ITER DOCUMENTATION SERIES No. 21

INIS-mf--12895

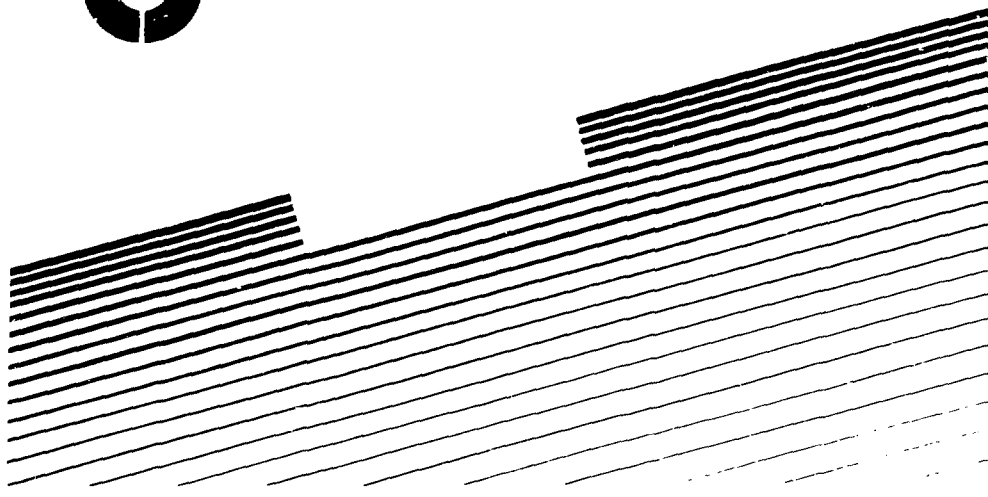

ITER PHYSICS

INTERNATIONAL ATOMIC ENERGY AGENCY, VIENNA, 1991

ITER PHYSICS

ITER DOCUMENTATION SERIES No. 21

ITER PHYSICS

D.E. POST, K. BORRASS, J.D. CALLEN, S.A. COHEN,
J.G. CORDEY, F. ENGELMANN, N. FUJISAWA,
M.F.A. HARRISON, J.T. HOGAN, H.J. HOPMAN,
Y. IGITKHANOV, O. KARDAUN, S.M. KAYE,
S. KRASHENINNIKOV, A. KUKUSHKIN, V. MUKHOVATOV,
W.M. NEVINS, A. NOCENTINI, G.W. PACHER,
H.D. PACHER, V.V. PARAIL, L.D. PEARLSTEIN,
L.J. PERKINS, S. PUTVINSKIJ, K. RIEDEL, D.J. SIGMAR,
M. SUGIHARA, D.W. SWAIN, T. TAKIZUKA, K. TANI,
T. TSUNEMATSU, N.A. UCKAN, J.G. WEGROWE,
J. WESLEY, S. YAMAMOTO, R. YOSHINO, K. YOUNG,
P.N. YUSHMANOV,
AND INTERNATIONAL CONTRIBUTORS

INTERNATIONAL ATOMIC ENERGY AGENCY
VIENNA, 1991

ITER PHYSICS
IAEA, VIENNA, 1991
IAEA/ITER/DS/21

Printed by the IAEA in Austria
May 1991

FOREWORD

Development of nuclear fusion as a practical energy source could provide great benefits for all mankind. This fact has been widely recognized and fusion research has enjoyed a level of international co-operation unusual in other scientific areas. From its inception, the International Atomic Energy Agency has actively promoted the international exchange of fusion information.

In this context, the IAEA responded in 1986 to calls for expansion of international co-operation in fusion energy development expressed at summit meetings of governmental leaders. At the invitation of the Director General there was a series of meetings in Vienna during 1987, at which representatives of the world's four major fusion programmes developed a detailed proposal for a joint venture called International Thermonuclear Experimental reactor Conceptual Design Activities. The Director General then invited each interested party to co-operate in ITER activities in accordance with the Terms of Reference that had been worked out. All four Parties accepted this invitation.

Joint work on ITER Conceptual Design Activities, under the auspices of the IAEA, began in April 1988 and was completed in December 1990. This work included two phases, the Definition Phase and the Design Phase. In 1988 the first phase produced a concept with a consistent set of technical characteristics and preliminary plans for co-ordinated R&D in support of ITER. The Design Phase produced a conceptual design, cost estimate, a description of site requirements, a preliminary construction schedule, and an ITER R&D plan. All information produced within the Conceptual Design Activities is being made available for all ITER Parties to use in reaching decisions about continuation of ITER into more extensive Engineering Design Activities. If carried out to fruition, the Engineering Design Activities would produce, by mid-nineties, sufficient design, R&D, and project information to allow a decision on the construction of ITER.

As part its support of ITER activities, the IAEA is pleased to publish the documents that summarize the results of the joint work.

CONTENTS

1.0 OVERVIEW 15
1.1 PHYSICS GOALS 15
1.2 DESIGN PHILOSOPHY 15
1.3 SUMMARY OF PHYSICS DESIGN GUIDELINES 17
1.4 SUMMARY OF PHYSICS ISSUES 17
1.4.1 Plasma Performance 19
1.4.2 Design Related Physics Issues 22
1.4.2.1 *Power and particle control* 23
1.4.2.2 *Disruptions* 25
1.4.2.3 *Auxiliary systems* 26
1.5 PHYSICS R&D FOR ITER 28
1.6 PHYSICS STATUS 29
REFERENCES (§1.0) 30

2.0 PLASMA PERFORMANCE 31
2.1 CONFINEMENT 31
2.1.1 Introduction 31
2.1.2 Confinement Requirements 32
2.1.3 Energy Confinement Database 32
2.1.3.1 *L-Mode* 32
2.1.3.2 *H-Mode* 38
2.1.3.3 *Additional confinement regimes* 43
2.1.4 Particle Confinement 45
2.1.4.1 *Parameter dependence of* τ_p *in OH and L-mode discharges* 45
2.1.4.2 *Local transport coefficients in ohmic and L-mode plasmas* 46
2.1.4.3 *Electron particle transport in improved confinement mode* 46
2.2.4.4 *Ion transport* 47
2.1.5 Momentum Confinement Database 47
2.1.6 Theory and Modeling 48
2.1.6.1 *Anomalous transport theory and modeling* 48
2.1.6.2 *Equivalence considerations* 50
References (§2.1) 51
2.2 MHD STABILITY 53
2.2.1 Introduction 53
2.2.2 Database 55
2.2.2.1 *Shape effects on beta limits* 55
2.2.2.2 *Profile effects on beta limits* 58
2.2.2.3 *Operation region and margin* 61

2.2.2.4 *The m = 1 phenomena* 65
2.2.2.5 *Non-ideal effects* 68
2.2.3 Predictions and Recommendations for ITER 68
2.2.3.1 *General conclusions* 68
2.2.3.2 *Shape effects* 69
2.2.3.3 *Profile effects* 69
2.2.3.4 *Summary and guidelines* 70
2.2.4 Major Issues Emphasized in the Future R&D Activity ... 70
2.2.4.1 *Issues* 70
2.2.4.2 *Future R&D tasks* 71
References (§2.2) 72
2.3 DENSITY LIMITS 74
2.3.1 Introduction 74
2.3.2 L-mode Density Limits 74
2.3.2.1 *General picture* 74
2.3.2.2 *Experimental studies* 75
2.3.2.3 *Modeling studies* 78
2.3.3 H-mode Density Limits 82
2.3.4 Projections to ITER 83
2.3.5 Summary and Conclusions 84
References (§2.3) 85
2.4 ALPHA PARTICLE PHYSICS 86
2.4.1 Introduction 86
2.4.2 Ripple Losses 87
2.4.2.1 *Qualitative analysis* 87
2.4.2.2 *Description of numerical codes* 90
2.4.2.3 *Numerical results for an ideal first wall* 90
2.4.2.4 *Heat load at limiters and port edges* 94
2.4.3 Collective Effects 94
2.4.3.1 *Toroidal Alfvén eigenmodes (TAE's)* 95
2.4.3.2 *Ballooning modes* 95
2.4.3.3 *Experimental results in relation to Alfvén and ballooning modes* 97
2.4.3.4 *Alpha particle driven fishbone oscillations* 99
2.4.3.5 *Concluding remarks* 99
2.4.4 Control of Fusion Power Production Rate (Burn Control). 100
2.4.4.1 *Introduction* 100
2.4.4.2 *Operating point (equilibrium) control* 100
2.4.4.3 *Fusion power stability control* 102
2.4.4.4 *Rapid termination of fusion power production* ... 105
References (§2.4) 106

3.0 POWER AND PARTICLE CONTROL 109
3.1 INTRODUCTION 109
3.2 EXPERIMENTAL DATABASE 110
3.2.1 General Characteristics of SOL and Divertor Plasmas 110

3.2.2 Upstream SOL Plasma Density and Temperature Characteristics 111
3.2.3 Effect of Additional Heating on SOL Plasma Density 111
3.2.4 Empirical Scaling for SOL Plasma Characteristics in Divertor Discharge 112
3.2.5 Transport Processes and Coefficients 112
3.2.6 Comparison of SOL Parameters for SN and DN Divertor 114
3.2.7 Characteristics of Heat and Particle Loads on Divertor ... 115
3.2.7.1 *Power load half-width* 115
3.2.7.2 *Asymmetry of heat and particle fluxes onto the divertor* 115
3.2.7.3 *Heat loads characteristics of DN divertor* 116
3.2.7.4 *Characteristic of ELMs* 118
3.2.8 Impurity Transport, Accumulation, and the Associated Radiation Loss 119
3.2.8.1 *Level of Z_{eff}: graphite divertor/ first wall components* 119
3.2.8.2 *Level of Z_{eff}: beryllium, boronized, and metal divertor/first wall components* 119
3.2.8.3 *Impurity transport and the associated radiation* . 120
3.2.8.4 *Edge radiation cooling of the edge* 120
3.2.9 Helium Transport and Exhaust 121
3.2.9.1 *Helium transport in the core plasma* 121
3.2.9.2 *Helium exhaust requirements* 122
3.2.9.3 *Tritium throughput* 122
3.3 STATUS OF MODEL VALIDATION 122
3.3.1 Models of the Edge Plasma Region 122
3.3.2 Scrape-off-Layer Parameters 123
3.4 MODEL PREDICTIONS OF DIVERTOR HEAT LOADS 125
3.4.1 Results of Model Predictions for ITER Divertor Plates .. 126
3.4.2 Effect of In/Out and Up/Down Asymmetry on Divertor Heat Load Specification 135
3.4.3 Physics Safety and Peaking Factor to be Applied to the Power Load 137
3.4.4 Improvement of Divertor Heat Loads by Ergodization and Sweeping 139
3.4.5 Peaking Factors for Plate Temperature and Sheath Potential 140
3.5 OPTIMIZATION OF DIVERTOR GEOMETRY 141
3.5.1 Divertor Depth 142
3.5.2 Plate Inclination 142
3.5.3 Plate Shape 143
3.6 COMPARISON OF SINGLE- AND DOUBLE-NULL DIVERTOR PERFORMANCE OF ITER 144
3.7 IMPURITY TRANSPORT AND RADIATED POWER 146
3.7.1 Divertor and SOL Regions 146
3.7.2 Core and Edge Regions 148

3.8 DIVERTOR PLATE EROSION AND REDEPOSITION 149
3.8.1 Low-Z Materials 152
3.8.2 High-Z Materials 155
3.9 HELIUM EXHAUST 156
3.9.1 Helium Transport in the Bulk Plasma 156
3.9.2 Helium Transport in the Edge Plasma 157
3.9.3 Helium Transport in the Pump Duct 158
3.10 FIRST-WALL OPERATING CONDITIONS 159
3.10.1 Heat Loads on the First Wall 159
3.10.2 Erosion 160
3.10.3 Plasma Contamination 160
3.10.4 Effects on the Divertor 160
3.11 STARTUP SCENARIO AND STARTUP LIMITER CONSIDERATIONS 161
3.12 CONDITIONING 163
3.12.1 Baking 163
3.12.2 Conditioning Techniques 163
3.13 PASSIVE SHUT-DOWN 164
3.14 PHYSICS R&D REQUIREMENTS 166
REFERENCES (§3.0) 167

4.0 DISRUPTIONS 171
4.1 CHARACTERISTICS OF TYPICAL DISRUPTIONS 171
4.1.1 Classification of Disruptions 171
4.1.2 Evolution of Disruptions 171
4.1.3 Disruption Frequency 172
4.1.4 Characterization of Disruptions for Representative ITER Scenario 173
4.2 CHARACTERISTICS OF VERTICAL DISPLACEMENT EVENTS 173
4.3 SPECIFIC ASPECTS OF DISRUPTIONS 178
4.3.1 Energy Deposition During Thermal Quench 178
4.3.2 Energy Deposition During Current Quench 178
4.3.3 Runaway Electrons 179
4.4 CONTROL AND AVOIDANCE OF DISRUPTIONS 181
4.4.1 Active Control Method 181
4.4.2 Stable Operational Range 182
4.5 REQUIREMENTS IN R&D 183
REFERENCES (§4.0) 184

5.0 CURRENT DRIVE AND HEATING 187
5.1 INTRODUCTION 187
5.2 IONIZATION, PREHEATING, AND CURRENT INITIATION 188
5.2.1 Experimental Results 189
5.2.2 EC Startup Theory: Status and Predictions for ITER 189
5.3 LOWER HYBRID PHYSICS 190

5.3.1 Physics Issues Relevant for High-β Operation 191
5.3.1.1 *Penetration limit due to wave damping* 191
5.3.1.2 *Penetration limit due to propagation effects in toroidal geometry* 192
5.3.1.3 *Spectral broadening issue* 193
5.3.1.4 *Consequences of restricted penetration: restricted total power and current* 193
5.3.1.5 *Current diffusion* 194
5.3.2 Selection of Frequency, Interaction with α-Particles 194
5.3.2.1 *Lowest frequency for avoiding interaction with α-particles* 195
5.3.2.2 *Coupling density* 195
5.3.2.3 *Selection of the frequency for the LHW system: Summary* 196
5.3.3 Current Drive Efficiency 196
5.3.4 Current Ramp-up Assist with LHW 197
5.4 NEUTRAL BEAM PHYSICS 198
5.4.1 Introduction 198
5.4.2 Status of Database 198
5.4.2.1 *Neutral beam current drive* 198
5.4.2.2 *Alfvén wave instability and beam slowing down* 199
5.4.2.3 *Neutral beam stopping cross-section* 200
5.4.2.4 *Plasma rotation* 201
5.4.3 Design Issues 202
5.4.3.1 *Current drive efficiency* 202
5.4.3.2 *Beam energy, beam aiming and beam penetration* 202
5.4.3.3 *Profile controllability of beam driven current* ... 205
5.4.3.4 *Beam shinethrough* 205
5.4.3.5 *Consistency with lower hybrid waves* 205
5.5 ION CYCLOTRON PHYSICS 206
5.5.1 Theory and Modeling of Fast Wave Current Drive 206
5.5.1.1 *Low frequency fast wave current drive scenarios* 206
5.5.1.2 *Intermediate frequency fast wave current drive scenarios* 207
5.5.1.3 *High frequency fast wave current drive scenarios* 207
5.5.2 Experimental Database 208
5.5.3 Ion Cyclotron Heating 208
5.5.3.1 *Deuterium minority heating* 208
5.5.3.2 *He^3 and other minority heating schemes* 209
5.5.3.3 *Heating and current drive at high frequency* 209
5.6 BOOTSTRAP CURRENT 210
5.6.1 Status of Database 210
5.6.2 Bootstrap Current in ITER 211

5.7 REFERENCE OPERATING SCENARIO 213
5.7.1 Current Profile Control 214
5.7.1.1 *Bulk current profile control* 214
5.7.1.2 *Detailed current profile control* 216
5.7.2 Start-up Assist 216
5.7.3 Noninductive Current Ramp-up and/or Current Ramp-up Assist 216
5.7.4 Plasma Heating and Burn Control 217
5.8 ALTERNATE OPERATING SCENARIO 217
5.8.1 Fast Wave Current Drive 218
5.8.1.1 *Scenarios with high bootstrap current* 218
5.8.1.2 *Long-pulse ignition and hybrid scenarios* 219
5.8.2 Fast Wave Heating and Burn Control 220
5.9 CONTROL OF MAJOR DISRUPTION BY EC CURRENT DRIVE 220
REFERENCES (§5.0) 221

6.0 AXISYMMETRIC MAGNETICS 229
6.1 INTRODUCTION 229
6.1.1 Axisymmetric Magnetics Design Issues 229
6.1.2 Topics and Organization 230
6.1.3 Relation to Other Design Elements 230
6.2 AXISYMMETRIC MAGNETICS REQUIREMENTS 231
6.2.1 Basic Requirements 231
6.2.2 Equilibrium Analysis Method and Validation 231
6.2.3 A1 Operational Scenario and Plasma Profile Parameters . 232
6.2.4 Plasma Volt-second Balance and Resistive Volt-second Requirements 234
6.3 PLASMA EQUILIBRIUM 237
6.3.1 Reference Plasma Configuration and PF Coil Locations . 237
6.3.2 PF System Optimization and Performance Evaluation 239
6.3.3 Alternate Plasma Configurations 241
6.3.4 Plasma Operations Cycle 242
6.3.5 Equilibrium Control 244
6.4 AXISYMMETRIC STABILITY AND DYNAMIC EVOLUTION 246
6.4.1 Axisymmetric Stability 246
6.4.2 Plasma Dynamics 249
6.5 SUMMARY AND FUTURE NEEDS 251
REFERENCES (§6.0) 252

7.0 DIAGNOSTICS 255
7.1 INTRODUCTION 255
7.2 SUMMARY 255
7.3 DIAGNOSTICS ISSUES 261
7.4 DIAGNOSTICS R&D PLAN 262
7.4.1 Examples of Diagnostics R&D Needs 262
REFERENCES (§7.0) 264

8.0 FUELLING 265
8.1 FUELLING REQUIREMENTS 265
8.1.1 Required Particle Fluxes 265
8.1.2 Control of Density and Density Profile 265
8.1.3 Fueling Requirements for Burn Control 266
8.1.4 Restriction on Density profile Choice 266
8.1.4.1 *Edge density* 266
8.1.4.2 *Beta limit* 266
8.1.4.3 *Damage to the first wall* 267
8.1.5 DT Mix Requirements and Tritium Inventory 267
8.1.6 Wall Conditioning 267
8.2 RELATION OF PARTICLE TRANSPORT TO FUELLING 267
8.2.1 Particle Confinement Time 267
8.2.2 Diffusivity and Inward Pinch 268
8.3 FUELLING METHODS 269
8.3.1 Gas Puffing 269
8.3.2 Pellet Injection and Pellet Ablation Physics 269
8.3.3 Alternative Methods 270
8.3.3.1 *NB injection* 270
8.3.3.2 *Ripple fuelling* 270
8.3.3.3 *Compact toroids* 271
8.4 MODES OF OPERATION 271
8.4.1 Fuelling During Burn 271
8.4.1.1 *Fuelling only by gas puffing* 271
8.4.1.2 *Fuelling only by pellet injection* 271
8.4.1.3 *Combination of pellet injection and gas puffing* 272
8.4.2 Compatibility of Pellet Fuelling with Lower Hybrid Current Drive 272
8.4.3 Density Ramp-up to Ignition 272
8.5 CONTROL OF DENSITY AND DT MIX 273
8.6 PHYSICS R&D NEEDS 273
8.6.1 Particle Transport 273
8.6.2 Pellet Ablation Physics 273
8.6.3 Innovative Fuelling Methods 274
REFERENCES (§8.0) 274

9.0 TOKAMAK OPERATIONS 277
9.1 OPERATIONAL PLANS 277
9.1.1 Zero-Activation Phase 277
9.1.2 Low-Activation Phase 277
9.1.3 High-Activation Phase 278
9.2 OPERATIONAL MODES 279
9.2.1 Major Characteristics of Operating Points: Inductive Operation 282
9.2.2 Major Characteristics of Operating Points: Long-Pulse Operation 283
9.2.3 Divertor Sweeping 285

9.3 OPERATIONAL SCENARIOS 285
9.3.1 Reference Ignition Scenario 285
9.3.2 Reference Long-Pulse Scenario 288
9.3.3 Nominal Steady-State 289
9.3.4 Variants Based on Noninductive Ramp-up Assist 292
9.3.5 Outboard Start-up 292
REFERENCES (§9.0) 293

10.0 PHYSICS R&D 295
10.1 INTRODUCTION 295
10.2 PROGRAMME 1989-1990 295
10.3 PROGRAMME 1991-1995 296
10.3.1 Approach 296
10.3.2 Programme 1991-1992 296
10.3.3 Diagnostics 297
REFERENCES (§10.0) 297

11.0 ACKNOWLEDGMENTS 299

1.0. OVERVIEW

The physics basis of ITER has been developed from an assessment of present tokamak physics and credible extrapolations of that physics. This assessment has been carried out with the assistance of the international fusion community, including participation by scientists from all of the major toroidal experiments in the world and a large portion of the theoretical plasma physics community. The basis consists of guidelines for energy confinement, operational limits, power and particle control, disruptions, current drive and heating, alpha particle physics, and plasma control. The development and implementation of the guidelines has been an integrated physics-engineering activity. In addition, a pre-conceptual design for plasma diagnostics for ITER has been developed and a plan for the operational program has been defined. In the cases for which the physics issues could not be fully resolved, a physics R&D program has been developed to provide the input required to complete the physics basis for ITER.

1.1 PHYSICS GOALS

The major goal of the physics program of ITER is to establish the physics basis for the design of a tokamak-based Demonstration Power Plant (DEMO). This means that ITER must study long pulse (200 s to steady-state), ignited plasmas [1.1]. A 200 s pulse is longer than all of the relevant plasma physics time scales except the time required to establish an equilibrium current profile (about 1000–2000 s). The DEMO plasma physics issues include:

- Energy confinement
- Operational limits and disruptions
- Power and particle exhaust
- Plasma shaping and control (including burn control)
- Plasma heating (including heating by auxiliary systems and alpha particles)
- Extension of the pulse length and profile control by non-inductive current drive

ITER will address all of these issues.

1.2 DESIGN PHILOSOPHY

To achieve the required level of plasma performance, the ITER plasma must have adequate energy confinement, MHD stability, power and particle exhaust, disruption control, auxiliary heating and current drive, plasma control, and alpha particle heating. The operational program must include a sufficiently broad range of plasma operating scenarios for flexibility and adequate plasma diagnostics to obtain both the required physics information during physics phase operation and integrated neutron wall loadings of ~1 MW•a/m^2 to carry out testing during the technology phase.

The present tokamak database has been assessed by the ITER team and the characteristics for the ITER plasma have been developed (Table 1-1). These general

requirements were derived by consideration of the data from the major toroidal confinement experiments in the international fusion program (including Alcator C, ASDEX, ATF, DIII, DIII-D, DITE, FT, JET, JFT-2M, JT-60, PBX/M, PDX, T-10, TEXTOR, TFR, TFTR, TORE-SUPRA, W-VIIA and -VIIAS, etc.), from general theoretical studies of the important physics issues, and from specific assessments of the physics issues by the ITER team.

TABLE 1-1. GENERAL CHARACTERISTICS OF ITER

Plasma current	$I \sim 20$ MA
Aspect ratio	$A = R/a \sim 2.5$–4.0
Plasma beta	$\beta \sim (2.5–3) \times I/aB$
Safety factor (at 95% flux)	$q_\psi(95\%) \geq 3$
Elongation (at 95% flux)	$\kappa_\psi(95\%) \sim 2$
Impurity control	Poloidal divertor
Auxiliary heating	NB, IC, EC, or LH
Current drive	NB, LH, and possibly IC plus bootstrap current
Disruption frequency	As low as possible

NB: neutral beam, IC: ion cyclotron, EC: electron cyclotron, LH: lower hybrid

A plasma current of about 20 MA has been judged to be needed for adequate energy confinement with H-mode operation. To develop this requirement, H-mode and L-mode data from the large tokamak experiments have been assembled and assessed (§2.1).

An aspect ratio range of 2.5–3.5 was chosen, because nearly all present tokamak data have been obtained in that range. The MHD stability requirement of $\beta \leq (2.5–3) \times (I/aB)$ is consistent with the experimental data and detailed theoretical/computational analysis (§2.2). The requirement for $q_\psi(95\%) \geq 3$ was set to ensure MHD stability with a minimum disruption frequency and to maintain favorable energy confinement. Plasma elongations of 2 are consistent with control of the plasma with respect to vertical stability.

The frequency of disruptions in ITER must be low enough so that lifetime of the plasma facing components is satisfactory (§3.0 and §4.0). The present concept allows for frequent replacement of the internal hardware during the physics phase operation when the disruption frequency is expected to be high. During the technology phase operation, the operating point selected will have to be sufficiently far from the operational limits so that disruptions and consequently replacement of internal components will be infrequent.

The best available method for power and particle exhaust appears to be the poloidal divertors that have been employed on ASDEX, DIII-D, JET, JFT-2M, JT-60, PBX/M, PDX,.... It is necessary to operate the poloidal divertor in ITER in a "high-recycling" mode to form a cold, dense plasma at the divertor plate to minimize erosion and impurity production and maximize the gas pressure, thereby decreasing the pumping speed required to exhaust the helium ash (§3.0).

The database obtained from present tokamak experiments indicate that the ITER plasma can be successfully heated to ignition with energetic neutral beams (NB), ion cyclotron (IC) waves, electron cyclotron (EC) waves, or lower hybrid (LH) waves (§5.0). The feasibility of current drive with NB and LH has been experimentally demonstrated. The IC waves are also a candidate for current drive but still require an experimental demonstration. Experiments indicate that a substantial fraction of the current in ITER (~30% or more) can be carried by the bootstrap current.

A full set of plasma diagnostics is needed for the physics phase (§7.0) [1.2]. A reduced set will be used during the technology phase to free up port space for technology test modules. A six year operational program is planned for physics studies. The program includes initial activation-free studies with hydrogen, low-activation heating and current drive studies with deuterium and He, and studies of long-pulse, ignited, and steady-state driven operation with deuterium and tritium. The physics phase will be followed by a technology phase of ~10 years dedicated to engineering tests.

Operational flexibility has been strongly emphasized in the design to provide margin for uncertainties in the physics guidelines and to ensure that there will be a choice of operating scenarios [1.3]. This includes the flexibility to operate with a range of plasma currents and incorporation of flexibility in the heating, current drive, fuelling, and power exhaust systems.

1.3 SUMMARY OF PHYSICS DESIGN GUIDELINES

The physics guidelines for the ITER design are based on reasonable extrapolations of the tokamak physics database as assessed during the ITER Conceptual Design Activities (1988–90) [1.4,5]. The physics guidelines that have been adopted for the ITER design are summarized in Table 1-2.

1.4 SUMMARY OF PHYSICS ISSUES

Although the physics issues are closely linked, it is useful to divide them into two groups: those that are related to achieving the level of plasma performance necessary to meet the goals of the experiment and those that are a consequence of the specific ITER design. The performance related guidelines define the machine concept and parameters. They include the energy confinement requirements necessary to achieve adequate plasma performance, determined primarily by the plasma current and aspect ratio. They also include the requirements to obtain the MHD stability needed to minimize the number of disruptions, determined primarily by the edge safety factor, beta limit, and density limit. These guidelines, together with the engineering considerations and the goals of the experiment, determine the overall machine configuration and size.

The fusion power, the divertor heat loads, the disruption mechanical loads, etc. are then determined by the configuration and size of the machine. These specific aspects of the design lead to guidelines for particle and power exhaust, disruptions, and for the auxiliary systems such as current drive and heating, plasma shaping and control, fuelling, and plasma diagnostics.

TABLE 1-2. SUMMARY OF ITER PHYSICS GUIDELINES

Units are mks, MA, MW, with $n_{20} = \langle n_e/10^{20}\ m^{-3}\rangle$ = volume-average electron density and $T_{10} = \langle T/10\ keV\rangle$ = density-weighted average temperature ($T_e \approx T_i \approx T$). Nominal profiles: n, $T \sim (1 - r^2/a^2)^{\alpha_{n,T}}$; with $\alpha_n \approx 0.5$, $\alpha_T \approx 1.0$. Where appropriate, one of two rules (x | y) may apply, referring to ("baseline performance" | "extended performance").

- Energy confinement: $I \geq 22$ MA with $A = R/a \approx 3$ for ignited operation in H-mode with $\tau_E(\text{required}) \leq \tau_E(\text{H-mode}) \sim 2 \times \tau_E^{ITER89\text{-}P}(\text{L-mode})$
- ITER (89) L-mode confinement scalings: power (P) law and off-set linear (OL)

  $\tau_E^{ITER89\text{-}P} = 0.048\, I^{0.85} R^{1.2} a^{0.3} \bar{n}_{20}^{0.1} B^{0.2} (A_i \kappa_x/P)^{0.5}$

  $\tau_E^{ITER89\text{-}OL} = 0.064\, I^{0.8} R^{1.6} a^{0.6} \bar{n}_{20}^{0.6} B^{0.35} \kappa_x^{0.5} A_i^{0.2}/P$
  $+ 0.04\, I^{0.5} R^{0.3} a^{0.8} \kappa_x^{0.6} A_i^{0.5}$.

  where $A_i = 2.5$ (isotopic mass for DT), $\kappa_x = \kappa$(at X-point), $\bar{n}$ = line-averaged density, $P(MW) = P_\alpha + P_{OH} + P_{aux} - P_{rad}$ = net heating power.
- ITER (90) H-mode confinement scaling:

  Typically, $\tau_E^{H\text{-}mode} \approx 2 \times \tau_E^{ITER89\text{-}P}$(L-mode)

  or τ_E(ELMy H-mode) $\sim 0.75 \times \tau_E$(ELM free H-mode)

  with

  $\tau_E^{ITER90\text{-}H}$(ELM-free) $= 0.064\, I^{0.87} R^{1.82} a^{0.12} \bar{n}_{20}^{0.09} B^{0.15} \kappa_x^{0.35} A_i^{0.5} P^{-0.5}$
- Beta limit: $\beta_{max}(\%) = gI/aB$

$g \leq 2.5$ | 3.0	for ignition studies
$g \leq 3.0$ | 3.3	for steady-state operation (current profile control is assumed)

- Safety factor: $q_\psi(95\%) \approx q_* f(\varepsilon)$

$q_\psi(95\%) \geq 3.0$ | 2.1	for $\kappa = b/a < 2$
$q_\psi(95\%) \geq 3.0$ | 3.0	for $\kappa = b/a \sim 2$ to 2.5

  where $q_* \approx (5a^2B/RI)[1 + \kappa^2(1 + 2\delta^2 - 1.2\delta^3)]/2$ is the cylindrical equivalent q and $f(\varepsilon) \approx (1.17 - 0.65\varepsilon)/(1 - \varepsilon^2)^2$ is the geometry factor ($\varepsilon = a/R$).
- Density limit:

  Imposes an upper limit on the plasma edge density. A tentative characterization:

  $n_{e,s20}^{crit} \propto C[q_\perp^{0.57} B^{0.31}/(q_\psi R)^{0.1}]$

  where $n_{e,s20}^{crit}$ (10^{20} m^{-3}) = critical density at the separatrix, $q_\perp$(MW/m^2) = mean heat flux across the separatrix, and $C \sim 0.5$ (depends on configuration).
- Power and particle control:

  Double null poloidal divertor with operational scenarios selected such that peak plate power loads ≤ 20 MW/m^2 and peak local $T_e^{div} \leq$ 10–20 eV.
- Disruption characteristics:

thermal quench time	0.1–1 ms (up to 3 ms infrequently)
current quench time	10 ms
runaway electron energy	up to 300 MeV

TABLE 1-2. (cont.)

- Z_{eff}: impurity and thermal alpha fractions ($f_j = n_j/n_e$)

$f_{DT} = 1 - 2f_{He} - 6f_C - 8f_O - 26f_{Fe}$	D+T fuel ions
$f_{He} = 0.1 \; / \; 0.05$	thermal alphas
$f_C = 0.009 + 0.006(0.7/\langle n_{20}\rangle)^{2.6}$	Carbon
$f_O = 0.001$	Oxygen
$f_{Fe} = 0.0005(0.7/\langle n_{20}\rangle)^{2.3}$	Iron

  $Z_{eff} = 1.6 \rightarrow 2.4$ for $\langle n_e\rangle = (1.4 \rightarrow 0.7) \times 10^{20}$ m^{-3}

- Toroidal field ripple: $\Delta B/B$ (outboard) $\leq 2\%$
  First wall peak heat load ≤ 0.5 MW/m^2
  A low ripple is needed in the center, and the ripple profile is important.

- Heating and current drive: CD efficiency (figure-of-merit) $\gamma = \langle n_{20}\rangle I_{CD} R/P_{CD}$
  Heating: $P_{aux} \sim 50$ MW (provided by CD system)
  Bootstrap: $I_{bs}/I \sim 15$–30%
  CD: NB: $E_{beam} \sim 1.3$ MeV; $\gamma_{NB} \sim 0.5$; $P_{beam} \sim 75$ MW
  LH: $f_{LH} \sim 5$ GHz, $P_{LH} \sim 50$ MW
  IC (alternative to NB): $f_{IC} \sim 15$-80 MHz; $\gamma_{IC} \sim 0.3$; $P_{IC} \sim 130$ MW
  Profile Control and plasma initiation: EC:
  $f_{EC} \sim 120$ GHz; $P_{EC} \sim 20$ MW

- Internal inductance and beta poloidal:

$0.55 \leq l_i(3) \leq 0.75$	all scenarios
$\beta_p \leq 0.75$	ignition studies
$\beta_p \leq 2.0$	long pulse/steady-state

  where $l_i(3) = (2V/R)\langle B_p^2\rangle/(\mu_o I)^2$

- Loop voltage/Volt-seconds/Pulse length:
  Loop voltage: calculated using neo-classical resistivity + bootstrap current
  Volt-second capability: sufficient to accomplish

Physics studies:	pure inductive (ignition)	~ 200 s ($l_i(3) = 0.75$)
	current drive ($Q > 5$)	steady-state
Technology testing:	hybrid (~0.8 MW/m^2)	> 1000 s

1.4.1 Plasma Performance

The performance-related physics guidelines, together with the engineering constraints, determine the size, configuration, and radial build of ITER. The first requirement is that ITER have sufficient energy confinement to achieve ignited plasma conditions. This means that ITER should be capable of achieving an $n_{DT}(0)T_i(0)\tau_E$ of about 8×10^{21} keV s/m^3, where $n_{DT}(0)$ is the central DT density, $T_i(0)$ is the central ion temperature and τ_E is the global confinement time. This translates into require-

ments for the minimum plasma current I, plasma size (R or a), and the aspect ratio (A = R/a). The second requirement is that ITER have sufficient MHD stability that the number of plasma disruptions can be kept to a minimum. This translates into requirements for the minimum MHD safety factor at the plasma edge, q_{edge}, and provision for operation sufficiently below the β limit. These MHD stability considerations set constraints on the plasma size, elongation, plasma current, and toroidal field. The major engineering constraints that contribute to the size are the thickness, d_{BS}, of the shielding needed to reduce the neutron heating of the superconducting coils to an acceptable level and the maximum magnetic field B_{Tmax} at the toroidal field coils consistent with the stress limits of the coils. Space for a central transformer capable of providing the inductive flux to drive the required current is also necessary.

The definition of $q_{cyl} = 5a^2B/RI$ and $B \propto 1/R$ can be used to illustrate how I, A, a, R, B_{Tmax}, d_{BS}, and q_{cyl} are related: $a = [IA^2q_{cyl}/5B_{Tmax} + d_{BS}]/(A - 1)$

Energy confinement: The confinement requirements for ITER are based on operation with the H-mode and other optimized confinement regimes (§2.1). An H-mode confinement database has been assembled for ITER using data from six machines: ASDEX, DIII-D, JET, JFT-2M, PBX/M, and PDX [1.7]. The H-mode scaling (see Table 1-2) developed from a preliminary analysis of these data predicts that the confinement time for ignited conditions and ELM-free operation in ITER will be ~ 5.9 s, corresponding to about 4.4 s when derated to allow for the level of ELM activity necessary to control impurities. [Note that ELM's reduce τ_E by about 25% so that τ_E(ELMy H-mode) ~ 0.75 × τ_E(ELM free H-mode).]. This predicted level of confinement (τ_E ~ 4.4 s) provides some margin with respect to the ~ 3 to 4 s needed for ignited and high-Q operation in ITER.

The initial confinement guidelines were based on using a multiplier of about 2 times the L-mode scaling for an H-mode scaling, since the L-mode data were more extensive and much better characterized than the H-mode data and $\tau_E^{H\text{-mode}}$ is generally close to a factor of $2 \times \tau_E^{L\text{-mode}}$ (§2.1). The ITER team assembled and assessed a database of L-mode data from the major tokamaks in the international fusion program. Analysis of the new database produced a new set of L-mode scalings (ITER89-P and ITER89-OL) [1.8] that predict an L-mode energy confinement time for the reference ITER ignition parameters of about 1.9–2 s.

Detailed analysis of the data has indicated that the data and most of the different scalings could be represented fairly well by an expression of the form:

$$\tau_E^{fit} = \tau_E^{ITER89}\, f_S^{\alpha}\, f_q^{\beta}\, f_{BR}^{\gamma}$$

where $f_S = 0.32(R/a)^{0.75}R^{0.25}\kappa^{0.5} = 1 \pm 0.1$ (shape-size index), $f_q = q_{edge}/3.2 = 1 \pm 0.35$ (safety factor, q-index), $f_{BR} = B(\kappa/R)^{0.9}(0.32/f_S)^{0.4} = 1 \pm 0.2$ (field-size index) with $|\alpha| \leq \sim 0.3$, $|\beta| \leq \sim 0.2$, and $|\gamma| \leq \sim 0.4$. Particular scalings, such as Goldston and Kaye-Big, can be reproduced by the choice of appropriate values of α, β, and γ. A major cause of the uncertainty is that the factors f_S and f_{BR} are close to 1 for all of the tokamaks in the database so that the data are collinear in f_S and f_{BR}. The other uncertainties are largely due to differences in the way τ_E scales with q and n for the different tokamaks in the database. For ITER, f_{BR} is about 1 but f_S is about 1.6, leading to some uncertainty in the scaling for ITER with respect to f_S. This uncertainty has been reduced this year with additional L-mode data with f_S ~ 1.4 to 2

from JT-60 and TFTR, which tend to support an upper limit of $|\alpha|$ of ~0.2, roughly consistent with the ITER89-P scaling. However, additional data with f_S and $f_{BR} \neq 1$ are needed to reduce the uncertainties.

This empirical approach to the development of confinement requirements is being supplemented by the research being done in the international fusion program to develop scalings based on physically meaningful parameters and to identify the basic physics mechanisms responsible for tokamak transport by comparing theoretical models with profile data and fluctuation measurements.

Given the uncertainties in extrapolating the confinement for ITER, provision of operational flexibility to maximize the confinement has been a high priority for the design. Energy confinement can be improved by optimization of the plasma, current, and heating profiles. Alpha particle, high-energy NB, and IC wave heating will provide highly peaked central heating profiles. The NB, LH, and EC current drive systems would allow partial control of the current profile, which will, among other effects, keep the q = 1 surface of the plasma from becoming too large. Pellet fuelling will also allow some control of the density profile. In addition, ITER has the potential of operating with 25 MA (full inductive ramp-up) and 28 MA (with LH assist) for a burn time of about 50 s, albeit at lower q_{edge}.

Operational limits: The second set of major physics constraints for ITER derive from the requirement that the number of plasma disruptions in ITER be minimized to the extent possible. This means that the operating point must be sufficiently far from the MHD operational limits for β, q_{edge}, and the plasma density.

Based on an assessment of the MHD stability achieved in present experiments, and extensive theoretical studies, a guideline of the form $\beta = gI/aB$ was chosen for computing the maximum beta for ITER (§2.2). Based on experimental results and theoretical calculations, the guideline for g has been chosen conservatively to be 2.5 for inductively driven operation and 3 for operation for which the current profile can be controlled by noninductive current drive. The experimentally observed beta limits are in close agreement with those predicted by ideal MHD theory. DIII-D has achieved betas of 11% transiently and 8% in steady state, corresponding to g values of 3.5 and 2.8 respectively. The data from DIII-D and PBX/M are generally consistent with a maximum transient beta at values of g ~ 3.5, but long pulse stable operation appears to require a slightly lower g. Profile effects are important and recent experiments on DIII-D and analysis of candidate ITER plasmas indicate that g of 4 to 5 can be obtained with edge q higher than 4 or 5 and appropriately broad current profiles.

Experimental studies on DIII-D, PBX/M, and other tokamaks indicate that plasma elongations of ~ 2 can be formed and controlled. The stability and MHD behavior of these plasmas can be predicted very well using present computational models. Since $q_{edge} \propto a^2B(1 + \kappa^2)/RI$, elongating the plasma is useful for increasing the plasma current to increase τ_E and β-limit for a fixed q_{edge}, magnetic field, major and minor radii.

The minimum value for q_{edge} has set at 3 due to both MHD stability and for energy confinement considerations. As q_{edge} decreases below 3, the frequency of disruptions increases and the operational window narrows. This is partially due to the reduced shear between the edge and the q = 1 surface and to the increase in the radius of the q = 1 surface. In addition, the dependence of τ_E on plasma current tends to saturate for $q_{edge} < 3$. Recent analysis of DIII-D has indicated that the saturation of τ_E

with I for $q \leq 3$ is due to poor beam penetration and sawtooth oscillations since I and n_e are correlated and the sawtooth inversion radius increases as q is reduced. Centrally peaked alpha heating and control of the m = 1 activity may therefore offer margin in the minimally acceptable q_{edge}, although the reduced shear as q_{edge} decreases reduces the stability margin for highly peaked pressure profiles.

ITER operational scenarios call for a volume averaged electron density of 7×10^{19} m^{-3} up to 1.5×10^{20} m^{-3} (§2.3). The experimental evidence indicates that the density limit observed in present experiments is due to a limit in the edge density. Most of the data supports the picture that, in the absence of sufficient heating power, densities at the edge above a critical value lead to rapid cooling of the edge plasma and shrinkage of the current profile, followed by a disruption. The usual empirical scalings, such as those of Hugill or Greenwald, are not consistent with the experimental scaling studies with respect to q, B and P_{input}, and do not reflect the dependence of the density limit on the edge density. The ITER group has thus developed and calibrated a model for the power balance in the edge which does reproduce the observed scaling in the experiments. Extrapolation of the model to ITER conditions indicates that operation of ITER will be close to the density limit, so that model development and validation is an important physics R&D task to improve the predictive capability.

Alpha particle physics: Efficient alpha particle heating will be necessary to achieve ignition with 22 MA (§2.4). The main issues related to alpha particle heating include loss of alphas due to ripple in the toroidal field and to MHD activity, collective effects due to the fast ion population, and control of the plasma burn. Detailed calculations indicate that the ripple losses are in the range of 1-to-3%. Although not a serious effect for plasma heating, these losses can lead to large localized peak heat loads on the first wall. The calculations indicate that the peak heat loads will be acceptable ($\leq$0.5 MW/m^2) provided the first wall tiles have been properly designed.

Experiments and theoretical analyses have been ongoing to assess the potential impact of possible collective effects due to the fast ion population in ITER, such as destabilization of Alfvén waves and MHD modes and the consequences resulting from such instabilities. Initial studies of the toroidal Alfvén eigenmode (TAE mode) suggested that it would be stable for the parameters of interest to ITER [§2.4]. However, recent studies indicate that, if the β_α profile is sufficiently peaked, the mode may be unstable, so that further studies are required, including fast ion simulation experiments and eventual DT operation in JET and TFTR.

Stable operation of ITER will require control of the level of alpha heating. The present strategy calls for operation of the plasma in a driven mode at conditions just short of ignition. With a Q (fusion power/auxiliary heating power) of ~ 40, this can be accomplished with ~ 30 MW of heating power.

1.4.2 Design-Related Physics Issues

The physics requirements in Tables 1-1 and 1-2, together with engineering constraints lead to the design parameters for ITER (Table 1-3). The high levels of heating power (200-to-300 MW), coupled with short power scrape-off widths of ~0.5 cm, lead to high peak heat fluxes on the divertor plates. These in turn can lead to high levels of sputtering erosion of the divertor plates and subsequent impurity contamination of the bulk plasma unless the edge plasma conditions are carefully controlled.

TABLE 1-3. DESIGN PARAMETERS OF ITER

R	6 m	P_{fusion}	1000 MW
a	2.15 m	P_{α}	200 MW (~ 4×10^{20} He atoms/s)
I	22 MA	$W_{thermal}$	600 MJ ($\beta \sim 4$ %, g ~ 2)
B	4.85 T	$W_{poloidal}$	600 MJ

Sustaining a fusion power of ~ 1000 MW requires the removal of approximately 4×10^{20} He atoms/s by the pumping system. The DT fuel converted to He "ash" plus the DT pumped away with the He "ash" must be replaced by the fuelling system.

The large plasma currents and stored thermal energy lead to strong electromagnetic forces on the tokamak structure from eddy currents induced during disruptions and to high peak heat fluxes on the plasma facing components during disruptions.

Approximately 50 MW of auxiliary heating is needed to heat the plasma to ignition. Depending on the density, approximately 100 MW of current drive power is needed to drive the part of the steady state plasma current of 15–20 MA not provided by the bootstrap effect.

To achieve the level of plasma performance potentially allowed by the performance guidelines, especially for long pulses, ITER must be designed to provide adequate power and particle control, to survive plasma disruptions, and to provide successful operation of the auxiliary systems for current drive and heating, plasma shaping and control, and fuelling. In addition, the diagnostics for the plasma must be adequate to provide the information necessary to control the plasma, to monitor the performance of the tokamak, and to do the measurements of the ITER plasma parameters necessary for the physics program.

1.4.2.1 Power and particle control

The ITER power and particle control system must remove about 200 MW of alpha heating power and about 120 MW of the auxiliary power provided for current drive (§3.0). This power exhaust must be accomplished a conditions that allow operating lifetimes on the order of a calendar year or more for the plasma facing components and do not lead to excessive plasma contamination. In addition, the He ash must be pumped with a reasonably sized pumping system.

The system is based on a double null poloidal divertor. The main advantages of a divertor are that a cool (~ 10–20 eV), dense (~ 4–6 $\times 10^{20}$ m^{-3}) plasma can be formed at the divertor plate due to intense local plasma recycling. The low divertor plasma temperature, T_{div}, minimizes the damage and erosion of the divertor plate and the production of impurities which might contaminate the plasma. The high particle flux and resulting high density leads to high gas pressures which minimize the size of the pumping system required for helium ash exhaust. This type of divertor operation has been verified on DIII, ASDEX and other divertor experiments. Graphite-based materials have been selected for the divertor plates and first wall tiles for the physics phase due to their refractory properties and wide operational experience in present tokamaks. The projections for the plasma performance of the ITER divertor have been

based on two dimensional computational models which include detailed treatments of the important atomic, molecular, and surface processes and which have been validated as much as possible by comparison with tokamak experimental data with limiters and divertors. However, the present database is insufficient to resolve many of the modelling uncertainties.

The models predict that low temperature (~ 10–20 eV) operation of the divertor should be possible for ignited operation in which the edge density is relatively high ($\geq 3 \times 10^{19}$ m^{-3}) and the total power incident on the divertor plates is ~100 MW; the other 100 MW is radiated to the wall as bremsstrahlung (~ 60 MW) and impurity line radiation (~ 40 MW, mostly from the plasma edge). In this case, the calculated net erosion rate of the graphite divertor plates is sufficiently low that the sputtering lifetime of the plates is longer than the physics phase, provided that the separatrix can be swept across the divertor plates sufficiently rapidly that the divertor plate surface temperature remains below about 1000°C.

This result is sensitive to the power scrape-off width. The best present estimates of this width are that it will be ~0.5 cm at the plasma midplane for ITER conditions. In the design, the effective area for power removal is increased by a factor of four by the expansion of the field lines near the divertor and by an additional factor of four by tilting the plate 15°. This results in a time-averaged peak power flux on the plate of ~8 MW/m^2 and a plasma temperature of ~10–20 eV at the divertor plate for ignited operation, including the penalty due to uncertainties in the edge transport, asymmetries in the power fluxes, and other effects; and the improvement due to separatrix sweeping at an adequately high frequency.

Technology phase operation will require extending the pulse length to at least 1000 s. This can be accomplished by lowering the plasma current sufficiently (to save volt seconds from the current ramp-up and reduce the loop voltage) by non-inductively driving part or all of the current not due to the bootstrap effect. Both the current drive power, P_{CD}, and the plasma temperature in the divertor, T_{div}, must be minimized simultaneously. Since $P_{CD} \propto n_e$ (n_e is the electron density at the separatrix at the plasma midplane) and $T_{div} \propto (P_\alpha + P_{CD})^2/n_e^3$, the high density necessary for acceptable divertor conditions is in contradiction to the low density needed for efficient current drive and acceptably low current drive powers. Furthermore, the power to the divertor is larger than for ignited operation due to the power required to drive the current. To resolve this dilemma, long pulse operating modes have been developed for which the density is sufficiently high that the divertor conditions are acceptable and sufficiently low that a large enough portion of current can be driven so that pulse lengths greater than 1000 s can be obtained.

Although steady state operation would have many advantages for the technology phase, it imposes the most demanding requirements since all of the current must be driven non-inductively except the bootstrap current. The additional current drive power and lower density lead to high peak heat fluxes and high plasma temperatures at the divertor plate. For such conditions, present modelling indicates that sputtering and radiation enhanced sublimation (such as observed in JET and other experiments) will lead to catastrophic carbon release. However, the reference specifications for the divertor conditions with steady state operation based on the present models might be too severe due to the uncertainties in the cross field plasma transport which determines the scrape-off width for the power, radiation losses due to impurities, the degree of

ergodization of the plasma edge, the potential for flatter density profiles, etc. However, it is clear that high edge densities are required for acceptable divertor conditions, He pumping and impurity retention. Improved model validation and measurements of divertor performance in prototypical conditions are required to clarify the issue.

While the sputtering erosion of graphite-based materials in the physics phase is anticipated to be acceptable, the integrated burn time in the technology phase will be 10^2 to 10^3 times longe so that sputtering will likely lead to the need for frequent replacement of the divertor plates. In addition, graphite-based materials have significant drawbacks in terms of hydrogen and impurity retention and are susceptible to radiation damage. Thus, while graphite-based materials may prove to be acceptable for both the physics and technology phases, alternative materials for the technology phase such as Be and W are being assessed. If temperatures at the divertor plate in the range of 10–20 eV or lower can be obtained, then the high sputtering threshold of tungsten would lead to very low erosion rates and long divertor plate lifetimes. However, even a very low level tungsten contamination of the plasma would prevent ignition ($n_W/n_e \geq 10^{-4}$). Experience with high-Z divertor plates is very limited (TiC coated Mo in JT-60) and the testing of high-Z divertor plates in tokamak experiments is a task for the ITER EDA Physics R&D Program. The operational experience with Be in divertor tokamaks is also limited, but the initial results in JET are promising.

Calculations of the pumping requirements for helium exhaust using the detailed models described above indicate that the proposed pumping speed should be adequate provided that the transport of helium ions from the plasma center where they are produced to the edge where they can be pumped is sufficiently rapid. Experimental results from TFTR, TEXTOR, and JT-60 indicate that the ratio of the particle confinement time for the thermalized alpha particles to the energy confinement time, τ_α/τ_E, is between 1 and 3, so that, at least for L-mode conditions, the ratio of the alpha-particle density to the plasma density, n_α/n_e, in the plasma core should not exceed the value of 10 % adopted in the guidelines.

1.4.2.2 Disruptions

Based upon a preliminary survey of the available disruption data and operational experience in tokamaks, guidelines for the timescales of the thermal quench and current decay, the location and magnitude of the peak heat fluxes, the energy and currents of the runaway electrons formed during disruptions, and the behavior of the plasma during the loss of position control leading to or occurring during a disruption have been developed.

During the thermal quench phase, a large portion of the plasma thermal energy (~ 500 MJ) can be deposited on the plasma facing components in 0.1-to-1 ms, leading to erosion and damage of the divertor plates and first wall tiles. The plasma current can decay in ~ 10 ms, inducing eddy currents in the structure and causing large impulsive force loads. Runaway electrons carrying up to half of the pre-disruption plasma current can be formed and accelerated during a disruption to energies of ~ 300 MeV, leading to the possibility of damage of the first wall components. Such damage due to high energy runaway electrons has been observed on JET, TFTR, and TORE-Supra.

Motion of the plasma into the plasma facing components due to loss of position control is expected to lead to large poloidal currents in the components and the

supporting structure and to produce large forces, as observed in DIII-D, JET, and PBX/M.

Although guidelines for the magnitude and frequency of these events have been drafted, much more information is needed. In particular measurements are needed to determine the timescales for the thermal and current quench more precisely, the energy deposition profile during the energy quench and the conditions which determine the runaway production. A relatively modest experimental program focussed on these topics should yield the necessary information in the next few years.

Given the severe impact of disruptions for ITER, their magnitude and frequency must be minimized. Operational experience with present experiments indicates that, with proper attention, the frequency of disruptions can be reduced to 2 to 5%. This is marginally acceptable for the physics phase, but must be further reduced to ~ 1 % for the technology phase. This should be possible if (1) plasma conditions close to the operational limits (beta, density, ...) are avoided, (2) plasma position control can be maintained as much as possible, even after the disruption, (3) proper start-up conditions are provided, (4) machine fault conditions (broken tiles, heating system failures, leaks, etc.) are minimized, and (5) the current profile is partially controlled by non-inductive current drive. Work on active control techniques such as feedback control of the m = 2 tearing mode and control of the current profile near the q = 2 surface is just beginning and needs increased emphasis. A major concern is the identification of pre-disruptive conditions early enough to activate control mechanisms and thereby avoid subsequent disruptive behavior.

1.4.2.3 Auxiliary Systems

In addition to the issues associated with power and particle control and disruptions, there are important physics aspects for the design of the auxiliary systems which are used to heat and control the plasma, to drive the plasma current, to fuel the plasma, and to measure the plasma parameters. In each of these areas, there is a good fundamental understanding of the relevant physical processes so that the physics performance of these systems can be predicted confidently.

Current drive and heating: The current drive and heating systems are required to (1) provide ionization and preheating to assist in the initiation of the plasma current, (2) provide or facilitate non-inductive assist of the current ramp-up including non-inductive ramp-up of all of the plasma current, (3) drive all or a portion of the plasma current for steady state or long pulse operation, (4) provide flexibility for control of the current profile, (5) heat the plasma to ignition, and (6) heat the plasma during driven operation with enough flexibility to provide burn control. Extensive analysis using experimentally validated theories and models has determined the design requirements for the current drive and heating system.

Due to the low resistance of the ITER vacuum vessel and structure, plasma breakdown and current initiation must be achieved with a relatively low toroidal electric field of ~ 0.3 V/m in the presence of the stray fields due to eddy currents. About 10 MW of electron cyclotron (EC) waves at 120 GHz can accomplish start-up on the outboard side of ITER as observed on DIII-D and other experiments. Increasing this to 20 MW offers the capability of partial control of the current profile for disruption control and profile optimization. In addition, noninductive current

ramp-up or ramp-up assist can be provided with 50 MW of 5 GHz lower hybrid (LH) waves to conserve volt seconds and extend the burn pulse.

In the reference current drive concept 75 MW of 1.3 MeV neutral beams and about 30 MW of 5-GHz LH waves are used to drive 15 to 22 MA of plasma current during the burn pulse. The neutral beams provide current drive in the plasma center and lower hybrid waves are used to broaden the current profile. The neutral beam energy is determined by the requirement that the beam penetrate to the plasma center. The LH waves will be absorbed in the outer portion of the plasma. Extensive operational experience and a good understanding of the underlying physics exist for current drive with neutral beams and LH waves. The alternative current drive option replaces the neutral beams with ion cyclotron (IC) waves. While IC systems have potential engineering advantages, the current drive efficiency is expected to be about 40% lower than for neutral beams, so that more IC power would be required. Experiments are also needed to demonstrate that IC waves can drive current.

A portion of the plasma current is expected to be carried by the neo-classical bootstrap current. The existence of this theoretically predicted current has been confirmed by experiments on TFTR, JET, JT-60, DIII-D, ATF and many other experiments. On JT-60 and TFTR, up to 75–80% of the current has been carried by the bootstrap current.

Axisymmetric magnetics: Because the ITER plasma will be highly shaped ($\kappa \sim 2$) and will require the flexibility to operate at high $\beta_{toroidal}$ and high $\beta_{poloidal}$, plasma shaping and control are important. A set of fourteen poloidal field coils located exterior to the toroidal field coils will provide shaping. Plasma control will be provided by active feedback of the currents in the external coils plus two internal control coils and by passive stabilizer elements close to the plasma. Extensive experience with high β plasmas with elongations comparable to 2 has been obtained on DIII-D and PBX/M ($\kappa \sim 2.5$–3). JET routinely operates with high elongations as well ($\kappa \sim 1.5$). The major requirements are:

(1) to ensure adequate shaping of the plasma equilibrium for the necessary range of plasma pressure and current profiles to provide the desired operational flexibility
(2) to provide the current waveforms necessary for the reference time dependent plasma scenarios, providing in particular the inductive flux necessary to produce and sustain the plasma current , and
(3) to provide adequate plasma position and stability control.

To develop the design, sophisticated computational models have been used that have been benchmarked extensively against tokamak operational experience so that the confidence in the design basis is high.

Fuelling: Fuelling is necessary to replace the deuterium and tritium either burned up by the fusion reactions or pumped away by the He exhaust system and to provide control of the total plasma density and density profile. Fuelling will be accomplished by a combination of gas puffing and pellet injection. In particular, the fraction of tritium injected by the fuelling system which is burned instead of being pumped out again should be as large as possible to minimize the tritium inventory and tritium gas handling and separation requirements. Gas puffing fuels the plasma via the scrape-off layer. The resulting density profile depends on inherent transport processes. To permit a degree of control allowing more peaked density profiles than the baseline gas puffing case, pellet injection is provided. Pellets launched at ~1 km/s

TABLE 1-4. DIAGNOSTICS COVERAGE

Operational Phase	Diagnostics Required
H/He/D Phase	Complete set
Physics D/T Phase	Complete set as far as possible plus alpha (α) diagnostics
Technology Phase	Diagnostics for machine control and monitoring plus those required to recover from faults

would penetrate inside the separatrix and those at ~5 km/s would penetrate to ~ 1/3 of the minor radius. The relative merits of fuelling with each of these techniques need to be determined. Pellet ablation and particle transport physics is an important part of the Physics R&D program. Present experiments indicate that the penetration of pellets with v_{pellet} ~ 1 km/s is proportional to $v_{pellet}^{1/3}$, but data is unavailable for higher velocities. Given the importance of controlling the plasma density and density profile, the design philosophy has been to provide as much flexibility as practical for fuelling.

Diagnostics: ITER is to provide a physics database adequate for the design of a demonstration power reactor. To achieve these goals, ITER must be equipped with as complete a set of diagnostics as is necessary to provide the information needed during each phase of operation (Table 1-4). Performing the required measurements in ITER will be difficult owing to the high levels of background radiation during DT operation, complicated by the long pulse lengths (10^2–10^5 s) and the need for detailed profile information, all combined with the limited access and the need for remote handling.

A list of parameters need to be measured and candidate methods for performing the measurement have been developed, and a preconceptual design study has been developed for those diagnostics. These studies have been used to integrate the diagnostics into the tokamak layout and access plans. In addition, these studies have been used to form the initial R&D plan for the development of diagnostics required for ITER. Substantial R&D is required in (i) reliability, (ii) development of new diagnostics, (iii) radiation effects, and (iv) demonstration of prototypes on tokamak experiments.

1.5 PHYSICS R&D FOR ITER

A number of questions which are either directly design-related, or which the ongoing fusion programs had not addressed sufficiently for ITER requirements, were identified during the first year of the ITER conceptual design. They formed the basis of an ITER-related physics R&D program comprised of twenty-three tasks covering 1989-1990 [1.9]. Thirteen of these tasks were design-related, that is, they addressed issues where the design constraints were difficult to specify or where the requirements were very demanding. Among these were divertor performance, disruptions, plasma break-down, and volt-second consumption. The other ten addressed plasma performance issues that were judged to be insufficiently covered in 1988 such as long

pulse operation in the H-mode, density limits, current drive, and alpha-particle physics. Twenty-five experimental facilities and many theoreticians participated in the program and the results of their work were reported to the ITER team in approximately 300 individual reports [1.9]. Many of the R&D reports formed much of the basis of the physics guidelines. Others confirmed the decisions made for the design. For example, the design related tasks yielded new information of practical value that helped the team develop algorithms for calculating the resistive volt-second consumption during current ramp-up, confirmed the feasibility of low voltage current initiation assisted by electron cyclotron waves, and confirmed the feasibility of assisting inductive current ramp-up with lower hybrid waves to save volt-seconds.

A more comprehensive physics R&D program has been developed for the Engineering Design Activity covering the period 1991-1995 so that a decision can be taken in 1995 on the construction of ITER [1.10]. For the detailed program in 1991-1992, twenty-two tasks were defined that cover the main areas of:

1. Power and Particle Exhaust Physics with primary emphasis on low temperature divertor operation (i.e. the combined areas of the physics of the plasma edge and plasma-wall interaction as well as impurity control, with due attention to new concepts),
2. Disruption Control and Operational Limits,
3. Steady-State Operation in Enhanced Confinement Regimes with emphasis on steady state H-mode operation,
4. Optimization of Operational Scenarios and Long-Pulse Operation (including the use of non-inductive current drive), and
5. Physics of a Burning Plasma with emphasis on fast ion physics and alpha particle physics.

The program presently includes the participation of the staff of approximately 50 experimental facilities and many theoretical and computational groups.

1.6 PHYSICS STATUS

The physics of ITER is based on demonstrated tokamak physics and credible extrapolations of that physics. The physics basis has been developed with the assistance of the international fusion community, including participation by all of the major tokamak experimental facilities and many theoreticians. The guidelines for energy confinement have been developed from data for H-mode operation, and indicate that ITER should be able to reach ignition. The guidelines for operational limits have been chosen to be conservative with respect to present experimental results in order to minimize the frequency of disruptions. Although the conditions for power and particle control by the divertor are very challenging, they are acceptable for ignited and long pulse operation. Steady state operation will require advances in the performance of the divertor. ITER has been designed to meet the demanding requirements posed by disruptions, but areas of concern remain, such as the lifetime of plasma facing components. Both power and particle control and disruptions are key physics R&D issues. The physics used in the design of the non-inductive current drive, plasma heating, plasma shaping and control, fuelling, and diagnostic systems for ITER is well understood and is based on extensive operational experience with

tokamak experiments and theoretical analysis. Operational flexibility has been emphasized in the design to provide contingency for uncertainties in the design assumptions. An extensive physics R&D program has been developed to improve and complete the physics database for ITER, and to address critical issues which have led to difficult design requirements so that the information necessary to support a decision on the construction of ITER in 1995 will be available.

REFERENCES (§1.0)

[1.1] *International Thermonuclear Experimental Reactor, Establishment of ITER: Relevant Documents*, IAEA/ITER/DS/1, ITER Documentation Series, IAEA, Vienna (1988).

[1.2] *ITER Diagnostics*, IAEA/ITER/DS/33, ITER Documentation Series, IAEA, Vienna, (1991).

[1.3] *ITER Operation and Research Program*, IAEA/ITER/DS/23, ITER Documentation Series, IAEA, Vienna (1991).

[1.4] *ITER Concept Definition: Vols. 1 and 2*, IAEA/ITER/DS/3, ITER Documentation Series, IAEA, Vienna (1989).

[1.5] *ITER Conceptual Design: Interim Report*, IAEA/ITER/DS/7, ITER Documentation Series, IAEA, Vienna (1990).

[1.6] *ITER Conceptual Design Report*, IAEA/ITER/DS/18, ITER Documentation Series, IAEA, Vienna (1991).

[1.7] J. CORDEY et al., "A Preliminary Analysis of the ITER Energy Confinement H-Mode Database," IAEA-CN-53/F-3-19, presented at the 13th Int. Conf. on Plasma Physics and Controlled Nuclear Fusion Research, Washington, D.C.October 1–6, 1990; to be published in the proceedings.

[1.8] P. YUSHMANOV et al., *Nucl. Fusion* **30** (1990) 1990.

[1.9] *Physics and Technology R&D for ITER Conceptual Design*, IAEA/ITER/DS/19, ITER Documentation Series, IAEA, Vienna (1991).

[1.10] *Research and Development Needs for ITER Engineering Design*, IAEA/ITER/DS/20, ITER Documentation Series, IAEA, Vienna (1991).

2.0. PLASMA PERFORMANCE

2.1 CONFINEMENT

2.1.1 Introduction

Energy, particle, and momentum confinement are key issues for the successful operation of ITER. Adequate energy confinement is essential for ITER to produce high levels of fusion power; it is one of the most important requirements for determining the plasma current of ITER. Particle transport is important for energy transport, fuelling, impurity effects, determination of the plasma profiles, and the exhaust of helium "ash". Momentum confinement is an issue primarily because momentum is injected into the plasma by the high energy neutral beams used for non-inductive current drive.

The energy confinement requirements are based on operation in the H-mode with sufficient ELM activity to avoid impurity accumulation. While the physical processes responsible for energy transport in tokamaks are beginning to be identified, the theories of such non-linear phenomena are not sufficiently well developed that they can be relied upon for confinement predictions. Therefore, the requirements were set on the basis of an assessment of the existing experimental data for tokamak energy confinement for both L-mode and H-mode operation. Initially, the available H-mode data were too sparse to develop a scaling so that the original confinement requirements were based on L-mode scalings. The predictions of these L-mode scalings diverged for candidate ITER parameters. To resolve this, a comprehensive database of L-mode energy confinement data was collected, and a new scaling was developed from this data. The analysis also identified lack of variation of some of the tokamak parameters as one of the primary causes for the multiplicity of L-mode scalings. New experiments were performed and the degeneracy in the data was reduced. In addition, a separate effort was initiated to collect and analyze H-mode confinement data. The results of both the L-mode and H-mode studies indicate that ITER should be able to ignite in H-mode operation with the reference parameters. Furthermore, operational flexibility to optimize the confinement is a key part of the ITER design. The heating and current drive, PF, and fuelling systems are designed to allow flexibility in the operational parameters. In addition, the device has the potential of operating at higher currents (25 and 28 MA) should additional margin in energy confinement be necessary.

The available data for particle transport indicates that the plasma and impurity density profiles as well as He transport should be acceptable for ITER conditions. However, since improvements in energy and particle confinement are linked, and the particle transport database in the H-mode in still limited, particle transport remains an important area of research.

Tangential neutral beam injection in present experiments often produces very high speed toroidal rotation due to the momentum injected by the beam. However,

due to the very high energy per particle (1.3 MeV/ion) compared to present beams (~90 keV), the calculated rotation speed in ITER does not appear to be large enough to be a concern.

While the present requirements for energy confinement are empirically based, identification of the primary mechanisms responsible for tokamak transport is a major focus of the research programs of the international fusion community. Although definitive results are not yet available, progress in the field has been steady so that it should be possible to predict the confinement capability of ITER with confidence in time to take a decision on the construction of ITER in 1996.

2.1.2 Confinement Requirements

ITER will require a level of energy (τ_E) and particle (τ_p) confinement adequate for reaching ignition and extended burn of DT plasmas, with steady-state, high-Q ($Q = 5P_\alpha/P_{aux}$) operation as an ultimate goal. This translates into a required confinement capability of $T_i(0)n_{DT}(0)\tau_E \sim 4\text{–}8 \times 10^{21}$ keV·s/m^3 for $Q \sim 5\text{–}\infty$ [where $T_i(0)$ is the central ion temperature, $n_{DT}(0)$ is the central DT fuel ion density, τ_E is the global energy confinement time]. In addition, $\tau_p^{He}/\tau_E < 10$ is required to ensure that the thermal alpha-particle (He) accumulation (n_{He}/n_e) is less than 10% (where τ_p^{He} is the global thermal alpha particle containment time). Furthermore, the tritium fuel burnup fraction under nominal burn conditions must be greater than 3%. While the ITER $Tn\tau_E$ requirement is about ten times the highest value achieved in JET, the extrapolation in plasma physics parameters is less. If β (ratio of plasma kinetic pressure to magnetic pressure), ν_* (collisionality), and ρ_L/a (ratio of the ion gyroradius to the plasma minor radius) are taken as the relevant dimensionless parameters to characterize the plasma, the extrapolation from present JET performance to ITER is a factor ≤ 2. The ITER concept is based on the expectation that H-mode confinement can be achieved for a long pulse.

2.1.3 Energy Confinement Database

The available energy confinement database is broad and contains discharges from a large number of tokamak experiments, including extensive data from large tokamaks with high levels of auxiliary heating (JET, JT-60, TFTR, DIII-D,...). Although a great deal is known about tokamak confinement scaling, uncertainties remain in extrapolation to future ITER-class machines. Recent work at ITER has concentrated on developing improved analysis and characterization of energy confinement in L- and H-mode discharges.

2.1.3.1 L-mode

Data characterization

L-mode confinement regimes in tokamaks with auxiliary heating have an extensive and well documented database. The most recent analysis of L-mode plasma confinement is based on the ITER L-mode database [2.1.1–2.1.7], containing more than 2000 shots from DIII, ISX-B, DITE, ASDEX, TFR, PDX, PLT, JT-60, DIII-D, TFTR, JET, T-10 and JFT-2M tokamaks. The parameter ranges in the ITER database are listed in Table 2.1-1.

TABLE 2.1-1. PARAMTER RANGE OF L-MODE DATABASE

Tok.	Config.	Heat	R(m)	a(m)	κ	I(MA)	B(T)	q(a)	$\bar{n}(10^{19})$	P_{abs}(MW)	A_p	A_b	N_{shot}
JET	Lim.	NB,IC	~2.9	~1.2	1.47–1.35	5–1	3.5–1.7	3.2–11	5–1	15–2	2	2–1	~620
JT-60	Lim.	NB,LH,IC	~3.05	~0.9	~1	3.2–1	4.8–4.5	2–0 6	11–1	23–2	1	1	~210
	Div.	NB,LH,IC	~3.1	~0.9	~1	2.7–1	4.8–4	2.3–0.6	6.5–0.5	28–2	1	1	~190
TFTR	Lim.	NB	~2.5	~0.8	1	2.5–0.8	5.2–3.9	3–10	7.5–1.5	20-3	2	2	~260
DIII-D	Lim.	NB	1.69	0.6?	1.8	1	2.1	7	3.5–1.5	6–2	2	1	~15
DIII	Lim.(?)	NB	~1.45	0.43–0.35	1.7–1.1	0.8–0.23	2.4–0.6	~(2–3)	10–3	5–1	2	1	~220
PLT	Lim.	NB	1.34	0.39	1	0.58–0.26	3.3–2	~(3–4.5)	6–1	3.5–1	1?	1?	~70
PDX	Lim.	NB	1.43	0.42	1	0.48–0.25	2.2–1	~(2–4)	7–2	5.5–1	2	1	~40
T-10	Lim.	EC	1.50	0.32–0.22	1	0.42–0.13	3–2.8	2.3–0.7	5.3–1.5	2.2–0.7	2	–	~30
ASDEX	Lim.	NB	1.64	0.39	1	0.38–0.19	2.2	~(2.7–5)	6–3	2.3–1	2	1	~30
JFT-2M	Lim.	NB,IC	~1.30	~0.32	1.5–1.35	0.35–0.16	1.3–1	2.3–0.7	4.5–1.5	2.7–0.6	2–1	1	~110
	Div.	NB	~1.30	0.29–0.24	1.5–1.35	0.28–0.15	1.3–0.7	2.4–0.5	4–1	1–0.6	2–1	1	~30
DITE	Lim.	NB	~1.17	0.26–0.18	1	0.26–0.07	2.5–0.9	~(2.3–6)	10–1	2–0.4	2	1	~200
ISX-B	Lim.	NB	0.93	0.25	1.5–1.1	0.2–0.06	1.5–0.8	~(2–5)	13–2.5	2.4–0.7	2	1	~110

A large number of empirical scaling expressions (see references in [2.1.1,2]) have been proposed to fit the energy confinement. The scaling analyses are based largely on subsets of this data, and often with additional information from the individual tokamaks. The existence of numerous scaling expressions reflects some characteristic features of the ITER L-mode dataset. These features are collinearity of data (i.e., weak variations of the data in some directions of the multi-dimensional parameter space) and variation of the τ_E dependencies from one parameter region to another (i.e, tokamak-to-tokamak variation, dependences due to heating methods and variations from different plasma configurations)

Within a given tokamak the dependence on the variables, I, P, n on a particular scaling [2.1.2], often reflect the properties of a specific regime only, whereas the dependence on R, a, and κ, which primarily comes from comparing different devices, is very poorly determined. Further, there is little B variation within any single tokamak and thus B scaling must also be determined by comparing different tokamaks.

Data analysis methods

Advanced statistical techniques have been used as a tool for analyzing and interpreting the global energy confinement data. Principal component analyses [2.1.3] and random coefficient models [2.1.4] have been found to be most useful. With a principal component analysis we find the directions of least data variation and thus determine plasma parameters combinations that introduce the largest errors into a scaling and into the corresponding predictions of τ_E. For the ITER database, these combinations are close to a

shape-size index: $f_s = 0.32\ R\ a^{-0.75}\ \kappa_x^{0.5} = 0.32\ R^{0.25}\ A^{0.75}\ \kappa_x^{0.5} = 1 \pm 0.1,$ (1)

q-index: $f_q = q_{eng}/3.2 = 1 \pm 0.35,$ (2)

field-size index: $f_{BR} = B\ (\kappa_x/R)^{0.9}\ (0.32/f_s)^{0.4} = 1 \pm 0.2.$ (3)

These indices have been normalized to a database averages of unity and the standard deviation of each of these indices is given. The first parametric factor, f_s, represents the fact that elongated tokamaks tend to have smaller aspect ratios than circular cross section tokamaks. The second parametric factor, f_q, represents both the tokamak to tokamak variation in q scaling and the lack of q variation in the present database. The third parametric factor, f_{BR}, represents the tendency of larger tokamaks to have stronger magnetic fields. All successful scalings, which represent the database reasonably well, differ from each other by some powers of these combinations of parameters [2.1.7].

New experiments on JT-60 [2.1.8] and TFTR [2.1.9] were performed to help reduce such scaling uncertainties. Figure 2.1-1 displays the values of the shape-size index f_s for the ITER database, for the new data from JT-60 LX (lower x-point configuration) and from TFTR where the aspect ratio was varied.

The random coefficient (R.C.) model is used to provide a systematic statistical description of the variation of the parameter dependencies between tokamaks. The data from different tokamaks is split into subgroups with similar transport properties, with similar heating methods and with similar plasma configurations. Considering the individual scalings of the subgroups as statistically independent observations, the correlation matrix can then be estimated by an iterative procedure and a statistically

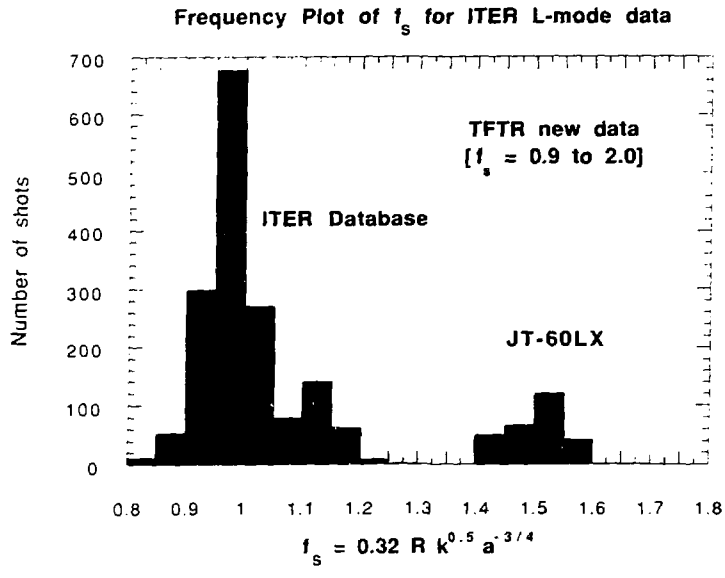

FIG. 2.1-1 Frequency of f_S in the ITER L-mode database with additional new data from JT-60 LX (lower X-point) and TFTR.

"optimal" scaling within the R.C. model can be obtained [2.1.4]. The R.C. model is appropriate when many small physical effects are responsible for the scaling differences. However, since there appear to be systematic differences between limiter and divertor discharges, and between neutral-beam (NB) and radio-frequency (RF) heated discharges only a single type of discharge should be analyzed statistically.

L-mode power law scalings

Only NB heated limiter discharges have sufficient data points in the present ITER L-mode database to produce a scaling from a single magnetic configuration and a single heating type The simplest exponential scaling form was found to be satisfactory for the limited NB heated data subset. The scaling, based on about 1000 data points from mainly DIII, TFTR, JET, JT-60, ASDEX, ISX-B and PDX has been developed [2.1.10], and was found to be close to Goldston scaling:

$$\tau_{ENB} = C\, I^{1.02}\, R^{1.71}\, a^{-0.39}\, \kappa_x^{0.65}\, \bar{n}_{20}^{0.08}\, B^{0.13}\, A_i^{0.5}\, P^{-0.53}. \qquad (4)$$

This scaling is dimensionally correct [2.1.5] and has been derived from a constrained random coefficient regression [2.1.6]. A similar approach, based on a constrained ordinary least squares regression has been applied to the JET-ASDEX dataset [2.1.11]. In comparison, an ordinary least squares regression, restricted to NB heated limiter discharges, yields a similar scaling.

Ion mass dependence in this scaling was not obtained by regression analysis but rather by comparing the τ_E dependence in deuterium vs hydrogen discharges for a

TABLE 2.1-2. COMPARISON OF NB LIMITER SCALINGS WITH DIVERTOR AND RF SCALINGS

Tokamak	dps	α_I	α_B	α_n	α_P
			NB, Limiter		
JET	94	0.85±0.07	0.44±0.05	–0.02±0.04	–0.56±0.03
JT-60	178	0.80±0.03	–	0.085±0.02	–0.58±0.03
JFT-2M	39	0.51±0.26	–	0.44±0.11	–0.71±0.12
TFTR	92	0.91±0.04	–	–0.26±0.04	–0.26±0.06
DIII	211	1.06±0.04	0.06±0.03	0.08±0.03	–0.71±0.02
ASDEX	28	1.11±0.07	–	–0.27±0.14	–0.31±0.18
PDX	41	1.14±0.06	–0.10±0.06	0.08±0.03	–0.61±0.03
ISXB	90	1.29±0.13	–0.11±0.06	0.08±0.03	–0.58±0.03
			NB, Divertor		
JET (fixed q_a)	35	0.72±0.04	0.72±0.04	0.14±0.04	–0.72±0.03
JT-60LX (little q_a variation)	264	0.38±0.04	0.38±0.04	0.13±0.03	–0.44±0.02
JT-60	92	0.55±0.06	–	0.02±0.05	–0.78±0.15
JFT-2M	30	–	–	0.69±0.08	–0.28±0.17
			RF, Limiter		
JT-60 (some density current correlation)	29	–	–	0.31±0.07	–0.38±0.03
JFT-2M	59	0.67±0.13	–	0.00±0.11	–034±0.04
T-10	25	0.43±0.11	–	0.84±0.10	–0.56±0.11

limited number of machines [2.1.12]. On small and medium size tokamaks this isotope scaling is almost uniformly seen. A comparison of confinement between JT-60 and TFTR supports the $A_i^{0.5}$ isotope scaling. Preliminary results in JET and DIII-D indicate a weaker isotope dependence in L-mode. These initial results are derived from a comparison of dissimilar discharges. We stress the importance of future systematic studies of isotope scaling.

One should note that the above [Eq. (4)] scaling was derived using a particular choice of missing data algorithm (no B dependence for some machines). Different algorithms leads to different scalings, with B and R exponents varying in the range $0.07 \leq \alpha_B \leq 0.20$ and $1.3 \leq \alpha_R \leq 1.6$. The situation becomes worse if other plasma configurations and other heating methods are taken into account. Table 2.1-2 presents scalings for tokamaks with different heating methods and different divertor configurations. Splitting the data into subgroups with different ranges of q, P/I, n/I also leads to different I, P, and B scalings [2.1.13].

From Table 2.1-2 we can see that the dependence on I is typically weaker for divertor discharges and RF heating. Similarly, the dependence on $\bar{n}$ is usually more pronounced for heating techniques other than NB. This difference may be due to beam penetration and fast ions effects important for NB heated plasmas. The exclusion of a fast ion component and/or beam penetration effects typically increases the $\bar{n}$ exponent by about 0.1–0.3 [2.1.14].

For the entire dataset, including the RF heated and divertor discharges, the ordinary least squares method yields the scaling

$$\tau_E = C\, I^{0.78}\, R^{1.15}\, a^{0.54}\, \kappa_x^{0.67}\, \bar{n}_{20}^{0.18}\, B^{0.15}\, A_i^{0.5}\, P^{-0.48}. \qquad (5)$$

The random coefficient model has its limitations, as it does not take into account the nonstatistical nature of subgroup scaling differences. Under these circumstances, the ITER L-mode power scaling was selected as a compromise between results from different heating methods and plasma configurations [2.1.7]:

$$\tau_E^{ITER89\text{-}P} = 0.048\, I^{0.85}\, R^{1.2}\, a^{0.3}\, \kappa_x^{0.5}\, \bar{n}_{20}^{0.1}\, B^{0.2}\, A_i^{0.5}\, P^{-0.5} \qquad (6)$$

This scaling can be made to satisfy the dimensional constraint by substituting $\alpha_n = 0.08$ for 0.1. The ITER89-P scaling is a good fit to not only NB limiter discharges but also to divertor and RF heated discharges. Figure 2.1-2 plots the residual error of the ITER89-P scaling, $ln\,(\tau_E/\tau_E^{ITER89\text{-}P})$ versus the cube root of the plasma volume. The new confinement studies in JT-60 and TFTR are also in good agreement with this scaling [2.1.8,9]. Table 2.1-2 demonstrates the importance of understanding the confinement difference between NB heated limiter discharges and RF heated divertor discharges. Unfortunately, the present ITER L-mode database contains insufficient RF heated, divertor discharges to permit a random coefficient analysis. Thus the ITER89-P scaling presently represents the most viable approach to extrapolating L-mode energy confinement to ITER.

L-mode offset linear scalings

Offset linear scalings separate the total stored plasma energy into an "Ohmic" plasma energy and an "incremental" plasma energy from auxiliary heating. This division into Ohmic and auxiliary energy is a physically reasonable way to describe a thermal pinch effect. However, as the plasma temperature increases, the Ohmic input power drops rapidly, which is a possible explanation as to why simple log linear scaling can be a good fit to strongly heated plasmas .

All the major offset linear scalings, ITER89-O, Rebut-Lallia, Shimomura-Odajima, and Takizuka, are a good fit to the weakly auxiliary heated discharges. For high power additional heated discharges the data scatter is higher. Thus, for large amounts of auxiliary heating, the use of an offset linear scaling requires more careful examination [2.1.7].

Historically, offset linear scalings have been advocated by groups working on tokamaks with divertors or RF heating. As Table 2.1-2 shows that divertor and RF heated plasmas do not follow the simple scaling of NB heated limiter tokamaks, offset linear scalings may be necessary to describe tokamak confinement with good accuracy.

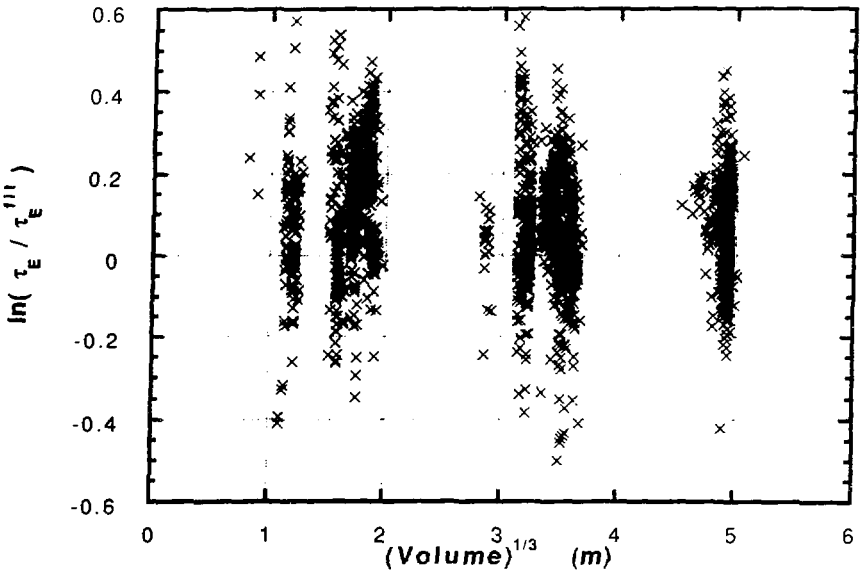

FIG. 2.1-2 Residual error of ITER89-P scaling: *ln* ($\tau_E/\tau_E^{ITER89\text{-}P}$) vs the cube root of the plasma volume.

Typically, offset linear scalings contain twice as many free parameters (unless additional assumptions are made). At present, physically compelling reasons for these assumptions are lacking. The existing ITER L-mode data is poorly structured for offset linear scalings since the database includes only a small number of discharges with P_{aux} comparable to P_{OH}. Although the ITER89-O scaling fits the existing data well, the lack of data makes many of the coefficients poorly determined. Thus we recommend the ITER89-O scaling only for comparison purposes and not for extrapolating tokamak confinement for ITER.

In conclusion, the ITER89-P L-mode scaling provides the most viable confinement prediction for ITER. For the proposed ITER physics baseline parameters, the predicted L-mode energy confinement is ~2.0 s. As discussed in Ref. [2.1.7], this extrapolation has an inaccuracy (one standard deviation) of 20-to-30%.

2.1.3.2 H-mode

Because ITER parameters are based on the working hypothesis that the device will be able to operate in the H-regime, the capability of accurately predicting the global energy confinement time τ_E for this regime is important. Therefore, upon request of ITER during the ITER Conceptual Design Activity, an H-mode database was assembled by Cordey et al. [2.1.15], using data from six machines: ASDEX, DIII-D, JET, JFT-2M, PBX/M and PDX. This database was then analyzed with the aim of deriving a scaling for the confinement time of H-mode plasmas. In this section, the work Cordey et al. is summarized, following closely reference [2.1.15].

The full H-mode database consists of 2120 datasets from 982 pulses. Measurements of the plasma energy content by several different techniques (diamagnetic, MHD and kinetic) have been assembled together with estimates of the fast ion energy content for most of the pulses. The 76 variables in each dataset include a simple label for type of ELM activity.

A "standard dataset" of 1239 observations has been selected, in which data from pulses with pellets, carbonized walls, high radiation $P_{rad}/P > 0.6$, low q_ψ (95%) < 3.1 (2.7 for JFT-2M), [dW/dt]/P > 0.35, or a high fast ion content $W_{fast}/W > 0.4$ are excluded. The standard dataset, which was used for the analysis, includes 693 ELM-free observations and 546 ELMy observations. An extensive report containing the details of the analysis will be available shortly along with the data itself. Essentially four questions are addressed in the following: (1) Do the existing L-mode scaling expressions multiplied by a scaling factor give a reasonable representation of the H-mode data? (2) Is the database well conditioned? (3) What are the best power and offset-linear fits to the data in terms of the variables I, n, P, B, R, R/a, κ ? (4) Does the data satisfy the constraints of plasma physics theory?

(1) Comparison with existing L-mode scaling expressions

The standard H-mode dataset has been fitted to four L-mode scaling expressions, Goldston [2.1.16], Kaye-Big [2.1.1], ITER89-P [2.1.7] and the offset linear scaling of Rebut and Lallia [2.1.17]. The factors of enhancement over these expressions are given in Table 2.1-3. The rms errors also given should be compared with 14% for a free fit to the standard dataset and 12% to the ELM-free dataset. The ITER89-P scaling gives the best fit to both datasets (shown in Fig. 2.1-3) since it has an aspect ratio dependence which is closest to that of the H-mode data. However, the rms error of 18% indicates that it is not a particularly good fit to the data. The comparison with the Rebut-Lallia scaling is degraded by the lack of data on Z_{eff}.

(2) Condition of the database

A detailed investigation has been made of the condition of the database with respect to the regression variables I, B, n, P, R, R/a, and κ. Two aspects are of interest. The first is to determine the directions in which the data is varied least and to check whether the data variation in these directions is larger than the associated measurement errors. The second aspect is to establish the distance needed in each direction to extrapolate to the parameters of the machine whose confinement is to be predicted, e.g. ITER. The directions of least variation are determined from a principal component analysis from which it can be concluded that the database is rather well conditioned for prediction of ITER, although it may be somewhat difficult to separate the effects of all 7 parameters [2.1.15].

(3) H-mode scaling expressions

Power law form: Direct regression on the standard data for each machine reveals differences between the machines in the scaling of τ_E with toroidal field B, ranging, at constant current, from no dependence with B in ASDEX, DIII-D, and JFT-2M, to an improvement with B in JET ($\sim B^{0.5\pm0.1}$), see also [2.1.18,19]. However, the variation of the scaling of B in the data may possibly overstate the "true" variation of the scaling of τ_E with B, since when the magnetic field is scanned for a given experiment, τ_E is usually observed to vary weakly with B. The reason for

TABLE 2.1-3.

	Standard dataset 1239 sets		ELM-free 693 sets	
Scaling Expression	Multiplication factor	σ %	Multiplication factor	s %
Goldston	1.57	25	1.50	27
Kaye Big	1.94	23	1.97	24
ITER 89-P	2.02	17	2.00	18
Rebut-Lallia	2.37	41	2.38	48

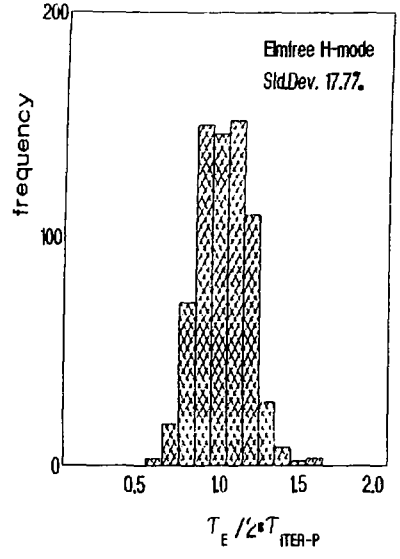

FIG. 2.1-3 Data frequency versus $\tau_E/2\tau_{ITER89\text{-}P}$ for the ELM-free dataset.

the strong improvement of τ_E with B in the JET data may be a consequence of the extensive helium conditioning that was used during the high field H-mode studies. In fact, recent B field scan experiments on JET at constant current have indeed shown that τ_E increases weakly with B, $\tau_E \propto B^{0.3\pm0.2}$. Thus B field scan experiments are needed to clarify this point. There is also some variation in the density dependence of τ_E in the different machines. Similar differences were seen in the L-mode database and several approaches were applied to handle these differences and produce combined scalings [2.1.7,10].

If the simpler approach of fixing the B dependence at the mean of the dependences seen in the individual machines $\tau_E \propto B^{0.15}$ is adopted and and standard multiple regression analysis to determine the remainder of the indices is applied, the

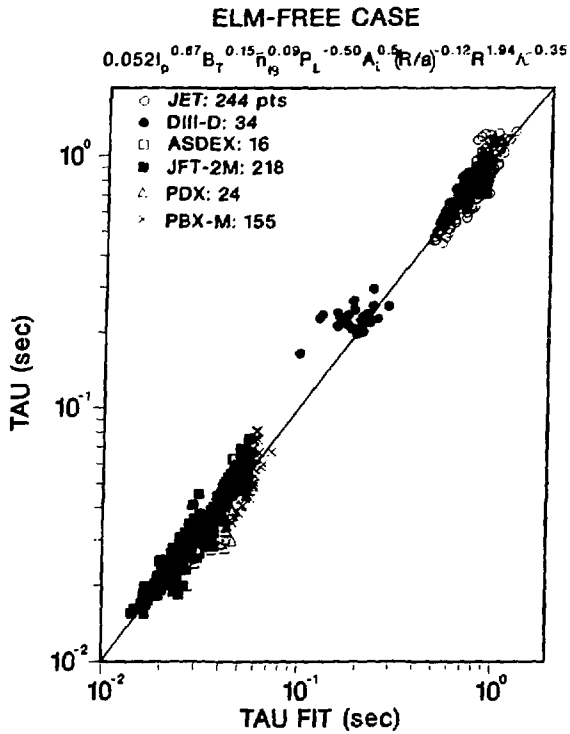

FIG. 2.1-4 τ_E versus the scaling expression of Eq. (7) for the ELM-free dataset.

resulting scaling expression (ITER H90-P) for the ELM-free dataset is

$$\tau_E(\text{ELM-free}) = 0.064 I^{0.87} B^{0.15} \bar{n}_{20}^{0.09} P^{-0.50} (R/a)^{-0.12} R^{1.94} \kappa_x^{0.35} A_i^{0.5} \quad (7)$$

The units in Eq. (7) are [s, MA, T, 10^{20} m^{-3}, MW, m], the root mean square (rms) error is 14%, the errors on the indices of I, B, etc., are: 0.04, 0, 0.03, 0.02, 0.06, 0.09, 0.07, 0, respectively, and the fit of the data to Eq. (7) is shown in Fig. 2.1-4. An addition to Eq. (7) could be to include the factor $(B\kappa/R)^{\alpha}$, where α is in the range $|\alpha| < 0.15$, which gives a range in B scaling that is identical to the range observed in the individual machines. In deriving Eq. (7) the diamagnetic loop measurement of τ_E was used for JET and the MHD data for the other devices, the atomic number A_i was not included in the regression. Expression (7) is similar to that obtained previously in a joint DIII-D/JET study [2.1.20] based on part of the present dataset. The addition of data from other machines has made it possible to determine the aspect ratio dependence, which is very weak. High-frequency, low-amplitude ELMs generally reduce τ_E by about 25% [τ_E(ELMy H-mode) = 0.75τ_E(ELM-free H-mode)]. The expression (7) gives τ_E(ELM-free) = 5.9 s [corresponding to τ_E = 4.4 s with ELMs] for nominal ITER parameters with I = 22 MA, B = 4.85 T, $\bar{n} = 1.24 \times 10^{20}$ m^{-3}, P(net heat) ≈ 150 MW, R = 6 m, a = 2.15 m, κ_x = 2.2, and A_i = 2.5.

Offset linear form: The fitting of data to an offset linear form has made extensive use of previous scaling studies on JFT-2M [2.1.21]. The offset linear form is expressed as $W_{th} = W_{os} + P\tau_{inc}$. The incremental confinement time τ_{inc} is assumed to depend only on I and R in the form $\tau_{inc} \propto I R^{\alpha} A_i^{0.5}$. The size dependence and constant of proportionality are then determined from the three D-shaped experiments with similar geometry JFT-2M, DIII-D, and JET. The energy offset term W_{os} is obtained in similar fashion. The final result is

$$W_{th} = 0.0495\, I^{1.13} R^{2.17} B^{0.56} A_i^{0.5} + 0.0212\, I R^{0.78} A_i^{0.5} P \qquad (8)$$

where the units are [MJ, MA, m, T, MW].

The rms error of this fit is 13.9% which is very similar to the rms error of the fits to expressions (7). Adding the data from the other machines does not reduce the goodness of the fit which is shown in Fig. 2.1-5. The ASDEX data appears marginally better than that of the scaling expression and this may be a consequence of the use of a closed divertor.

The predicted confinement time for ITER using Eq. (8) is 5 s, in agreement with the predictions from the power law form.

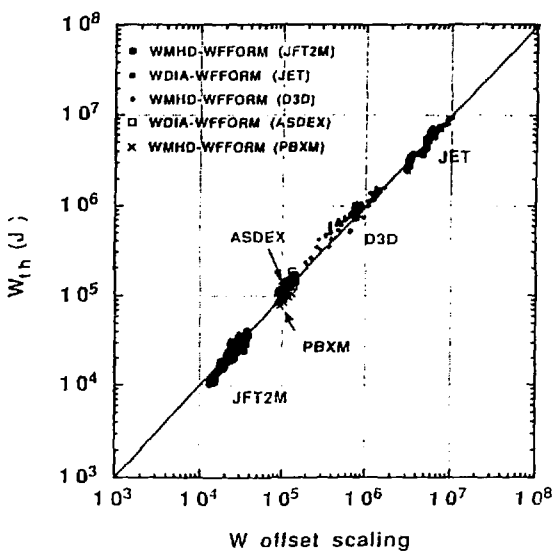

FIG. 2.1-5 $W_{thermal}$ versus the offset linear scaling expression of Eq. (8). Note in deriving $W_{thermal}$ here the fast ion contribution has been assumed to be isotropic in all devices.

(4) Physics constraints

The scalings given in Eqs. (7) and (8) do not precisely satisfy the theoretical physics constraints derived by Kadomtsev [2.1.22], Connor and Taylor [2.1.23] and Rebut [2.1.24]. However, only very small changes to the indices in Eq. (7) give expressions that indeed satisfy such constraints. Following the procedure outlined in

reference [2.1.25], he confinement time can be expressed in terms of the dimensionless variables as follows

$$\tau_{E,thermal} \propto \tau_B^{x1} (\rho/a)^{x2} \nu_*^{x3} \beta^{x4} \varepsilon^{x5} \kappa^{x6} q^{x7} A_i^{x8} \quad (9)$$

τ_B is the Bohm time, ρ/a is the normalized gyroradius, ν_* the normalized collisionality, β (= β_p) the poloidal plasma beta, ε the inverse aspect ratio (= a/R), κ the plasma elongation (= b/a) and q the cylindrical safety factor. These variables are expressed in terms of those available in the database as follows:

$$\tau_B \sim a^4 n I \kappa / \varepsilon P \tau_E, \qquad \rho/a \sim [(\varepsilon P \tau_E A_i)/(a^3 n I^2 \kappa)]^{1/2},$$
$$\nu_* \sim a^7 n^3 \kappa^2 / \varepsilon^2 P^2 \tau_E^2, \qquad \beta \sim \varepsilon P \tau_E / I^2 a, \qquad q \sim \varepsilon a \kappa B / I.$$

The physics constraints are then introduced by imposing linear restrictions on x_1, x_2, etc. The test of the acceptability of a single restriction is that the change in the mean square error is negligible (i.e., $\delta\sigma < 2\sigma/N^{1/2} \sim 1.2\%$). The result is [2.1.15] that the high β-collisional constraint of Kadomtsev [2.1.22] is well satisfied. In addition, the short wavelength ($\lambda \sim \rho$) constraint is also satisfied. The constraints of resistive and ideal MHD and the long wavelength ($\lambda \sim a$) turbulence are clearly not satisfied. The thermal energy confinement time for ITER, for the above representative parameters, with the short wavelenght constraint satisfied is 4.9 s.

(5) Summary

The ITER H-mode database is well conditioned for predictions of τ_E in ITER, as the extrapolation in the ITER parameters is not large in the least well known direction.

The two scaling expressions for the confinement time of ELM-free H-modes that have been derived under different assumptions give similar predictions for τ_E in ITER (5.5 to 5.9 s). Both scalings are somewhat more favorable than about 2 times the ITERP-89 L-mode scaling, which would predict ~4 s in ITER. However, the ELM-free confinement time have to be derated by about 25% for the level of ELM activity necessary to avoid impurity accumulation. This gives a predictive confinement time of ~4–4.4 s, consistent with the 3.8 s needed for ignition.

The data have been shown to satisfy the high β-collisional constraint of Kadomtsev, and in addition that of the short wavelength turbulence model.

The preliminary status of these results has to be stressed. As an outcome of the ongoing work, changes and improvements, to the ITER H90-P power law) and ITER H90-O (off-set linear) scaling expressions, are expected.

2.1.3.3 Additional confinement regimes

Several other types of improved confinement modes have been found in ohmic and neutral beam heated tokamak plasmas. (It must be noted that these improved modes were partly machine specific.) In ITER, operational flexibility has been stressed in the design so that these regimes can be investigated.

Improved confinement for Ohmic heated plasmas

The scaling of Ohmic confinement time in the low-density regime is given as

$$\tau_{LOH} \sim 0.1\, \kappa R^{1.5} a q \bar{n}_{20}.$$

The confinement time usually saturates in the high-density regime ($n > n_{sat}$) and takes the form

$$\tau_{SOH} \sim 0.03\, A_i^{0.5}\, \kappa\, R^{1.5}\, a^{0.5}\, B,$$

for $\bar{n}_{20} > \bar{n}_{sat,20} \sim 0.06\, I\, R\, A_i^{0.5}\, \kappa^{-1}\, a^{-2.5}$.

When pellet injection fuelling is used, τ_{OH} increases in proportion to n_e without saturation even for high-n_e discharges in Alcator [2.1.25], D-III [2.1.26] and ASDEX [2.1.27]. By using feedback control of gas fuelling, improvement of Ohmic confinement (IOC), $\tau_{OH} \sim n_e$, is obtained in ASDEX [2.1.28]. For both cases, pellet injection and IOC, the density profile becomes peaked compared with the case of saturated Ohmic confinement, and the stabilization of η_i mode might be responsible for the improved confinement.

Z-mode in ISX-B [2.1.29]

A small amount of neon was injected into ISX-B shortly after the start of NB heating. The scaling of τ_E that had no n_e-dependence changed with neon-injection such that $\tau_E \sim n_e$ with an enhancement factor up to 1.8 at $\bar{n}_e \sim 0.6 \times 10^{20}$ m^{-3}. Simultaneously, there was only a modest rise in Z_{eff}, $Z_{eff} = 1.6$ without neon and $Z_{eff} = 2.0$ with neon at $n_e \sim 0.5 \times 10^{20}$ m^{-3}. The particle confinement was also improved by neon-injection. The possibility of stationary operation with the Z-mode has not been evaluated.

P-mode in D-III [2.1.26] and JT-60 [2.1.30]

Pellet-fuelled limiter discharges in Doublet III exhibit low edge recycling with a doubling of τ_E, similar to that for divertor H-mode discharges. The density profile is peaked in this P-mode, $n_e(0)/n_e \sim 2$, while $n_e(0)/n_e \sim 1.2$ for gas-fuelled plasmas. By adopting an interrupted-beam scheme (neutral beam is interrupted just before each pellet is injected), the pellet ablation in the peripheral region, $\Delta r \sim 10$ cm, is reduced, and the improvement of τ_E is maintained for a time greater than 100 ms.

The energy confinement time is improved by ~40% in low-q ($q < 3$) JT-60 plasmas, when pellets are injected just before the NB injection. Sawtooth activity is suppressed, and a peaked n_e profile inside the sawtooth inversion radius is obtained. The enhanced stage ends when a large sawtooth develops.

Supershot in TFTR [2.1.31]

The improved performance of TFTR, $T_i(0) \sim 32$ keV and $T_i(0)n_e(0)\tau_E \sim 4.2 \times 10^{20}$ keV•m^{-3}•s, is achieved with D^0-NB heating by up to 30 MW in the supershot regime. Enhancement of τ_E for the supershot correlates with the peaking of the n_e profile, and is the order of $3 \times \tau_E^L$ for I = 1–1.6 MA and $P_{NBI} > 10$ MW. The energy confinement time is weakly dependent on I and P_{NBI}. Good confinement is achieved for the low-n_e target plasma. A necessary condition for the supershot is a reduction in deuterium recycling at the limiter, which is accomplished with the combination of helium degassing discharges and extensive operation with NBI at higher I.

Improved confinement with counter neutral beam injection in ASDEX [2.1.32]

Counter neutral injection (ctr-NI) into ASDEX leads to improved particle confinement and an increase in the impurity accumulation which is similar to other

tokamaks with ctr-NI. However, energy confinement is also improved in ASDEX with τ_E(ctr-NI) ~ $2\tau_E$(co-NI) in contrast with other experiments. The improved confinement correlates with a simultaneous peaking of the density profile. This persists on average despite the fact that sawtooth instability flattens the density profile and transiently reduces the energy content.

IL-mode in JFT-2M [2.1.33]

An improved stationary confinement mode (IL-mode), $\tau_E \sim \tau_E$(H-mode), is obtained after ELM-free ordinary H-mode in single-null JFT-2M plasmas with q ~ 3 (it is also possible to achieve the IL-mode in limiter discharges). Edge phenomena are similar to those in the L-mode rather than the H-mode, and the density profile is highly peaked. The radiation loss is stationary but has a peaked profile. Suppression of sawtooth activity is necessary to obtain a long pulse IL-mode.

IDC in JT-60 [2.1.34]

The improved divertor confinement (IDC) regime for high-power NB heating (> 10 MW) develops in the lower X-point configuration of JT-60 if the ∇B drift is towards the X-pont. The carbon impurities accumulate near the X-point and enhance the divertor radiation by up to 50% of the input power, while oxygen impurities are reduced. The 20% improvement in energy confinement is correlated with an improvement in particle confinement.

2.1.4 Particle Confinement Database

Knowledge of DT and electron particle transport is important for density control, density profile control and fuelling. Helium ash transport and impurity transport must also be understood to evaluate helium accumulation and the required helium pumping speeds. The database for the latter is described in §3.0.

The global confinement time of the particles inside the separatrix (τ_p) may be strongly affected by the scrape-off layer (SOL) plasma condition, especially when the penetration of neutral particles inside the separatrix is reduced. While the ITER plasma will be operated under these conditions, in present experiments the neutrals can penetrate the SOL. To permit extrapolation to ITER, the diffusion coefficient and inward pinch must therefore be determined locally, taking account of the sources. In most investigations, however, only the global particle confinement time τ_p and its dependence on global plasma parameters are determined experimentally. The local transport coefficients, D and v_{in} (inward pinch velocity), determine the global particle confinement time or particle outflux from the core plasma. The profile of plasma density is determined by the ratio of v_{in}/D in steady state and in the absence of volume sources. When the ratio v_{in}/D is given by $2C_v r/a^2$, n(r) has the form $\exp(-C_v r^2/a^2)$. Higher pinch velocities (larger values of C_v) lead to more peaked density profiles.

2.1.4.1 Parameter dependence of τ_p in OH and L-mode discharges

The particle confinement time in OH discharges with low $\bar{n}_e$ increases with increasing density, τ_p (~ a^2/D) $\propto \bar{n}_e$, which suggests $D \propto 1/\bar{n}_e$. On the contrary, for higher $\bar{n}_e$ discharges, the particle confinement time decreases with density, $\tau_p \propto 1/\bar{n}_e$, an effect which may be related to the reduced neutral penetration. These experimental observations are common to JET, Alcator, JT-60, and TEXT [2.1.35].

For neutral-beam (NB) heated L-mode discharges in JT-60 in the outer X-point configuration [2.1.36], τ_p degrades with heating power, $\tau_p \sim P^{-0.5}$. This tendency is basically the same as the power degradation in the energy confinement time. For ion cyclotron heated plasmas in JET [2.1.37], τ_p is also found to degrade with P much the same as for JT-60 experiments. The I dependence of τ_p ($\tau_p \propto I^{\alpha}$) is weak ($\alpha \sim 0$) for JT-60 divertor discharges, while $\alpha \sim 1$ for JET limiter discharges. This I dependence of τ_p (in JET) is similar to that of the L-mode energy confinement time, τ_E. From these limited results, the approximate τ_p scaling for L-mode discharges is

$$\tau_p \sim I^{\alpha}/(\bar{n}_e P^{0.5}) \quad (\alpha = 0\text{-to-}1).$$

The dependence of the particle confinement time on B and size is not clear.

2.1.4.2 Local transport coefficients in ohmic and L-mode plasmas

The local transport coefficients, D and v_{in}, have been measured in several tokamaks in ohmic and L-mode plasmas. In ohmically heated TEXT plasmas, gas-feed modulation experiments showed that $D_{eq} \propto I/\bar{n}_e B$, $\chi_e/D_{eq} \approx 2$–4 and $C_v \approx 1$ [2.1.38]. On the contrary, measurement of the propagation of the density pulse produced by sawteeth in the same TEXT plasma suggested that the value of D is larger transiently than the equilibrium value, i.e. $D_{tr} \approx (2\text{–}5)D_{eq}$, $D_{tr} \propto I/B$ and $C_v \approx 0$ [2.1.39]. For OH discharges in JET [$0.15 < \bar{n}_e$ (10^{20} m^{-3}) < 2.7, $2.8T < B < 3.4$ T, I ~ 3 MA], $D \approx 0.4$ m^2/s ($\sim \chi_e/7$) and $v_{in} \approx 1 \times (r/a)^4$ m/s [2.1.40].

Local particle transport coefficients have only rarely been measured in experiments with additional heating. Some results of auxiliary heated experiments in JET, JT-60 and ASDEX were discussed during the ITER Workshop on Fuelling and Plasma Operation Control (July 9–20, 1990). In the JET plasma, typical values of D and v_{in} are $D(m^2/s) \approx (0.3\text{–}0.5) \times (1 + 2r^2/a^2)$ and $v_{in}(m/s) \approx (0.4\text{–}1.0) \times (r/a)^{2.5}$ [2.1.41]. (Note that Be and C operation may be different). JT-60 experiments [2.1.42] for L-mode were simulated by : $D(m^2/s) = [0.2 + 0.015\ P(MW)] \times q(r)$ for the region $q > 1$ and $D(m^2/s) = 0.1$ for the region $q < 1$ (where q is the safety factor). The inward pinch rises to $v_{in}(m/s) = (0.4\text{–}0.5) \times r/a$ just after a pellet injection and drops to zero after a sawtooth crash. In neutral-beam heated ASDEX plasmas, $D(m^2/s) \approx (0.2\text{–}0.3) \times [P(MW)/1.5]^{0.5\text{–}1.0}$ and $v_{in}(m/s) \approx (r/a) \times [P(MW)/1.5]^{0.5}$ [2.1.43].

2.1.4.3 Electron particle transport in improved confinement modes

Particle transport in the improved Ohmic confinement regime (IOC) is significantly lower than in the saturated Ohmic confinement (SOC) regime, i.e., $D(2a/3) \approx 0.06 \ll D_{SOC}$ (m^2/s) ≈ 0.5 and $v_{in}(2a/3) \approx 1.5$ m/s $< v_{in,SOC} \approx 4$ m/s [2.1.28]. In other improved confinement modes, such as the Z-mode in ISX-B [2.1.30] and ctr-NI (counter neutral injection) operation in ASDEX [2.1.33], both particle and energy confinement improved also.

The global particle confinement time of L- and H-modes was compared in NB heated ASDEX plasmas at P = 3 MW and $\bar{n}_e \approx 3 \times 10^{19}$ m^{-3} [2.1.44]. Here, $\tau_p^L \approx 0.01$ s and $\tau_p^H \approx 0.15$ s. The latter is larger than in OH discharges for which $\tau_p^{OH} \approx 0.05$ s. In H-mode, τ_p^H is larger than $\tau_E^H \approx 0.06$ s, whereas in L-mode, τ_p^L is smaller than $\tau_E^L \approx 0.03$ s. The particle confinement is improved mainly in the

peripheral region just inside the separatrix by an appreciable reduction of D and/or a strong increase of v_{in}. There seems to be little change in local transport coefficients in the central region [2.1.45].

The dependence of τ_p on plasma parameters in H-mode discharges in NB-heated JET plasmas was also investigated [2.1.46]. τ_p^H increases slightly as $\bar{n}_e$ increases in H-modes, while τ_p^L decreases as $\bar{n}_e$ increases in limiter L-modes. Accordingly, $\tau_p^H \approx 0.5$ s becomes a factor of two larger than τ_p^L at higher density, $\bar{n}_e > 2.5 \times 10^{19}$ m^{-3}. This H-mode value is still lower than $\tau_E^H \approx 0.6$ s. A favorable dependence of τ_p upon I is found, $\tau_p(I=3\ MA) \geq 1.5\ \tau_p(I=2\ MA)$. These results were obtained for $P_{NB} \sim 10$ MW. The dependence of τ_p^H on heating power is not known.

2.1.4.4 Ion transport

Differences in local particle transport of impurities relative to DT determine the relative degree of central accumulation of the various species and also influence the electron density profile by variation of the particle sources. For example, the deuterium density profiles in the ASDEX plasma were compared for the ctr-NI phase and for the H phase [2.1.47]. The electron density profile for the ctr-NI phase was peaked, while that for the H phase was rather broad. An accumulation of C, O, B and Cu impurities in the central region is observed for the ctr-NI phase, while a flat or slightly-hollow impurity profile is observed for the H-phase, leading to similar deuterium profiles for both cases. This difference in accumulation suggests that the value of C_v for the ctr-NI phase is larger than that for the H phase. Central peaking of impurities was observed to increase with Z. Injection of higher-Z impurities may reduce accumulation of lower-Z impurities present.

2.1.5 Momentum Confinement Database

The knowledge of the toroidal momentum confinement time, τ_ϕ, is important for evaluating the toroidal rotation speed which could be induced in ITER by the presence of momentum sources (such as that due, for instance, to unbalanced tangential neutral beam injection aiming at driving a fraction of plasma current).

Toroidal plasma rotation could affect energy transport through the excitation of MHD turbulence (for $v_\phi > v_{th,i}$); beam-induced toroidal plasma rotation, by reducing the neutral beam energy in the rotating plasma frame, could increase the ionization cross-section, broadening the power and current deposition profiles. Preliminary studies assuming similar values for the momentum and energy confinement times suggest that the rotation induced in ITER by neutral beam injection, under conditions representative for beam driven current drive, should reach relatively modest values, at which none of these two effects is significant [2.1.48, also see §5.4].

Correlation of momentum and energy confinement

Many tokamaks have reported similar magnitudes for the global momentum and energy confinement times. On the other hand, there is conflicting evidence for such questions as whether the correlation is more with ion or electron energy confinement and whether the parameter dependence is the same.

In Doublet III, careful toroidal rotation speed profile measurements during L- and H-mode operations have shown that, in L-mode, τ_ϕ is less than the global energy

confinement time τ_E, and decreases faster with increasing beam power while in H-mode discharges τ_ϕ and τ_E have the same value and the same dependence on plasma current and beam power [2.1.49]. The L-mode data were obtained in limiter discharges for deuterium beam injection into deuterium plasmas, whereas the H-mode data were obtained in divertor discharges for hydrogen beam injection into a deuterium plasma. A saturation of rotation speed with increasing beam power was seen in the L-mode plasmas, but not in the H-mode, indicating that the degradation of τ_ϕ with increasing beam power was much stronger in L-mode. More recently, measurements in hot-ion discharges in DIII-D show that the angular momentum diffusivity χ_ϕ is basically equal to the electron thermal diffusivity χ_e in both L-mode and H-mode [2.1.50].

In TFTR, a transport analysis of simultaneous measurements of the toroidal rotation speed and ion temperature profiles during unbalanced neutral beam injection has shown that the ion momentum and thermal diffusivities are comparable in magnitude ($\chi_\phi \approx 1.5\ \chi_i$) and vary similarly with plasma current and radius [2.1.51].

In JET, a very few discharges have been recently analyzed and their local transport properties determined [2.1.52,53]. A hot-ion H-mode discharge and of a monster sawtooth shot have shown a momentum diffusivity equal, within a factor of 2, to the electron energy diffusivity ($\chi_\phi/\chi_e \sim$ 1-to-2). A similar conclusion (with larger error bars) has been obtained in the case of an L-mode discharge with strong (17.8 MW of neutral beam injection) additional heating. On the other hand, $\chi_\phi/\chi_e \sim$1-to-5 in the case of an L-mode discharge with lower (9.2 MW of NB injection) additional heating and $\chi_\phi/\chi_e \sim$ 1-to-6 in the case a "normal" H-mode shot.

2.1.6 Theory and Modeling

2.1.6.1 Anomalous transport theory and modeling

The physical processes that underlie plasma transport in tokamaks are not well understood at present. Plasma confinement has mostly been characterized by empirical scaling relations derived from statistical analyses from a variety of experimental devices [cf. §2.1.3]. The plasma transport induced by Coulomb collisions (neoclassical in a 2D or 3D geometry) is much less than what is actually observed. The standard concept for this "anomalous" transport is that the free energy associated with confinement of the plasma drives microscopic instabilities that induce enhanced, turbulent fluctuations in the plasma which in turn cause the anomalous plasma transport. Linear plasma stability theory is a highly developed subject and fluctuations are observed at roughly the predicted wavelengths, frequencies and amplitudes.

The ultimate challenge lies in developing complete theories of plasma turbulence and turbulent transport for specific experimental situations, experimentally identifying the fluctuations (or other phenomena) responsible for the local plasma transport, and making detailed comparisons between theory and experiment. Like their fluid turbulence counterparts, these studies are at the forefront of scientific research.

Increased understanding is required to optimize plasma confinement in tokamaks and to improve the predictability of confinement in ITER. The development of a complete characterization and understanding of transport in tokamak plasmas is a long-term goal of the world research programs. While it is not known how long it will take to achieve this goal, the recent increasing emphasis on transport studies should

produce sufficient progress toward this goal so that in a few years, confinement in ITER can be predicted with an accuracy sufficient to start construction of the device.

While the plasma transport processes throughout the plasma volume are not well understood, there is substantial experimental evidence that the anomalous transport is a local, diffusive process. Most generally, there are many indications that in the absence of macroscopic phenomena such as sawteeth, Mirnov oscillations, etc., the plasma density and temperature in radial layers within the plasma act independently on time scales shorter than diffusive transport time scales. In addition, the responses to localized transients in electron temperature, density, toroidal momentum and impurity densities have all been shown to be governed by diffusion equations, sometimes with significant coupling between them. The diffusion coefficients deduced from these "small signal" localized transient responses are often larger than the analogous "effective diffusion coefficients" deduced from equilibrium energy and particle balance analyses. Much work remains to develop a good characterization of anomalous transport processes in a plasma. The combination of the couplings between various transport processes and the increased transport for localized transient responses indicate that the transport fluxes are nonlinear functions of a combination of plasma parameters and their radial gradients, and/or have significant "off-diagonal" components, pinch terms, etc.

Theoretical models of anomalous transport are based primarily on studies of plasma turbulence and the plasma transport they induce. The underlying source of "expansion" free energy for the plasma turbulence is principally the plasma pressure gradient associated with the confinement of the hot plasma away from the cold, material boundaries. Both direct measurements of radial correlations of plasma fluctuations and the diffusive localized transient responses discussed in the preceding paragraph indicate that the turbulent radial decorrelation lengths in tokamak plasmas are quite short, less than 5% of the plasma minor radius. Thus, most of the theoretical models study turbulence in thin layers of the plasma, driven by equilibrium gradients in the plasma parameters across the layer.

Many types of collective modes and mechanisms for releasing the expansion free energy are considered individually or in combinations--dissipative fluidlike modes (resistive, neoclassical MHD, etc.), drift waves ("universal" microinstabilities, trapped-particle modes, η_i-modes, etc.), and electromagnetic skin depth modes (η_e-modes, cascades to short wavelengths, etc.). Numerical simulations of plasma turbulence have been developed for many types of models (fluidlike, particle-pushing, etc.) and modes. They form a basis of comparison for the various types of nonlinear models of plasma turbulence and turbulent transport that are being developed.

The Direct-Interaction-Approximation (DIA) approach [or the Eddy Damped Quasi-Normal Markovian (EDQNM) approximation to it] has proved to be one of the most successful and pragmatic in developing models for the numerical plasma turbulence simulation results. DIA models of transport in the core plasma region of tokamaks have, however, had very limited success to date clarifying the responsible component of plasma turbulent transport or in predicting the level of anomalous transport in tokamak plasmas.

On the other hand, considerable progress has been made over the past few years in connecting together DIA-based theory, modeling and experiments with regard to the turbulent fluctuations and the local transport fluxes in the plasma edge region. The

underlying unstable modes are fluidlike modes that include the resistive MHD rippling mode and drift waves. Temperature dependent impurity radiation effects are included in the models. The edge fluctuations and the transport they induce have been shown to depend on the radial electric field when the shear in the poloidal flow velocity (radial electric field) is large enough so that the Doppler shift of the turbulent eddies is significantly sheared over the relevant radial decorrelation length. The strongly sheared edge radial electric field can be induced externally (with a biased probe) or via ion charge losses near the limiter or near the separatrix in a divertor plasma. Models of the L-H transition in tokamak experiments based on these effects (radial ion charge loss → large radial E field with strong shear → reduced fluctuations → reduced transport) are looking quite promising.

The global energy confinement time in a tokamak is an aggregate of many effects — macroscopic phenomena (sawteeth, Mirnov oscillations/locked modes, ELMs, etc.), edge conditions, fast ion components, radiation, and finally plasma transport. Therefore it is intrinsically difficult to derive scalings for the global energy confinement time from local transport models. Nevertheless, it has been possible, in specific cases, to quantify the effects due to sawteeth, Mirnov oscillations and locked modes, as well as the heating and radiation profiles. Also scaling expressions for the global confinement time have been derived from local transport models that are roughly consistent with the experiments. However, the identification of a prevalent transport mechanism has not yet been possible either following this approach.

2.1.6.2 Equivalence considerations

The most promising way to find the scaling relations for the plasma transport properties and, hence, the global energy confinement time is to combine the theoretical analysis of possible mechanisms with equivalence considerations in terms of dimensionless parameters characterizing the plasma conditions [2.1.22,23]. In fact, it appears that a quasi-neutral, collisional, high-β model is adequate for hot tokamak plasmas. The relevant dimensionless plasma parameters, in this case, are a/ρ_L, ν_*, β, q, A_i, etc., to be supplemented by the dimensionless parameters describing the configuration, viz. R/a (aspect ratio) and κ (elongation). The confinement time τ_E, for discharges having similar heating, fuelling, and radiation profiles, is then given by $\omega_c\tau_E = F(a/\rho_L, \nu_*, \beta, q, A_i, \ldots,$ configuration) with F an arbitrary function (and where ω_c is the gyrofrequency). Equivalent plasma states have identical dimensionless parameters, but actually may differ as one of the dimensional parameters n, T, a, and B remains free.

The above relation will allow a prediction for τ_E for any plasma condition if the global confinement time is known for an equivalent state. For ITER this is, however, not applicable in this form as its dimensionless size a/ρ_L is about a factor of 2 larger than in the largest operating tokamak (JET). Additional theoretical and experimental information is therefore needed to determine the functional dependence of the transport properties on a/ρ_L. In a given device, this can be obtained by varying the magnetic field, and using data from various devices so that a wide interval can be covered. Most relevant are medium-to-large tokamaks able to operate in an elongated divertor configuration (JET, JT-60U, DIII-D, ASDEX-Upgrade). Theory provides a relation between simple transport mechanisms and the dependence of the transport coefficients

on a/ρ_L. Many kinds of turbulence (such as drift waves, resistive ballooning modes, magnetic perturbations including overlapping islands, electromagnetic skin depth modes, etc.) are predicted to lead to a gyro-reduced Bohm scaling of the diffusion coefficients, corresponding to an energy confinement time given by

$$\omega_c \tau_E = (a/\rho_L)^3 F(\nu_*, \beta, q, A_i, \ldots, \text{configuration}).$$

If this scaling relation (or a similar one in which the cubic dependence on a/ρ_L is replaced by another known functional dependence) can be confirmed, τ_E can be obtained by a "partial equivalence" argument in the other dimensionless parameters for which the values needed in ITER can be obtained simultaneously in the present generation of tokamaks. It must however be noted that the dependence on a/ρ_L must be determined with high precision to be able to predict the confinement properties of the ITER plasma with satisfactory accuracy.

The intense activity ongoing on all fronts of theoretical analysis and modelling, combined with a systematic comparison with a fast growing database especially for the H-mode, can be expected to provide the needed predictive capability within the next few years.

REFERENCES (§2.1)

[2.1.1] S. KAYE, C. BARNES, M. BELL, et al., "Status of global scaling expressions," *Phys. of Fluid* (to be published).

[2.1.2] See (and references therein) *ITER Concept Definition*, Vol. 2, p. 1–12, ITER Documentation Series, No. 3, IAEA, Vienna (1989).

[2.1.3] K. RIEDEL, *Comments Plasma Phys. Cont. Nucl. Fusion* **12** (1989) 279.

[2.1.4] K. RIEDEL, *Nucl. Fusion* **30** (1990) 755.

[2.1.5] B.B. KADOMTSEV, *Soviet J. Plasma Physics* **1** (1975) 295

[2.1.6] K. RIEDEL, "On dimensionally correct power law scaling laws for neutral beam heated limiter L-mode confinement," submitted to *Nucl. Fusion*.

[2.1.7] P. YUSHMANOV, T. TAKIZUKA, K. RIEDEL, O. KARDAUN, J.G. CORDEY, S. KAYE, D. POST, *Nucl. Fusion* **30** (1990) 1990.

[2.1.8] T. TAKIZUKA, O. NAITO, JT-60 Team, "Global confinement data from JT-60 with lower X-point configuration," ITER-IL-PH-4-0-J-2 (1990).

[2.1.9] GRISHAM, L. et al., 17th EPS Conference on Controlled Nuclear Fusion and Plasma Heating, Amsterdam, 1990, Vol 1, p. 146.

[2.1.10] RIEDEL, K., KAYE, S., *Nucl. Fusion* **30** (1990) 731.

[2.1.11] O. KARDAUN, K. THOMSEN, J. CORDEY, F. WAGNER, JET Team, ASDEX Team, 17th EPS Conference on Controlled Fusion and Plasma Heating, Amsterdam, 1990, Vol. 1, p. 110.

[2.1.12] F. WAGNER, M. BESSENRODT-WEBERPALS, H. FAHRBACK, O. GRUBER, W. HERRMAN, et al, "Isotope dependence of ohmic discharge parameters of ASDEX," Proc. 16th European Conference on Controlled Fusion and Plasma Physics, Venice, 1989, Vol. 1, p. 195.

[2.1.13] J. CHRISTIANSEN, J.G. CORDEY, K. THOMSON, *Nucl. Fusion* **30** (1990) 1183.

[2.1.14] J.G. CORDEY, private communication.

[2.1.15] J. CORDEY et al., "A Preliminary Analysis of the ITER Energy Confinement H-Mode Database," IAEA-CN-53/F-3-19, presented at the 13th Int. Conf. on Plasma Physics and Controlled Nuclear Fusion Research, Washington, D.C.October 1–6, 1990; to be published in the proceedings.

[2.1.16] R.J. GOLDSTON, *Plasma Physics and Controlled Fusion* **26** (1984) 87.
[2.1.17] P.H. REBUT, P.P. LALLIA, M.L. WATKINS, Plasma Physics and Controlled Nuclear Fusion Research (Proc. 12th Int. Conf., Nice 1988), IAEA, Vienna, paper IAEA-CN-50/D-4-1.
[2.1.18] M. KEILHACKER and the JET Team, Plasma Physics and Controlled Nuclear Fusion Research (Proc. 12th Int. Conf., Nice 1988), IAEA, Vienna, Vol. 1, 159 (1989) 159.
[2.1.19] O. KARDAUN et al, Proc. of 16th Eur. Conf. on Cont. Fusion and Plasma Physics, Venice, **13B** (1989) 253.
[2.1.20] D.P. SCHISSEL et al., and B.J.D. TUBBING et al., GA-A19925 (1990) and JET-P (90) 16 1990.
[2.1.21] N. SUZUKI et al., Plasma Physics and Controlled Nuclear Fusion Rsearch (Proc. 12th Int. Conf., Nice, 1988), IAEA, Vienna, Vol. 1, 207 (1989).
[2.1.22] B.B. KADOMTSEV, *Sov. J. Plasma Physics I.* **1** (1975) 295.
[2.1.23] J.W. CONNOR, J.B. TAYLOR, *Nucl. Fusion* **17** (1977) 1047.
[2.1.24] P.H. REBUT, M.L. WATKINS, P.P. LALLIA, Proc of 14th Eur. Conf. on Cont. Fusion and Plasma Physics, Madrid, (1987), Vol. 11d (1) EPS (1987) 172.
[2.1.25] M. GREENWALD et al., *Phys. Rev. Lett.* **53** (1984) 352.
[2.1.26] S. SENGOKU et al., Plasma Physics and Controlled Nuclear Fusion Research (Proc. 10th Int. Conf., London, 1984), IAEA, Vienna, Vol. 1, 405 (1985).
[2.1.27] M. KAUFMANN et al., *Nucl. Fusion* **28** (1988) 827.
[2.1.28] F.X. SÖLDNER et al., *Phys. Rev. Lett.* **61** (1988) 1105.
[2.1.29] E.A. LAZARUS et al., *J. Nucl. Mater.* **121** (1984) 61; M. MURAKAMI et al., Plasma Physics and Controlled Nuclear Fusion Research (Proc. 10th Int. Conf., London, 1984), IAEA, Vienna, Vol. 1, p. 87 (1985).
[2.1.30] Y. KAMADA, *Nucl. Fusion* **29** (1989) 1785.
[2.1.31] R.J. HAWRYLUK et al., Plasma Physics and Controlled Nuclear Fusion Research (Proc. 11th Int. Conf., Kyoto, 1986), IAEA, Vienna, Vol. 1, 51 (1987); M.G. BELL et al., Plasma Physics and Controlled Nuclear Fusion Research 1988 (Proc. 12th Int. Conf., Nice, 1988), IAEA, Vienna, Vol. 1, 27 (1989).
[2.1.32] O. GEHRE et al., *Phys. Rev. Lett.* **60** (1988) 1502.
[2.1.33] M. MORI et al., *Nucl. Fusion* **28** (1988) 1892; M. MORI et al., in Controlled Fusion and Plasma Heating (Proc. 16th Eur. Conf. Rome, 1989) p. 217.
[2.1.34] S. TSUJI et al., Plasma Physics and Controlled Nuclear Fusion Research (Proc. 12th Int. Conf., Nice, 1988), IAEA, Vienna, Vol. 1, 265 (1989).
[2.1.35] A.J. WOOTTON et al., *Plasma Phys. and Contr. Fusion* **30** (1988) 1479.
[2.1.36] S. TSUJI, JT-60 Team, Proc. 14th EPS, Madrid, 1987, Part I, p. 57.
[2.1.37] M. BURES et al., *Plasma Phys. and Contr. Fusion* **30** (1988) 1833.
[2.1.38] K.W. GENTLE et al., *Plasma Phys. and Contr. Fusion* **29** (1987) 1077.
[2.1.39] S.K. KIM et al., *Phys. Rev. Lett.*, **60** (1988) 577.
[2.1.40] A. GONDHALEKAR et al., *Plasma Phys. and Contr. Fusion* **31** (1989) 805.
[2.1.41] A. GONDHALEKAR, "Fuelling and density behaviour in JET," ITER-IL-PH-9-0-E-8, presented at the *ITER Workshop on Fuelling and Plasma Operation Control*, 9–20 July 1990, Garching.
[2.1.42] K. SHIMIZU, "Simulation analysis of JT-60 pellet injection experiments," ITER-IL-PH-9-0-J-3, ibid.
[2.1.43] K. BUCHL et al., "Double-feedback controlled pellet refuelled plasmas: density profile control by pellets and related particle transport," ITER-IL-PH-9-0-E-6, ibid.

[2.1.44] ASDEX Team, *Nucl. Fusion* **29** (1989) 1959.
[2.1.45] K.W. GENTLE et al., "Determination of particle transport coefficients in ASDEX by gas modulation," ITER-IL-PH-9-0-E-12, *op. cit.* [2.1.41].
[2.1.46] A. TANGA et al., *Nucl. Fusion* **27** (1987) 1877.
[2.1.47] G. FUSSMANN, "Impurity transport in tokamaks (overview)," ITER-IL-PH-9-0-E-11, *op. cit.* [2.1.41].
[2.1.48] S.D. SCOTT, "Projections of rotation velocity for ITER," presented at the ITER Specialists' Meeting on Confinement, 24–27 May 1988, Garching.
[2.1.49] K.H. BURRELL et al., *Nucl. Fusion* **28** (1988) 3.
[2.1.50] K.H. BURRELL et al., Proc. 17th EPS Conf. on Controlled Fusion and Plasma Heating, Amsterdam 1990, Vol. 1, p. 271.
[2.1.51] S.D. SCOTT et al., *Phys. Rev. Lett.* **64** (1990) 531.
[2.1.52] B. BALLET et al., Proc. 17th EPS Conf. on Controlled Fusion and Plasma Heating, Amsterdam 1990, Vol. 1, p. 162.
[2.1.53] B. BALLET et al., "Determination of local transport coefficients by heat flux analysis and comparisons with theoretical models," JET Report, JET-P(90)51 (1990).

2.2 MHD LIMITS

2.2.1 Introduction

To attain its objectives, in particular long-pulse operation ITER must be capable of routinely operating at or near the maximum expected steady-state beta, β, hence it is critical that there be high performance near the MHD limits. Raising the plasma current (to lower β_{pol}) is a route to both high beta stable discharges and to improved energy confinement time, provided the safety factor, q_ψ, is at least kept above two (even at low β). However, operating in the range as low as $2 < q_\psi < 3$ though possible is considered unreliable for the reasons described below. Still, further improvements can be made by maximizing the Troyon parameter, $g = \langle\beta\rangle/(I/aB)$, through optimizing the tokamak cross-section shape (chiefly the elongation and triangularity) and optimizing plasma profiles (current density and pressure). Such information can then be used in systems studies to optimize the operating scenarios.

Although some present experiments attain their highest β values for $2 < q_\psi < 3$, these devices have a relatively close-fitting poloidal field system, which may add to the stability. However, wall stabilization is not considered to be a safe option for ITER. Theoretical analysis for cases without a conducting wall indicates that stability is sensitive to the current density profile near the plasma edge for $2 \leq q_\psi < 3$, and a strong degradation in the beta limit appears due to the onset of external modes. This degradation is even present for higher q_ψ values, when the current density at the edge (or its derivative) exceeds a certain value. Consequently, the safe range for the safety factor to be adhered to is $q_\psi > 3$. Another effect of the wall in present experiments may be the avoidance of locked external kink modes; again, this stabilizing influence is not likely to be effective during long burning pulses.

With this constraint of $q_\psi > 3$, increasing the plasma current to improve the energy confinement time requires an increase in the plasma elongation, κ. However there is an upper limit on the allowable elongation set by the requirements of the feedback control system for axisymmetric modes (i.e., vertical position control).

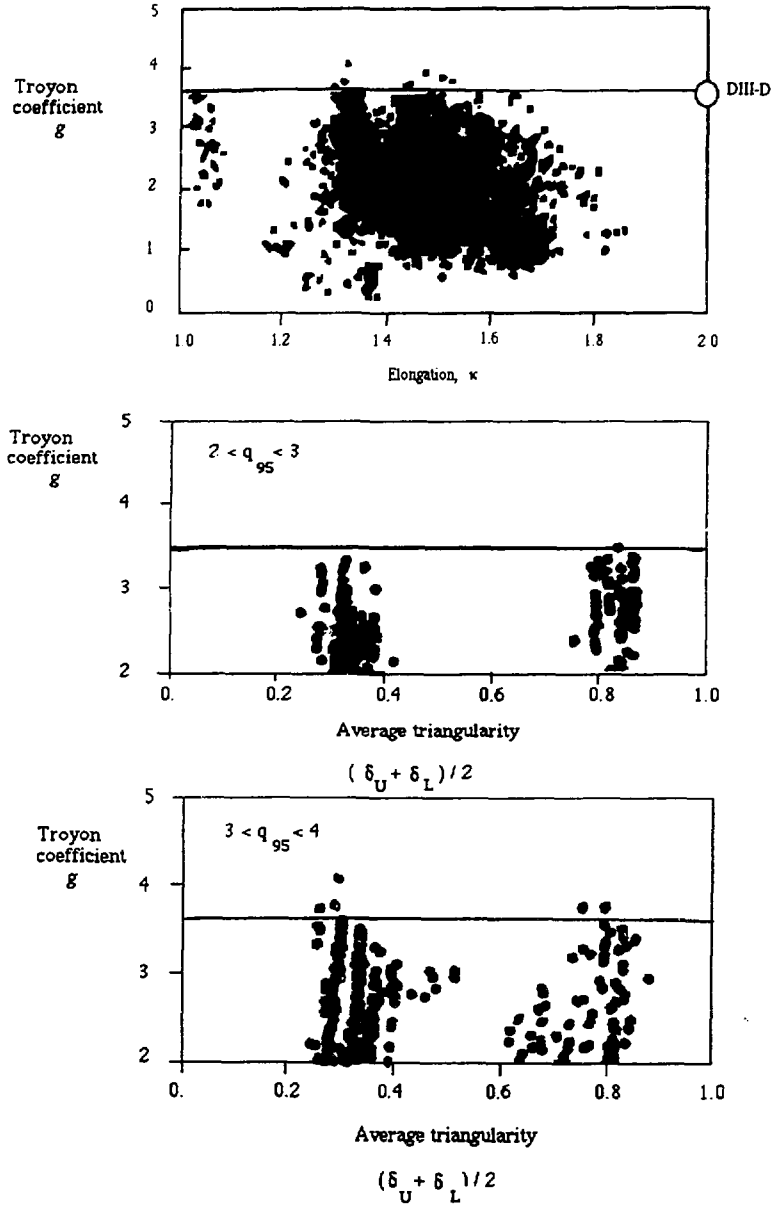

FIG. 2.2-1 Dependence of g on κ (top) and δ (middle for $2 < q_\psi < 3$ and bottom for $3 < q_\psi < 4$) in DIII and DIII-D experiments. g^{max} is almost independent of κ and has a weak dependence on δ.

The pressure and safety factor (or current density) profiles needed to achieve stable high beta states may also have an important impact on ignition conditions. Compatibility of the optimal profiles with neutral beam, RF and alpha particle heating profiles must be considered. The effect of fast ions and alpha-particles on the stability of the m = 1 mode and on the energy and particle confinement time in the central region of the plasma is also important.

In addition to these operational requirements, it is important to know the maximum power density ITER would reach during possible operational transients (such as α particle-heated thermal excursions). Knowledge of this maximum transient beta limit, which will be larger than that obtained during steady-state conditions, may be needed to avoid disruptions during such transient excursions.

Lastly, while ideal MHD models can predict the overall limits to plasma performance, plasma behavior near these limits is often dominated by non-ideal (dissipative) effects. Resistive-fluid tearing modes have often been identified in tokamaks, and a good correlation of theoretical models with experiments has been achieved. Typical ITER profiles are found to be stable to resistive-fluid modes because of the strong plasma shaping. However, the very low collisionality expected in ITER requires qualitative changes in the present models of dissipation; specifically, there is a need to include kinetic and neoclassical effects. Ideal MHD stability can also be modified by high energy ions. The "fishbone" instability is seen in experiments in which neutral beam heating is carried out perpendicular to the magnetic field lines. This instability could also occur when the plasma is heated by alpha-particles, and may limit the central electron temperature. Alpha-particle induced instability, whether of low- or high-n (ballooning) modes, may also reduce the "safe" β-limit for ITER.

2.2.2 Database

2.2.2.1 Shape effects on beta limits

Experiments in Doublet-III and DIII-D show that g^{max} is independent of κ, for κ below 2.0 [2.2.1] and, in DIII-D single and double-null configurations there is only a weak dependence on triangularity (see Fig. 2.2-1 [2.2.1]). Typically, $g^{max} = 3.5$ for $2 < q_\psi < 3$ both for $\delta = 0.25$–0.35 and for $\delta = 0.8$–0.85. Similarly, in the higher q region, $g^{max} = 3.5$, both for $\delta = 0.25$–0.4 and for $\delta = 0.7$–0.8, for $3 < q_\psi < 4$. PBX-M shows a similar trend with the maximum β rising approximately linearly with κ for $\kappa < 2$ and saturating for $\kappa > 2$, but there is a more pronounced dependence on triangularity with g^{max} increasing with δ up to $\delta = 0.5$ and then saturating [2.2.2].

Some caution must be paid in extrapolating these shaping results directly to ITER because a conducting wall is calculated to be an important stabilizing mechanism for external modes in DIII-D (with $a_w/a \sim 1.5$) [2.2.1], and may be active in the experiments. This is true also for closely fitting passive stabilizers in PBX-M, which are expected to serve as conducting shells for fast time scale MHD modes. Further, in PBX-M there is a small "bean-like" indentation (~ 15%) present for high β_{pol} experiments [2.2.2]. Theory predicts that this shaping will have an additional stabilizing influence on high-n modes (n = toroidal mode number). Another point to be stressed is that maximum operational values of g, or other limits to the operational space may be the result of limitations in available power, or the degree to which experimental operation has been dedicated to exploring this regime, or other

constraints, unrelated to actual stability limits. Thus, there is a need for continued study as part of the long range R&D programme in this area.

Studies of the effects of shaping on ideal MHD predictions of beta limits in ITER consider both low-n kink ($n \leq 3$) and $n = \infty$ modes. The goal has been to find the optimal elongation and to determine the effects of profiles on the optimal triangularity. To determine the optimal elongation we consider three profile cases:

Case 1 [2.2.3] $q = q_0 + q_1\psi^{\alpha_1} + (q_\psi - q_0 - q_1)\psi^6$,

$p = p_0[(1 - \psi^{\beta_1})^{\beta_2} + p_1\psi^3(1 - \psi)^{\beta_3}]$, (1a)

Case 2 [2.2.4] $q = q_0 + 0.5\psi^2 + (q_\psi - q_0 - 0.5)\psi^6$, (1b)

or q-profile obtained from $Rj_\phi = j_0(1 - \psi^{\alpha_1})^{\alpha_2}$ at low beta,

p: optimized to ballooning mode, with $p'(\psi)$ reduced near the edge to stabilize the kink,

Case 3 [2.2.5] $\langle \mathbf{j}\cdot\mathbf{B}\rangle/\langle \mathbf{B}\cdot\nabla\Phi\rangle = j_0 (1 - \psi^{\alpha_1})^{\alpha_2}$, (1c)

p: optimized for ballooning with smooth reduction for $0.8 < \psi < 1.0$,

where ψ is the normalized flux function, $0 < \psi < 1$. The safety factor at the magnetic axis, q_0, is chosen to be between 1.01 and 1.05 for most of these cases to avoid local interchange modes. Cases with $q_0 < 1$ have been studied separately [2.2.6, 2.2.7]. The plasma shape is specified by the formulae

$$R = R_0 + a\cos(\theta + \delta \sin\theta), \qquad z = \kappa a \sin\theta. \tag{2}$$

Fixed boundary equilibria are used and q_ψ, κ, and δ at the boundary are interpreted as the value at the 95% flux surface in a divertor configuration. The aspect ratio, $A = R_0/a$, is chosen to be about 3.

Figure 2.2-2 shows the beta limits for $A = 3$ (profile cases 1 and 2) and 3.3 (profile case 3) as a function of κ, with $q_\psi = 3$. For cases 1 and 2, there appears a maximum in β. The corresponding value of κ depends on the pressure profiles. Case 3 shows a monotonic increase in the beta limit with κ for $\kappa \leq 2.5$. For $\kappa \geq 2.5$, the beta limit decreases mainly due to the external kink mode. It may be possible to enhance the beta limit for $2 < \kappa < 2.5$ by shaping and by careful optimization of the pressure and current density profiles. The g-limits for $q_\psi \geq 3$ as a function of κ are shown in Fig. 2.2-3. For $\kappa \leq 2$, g takes on values between 2 and 3.8 depending on the profile. The difference is mainly due to different profiles near the plasma edge. For $\kappa > 2$, g decreases as κ increases. The average of the three cases gives

$$g = 3.4 \qquad (\kappa \leq 2 \text{ and } q_\psi \geq 3) \tag{3a}$$

$$= -9.12 + 12.3\kappa - 3.02\kappa^2 \qquad (2 < \kappa < 2.5 \text{ and } q_\psi > 3). \tag{3b}$$

For $\kappa \geq 2$, the g-limit due to the external kink is insensitive to triangularity, δ, for $q_\psi \geq 3$ and high magnetic shear (low current density) near the plasma edge. The beta limit will increase with increasing plasma current if δ increases at fixed q_ψ.

The effect of triangularity on the beta limit has also been examined in detail both for cases with $q_0 > 1$ [2.2.8] and $q_0 < 1$ [2.2.6]. For $q_0 > 1$, several general classes of profiles are used [2.2.8]: broad current density with optimized pressure,

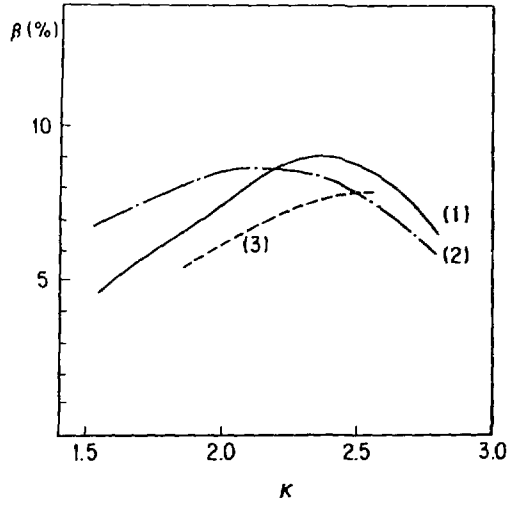

FIG. 2.2-2 β vs κ for $q_\psi \sim 3$. The curves (1), (2) and (3) denote the profile cases 1, 2, and 3. For Cases 1 and 2, the aspect ratio is A = 3; and A = 3.3 for case 3. The envelope of beta limits for different equilibria gives an almost constant limit for $2 < \kappa < 2.5$.

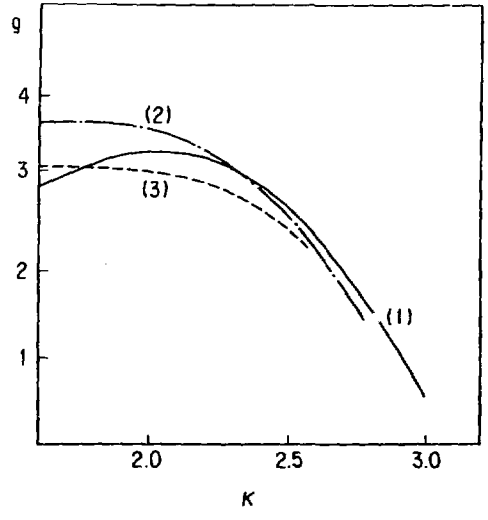

FIG. 2.2-3 g vs κ. For $q_\psi \geq 3$ and $\kappa \leq 2$ g reaches about an average value of 3.4 and decreases for $\kappa > 2$.

moderately peaked pressure with optimized current density, strongly peaked pressure with high-shear, optimized current density and highly peaked pressure with optimized q_o. For these cases the flux-surface averaged toroidal current density is specified, $I'(\psi) = \langle J_\phi \rangle$. Polynomial forms are chosen for $I'(\psi)$ and $p'(\psi)$. The optimum β is obtained with broad pressure profiles and triangularity has a weak effect for these profiles. In contrast, increased triangularity is found to be clearly favorable for peaked pressure profiles due to the increase in the magnetic shear near the plasma center. For an ITER configuration with $q_\psi \sim 3.1$, however, the predicted improvement in raising δ from 0.4 to 0.6 is shown to be small even for strongly peaked pressure profiles.

The stability of the internal modes depends strongly on δ when $q_o \leq 1$ [2.2.6]. Figure 2.2-4 shows that for internal kink modes the g-limit increases as a function of δ for three different pressure profiles [see 4(a)] and the flattest pressure profile near the axis reaches the highest g (and β) [see 4(b)]. This has been further demonstrated for profile case 2 by adopting an optimization procedure in which the pressure gradient is required to vanish in the region $q(\psi) < 1.1$ [2.2.9]. The profile with the lower central q produces higher magnetic shear in the outer plasma region and thereby supports a larger pressure gradient in this region. Using this optimization technique, the average beta value is increased for $q_o < 1$ due to the volume weighting effect.

An indication of the beta limit for a single null configuration compared with that of a double null for ITER is given in [2.2.9] for a restricted database. Pressure profiles optimized for ballooning modes are used in the analysis and for this study it is seen that external kink modes are more unstable for the asymmetrical configuration, for $\kappa_{upper} = 1.6$, $\kappa_{lower} = 2.4$ and $\delta_{upper} = 0.2$, $\delta_{lower} = 0.6$, $g^{max} \leq 2$ is found.

2.2.2.2 Profile effects on beta limit

A high beta discharge in DIII-D shows that $g = 3.3$ is attained ($\beta = 9.5\%$) with a pressure profile close to the form $p = p_o(1 - r^2)^{1.5}$, where r^2 is the normalized volume of a tube of flux; however near the edge the pressure falls off more rapidly. The density profile is flat to hollow and the temperature profiles fall off smoothly. This functional form of the pressure profile is roughly that of the ITER guidelines, where the recommended expression as a function of flux is $p = p_o(1 - \psi)^{\alpha_p}$ (with $\alpha_p \sim 1.0$–1.3). The pressure gradient near the edge, as indicated above, is somewhat larger than that of the ITER guidelines. Examination of the DIII-D operational space for q-values $2.2 < q_\psi < 2.8$ shows that the $l_i(1)$ values corresponding to $g > 3$ lie in the range $0.8 \leq l_i(1) \leq 0.9$, where $l_i(1) \equiv \langle B_p^2 \rangle / \langle\langle B_p \rangle\rangle^2$ [2.2.1], which is nearly equivalent to $0.6 \leq l_i(3) \leq 0.7$, where $l_i(3) \equiv (2V/R_o)\langle B_p^2 \rangle / (\mu_o I)^2$. These observed values correspond to ITER recommended values.

A β-saturation or decline (without disruptions) for peaked pressure profiles is observed on JET. The pressure profile is "triangular" (linear in the effective radius) with a flat to hollow density profile. The current density is relatively broad for these cases and is characterized by $l_i(3) \sim 0.7$. The beta limit on JET occurs for $g^{max} \sim 2.8$ by reducing the toroidal magnetic field. The limit is accompanied by beta clipping (a fast decline), beta collapse (a slow decline) and an increase in high frequency density fluctuations as g approaches g^{max}. Beta clipping is characterized by a rapid decline, on a time scale much faster ($\tau_{clip} \sim 100$ μs) than for the sawtooth crash ($\tau_{saw} \sim 10$ ms at low β). Beta collapse (or decline) occurs over a period of ~1–200 ms [2.2.10].

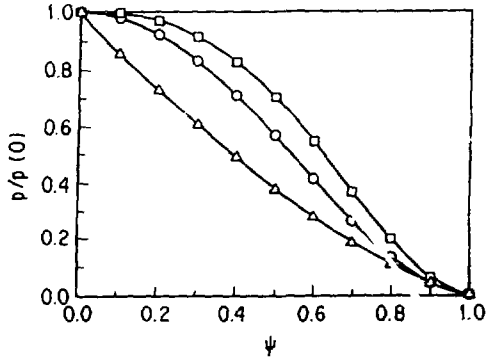

FIG. 2.2-4 (a) Pressure profile used for the analysis of internal kink modes.

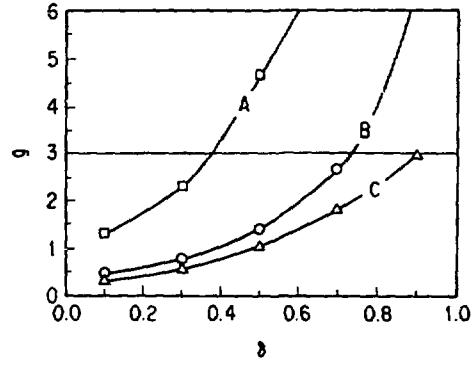

FIG. 2.2-4 (b) g vs δ. The symbols correspond to those in Fig. 2.2-4 (a). A flat pressure profile is favorable to reach high beta

Ballooning analyses of peaked (triangular) pressure profiles indicate that the stability of much of the volume is marginal ($0.28 \leq (\psi/\psi_{wall})^{0.5} \leq 0.55$) and near the center the plasma is unstable to ballooning modes. Extremely peaked pressure profiles, having a central region with $\alpha_p \gg 2$, and a broad pedestal from r/a = 0.5 to the edge, are produced by pellet injection, and a ballooning analysis in the center indicates that the stability limit for these profiles is exceeded by a factor 2. A q-profile with negative shear on axis is required to produce stability in this case [2.2.11].

Pellet injection in JT-60 generates very peaked density profiles with $n_e(0)/\langle n_e \rangle$ up to ~2.8. The profile is maintained for about 1 second. The measured electron density and temperature profiles are used for the analysis of n = 1 modes and the pressure and surface averaged parallel current profiles are parameterized to fit the measured pressure profile, q_o, l_i and the position of the q = 1 surface. The resultant q-profile shows high shear in the central region as $q_o < 1$, and in that region the high-n modes are stable even in the presence of a large pressure gradient. In the immediate vicinity of the magnetic axis this analysis assumed that the derivative of the pressure

with respect to poloidal flux was zero. JT-60 has a weak elongation and analysis shows the degradation in the internal kink limit for increasing κ [2.2.12]. Stabilization with increased triangularity is also suggested for higher κ.

Analysis of pellet injection cases in JET shows that "infernal" modes are unstable for very peaked pressure profiles with very flat central q profiles and $q_0 > 1$. An observed m=3/n=2 pressure collapse is suggested by a nonlinear MHD calculation for toroidal geometry and shaped cross-section. This linearly unstable mode at $q(\psi) \sim 1.5$ is shown to grow nonlinearly and lead to a ~30% collapse in the pressure [2.2.13].

In TFTR a wide range of density profiles are obtained in L-Mode, supershot, limiter H-mode, pellet fuelled, and detached-mode plasmas. While TFTR typically has large values of q_ψ, the supershot regime has only produced g values in the range of 2–2.5 for highly peaked current density profiles with $l_i > 1.4$ [$l_i(1) \sim l_i(3)$]. These highly peaked pressure profiles and the attained g values [2.2.14] correspond to a range of importance to ITER. In PBX-M quiescent discharges with $g > 2.5$ are obtained with low inductance ($0.45 < l_i(3) < 0.65$) and with moderate pressure profile peaking factors ($2 < p(0)/\langle p \rangle < 4$) [2.2.2].

Theory predicts that stability requires a lower l_i for a peaked pressure profile [2.2.15,16]. The results are shown with pressure profiles of the form of case 1 [Eq.(1a)] and with $\langle j \cdot B \rangle = j_0(1 - \psi^{\alpha_1})^{\alpha_2}$. Figure 2.2-5 shows the dependence of g on the exponent of the pressure profile (α_p) at marginal stability to $n = \infty$ modes for different l_i's. The case with $l_i(3) = 0.6–0.65$ corresponds to $\alpha_2 = 0.5$ and $l_i = 0.8–0.9$ to the choice of $\alpha_2 = 3.0$. However, the growth parameter (γ^2) oscillates continuously with n. This shows that the most unstable mode number is sensitive to q_0, since a small change in q_0 changes the peak position of $\gamma^2(n)$. The magnetic shear is very weak near the center for $q_0 \sim 1$ and the limitation on the pressure gradient near the center is more stringent when l_i is large and I is fixed. This shear profile causes an internal mode-like structure. The optimized pressure gradient has a maximum in the outer region of the plasma and a small reduction of the pressure gradient in the center can enhance the ballooning limit. In another calculation it was shown that the g limit for $n \leq 3$ is not much smaller than those for $l_i = 0.6–0.65$ for $q_0 = 1.1$. However, the sensitivity to q_0 may be stronger due to the weak shear and mode coupling.

The effect of pressure profiles is studied using data from DIII-D experiments [2.2.17]. Starting with an experimentally fitted p' profile with a nearly linear dependence on ψ, the pressure profile is adjusted to be optimized to ideal MHD modes. The average current density at the separatrix is constrained to vanish for this study and the value of $l_i(1)$ varied from 0.6 to 1.2. Placing the maximum p' near the edge produced a significant increase in the predicted g value for external modes (from ~3 to 6) for $q_\psi \sim 3.2$. In contrast, a significant increase in g^{max}, up to 6 for the kink limit, is obtained for a broad pressure profile of the form $dp/d\psi = p_0(\psi^2 - \psi^3)$ with a perfectly conducting wall at $a_{wall}/a = 1.5$. However, the high n ballooning limit is now more restrictive, with $g^{max} \sim 4.5$. Hence, for broad pressure profiles g increases with l_i, with beta limited by kink modes, while for peaked pressure profiles g decreases with l_i with beta limited by ballooning modes near the plasma center.

Peaked pressure profiles have been obtained in many experiments (DIII-D, JET, JT-60, TFTR results were described earlier). The analysis of experimental results in some instances has shown that the assumption of $q_0 < 1$ (suggested by the data) leads to an increase in shear that stabilizes localized modes. Analysis of the mode structure

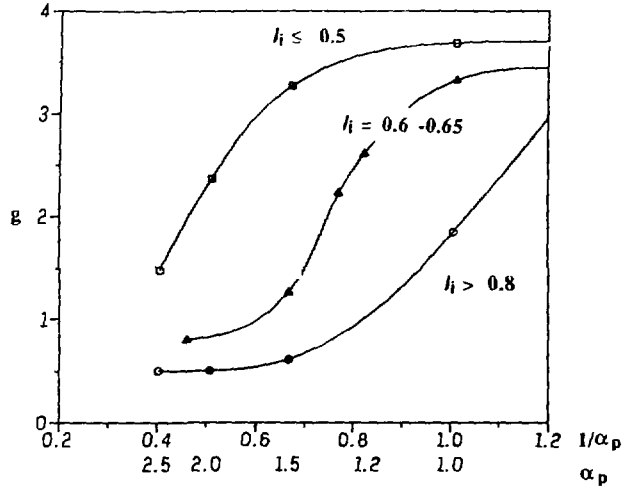

FIG. 2.2-5 g vs the peakedness of pressure profile for different l_i, when $q_0 \sim 1$. As the pressure becomes peaked, lower l_i is required to stabilize the ballooning modes near the plasma center.

of instabilities for strongly peaked pressure profiles has been made [2.2.18]. It is shown that broad pressure profiles may lead to a peeling type instability at the edge. On the other hand, peaked pressure leads to a strong coupling between a high-m (~6) external mode structure and the m=1/n=1 internal kink structure for $q_\psi \sim 5$.

Predictions for ITER must account for self-consistent neoclassical steady state profiles expected during long pulse inductive operation. The equilibrium profiles to be expected and the localized stability analysis have been studied [2.2.19]. It is shown that the bootstrap current is not the most important neoclassical effect for the physics phase, rather it is the large number of trapped electrons which increase the resistivity in a low collisionality plasma and steepen the conductivity profile on axis. This leads to highly peaked current density profiles with $q_0 \ll 1$ (as low as 0.24) where sawteeth effects are neglected. The strong shear created by such low q_0 stabilizes the Mercier and ballooning modes near the magnetic axis as shown in Fig. 2.2-6 [2.2.19].

2.2.2.3 Operation region and margin

Data in DIII-D shows an operational range at high values of g as well as higher absolute values of β which are up to ~ 9.5–11% (g ~ 3.1–3.3) transiently and at the level of 8% (g ~ 2.7) for 1 second. Improvements in the maximum values result from the ability to use $D^0 \rightarrow D^+$ injection. Double null diverted plasma operation allows attainment of I_N (≡ I/aB) as high as 3.3 for $q_\psi = 2.2$. The highest (transient) g value is reached at $I_N \sim 1.1$ while the highest absolute value of β is reached at $I_N = 2.7–3.3$. The highest value of I_N with a single null configuration is 2.5.

The accessible region in g–l_i operational space is also studied in DIII-D, through operation with q_ψ in the range 3–5. For $1.8 < \kappa < 2.2$, and $2 < q_\psi < 3$ the g–l_i

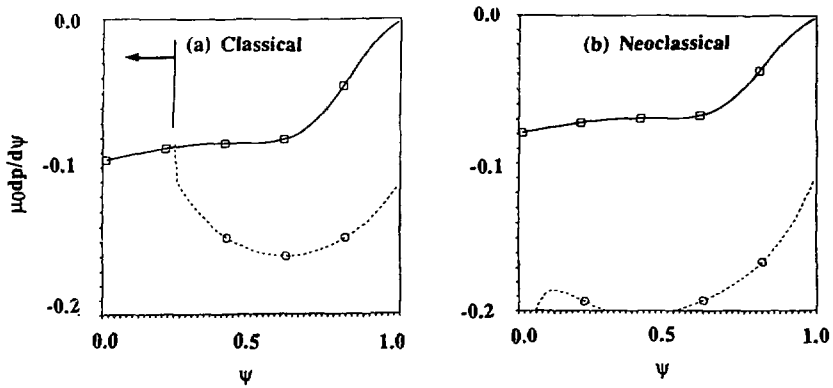

FIG. 2.2-6 Stability of localized modes for the classical (a) and neoclassical (b) current distributions.

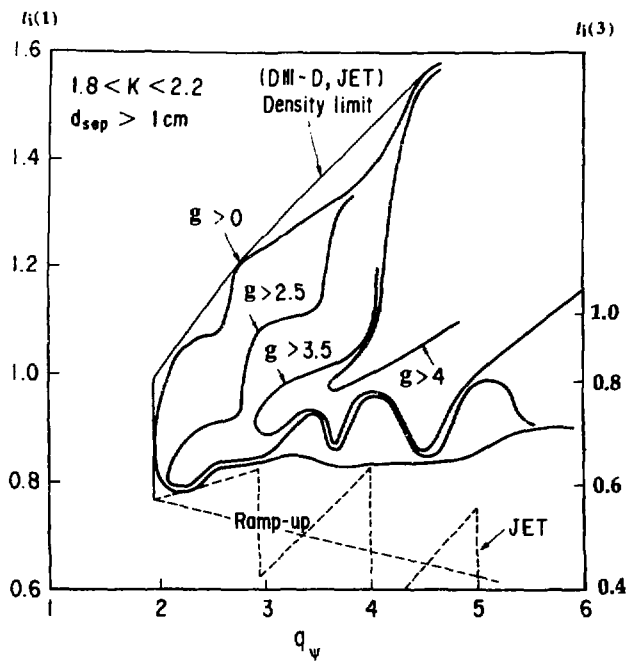

FIG. 2.2-7 The contour of g in l_i–q space of DIII-D experiments. The higher g values at $q_\psi \sim 3$ are obtained in lower l_i region. [$l_i(1) \sim 0.8$, $l_i(3) \sim 0.65$].

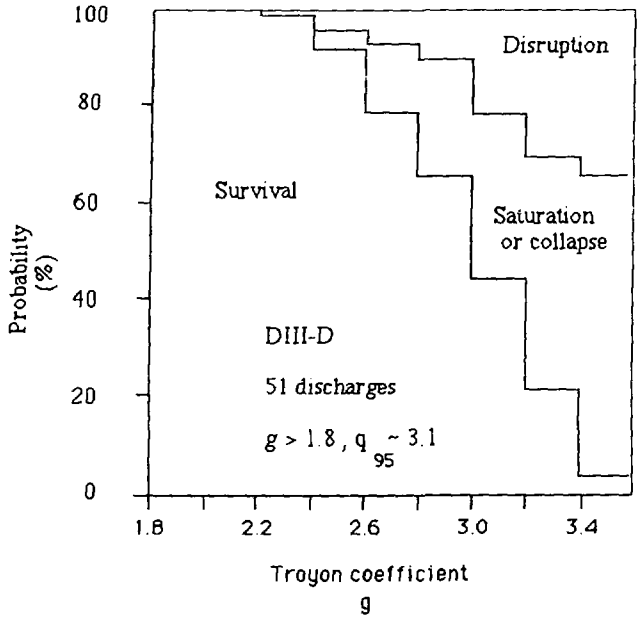

FIG. 2.2-8 Disruption and beta-collapse frequencies vs g in DIII-D experiments. For g > 2.5, the frequency of disruption and beta-collapse increases.

operating space is very narrow with values of g ~ 2.5 provided $l_i(1)$ is in the range 0.8 - 0.9 ; for $q_\psi \sim 3$ the range can be extended to 0.8–1.1. However, for $3 < q_\psi < 4$, g values above 3 are found for $0.9 < l_i(1) < 1.4$. For higher q_ψ (~4–6), g > 3 are found for $l_i(1) > 0.9$, and values g > 4 are generated for $1 < l_i(1) < 1.6$. Thus the following picture emerges: as q_ψ increases the available $l_i(1)$ space opens up with a simultaneous increase in the g values. This behavior is depicted in Fig. 2.2-7 where contours of constant g are shown in q_ψ–$l_i(1)$ operational space. The lower boundary is the standard one where there is some q-dependent limit that is observed to restrict current ramp-up. The upper boundaries are the improvements in stability with increasing q_ψ. Conversely the operating space shrinks as g increases. The "steady state" dependence of g on q_ψ has also studied in DIII-D. The discharges can be maintained for times ≥ 1 second with $g \geq 2.7$ for $q_\psi = 2.3$, with $g \geq 3$ at $q_\psi = 3.1$ and with $g \geq 3.4$ at $q_\psi = 3.8$. The reliability of operation in the regime where g approaches g^{max} has also been studied in DIII-D (Fig. 2.2-8, [2.2.1]) for 51 discharges with g > 1.8 at $q_\psi \sim 3.1$. Of these, 100% of the shots survived during the high-β phase for $g \leq 2.3$ [2.2.1], while for $g \leq 2.5$, the physics phase value of ITER, more than 90% avoided disruption, and as g increased further the frequency of disruption and saturation or collapse increased directly proportional to g.

To maximize the current it is preferred to limit the operation to $q_\psi \sim 3.1$ where g = 2.4–2.5 can be obtained for nearly steady state operation. For $2.5 < g < 2.7$, either a strong saturation in beta value (JFT-2M, Fig. 2.2-9 [2.2.20]), or a beta

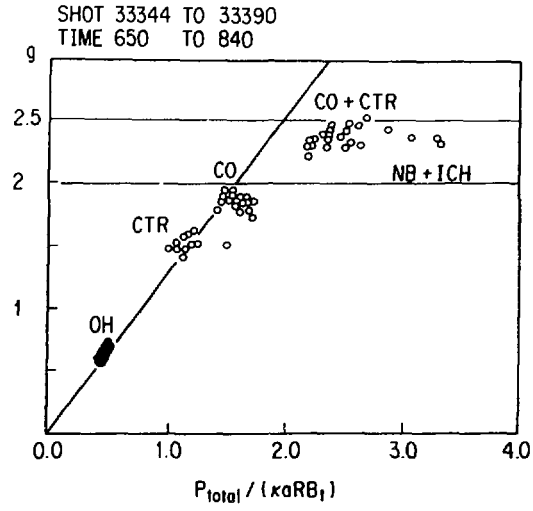

FIG. 2.2-9 g vs heating power in the JFT-2M tokamak. The g-value is limited to g = 2.5. For the combination of neutral beam and ICRF heating, the g value is limited to g ~ 2 for most cases.

TABLE 2.2-1. q-LIMITS IN EXPERIMENTS

Device	A	κ	I_N^{max*}	q_J
DIII (NB)	4.	1.6	1.1	2.0
PDX (NB)	3.2-4	1.	0.6	2.1-2.6
PBX (NB)	4.	2.0	1.5	2.1
ASDEX (NB)	4.1	1.	0.5	2.3
JFT-2M (NB+IC)	4.3	1.5	1.0(0.8)**	1.9(2.4)
DIII-D (NB)	2.7	2.0	2.5	1.9

* I_N^{max} is the maximum normalized current above which disruption or serious beta degradation occurs,
** Long duration with ELMs.

collapse/disruption occurs (DIII-D and ASDEX [2.2.21]) and higher beta (g ≥ 3) can only be attained transiently. It is not clear whether the transient profile can be sustained by a careful control of the profiles. The limits on I_N and q_J for high beta with g ≥ 2.4 are summarized in Table 2.2-1 [where $q_J = 5a^2B(1 + \kappa^2)/2RI$]. The condition $q_J > 2$ appears to describe the limit for plasma current in the experiments.

A new regime with ultra-high β_{pol} (~3.6), with $\varepsilon\beta_{pol} \sim 1.2$, has been obtained on TFTR, with $q_\psi \sim 20$–30 and $q_o \sim 2$. This profile should produce strong shear over the whole plasma. Detailed analysis is underway.

2.2.2.4 The m = 1 phenomena

Sawteeth oscillations of the electron temperature near the plasma center have been observed on most tokamaks and as much as 10% of the thermal energy can be lost in about 100 μs for intensely heated plasmas. During the process, the poloidal magnetic flux may be redistributed near the plasma center. Such m = 1 activity is considered to be a serious problem for controlling the burn of high-Q plasmas where the major heating power is supplied by alpha particles; in addition, sawtooth activity has a negative impact on plasma position control through possible uncontrolled changes in the internal inductance. On the other hand, sawtooth activity could help ITER performance by removing impurities (including He ash) from the plasma center.

The typical sawtooth oscillation cycle consists of a long period (up to seconds) of gradual change in the plasma equilibrium parameters, a precursor phase (not always observed) that may last from 10-to-100 ms and a sudden crash phase on the 10–100 μs time scale. During the precursor and crash periods a localized region of intense soft X-radiation is observed ("hot spot") along with a colder surrounding region with an m = 1 structure ("T_e island") [2.2.22, 23]. The magnetic field topology is an important determinant of the plasma behavior during a sawtooth cycle; however, it is not directly observable. Time and space-resolved soft X-ray emission (SXR), electron cyclotron emission (ECE) and time resolved external magnetic diagnostics are usually available. Some time- (or shot) averaged polarimeter or beam measurements of the q-profile (on JET, TFTR, TEXTOR [2.2.24], PBX-M [2.2.25], and ASDEX [2.2.26]) are available for the plasma state just before or after the sawtooth. Nonlinear, 3D MHD predictions of SXR and ECE signals are compared with these observations.

The experiments report a variety of sawtooth phenomena (Figs. 2.2-10 and 11). A "full" reconnection is observed on TFTR where the hot spot disappears during the fast crash phase (see Fig. 2.2-11). On the other hand, "partial" reconnections are observed on JET (see Fig. 2.2-10), TEXTOR and T-10 [2.2.27], while some nonlinear simulations predict only Kadomtsev-like, or "full" reconnection [2.2.28, 29]. Partial reconnection has been calculated in studies of hollow current density profiles. According to the full reconnection model the poloidal flux is exchanged during the crash within a region larger than the q = 1 radius. Experiments show values of $q_0 \sim 0.65$–0.77 [2.2.22], that is maintained during the whole sawtooth period [2.2.24], which is inconsistent with the full reconnection model. The sawtooth crash time is observed to be as much as 10 times faster than model predictions.

The length of the sawtooth period is required to estimate the impurity accumulation (or ash removal efficiency). Based on considerations of 3D modeling and fits to some experiments a semi-empirical model predicts the sawtooth time is proportional to $R^2T^{3/2}$ [2.2.28]. Among the present experiments, however, neither the temperature nor the size scaling are clear, although an increase of the sawtooth period with T is observed. Experiments show that the sawtooth period may easily be made as long as the experimental pulse length by using co-parallel injection, and with increasing difficulty by using balanced parallel and counter-parallel injection on TFTR [2.2.23]. This indicates that with heating or current-drive the q and/or j profiles can be changed and thereby lengthen the sawtooth period. Thus, the semi-empirical scaling of the period should probably be regarded as a scaling for the minimum time in ITER.

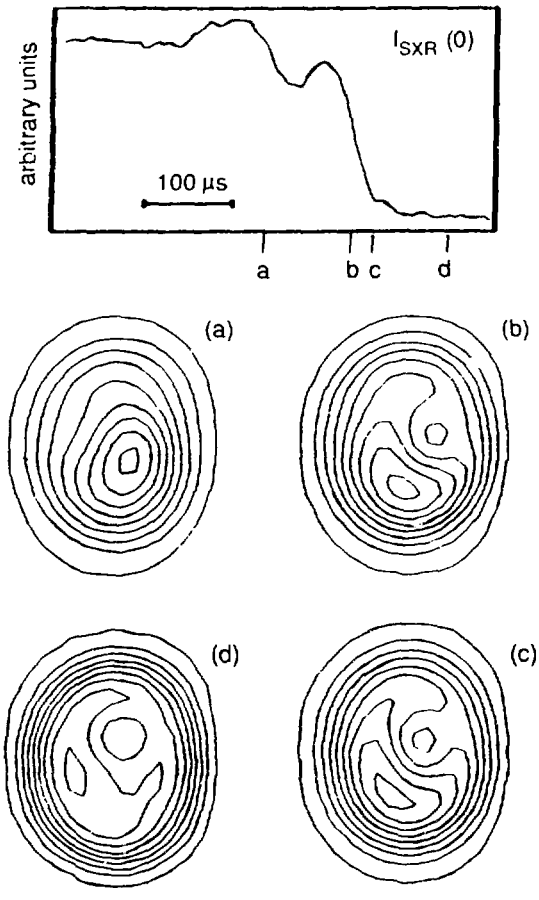

FIG. 2.2-10 Time evolution of T_e-island during a sawtooth crash on JET. The hot spot exists even after the crash (partial reconnection).

Reliable identification of sawtooth precursors is required for control. Numerical studies predict the existence of modes which grow slowly for the entire time of the sawtooth period, but for which the experimentally observable quantities such as "hot spot" displacements are detectable only milliseconds before the crash [2.2.29]. It seems that effects on the transport timescale, which are not included in the numerical models, may modify the detailed behavior, so that the prediction of crash times depends on detailed knowledge of the resistivity and thermal conductivity profiles. Experiments on TFTR show that there are often no precursors. Thus, no reliable predictions of sawtooth precursor phenomena can be made for ITER at this time.

Suppression of the sawtooth has been demonstrated experimentally with various methods: LHCD and counter NB injection on ASDEX [2.2.26], pellet injection and

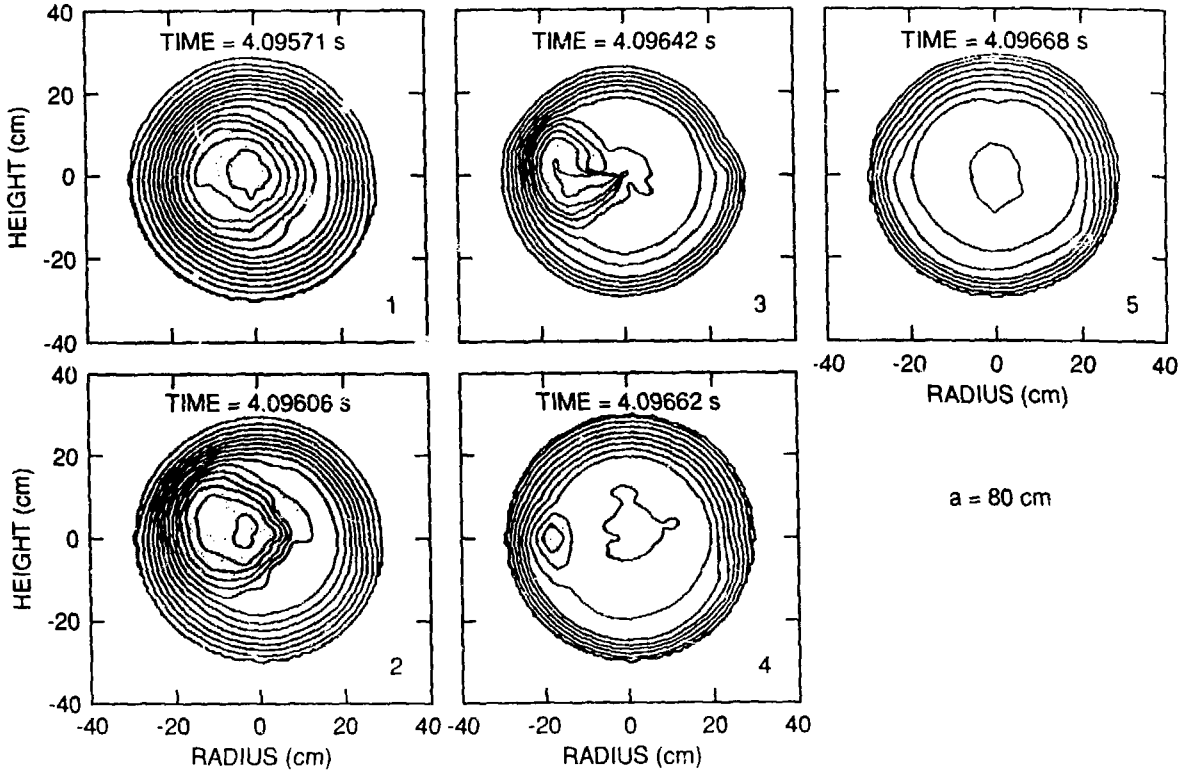

FIG. 2.2-11 Time evolution of T_e-island during a sawtooth crash on TFTR. The hot spot disappears after the crash (full reconnection).

ICRF heating on JET [2.2.22], parallel NB heating on PBX-M [2.2.25], co-injection on TEXTOR [2.2.30], and EC heating near the q = 1 surface on T-10 [2.2.27]. Among these methods, LH and NB are available for sawtooth control of ITER in the reference scenario for current drive and others may be available as alternative methods

Sawtooth stability is a fundamental problem for the steady state phase, since the neoclassical Ohm's law predicts that $q_0 < 1$. However, current can be injected in the direction of the main plasma current to broaden the j profile, especially near the edge, and to use the naturally peaked ohmic current in the center to provide the necessary shear. A relatively small counter-driven current (~38 kA), localized near the axis, can be used to raise q_0 to near unity (~0.9) [2.2.31].

Theoretical models do not make specific predictions of sawtooth effects on impurity accumulation or dispersal. Dispersal of central impurities is a qualitative prediction of full reconnection model, but there are discrepancies between experiments and this model regarding the degree of reconnection and its effect on plasma parameters.

2.2.2.5 Non-ideal effects

Dissipative effects are expected to modify the predicted beta limits for ITER. The predicted level of such modifications is usually estimated with a classical resistivity. Resistive MHD calculations show that the ITER optimized profiles with $q_\psi = 3.1$ are stable to resistive modes for $\kappa > 1.5$ [2.2.13]. Studies have also been made for non-optimal profiles in which both the current and pressure profiles are peaked [2.2.32]. For such profiles, $q_0 = 0.8$, and the resistive kink modes are unstable at zero beta. Perhaps more importantly, the classical resistive MHD model is inconsistent with the neoclassical equilibrium. Calculations show that the tearing modes which can be stable with classical resistivity, become destabilized with a neoclassical MHD model and that the island widths of saturated modes are increased [2.2.13]. There is no detailed comparison of this model with experiment as yet and this is a topic proposed for further study in the ITER long-term R&D plan.

A numerical study of possible stabilization of m = 2 instabilities with local current density around the q = 2 surface has been conducted for ITER. In addition, in an analytic calculation a more restrictive necessary condition can be found using a single helicity test function in a toroidal geometry. Application of this criterion shows a weak destabilizing influence on triangularity. The numerical results and ideal MHD studies show the opposite tendency, triangularity improves stability [2.2.33].

2.2.3 Predictions and Recommendations for ITER

2.2.3.1 General conclusion

Ideal MHD theory predicts a maximum value $g = g^{max} = 3\text{-}3.5$. However, this value is not a universal limit, but depends on the plasma shape and profiles. The range where g is almost constant is given by $q_J > 2$ with $\kappa \leq 2.0\text{–}2.2$; in this range q_ψ can be less than 3, but as indicated earlier, a conservative limit of $q_\psi \geq 3$ is recommended. These beta and g values are obtained from ideal MHD calculations for ballooning and low-n modes with optimized profiles of pressure and safety factor (or current density). Near the beta limit resistive and kinetic effects are expected to be important.

In experiments stable and nearly stationary operation is obtained with $g \leq 2.7$ (DIII-D), $g \leq 2.5$ (JFT-2M), and $g \leq 2.3$ (ASDEX). In ASDEX, g can reach 2.4 if the parallel beam pressure is included. The maximum value of g seems to be determined by current diffusion affected by impurity accumulation at the plasma center. In DIII-D large amplitude magnetic fluctuations are observed as g approaches 2.7, and beta disruption or collapse occurs for $g > 2.7$, the maximum achievable g being 3.5. The corresponding q-limits are $q_\psi \sim 2.2$, $q_J \sim 1.9$ (DIII-D and JFT-2M) and $q_\psi \sim 3$, $q_J \sim 2.3$ (ASDEX) (see Table 2.2-1). In DIII-D operation at lower q_ψ (~2.2) is possible with low beta, where the beta value is limited by energy confinement and available heating power. In ASDEX, the beta limit for $q_\psi \geq 3$ is usually non-disruptive, whereas disruption occurs during a transient phase for $q_\psi < 3$. For a relatively clean plasma and $\kappa \leq 2$, for performance predictions in ITER, $g = 2.5$ is recommended in the absence of efficient profile control (which is the case for ignition studies). For steady state operation with the use of current profile control, $g = 3$ is recommended. Optimistic projections to be covered as far as possible by the technical capability of the machine are $g = 3$ for ignition studies and $g = 3.3$ for steady-state operation.

2.2.3.2 Shape effects

In DIII-D the maximum g is almost independent of κ, for $\kappa \leq 2$. There is limited experimental data for $\kappa > 2$ and ideal MHD analyses are then used to predict the beta limit. An optimum shape, where the beta value takes its maximum, exists for the range $2 < \kappa < 2.5$ and the optimum value for κ depends on profiles and δ. For $\kappa > 2$, the triangularity plays an important role in the stability of the internal modes, e.g., at $\kappa = 2$ the minimum δ needed to achieve an appreciable beta is ~ 0.4. For $\kappa \leq 2$, theory shows that the envelope of the optimum beta values obtained for different profiles and $\delta \leq 0.5$ is essentially constant. Studies on aspect ratio dependence in the range $2 < A < 4$ with $\kappa > 1.6$ show a weak dependence of g^{max} on A. Calculations using non-optimized profiles have shown a dependence $g^{max} \sim A^{-1}$ [2.2.7], whereas $g^{max} \sim A^0$ when profiles are optimized for each aspect ratio [2.2.34].

2.2.3.3 Profile effects

Stable discharges are possible in the range $2 < q_\psi < 3$ but g may be small depending on profiles and δ and stability may require the presence of a conducting wall to eliminate external kinks. In addition, while the energy confinement in this region is much affected by sawteeth, ITER should however have the technical capability to operate in this range. For performance predictions though, $q_\psi \geq 3$ should be used. In the range $3 \leq q_\psi \leq 4$ the value $g = 3$–3.5 is theoretically achievable for optimized profiles. However, as said above, stable and stationary discharges in the experiment are limited to $g \leq 2.5$. For $q_\psi \geq 4$, a higher value of g may be possible with optimized profiles approaching the experimentally observed ones.

Operating with $q_0 < 1$ is possible, but there is the threat of an internal kink instability. When the radius of the $q = 1$ surface exceeds half the plasma radius the beta limit decreases rapidly. However, if the pressure profile can be flattened in the region $q(\psi) < 1.1$ region, the beta limit can be increased as a result of higher shear in the plasma exterior and an increase in the volume where the pressure is high.

Moreover, at large κ, triangularity can be very beneficial in improving the internal kink stability, again through an increase in the edge shear.

For a given current profile, elongation weakens the magnetic shear near the magnetic axis and, in this region the marginal pressure gradient for MHD modes becomes small and the peaking factor of the pressure $\langle p^2\rangle/\langle p\rangle^2$ is about 1.2 for profiles optimized for ballooning, internal and external kink modes. Optimized pressure profiles with $g \sim 3.5$ are close to $p = p_0(1 - \psi)^{0.7}$ and theory shows a decreasing g-limit as the peaking factor increases.

For $q_0 \sim 1.1$, the beta limits are larger for smaller l_i. Again, this is due to weak shear near the plasma center for large l_i when the central current density (or q_0) is fixed. The structure of the global modes shows a strong mode coupling between low-m and high-m components (m = poloidal mode number). The low-m components become large for a peaked pressure profile and large l_i. This indicates that the most unstable toroidal mode number is sensitive to q_0. Thus the ballooning limit for $l_i \geq 0.8$ is much reduced due to a weak shear near the plasma center; however, with a small local reduction of the pressure gradient the limit can be increased. On the other hand, for broad pressure profiles, kink modes limit the beta value and g^{max} increases with l_i due to increasing shear near the edge.

2.2.3.4 Summary and guidelines

From the data presented and discussions at several the specialists' meetings, the following conclusions are reached:

- No strong enhancement of the beta limit has yet been observed for $\kappa > 2.2$. The experimental results from DIII-D and PBX-M show $g \sim$ constant for up to $\kappa = 2$.
- The accessible domain in the $(g–l_i)$ space is considerably narrower for lower q_ψ than for higher q_ψ. For $q_\psi \sim 3$ and $g = g_s = 2.5$, which is recommended for the ITER physics phase, $l_i(3)$ has to be between 0.6 and 1.0 and g^{max} is obtained at $l_i(3) \sim 0.65$ [$l_i(1) \sim 0.9$]. To keep the operation margin (e.g., $g_s \sim 0.7g^{max}$) for reducing the disruption frequency, operation around $q_\psi \sim 3$ and $l_i(3) \sim 0.65$ is recommended. Operation with $q_\psi < 3$ may be possible but only a narrow stable region exists around $l_i(3) \sim 0.6$.
- At high q_ψ, the operation range in the $(g–l_i)$ space is wider and the possibility of higher g operation ($g^{max} > 3.5$) depends on pressure profiles. Theory suggests that high g operation may be possible for broad pressure profiles and high l_i.
- For current-driven operation in the steady-state phase, it is recommended that the value of $q_\psi–q_0$ be larger than 2 to provide sufficient global shear to reach the g values needed for stabilizing kink modes.
- The limit for the central beta of the fusion alpha-particles, due to the fishbone instability, is $\beta_\alpha(0) \sim 1–4\%$. This implies that there is a limit on the central electron temperature, typically at $T_e(0) \sim 30$ keV.

2.2.4 Major Issues Emphasized in the Future R&D Activity

2.2.4.1 Issues

To some extent theory can predict the boundary where the beta collapse and/or disruptions occur. However, the modes responsible for this at $g > (0.7–0.8) \times g^{max}$ vary with operational regimes and devices. Thus more detailed comparison between

theory and experiment is required to clarify the effect of pressure profiles, current density profiles and conducting walls. Similarly, the m /n= 1/1 instability responsible for sawtooth activity, which will strongly impact the burning plasma, is sensitive to the current profiles. It is important to have detailed experimental information on the current density profiles and the time dependent magnetic topology to compare with theory. There are of course shortcomings in theoretical models; for example it is thought that neoclassical and kinetic effects at the mode rational surfaces can be quite important. Most of the unresolved issues have been included in the future R&D programme [§10.0].

2.2.4.2 Future R&D tasks

The recommendations for future tasks that will resolve the remaining issues cover 5 areas: (1) characterization and control of β-limiting phenomena, (2) impact of profiles on the beta limit, (3) steady-state pressure and current density profiles in inductive operation, (4) impact of the m = 1 (sawtooth) mode on high beta operation, and (5) impact of fast-ion population on high beta operation.

Characterization and control of β-limiting phenomena

The detailed characterization of the high-β disruption and collapse phenomena is required to establish means to prevent their occurrence. This can be done by an experimental delineation of the accessible operational regime in the g-l_i and g-q_ψ spaces to distinguish the beta limit from other operational limits such as available power, confinement, and density. It is important to determine the parameter ranges in these spaces which are free of high β disruption and β-collapse (e.g., for times > 1 s, the duration of time depends on the device), and to further characterize the parameter ranges with regard to the frequency of high β disruption and/or collapse. It is also important to determine the responsible mode(s) for the disruption/collapse using high resolution diagnostics and detailed comparison with codes.

Impact of profiles on the beta limit

It is important to experimentally determine the explicit relation between the beta limit and pressure and current density profiles, and to make detailed comparisons of this limit with theoretical models relevant for ITER conditions. Peaked pressure profiles in ITER are favorable for high fusion reactivity at given β, and flexibility in the current density profile is desired both for the physics and the steady state (technology) phases. No definitive experimental data on these dependences are presently available.

For example, to study the pressure profile dependence, experiments should be performed in the same device, with the same global parameters (I,B), to make comparisons of the beta limits with NB and RF heating, with pellet and gas fuelling, for supershot and L/H mode conditions (if high-β is possible in an L-mode discharge). To explore the effects of current density profile, one can use NB and RF heating with the same P_{ext} and in the same device with the same global parameters to generate similar pressure profiles and then study plasmas with significantly different values of l_i. To explore the theoretically predicted 'ravine' phenomenon (regions with very low β-limit) one can use current ramp to produce finite dj/dr at the edge.

Steady-state pressure and current density profiles in inductive operation

The stability properties of steady state pressure and current density profiles arrived at during inductive operation must be determined. In prior analyses self-consistent profiles were rarely studied, rather analytic forms that covered a wide range of profiles were used. In the steady state of the inductive operation profiles will be constrained by Ohm's law. Direct experimental validation of the neoclassical form of Ohm's law is lacking, as are self-consistent theoretical evaluations of the beta limits for this unique profile. It is important to assemble experimental measurements to establish the proper form of the Ohm's law to use in shaped plasmas at high-β. It is also necessary to determine how recurrent sawtooth phenomena might modify the steady-state profile and change stability predictions.

Impact of the m = 1 (sawtooth) mode on high beta operation

Since the m = 1 mode has a strong influence on the current density profile it also has an impact on other modes responsible for setting the beta limit; consequently a detailed characterization of this m=1 mode in the high-β regime is required to develop means for control. This can be accomplished empirically by delineating experimental regimes which are free of sawtooth phenomena in $g–l_i$ and $g–q_\psi$ spaces. It is equally important to determine to which extent sawtooth activity can purge impurities from the interior. Detailed work is needed to characterize sawtooth behavior experimentally in the high-β regime in terms of frequency and amplitude, dependence on plasma shape, and its role in destabilizing other modes: e.g., 2/1, 3/2, continuous 1/1. Also attention should be paid to the "m = 1" induced major disruptions. Detailed comparisons with theoretical predictions are required.

Impact of fast-ion population on high beta operation

Lacking D-T operational capability in the short term, experimental tests must be devised to test the models using the production of energetic tails in the ion distribution functions to experimentally determine the role of fast particles in setting β and confinement limits. It is required to devise experiments which can be compared to theories which predict instability driven by fast-ion tails. For example, energetic ions produced with neutral beams or RF waves in existing experiments can be used to evaluate both the sawtooth stabilization as well as resonant particle driven MHD instability.

REFERENCES (§2.2)

[2.2.1] E.J. STRAIT, "Beta limits and low-q operation in DIII-D, " ITER-IL-PH-11-0-01-U.

[2.2.2] H. TAKAHASHI, "Pressure and current profiles and MHD activities in PBX-M," presented at ITER Specialists' Meeting on Beta Limits and Profiles, 5-7 March, 1990, Garching.

[2.2.3] J. HOGAN, "Linear ideal MHD stability calculations for ITER," presented at ITER Specialists' Meeting on Operational Limits, 6-10 June 1988, Garching.

[2.2.4] L. DEGTYAREV et al., "Linear ideal MHD beta limits in tokamak," ibid.

[2.2.5] M.W. PHILLIPS, "Effect of shaping on the stability of high current, high beta tokamaks," ibid.

[2.2.6] J. MANICKAM, "Effect of shaping and profiles on high beta tokamaks," ibid.
[2.2.7] J. HOGAN, "ITER beta limits and profiles", ITER-IL-PH-11-0-04-U, presented at ITER Specialists' Meeting on Beta Limits and Profiles, 5-7 March 1990, Garching.
[2.2.8] G. SCHULTZ et al., "Influence of triangularity and plasma profiles on ideal-MHD beta limits," ITER-IL-PH-11-0-02-E.
[2.2.9] L. M. DEGTYAREV et al., "Linear ideal MHD beta limits in tokamak, supplement to the report on the ITER Specialists' Meeting on Operational Limits," internal ITER memorandum (1989).
[2.2.10] P. SMEULDERS, "High beta regimes in JET," presented at ITER Specialists' Meeting on Beta Limits and Profiles, 5-7 March 1990, Garching.
[2.2.11] G.T.A. HUYSMANS et al., "Ballooning stability of JET high beta discharges," ITER-IL-PH-11-0-01-E.
[2.2.12] Y. KAMADA et al., "Ideal MHD stability of pellet fuelled plasmas in JT-60, " ITER-IL-11-0-02-J.
[2.2.13] B. CARRERAS et al., "Resistive stability in the region $2.5 < q < 3$," presented at ITER Specialists' Meeting on Beta Limits and Profiles, 5-7 March 1990, Garching.
[2.2.14] K. MCGUIRE et al., "Beta limit in TFTR," ITER-IL-PH-11-0-02-U.
[2.2.15] T. TSUNEMATSU, et al., "Pressure profile effect on ideal MHD stability," ITER-IL-11-9-01-J.
[2.2.16] J. HOGAN, "MHD equilibrium and stability studies for ITER physics work plan," ITER-IL-11-9-01-U.
[2.2.17] A.D. TURNBULL et al., "Dependence of tokamak beta limits on the pressure profiles," ITER-IL-PH-0-03-U
[2.2.18] J. MANICKAM, "The role of ideal instabilities in experiments," presented at ITER Specialists' Meeting on Beta Limits and Profiles, 5-7 March, 1990, Garching.
[2.2.19] S. TOKUDA et al., "MHD stability of tokamak plasmas obeying neoclassical Ohm's law," ITER-IL-11-0-03-J.
[2.2.20] H. MATSUMOTO, "Operational limits in JFT-2M," presented at ITER Specialists' Meeting on Operational Limits, 6-10 June 1988, Garching.
[2.2.21] O. GRUBER, "Energy Confinement and MHD Stability in ASDEX near the Beta Limit," presented at ITER Specialists' Meeting on Beta Limits and Profiles, 5-7 March, 1990, Garching.
[2.2.22] D. CAMPBELL, "Sawtooth activity in high beta plasmas in JET," ITER-IL-PH-11-0-8, presented at ITER Specialists' Meeting on Sawtooth Behavior at High Beta, 6-8 August, 1990, Garching.
[2.2.23] K. MCGUIRE, "Sawtooth effects on TFTR," ITER-IL-PH-11-0-9, ibid.
[2.2.24] H. SOLTWISCH, "Sawtooth activity in TEXTOR: magnetic field measurements," ITER-IL-PH-11-0-13, ibid.
[2.2.25] S. SESNIC, "q-profile measurements and fast-ion transport during sawtooth oscillations in NB heated plasmas," ITER-IL-PH-11-0-14, ibid.
[2.2.26] R. BUECHSE, "Tomographic studies of $m = 1$ sawtooth in various heating methods and confinement conditions on ASDEX," ITER-IL-PH-11-0-11, ibid.
[2.2.27] P. SAVRUKHIN, "Internal disruptions on T-10," ITER-IL-PH-11-0-10, ibid.
[2.2.28] W. PARK, "Finite pressure effects on sawtooth oscillations," ITER-IL-PH-11-0-18, ibid.
[2.2.29] A. AYDEMIR, "Tokamak sawtooth oscillations," ITER-IL-PH-11-0-19, ibid.

[2.2.30] H. CONRADS, "Sawtooth activity in TEXTOR during additional heating," ITER-IL-PH-11-0-12, ibid.
[2.2.31] S. TOKUDA, "Requirement for current density profile for sawtooth suppression," ITER-IL-PH-11-0-16, ibid.
[2.2.32] A. BONDESON, "Shaping and pressure effects on MHD stability of internal kinks," ITER-IL-PH-11-0-15, ibid.
[2.2.33] L.E. ZAKHAROV, et al., "m = 2 tearing mode stabilization with local Current Drive in ITER", ITER-IL-11-0-02-S.
[2.2.34] L.M. DEGTYAREV et al., "Shear and current density effect on tokamak kink mode instability," ITER IL-PH-11-9-01-S.

2.3 DENSITY LIMITS

2.3.1 Introduction

The necessity of achieving a prescribed wall load or fusion power essentially determines the plasma pressure in a device like ITER. The range of operation densities and temperatures compatible with this condition is constrained by the problems of power exhaust and density limits. The maximum allowable heat loads on the divertor plates and the maximum allowable sheath edge temperature, as well as considerations of pumping speed, impurity reduction, and runaway production impose a lower limit on the operating densities, whereas the density limit imposes an upper limit. For most of the density limit scalings proposed in the past an overlap of the two constraints or at best a very narrow accessible density range is predicted for ITER. Safe prediction of the densities accessible in ITER is therefore crucial for achieving the projected performances of ITER.

Density limits may be associated with the occurrence of disruptions (disruptive density limit), confinement regime transitions (H-L transition) or resistance to further density increase (refuelling limit). Most of the effort on density limits has concentrated on the disruptive density limit in L-mode discharges. Refuelling limits have been observed only recently in JET and JT-60.

In this summary emphasis is placed on the results and concepts that have played a major role during the ITER conceptual design phase, but it is not intended to give an exhaustive review the field.

2.3.2 L-mode Density Limits

2.3.2.1 General picture

In the overwhelming majority of L-mode discharges the density limit is a disruptive limit. A widely accepted picture of the general mechanism that triggers high-density disruptions and thus determines the density limit has evolved. In this picture cooling of the plasma edge leads to shrinking of the current channel, which destabilizes the m/n = 2/1 tearing mode when the $q_\psi = 2$ surface is reached. In principle, a variety of mechanisms may cause edge cooling. Charge exchange and ionization losses as well as anomalous transport may have an indirect impact because it affects the plasma density at the edge and is important in determining recycling. The triggering mechanism is conceived as a loss of thermal equilibrium or destabilization of thermal equilibrium somewhere outside the $q_\psi = 2$ surface. Different concepts have

been proposed, which differ in the weight given to the different loss mechanisms and the part of the discharge where the initial loss of equilibrium/stability is localized (edge cooling by anomalous transport in the bulk plasma periphery, loss of thermal equilibrium in the divertor region, radiation from the bulk plasma edge, etc.).

Schematically, three phases can be distinguished in a typical discharge ending in a density limit disruption: the quasi steady-state phase, a nonlinear phase, where some characteristic parameters show strong nonlinear variation (e.g. radiation), and the final disruptive phase. Experimental studies focus on all three phases. Modelling studies up to now have been limited to the quasi-steady-state phase and the evolution of threshold conditions for the onset of the nonlinear phase. In addition, both experiment and theory provide information on the scaling of the critical density. The material presented in the following is structured along these lines.

2.3.2.2 Experimental studies

General aspects:

In dedicated density limit studies the critical density is usually approached by a slow, quasi-steady-state density rise. Other ways of approaching the limit (slow I reduction, B reduction) do not change the picture. In this way steady-state or near-stady-state situations are obtained. Density limit disruptions may also occur during transient phases (density ramp-up, end of heating phase, current decay). There is no indication of an intrinsic difference between these two different cases and transient density limit disruptions are naturally explained as an approach to the density limit in the course of variation of discharge parameters.

One of the most important results obtained during the past years has been the direct experimental confirmation that the density limit is an edge density limit (ASDEX [2.3.1], JET [2.3.2,3], JT-60 [2.3.4], TFTR [2.3.4]). In particular, improvement of the line average density limit as observed on ASDEX in confinement regions with peaked density profiles and generally in pellet-fuelled discharges is naturally explained as a profile effect.

The question of the radiative power fraction at the density limit has recently gained considerable interest, which was triggered by the observation made on JET carbon limiter discharges [2.3.5,6] that ("radiative edge"): (i) $P_{rad} = P_{in}$ holds at the limit (where P_{in} is the total input power and P_{rad} is the radiated power), which is predominantly radiated from the plasma periphery and (ii) the radiation mantle grows inwards and the disruption occurs when the $q_\psi = 2$ surface is reached.

There is now overwhelming evidence from different devices (JET [2.3.4], ASDEX [2.3.1], JT-60 [2.3.4], T-3 [2.3.7]) that P_{rad}/P_{in} may be considerably below unity when the disruptive process develops. This rules out the radiative edge concept as unique triggering mechanism. In this context it is essential to distinguish carefully between P_{rad}/P_{in} at the onset of the disruptive phase and later, when 100% radiation is always found (JT-60). 100% radiation seems to be associated with high Z_{eff} but is obviously not intrinsic to limiter configurations as suggested by previous results (JET, TEXTOR, TFTR). ASDEX observations strongly support a divertor-based picture [2.3.4]. The strong impact of recycling on the density limit, in TUMAN 3 [2.3.4] as well as the interpretation of T-10 results (see §2.3.2.3) point in the same direction. Despite some progress the problem of the underlying triggering mechanism

remains, however, unresolved. In particular, it is not clear whether a universal triggering mechanism exists at all.

Selective scaling studies:

Experimental scaling relations, together with model predictions, provide the basis for extrapolation to ITER. From the general picture it is concluded that the critical (separatrix or plasma boundary) density has the form

$$n_s^{crit} = n_s^{crit}(a,R,\kappa,q,B,P_{in},...) \quad (1)$$

provided that a simple description by global parameters is possible. Scaling studies, including systematic experimental scans and statistical analysis of accidental data, are reported from practically all tokamaks. Apart from a reported DIII-D size scaling study [2.3.8], these investigations are typically restricted to variations of q (safety factor), B (toroidal field), P_{in} (input power) and κ (elongation). In the ohmic domain a Hugill-type scaling is generally observed [$n^{crit} \sim B/qR$; there is some difference in the q definition applied (q_ψ, q_I, q_c), but in most cases the current q, $q_I = (2\pi/\mu_0)(a^2B/RI)(1 + \kappa^2)/2$, seems to be the most appropriate scaling parameter]. Studies in the ohmic domain are hampered by the intrinsic dependence of P_{in} on q, B,... and results from discharges with strong additional heating are therefore needed to determine the power dependence of n^{crit}. Considerable divergence is observed in the power scaling ($n^{crit} \sim P^\alpha$). Very weak power dependence is observed in DIII-D [2.3.2,8], JFT-2M [2.3.2], and TEXTOR [2.3.4] ($\alpha \approx 0.1$–0.3). JET and JT-60 [2.3.4], however, report $\alpha \approx 0.5$. This holds in both devices also for discharges where the disruption is not triggered by radiative collapse ($P_{rad}/P_{in} < 1$). A particular situation is given in ASDEX, where $\alpha \approx 0.5$ has been observed in the "old" divertor configuration [2.3.9], while much weaker power dependence is observed in the present divertor configuration, which is characterized by a reduced escape probability of neutrals [2.3.1,10]. The dataset also suggests a correlation between the power and q-dependence. While in the "old" ASDEX and in JET the q-dependence is weak ($n^{crit} \sim 1/q^{0.2-0.4}$) [2.3.9,11], one has $n^{crit} \sim 1/q$ in cases where α is small (~0.1–0.3 "new" ASDEX [2.3.1], DIII-D [2.3.2,8], JFT-2M [2.3.2]). Typically the latter group seems to be described by a Hugill/Greenwald-type scaling (see Fig. 2.3-1), while devices of the first group clearly violate this kind of scaling.

The JT-60 data reported ($\alpha \sim 0.5$; Hugill-type scaling in the presence of additional heating [2.3.4]) seem to contradict this picture. Detailed inspection shows, however, a flattening of the power dependence for high powers, i.e. for those points which define the high-density boundary in the Hugill plot. In TEXTOR the situation remains somewhat unclear due to the limited number of discharges with additional heating. Recently, edge-based density limit models have been proposed which predict both kinds of behaviour (see §2.3.2.3).

Discrete parameters include first-wall/limiter material (ASDEX, JET, JFT-2M, TEXTOR), the working gas (JFT-2M), and the magnetic configuration (X-point/limiter; JFT-2M) [2.3.4,8]. The main impact of different first-wall conditions seems to occur through the impact on the bulk plasma purity, which determines the power flux into the plasma edge. The improvement usually observed with higher purity would thus essentially reflect the power dependence. The impact of the working gas and the configuration on the critical density are moderate. Generally, these discrete parameters

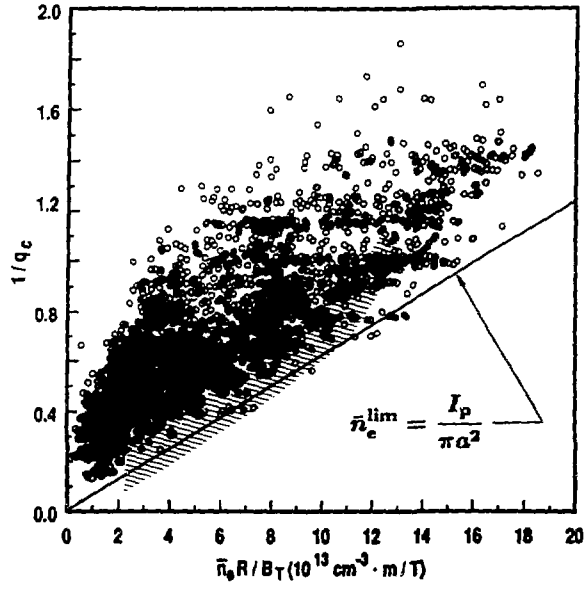

FIG. 2.3-1 Data from the DIII-D data bank. The Greenwald limit is also shown. Most of the data points are H-mode discharges. The cross-hatched region is covered by ohmic/L-mode study. In this case the Greenwald limit appears to apply to ohmic, L-mode and H-mode discharges.

do not seem to affect the scaling of the critical density. Pellet refuelling versus gas puffing studies have been reported from ASDEX [2.3.1], JET [2.3.2], JT-60 [2.3.4], JFT-2M [2.3.4] and TFTR [2.3.4]. Pellet refuelling generally leads to significantly higher line average densities, but no effect on the critical edge density is observed (ASDEX, JET, JT-60, TFTR), confirming that the density limits are edge limits.

General scaling relations:

For extrapolation to ITER the scaling with respect to all relevant parameters has to be known. The first scaling, which was frequently interpreted as a universal density limit scaling, was proposed by Hugill for the line-averaged density:

$$\bar{n}_e^{crit} = h\,(B/Rq) \qquad (2)$$

with $h = 2$ for $\bar{n}_e^{crit}$ in 10^{20} m^{-3}, B in T, and R in m. (As to the q definition to be used see earlier discussions.) As noted this form of scaling is generally observed in ohmic discharges but the coefficient varies between different devices, indicating hidden parameters. The Hugill value of $h = 2$ seems to be the optimum that can be achieved in clean gas-puff fuelled discharges.

On the basis of the analysis of data from ALCATOR C, Doublet III, and PBX, Greenwald proposed the scaling [2.3.12]

$$\bar{n}_e^{crit} = f\,\kappa J, \qquad (3)$$

where the units are (10^{20} m^{-3}; MA/m^2), κ is the elongation, J is the mean plasma current density, and $f \sim 1$ is claimed to hold independently of the heating mechanism or refuelling method. Apart from the beneficial dependence of elongation, Eq. (3) is essentially identical to the classical Hugill limit when $q = q_c$ is adopted.

Both scalings are hampered by the fact that they do not reflect the frequently observed power dependence and that the density limit is an edge limit. Also, the beneficial scaling with elongation, as predicted by the Greenwald scaling, has not been confirmed in dedicated studies on JFT-2M [2.3.8]. Thus the proposed scalings, although adequate in certain cases, do not provide a universal description of the experimental observations and hence do not provide a reliable basis for extrapolation to ITER.

2.3.2.3 Modelling studies

Borrass model:

K. Borrass proposed an analytical model of the scrape-off layer/divertor region where loss of thermal equilibrium in front of the divertor plate is the basic triggering mechanism for a density limit disruption [2.3.13]. The model is basically a 1-D edge model from which a global, two-temperature model is derived. It provides a relation between the separatrix density, n_s and the divertor temperature T_D which is the basis for the derivation of a density limit:

$$n_s = C \frac{B^{5/16} Q_\perp^{10/16}}{L^{1/16}} \frac{T_D^{11/32}}{\left\{ \xi\beta + \frac{Q_{rad}}{\bar{c}\, T_D^{1/2}} + \gamma T_D \right\}^{11/16}} \qquad (4)$$

Here $Q_\perp$ the net power flux across the separatrix, L is the connection length ($L \sim qR$), and Q_{rad} is the impurity radiation loss term in the power balance equation. $\bar{c}$ is defined by $c_s(T) = \bar{c}\, T^{1/2}$, where c_s is the ion sound speed. The shape of n_s vs T_D is determined by the last term of Eq. (4). The terms in the curly brackets are the loss terms associated with ionization, impurity radiation, and the power flux into the sheath region. ξ is the average ionization energy of a neutral and β is the fraction of neutrals that are ionized in the flux tube under consideration, while $1 - \beta$ is the fraction of pumped neutrals. γ is the sheath energy transfer coefficient. A typical shape of the right-hand side of Eq. (4) is shown in Fig. 2.3-2. Formally, a density limit is established by the fact that n_s [$\propto f(T_D)$] has a maximum, which is interpreted as the critical density. For points above the limit curve of Fig. 2.3-2 the energy balance in front of the divertor plate is negative. Therefore, for $n_s > n_s^{crit}$ the divertor temperature collapses. This collapse is taken as the triggering mechanism for a density disruption.

An essential ingredient of the model is the treatment of recycling and impurity radiation. Mainly as a consequence of the pressure balance $Q_{rad} \sim T_D^{-3/2}$ holds for fixed n_B. Therefore, though impurity radiation is only a small loss at $T_D = T_D^{crit}$ (where T_D^{crit} is the temperature where n_s has its maximum), it rapidly grows for low T_D. For high T_D the term γT_D dominates ($\gamma \approx$ const.). These two terms always provide the existence of a maximum and hence a density limit. A diffusion model for recycling, based on diffusion of neutrals by charge exchange reaction, has been proposed which includes outward diffusion of neutrals near the plate, diffusion into the fan and pumping [2.3.13] and is comprised by β in Eq. (4). While ξ is nearly

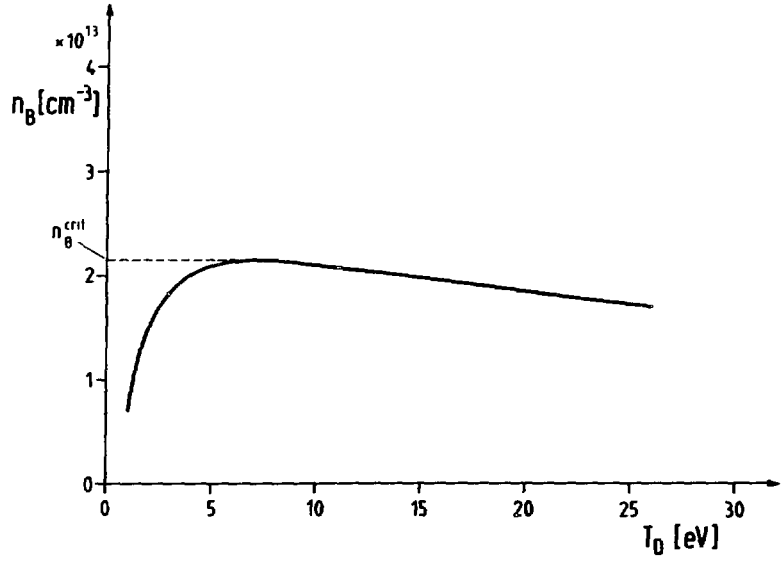

FIG. 2.3-2 n_S (=n_B) vs T_D: typical shape of the right-hand side of Eq. (4).

constant, β may show larger variation and is responsible for details of the density limit behaviour (see below).

The density limit model has been extensively validated using ASDEX density limit results. As noted, the ASDEX density limit behaviour changed significantly after reconstruction of the ASDEX divertor [2.3.10]. A q-scan for ohmic and constant neutral beam power of 1.7 MW obtained in the old configuration is shown in Fig. 2.3-3 [2.3.9]. [Note: if not otherwise stated, q is the cylindrical safety factor.] The results are well described by the model (except for very low q-values, where ASDEX shows a characteristic depletion which is presumably related to MHD phenomena). In this regime numerical sensitivity studies yield the scaling

$$n_s^{crit} \approx 1.54\ (Q_\perp^{0.43}\ B^{0.31})/(qR)^{0.45} \qquad (5)$$

(n_S in $10^{20}\,m^{-3}$; B in T; $Q_\perp$ in MW/m^2, R in m), where n_s is the electron density at the separatrix, $Q_\perp$ is the net power flux across the separatrix. A much weaker power dependence was observed in the new configuration (see Fig. 2.3-4). The difference between the two configurations is interpreted as being a consequence of the different divertor designs (characterized by the pumping probability of neutrals hitting the wall in the present model). This probability (estimated in ASDEX from gas consumption measurements and the divertor geometry) is found to be ≈ 0.1 in the old and ≈ 0.05 in the new configuration. With this input the model reproduces the weak power dependence in the new configuration (see Fig. 2.3-4). In this regime of weak power dependence also an inverse q-scaling ($n^{crit} \sim 1/q$) is predicted in agreement with recent ASDEX results [2.3.14]. The model thus allows both types of scalings observed experimentally and gives a physical picture for the different types of behaviour.

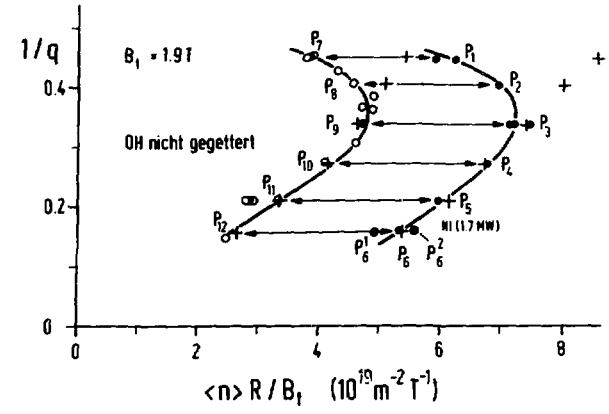

FIG. 2.3-3 Hugill plot for the ohmic case and neutral injection of 1.7 MW measured in the old ASDEX configuration. Experimental points are redrawn from Fig. 2.3-1 of [2.3.9]; calculated points (+) are added.

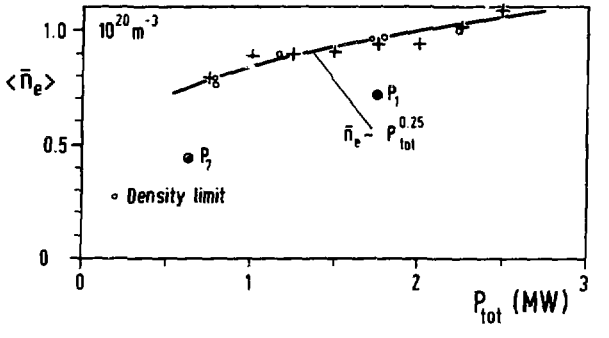

FIG. 2.3-4 Power scan obtained in the new ASDEX configuration at q = 1.96 and B = 1.9T. Experimental points are redrawn from [2.3.10]; calculated points (+) are added.

The different regimes discussed so far resulted from different recycling conditions. In these regimes $\beta < 1$ holds and formally the different regimes are distinguished by the way in which β varies with external parameters (q, $Q_\perp$, B,...). In ITER, since the divertor temperature will be higher (see below) and the divertor plasma in an open configuration is thicker, the probability that a neutral may escape from the divertor plasma is very low (~10^{-3}) and therefore $\beta \approx 1$ holds [2.3.15]. In this regime numerical scaling studies result in [2.3.15]

$$n_s^{crit} \approx 0.5\ (Q_\perp^{0.57} B^{0.31})/[q_\psi(95\%)R]^{0.09} \qquad (6)$$

which applies to an ITER-like double null divertor configuration [units as in Eq. (5)].

The proposed model has a number of implications for edge physics and the related problem of divertor design. As follows from Fig. 2.3-2, the critical density is reached at a finite divertor temperature T_D^{crit}. Values of T_D^{crit} of 20–40 eV result for ITER [2.3.13], but this prediction may be modified when improved models become available. Erosion of the divertor plates is largely determined by the sheath edge temperature. Values of up to about 30 eV would be acceptable for graphite plates, while the acceptability for tungsten plates essentially depends on the retention of tungsten. The divertor temperature might therefore be a matter of concern. In present 2-D modeling of ITER edge conditions impurity radiation is not included. In that case the n_s–T_D relation according to Eq.(4) becomes monotonic, formally permitting arbitrarily low T_D values [2.3.13]. Present values resulting from 2-D modeling range from 6–20 eV for the reference scenarios [2.3.16, also §3.4]. Impurity transport and impurity radiation must be included in future 2-D modeling for further clarification.

In principle, all edge physics conditions adopted with a view to divertor design requirements should be compatible with scrape-off layer based density limits if the underlying physics assumptions are the same. The most favorable divertor conditions would be achieved by operation close to the limit. A problem arises in situations with asymmetric power distribution between the outboard and inboard scrape-off layer as is expected in double-null configurations like ITER (4:1 ratio according to ITER guidelines), although more recent observations in ASDEX H-mode discharges suggest a ratio of 2:1. Under these conditions the inboard channel determines the critical density while the outboard channel, which is most critical for divertor design, is still relatively far away from its limit [see the $Q_\perp^{0.5}$-dependence in Eq.(6)]. This problem is characteristic of all scrape-off layer based density limits with power dependence.

Loss of cooling in the ITER divertor region or failure of the burn stability control system will result in significant damage to plasma-facing components unless the fusion power is reduced to zero within a few seconds (emergency shutdown) [2.3.17]. In the presence of a power-dependent scaling according to Eq.(6) and for an operation point close to the critical density, ramp-down of the power flux into the scrape-off layer requires simultaneous density decrease to avoid a density limit disruption. Non-disruptive emergency shut-down is therefore intrinsically limited by the particle confinement time under these conditions.

Krasheninnikov-Yushmanov model

This model includes, in addition to the scrape-off layer, the bulk plasma periphery. A global scrape-off layer model, including analysis of the plasma energy and particle balances, neutral particles and impurity radiation, is used to derive the relations between edge values of temperature and density (T_s,n_s) and the corresponding total fluxes across the bulk plasma boundary (Q_s,Γ_s), which are used as boundary conditions for the 1-1/2 D description of the bulk plasma [2.3.18,19]. The scrape-off layer model has been analyzed analytically and numerically. The solutions of this model are conveniently expressed in terms of Q_s and Γ_s. Various regimes in the Q_s–Γ_s plane can be distinguished by (i) characteristic values of the recycling coefficient R, the convective fraction of the heat flux to the scrape-off layer and the radiative loss fraction in the scrape-off layer and (ii) the way in which the boundary density n_s depends on Γ_s. The existence of a density limit is associated with regimes where $n_s(\Gamma_s)$ shows weak or even negative dependence. In this regime even

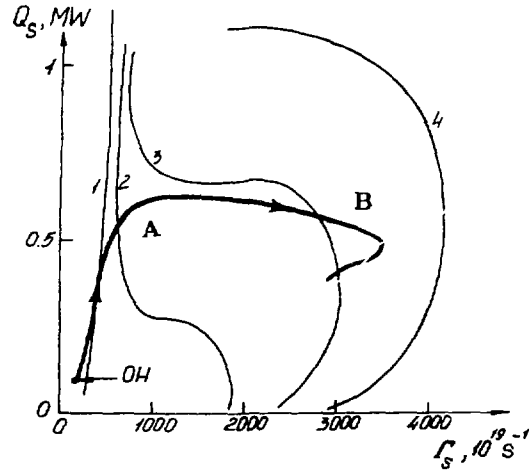

FIG. 2.3-5 Simulation of T-10 density limit discharge with additional heating (shot No. 48225). The heavy solid line is the calculated trajectory (coupled 1-1/2-D code plus edge model) in the $Q_s - \Gamma_s$ plane. The thin lines are lines of constant boundary density, with the densities given in units of 10^{19} m^{-3}. Between points A and B n_s is approximately constant. Nevertheless Γ_s increases due to the weak dependence of n_s on Γ_s (see adjacent curve with $n_s = 3 \times 10^{19}$ m^{-3}). The decrease of Q_s near B is caused by the increased radiation losses.

a small increase of n_s leads to a strong increase of Γ_s (see Fig. 2.3-5), this being associated with a corresponding increase of the influx of recycling neutrals which leads to cooling of the edge. Increased impurity influx, associated with enhanced recycling, as well as an edge transport law with adverse density and temperature dependence are supposed to amplify this effect. The thick line in Fig. 2.3-5 is the trajectory of a disruptive T-10 discharge. In Fig. 2.3-6 the time evolution of the same shot is given and compared with modeling results [2.3.20].

More detailed validation of the model by T-10 results and data from other machines are needed. The analysis for ITER-like devices remains to be done.

2.3.3 H-mode Density Limits

Experimental data on the H-mode density limit are very scarce. Studies have been performed on DIII-D [2.3.2], JFT -2M [2.3.4] and ASDEX [2.3.21,22].

On DIII-D the H-mode density limit seems to be disruptive and, if expressed in terms of the line average density, obeys the same scaling as the L-mode limit (see also Fig. 2.3-1). Recently two low-q H-mode density limit shots have been performed on ASDEX, where the limit was approached by slow density ramp-up (P_{NB} = 2 MW). The line average density exceeds that in similar L-mode shots (P_{NB} = 1.7 MW [2.3.1]) by about 20%. Comparison of the edge density is under preparation. Both discharges end in a disruption without re-entering the L-mode.

In JFT-2M the H-mode density limit is manifested as an H-L transition [2.3.2,4]. The H-mode in JFT-2M is almost ELM-free so that the density generally

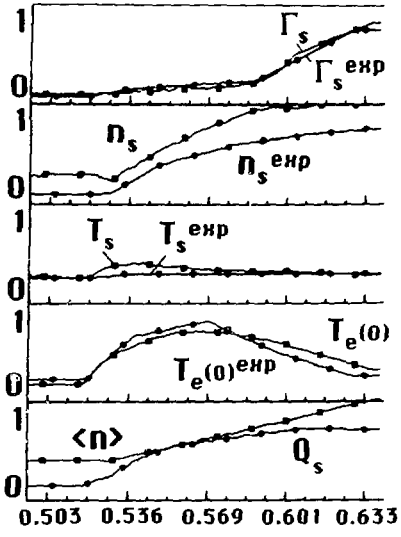

FIG. 2.3-6 Time evolution of T-10 shot No. 48225. Given are experimental and calculated values for volume-averaged density (n) (in units of 5×10^{19} m^{-3}), total heat flux across the plasma boundary Q_s (in units of 2 MW), central electron temperature $T_e(0)$ (in units of 6 keV), boundary temperature T_s (in units of 100 eV), edge density n_s (in units of 3×10^{19} m^{-3}) and the particle flux across the boundary = Γ_s (in units of 3×10^{22} s^{-1}) versus time (in s).

increases until the transition occurs. Enhanced radiation triggers the H-L transition and it is expected that higher densities could be achieved in cleaner discharges. The H-mode density limit in JFT-2M shows weak power dependence ($\sim P_{in}^{0.2-0.3}$).

These results indicate that for sufficiently clean discharges the H-mode density limit is disruptive and that the achievable line average densities are comparable to or higher than those achieved under L-mode conditions. In the light of the comparatively flatter shape of H-mode density profiles this indicates a gain in edge density.

The models discussed should apply equally well to H-mode discharges with the proper perpendicular transport adopted. The tentative values given in Table 2.3-1 (see §2.3.4) are consistent with the above picture.

2.3.4 Projections to ITER

From the preceding discussion it follows that the basis for extrapolation to ITER is still limited. Table 2.3-1 summarizes some projections for three representative ITER operation scenarios. The steady-state, low-density/high-temperature scenario is the least critical one, but it is rather questionable as regards divertor design limitations because of the high divertor temperature resulting as a consequence of the low separatrix density.

The empirical Hugill and Greenwald scalings are only given for comparison. For the ignition and hybrid scenarios the Borrass model predicts somewhat lower values than assumed. This is obvious from the preceding discussion (§2.3.2.3).

TABLE 2.3-1. DENSITY LIMIT PROJECTIONS FOR ITER

[$\bar{n}_e$ = line-average electron density (in units of 10^{20} m^{-3}). $\bar{n}_e/n_s = 4.13$ is assumed in accordance with the ITER physics guidelines. $P_{in} = P_\alpha + P_{add} - P_{rad}$ is the net input power. Device parameters: a = 2.15 m, R = 6 m, $\kappa_{95} = 1.98$, and $B = 4.85$ T.]

Operation scenario			Ignition	Steady-state	Hybrid
P_f	MW		1081	750	860
P_{add}	MW		-	113	109
P_{rad}	MW		102	76	185
P_{in}	MW		114	74	96
I	MA		22	19.8	15.4
$q_I/q_\psi(95\%)$			2.3/3.0	2.6/3.5	3.3/4.4
$\bar{n}_e$	10^{20} m^{-3}	required	1.44	0.76	1.25
		L-mode			
$\bar{n}_e$	10^{20} m^{-3}	*Hugill*	0.72	0.64	0.51
$\bar{n}_e$	10^{20} m^{-3}	*Greenwald*	1.4	1.3	1.0
$\bar{n}_e$	10^{20} m^{-3}	*Borrass*	0.88	0.70	0.77
		H-mode			
$\bar{n}_e$	10^{20} m^{-3}	*Borrass*	1.24	0.97	1.09

Contrary to a widespread opinion, a strong power dependence of the critical density, such as predicted by Eq. (6) or observed in JET [2.3.4], does not automatically solve the problem [2.3.23]. In fact, what counts is, irrespective of the underlying model, the power flux into the boundary region, which is comparable in ITER and current tokamaks with strong additional heating.

For the H-mode regime the situation is even more uncertain. The experimental data do not provide any basis for extrapolation. The models discussed should, in principle, also apply to H-mode plasmas, but the uncertainties about perpendicular transport in H-mode scrape-off layers excludes straightforward application. Tentative "H-mode" values as predicted by the Borrass model with the assumption $\chi_\perp$(H-mode) = $\chi_\perp$(L-mode)/3 are also given in Table 2.3-1. There is an increase in $n^{cri.}$ which seems to be in accordance with the limited experimental observations (§2.3.3).

2.3.5 Summary and Conclusions

Considerable progress has been made during the ITER conceptual design phase in improving the experimental data base and density limit modeling.

- There is now clear confirmation from a number of devices that density limits are edge density limits. Density limits are thus potentially competing with divertor design related requirements on edge densities.

- There is also clear empirical evidence that 100% radiation losses ($P_{rad} = P_{in}$) at the density limit is at least not a universal phenomenon. Instead the scrape-off layer seems to play a decisive role.
- Devices with strong additional heating show a quite different picture as regards the power and q-scalings of the critical density. Proposed scaling expressions cover only part of the observations and hence do not provide a basis for extrapolation to ITER.
- Edge-based models have been successful in modeling details of specific devices and in reproducing the various types of scaling observed experimentally. They also imply a close connection to edge physics and the plasma exhaust problem:
  - o Operation close to the density limit will be required to have acceptably low divertor temperatures.
  - o Disruption-free emergency discharge termination on the technically required time scales of about 1 s is questionable under these conditions.
  - o In configurations with asymmetric power distribution between inboard and outboard channels the critical density is determined by the channel with the lower power influx. Proximity to the critical density will generally be possible only for this channel, while the other ones may be far away from the limit, depending on the power distribution.
  - o In principle, the edge plasma conditions predicted with a view to divertor design requirements should be compatible with scrape-off layer based density limits. The existing divergences are caused by differences in the underlying physics assumptions (transport, radiation) and the level of modeling (1-D/2-D). Improvement of the edge physics data base and of edge modeling in the future R&D activity is needed to remedy the situation.
- The data base on H-mode density limits is very scarce and further improvement is an important part of the Physics R&D programme for ITER.

REFERENCES (§2.3)

[2.3.1] A. STÄBLER et al., "Density Limit in ASDEX Discharges with Peaked Density Profiles," 16th Eur. Conf. on Contr. Fus. and Plasm. Physics, Venice 1989, Part 1, p. 23.

[2.3.2] ITER Physics R&D Reports (by ASDEX, ATF, JET, JFT-2M, DIII-D, TFTR, TUMAN3/FT-2 Teams), Task PH17, Density Limit, September 1989, ITER-TN-PH-9-7/PH17.

[2.3.3] The JET Team, "High density regimes and beta limits in JET," 13th Int. Conf. on Plasm. Physics and Contr. Nucl. Fus. Research, Washington DC, 1990, paper IAEA-CN-53/A-3-4.

[2.3.4] ITER Physics R&D Reports (by ASDEX, ATF, JET, JFT-2M, JT-60, DIII-D, TEXTOR, TFTR, TUMAN3 Teams), Task PH17, Density Limit, March 1990, ITER-TN-PH-0-3/PH17.

[2.3.5] F.C. SCHÜLLER, "Operational aspects of JET disruptions," presented at the IAEA Technical Committee Meeting on Density Limit and Disruptions, JET Joint Undertaking, 26-28 January 1988.

[2.3.6] F.C. SCHÜLLER et al., "Experimental observations of disruptions in JET," 12th Eur. Conf. on Contr. Fus. and Plasm. Physics, Budapest, 1985, Part 1, p. 151.

[2.3.7] V.A. VERSHKOV, S.V. MIRNOV, *Nucl. Fusion* **14** (1976) 383.

[2.3.8] K. BORRASS, Y.L. IGITKHANOV, N.A. UCKAN, "Report of the ITER Experts' Meeting on Density Limits, Garching, September 20-22, 1989," ITER-TN-PH-9-6.
[2.3.9] H. NIEDERMEYER et al., "Investigation into the density limit of the tokamak with Ohmic and neutral beam heating," Proc. 12th Eur. Conf. on Contr. Fus. and Plasm. Physics, Budapest, 1985, Vol. 1, p. 159.
[2.3.10] H. NIEDERMEYER et al., *Plasma Phys. Contr. Fusion* **30** (1988) 1443.
[2.3.11] C.G. LOWRY et al., Density Limit in JET with Beryllium, 17th EPS Conf. on Cont. Fus. and Plasma Phys., Amsterdam 1990, Vol. 1, p. 339.
[2.3.12] M. GREENWALD et al., *Nucl. Fusion* **28** (1988) 2199.
[2.3.13] K. BORRASS, "Disruptive Tokamak Density Limit as Scrape-off Layer/Divertor Phenomenon," NET Report No. 95, EUR-FU/80/89-95.
[2.3.14] A. STÄBLER et al., "Density limit in ASDEX under clean plasma conditions," 17th EPS Conf. on Contr. Fus. and Plasma Heating, Amsterdam 25-29 June 1990 contributed papers, Part 1, p. 395.
[2.3.15] K. BORRASS, "Scrapeoff layer based model for disruptive density limit and implications for next-generation tokamaks," ibid, Part 3, p. 1393.
[2.3.16] S.A. COHEN et al., "Power and Particle Control for ITER," 13th Int. Conf. on Plasm. Physics and Contr. Fusion, Washington DC, 1990, paper IAEA-CN-53/F-3-3.
[2.3.17] K. BORRASS et al., "Plasma Operation Control in ITER," ibid, paper IAEA-CN-53/F-3-6.
[2.3.18] S. KRASHENINNIKOV, P.N. YUSHMANOV, ITER Report ITER-IL-PH-13-9-S-6.
[2.3.19] A.Yu. DENESTROVSKIJ et al., ITER Report ITER-IL-PH-13-9-S-11.
[2.3.20] V.V. ALIKAEV et al., 12th Int. Conf. on Plasma Phys. and Contr. Nucl. Fus. Research, Nice, Vol. 1, p. 513, 1988.
[2.3.21] ASDEX Team, The H-mode of ASDEX, *Nucl. Fusion* **29** (1989) 1959.
[2.3.22] A. STÄBLER, private communication
[2.3.23] The JET Team, "Recent Results and Future Prospects," 13th Int. Conf. on Plasm. Phys. and Contr. Nucl. Fus. Research, Washington D.C., 1990, paper IAEA-CN-53/A-1-2.

2.4 ALPHA-PARTICLE PHYSICS

2.4.1 Introduction

ITER is to operate with heating by fusion alpha (α) particles as the dominant power source. This implies that the device will work under conditions characterized by the presence of an appreciable population of of fast ions in the plasma. Therefore, the confinement of this population and its impact on plasma performance are important issues. Also the dynamical behavior of the plasma will be profoundly affected by α-particle heating, as it leads to a strong correlation between the plasma conditions and heating. Consequently, burn control arises as a new issue to be addressed. Of course, all these issues are the very subject of investigation on ITER in its physics phase, but careful analyses are needed to develop an appreciation of their impact and, in particular, a concept for burn control.

Alpha-particle losses also have a direct impact on ITER design [2.4.1], although power balance considerations would allow rather high losses; a loss fraction of ~0.05–0.1 is not critical for ignition in ITER. The actual limitation is related to heat load restrictions on the first wall as losses induced by the presence of the ripple of the

toroidal field generate a highly peaked heat deposition profiles. The larger the peaking factor of the heat load, the less is the tolerable α-particle loss fraction. For example, for a neutron wall load of P_n = 1 MW/m^2, ripple-trapped particle losses with a peaking factor above 10^2 impose an upper boundary of the loss fraction of just a few percent. For an unfavorable ripple profile the banana diffusion enhanced by other loss channels such as MHD modes or α-particle induced instabilities may enhance ripple-trapped losses and the peak power flux to the first wall.

Therefore condideration of the various α-particle loss channels is of direct importance for the first wall and TF coil design. It is important that comprehensive analyses of these loss channels continue at the theory level to improve understanding of collective effects and at the code development level to improve tools so as to evaluate the impact of α-particle losses. Detailed code development work for ITER in this area has started in 1988, and is still in progress.

2.4.2 Ripple Losses

Ripple-induced losses generating highly peaked fluxes to the wall, together with possible synergistic effects, are the most critical channel of α-particle losses with respect to the impact on the shape of the TF coils and the first wall.

Experimental studies of high energy ion ripple losses have been recently started on TFTR [2.4.2] where it is possible to change the ripple value by changing the radial position of the plasma. Initial results were obtained and are being analyzed.

Because of the lack of experimental data on fast ion ripple losses in tokamaks, numerical modeling of α-particle ripple losses was the only means of predicting the loss fraction and first wall heat load in ITER. There was already a detailed study for the INTOR parameter range. In ITER the plasma current is approximately 4 times larger than in INTOR, the aspect ratio is lower, and the elongation is as high as 2. As a result the ripple profile differs significantly from the INTOR case and different loss mechanisms become operative. Studies of α-particle ripple losses in ITER have been started in 1988 and have considerably improved the understanding of the phenomenon.

2.4.2.1 Qualitative analysis

There are different channels [2.4.3 through 2.4.12] of α-particle ripple losses in a tokamak, which dominate in different parts of the plasma cross section and for different ranges of α-particle energy. All relevant channels are related to banana-trapped particles. Passing particles are not sensitive to the TF magnetic field ripple, which, e.g., implies that the quasi-tangential NB injection in ITER will not suffer serious ripple losses.

The ITER plasma cross section and the reference ripple contours used for the modeling are shown in Fig. 2.4-1 [2.4.8]. Figure 2.4-2 displays the regions in which determined loss mechanisms prevail. In region 1, in which the ripple value is low, one has collisional ripple induced banana diffusion. Theoretical analysis [2.4.3] here predicts a low diffusion rate for both high (> 1 MeV) and low (< 100 keV) energy α-particles. The diffusion rate is highest in the energy range of 300–700 keV where the α-particle scattering on the background ions is largest. The diffusion coefficient is sufficient to produce a large displacement and a noticeable particle flux, however the energy is low and the energy loss fraction is of the order of a percent.

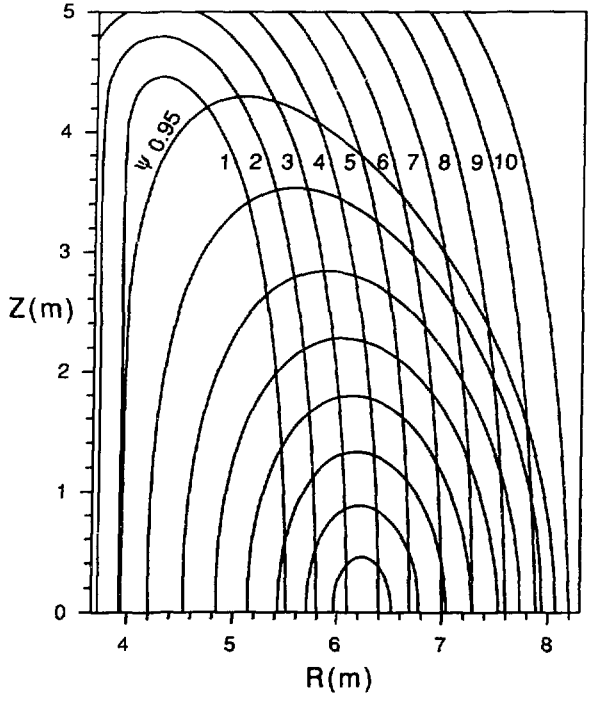

FIG. 2.4-1 Plasma magnetic surfaces and ripple contours:
1- $\delta(\%) = 3.44 \times 10^{-3}$; 2- $\delta(\%) = 7.95 \times 10^{-3}$; 3- $\delta(\%) = 1.77 \times 10^{-2}$;
4- $\delta(\%) = 3.79 \times 10^{-2}$; 5- $\delta(\%) = 7.84 \times 10^{-2}$; 6- $\delta(\%) = 1.57 \times 10^{-1}$;
7- $\delta(\%) = 0.305$; 8- $\delta(\%) = 0.578$; 9- $\delta(\%) = 1.07$;
10- $\delta(\%) = 1.92$;

In region 2, the ripple value is large leading to stochastic diffusion [2.4.4,5]. When banana tips are in this region, the α-particle leaves the plasma very fast, typically after 10^2–10^3 bounce periods. The boundary of the stochastic region, shown in Fig. 2.4-2 by a dashed line, depends on the particle energy; it is approximately given, for circular cross-section, by the simple analytic expression [2.4.4]

$$\delta_{cr} \approx (\varepsilon/\pi Nq)^{3/2}\kappa/\rho_L q, \qquad (1)$$

where ε is the inverse aspect ratio, κ is the plasma elongation, ρ_L is the gyroradius, and N is the number of TF coils. Region 3 is the ripple well region in which direct losses of the ripple trapped particles occur. The banana diffusion also is enhanced in this region. For the standard tokamak approximation, the position of the boundary of the ripple-well region is given by

$$\delta = B_r/NB, \qquad (2)$$

where B_r is the radial component of poloidal field and B is the toroidal field at the

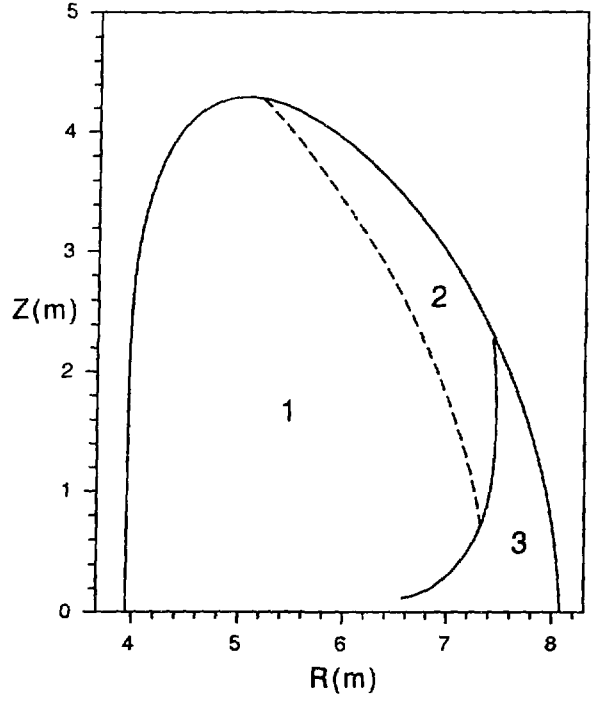

FIG. 2.4-2 ITER plasma cross section and regions where different loss mechanisms prevail: 1- collisional ripple enhanced diffusion; 2- stochastic diffusion; 3- ripple well region.

plasma center $R = R_0$. The most important process taking place in this region is the collisionless transformation of banana orbits into ripple-trapped particles, which do not sense the rotational transform of the field and drift out of the plasma, on the average, in vertical direction. The probability of this transformation, for α-particles with energy $E > 1$ MeV, is very high [2.4.6,7]. It takes only a few bounce periods. The total number of the α-particles born as ripple-trapped particles is small, $\sim\varepsilon^{1/2}P_{\alpha 3}$, where $P_{\alpha 3}$ is the total α-particle source in region 3, but with an unfavorable ripple profile the ripple-well region may be filled with banana particles escaping from the central region due to collisional or stochastic diffusion. While the transformation of the banana-trapped into ripple-trapped particles does not change the total loss fraction, it strongly affects the distribution of the first wall heat load.

Analytical expressions for α-particle ripple loss were obtained for a high aspect ratio plasma with circular cross sections of the magnetic surfaces. For the actual plasma geometry and ripple profiles, the α-particle loss fraction and especially the profile of the first wall heat load are obtained by direct Monte-Carlo modeling.

2.4.2.2 Description of numerical codes

The numerical analyses were performed with several codes using different approaches. The main results discussed in this section have been obtained by the following codes:

1. A three dimensional Orbit Following Monte-Carlo code (3D OFMC) developed (*by K. Tani, JAERI* [2.4.8]) for evaluation of the ripple-loss of high-energy ions in tokamaks: The numerical procedures are based on following the guiding center orbits in 3-D space. The finite gyro-radius is taken into account when the particle approaches the wall. Coulomb collisions with bulk electrons and ions are simulated by Monte-Carlo techniques. The orbit of a test particle is computed until either its energy is reduced to the thermal level or the particle is lost to the wall.
2. A combination of an OFMC code and a Mapping code (*by S. Konovalov, V. Saplahidi, Kurchatov Institute and Moscow University* [2.4.9]): A mapping code that follows banana orbits and calculates banana tip positions after each bounce period, is used in the central plasma region. If the banana tip reaches an intermediate boundary located either near the plasma boundary or the boundary of the local well region, exact trajectories are calculated with an OFMC code. This procedure reduces computing time, yet obtains good statistics in the calculation of the first wall heat load profile.
3. An OFMC code (by *L.M. Hively and J.A. Rome, ORNL,* [2.4.10]), which has been used for ripple loss studies of α-particles with an energy below the critical energy (800 keV): The magnetic field was modeled as the sum of an axisymmetric (2D) equilibrium and the ripple fields calculated from the Biot-Savart law from discrete TF coils (taken to be 14 in this analysis). The guiding center equations were used to follow the α-particle orbits until slowing down to the thermal energy or loss to the wall (which was taken to be elliptical).
4. The code RIPLOS (by *H.E. Mynick and R. White, PPPL,* [2.4.5]), which replaces orbit following by the evaluation of an analytic stochastic loss condition: As the particle confinement time for the banana particles having their tips in the stochastic region (region 3 in Fig. 2.4-2) is much smaller than the slowing down time, it is possible to treat this region as a loss cone for banana particles. This approach is just useful for an order magnitude estimate of ripple losses, but the peak heat wall load is not obtained and α-particle transport into the stochastic region is disregarded.
5. An OFMC code (by *E. Bittoni and H. Haegi, Bologna and Frascati,* [2.4.13]), which was applied to various aspects of the problem.

Theoretical studies of ripple-enhanced diffusion are being continued [2.4.11], [2.4.12], with the aim of obtaining a deeper understanding of the ripple loss physics.

2.4.2.3 Numerical results for an ideal first wall

The ripple loss calculations were performed for various plasma scenarios both for ignited plasma in the physics phase and for technology phase cases taking a reduced plasma current. The numerical results and the plasma parameters used in the calculations are shown in Table 2.4-1. The calculations were performed for fixed profiles of temperature $T_{e,i} = T_0(1 - \psi/\psi_s)$ and density $n_e = n_0(1 - \psi/\psi_s)^{0.5}$, whereas other parameters varied in the different calculations. Part of the modeling was made for the ITER parameters as of 1988.

TABLE 2.4-1. SUMMARY OF NUMERICAL RESULTS AND PLASMA PARAMETERS USED

Code(*)	Physics Phase 1	2	3	4(1)	Technology Phase 1	2
Major radius, R (m)	5.8	6.0	5.8	5.8	6.0	6.0
Minor radius, a (m)	2.2	2.15	2.2	2.2	2.15	2.15
Plasma elongation, κ	1.96	2.05	2.13	1.96	2.05	2.05
Triangularity,	0.55	0.38	0.51	0.55	0.38	0.38
Plasma current, I (MA)	22	22	22	22	14	14
Toroidal field, B (T)	4.4	4.85	5	4.4	4.85	4.85
Number of TF coils, N	16	16	14	16	16	16
Maximum ripple value, δ (%)	1.5	1.7	3	1.5	1.7	1.7
Central temperature, T_0 (keV)	17	17	20	17	30	30
Central density n_{e0} (10^{20} m^{-3})	2	2	2	2	1	1
Z_{eff}	1.5	1	2.15		1.5	1
α-particle energy range, MeV	<3.5	1–3.5	< 0.8	3.5	<3.5	<3.5
Power loss fraction, G (%)	0.65	0.3	0.61	0.3	1.9	0.8
Ripple trapped,%	0.12	small	0.59(2)		0.1	small
Banana,%	0.56	0.3	0.02(2)		1.8	0.8
Particle loss fraction%	0.88	0.4	6	0.3		1.2
Ripple trapped,%	0.32	small				small
Banana,%	0.56	0.4				1.2
Peak heat load, MW/m^2	0.1	<0.05(3)	0.35(2)		<0.1(3)	0.07
Provided by	rip.trap	banana	rip.trap		banana	banana
Peak location Z (m)	3 peaked	<3 broad	3.5 peaked			< 3 broad

(*) See text (Sect. 2.4.2.2)
(1) Only stochastic banana diffusion losses; the loss fraction was found to be sensitive to plasma profiles (0.03% - 0.9%)
(2) This estimation comes from Fig. 8 of Ref. [2.4.7].
(3) The accuracy of the code was not sufficient to obtain the actual figure.

The results indicate a low power and particle loss fraction for the ITER physics phase. The energy loss fraction is below 1% which also leads to low first wall heat loads. A typical heat load distribution over a first wall, following a magnetic surface, as due to ripple-trapped particles is shown in Fig. 2.4-3. The ripple-trapped losses are localized between TF coils with the maximum at the point with Z ~ 3 m. The escaping banana particles are distributed over the first wall more or less uniformly with a toroidal peaking factor of 1–2. The poloidal distribution is rather broad, $0 < Z < 3$ m, with very low peak heat loads, well below the allowable limit.

A reduced plasma current of 14 MA and an increased α-particle slowing down time owing to the higher temperature and lower density ($\tau_s \sim T^{3/2}/n$) are typical features of steady-state scenarios for the technology phase. This tends to increase the α-particle ripple losses. The loss fraction is larger than for the physics phase but the

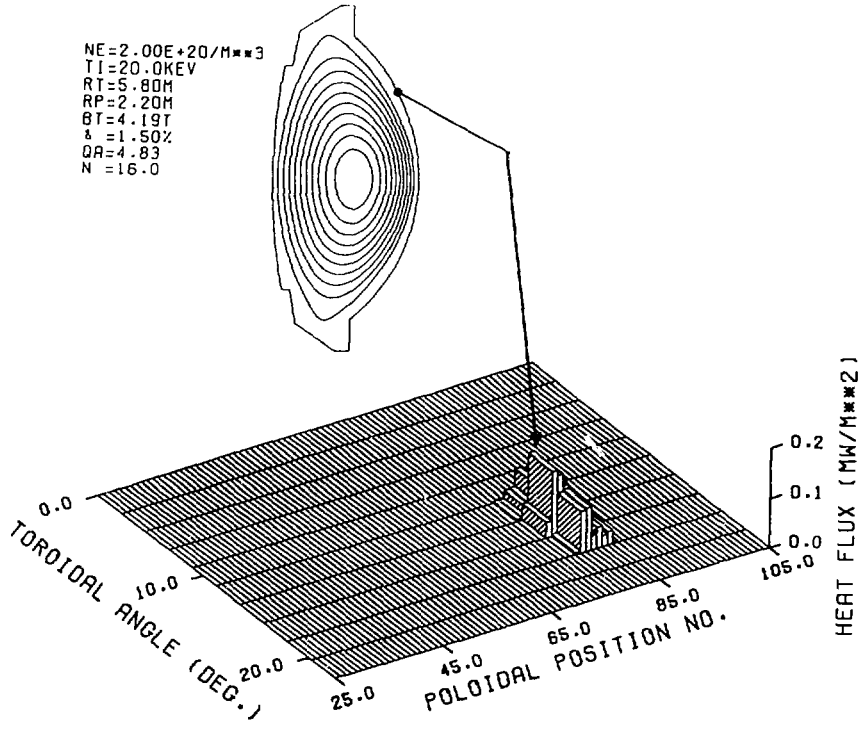

FIG. 2.4-3 Heat wall load due to ripple trapped particles [2.4.8] for the case of the first column of Table 2.4-1.

increase is not as large as it had been expected from an earlier scaling predicting a dependence as q^4 [2.4.8,9]. This may be explained by the following characteristics of the plasma current and ripple profiles in ITER:

(i) The ripple value is very low almost everywhere in the plasma cross section except at the outer edge of the plasma (Fig. 2.4-1) with a steep radial gradient.

(ii) In the highly elongated ITER plasma cross section the q-profile has a wide region where q is low, $q \approx 1$; conversely q and shear are only large near the plasma boundary where the α-particle source is small.

These properties of the profiles strongly reduce the ripple losses from the central plasma region where fusion α-particles are born and make the position of the stochastic and the ripple-well regions rather insensitive to the plasma current. The ratio ≈ 0.3 obtained from two different codes for the losses in the physics and steady-state technology phases agrees very well, yet there is a factor of two difference in the total power loss fraction predicted. The reason for this may be the different Z_{eff} used in the calculations. Both results were obtained for the ripple profile shown in Fig. 2.4-1. For this profile the heat wall load is mainly due to banana particles. Typical banana heat load profiles are shown in Fig. 2.4-4.

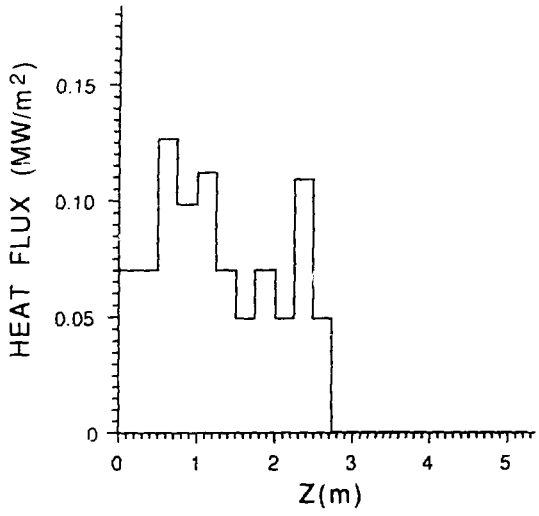

FIG. 2.4-4 Heat wall load due to banana particles [2.4.9] for the case of the last column of the Table 2.4-1.

It was found that the poloidal profile of the first wall load is very sensitive to the ripple profile and the location of the ripple well region. The code 2 [2.4.9] was used to analyze a ripple profile corresponding to a slightly different shape (smaller height) of the TF coil. The difference mainly was in the regions of larger ripple values above and below the equatorial plane while the ripple profile in the equatorial plane was almost unchanged. This change in the ripple profile leads to a deviation of the upper part of the ripple well region boundary from the vertical (Fig. 2.4-5). In this case the ripple-trapped particle loss region appears in the upper part of the ripple-well region. The banana particles leaving the plasma by ripple enhanced stochastic diffusion are transformed into ripple-trapped ones when the banana tip intersects the ripple-well region boundary. Because of the high probability of this collisionless transformation the vast majority of the ripple-trapped particles with $E > 1$ MeV leaves the plasma near the left boundary of the ripple-well region and provides the very peaked heat load shown in Fig. 2.4-3. The peak heat load was found to be about 0.5 MW/m^2, which is approximately ten times larger than that for the reference ripple profile while the power loss fraction of 0.9% is close to the reference one.

In summary, the power ripple losses fraction was found to be less sensitive to the plasma current than expected. At the reference ripple profile the loss fraction is low (< 2%), even for low plasma current (14 MA) technology phase scenarios. A high sensitivity to the ripple profile has been found. To prevent a highly peaked heat load, the ripple profile should be such that ripple-trapped losses are minimized.

It was found that α-particle divertor heat load is negligibly small in the ITER configuration, but this result may depend on the fact that the scrape off layer (SOL) was not realistically modeled. A more detailed analysis of α-particle interaction with the SOL plasma is necessary.

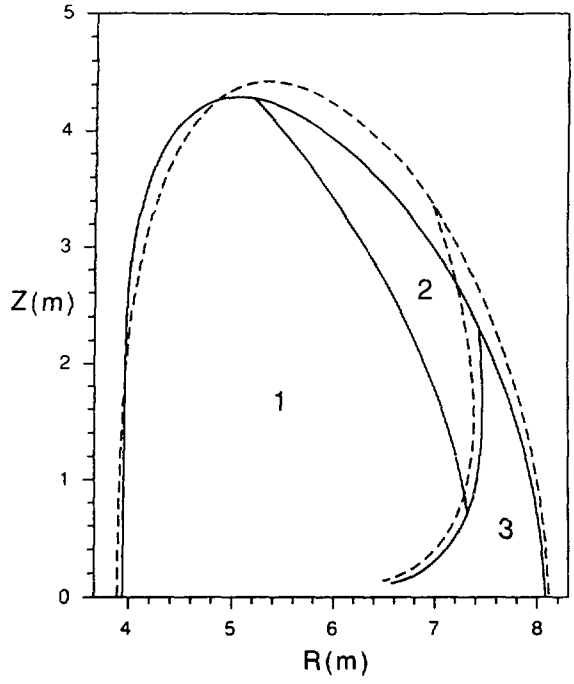

FIG. 2.4-5 Plasma shape and ripple well region boundary for the two cases discussed in the text; the dotted lines refer to the case leading to efficient collisionless transformation and high heat wall load due ripple trapped particles.

2.4.2.4 Heat load at limiters and port edges

Because of the very small incident angle of the α-particles escaping to the wall, the heat load at limiters and edges of ports and of blanket modules (due to misalignments in assembly) can be much larger than the values given in Table 2.4-1. The heat load provided by escaping banana particles is located at the plasma current facing side of the limiters, ports and blanket modules located at the outer part of the first wall. The inclination of the drift trajectory to the first wall which defines the depth of the heat deposition profile at the side plates can be estimated from $\alpha = v_{dr,normal}/v_{\|}$. For example the depth d_0 of the heat load at the edge of a port with toroidal length of 1 m is equal to $d_0 = 2.4 \times 10^{-3}$ Z, where Z is the vertical position at the port edge. For Z = 1 m the depth is few millimeters, which implies an extremely high heat load, of about 30 MW/m^2. To avoid heat concentration at the edges, an appropriate shaping of the first wall is necessary.

2.4.3 Collective Effects

The most critical collective effects produced by fusion α-particles appear when the fast particle velocities parallel to B ($v_{\alpha\|}$) extend beyond $v_{Alfvén}$. ITER will operate in this regime that is difficult to simulate in present tokamaks. In fact, the condition

could be met using parallel neutral beam injection at high energy and/or low B, but the regime can by now only be marginally achieved. Ion cyclotron minority heating appears unsuitable because it generates an energetic tail in the perpendicular direction. Therefore, validation of theoretical predictions by experiments in this area may have to await neutral beam injection at 0.5 MeV as considered on JT-60U, and/or DT operation in TFTR and JET. A well coordinated research work combining theoretical and experimental efforts is particularly essential in this area.

2.4.3.1 Toroidal Alfvén eigenmodes (TAE's)

By the mid 1970's Mikhailovskii et al [2.4.14] and Rosenbluth et al [2.4.15] had discovered the fundamental instability mechanism of low mode number Alfvén eigenmodes (albeit for cylindrical geometry, cf. [2.4.11]) with a growth rate of 10^{-2} the Alfvén frequency. After the discovery of the toroidicity-induced spectral gaps by Kieras et. al [2.4.16] and C.Z. Cheng et. al [2.4.17], Fu and Van Dam [2.4.18] demonstrated analytically an even faster growth rate of $2.5 \times 10^{-2}\ \omega_A$ in toroidal geometry, verified numerically by the Nova-K code of C.Z. Cheng et al., [2.4.19].

There are two necessary conditions for the TAE instability to occur, namely: $v_\alpha \geq v_A$ and $\omega_{*\alpha}/\omega_A > 1/2$, where $\omega_{*\alpha} = mv_\alpha\rho_\alpha/L_\alpha^2$, $\omega_A = v_A/2R_0q$ (gap) and L_α is the $n_\alpha(r)$ scale length. The first condition is easily fulfilled in ITER where for the reference scenario $v_\alpha/v_A = 1.5$. The second inequality, for given v_α/v_A and β_α, is actually a condition on the α-particle density gradient. For the α-particle slowing down profile $n_\alpha \sim n\langle\sigma v\rangle T^{3/2}$ and ITER reference plasma profiles (see §1.3), one has $L_\alpha = 0.25a$. Figure 2.4-6 shows the threshold for the α-particle beta for ITER [2.4.8]. For steep α-particle gradients the α-particle beta limit is very low but rapidly increases with increase of L_α.

Sigmar et al [2.4.20] investigated the single α-particle guiding center resonant motion, given the exact radial mode structure from Nova-K and assuming perturbed amplitudes $10^{-5} \leq B_r/B_0 \leq 10^{-3}$. They also performed a Monte Carlo simulation of 5120 randomly distributed α-particles. Resonant ($\omega - k_\parallel v_{\alpha\parallel} - k_\perp v_{D\alpha} = 0$) losses of circulating α-particles producing secular radial motion out of the system were observed for $B_r/B_0 \geq 10^{-4}$, indicating possible fast α-particle anomalous transport on a time scale comparable to the slowing down time. However, this simulation, by assuming B_r as given, was not self-consistent and cannot answer questions about the wave particle resonance coherence time in the fully developed multi-mode turbulence. A step in this direction is the work reported in Refs [2.4.20,21] on the diffusion in angle-action space, with finite orbit and mode structure effects, is in progress. Also, under investigation is the linear damping of the α-particle driven TAE due to a stabilizing coupling effect of the main gap mode to continuum modes near the plasma edge [2.4.22]. A fully self-consistent computational effort evolving the finite amplitude MHD waves nonlinearly with a fluid code and the α-particles by a particle pushing algorithm has been started recently [2.4.23], results are still withstanding.

2.4.3.2 Ballooning modes

After early suggestions by Rosenbluth et al. [2.4.24] to stabilize the low frequency ($\omega_r \sim \omega_{*i}$) branch of the ballooning mode using energetic trapped ions, Spong et al. [2.4.25,26] and Rewoldt [2.4.27] found destabilization of the ballooning mode due to trapped and circulating α-particles to occur at higher values of ω_r

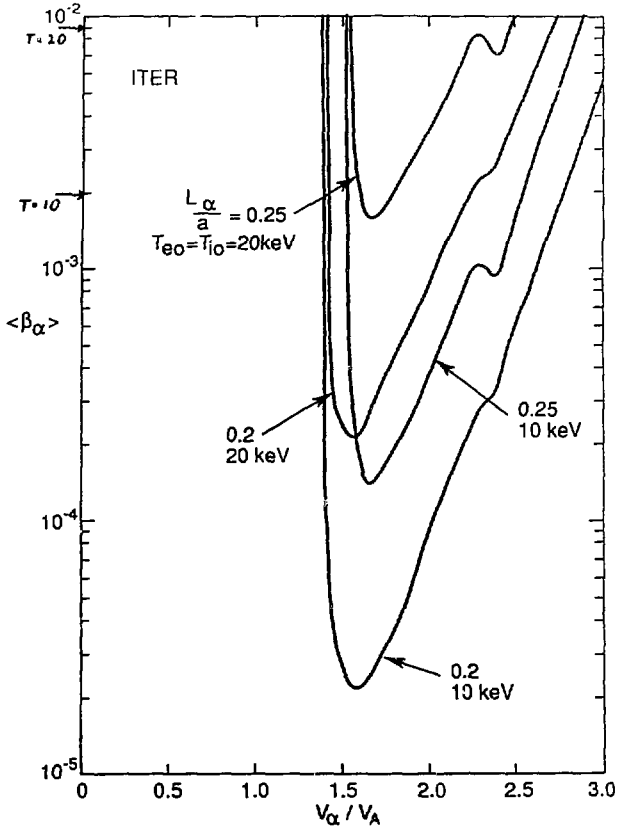

FIG. 2.4-6 TAE stability boundaries as given in [2.4.19] for the standard ITER equilibrium. L_α/a is the ratio of the α-particle density gradient scale length to the plasma minor radius. For, $\beta_{thermal} = 4\%$, $\bar{v}/v_A \approx 1.5$ and thermal DT fusion, one has $T_e = 10$ keV, $\beta_\alpha \leq 2 \times 10^{-3}$; at $T_e = 20$ keV, $\beta_\alpha \leq 8 \times 10^{-3}$, see arrows.

(reaching up to the Alfvén frequency $\omega_A = k_{||}v_A$). In fact, in this range, the underlying MHD oscillations have been identified as high mode number TAE (gap) modes [2.4.28]. For trapped α-particles the instability mechanism is the banana precession frequency resonance with ω_r, for the circulating α-particles it is a transit resonance near the circulating trapped boundary. Figure 2.4-7 from Ref. [2.4.28] shows the critical flux-surface-averaged <β> as a function of normalized flux surface radius, for an ITER equilibrium. One notices a lowering of the <β> threshold (due to the intrinsic trapped α-particle population). Reference [2.4.27] shows a similar effect obtained from an entirely different kinetic code that includes trapped and circulating α-particle contributions. This lowering of the high mode number instability threshold could affect the α-particles by producing an anomalous α-particle diffusion (which is estimated in [2.4.27] to be characterized by $D_\alpha = 1$ m^2/s without, however, providing a self-consistent saturation calculation for this microturbulence). Concerning the

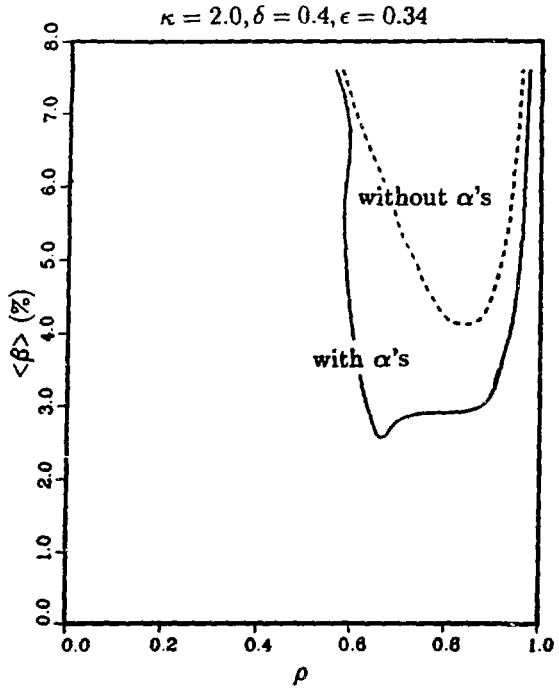

FIG. 2.4-7 Critical β for α-particle destabilized ballooning mode vs normalized flux surface radius [2.4.31] for ITER parameters. The beta limit is significantly reduced by the presence of the α-particles.

anomalous diffusion of alpha-particles due to higher mode number ballooning perturbations it has been shown [2.4.29] that stochastic transport is reduced inversely with $k_\perp \rho_\alpha > 1$ due to the "orbit averaging" effect. Thus only intermediate mode numbers ($n < 10$) may be contributing to transport.

2.4.3.3 Experimental results in relation to Alfvén and ballooning modes

The intense theoretical and numerical effort has stimulated experimental efforts [2.4.30–34] to verify the theoretical predictions. Historically, NB driven instabilities in conditions with $v_{b\|} > v_{Alfvén}$ were suspected in ISX-B [2.4.33] and JFT-2, and reported in T-11 by Leonov et al. [2.4.30] when the volume-averaged beta ⟨β⟩ exceeded 2% [with a highly peaked profile, β(0) ≈ 9%]. The latter authors observed sharp periodic drops in the β_p (diamagnetic) signal accompanied by a positive voltage spike that may suggest a super-Alfvénic beam destabilization of the ballooning mode rather than of the low mode number TAE. Note that both of these modes are toroidal Alfvén gap modes destabilized by fast ions, plus - in the case of the ballooning mode - the additional pressure drive of the bulk plasma. In fact, Heidbrink [2.4.32] mentions the possibility of a relation with pressure driven fluctuations.

Recently, K.L. Wong has started systematic experiments on TFTR [2.4.31] at low values of B = 1 T, I > 400 kA, E_b = 95–110 keV. When $\bar{v}_b/v_{Alfvén} > 0.7$, Alfvén

frequency bursts (≤ 90 kHz) were observed with mode numbers around n = 3 and fast ion losses of ~5% are inferred from the neutron signal drop. For the next four years of TFTR operation (through its D-T phase), a programme has been outlined to compare the theoretical and experimental threshold conditions, and the effect of Alfvén turbulence on fast ion and α-particle confinement.

On DIII-D, Heidbrink et al. [2.4.32] have conducted a series of experiments focussing on realizing the necessary conditions for the TAE instability, namely $v_b \geq v_{Alfvén}$, $\beta_b > \beta_{b,crit}$ (a threshold value) and the beam density profile scale $L_b^{-1} = (dn_b/dr)/n_b$ being short enough to allow $\omega_{*b}/\omega_A > 1/2$. Toroidal mode numbers n = 4-9 and new features in the frequency spectrum around the Alfvén frequency (78 kHz for n = 4) were observed when the beam beta exceeded ~2%, at $\bar{v}_{b\|}/v_{Alfvén} > 0.8$. Here, $\bar{v}_{b\|}$ is the parallel beam velocity averaged over a slowing down distribution. Theoretically, for the DIII-D q-profile and device parameters, the n = 4 TAE should indeed be unstable, but the $\langle\beta_b\rangle$ threshold observed to be necessary for instability (~2%) is about 7 times larger than the theoretical prediction. This discrepancy may indicate that the "standard" TAE mode (with its theoretical $\langle\beta_\alpha\rangle$ threshold of ≈ 2%) is damped more strongly than presently expected; however, it may be triggered in high β_p discharges approaching the β limit.

Ion cyclotron minority heating has been used in JET [2.4.34] to produce 1.5 MeV He^3 ions with an energy content up to 2.4 MJ corresponding to almost 50% of the total plasma energy. The parameters achieved in JET of the superthermal component and those of the ITER α-particles are as follows:

Parameter	Achieved in JET	Expected in ITER
n_{fast}/n_{eo}	1–3%	0.1–2%
$\langle E_{fast}\rangle$	1–5 MeV	1–2 MeV
$\langle\beta_{fast}\rangle/\beta$	50%	30%
$p_\perp/p_\|$	10–50	1
$\Delta r_b/a$	0.3	0.1
v_{fast}/v_A	2-4	1.7–2.5
τ_{eff}/τ_s	1	–

The parameter range achieved in JET covers that expected in ITER, except for the high anisotropy and larger banana width. The major part of the results corresponds to sawtooth-free (Monster), L-mode discharges. The superthermal ion energy W_f follows the fundamental scaling relation $W = kP_{rf}\tau_s(0)$, where P_{rf} is the ICRH power, $\tau_s(0)$ is the slowing down time at the plasma center, and k is a form factor for the fast ion radial distribution, showing that the interaction of fast ions with the plasma is collisional. Exceptions that were found for low plasma current can be explained by finite ion orbit effects. The D-He^3 fusion rate, for on-axis heating, is in good agreement with calculations of RF power deposition and fast ion generation. The fast ion diffusion coefficient was found to be very low, $D_{fast} < 0.2$ m^2/s which is approximately 10 times less than the critical value $D_{alpha} = 2$ m^2/s necessary for good confinement of α-particles in ITER.

The termination of the sawtooth-free period leads to significant fast ion transport. Typically 50% of the fast ions are expelled from the plasma core in a large sawtooth crash. After the crash the remaining ions continue to slow down at approximately the collisional rate.

So far, the fast ion driven ballooning and TAE instabilities and transport induced by them have not yet been clearly identified. It must be noted that the anisotropy of the fast ion population in the recent JET experiments [2.4.34] may exclude these instabilities. More detailed experimental and theoretical work is required.

2.4.3.4 Alpha-particle driven fishbone oscillations

NB driven fishboning was a strong effect in PDX. Similarly, in a burning plasma, α-particles can affect the $m = n = 1$ internal kink modes in the vicinity of the $q = 1$ surface. With an appropriate density of fast trapped ions such as produced by ICRH or fusion burn, the sawtooth oscillations are found to be stabilized [2.4.35,36], but C.Z. Cheng recently found (using the Nova-K code's capability to cover a complete fast ion pitch angle distribution and a finite aspect ratio, shaped plasma cross section equilibrium) that α-particles near the passing/trapped boundary may overwhelm the stabilizing effect of the strongly trapped ions. Thus again, ICRH produced energetic trapped ions may not adequately simulate the collective α-particle effects. Verification will have to await further combined ICRH/NB heating experiments of TFTR, JET and JT-60U.

When the density of fast ions or α-particles becomes too large, the fishbone instability is triggered by the trapped particle precession resonance with the mode frequency. This instability exists over a range of frequencies ranging from ω_* to $\omega_{D\alpha}$, carried by a low frequency MHD oscillation of the background plasma [2.4.36] or undergoing a transition to an oscillation of the fast ion species at high frequencies [2.4.35]. In either case, energetic banana particles may be ejected in bursts, periodically increasing the wall loading on the outboard side of the tokamak and reducing the energy transfer from fast particles to the bulk plasma. On the other hand, theoretical investigation of the high energy ion confinement in the presence of low-frequency MHD modes ($\omega \ll \omega_*, \omega_{D\alpha}$) [2.4.37] shows that the drift orbits of the fast ions are more stable than those of low energy particles. Thus the lower frequency fishbone branch may even produce a desirable loss of epithermal He-ash.

2.4.3.5 Concluding remarks

Theoretical and experimental evidence for the α-particle driven collective effects such as resonant excitation of the shear Alfvén spectrum, as well as α-particle driven ballooning (at medium range toroidal mode numbers $3 \leq n \leq 10$) and fishboning is firm enough (and growing) to warrant R&D efforts to determine a possible anomalous fast α-particle diffusion due to these effects. Close collaboration has been started between analytical and numerical physicists and experimentalists on several large tokamaks. The importance of producing a velocity distribution function approaching the isotropic one of the fusion born α-particles has been recognized and will require additional experiments with a combination of strong high energy neutral beam injection and ion cyclotron minority heating. DT operation in TFTR and JET may provide answers in the longer term.

2.4.4 Control of the Fusion Power Production Rate (Burn Control)

2.4.4.1 Introduction

One of the primary goals for ITER is the study of long pulse, equilibrium ignited plasmas, i.e. high-Q plasmas with $Q = P_{fusion}/P_{aux} \geq 30$. This requires control of three aspects of the operating conditions:

- Control of the operating point: The establishment of plasma conditions and adjustment of the parameters of operation to attain the desired equilibrium operating point at a given fusion power while satisfying the relevant physics and engineering constraints. The characteristic time scales are seconds to minutes. Adjustment of the conditions necessary to obtain the desired operating point can be made prior to the establishment of the burn pulse.
- Control of the stability of the fusion power production: The detection and feedback-stabilization of the thermal instabilities which may be present in the thermonuclear burn process at the low temperature (~10 keV) operating points. The characteristic time scales are ~1–10 s and time-dependent control is required.
- Capability to terminate the fusion power production quickly: Rapid reduction of the fusion power will be required in response to component failures or loss of control of burn stability to avoid damage to the tokamak and possible safety problems. Time scales required are < 10 s and, ideally, ~1 s. These control functions must be part of the integrated, overall control process that also includes, for example, particle control and current-profile control.

2.4.4.2 Operating point (equilibrium) control

The basis of operating point (equilibrium) control is to select the working parameters in order to operate: (1) at the desired fusion power, (2) at the highest Q attainable, (3) in a controllable manner (i.e the equilibrium point must be stable), (4) within the operating constraint boundaries (§1.0). Since the exact final operating point will depend on a number of physics performance issues such as energy confinement, impurity level, etc., which will only be definitely known with precision after some operational experience has been obtained on ITER, flexibility in the control systems is essential.

The constraints that limit the choice of the operating point are illustrated in Fig. 2.4-8 which shows the ITER plasma operation contours (POPCON's) in n-T space with energy confinement defined by 2 × ITER89-P (L-mode) power law scaling (§2.1). For a wall load of 1 MW/m^2 (1080 MW fusion power), two possible operating regions exist within the boundaries of the beta limit, density limit, and ignition curve: a high-n, low-T region and a low-n, high-T region. The low-n, high-T operating point possesses inherent thermal stability but has the twin disadvantages of deleterious divertor heat loads and greater sensitivity to confinement scaling [2.4.38]. In the latter instance, low density operating points which otherwise meet wall load and beta constraints in Fig 2.4-8 would be well into the super-ignited region (and therefore uncontrollable) had the ITER offset-linear scaling been used instead.

Consequently, operating points in the high density region of Fig 2.4-8 are preferable even though they require active burn control to achieve thermal stability. The reference ignition scenario A1 (Fig. 2.4-8) (§9.0) is a fully ignited point on the

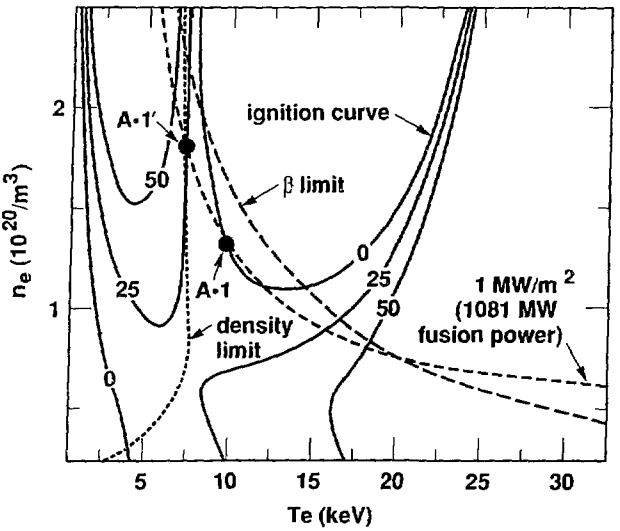

FIG. 2.4-8 ITER plasma operating contours (POPCONS) in n-T space for ITER power energy confinement scaling (H = 2.0). Contours denote auxiliary heating power $P_{NB,Eq}$ required to maintain equilibrium power balance. The $P_{NB,Eq} = 0$ contour is the true ignition boundary. Operational constraints of beta limit, density limit and required neutron wall loading (fusion power) are shown. Point A.1 is the (true) ignition reference baseline (see Sect. 9.0) while point A.1' is our recommended operating point for stability control with $P_{NB,Eq} \sim 25MW$, $Q \sim 43$.

ignition contour (i.e. $Q = \infty$). The recommended stability control scheme (§2.4.4.3) requires operation at the slightly sub-ignited point A.1' with $P_{NB,Eq} \sim 25MW$, $Q \sim 43$.

The control variables which can be used to define the operating point include the magnetic field on axis (B), plasma current (I), plasma density and, perhaps, control of Z_{eff} via, say, impurity injection. These variables cannot be adjusted independently. For example, B and I must satisfy engineering and physics constraints such as the maximum beta (§1.0,2.2) and minimum q_ψ (§1.0,2.2). These parameters would, in general, be set prior to the burn pulse.

Achievement of an acceptable operating point can be obtained with some degradation of the energy confinement below the reference assumptions (§2.1) by increasing B and I, except that higher current would reduce the volt-seconds and require either a shorter burn pulse or additional volt second savings from the non-inductive current drive system. Due to constraints on beta caused by the need to keep the fusion power at 1080 MW to achieve a wall loading of 1 MW/m^2, achievement of a stable burn with confinement better than the reference assumptions (§2.1) by reducing B and I is difficult. For H = 2.5, it is not possible. We could still obtain controlled ignition but only at lower fusion powers. For higher fusion powers, confinement would have to be actually degraded. An alternative solution to "over-confinement" might be impurity injection to promote radiation loss. Control of confinement by, for example, degraded H-mode operation, would, if feasible, be a highly desirable operating-point control method.

2.4.4.3 Fusion power stability control

Overview

The requirements for the ITER fusion power stability control systems at the chosen operating point [low temperature (~10keV) and high density] have been defined for various confinement scalings by time-dependent transport simulations. Without control, these ignited and near-ignited plasmas are susceptible to thermal instabilities with a time constant of 3–10 s [2.4.39]. Fluctuations in the plasma temperature would then lead either to a positive thermal excursion resulting in a beta-limit disruption or to a negative excursion which would terminate the fusion power production with the possibility of a density-limit disruption. An uncontrolled positive excursion could also lead to elevated fusion powers ($\geq$ 2000 MW) with the possibility of damage to plasma-facing components. We have selected active feedback of power and particle sources based on standard diagnostic signals as the reference fusion power control systems since they have been identified as the most direct and the most credible control strategies available at present [2.4.40,41].

Primary stability control scheme: modulated neutral beam heating

The primary stability control system is feedback control of the external heating power based on total neutron flux measurements of the instantaneous total fusion power. The performance of this system is governed by constraints on the heating and diagnostic systems. The proposed ITER power handling system limits the rate at which the neutral beam power can be varied to $R_{NB} \sim \pm 10$ MW/s. The neutron flux measurements $|\Delta\Phi_N/\Phi_N|_{Diag}$ are predicted to have accuracies no better than 5% (§7.0). Based on time-dependent simulations of a volume-averaged (0–D) plasma model [2.4.39], the maximum positive and negative fractional neutron flux perturbations $\Delta\Phi_N/\Phi_N$ that can be stabilized as a function of the equilibrium power $P_{NB,Eq}$ depend on the neutral beam power ramp-rate $|R_{NB}|$ (Fig. 2.4-9). The two curves labeled by the same $|R_{NB}|$ value bound the maximum positive and negative perturbations in Φ_N that can be stabilized at a given equilibrium point characterized by $P_{NB,Eq}$. Increasing the neutral beam power ramp-rate $|R_{NB}|$ is useful for either increasing the size of perturbations that can be stabilized or decreasing the minimum value of $P_{NB,Eq}$ (i.e., increasing the Q) at the operating point. Positive excursions are the most difficult to control at high-Q operating points (i.e. low values of $P_{NB,Eq}$) while negative perturbations are the most difficult to control at low-Q operating points (i.e. high values of $P_{NB,Eq}$).

To account for 0-D modeling uncertainties and large-amplitude transients such as sawteeth, we have assumed that we must control 10% positive and negative perturbations in Φ_N (i.e., twice the diagnostic threshold). With this assumption, $P_{NB,Eq} \sim 25$ MW (yielding an operating point with $Q \sim 43$) with the present ITER neutral beam power ramp-rate of $|R_{NB}| = 10$ MW/s, can provide time-averaged stability. This performance level requires that, at least, 50 MW of NB power be held in reserve in order to stabilize negative excursions for the operating point A.1' (Fig. 2.4-8). Other forms of heating, such as ICRH and ECRH have also been considered for auxiliary power feedback control. For the high densities ($\sim 1.2–1.4 \times 10^{20}$ m^{-3}) of the near-ignited operating points, ICRH has advantages for control applications relative to neutral beams in term of better penetration to the plasma center and the ability to directly heat the ion species. Recent studies predict effective control by

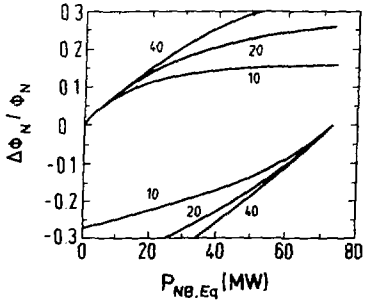

FIG. 2.4-9 ITER burn stability control diagram for ignited operation -- 0-D analysis: Plot of critical positive and negative neutron flux perturbations $\Delta\Phi_N/\Phi_N$ which can be stabilized at a given equilibrium auxiliary power $P_{NB,Eq}$ for several values of neutral beam ramp-rate: 10, 20 and 40 MW/s. Our reference ignition baseline A.1 would be at $P_{NB,Eq} = 0$ and thus would be uncontrollable relative to positive excursions. Our selected operating point (A.1' in Fig. 2.4-8 above) is at PNB,Eq = 25MW, Q~43

ICRH with operation at the second harmonic of deuterium, $2\omega_{cD}$ [2.4.42]. Similar advantages for high density discharges have been predicted for ECRH [2.4.43].

Alternative stability control schemes

Simultaneous modulation of the plasma density and composition by control of the: (a) total core density, (b) density profile, (c) DT fuel mix, or (d) impurity concentration offers an additional dimension to the control phase space when taken together with auxiliary heating. Particle control through fuelling modulation is applicable to both sub-ignited and, under certain conditions, truly ignited (i.e., $Q = \infty$; $P_{NB,Eq} = 0$) operating points [2.4.39]. However, divertor operation constraints and density limit considerations dictate rather stringent limitations on the edge density. Therefore, this scheme is generally considered as a supplemental system to improve the performance of the primary (auxiliary heating) method [2.4.39,44,45].

Another alternative approach is variation of the D-T mix about a slightly off-optimum equilibrium value (e.g., $n_D/n_T \sim 1.2$). Provided that the fuelling system can vary the D-T mix on the required time scale of several seconds, this could be an option for a stand-alone control system since the constraints imposed by divertor operation and density limit can be more easily fulfilled.

Controlled injection of impurities to enhance the total radiation loss has also been considered as a means of ITER burn control [2.4.39]. 0-D analyses have suggested that, in principle, injection of tungsten impurities (using seeded fuel pellets) could serve as a back-up to neutral beam power modulation, but the build-up of tungsten plasma contamination is a concern. Other stability control schemes have also been identified such as plasma compression/decompression, control of toroidal field ripple, etc [2.4.40]. However, not only are the physics and technological requirements of such schemes insufficiently developed at this time but, in many cases, there appear to be fundamental reasons why they would not be applicable to ITER.

Such alternative stability control schemes, even if not appropriate as a stand-alone method, may provide additional flexibility and help to reduce the power needs if applied in combination with feedback-controlled external heating.

Profile effects

Because of their simplicity and speed, 0-D models have been used extensively in fusion power control analyses. However, a number of important effects such as radially dependent transport coefficients, density and temperature profile shape evolution, realistic plasma geometry, off-axis heating, large-amplitude transients (e.g. sawteeth, pellets, etc.), are either neglected or incompletely handled in the 0-D approach. The correct treatment of these effects requires 1-1/2-D plasma modelling. In general, the differences between 0-D and 1 1/2-D formalisms for burn-control can be attributed to [2.4.38]:

- *Profile effects:* Depending on the form of the transport coefficients, the resulting profiles can vary considerably over operating space relative to the fixed profile assumed in a 0-D model.
- *Beam penetration:* At higher densities ($> 1.3 \times 10^{20}$ m^{-3}), the 1.3 MeV ITER beams cannot penetrate to the plasma core resulting in inefficient heating profiles and higher requirements of auxiliary heating power. Furthermore, this decoupling of the NB power-deposition region from the central region of peak fusion power production sometimes leads to power oscillations across the plasma radius.
- *Impurity radiation:* Radial-dependent line and recombination radiation may be an important part of the total radiation loss and the overall energy balance.
- *Profile transients:* Profile transients such as sawteeth may make it difficult for diagnostics to distinguish between a burn runaway excursion and a benign profile relaxation.

Time-dependent 1-1/2-D simulations have been undertaken to determine the effectiveness of neutral beam power feedback for control of thermally unstable operating points and to validate the 0-D conclusions described above. The results, so far, confirm the broad predictions, but not the details, of the 0-D calculations indicating that control is possible, at least for medium densities. However, some of the above 1-D effects have not yet been included. At higher densities ($>1.3 \times 10^{20}$ m^{-3}), off-axis heating due to the poor beam penetration makes control problematic, especially for negative perturbations. Further issues that are being addressed are the effect of perturbations introduced by pellet injection and sawteeth and the feasibility of alternative control methods such as fueling and density control, used either alone or in conjunction with neutral beam feedback. Faster 1-1/2-D transport codes are being developed for these studies.

In contrast to the conclusions of the 0-D analysis, the 1-1/2 D codes indicate that observation of only one global variable such as total neutron flux may not be sufficient to guarantee global controllability. Measurement uncertainties for the plasma quantities used as control input are one of the main perturbations in the control process[2.4.46]. On-going work in stability control should seek to specify a minimum set of diagnostic observables to ensure stability in a 1-1/2-D context including the accuracy and resolution (time and space) requirements for such observables as the global neutron flux, spatially-resolved flux, ion temperature, etc. Transient profile effects such as sawteeth and their detection are also important.

2.4.4.4 Rapid termination of the fusion power production

Methods to terminate the fusion power production rapidly are required:

(1) When the normal burn stability control system fails and the plasma becomes super-ignited. Nearly-ignited, high-Q operating points at high density have a positive temperature coefficient of reactivity so that once the plasma temperature has crossed the ignition boundary (Fig. 2.4-8), the baseline scheme of modulated control of auxiliary power cannot restore the equilibrium.

(2) When the plasma is operating stably at the desired operating point but an external accident event (for example a loss-of-coolant or loss-of-flow accident (LOCA/LOFA) in a torus component) necessitates a rapid reduction of fusion power on a time scale much shorter than the conventional shutdown period.

A LOCA/LOFA in the divertor will result in significant damage to the plasma-facing components unless the fusion power can be reduced to zero in less than 10 s [2.4.47]. For some divertor designs, the required time scale is as low as 1-3 s. Similar damage can occur in the event of a failure of the fusion power stability control system where fusion powers of ≥2000 MW can be reached in time scales of ~5-15 s, depending on the confinement scaling [2.4.39].

The timescales required for rapid fusion power termination (1-10 s) relative to normal, controlled shutdown at the end of a conventional burn pulse (several tens of seconds) are very short. A number of candidate techniques for rapidly terminating the

TABLE 2.4-2. CANDIDATE EMERGENCY SHUTDOWN SCHEMES

METHOD	TIME SCALE[a]	PROBABILITY OF DISRUPTION	POTENTIAL for PASSIVE SYSTEM[b]
Controlled reduction of aux heating and fuelling[c]	slow	low	n.a
H to L-mode transition	medium	low	low
Controlled impurity injection:			
- hydrogen	medium	low	low
- medium to high Z	medium	moderate	medium
Rapid shutoff of auxiliary heating and fueling	medium	moderate to high	moderate
Vaporization of divertor substrate	medium	moderate to high	high
Uncontrolled central impurity injection (gravity-driven rod, pressure-driven bullet)	fast	moderate to high	moderate
Uncontrolled edge impurity injection (pressurized burst diaphragm, pressurized He capsules)	fast	high	moderate
Interruption of vertical control	fast	100%	moderate

[a] Relative to accident transients (LOCA/LOFA and thermal runaway).
[b] i.e, able to operate without active detection, intervention or control.
[c] Normal method for conventional plasma shutdown (~tens of seconds). Shown for completeness only.

fusion power production in ITER have been identified (Table 2.4-2) [2.4.38,11]. A potential characteristic of several of the faster schemes in Table 2.4-2 is the tendency to initiate a density limit disruption because the fusion power decays at a faster rate than the density. However, as ITER is designed to accommodate a number of disruptions, the termination of the discharge by a disruption would be preferable to more severe damage to the machine. It would be highly desirable if the fusion power production could be terminated passively when needed, i.e without any active detection, intervention or control. Although studies have only begun, this appears difficult to achieve in practice [2.4.48]. This is primarily because the power producing element (the plasma) is not in intimate contact with the medium undergoing the off-normal event (the plasma facing components, blankets, etc.). A qualitative assessment showing which schemes have the potential for passive operation and which schemes will probably operate only under active means (i.e., active detection and/or active intervention) is given in Table 2.4-2. Of the eight methods in the table, only one really lends itself to a truly passive system, i.e. vaporization of the divertor substrate due to a local LOCA/LOFA.

REFERENCES (§2.4)

[2.4.1] *ITER Conceptual Design Report*, IAEA/ITER/DS/18, ITER Documentation Series, IAEA, Vienna (1991).

[2.4.2] R.L. BOIVIN, et al., TFTR contributions to the ITER Physics R&D, Task PH12, Alpha Particle Losses Induced by the Toroidal Magnetic Field Ripple, March 1990, ITER-TN-PH-0-3/PH12.

[2.4.3] P.YUSHMANOV, Review of Plasma Physics, Ed. B.B.Kadomtsev, Vol. 16, Consultants Bureau, New York - London, 1987.

[2.4.4] R.J. GOLDSTON, R.B. WHITE, A.H. BOOZER, *Phys Rev.Lett.* **47** (1981) 647.

[2.4.5] R.B.WHITE et al., Plasma Phys. Controlled Nuclear Fusion Research, IAEA. Vienna, 1982, Vol. 3. p. 391.

[2.4.6] R.J.GOLDSTON , H.H.TOWNER, J. Plasma Phys. 26 (1981) 283.

[2.4.7] V.Ya. GOLOBORODKO, V. YAVORSKIJ, *Nucl.Fusion* **24** (1984) 627.

[2.4.8] K.TANI et al., ITER reports 1989-90: ITER-IL-PH-1-9-J-1, ITER-IL-PH-1-9-J-2, ITER-IL-PH-1-0-J-1.

[2.4.9] S.KONOVALOV et al., ITER reports 1989: ITER-IL-1-9-S-1, ITER-IL-1-9-S-1, ITER-IL-1-9-S-1, and ITER-IL-1-9-S-1.

[2.4.10] L.M. HIVELY, J.A. ROME, Nuclear Fusion 30 (1990) 1129.

[2.4.11] *IAEA Technical Committee Meeting on Alpha Particle Confinement and Heating*, Kiev, USSR, October 1989.

[2.4.12] V.Ya. GOLOBORODKO et al., ibid; P. GRUA, J-P. ROUBIN, "Collisionless regimes of trapped particles in tokamak," ITER-IL-PH-1-0-E-1.

[2.4.13] E. BITTONI, M. HAEGI, ibid, to appear in *Fusion Technol. 1990.*

[2.4.14] A. MIKHAILOVSKIJ, *Zh. Eksp. Teor. Fiz.* **68**, 1772 [*Sov. Phys. JETP* **41** (1975) 890].

[2.4.15] M. ROSENBLUTH,P. RUTHERFORD,*Phys.Rev. Lett.* **34** (1975) 1428.

[2.4.16] C. KIERAS, J. TATARONIS, *J. Plasma Phys.* **28** (1982) 395.

[2.4.17] C.Z. CHENG, L. CHEN, M.S. CHANCE, *Ann. Phys.* **161** (1984) 21.

[2.4.18] G.Y. FU, J. VAN DAM, *Phys. Fluids* **B1** (1989) 1949.

[2.4.19] C.Z. CHENG, Kiev Conf. op. cit. in [2.4.11]; submitted to *Phys. Fluids.*

[2.4.20] D.J. SIGMAR, C.T. HSU, R. WHITE, C.Z. CHENG, op. cit in [2.4.11], and MIT Report PFC/JA-89-58 (1989).

[2.4.21] H. BERK, B. BREIZMAN, *Phys. Fluids* **B2** (1990) 2246.
[2.4.22] J. VAN DAM, *Bull. Am. Phys. Soc.* 35 (1990), paper 1P25.
[2.4.23] D. SPONG et al., *Bull. Am. Phys. Soc.* 35 (1990), paper 1P18.
[2.4.24] M.N. ROSENBLUTH et al., *Phys. Rev. Lett.* 51 (1983) 1967.
[2.4.25] D. SPONG et al., *Phys. Fluids* 28 (1985) 2494.
[2.4.26] D. SPONG, D. SIGMAR, J. RAMOS, *Fusion Technol.* 13 (1988) 428.
[2.4.27] G. REWOLDT, *Phys. Fluids* 31 (1988) 3727.
[2.4.28] D. SPONG et al., op. cit, in [2.4.11], to appear in *Fusion Technol.* 1990.
[2.4.29] H. MYNICK, R. DUVALL, *Phys. Fluids* **B1** (1989) 750.
[2.4.30] V. LEONOV et al., IAEA-CN-38/M-2, Vol. I, p. 393, Brussels, 1980.
[2.4.31] K.L. WONG, *Bull. Am. Phys. Soc.* 35 (1990), paper 7Q8.
[2.4.32] W. HEIDBRINK, *Bull. Am. Phys. Soc.* 35 (1990), paper 3P5.
[2.4.33] M. MURAKAMI and ISX-B Team, Plasma Phys. Controlled Nuclear Fusion Research, IAEA. Vienna, 1984, Vol. 1, p. 87.
[2.4.34] D.F. START et al., op. cit in [2.4.11], G. COTTRELL et al., "Alpha particle simulation experiments in JET," APS 1989
[2.4.35] R. WHITE et al., *Phys. Fluids* 32 (1990) 745, and references therein.
[2.4.36] B. COPPI et al., *Phys. Fluids* **B2** (1990) 927.
[2.4.37] S.KONOVALOV, S.PUTVINSKIJ, op. cit in [2.4.11],to appear in *Fusion Technol.* 1990.
[2.4.38] L.J.PERKINS et al., "US studies in burn control for the ITER Conceptual Design Activity," UCRL-ID-105546, Lawrence Livermore Laboratory, 1990.
[2.4.39] S.W. HANEY et al., "Active Control of Burn Conditions for ITER," to be published in *Fusion Technol.* (1991).
[2.4.40] See, for example, K.BORRASS, "Burn temperature control and stabilization of thermal runaway in tokamaks," *Physics Scripta* **T16** (1987) 107; G.T. SAGER, "Review: tokamak burn control," DOE/ER/52127–36, Fusion Studies Laboratory, Univ. of Illinois (1988).
[2.4.41] L. BROMBERG, J.L. FISHER, D.R. COHN, "Active Burn Control of Nearly Ignited Plasmas," Nucl. Fusion, 20, 203 (1980).
[2.4.42] H.KIMURA et al. in Final Report of Fast Wave Current Drive and Ion Cyclotron Heating System for ITER, D.Swain (Ed.) (1990). See also."Ion Cyclotron Physics," Sect. 5.5, this report
[2.4.43] N.N.VASILIEV, V.E.LUKHASH, R.R.KHYRUTDINOV, "ITER fusion power control," ITER-IL-PH-06-0-S-10 (1990)
[2.4.44] S.G.BESPOLUDENOV, S.A.GALKIN, "Possibility of burn control in ITER at high density and low temperature," ITER-IL-PH-06-0-S-12 (1990)
[2.4.45] A.FUKUYAMA et al., "Dynamic response of stationary burning plasma," in Proc. of 13th Int. Conf. on Plasma Physics and Controlled Nuclear Fusion Research, Washington, DC,1990, IAEA-CN-53/G-2-7.
[2.4.46] T.ELEVANT, presented at the ITER Specialists' Meeting on Burn Control, Garching, July 1990
[2.4.47] *ITER Plasma Facing Components*, IAEA ITER Documentation Series, No.30, International Atomic Energy Agency (1990)
[2.4.48] R.B.CAMPBELL, S.W.HANEY, L.J.PERKINS, "An investigation of emergency plasma shutdown methods for ITER," Lawrence Livermore National Laboratory, UCRL-JC-104201 (1990), submitted to Nucl. Fusion.

3.0. POWER AND PARTICLE CONTROL

3.1 INTRODUCTION

The ITER power and particle control concept is based on a poloidal double-null divertor operating in a high recycling mode. Particle exhaust is performed via pump ducts opening on the lower divertor.

Assessment of recent experimental data and of the validity and applicability of plasma edge models lead to updated information on the impact of power and particle control issues on ITER plasma operational scenarios, materials selection for plasma-facing components, divertor geometry, impurity content, and the exhaust of He ash. Emphasis has been given to determining the uncertainties in predicted divertor performance and how these uncertainties (especially those relating to divertor plate power load, local plasma temperature, and plate erosion) influence the physics guidelines. Analyses have been performed for four plasma operational scenarios which typify those presently being considered for ITER (see §9.3). They are: A1 (the reference physics phase ignition scenario), B1 [the reference, long-pulse, hybrid (30% current drive) scenario for the technology phase with trace Fe seeding to enhance edge radiative power loss], B6 (a steady-state technology phase scenario), and B4 (an 18% current drive, hybrid scenario without impurity seeding, also for the technology phase). These analyses assume up/down-balanced DN performance; there are also assessments of the consequences of up/down imbalance and of operation with a strong SN configuration.

The two-dimensional plasma models used necessarily assume idealised toroidal symmetry and, to date, relate only to a stationary divertor plasma. To compensate, the likely magnitude of toroidal peaking and the consequences of sweeping the plasma across the divertor plate have been examined. There is also preliminary assessment of the effect of edge plasma ergodisation on divertor heat load. Surveys of compatibility with main plasma conditions have been extended to limiter operation during both inductive and non-inductive start up. Helium ion transport from the core plasma has been studied both experimentally and theoretically. Calculations of He pumping requirements have been updated and extended to the detailed geometry of ITER. The potential for improving divertor performance by means of high radiative power losses in the edge or divertor plasmas has been evaluated in the light of both experimental data and the results of modeling. There is updated quantification of the erosion of carbon-based divertor plates when exposed to the expected plasma condition. The potential of tungsten as a divertor plate material has been further explored.

The main conclusions are:

1. The predicted value of the divertor plate power load is robust although uncertainties remain with respect to the fraction of power that can be radiated. Both the reference physics (A1) and technology (B1) phase scenarios are expected to have acceptable power loads, especially if the plasma is swept across the plate.
2. The predicted peak plasma temperature at the divertor plate is less certain, as are the energy of the incident D^+/T^+, He^{++}, and impurity ions and the associated plate

erosion. This is probably not important for the low divertor-sheath temperature (10 to 25 eV) scenarios, A1 and B1, or for the excessively high temperature (100 to 220 eV) scenario B6. In scenario B4, the temperature ranges from acceptable (25 eV) to unacceptable (75 eV). The presence of suprathermal particles, which are not adequately treated in fluid modeling, is expected to increase the energy of incident ions and hence impose more severe constraints.

3. At a peak surface temperature of 1000°C, net carbon erosion in A1 and B1 is modest (< 0.15 m/integrated burn year). Erosion in scenario B4 ranges from marginally acceptable (about 0.25 m/integrated burn year) to unacceptable (100 m/integrated burn year). Scenario B6 exhibits runaway erosion conditions. Erosion is reduced at lower surface temperatures, but the same groupings of acceptability apply. Furthermore, lower surface temperatures are unlikely to be obtained because of the high power loads. Due to low plasma sheath temperature and low impurity charge states, scenarios A1 and B1 are predicted to have acceptable erosion at divertor plate temperatures even near 2000°C, though operation above 1500°C is not recommended.

4. There is now improved convergence in the predictions of the He ash exhaust requirements. To maintain a He ash concentration in the plasma below 0.1, the combined pumping speed of the ducts and the vacuum pumps for scenarios A1 and B1 is in the range 300-to-700 m^3/s of He at room temperature. Scenario B4 requires 340 to 800 m^3/s and B6 requires 1060-to-1970 m^3/s. The ratio of He atom flux exhausted to that of (D + T) equivalent atoms is expected to be greater than 0.025.

5. The relatively low plasma temperature predicted by fluid modeling for scenarios A1 and B1 may be compatible with the use of a tungsten diveror plate. However, the presence of suprathermal particles would have a potentially deleterious effect and the predicted temperature would be expected to increase for tungsten with respect to carbon. Further reassessment of the problem is also required with respect to tritium retention in the materials, impurity (ion) retention in the divertor region, and the effects of impurities on erosion. Compatibility with scenario B4 is much less certain and with B6 is clearly not obtained.

3.2 EXPERIMENTAL DATABASE

3.2.1 General Characteristics of SOL and Divertor Plasmas

The formation of cold and dense divertor plasmas is an essential condition for long-lived operation of ITER divertor plates, impurity control, and adequate He ash exhaust. It reduces the peak power load per unit area on the divertor plates, divertor plate erosion, and required pumping speed for He exhaust (due to increased neutral He pressure by high recycling). Cold, dense divertor plasmas were first observed in DIII [3.1] and ASDEX [3.2] and later in all divertor tokamaks, PDX/PBX, JET, DIII-D, JFT-2M, JT-60. In some cases (DIII, ASDEX), the divertor plasma temperature drops below 10 eV even with large auxiliary heating power. However, in many cases it is still in the range of several tens of eV, a value marginally low in the ITER design because of erosion as described in §3.8. Although conditions for the formation of sufficiently cold and dense divertor plasma are not fully understood yet, heating power (power input to the SOL) and main plasma density (particle flux to SOL) are clearly important parameters. High radiation levels from the plasma edge or

divertor promote low divertor sheath electron temperatures. Moreover, a nonlinear increase of the divertor plasma density (and an associated decrease in divertor electron temperature) as the main plasma density is increased was observed in DIII, ASDEX and other devices. In the same context, dependence of high recycling on the confinement mode of the main plasma is especially important in the ITER design because the particle flux into the SOL generally decreases in the improved energy confinement modes, e.g., H-mode. Relatively low peak divertor plasma temperatures, 20-40 eV, are observed even during H-mode discharges in DIII-D, JFT-2M and JET. During H-mode operation with I = 4.6 MA and P_{NB} = 14 MW, JET reported a flow reversal in the SOL [3.3] where plasma particles flow towards the divertor in the outer region of the SOL and away from the divertor in the SOL closer to the separatrix. This provides an indication of high recycling conditions at divertor plate.

The routine achievement of high recycling conditions in H-mode plasmas and the apparent benefits to be gained support the choice of this mode for ITER operation.

3.2.2 Upstream SOL Plasma Density and Temperature Characteristics

Characteristics of the upstream SOL plasma are closely correlated with divertor plasma performance, i.e., theoretical and modeling predictions indicate that the plasma density at the separatrix in the midplane is of crucial importance for the formation of cold and dense plasmas at the divertor plate. This is also predicted to be one of the key factors determining the peak power load on the divertor plate. Additionally, recycling on the first wall and coupling of RF waves are greatly affected by the midplane SOL density and its profile. In JET limiter discharges [3.4] the midplane separatrix density, n_s, is observed to increase in proportion to the line-average density, $\bar{n}_e$, for low plasma current with constant input power (e.g., $n_s \sim 0.055\ \bar{n}_e$), whereas $n_s \propto \bar{n}_e^2$ for high plasma current ($\geq$ 4MA), reaching $n_s/\bar{n}_e \sim 1/4$ for $\bar{n}_e \sim 4 \times 10^{19}\ m^{-3}$. Consistent with the increase of n_s, the separatrix temperature decreases as $T_s \propto \bar{n}_e^{(-2 \rightarrow -3)}$; T_s increases naturally with the increase of the input power. Increase of the separatrix density is also observed in limiter Ohmic discharges of T-10, [$n_s \propto n_e^2(0)$] [3.5] and by Li beam measurement of TEXTOR SOL plasma [3.6]. TEXTOR observes an isotope dependence of n_s, $n_s(H+) = (1.3–1.7) \times n_s(D+)$, which is consistent with the peaking of the density profile in D plasma. The increase of edge density seems to continue until the plasma detaches from the limiter. TEXTOR observes a decrease of n_s with increasing $\bar{n}_e$ after the plasma detaches. In DIII-D, values of $n_s/\bar{n}_e$ sometimes reach 1/2, as in H-mode discharges with hollow density profiles.

3.2.3 Effect of Additional Heating on SOL Plasma Density

The increase of the SOL plasma density may be greatly enhanced with additional heating, PLT [3.7], ASDEX [3.8], JET [3.3]. The degree of the enhancement depends on the heating scheme and wall conditions. Early ICRF experiments on JET and PLT observed fairly large increases of n_s (a factor of 5 in JET with 12 MW, and $\geq$70% in PLT with 800 kW) with a power dependence of $P^{1/2}$. But virtually no density rise was observed in JET after the installation of Be plasma-facing components [3.9]. The decay length of the SOL density, λ_n, is increased with power, especially in the outer SOL region. This is likely due to direct power deposition in the SOL and the associated increase of ionization of neutral particles from the limiter. An increase of λ_n is also observed in T-10 with high power ECRF heating [3.10]. In NB

heating, the separatrix density increases, in part due to beam fueling, also as ~$P^{1/2}$. No substantial increase of λ_n is observed in JET limiter discharge and only gradual increase in ASDEX divertor discharges. Increase of the separatrix or LCFS (last closed flux surface) density with heating power may be related to the degradation of the particle confinement, consistent with L-mode power scaling and the other experimental tendency that discharges with degraded confinement have higher edge density.

3.2.4 Empirical Scaling for SOL Plasma Characteristics in Divertor Discharge

In divertor discharges of ASDEX, density and temperature profiles in the SOL and the empirical scaling for separatrix density and its decay length λ_n are extensively studied by measuring the density and temperature profile at the midplane SOL by use of a Li beam calibrated by Thomson scattering [3.11]. (The difficulty in determining the separatrix position must be noted). Both n_s and λ_n depend not only on the main plasma parameters (e.g., n, I, P_{input}, etc.), but also on the confinement mode of the main plasma. Typical scalings obtained by regression fitting are:

$$n_s(\mathrm{OH}) \propto \bar{n}_e\, I^{0.25}, \qquad n_s(\mathrm{L}) \propto \bar{n}_e\, I^{-0.5},$$
$$\lambda_n(\mathrm{OH, L}) \propto \bar{n}_e^{-0.22} I^{-0.6}\, P_{tot}^{0.19}. \qquad (I)$$

In general, n_s increases in proportion to the main plasma density, similar to the limiter discharges. No dependence on the power is observed. Typically, $n_s/\bar{n}_e$ ~ 1/4.4 (OH) and 1/4.7 (L). In H-mode discharges, both n_s and λ_n are found to be nearly independent of main plasma density, with $n_s/\bar{n}_e$ occasionally reaching 1/2. DIII-D sees the same variability. Similar to limiter discharges, good confinement discharges have lower values of n_s: $n_s(H+)$ ~ $1.7n_s(D+)$ and $n_s(IOC)$ ~ $0.6n_s(SOC)$. In contrast to n_s, λ_n has no substantial dependence on isotope, $\lambda_n(H+)$ ~ $\lambda_n(D+)$. In NB-heated H-mode discharges of JET, both density and temperature profiles have a plateau-like feature in the outer SOL region, which is similar to the ASDEX divertor discharges.

In the present divertor experiments, neutral particles play a dominant role in the particle balance within the separatrix surface, which will be quite different from the ITER case. Thus n_s and λ_n in ITER could be very different.

Based on the available data, $n_s/\langle n_e \rangle$ = 1/3.5 was chosen as input to the 2-D models of the ITER SOL (see §3.4).

3.2.5 Transport Processes and Coefficients

It is generally accepted that transport along the field line is dominated by collisions that is supported by numerical simulations of the experimental data from the midplane and divertor regions. For example, ASDEX demonstrated electron pressure balance between the midplane and the divertor, which can be evidence of momentum conservation in collisions [3.12]. Although there exist several uncertainties in this experimental evidence, e.g., separatrix position and the ion contribution to the pressure balance [3.13], the collisional transport process seems to dominate, in a global sense, transport along the field line.

The cause of transport perpendicular to the field line is poorly understood. Transport is anomalous. Furthermore, there is a large uncertainty in the present experimental database for χ and v_{pinch}. The data that exist are not for the same plasma parameters as expected in the ITER SOL. In principle, $D_\perp$ and $\chi_\perp$ can be derived

from the measurement of λ_n and λ_T (temperature decay length). In JET divertor and limiter discharges, $D_\perp$ scales as $\bar{n}_e^{-1}$ near the separatrix in the SOL [3.4]. Since $T_e(a) \propto \bar{n}_e^{-1}$, $D_\perp$ could be interpreted as Bohm-like ($\propto T$). However, the density profile usually has a plateau-like feature in the outer region of the SOL, which cannot be reproduced by Bohm-like diffusivity and suggests that $D_\perp$ should have an increasing feature in the radial direction such as $\propto n(r)^{-1}$, with which ASDEX data is well reproduced by 2-D divertor simulations. In contrast to the case of $D_\perp$, there exists large uncertainties in determining $\chi_\perp$ from measurements of T_e and T_i profiles, in part due to uncertainties of the sheath heat transmission coefficient, which can be affected by the secondary electron emission and by T_e - T_i equi-partitioning in the SOL. Thus far, very few estimations of χ_e have been obtained, and no estimation of χ_i exists since there is no reliable experimental data on ion temperature in the SOL.

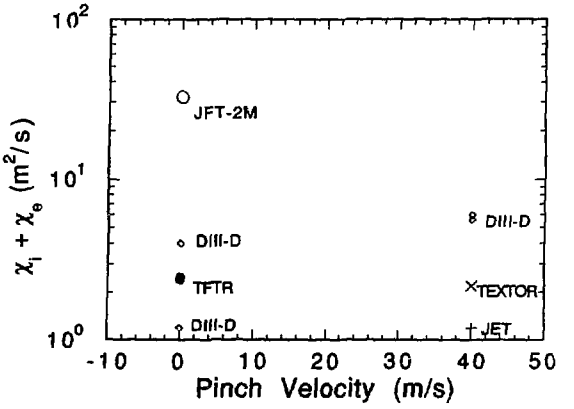

FIG. 3-1 Reported values of heat conduction χ and inward pinch v for fits to various experiments (JFT-2M, DIII-D, TFTR, TEXTOR, JET).

The method by which perpendicular transport coefficients were extracted from the experiments for ITER use was to simulate the tokamak edge plasma database with the 2-D codes and vary the transport coefficients to match the observed electron temperatures, densities, and divertor plate power loads (§3.2.7). The best fits from the simulations are summarized in Fig. 3-1. Average values chosen for the ITER simulations are described in §3.3.2.

Other important transport processes that can affect the divertor and SOL plasma characteristics are drift effects and SOL plasma currents. Both particle and heat fluxes are affected by classical drift effects, $\mathbf{B}\times\nabla P_e$ and $\mathbf{B}\times\nabla T$. Direct discrimination of this drift process from anomalous transport is difficult to demonstrate in experiments. Indirect indications have been obtained in various ways, e.g., modification of heat flux and impurity radiation asymmetry between inboard and outboard divertor region in the SN divertor discharge when the direction of the toroidal magnetic field is reversed. Direct measurement of SOL currents by Langmuir probes was first done in JET SN divertor discharges [3.3]. It was concluded that a large SOL current, up to 10^5 A/m^2 (see Fig. 3-2), was driven by the thermoelectric force due to the potential

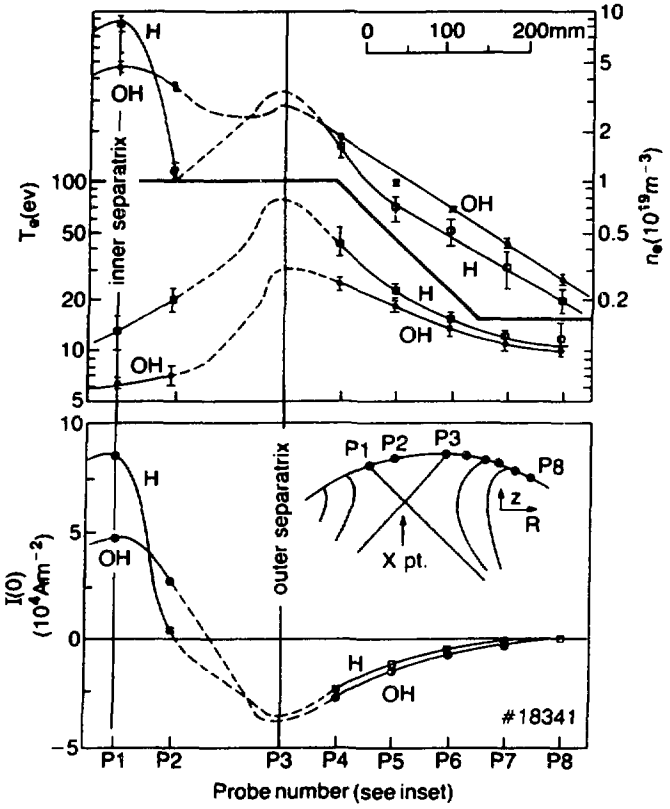

FIG. 3-2 Profiles of density, temperature, and net current density at the target plates. Net current density is measured with Langmuir probes P1 to P8 at torus potential mounted in these plates. Figure taken from JET TEAM (presented by M. Keilhacker), Proc. 12th Int. Conf. on Plasma Physics and Controlled Nucl. Fusion Research, Nice, France, (1988), IAEA, Vienna, p. 159.

difference between the inner and the outer divertor plates. This was generated by the heat and particle flux asymmetry between them - a larger heat flux with less particle flux to the outer plate. An electrical potential difference between inner and outer divertor plates is also observed in other divertor tokamaks, JFT-2M, DIII-D. Thus, a SOL current may play a role in SOL and divertor plasma characteristics.

Viscosity coefficients have not been measured in the edge region of tokamaks. Their effects on transport, as investigated by the fluid models, have not been studied. In the fluid codes the viscosity values are taken to be near neoclassical, or a small fraction, < 0.2, of the anomalous value.

3.2.6 Comparison of SOL Parameters for SN and DN Divertor

Systematic investigations of the SOL parameters both for SN and DN configurations have been done only in ASDEX [3.14]. It is shown by Li beam measurement

that the separatrix densities n_s both for SN and DN are similar both in L- and H-mode discharges, and for wide range of density, power and current scans.

3.2.7 Characteristics of Heat and Particle Loads on Divertor

Heat load and particle flux onto divertor plates have been measured by IRTV and/or Langmuir probes in many divertor tokamaks. A larger database is available for SN divertor discharges than for DN. Understanding of these characteristics is far from sufficient for ITER design.

3.2.7.1 Power load half width

In DIII-D, extensive measurements of the heat load on the divertor are done for SN divertor discharges in various confinement modes [3.15]. The half width of the heat load (Δ) is greatly affected by the confinement mode. In DIII-D Δ is reduced by a factor of 2 after the H-mode transition. Δ is also affected by other parameters of the main plasma, such as plasma density and input power into SOL. Model predictions based on a collisional transport along the field lines and anomalous transport across the field lines indicate that Δ increases with (separatrix) density and decreases with input power into SOL. IRTV measurement on JT-60 show qualitative agreement for this prediction [3.16]. Definitive experimental identification of these dependences has not yet been fully done. The experimentally determined geometrical dependence of Δ seems obvious, e.g., Δ varies with the variation of the flux tube width at the divertor strike point, as is shown by changing the X-point height in DIII-D [3.17] and JT-60 [3.16]. Another obvious geometrical effect is that of connection length (Δ increases as the connection length increases due to increased perpendicular transport) qualitatively supported in DIII-D SN divertor configuration [3.17], in which Δ is much smaller on one side of the divertor plate with larger heat flux, than on the other. This is emphasized when the heat flux asymmetry between the inner and outer plates is large.

3.2.7.2 Asymmetry of heat and particle fluxes onto the divertor

Asymmetry of the heat flux onto the inner/outer divertors for SN and upper/lower divertors for DN is important in the ITER divertor design since it directly affects the peak heat load, $\hat{P}$. A systematic experimental database is still lacking, especially for the DN divertor configuration. Generally acceptable qualitative features so far obtained are that these asymmetries surely exist both in SN and DN configurations, and they are greatly modified by the direction of the toroidal magnetic field, which is represented by the ion ∇B drift direction. When the ion ∇B drift direction is toward the X point in a SN configuration, the heat load (total integrated) on the outer divertor is generally larger than that on the inner, e.g., in DIII-D and ASDEX, inner-to-outer ratio is 1:2 (OH), 1:4 (L) and 1:2 (H) [3.15, 18]. In addition, the feature of this larger heat load on the outer may not be universal, since, in JT-60 [3.16], a larger heat load (total integrated) on the inner divertor is observed (≈2:1) for low density discharges, though the outer heat load becomes larger when the density is increased. When the ion ∇B drift direction is reversed (away from the X point), this asymmetry tends to be equalized or the inner can be rather larger than the outer. In DIII-D, the asymmetry is almost equalized in L-mode discharges, while the peak heat load on the inner divertor is larger than the outer by a factor of ~2 in H-mode discharges. In JT-

60, the total integrated power almost doubles at the peak in the inner divertor for L-mode discharges. In these experiments, the density range is still narrow; careful discrimination between total and peak heat load asymmetry must be done.

There are several physical mechanisms that could produce this asymmetry. One is a geometrical effect - the area of outer separatrix surface is larger than inner; another effect is that larger radial gradients at large major radii because of the smaller distances between the flux surfaces. Another possibility is microinstabilities localized near the outer midplane and the associated increase in heat/particle transport. Numerical calculations show that the geometrical mechanisms explain an asymmetry of factor 2. Thus, the transport process may also play an essential role. This is supported by experiments in DIII-D showing the asymmetry increases up to 1:4 in L-mode discharges as the heating power is increased [3.15]. This speculation is also supported by the fact that the direction toroidal magnetic field modifies the asymmetry observed in many divertor tokamaks. In particular, the observation in DIII-D that, at the H-mode transition, the heat load is reduced only on the outer divertor suggests that the enhanced energy loss associated with L-mode is probably localized near the outboard midplane.

Asymmetry of particle flux is relevant to He ash exhaust. In the SN divertor, the in-out asymmetry of the particle flux is opposite to the heat flux asymmetry because of pressure balance and enhanced radiation at higher density. This expectation is supported by many divertor tokamaks, JET, JT-60, JFT-2M, and DIII-D. In JFT-2M, the particle flux is larger and the heat flux is smaller, on the ion side. Although this is not inconsistent with the physical picture obtained in other divertor tokamaks that transport (correlated with the direction of ion ∇B drift) modifies the in-out asymmetry of the heat flux, it is not clear whether this feature is universal.

3.2.7.3 Heat load characteristics of DN divertor

The 2-D SOL models assume a 1:1 split of power between upper and lower divertors. This equal partitioning is closely related to the accuracy of vertical plasma position control. Slight vertical displacement ($\Delta_z \sim \pm 10$ mm) is expected to be sufficient to produce enough separation of the active and passive separatrix surfaces (5 mm at the midplane) that a large asymmetry of heat load on the upper and lower divertor plate would result. In ASDEX [3.8], intentional displacement of the vertical position is done to measure the transition from DN to up or down SN configurations by measuring the floating potential dip due to fast electrons. Transition from DN to SN requires displacement of the magnetic axis by ± 1 cm vertically, consistent with the displacement required to produce asymmetry of the threshold power for L-H transition. A few mm displacement appears sufficient to produce such a DN/SN transition, as fast electrons are expected to be strongly localized at the separatrix surface, thus suggesting unknown mechanisms that broaden the orbit of fast electrons.

With a magnetics control scheme, DIII-D [3.17] performed an experiment to maintain a DN configuration throughout an H-mode discharge, with the two separatrix surfaces coincident to ± 2 mm at the midplane. The total power to each divertor target was balanced to within 20%, but the peak heat flux on the lower target plate (in the ion ∇B drift direction) is nearly twice that on the upper target. This feature is shown in Fig. 3-3. These results suggest that it may be impossible to equalize the heat load solely by a magnetics control scheme, and that the imbalance of the peak heat

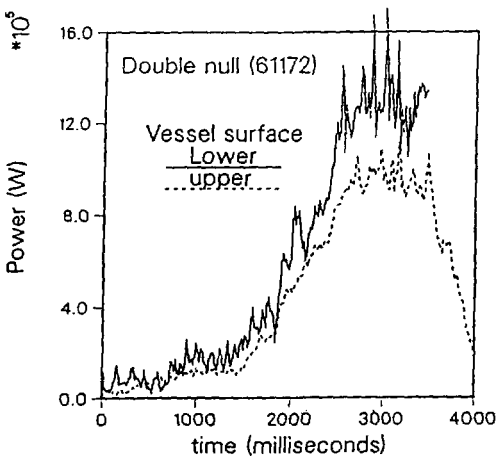

(a)

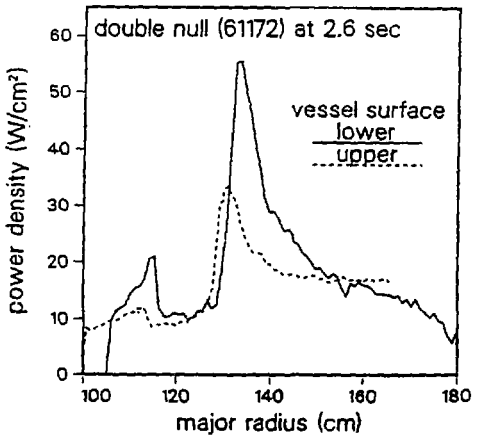

(b)

FIG. 3-3 Divertor heat flux for DN H-mode with ELMs. Ion grad B drift is towards lower divertor. Profiles are at 2.6 s. Figure taken from D.N. HILL et al, "Divertor Plasma Studies on DIII-D," Proc. 13th Int. Conf. on Plasma Physics and Contr. Nuclear Fusion Research, washington, D.C. (1990).

load can be larger than that of the total heat load. The result that, for this DN case, the heat load on the inner divertor target is considerably smaller than the outer (typically 1/3–1/4) for both upper and lower divertor, seems contradictory to the SN database since the ion VB drift direction is away from X point for the upper divertor target.

In ASDEX [3.12], toroidal asymmetry of the divertor heat load is observed by measuring the temperature rise of the cooling water in eight toroidal segments after the discharges for OH, LH-heated and NB-heated H-mode discharges with ELMs. The

toroidal phase of this asymmetry exhibits n=1 mode structure and is locked, probably to a static external perturbation. The degree of the asymmetry strongly depends on the safety factor. With strong LH heating in an upper SN configuration, the asymmetry becomes ~2 for $q_{cyl} = 2.5$ and it reduces down to ~20% for $q_{cyl} = 3.7$. One possible cause of this asymmetry is speculated to be a small misalignment of the divertor coil.

3.2.7.4 Characteristics of ELMs

Transient phenomena that cause periodically large heat loads on the divertor plates will have a great impact on the divertor design for ITER. Such transient phenomena are expected to be present in the ITER scenarios. In particular, edge localized modes (ELMs) are transients that are an essential part of a candidate scheme to attain steady-state H-modes without uncontrolled density and impurity increase. Characteristics of ELMs have been studied in DIII-D [3.17]. The major points are as follows:

(i) Frequency and amplitude of ELMs

At low input power, ELMs occur infrequently and have a relatively large amplitude (> 0.1 E_{tot} loss per ELM). At higher power, the ELM frequency increases and the amplitude falls (~1-2% of E_{tot} loss per ELM with frequency of ~100 Hz for P_{tot} ~ 12 MW). An increase of the ELM frequency with the input power is consistent with the physical picture that ELMs occur when the edge pressure gradient exceeds the ballooning stability limits. However, the decrease of the ELM amplitude cannot be explained by this picture. X-point location affects the edge magnetic shear and consequently the stability limit of the ballooning mode (higher X-point generally gives fewer ELMs), which support the ballooning feature of ELMs.

Grassy ELMs and the consequent steady H-mode discharge can be produced and controlled by the application of perturbed helical field on the plasma periphery (EML; Ergodic Magnetic Limiter) as shown in JFT-2M [3.19].

(ii) Power load characteristics on divertor plate during ELMs

The peak heat load onto the divertor plate during giant ELMs is about 10-20 times the value between ELMs. In DIII-D and ASDEX SN divertor [3.15], a large peak heat load (~ 55 MW/m^2 for P_{NB} = 5 MW) is observed and ~10 % of total stored energy E_{tot} is lost per ELM. In this case, the power deposition profile is substantially broader, 8 cm 1/e width, compared with 3–4 cm 1/e width in the quiescent H-mode [3.15, 18]. For grassy ELMs, direct, time-resolved power load measurements are more difficult.

The fraction of total energy deposited on the inner and outer divertor plate seems to depend on the discharge conditions. In some cases, the outer plate receives dominant energy lost by ELMs, consistent with the ballooning picture of ELMs localized near the outer boundary. However, the fraction can be equal and, in some cases, the inner plate is observed to receive greater energy than the outer, which could possibly be due to a toroidal mode structure [3.17].

(iii) ELM effects on divertor plasma characteristics

The divertor electron temperature and density are modified by the ELMs, as observed in DIII-D [3.17]. For giant ELMs, the ion saturation current increases by a factor of 5-10, and the heat flux to the divertor increases more. This suggests that the ELMS produce a temperature modulation. The impact of this transient modification of the divertor plasma characteristics on the plate erosion is not yet clearly identified.

3.2.8 Impurity Transport, Accumulation, and the Associated Radiation Loss

3.2.8.1 Level of Z_{eff}: graphite divertor/first wall components

Impurity contamination in the main plasma degrades the plasma performance of ITER in two ways, depending on the impurity species: fuel dilution is dominant by low Z impurities and radiation losses by high Z impurities. The contamination level, Z_{eff}, has been measured in existing devices with graphite or other low-Z divertor/first wall materials such as boron and beryllium. Reduction of Z_{eff} with increasing plasma density is observed in all of the existing and previous devices.

Z_{eff} increases with plasma current in Ohmic discharge of JET, due probably to the increase of edge temperature with current [3.20]. Z_{eff} also increases with current in NB-heated discharges in JT-60 [3.21]. The absolute value of Z_{eff} depends on the heating mode (OH or auxiliary), power level, and confinement mode. In the case of graphite divertor/first wall components, the minimum value of Z_{eff} attained so far is ~1.5–2.0. When heating powers become large (e.g., ~10 MW for JT-60, ~20 MW for JET, ~25 MW for TFTR), abrupt increases of Z_{eff} are frequently observed, corresponding to the initiation of carbon blooms due to inaccuracy of graphite tile alignment and other effects. In TFTR, with a tile alignment accuracy of 1–2 mm, the surface temperature of locally heated parts exceeds ~1700°C, which is beyond the threshold temperature for radiation enhanced sublimation at electron temperatures of ~ 50 eV. This leads to the bloom [3.22]. Better tile alignment in TFTR, to 0.2 mm, has reduced the occurrence of the blooms and raised the power/energy threshold about a factor of 2.

Abrupt increases of Z_{eff} are more pronounced in the case of LHCD discharges. Less power, compared to NB, is sufficient to produce blooms. This result is likely caused by localized impacts of fast electrons or increased edge electron temperature.

The level of Z_{eff} in the improved confinement mode regime is particularly important for ITER. In the quiescent H-mode, Z_{eff} is usually higher. Radiation increases, associated with the increase of density of hydrogen and impurity ions; the discharge finally terminates due to radiative collapse. Impurity accumulation in H-mode discharges is avoided by ELMs. Grassy ELMs with small amplitude and high frequency are particularly efficient in this respect. Steady H-modes are maintained for > 10 s in DIII-D [3.23] when accompanied by grassy ELMs. In this discharge, $Z_{eff} < 1.7$ is attained with a confinement enhancement factor of ~ 1.4 (DIII-D data in the ITER H-mode databasehave an overall average value of enhancement of 1.7). Avoidance of impurity accumulation is also observed in JFT-2M experiments, in which grassy ELMs are triggered by the application of the perturbing magnetic field on the periphery [3.19].

3.2.8.2 Level of Z_{eff}: beryllium, boronized, and metal divertor/first wall components

With beryllium-coated (JET) and boronized (TEXTOR, ASDEX) divertor and first wall components, lower Z_{eff} is observed, i.e., 1.4 (OH) and 2–3 (strong heating) in JET [3.24] and 1.4 in TEXTOR OH discharge [3.25]. This is mainly due to the reduction of O impurity and the associated reduction of C (generated in the form of hydrocarbons). However, blooms cannot be prevented even by beryllium. Due to this reduction of impurities, plasma detachment has been rarely observed and the critical density limit for disruption is found to be greatly increased in TEXTOR [3.24].

The lowest Z_{eff} values have so far been achieved in metal divertor/first wall discharges. In JT-60 [3.26] TiC coated molybdenum divertor/first wall discharges, Z_{eff} is reduced down to ~1 in the OH discharge, and to ~1.4 even with 22 MW of NB heating discharges in divertor configurations. However, in the NB-heating case, abrupt increase of metal impurity influx have been frequently observed in the divertor discharges. Z_{eff} is fairly high in the limiter discharges.

3.2.8.3 Impurity transport and the associated radiation

The level of Z_{eff} and the associated radiation loss and its profile are strongly affected by the transport of impurities generated at the divertor/first wall. Impurity transport in the edge/SOL region determines the impurity retention efficiency. Divertor plasma have higher retention capability for impurities owing to the shielding effect of the SOL plasma. This is clearly demonstrated in all divertor tokamaks. In general, retention efficiency for heavy metal impurities is much higher than for light gaseous impurities. Retention efficiency also depends on the main plasma density and the SOL density; at low density, the efficiency decreases significantly [3.27], which partially explains the increase of Z_{eff} in low density discharges. Transport in the main plasma determines the accumulation of impurities, and thus, has a crucial effect on the plasma performance. Impurity transport in improved confinement modes is particularly important. In most improved confinement mode discharges, especially quiescent H-modes, strong impurity accumulation near the plasma center is generally observed. Impurity accumulation is found to be absent in the H-mode regime with grassy ELMs. Large increases of radiation near the plasma center are due partially to the increase of the density. Additionally, measurements of the impurity line emission leads to the conclusion that the impurities actually accumulates near the center, which is usually modelled by inward pinch velocity in the transport equation.

3.2.8.4 Radiation cooling of the edge

Substantial cooling in plasma periphery or divertor region by impurity radiation is fairly beneficial for divertor design, particularly if stable and controllable. Radiative cooling in the divertor region was first observed in DIII [3.28] and ASDEX [3.29], in which almost half of the input power was radiated. Recently, in the JT-60 IDC mode also, up to 50% of the input power is radiated by carbon from the inboard region of the divertor, without significant increase of the radiation from the main plasma [3.30].

In many limiter discharges, strong edge radiation (~100% of the input power) is often observed at high plasma density, especially, with graphite limiters. Due to this large edge radiation, the plasma current channel shrinks and detaches from the limiter. The particle flux to the limiter decreases and that to the first wall increases. Marfe phenomena often precede detachment. Reattachment is generally caused by strong NB heating. The detached state can be recovered with hydrogen gas-puffing or impurity (neon) puffing, TFTR [3.31]. It has been shown that both Ohmic and NB TFTR detached plasmas are nearly devoid of metallic impurities and often have $Z_{eff} < 2$.

For the application of these large radiation discharge scenarios to ITER, there exist several related issues: stability, controllability, and purity of the main plasma. In the case of divertor radiation, too much reduction of the divertor plasma temperature (below several eV) could lead to disruptions due, possibly, to thermal instability in the

divertor configuration, as suggested by ASDEX [3.32]. In the case of edge radiation in detached discharges, the discharge condition is very close to the plasma disruption due to the shrinkage of the current channel. The rapid increase of the radiation at detachment occurs within a small range in the density. Contamination of the main plasma, when the edge radiation is fairly large, is another concern, especially, in the improved confinement modes, where significant inward pinch may occur.

3.2.9 Helium Transport and Exhaust

This issue is divided into three categories. First is the transport of He in the main plasma. Slow He transport out of the core region will degrade fusion power due to fuel dilution (at constant β). Second is the absolute value of the neutral He pressure in the duct region. This determines the required exhaust speed of the pumping system. Third is the relative pressure of He to the fuel particles in the pump duct region. This determines the tritium throughput and associated reprocessing requirements, topics of great concern from a safety perspective.

3.2.9.1 Helium transport in the core plasma

The minimum level of He that accumulates in ITER is directly correlated with He transport in the core plasma, although pumping conditions (i.e., boundary conditions) naturally also have a substantial effect. Particle transport of hydrogen/deuterium in the main plasma may provide useful information on the He transport, since their masses and mass-to-charge ratios are similar. The ratio of H/D particle diffusivity D to the energy diffusivity χ was studied in JET and JT-60 by the measurement of heat and density pulse propagation (after the sawtooth crash). The results of these perturbative measurements showed $5 > \chi/D > 12$ in JET and $\chi/D \sim 3$–6 in JT-60. Measurements by profile analysis in JET [3.33] show smaller values, $\chi/D \sim 2$–3. In TFTR, χ/D for deuterium is determined from measurements of density and temperature profiles under steady-state conditions. They obtained $\chi/D \sim 4$ for L-mode and ~1 for supershot conditions [3.34]. Differences of the χ/D values for JET, JT-60, and TFTR may be attributed to profile differences and pulse propagation versus profile analysis of experimental conditions.

Indications of differences between He and H/D particle transport are obtained by direct measurements of He transport in TFTR [3.35], JT-60 [3.36] and TEXTOR [3.37]. Analysis of the transient behavior of the He density profile after gas-puffing in TFTR shows a strong hollow spatial dependence of particle diffusivity with fairly large convective inward velocity (> 30 m/s). A large diffusivity (~10 m^2/s) is necessary in the edge region to model the data. Both JT-60 and TEXTOR observe the quasi-steady behavior of the He density profile and report that an inward pinch plays an important role (1–2 m/s) with a diffusivity of ~ 1 m^2/s. Indication that the inward pinch velocity of the He is larger than that of the background H/D is also suggested by comparison of quasi-steady profiles of He and background hydrogen/deuterium in JT-60 (c_v = 1–2 for He and 0–1 for hydrogen where the inward pinch velocity v_{pinch} is expressed as $v_{pinch} = 2c_v Dr/a^2$) and TFTR (where the peaking factor is ~ 1.6 for deuterium and ~ 2 for He). Note that, despite the large values for v_{pinch}, these are small values of c_v, corresponding to increases in He concentration less than a factor of 2 over $v_{pinch} = 0$.

Additional information on He accumulation levels is from global values of (τ_{He}/τ_E). This is obtained from transport analysis in TEXTOR ($\tau_{He}/\tau_E \sim 3$) [3.37] and TFTR ($\tau_{He}/\tau_E \sim 2$–3) [3.35]. All of these results indicate that the minimum He concentration in ITER, with the installation of proper pumping capacity, will be in the range of (5–10)%.

Note that all of these experiments are L-mode or slightly improved confinement mode discharges and the empirical scaling for τ_{He} core, especially for the improved confinement modes, is needed to extrapolate more directly to ITER.

Helium transport was shown to be affected by edge recycling or deuterium fueling conditions in TEXTOR, where large pumping (and/or large deuterium gas-puffing) is speculated to reduce the coefficient of inward pinch velocity of He. Detailed profile information is needed to prove that the pinch velocity is really reduced. This feature may have some similarity to peaked density profiles in enhanced confinement regimes like the IOC in ASDEX and T-10, observed when gas-puffing is reduced.

3.2.9.2 Helium exhaust requirements

DIII and JT-60 have measured the neutral He pressure (both absolute and relative to the background H/D pressure) in the divertor duct region. In DIII ohmic discharges with He gas-puffing [3.38], neutral He pressure increases non-linearly with the $\bar{n}_e$, reaching 0.026 Pa. In JT-60 NB-heated L-mode discharges [3.39], both hydrogen and He neutral pressure rise as $\bar{n}_e^3$ and the He pressure reaches 0.02 Pa for $\bar{n}_e = 5 \times 10^{19}$ m^{-3}, which, with no extrapolation, implies that a pumping speed of ~100 m^3/s is sufficient for ITER. An exhaust efficiency of 0.92 (recycling coefficient) for He was demonstrated in the TEXTOR [3.37] pump-limiter experiment.

3.2.9.3 Tritium throughput

Tritium throughput to the pump is determined by the He enrichment factor, defined as $R_e = (P_{He}/P_{D+T})_{duct}/(n_{He}/n_e)_{main}$. In DIII-D Ohmic discharges with He gas-puffing [3.38], $R_e \sim 0.5$ (a de-enrichment). In JT-60, the neutral He pressure and R_e were measured in hydrogen-NB heated L-mode discharges with He gas-puffing and He NB fueling [3.39]. R_e depends strongly on the fueling scheme of He, i.e., deep fueling reduces R_e in the divertor region, an effect which is attributed to the reduction of recycling of He in the SOL. In support of this picture, $R_e \sim 0.4$–0.5 was obtained with NB He-injection and $R_e \sim 0.8$ was obtained in small He gas puffing case. Pump-limiter experiments in TEXTOR also obtained similar R_e values (~0.5 for low- and ~1.2 for high-$\bar{n}_e$ discharges) [3.37].

3.3 STATUS OF MODEL VALIDATION

3.3.1 Models of the Edge Plasma Region

The design database for the ITER divertor plasma performance has been based on 2-D computational models that include detailed fluid treatments of plasma behavior in the SOL and in the divertor volume. Five [3.40-44] of the dozen or so existing models have been predominantly used for 2-D modeling of the edge plasmas in tokamaks prototypical of reactors. Their comparative characteristics are given in Table 3-I. All the codes employ multi-fluid hydrodynamics equations with anomalous transport across and classical transport (modified to include some kinetic effects) along the magnetic field line. Some of the codes use Monte-Carlo techniques, others use analytic models, to simulate neutral gas behavior. Two of the models (EDGE2D and B2) include a part of the main plasma inside the separatrix. Most of the codes use curvilinear, orthogonal coordinates and a geometry consistent with the MHD equilib-

TABLE 3-1. CHARACTERISTICS OF 2-D EDGE MODELS

Braams B2	Edge 2D	UEDA	DDC 83	DDIC 89	Characteristics of 2-D fluid edge plasma codes	
x	x	x	x	x	Braginskii basic equations	
x	x		x	x	Finite difference	Calculation method
		x			Particle in cell	
			x	x	Rectangular mesh	Geometry
x	x	x			Orthogonal curvilinear	
x	x	x			Linked to MHD	
x		x			Trace concentrations	Impurities
				x	Unlimited concentrations	
x	x	x	x	x	Flux limiter	Additional transport
x	x				Inward pinch velocity	
	x	x			B×∇T drifts	
	x				Edge currents ($B_{\parallel}$)	Sheath boundary
x		x	x	x	Local ambipolarity	
x	x	x			Mach number = 1	
			x	x	Continuity conditions at λ_{ee} from sheath	
x			x	x	Non-statistical	Neutral transport
x	x	x	x		Monte Carlo	
x				x	Release of plate/wall impurities	

rium surfaces. Impurities are mainly described in the test particle approximation, except DDIC89, where an arbitrary impurity concentration can be included.

3.3.2 Scrape-off-Layer Parameters

To predict plasma edge behavior by means of two-dimensional fluid models, it is first necessary to postulate the plasma conditions [i.e., density (or particle flux) and temperature (or energy flux) of both electrons and ions] at the interface between the main plasma and the edge region, which is encompassed by the model. Then, it is necessary to prescribe the coefficients for radial thermal diffusivity ($\chi_{\perp}^{e}$ and $\chi_{\perp}^{i}$), particle diffusivity ($D_{\perp}$), and parallel transport. To the extent possible, this has been accomplished by a comparison with experimental data from tokamaks and other plasma devices (see §3.2). To compensate for the lack of detailed theoretical understanding of the transport mechanisms, selection of transport coefficients is made by matching the main parameters of the SOL plasma, e.g., electron temperature and density profiles and divertor power load profiles, observed in the experiments with those reproduced in the calculations. Basic characteristics predicted by modeling, e.g., pressure balance along **B** (ASDEX/B2 and DDC83 codes), and B×∇T drift effects (JFT-2M/UEDA code), have been validated for a limited number of discharges. However, inadequate cross checking, due to a lack of data over a wide parameter range, is the rule. This arises from a combination of inadequate diagnostic facilities, complex divertor geometries, and lack of machine time dedicated to edge plasma problems. This has limited the ability to study scaling of edge conditions. A

particular difficulty has been the need to identify the location of the separatrix with the high precision (< 1 cm) required for comparisor. of radial profiles in the SOL with those at the divertor plates. Furthermore, boundary conditions must be imposed that describe energy transport through the sheaths at the divertor targets, e.g.,

$$q_{\parallel,sheath} = \Gamma_{\parallel} (\gamma_e T_e + \gamma_i T_i) \qquad (2)$$

where $\Gamma_{\parallel}$ is the particle flux and γ_e and γ_i are the appropriate sheath heat transport coefficients for electrons and ions. Similarly, at the first wall, temperature (or energy flux) and density (or particle flux) conditions must be postulated. The recycling of particles at each boundary must be described.

Guidelines to the modeling parameters have been evolved, based upon assessments of experimental (§3.2) and theoretical results, and are as follows:

(i) Edge plasma density

For a DN configuration, it is assumed that the density at the separatrix on the outer mid-plane is $n_s \approx \langle n_e \rangle / 3.5$. This is a somewhat smaller density ratio than is observed in ASDEX but it takes account of H-mode discharges for SN configurations in both JET and DIII-D (see §3.2.2 and 3.2.4). Furthermore, there is evidence that $n_s \propto \langle n_e \rangle^2$ so that a larger value of n_s could be envisaged for ITER.

(ii) Cross-field transport coefficients

At present there is insufficient evidence to reject the simplistic assumption that anomalous transport can be simulated by a constant coefficient which is independent of plasma parameters. The values given in Table 3-2, independent of T_e, n_e and r, have been used for a number of simulations of ITER:

TABLE 3-2.

	$\chi_{\perp}^{e}$ [m^2/s]	$\chi_{\perp}^{i}$ [m^2/s]	$D_{\perp}$ [m^2/s]	v_{pinch}
L-mode	3	1	1	0
H-mode	1	1/3	1/3	0

The confinement mode envisaged for ITER is the "ELMy" H-mode chosen for long energy confinement time and low impurity content. Detailed assessment of the DIII-D data implies that only a small fraction (< 0.1) of the contained energy will be lost in "ELMy" H-mode conditions that correspond to the surface power densities envisaged for ITER. For all four scenarios (A1, B1, B4, and B6) the cross-field transport coefficients summarized in Table 3-3 were used in the modeling.

TABLE 3-3.

	$\chi_{\perp}^{e}$ [m^2/s]	$\chi_{\perp}^{i}$ [m^2/s]	$D_{\perp}$ [m^2/s]	v_{pinch}
"ELMy" H-mode	2	2/3	2/3	0

(iii) Parallel transport

Thermal transport along the field is limited to a fraction of the free streaming value by a flux limit factor, taken to be $F_l = 0.2$ for both electrons and ions, from

kinetic models of the edge [3.45]. The heat flux is then given by

$$q_{\parallel}(\text{sheath}) = F_1\, q_{SH}\, q_{fs}/(q_{SH} + F_1\, q_{fs}) \qquad (3)$$

where q_{SH} = the Spitzer-Härm heat flux and $q_{fs} = n\, v\, T$, the free streaming value.

(iv) Z_{eff} in the scrape-off layer

The values of Z_{eff} quoted for the various options of ITER make allowance for the edge localised nature of power losses for partially stripped impurities. From purely global considerations it may be expected that the same composition of impurities could result in a lower value of Z_{eff} in the SOL due to the lower average charge state of the impurity ions. Assuming that the average charge state is 12 for iron and 3 for carbon provides a crude estimation that

$$Z_{eff}(\text{SOL}) = 1 + 0.8\,[Z_{eff}(\text{core}) - 1] \qquad (4)$$

It is stressed that this is only a global value (which is presently used in systems code analysis) and that, for 2-D analyses, the local Z_{eff} should ideally reflect the local concentration of impurities due to release from boundary surfaces etc. Indeed, some experiments exhibit a Z_{eff} which increases towards the edge.

(v) The influence of $Z_{eff} > 1$ upon collisionality in the SOL

This reduces the classical coefficient for parallel transport of heat, i.e., $\chi_{\parallel} \propto 1/Z_{eff}$ and so the influence of the F_1 may be reduced. A further effect is that $n_e = n_i$ is no longer a valid assumption.

(vi) Interface to core plasma

The location of the interface between the main and edge plasma should be inboard of the separatrix in order that simplifying assumptions such as uniformity of density and temperature (or power flow) are appropriate. It is assumed that there is no poloidal variation of χ.

(vii) Power flow channels

The prediction of edge plasma conditions is sensitive to the assumed values of $P_{\perp}^{e}/P_{\perp}^{i}$. Both power load and local plasma temperature increase with increasing $P_{\perp}^{e}/P_{\perp}^{i}$. The experimental database is sparse but it appears to favour values somewhat lower than $P_{\perp}^{e}/P_{\perp}^{i} = 3$, which is what is conservatively assumed for ITER.

(viii) Power flow

It is assumed that the non-radiated plasma power which enters the (inner/outer) SOLs of a balanced DN configuration is $P_{in}/P_{out} = 1/4$, somewhat smaller than the experimental data reported in §3.2.7.2.

The consequences of uncertainties in these guidelines and their inclusion in the physics specifications are discussed in §3.4.

3.4 MODEL PREDICTIONS OF DIVERTOR HEAT LOADS

Two-dimensional modeling of the scrape-off layer and divertor of ITER has been used to predict the performance of the edge plasma. The reference cases were generated using the Braams B2 code in several different versions. Benchmark comparisons against calculations using the UEDA and DDIC codes have been performed.

Assuming symmetry, 2-D modeling [3.46,47] with the Braams code has been carried out for one half of the DN ITER configuration, as well as for SN cases.

Reflecting cuts are imposed at the separation of inner and outer scrape-off layer. Null-to-strike point distances are 1.5 m (outer plate, connection length 84 m at 22 MA) and 0.6 m (inner plate, connection length 79 m at 22 MA). The plate inclination is assumed to be 15° to the separatrix magnetic surface for the outer plate (field line angle to plate 1.6°) and 45° for the inner plate (field line angle to the plate 1.9°). The interface to the core plasma is 2.5 cm inside the separatrix.

All 2-D calculations presently carried out refer to the reference divertor plate material for the physics phase, graphite. Transport coefficients used are for "ELMy" H-mode conditions; see §3.3.2. Recycling of deuterium and tritium at the plates is treated in an analytical local model corrected for plate inclination. Recycling processes include molecular and atomic processes and energy losses due to dissociation, ionization, and charge exchange. Neutral exhaust is treated by assuming a very small divertor plate porosity for D/T(~ 0.005). Coupled Monte Carlo calculations are in preparation to improve treatment of He exhaust and recycling.

The erosion calculation includes physical sputtering, self sputtering, radiation-enhanced sublimation for D, T and C, and chemical sputtering for D and T. Net erosion is calculated taking plate inclination into account. The excess of plate temperature over the cooling water temperature is assumed to vary as the power load on the plate.

3.4.1 Results of Model Predictions for ITER Divertor Plates

Input parameters for the model calculations for four standard ITER scenarios are given in Table 3-4. The results of these ideal 2-D modeling calculations are given in Tables 3-5 (parameters other than power load) and 3-6 (power load). Power load profiles on the divertor plate are given in Fig. 3-4; profiles of radial power flow at the midplane are given in Fig. 3-5; temperature profiles on the divertor plate are given in Fig. 3-6; and density and flux profiles on the divertor plate are in Figs. 3-7 and 3-8, respectively.

The scenarios have been chosen to offer a representative cross-section of proposed ITER scenarios, including the reference, physics , ignition scenario A1 and the reference, technology phase, long-pulse scenario B1 (which satisfies wall loading requirements with an acceptable number of shots). According to the present calculations, both of these scenarios are acceptable from the points of view of erosion, impurity release, required/available He pumping speed, and power load Admittedly, improvements in any of these quantities are highly desirable. The nominal steady-state scenario B6 and an alternate, unseeded, long-pulse scenario B4, as presently evaluated, both present serious problems.

The contents of Tables 3-5 and 3-6 will now be discussed in more detail. The results of model calculations for power load are considerably more robust than for sheath electron temperature. Therefore, it is possible to quote a single number for power load for each scenario. On the contrary, a range of sheath electron and ion temperature values is given. This range represents the results of two similar calculations and therefore gives a first indication of the uncertainty in these values. (Where only one value is given, only one calculation exists. For a safety factor to be applied to the electron sheath temperature as well as the necessity to avoid lower edge densities than those assumed here, see §3.4.5).

TABLE 3-4. INPUT PARAMETERS FOR 2-D MODELS

	A1 Reference Ignition	B1 Reference Long-Pulse Hybrid, 30% CD, impurity-seeded	B6 Nominal Steady-State	B4 Long-Pulse, Hybrid 18% CD no impurity seeding
Plasma current [MA]	22	15.4	18.9	7.6
$\langle n_e \rangle$ [10^{20} m^{-3}]	1.22	1.06	0.64	1.31
$n_e(a)$ [10^{20} m^{-3}]	0.35	0.30	0.18	0.37
Iron seeding concentration		0.07%		
Z_{eff} (core plasma)	1.66	2.2	2.2	1.6
Z_{eff} (SOL)	1.53	1.96	1.96	1.48
Pulse length [s]	400	2520	steady-state	960
Fusion power [MW]	1080	860	750	865
Current drive power [MW]	0	110	113	113
Plasma Power (Ohmic+alpha+CD) [MW]	218	283	263	288
Power radiated [MW]	102	185	76	110
Power into SOL (all plates) [MW]	116	98	187	178
Power for each top/bottom divertor segment (outer/inner) [MW]	46/12	39/10	75/19	71/18

The net erosion rates are calculated for the given range of plasma temperature profiles assuming a maximum plate temperature of 1000°C - the large variation is caused by the variation in plasma temperatures. A higher plate surface temperature would lead to larger erosion. The total C release from the plate should remain much smaller than the total DT flux to the plate to avoid large impurity reflux from the divertor. Detailed analysis of impurity transport is needed to quantify this reflux.

The required pumping speed for He exhaust and its uncertainty is treated in §3.9. Uncertainty in the value comes from the assumptions on core He transport and on the He profile at the plate. Some improvement is possible by optimization of the pump duct and divertor plate geometry.

In Table 3-6, the peak power loads are given for the various scenarios. When multiplied by the physics safety factor discussed in §3.4.3, the static peak power loads with physics safety factor are obtained. These include both reductions in width of the profile (with consequent increases in height at constant total power) and asymmetries and nonuniformities in the total power flowing to the plate. These values are in the range of 10-20 MW/m^2 for the reference scenarios and higher for the nominal steady-state and alternate long-pulse scenarios. It is noted that the static peak power load is similar for outer and inner divertor plates (e.g. 20 MW/m^2 vs 17 MW/m^2 for scenario A1).

A considerable improvement is achieved when X-point sweeping, sinusoidal in time (±3 cm at the X-point and ±11.6 cm at the tilted divertor plate), and active er-

TABLE 3-5. PERFORMANCE OF ITER OPERATING SCENARIOS: IDEAL 2-D MODEL

	A1 Outer/Inner Plate	B1 Outer/Inner Plate	B6 Outer/Inner Plate	B4 Outer/Inner Plate
T_e at midplane [eV]	193/149	231/178	324/248	254/196
T_i at midplane [eV]	283/205	338/245	579/422	391/282
T_e at plate [eV]	12-17/5	10-20/6.6	100-160/ 25-75	50/220
T_i at plate [eV]	6-10/5[a]	7-9/6[a]	30-40/20	10/9
Peak DT flux to plate [10^{23} m^{-2} s^{-1}]	4.3/4.2	2.7/2.3 to 3.9	1.7/1.8 to 2	3.6/3.3 to 4.3
Total DT flux to plate [10^{24} s^{-1}]	4.4/1.6	3.5/1.3	2.5/0.9	4.4/1.6
Net erosion (at 1000°C) [m/burn year]	0.04/0.007 to 0.13	0.01/.005 to 0.16	79.0 / run-away to run-away	0.26/0.97 to 102.
Total C release flux from plate [10^{24} s^{-1}]	0.047/0.016 to 0.06	.0266/.014 to 0.062	2.38 / run-away to run-away	0.23/0.07 to 3.04
DT radiation from divertor [MW]	4.1/1.8	3.4/1.5	2.9/1.2	4.0/1.7
Required pumping speed for He exhaust* [m^3 s^{-1}] (from §3.9)	310[b]- 700[c]	340[b]-800[c]	1060[b]- 1970[c]	180[b]-470[c]

[a] These low temperatures may be incompatible with the density limit.

* Required pumping speed from:

[b] core He transport model.

[c] edge concentration = 0.1 (Rev A04).

godization, possibly with toroidal rotation, is applied (see §3.4.4). While these calculations have not yet been performed for the inner plate, for the case of the outer plate and for profiles that include the physics safety factor (i.e., narrower by a factor 2 than those of Fig. 3-4, see §3.4.3), the time-averaged peak power load has been calculated in [3.48] and shows a reduction of 0.23 to 0.4 of the static peak power value. The time-averaged peak power loads for the reference ignition and reference long pulse hybrid cases lie between 5 and 8 MW/m^2, with the higher power load for the ignited scenario. The improvement with sweep and ergodization, more marked for narrower power load profile, is scenario-dependent. The ratio of the time-averaged peak power load to the ideal 2-D model peak power load is defined as a scenario-dependent effective physics safety factor (time-averaged, with sweep and ergodization). It lies between 0.79 and 1.36 depending on the scenario, i.e., much lower than the original static value of 3.4 for the outer plate. The time-averaged value represents an upper bound to the improvement expected from sweeping (see §3.4.4).

TABLE 3-6. DIVERTOR POWER LOADS FOR ITER OPERATING SCENARIOS: 2-D MODELS INCLUDING PHYSICS PEAKING AND SAFETY FACTORS (GRAPHITE PLATES)

	A1 Outer/Inner Plate	B1 Outer/Inner Plate	B6 Outer/Inner Plate	B4 Outer/Inner Plate
Peak power load from 2-D Model [MW/m^2]	6/3.2	4.2/2.2	22/16	12.5/9
Physics Safety Factor (See Table 3-8)	3.4/5.2	3.4/5.2	3.4/5.2	3.4/5.2
Static peak power load with Physics Safety Factor [MW/m^2]	20/17	14/11	75/83	43/47
Time-averaged peak power load[a] with ± 0.116 m sweeping and 0.06 m ergodization [MW/m^2]	7.7/tbd	5.6/tbd	17/tbd	13/tbd
Effective Physics Safety Factor:[b] time-averaged, with ±0.116 m sweep and 0.06 ergodization	1.26/tbd	1.36/tbd	0.79/tbd	1.03/tbd

* Engineering peaking factor (estimated to be of the order of 1.3) not yet taken into account in this table

a Indicates maximum improvement possible to be obtained by sweeping (see §3.4.4). The surface temperature excursion is design-dependent and must be calculated from the static peak power load and the applied frequency and amplitude.

b Ratio of time-averaged peak power load to static peak power load.

On examination of the present data, the following conclusions are drawn:

1. The reference ignition scenario for the physics phase is acceptable from the points of view of net erosion (of the order of 0.1 m per burn year), carbon impurity release, required He pumping speed (310–700 m^3/s), and marginally for time-averaged peak heat load (7.7 MW/m^2), assuming adequate sweep frequency.

2. The reference long-pulse hybrid scenario for the technology phase is acceptable from the points of view of net erosion (up to 0.16 m per burn year), carbon impurity release, required He pumping speed (340–800 m^3/s) and time-averaged peak heat load (5.6 MW/m^2), assuming adequate sweep frequency. Advances in edge density control could reduce the erosion figure further. The low current of this scenario might necessitate an adjustment of the angle of the divertor plate (less grazing incidence), leading to an upward adjustment of the heat load. Modest impurity seeding (or other methods to reduce power) are required for feasibility, since the alternate long-pulse hybrid scenario without impurity seeding leads to unacceptably high values of divertor power load. The compatibility of Fe-seeding with long-pulse carbon divertor operation is yet to be experimentally verified.

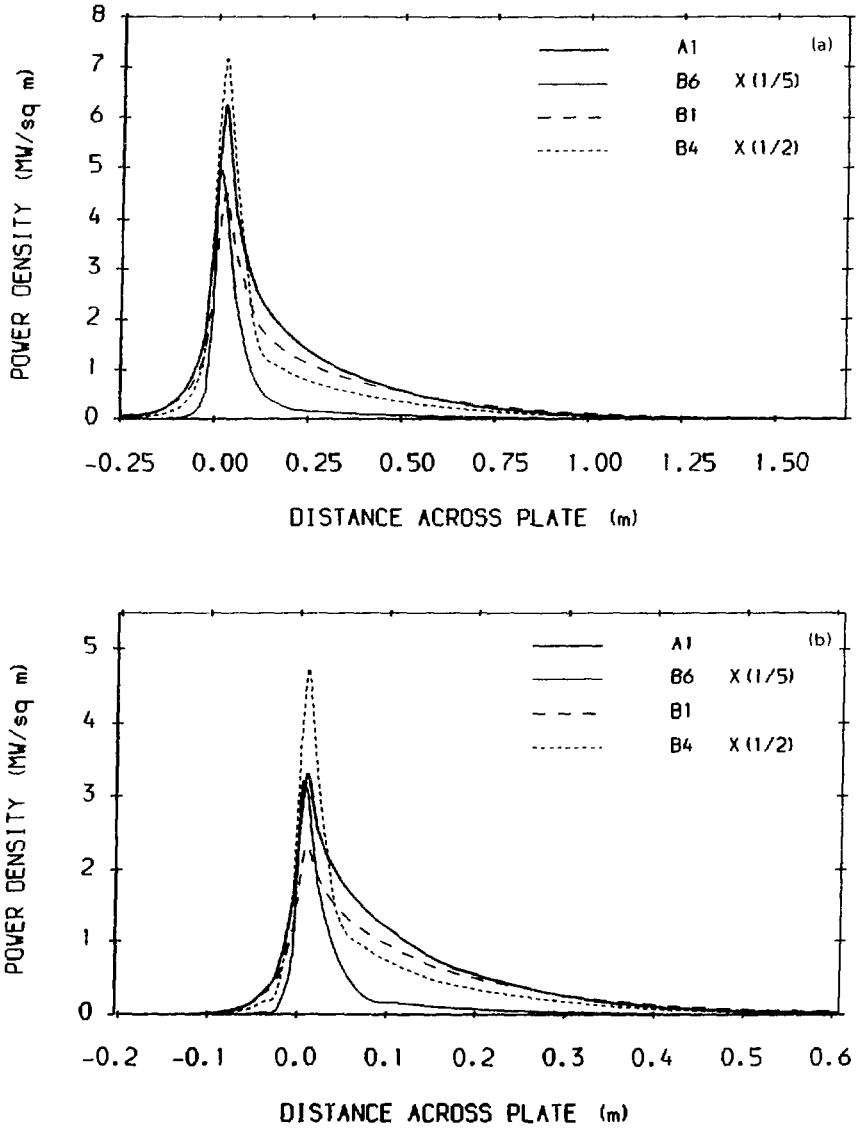

FIG. 3-4 Ideal Power Load on (a) outer plate, (b) inner plate for ITER scenarios A1,. B1, B6, and B4, as a function of distance on the inclined divertor plate. To be multiplied by Physics Safety Factor (see §3.4.3)

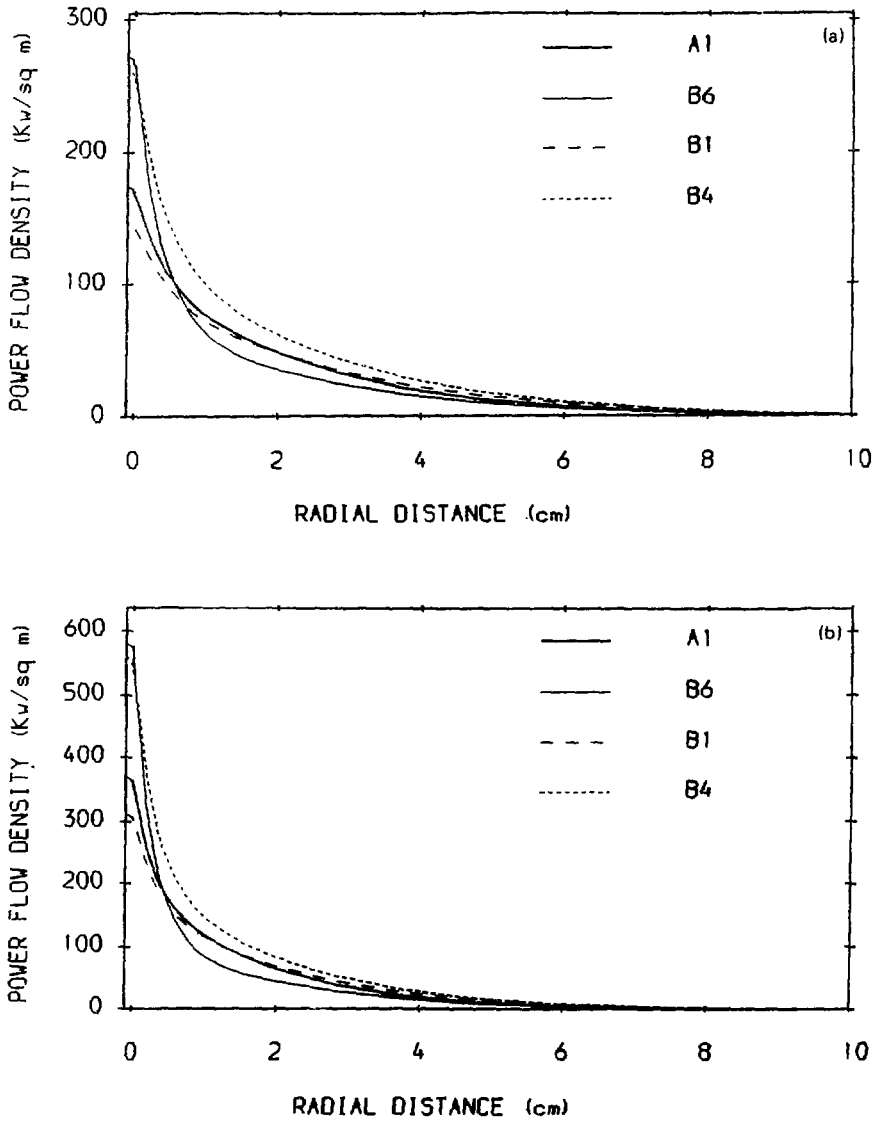

FIG. 3-5 Profile of radial power flow per unit area at (a) outer midplane (b) inner midplane for ITER scenarios A1, B1, B6, and B4.

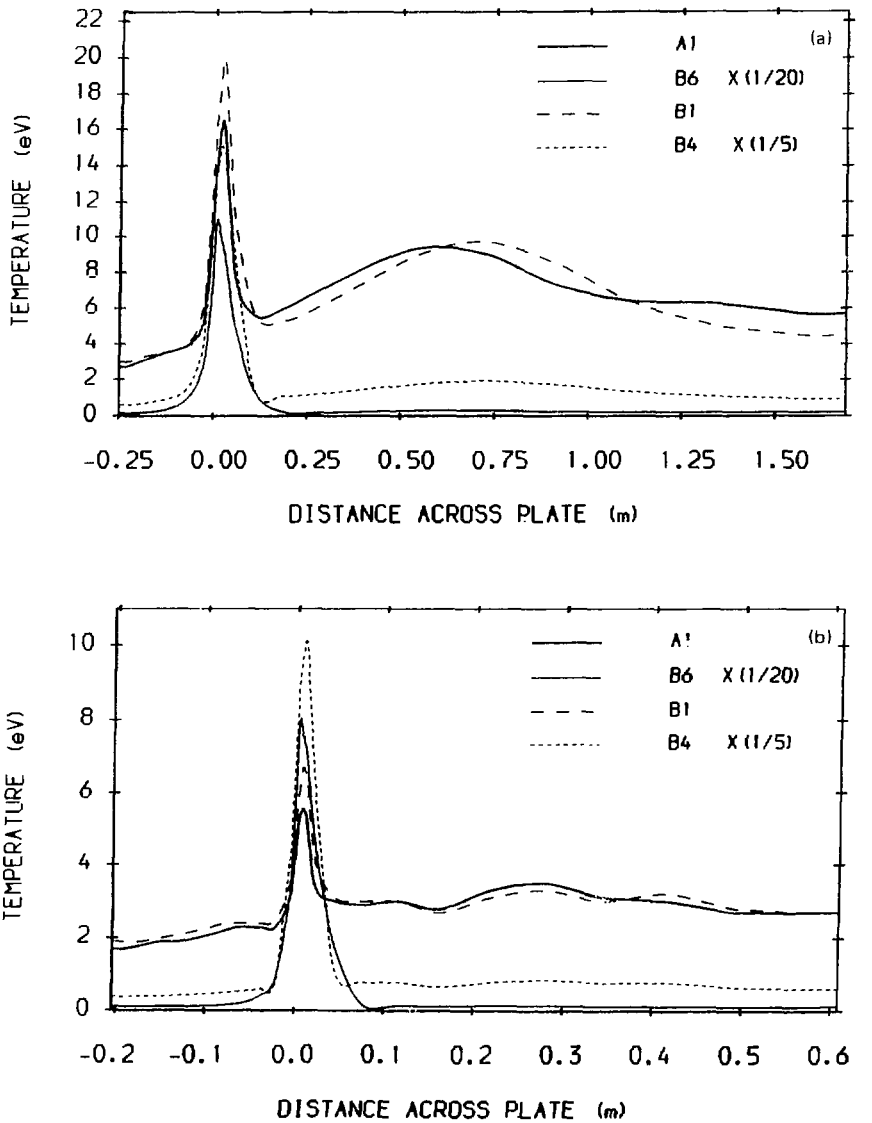

FIG. 3-6 Electron temperature at sheath at (a) outer plate, (b) inner plate for ITER scenarios A1,. B1, B6, and B4, as a function of distance on the inclined divertor plate.

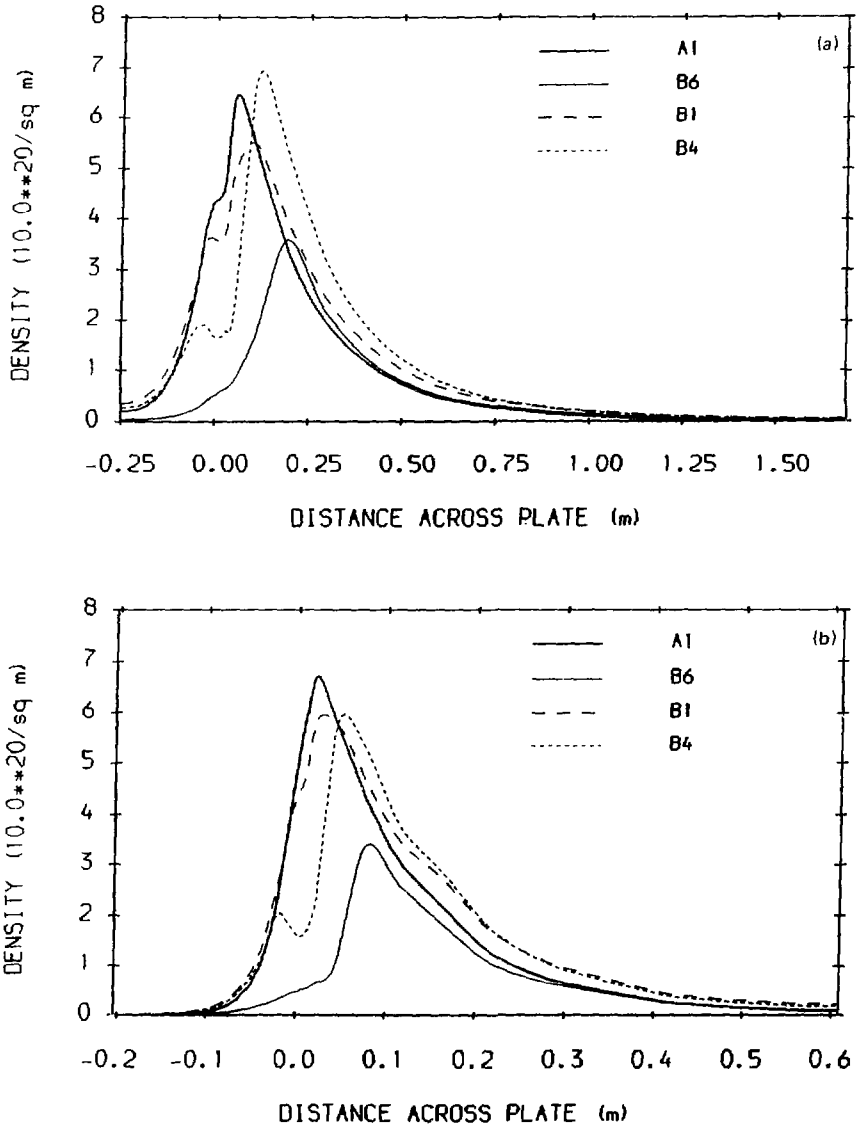

FIG. 3-7 Plasma density at (a) outer plate, (b) inner plate for ITER scenarios A1,. B1, B6, and B4, as a function of distance on the inclined divertor plate.

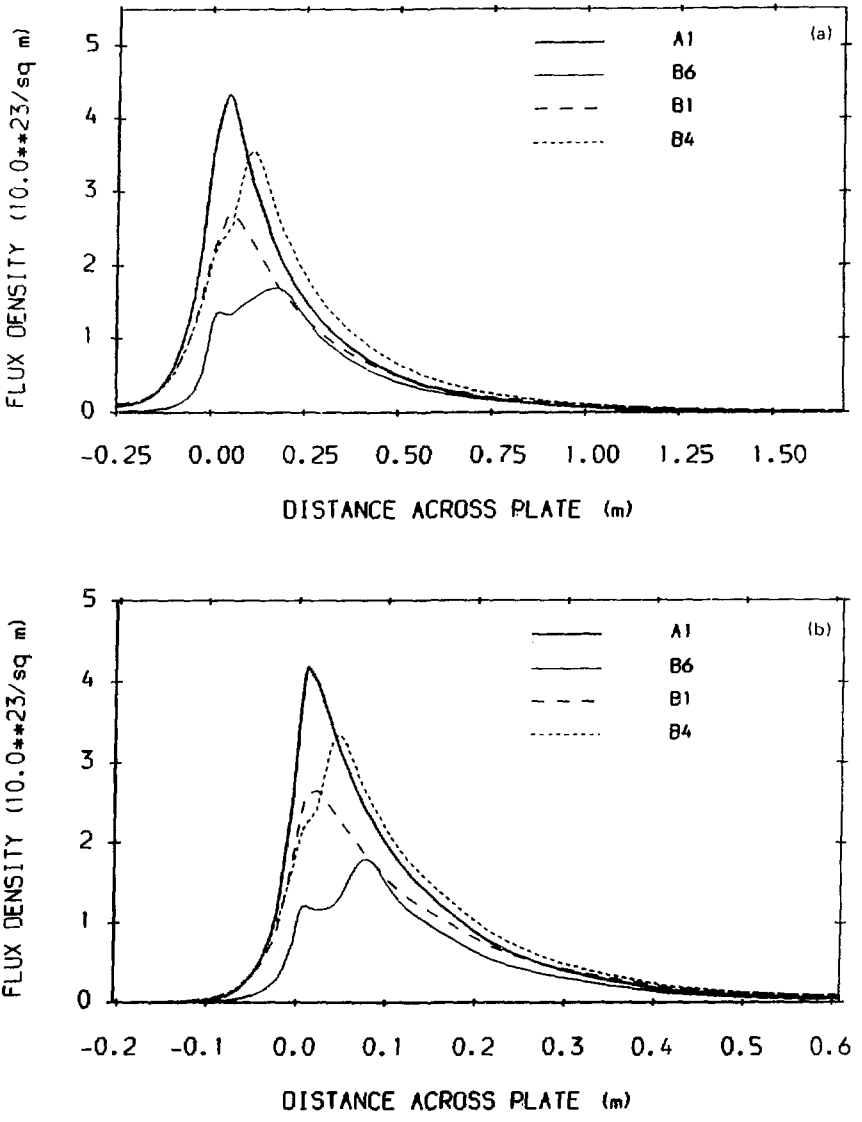

FIG. 3-8 Particle flux per unit area to (a) outer and (b) inner plate for ITER scenarios A1, B1, B6, and B4, as a function of distance on the inclined divertor plate.

3. The specific nominal steady-state scenario B6, as defined in Table 3-4 and evaluated with the assumed parameters and uncertainties, is not acceptable from the points of view of net erosion (possibility of runaway erosion at 1000°C) carbon release (greater than DT flux to the plate), He pumping (with present assumptions), and time-averaged peak power load (17 MW/m^2, with a narrow profile exacerbating surface temperature excursions). While this particular scenario, B6, is not acceptable, improvements mentioned below could lead to the generation of new and acceptable steady-state operating scenarios.

In addition, the following general conclusions should be drawn on the relation of divertor conditions to scenarios as presently understood:

1. Power flows of 100-120 MW into the scrape-off layer at edge densities of about 3-4.$\times$ 10^{19} m^{-3} lead to acceptable conditions for the present ITER.
2. Significantly higher power levels and/or lower edge densities can not be accommodated in the present conceptual design. While higher power levels can be partially mitigated by increased radiation (e.g. scenario B1, in which 2/3 of the power is radiated using impurity seeding), low edge densities lead to unacceptably high divertor plate plasma temperatures, erosion rates, required He pumping speeds, and power loads. In addition, low edge densities are expected to reduce impurity retention by the divertor and to increase the likelihood and severity of runaway electron production during disruptions.
3. To demonstrate the feasibility of the steady-state mode of operation, better optimized scenarios (higher edge density) should be identified. A concerted research and development effort is required to reduce the present uncertainties in scrape-off layer parameters and modeling, and to develop plasma control schemes which maximize the ratio of edge to bulk density (i.e. increase the edge density while not increasing the input power). During physics phase operation, these control schemes should be implemented to establish experimentally the characteristics and feasibility of a future steady-state scenario.
4. Finally, sweeping of the separatrix at adequately high frequency, possibly combined with ergodization, is an essential ingredient of the divertor design to reduce the peak heat loads and surface temperatures.

3.4.2 Effect of In/Out and Up/Down Asymmetry on Divertor Heat Load Specification

Up-down motion of the plasma due to imperfect position control constitutes a significant modification of the ideal DN heat load specification. Experimentally, it has been established (in DIII-D and JT-60) that reversing the toroidal magnetic field in SN operation can lead to a factor 4 change in the power load to the inner divertor plate. Applied to ITER, top and bottom SN power loads would then differ by the same factor. This magnetic field dependence, not included in the 2-D modeling, has been attributed to neoclassical drift terms and poloidal electric fields. Although further experimental corroboration is required (in particular, increase of radiated power in one configuration could conceivably account for the factor), it is assumed conservatively that the power load to the top (bottom) inner plate is increased (decreased) by a factor of 2 relative to an ideal SN case.

From ideal DN 2-D modeling of ITER (see §3.4.1), it was concluded that displacing the plasma vertically by 3 mm produced a separation of 1.2 mm in the

horizontal plane between the separatrices emanating from the top and bottom X-points and could therefore produce a 60:40 imbalance in the power deposition to top and bottom divertors. This imbalance is considered to delimit the threshold between ideal, but unbalanced, DN operation and nonideal SN-like operation susceptible to the modified power loads given in the previous paragraph. Since the vertical control system is presently not able to guarantee vertical control to 3 mm, it is assumed that the displacements are larger and that therefore nonideal SN-like behaviour affects the heat load estimates even for DN operation. Naturally, effects tending to broaden the scrape-off layer would reduce the vertical control requirement implicit in this evaluation. Further experimental data may modify the above assumptions.

The results of this evaluation are quoted in Table 3-7. The SN values are scaled from SN calculations, which had used a geometry similar but not identical to ITER (see §3.6). Both total power to the plates and power load normalized to that on one ideal DN outer divertor plate are given.

As seen in Table 3-7, for 50:50 up-down oscillation, the power load to one of the inner plates is a factor of 1.5 higher than the reference power load of the outer plate in ideal DN operation, i.e. a factor of 2 higher than the power load of the inner plate in ideal DN operation. A factor of 2 relative to the model calculation is therefore adopted for the inner plate as safety factor for up-down and in-out asymmetry. For the

TABLE 3-7. UP/DOWN AND IN/OUT ASYMMETRY

TOTAL POWER	Bottom "good" drift inside	Bottom "good" drift outside	Top "bad" drift inside	Top "bad" drift outside
DN	0.1	0.4	0.1	0.4
Ideal SN				
Bottom	0.3	0.7		
Top			0.3	0.7
Nonideal SN				
Bottom	0.15	0.85		
Top			0.6	0.4
POWER LOAD PER AREA normalized to DN outer plate	Bottom "good" drift inside	Bottom "good" drift outside	Top "bad" drift inside	Top "bad" drift outside
DN	0.75	1	0.75	1
Ideal SN				
Bottom	1.5	1		
Top			1.5	1
Nonideal SN				
Bottom	0.75	1.2		
Top			3	0.6
Nonideal SN 50% time averaged				
Bottom	0.4	0.6		
Top			1.5	0.3

outer plate, the worst case corresponds to a vertical offset of about 3 mm with ideal DN-like behaviour, i.e. an average imbalance of 25%. A factor of 1.25 relative to the model calculation is therefore adopted for the outer plate as safety factor for in-out asymmetry.

While the factors given above represent the design guideline, improvements of these factors may be possible in the course of machine operation once the exact value of the drift effects for ITER is known, provided vertical control and heat flux diagnostics can be rendered accurate enough and assuming routine repetitive operation. By adjusting the relative time for which the power is deposited to the top or bottom plates, the power load to the inner plates can be minimized (to 0.6 of the ideal double null outer plate value) or the largest power load to any of the four plates can be minimized (to 0.9 of the ideal double null outer plate value. Further work in this area, called for in the R&D program, demands more experimental data on asymmetries and improved modeling to take account of drift effects.

3.4.3 Physics Safety and Peaking Factors to be Applied to the Power Load

2-D models of the scrape-off layer rely on inputs from experiment, basic theory, and plasma operations scenarios. In many cases the data and calculations are insufficient in number and detail. Consequently, a "physics safety factor" must be applied. This factor represents a combination of asymmetries (due to operations, physics, and geometry), temporal variations, and uncertainties. The factor does not represent a range of possible values, which would be significantly larger. Rather, the physics safety factor is the result of an assessment by the ITER Power and Particle Control Group on the basis of available information of the plausible mean deviation of power loads from the model values. Synergism between the various effects was included in the assessment as far as possible. The result of this assessment is given in Table 3-8. The "physics safety factor" consists of two multiplicative factors: a power load safety factor due to SOL width variation, and power load safety factor due to total power variation or asymmetry. The first, the width-dependent part, includes effects tending to reduce the scrape-off layer width and thereby increase the peak power load at constant input power. The second, the power-dependent part, includes effects tending to change the total power reaching the plate either directly (e.g. impurity radiation in the divertor) or by modifying the distribution of power among the plasma-facing components (e.g. poloidal and toroidal peaking). The effect of the width-dependent part can be mitigated by space-averaging techniques such as ergodization and sweeping. This is already included in Table 3-6, in the row labeled "time-averaged peak power load."

The perpendicular heat conduction and the edge density, both imperfectly known, affect the width of the scrape-off layer and the sheath temperature. Comparison of models with the experimental results indicate that various combinations of heat conduction and inward pinch fit the data equally well, so that a large degree of uncertainty exists in determining the correct combination and scaling of these parameters. It is, however, expected that unfavourable effects in one parameter will be partially offset by favourable effects in the other, e.g. that low edge density would be associated with an inward pinch, but a higher $\chi_{\perp}^{e}$. The cumulative effect of these uncertainties is evaluated at a factor of 1.7, and is considered to affect mainly the width of the profile.

Previously, Z_{eff} in the scrape-off layer and nonlocal kinetic effects leading to the application of a flux limiting factor (§3.3.2) had not been included in the model

TABLE 3-8. PHYSICS SAFETY FACTOR FOR PEAK POWER LAND

	Power Load Safety Factor due to SOL Width Variation	Power Load Safety Factor due to Total Power Variation or Asym metry
	Either Plate	Outer/Inner Plate
$\chi_\perp$, v_{pinch}, $n_s/\langle n_e \rangle$	1.7	
Impurity radiation in SOL		0.85
Finite Larmor radius	0.9	
Additional physics	1.3	
Poloidal peaking: in-out (drifts) and up-down		1.25/2.0
Toroidal peaking: ripple and locked# modes		1.5/1.4
Time peaking (burn control)		1.08
Physics Safety Factor due to SOL Width (either plate)	2.0*	
Physics Safety Factor due to total power variation or asymmetry (inner/outer plate)		1.7/2.6

	Outer Plate	Inner Plate
TOTAL Physics Safety Factor	3.4	5.2

Note: Engineering peaking factor (usually taken to be 1.3 for 1.7* angle between field line and plate) must be applied in addition.

The peaking factor due to locked modes may be reduced if means of unlocking the locked modes is found (R&D).

* The width-dependent part of physics safety factor should be reduced if the power load profile is extremely narrow (e.g. midplane SOL width < 3 mm) and ergodization or separatrix sweeping is applied.

calculation. However, these effects are now included and therefore no longer give rise to a safety factor.

Impurity radiation in the scrape-off layer is not presently taken into account. It is expected that impurities will radiate 30% of the power entering the divertor (i.e. over and above the power already radiated from core and edge plasma) and therefore the peak power (per unit area) to the plate will be reduced by a factor estimated at 0.85.

Finite Larmor radius effects have not yet been evaluated in detail but are expected to broaden the scrape-off layer, leading to an improvement by a factor of 0.9 in the width-dependent part for typical scenarios.

Among the many uncertainties and omissions in the model not specifically mentioned are: kinetic effects (uncertainty in flux limit factor); refined sheath conditions (non-ambipolarity and variation of heat transmission coefficients); improved atomic physics and recycling models; variation of the impurity concentration along the field lines; finite mesh size; inclined plates; and non-orthogonal meshes. All are candidate effects tending to modify the power load. Further important effects are

the variation of the transport coefficients with plasma parameters (e.g., Bohm vs. constant) and the ratio of power carried by electrons and ions. All these additional physics and numerical factors are assumed to require a safety factor of 1.3 relative to present modeling, and to affect mainly the width of the scrape-off layer.

Poloidal peaking, i.e. the effect of up-down and in-out asymmetries, has been discussed in §3.4.2. The safety factors to be applied are 1.25 for the outer plate and 2.0 for the inner plate. Although some indication of a change in profile is seen in experiments, these factors are entirely attributed to the power-dependent part of the safety factor because of the sparsity of available data.

There are two sources of toroidal peaking: toroidal field ripple and MHD effects. Ripple acts to increase the heat load locally, essentially by modifying the (very grazing) angle of incidence of the field line on the plate. At the outer strike point, the peak-to-peak ripple of 1.8% leads to a local increase of a factor 1.18 over the ideal value, while the smaller ripple on the inner plate yields only an increase of 1.044. Final evaluation of the effect of locked modes requires further experimental data; Presently available data indicate asymmetries of ± 50% at q ~ 2.5, and ±20% for q = 3.7. A factor of 1.3 has therefore been assumed for these asymmetries for ITER. (Schemes to reduce this effect by unlocking locked modes using rotating error fields should be considered in the framework of the Physics R&D program.) The combined effect of ripple and locked modes, therefore, yields a safety factor for toroidal asymmetry of 1.5 for the outer plate, and 1.4 for the inner plate.

It is expected that some temporal variation in power load over a period of seconds is unavoidable. In particular, high density, low-temperature operation would require burn control using additional heating. This is estimated to result in excursions of the power to the scrape-off layer of the order of 5% and consequent excursions of the power load by 8%. A factor 1.08 is adopted for temporal variations of power load.

The physics safety factor is the product of the various factors, assessing the effect of asymmetries (due to operations, physics, and geometry), temporal variation, and uncertainties. The width-dependent factor to be applied to the ideal 2-D model values of ITER, presented in §3.4.1, is 2.0. In addition, the power and asymmetry dependent factor to be applied is 1.7 for the outer plate and 2.6 for the inner plate. This leads to a total physics safety factor (before ergodization and sweeping) of 3.4 for the outer plate and 5.2 for the inner plate.The safety factor is expected to be smaller for extremely narrow profiles, and is subject to a greater improvement by sweeping and ergodization.

Several further comments are indispensable. The present calculations apply only to divertor tiles consisting of carbon-based materials, so that the guidelines above are for the reference physics phase design. Electron temperatures and plate erosion rates are subject to larger modeling uncertainty than the power loads (§3.4.5).

3.4.4 Improvement of Divertor Heat Load by Ergodization and Sweeping

Sweeping of the X-point (separatrix) over a relatively small distance using the plasma position control system is an essential tool for reducing time-averaged power loads and peak surface temperatures on the divertor plate. To minimize the latter, it is assumed that sweeping is carried out at the highest allowable frequency, that therefore higher harmonics are absent and the sweep is then sinusoidal in time with an amplitude of ± 3 cm at the X-point, or ± 11.6 cm on the inclined divertor plate. This sinu-

soidal dependence is also appropriate if the X-point is moved in a circle so as to maximize the benefit of sweeping at the inner plate. Calculations were performed in [3.48,49,50] to investigate the effect of sweeping on the various scenarios of §3.4.1 including the calculated profiles peaking by a factor 2 (§3.4.3, physics peaking factor). It is concluded that sweeping yields a time-averaged peak heat load lower than the static peak heat load by a very significant factor, 0.23 to 0.37, depending on the scenario. Therefore this option should become an integral part of the machine design. It should be emphasized that the actual temperature rise must be calculated from the original power load profile (with the width reduced by the width-dependent part of the physics safety factor and the amplitude increased by the total physics safety factor), the detailed tile design, and the applied frequency and amplitude of the sweeping.

Ergodization, using an $n = 1$ perturbation near the midplane employing the existing saddle coils (20 kA), was proposed in [3.51] as a method for flattening the power load profile over 1 mm in the midplane. Since a static perturbing field creates toroidally asymmetric regions of localized power deposition, these must be averaged by toroidally rotating the perturbing field (at a frequency ~ 1 Hz). When this is done, a region of 2.6 mm in the midplane and therefore 6 cm along the divertor plate is averaged. Application of 2-D modeling to ergodization is under way, and preliminary results [3.52] show that the improvement to be expected from ergodization ranges up to 15% depending on profile width. An evaluation [3.48,49] assuming the scheme corresponds to simple averaging over 6 cm (separatrix sweeping linear in time) showed that ergodization alone was effective for reducing the power load of very narrow profiles. When combined with sweeping, the time-averaged peak heat load was 0.17-to-0.37 of the static value [3.49], i.e. somewhat improved over the effect of sweep alone. Further study and optimization of ergodization in the presence of sweeping is recommended, particularly including toroidal rotation which may well relax the toroidal asymmetry (locked mode) factor in Table 3-8.

3.4.5 Peaking Factors for Plate Temperature and Sheath Potential

2-D fluid modeling of the plasma and neutral transport processes in the ITER divertor shows conditions under which relatively low values of the plasma temperature near the divertor plate ($T_e \leq 10$ eV) and the sheath potential ($U \leq 30$ eV) can be obtained. Plate erosion under these conditions is relatively low. For this energy range ($E \sim 2T_i + U \leq 50$ eV) of the incident ion, the sputtering yield has a strong dependence on the ion energy. Therefore, account must be taken of plasma temperature and sheath potential peaking factors, caused by uncertainties in the 2-D model input assumptions as well as reasons which were not considered in 2-D modeling.

There are two main reasons for changes of the incident ion energy in comparison with 2-D fluid model, and accordingly the peaking factor is the product of two factors, f_1 and f_2. Of these, the electron temperature peaking factor f_1 is related to on the power load peaking factors and uncertainties of the midplane electron density n_s, and may be estimated by using the scaling law for the plate temperature [3.47]: $(T_e \propto q_{\|}^{20/9} n_s^{-28/9} L^{2/9}$. Here $q_{\|}$ is the heat flux at the plate along the magnetic field line and L is the field line connection length. The value of f_1 depends strongly on edge electron density and heat conductivity χ across the magnetic field. Uncertainites in these parameters must be investigated in detail, in accordance with the Physics R&D

program. We note that the strong dependence of f_1 on n_s necessitates that appropriate control mechanisms be available to keep n_s high, roughly above 3×10^{19} m^{-3}.

The effects of the ripple power load peaking factor should be omitted, since the ripples does not affect the $q_{\parallel}$ value. The other power load peaking factors pointed out in the §3.4.3, give rise to temperature peaking factors

$$f_1 \text{ (outer plate)} = 1.6, \qquad f_1 \text{(inner plate)} = 3.2, \tag{5}$$

provided, as mentioned above, that the edge density is kept above 3×10^{19} m^{-3}

The second reason is the influence of kinetic effects on the $B_{\parallel}$ transport processes in the divertor plasma. The Coulomb-scattering mean-free-path of the electrons and ions at the midplane, λ_e and λ_i respectively, are comparable with the magnetic field line connection length, L. Typically, $3L < \lambda_e, \lambda_i < 30L$. This low collisionality may cause a deviation from Maxwellian of the electron and ion distribution functions near the plate. The suprathermal electrons may change the local relation between the plate electron temperature and sheath potential, increasing the latter. Kinetic modeling of the ITER divertor plasma shows an increase of the sheath potential by a factor of 1.5 in comparison with its local value [3.53]. Thus, the kinetic peaking factor, f_2, for the energy of the incident ions is estimated as 1.3. Here, it is also assumed that the edge density remains above 3×10^{19} m^{-3}. Further investigation of this problem is needed.

The global peaking factor $f_E = f_1 \times f_2$ for the ion energy hitting the plate is:

$$f_E = 1.6 \times 1.3 = 2.1 \text{ (outer plate)} \quad \text{and} \quad f_E = 3.2 \times 1.3 = 4.2 \text{ (inner plate)} \tag{6}$$

3.5 OPTIMIZATION OF DIVERTOR GEOMETRY

The shape and orientation of the divertor plate relative to the pump duct opening (as well as the plasma parameters near the plate) clearly can play an important role in determining the peak power loading per unit area, $\hat{P}$, and peak electron temperature $\hat{T}$ on the divertor, the ability to exhaust He and, more subtly, the amount of tritium throughput. There is a speculated link between heat exhaust and He ash removal. That is, one cannot channel He into the divertor region without also extracting a minimum heat. In a related manner, a minimum power must also flow to the material boundaries to maintain H-mode confinement. As a rough estimate of the minimum required power loading onto the divertor plates for the ITER specification, one could choose values from the present machines for the power flow to divertor plates (per unit area) per unit of "exhausted" gases or the power required to sustain H-mode behavior, whichever is larger. Both give values for the minimum required power loading $P_m > 4$ MW/m^2 measured at the divertor plate, parallel to flux surfaces in the poloidal plane. However, divertor plates in present machines are oriented approximately normal to flux surfaces, are close to the X-point, and are flat. Changes in peak heat load could be result from changes in divertor plate inclination, depth, and shape. (This is clearly an optimistic interpretation for power handling requirements.)

An additional parameter to be considered is the peak plasma temperature, $\hat{T}$, at the sheath. Greater divertor depth will promote lower $\hat{T}$ because of the greater distance along **B** over which a gradient can be established. Because power flows radially outward across most of the separatrix, the gradient is influenced more by the distance

from the x-point region to the divertor plate than by the distance from the midplane (stagnation point in the DN configuration) to the divertor. Low $\hat{T}$, below ~ 50 eV, is desirable because of reduced divertor plate erosion, predominantly for high-Z materials, and also because of the associated higher density which eases the He pumping requirements.

All peak power loads and electron temperatures described in this section do not include the model safety or peaking factors described in §3.4.3 and 3.4.5.

3.5.1 Divertor Depth

The depth of the divertor is defined as the distance from the X-point to the strike point (the intersection of the separatrix with the divertor plate) in the poloidal plane. Increasing the divertor depth increases the height of a tokamak and moves the divertor coils further from the minor axis, requiring greater divertor coil currents and stronger divertor coil support structures. Because these changes are expensive, a deep divertor must have clear operational advantages.

Improvements to be gained from deep divertors are assessed by 2-D models of the magnetic field and of the edge plasma. From flux surface calculations it is clear that flux surfaces converge the further one proceeds away from the X-point. This concentrates the heat flux, and at the simplest level, appears to recommend strongly against deep divertors. However, the polodal field increases away from the X-point, thus permitting smaller angles between the magnetic surfaces and the plate in the vertical plane (§3.5.2). The effect of magnetic surface compression and the effect of grazing incidence then cancel each other. Radial diffusion of heat then spreads the heat load as the distance to the x-point is increased. Fluid models of the plasma show ameliorating effects which are strongly density and input power dependent. As described in the next paragraph, the main advantage to be gained from a deeper divertor is the lowering of sheath plasma temperatures which results in reduced divertor plate erosion.

For L-mode transport parameters and 70 MW of power to an outer divertor, corresponding to a fusion power of ~ 1.5 GW in the DN configuration, an increase in divertor depth from 0.8 to 1.5 m is predicted to drop T_e at the plate from 80 to 50 eV at $\langle n_e \rangle = 0.9 \times 10^{20}$ m^{-3} and to <10 eV at $\langle n_e \rangle = 1.5 \times 10^{20}$ m^{-3} (see Fig. 3-9 [3.54]). Simultaneously, the power loading onto these divertor plates would increase 30% to 12 MW/m^2 (times the physics safety factor of 3.4) at 0.9×10^{20} m^{-3} and decrease 80% to less than 1 MW/m^2 (times the Physics Safety Factor of 3.4) at $\langle n_e \rangle = 1.5 \times 10^{20}$ m^{-3}. Operation at 1 GW fusion power would reduce the heat load ~ 50% for the lower density case and ~ 80% for the higher density case.

3.5.2 Plate Inclination

The power load on a divertor plate is proportional to the power flow in the poloidal direction times sin θ, where θ is the angle between the plate and the flux surface in the poloidal plane. As a reference, and because the peak power loading occurs within a few cm of the separatrix, we use the value of θ evaluated at the strike point instead of on each field line. Smaller values of θ lower the peak power load.

A constraint is placed on a minimum value for θ, based on the allowed angle, ζ, for the total magnetic field with respect to the tile surface. Tolerances in the mechanical alignment of the tiles sets a limit of 1.6° on ζ. The relation between the

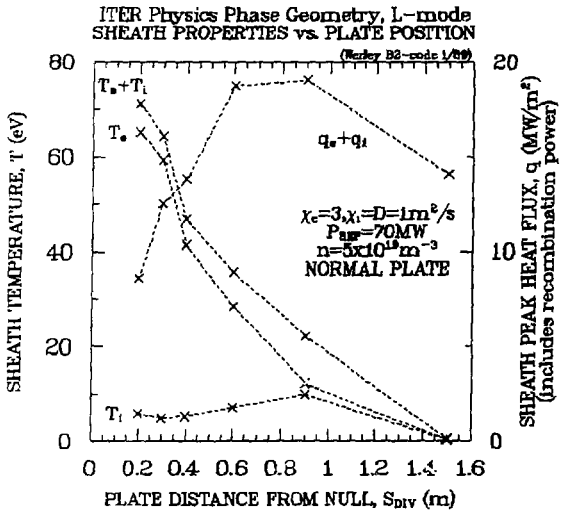

FIG. 3-9 Electron temperature, ion temperature and ideal heat flux (to be multiplied by Physics Safety Factor) as the distance between the X-point and the strike point is varied.

angles θ and ζ and the poloidal and toroidal field magnitudes, B_p and B_T, is

$$(\sin\theta)\, B_p/B_T = \tan\zeta = \tan 1.6^\circ. \qquad (7)$$

The inclination of $\theta = 15^\circ$ specified for ITER corresponds to $B_p/B_T = 0.107$, conditions present in the ignited physics phase with a plasma current of 22 MA.

Lower plasma currents reduce B_p, and hence require larger values of θ to satisfy Eq. (7). This is problematic in two respects. First, it is impossible to change the plate inclination during or between discharges to satisfy the changing currents. (The longer connection length along **B** at lower current helps little to reduce the peak power load.) Secondly, the value of θ was chosen to reduce the heat flux in the physics phase. Greater power loads are expected in the technology phase, which has a lower current.

3.5.3 Plate Shape

Divertor plates may be flat or curved. A slight curve has been favored by the engineering groups to allow thicker neutron shielding in sensitive regions. Shaped divertor plates, in principle, could promote different plasma and atomic physics at the plates. This has yet to be studied in detail, though speculated improvements have been proposed. The clearest improvement to be gained from divertor plate shape comes from flattening the plate to promote the reflection of He into the pump duct. Combined with an altered pump duct conductance, this can improve the He exhaust ~ 50% and reduce the D/T exhaust ~3-fold (see §3.9) [3.55]. The latter gain comes most strongly if the He flux profile on the divertor plate is displaced outwards in major radius relative to the D/T flux profile, as predicted by 2-D fluid modeling [3.56,57].

3.6 COMPARISON OF SINGLE- AND DOUBLE-NULL DIVERTOR PEFORMANCE OF ITER

The tokamak concept of a highly elongated, SN poloidal divertor located at the bottom of the vessel offers a number of potential advantages: (a) it provides, within the constrains of the vessel and main plasma geometry, the maximum practicable null to strike-point distance; (b) it is thereby expected to minimise (for a fixed divertor power load) the plasma temperature adjacent to the plate; (c) it provides flexibility in respect to size and shape of the main plasma because the null-point can generally be located so as to ensure satisfactory positioning of the inner and outer plasma channels on the plate; (d) He ions can flow to only one divertor and hence the the exhaust efficiency of He gas may be superior to that of a DN; and (e) the absence of an eroding upper divertor plate reduces the possibility of debris falling into the plasma and causing disruptions. It does however have disadvantages. There is only one divertor and hence it must handle twice the power of an up/down balanced DN configuration. The intrinsic power loading will therefore be higher provided that this not be offset by an increase in thickness of the power flow scrape-off layer. Increased power load results in an increased plasma temperature at the plate unless this can be offset by an increase in the null-to-strike-point distance. If this is not the case, higher erosion and higher release rate of impurities are to be expected.

Further interest in the SN stems from the potential difficulty of producing an ideally balanced, up/down DN configuration. Calculation of MHD equilibria has indicated that an up/down displacement of the plasma axis by 3 mm could result in a mid-plane separation of 1.2 mm between the separatrices which are linked to the upper and lower nulls. This separation is a significant fraction of the expected thickness of the power flow scrape-off layer, hence this unbalanced configuration is expected to behave in a comparable manner to a SN with most of the power flowing to the dominant one of the two divertors.

Analysis of the SN divertor is a relatively recent ITER activity and hence information has been sought from previous studies such as INTOR. Although the earlier configurations differ in detail from ITER, trends are noted whose origins appear to be sufficiently basic for them to be applied in general.

In respect to the topology of the edge region, the main difference between a DN and SN divertor is that the inner and outer divertor plates of the latter are linked by continuous flux tubes. In the case of the DN, the top and bottom plates are linked whereas the inner and outer are linked only in the private flux regions. The following conclusions regarding the behavior of the divertor and scrape-off layer in SN configurations are derived from two-dimensional modeling of NET and INTOR.

The location of the stagnation zone of the power and particle transport along the magnetic field in the scrape-off layer can be identified only by two-dimensional modeling, lies close to the top of the plasma, but is sensitive to plasma shape. (There is as yet no simple, i.e., analytical, method for identifying the stagnation zone.) If a uniform distribution of power flow is assumed at the interface surface inboard of the separatrix, two-dimensional modeling indicates that power flow across the separatrix into the scrape-off layer is peaked at the outer mid-plane, mainly due to the poloidal variation of the flux surface. Nevertheless, power flow into the inner and outer divertors is distributed in the ratio of the inner and outer areas of the separatrix, i.e.

the areas between the stagnation zone and the null-point. This power distribution is insensitive to the (inner : outer) ratio of the magnetic connection lengths between the stagnation zone and divertor throats. The predicted ratio of (inner / outer) power flows for the various SN configurations ranges from 0.3:0.7 to 0.4:0.6 which is substantially greater than the guideline value of 0.2:0.8 used for modeling of the DN configuration. It is therefore expected that the power load, at least on the SN inner plate, will be larger than that of the DN. There are experimental data which exhibit these ratios but, especially in the case of the SN, the ratio is sensitive to the operation of the main plasma. In particular, it varies with the direction of $\mathbf{B}_{tor}$ relative to the null-point. This has been attributed to the $\mathbf{B}\times\nabla T$ drifts (which are not generally included in plasma modeling) but this appraisal is not conclusive. Additional strong dependences on plasma density have been observed in JT-60.

An example of the radial profiles of power flow (per unit area) at the inner and outer mid-plane of a SN configurations (NET 3A) is provided by Fig. 3-10. The 1/e scale length for the inner divertor is about twice that for the outer. This ratio corresponds closely to the corresponding (in/out) spacing of the magnetic flux surfaces. The radial profiles of both plasma density and temperature exhibit similar behavior and the implication is that the scrape-off layer width is governed by the radial profile of plasma transport processes into the scrape-off layer at the region of maximum outward flow, i.e. at the outer mid-plane. This imprint is projected along the magnetic field to the inner and outer divertors because of the dominance of parallel transport. Figure 3-5 shows the inner and outer profiles of power flow at the mid-plane for the scenarios of the DN ITER configuration, including A1. It is important to note that the scale-length ratio is comparable to that of the SN case even though the flux tubes in the scrape-off layers are not connected.

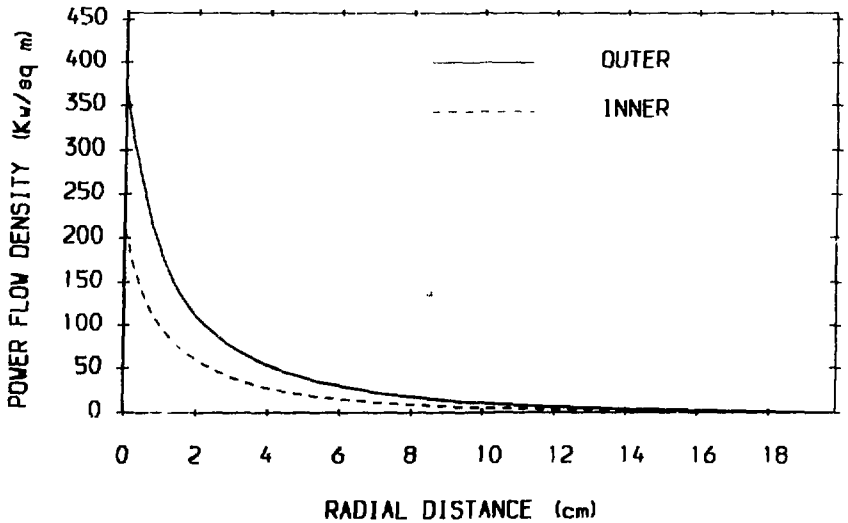

FIG. 3-10 Ideal Power Load on outer plate and inner plate for typical single null case (NET parameters, version 3A). To be multiplied by Physics Safety Factor (see §3.4.3)

Simple scaling [3.47] of the radial power flow scale length , Δ_{power}, is of the form

$$\Delta_{power} \propto [(n_s \chi_\perp)^{7/9}/P_\perp^{5/9}] (Z_{eff}/\chi_{||})^{2/9} L_t^{4/9} \quad (8)$$

where n_s is the plasma density at the separatrix at the stagnation zone, $P_\perp$ the average radial power flow (per unit area) across the separatrix, $\chi_\perp$ and $\chi_{||}/Z_{eff}$ are, respectively, the coefficients for transverse thermal diffusivity and classical parallel heat transport and, for the SN divertor, L_t is the throat to throat magnetic connection length. For the DN configuration, L_t is the stagnation zone to throat connection length. Application to the modeling results indicates that, if the divertor magnetic topology and plate geometry are similar for the SN and DN cases, then the ratio (SN/DN) of their peak plate power loads are

$$\hat{P}_{SN}/\hat{P}_{DN} \approx 2.4 \text{ (Inner)} \quad \text{and} \quad \approx 1.1 \text{ (Outer)}. \quad (9)$$

These ratios have been taken as a guide when deriving the "model safety factors" described in §3.4.3.

3.7 IMPURITY TRANSPORT AND RADIATED POWER

Impurities originate predominantly from the direct contact of plasma with divertor, sublimiter, and wall surfaces. Impurities may rapidly return to near their birth location or be transported throughout the SOL, edge, and core plasmas. Fuel dilution and impurity radiation from the core are clearly detrimental. Increases in SOL Z_{eff} and edge and SOL impurity radiation are beneficial because of the reduced divertor power load they effect. However, impurities in the SOL will increase divertor erosion rates. In this section we discuss impurities after release from divertor surfaces only. Later sections (3.8 and 3.10) focus on impurities from the walls and sublimiters, release mechanisms, and associated net erosion rates.

3.7.1 Divertor and SOL Regions

Impurities ejected from the divertor plate typically have energies below 50 eV. They penetrate a short distance, < 1 mm, through the dense divertor region plasma before ionization. The exact distance of penetration is extremely important for determining whether these impurities will escape the divertor region and enter the core plasma and if they will radiate much power. The further they penetrate before first ionization, the greater the likelihood of migrating upstream, crossing the separatrix, and radiating copiously.

Forces on impurity ions in the divertor region are due to the sheath electric field, to D/T drag, and to the temperature gradient. The latter force is away from the divertor plate, while the first is generally towards the divertor plate. Drag from D/T is towards the plate in the high ionization/recycling region, but may be away from the plate outside the region of high recycling. Simulations of impurity ionization and transport with a Monte Carlo/Fokker Planck code (ZTRANS) which assumes a fixed set of SOL plasma parameters, show good retention of impurities in the sheath, particularly if a magnetic sheath is included in the analysis [3.58]. Simulations of impurity ion transport using a 2-D fluid code (DDIC89) [3.59] show that poor retention is likely at

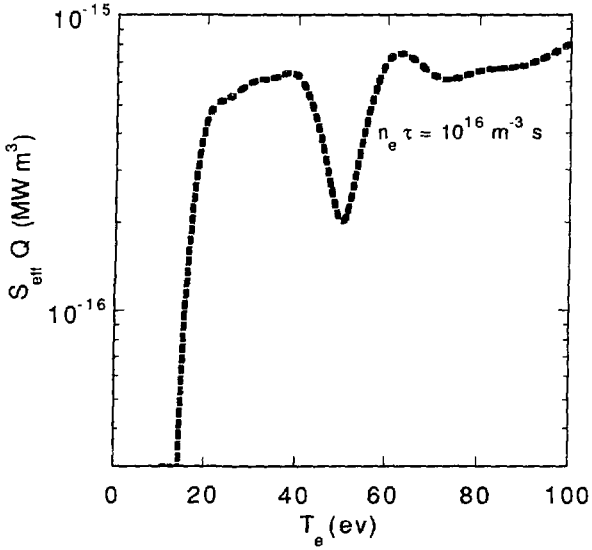

FIG. 3-11 Effective emissivity of carbon impurity radiation as a function of electron temperature for impurity confinement time of $10^{16}/n_e$ m^{-3} s.

high impurity generation rates when intense impurity radiation in the divertor region alters the plasma parameters, and hence the relative magnitudes of the forces there. Experimental studies of impurity retention in the ASDEX divertor show variation similar to that noted above. However, there is no detailed quantitative corroboration of the modeling at present.

The amount of impurity radiation depends on the impurity charge state and the electron energy distribution functions. For a fixed impurity density, processes which lower the charge state increase the radiation level. Finite confinement time of impurities in the SOL region causes the average impurity ion charge state to be lower than the coronal value. Calculations [3.60] of the effect on radiation from Be and C sputtered from divertor plates have been made under the assumption of a fixed impurity confinement time, ~ 5 ms. In this time period, impurities would move in the poloidal direction a distance of ~ 1 m above the divertor plate, well away from the region where the sheath or D/T drag would cleanse the plasma. As shown in Fig. 3-11, the predicted impurity radiation versus electron temperature has a negative slope region where increases in temperature result in decreases in impurity radiation. With this prescription, time-dependent solutions of impurity generation and radiation processes predict that a relaxation oscillation will occur with a period of several ms. Under power load conditions typical for the ITER divertor during the physics phase, the total time-averaged radiation from the SOL predicted for C divertor plates is ~ 50 MW and for Be is about 12 MW. D/T radiation and charge exchange losses from the divertor region are typically < 5 MW, though higher percentages are predicted for higher plasma densities. JT-60 and JET (see §3.2.8.3) have reported that radiation from the divertor region can exceed 60% of the input power during intense auxiliary

heating, > 20 MW. Recently, DIII-D has attained similarly high fractions of power radiated by seeding the divertor plasma with impurity gases [3.61]. At increasing SOL plus edge radiation fractions, typically > 0.7, Marfes form. Eventually both limiter and divertor plasmas detach. H-mode confinement is lost for edge plus SOL radiation fractions above ~ 0.8.

Charge exchange of impurities with neutral D/T is another process which lowers the charge state. Its effects have not yet been included self-consistently into these models of impurity radiation.

Modeling of the ITER SOL (see §3.4) does not include SOL radiation levels as high as those seen in experiments. The physics safety factor (§3.4.3) does allow a 15% decrease in divertor power load due to SOL radiation, much below the values seen in JET, JT-60, and DIII-D.

3.7.2 Core and Edge Region

Tokamak experiments show mainly diffusive impurity transport (i.e., no accumulation) for H-modes with grassy ELMs, but inward convection and accumulation during quiescent H-modes. Whether this phenomenon is dominated by SOL or edge

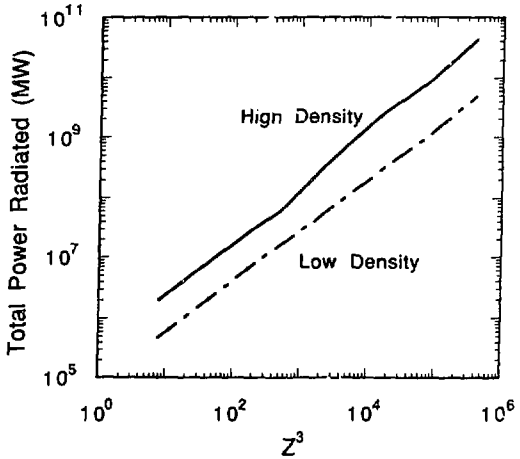

FIG. 3-12 Radiated power, as a function of Z^3 for $\langle n_e \rangle = 1.2 \times 10^{20}$ m^{-3} and for $\langle n_e \rangle = 0.6 \times 10^{20}$ m^{-3}.

plasma behavior is unclear. The ITER impurity control concept is based on maintaining grassy ELM conditions, including diffusion-dominated transport. After impurities cross the separatrix, noncoronal charge state distributions remain important to radiation. Impurity radiation depends strongly on: (1) Z of the impurity; (2) the electron density; (3) and the transport coefficients. Figure 3-12 shows [3.62] that the radiated power, P_{rad}

$$P_{rad} \propto Z^3 \langle n_e \rangle^2 \tag{10}$$

Based on the ITER specifications for Z_{eff} [3.63], the total power radiated from ITER by impurities has been calculated [3.62] using the MIST code considering a

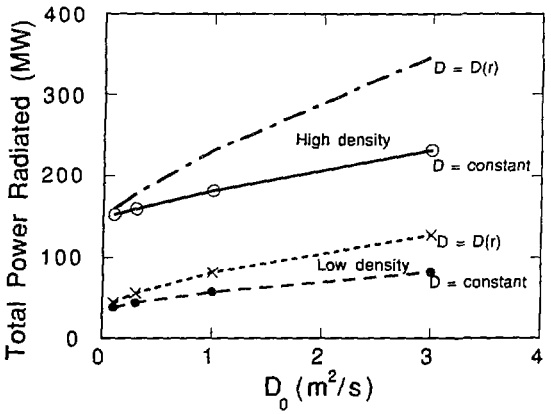

FIG. 3-13 Radiated power, as a function of diffusion coefficient for $\langle n_e \rangle = 1.2 \times 10^{20}$ m^{-3} and for $\langle n_e \rangle = 0.6 \times 10^{20}$ $m^{-3}$for constant and spatially varying diffusion coefficent.

variety of diffusive transport models, see Fig. 3-13. The upper pair of curves are for the ignited scenario, $\langle n_e \rangle = 1.2 \times 10^{20}$ m^{-3} and the lower are representative of steady-state operation, $\langle n_e \rangle = 0.6 \times 10^{20}$ m^{-3}. A particle diffusion coefficient of D = 0.67 m^2/s, the ITER reference value, results in ~180 MW of radiated power in the ignited scenario but only ~50 MW in the steady-state one. The latter value is not adequate to reduce the power into the SOL to an acceptable value for divertor plate lifetime. About half the radiated power arises from C and half from Fe. [Inaccuracies of the impurity radiation rates could be compensated by choosing materials of slightly different Z, Eq. (10).]

In the diffusion-only calculations, about half the radiated power originates from $0.9 < r/a < 1.0$, and half from $r/a < 0.9$. If an inward pinch v_{pinch} is included in the impurity transport equation, the total radiation and the fraction from the edge (see Fig. 3-14) decrease for fixed core impurity concentrations.In Fig. 3-14, the radiation from the edge and from the core is plotted for several impurities, normalized to the total radiated by that impurity. If $v_{pinch} > 2\, c_v\, D\, r/a^2$ with $c_v = 2$, the increase in impurity confinement and the decrease in radiation, i.e. increase in power load on the divertor, both cause serious problems. As noted before, quiescent H-modes show impurity accumulation equivalent to $c_v \equiv Z$ while L-modes and ELMy H-modes show $c_v < 2$. Some transport experiments do show $D = \chi$ for non-recycling impurities, equivalent to $\tau_p < 2\, \tau_E$ for $c_v < 2$. Thus, our assumption that $D = \chi/3$, equivalent to $\tau_p = 3\, \tau_E$, may be pessimistic.

3.8 DIVERTOR PLATE EROSION AND REDEPOSITION

The selection of both divertor geometry and plasma operational scenarios of ITER has been influenced by the need to minimise both surface erosion of the plates and the ingress of impurity ions into the hot plasma core. Conditions in the plasma adjacent to the divertor plates have a strong impact upon the choice of plate material. If

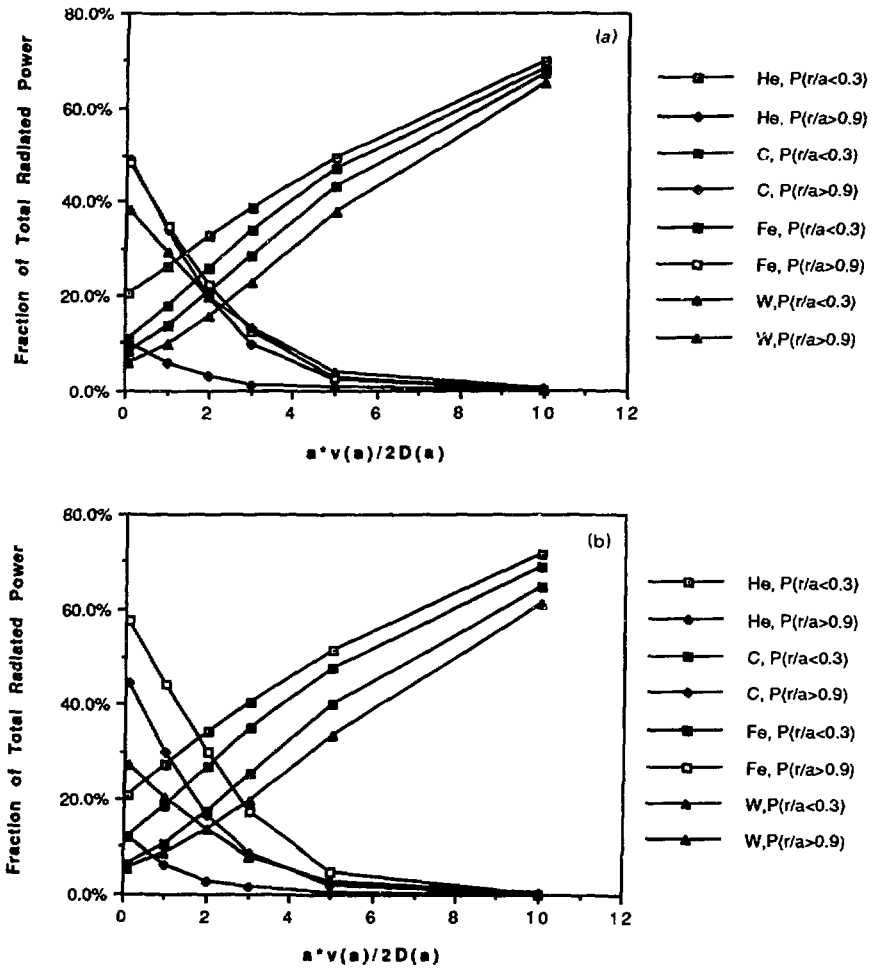

FIG. 3-14 Power radiated in core (r/a<0.3) and in edge (r/a>0.9) for (a) $\langle n_e \rangle = 0.6 \times 10^{20}$ m^{-3} and (b) $\langle n_e \rangle = 1.2 \times 10^{20}$ m^{-3}, given as a fraction of the total power radiated by each impurity.

a relatively low plasma temperature can be ensured, then a high-Z material, such as tungsten, offers the prospect of low erosion, hence long lifetime of the plates. But there is a risk of contaminating the core plasma with powerfully radiating ions whose allowable concentration is only ~10^{-5}. Low-Z materials, such as those based on carbon, exhibit much higher erosion but they radiate less, especially at high temperature. Their allowable concentration, which is determined largely by fuel dilution, is about 10^3 times greater than that of high-Z materials. Medium-Z materials are generally unsatisfactory due to the combination of their relatively high erosion yields and low

allowable concentrations. It is possible, though, that some operational scenarios would function well with medium-Z materials.

Erosion issues must be considered throughout the operational cycle of the device so that behavior during start-up (and possibly during shut-down), when the plasma is in contact with a limiter, is also important. Contamination of the start-up limiter may be an important issue if more than one material is used for plasma-facing components and the mixing of materials is not recommended. On balance, it appears that low Z materials offer a high degree of flexibility. Since this is desirable during the physics phase of ITER, they have been chosen, at least, for initial operation. In particular, C-based materials are favored because of their good refractory and disruption resistant properties. However, and especially in the case of carbon, there are many problems associated with the tritium inventory, chemical reactivity, and the effects of neutron irradiation (e.g. swelling, reduction of thermal conductivity, etc.). High-Z materials are less susceptible to these defects, which, together with their low erosion, makes them more attractive for long term operation during the technology phase provided that suitable plasma conditions can be attained and the generation and accumulation of transmutation products be tolerated. In view of the critical nature of the materials problems, an aggressive search for improved materials is both necessary and urgent.

One cause of erosion of both low and high Z elements arises due to physical sputtering by D^+ and T^+ bombardment. The released atoms become ionised by collisions with plasma electrons and thence return, guided by the magnetic field, back to the surface. Redeposition may occur. During this cycle they reach relatively low charge states (2 to 3) but, nevertheless, are accelerated by the electric field in the locality of the surface to energies which can be higher than those of the D^+/T^+ ions. Self sputtering due to bombardment by recycling ions of divertor plate material is a very important contributor to erosion because its yield can exceed unity and thereby lead to runaway erosion conditions. Physical sputtering and self sputtering are sensitive to the energy of the incident ions. Thus the radial profiles of their yields across the divertor plate depend upon the profiles of the local electric field, i.e., upon the profile of the plasma sheath potential which is itself dependent upon T_e.

Detailed conditions at the plate surface are complex because both the magnitude of the sputtering yields and the angle of release are sensitive to the distributions of both energy and angle of incidence of the bombarding ions. Furthermore, the magnetic field lines in ITER lie at grazing incidence ($\approx 1.5°$) to the surface. Kinetic modeling indicates that the range of the local field is thereby enhanced. The extent of this "magnetic sheath" appears, from kinetic modeling, to be sufficiently great for slowly moving sputtered atoms (e.g., atoms of tungsten) to be ionised and returned to the plate without experiencing the full sheath acceleration potential and without equilibrating with the D/T plasma [3.58]. The tendency of this combination of effects is to reduce the charge state and also the energy of the returning ions. Light ions such as carbon penetrate further into the sheath because of their greater release velocity. A further complication is the influence of the charge-to-mass ratio upon the angle of incidence of the returning ions due to its effect upon the ion Larmor radius.

The penetration range of the neutral particles into the plasma depends upon atomic interactions close to the plate. These are predominantly electron impact ionisation of the atoms (for which there are no experimental data for high Z elements) but in the case of carbon, which can release hydrocarbons (see §3.8.1), the range depends

upon a complex chain of neutral and ionised molecule dissociation processes in which charge exchange with protons plays a role.

In addition to the release of atoms of divertor plate material by particle bombardment, erosion can also occur due to evaporation (or sublimation) and also chemical reactions. For these it is also necessary to know the profile of surface temperature across the plate. Arcing, especially unipolar arcing, may also contribute if the sheath potential is high or if there is highly localised power and particle deposition. Detailed experimental data are sparse. They indicate that arcing is often transient and occurs during startup, but it has also been observed during neutral beam injection or lower hybrid current drive. Arcing has not been yet been considered in detail for ITER.

3.8.1 Low-Z Materials

Due to its chemical reactivity, carbon releases hydrocarbons when bombarded by hydrogenic ions. Experimental data show that the yield is sensitive to both surface temperature and incident particle energy and possibly to the intensity of the incident particle flux. Tokamak data are ambiguous regarding chemical erosion in reactor-relevant conditions, due, possibly, to the powerful suppressing effect of small concentrations of surface impurities such as metals. In the presence of oxygen, chemical erosion of carbon is enhanced due to the formation of CO molecules, their yield being ~1. An apparently unique property of carbon is that particle bombardment can cause the release of atoms from a hot surface due to radiation-enhanced sublimation (RES), the yield being sensitive to both the momentum flux of the incident particles and the temperature of the surface. Thus both D^+/T^+ ions and recycling carbon ions can give rise to radiation enhanced sublimation which thereby enhances the effective yields for both D/T sputtering and for carbon self sputtering. The additional components are dependent upon both incident energy and surface temperature. The runaway condition (which sets in when the self-sputter yield exceeds unity) can occur at relatively low T_e if the surface temperature is high. An example of the radial variation of the various yields across the carbon outer plate of the physics A1 scenario of ITER is shown in Fig. 3-15. The profile of the surface temperature is assumed to have the same shape as that of the power load when the plasma is stationary. The peak temperature, which is a feature of the engineering design, is assumed to be 1000°C. The results, which were obtained using a relatively simple model, are based upon the assumption that the average charge states of recycling carbon ions are 1 for RES, 2 for physical sputtering, and 1 for molecular species. Neither contributions from more highly charged carbon ions which could reach the plate from distant regions of the SOL and the edge plasma nor contributions from impurities such as He or oxygen are included in this particular graph. (They are, however, included in the full erosion analyses.) For these conditions the peak yield of carbon self sputtering is about 0.1 and the RES contribution due to recycling carbon ions is about 0.03. Runaway erosion will not occur as the surface temperature is increased and the limiting surface temperature will depend upon the onset of gross thermal sublimation. In contrast, a similar calculation for the B4 ITER scenario indicates that (for a peak $T_e \approx 75$ eV) the peak self-sputtering yield is about 0.8 and the peak RES yield about 0.2. For this runaway erosion is likely even at a surface temperature as low as 1000°C. This analysis does not include time-dependent effects. Self-consistent impurity radiation from the SOL would be extremely important in this context.

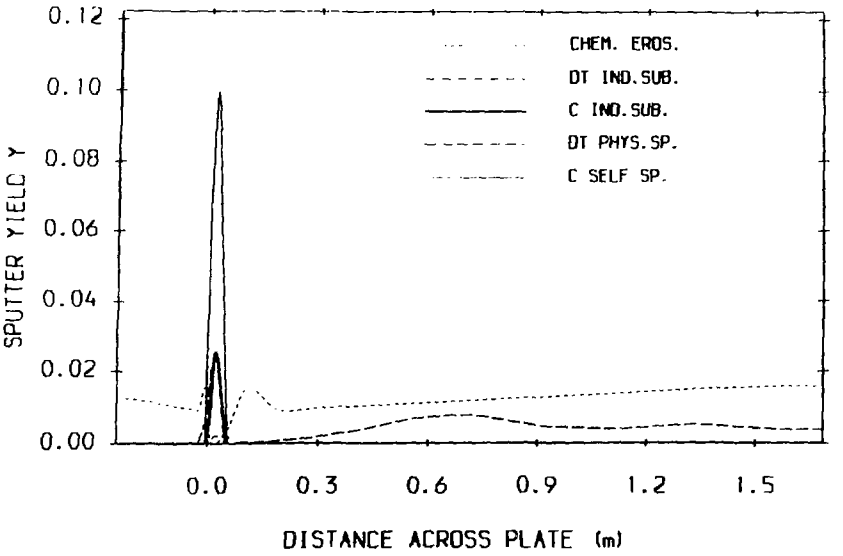

FIG. 3-15 Variation across the inclined divertor plate of ITER (Physics Ignited scenario) of the yields for chemical erosion, for physical sputtering due to D/T and recycling C ions and also for RES (The figure legend for RES is D/T and C induced sublimation).

Present predictions are uncertain in respect to both the plasma temperature adjacent to the divertor plate and to the corresponding D^+/T^+ flux. To take this into account, upper and lower values of T_e are given in the physics guidelines (see Table 3-5). Fig. 3-16 shows the corresponding values of peak net erosion for the outer divertor plates of ITER options A1, B1, B4,and B6 at a peak surface temperature of 1000°C. Only options A1,B1 and the lower T_e case of B4 have peak net erosion of less than 1 m/(integrated burn year). The corresponding release rates of carbon atoms and hydrocarbon molecules are shown in Fig. 3-17 where the same groupings of options apply if the release rates are to be less than about 10% of the incident D^+/T^+ ion flux. (The incident D/T flux is typically 2-to-4 $\times$ 10^{24} s^{-1}).

The implication of the results at a peak surface temperature of 1000°C is that options A1 and B1 provide acceptable performance in respect to both net erosion and release rate of carbon. While the low peak electron temperature for these cases would allow temperatures higher than the 1000°C usually permitted, the actual electron temperature could be higher than calculated because of the temperature peaking factor (§3.4.5), time-dependent effects (ELMs), or the imposition of a lower bound on the electron temperature by density limit considerations. Accordingly, the recommended temperature should remain below the material-dependent threshold for RES. This threshold has been evaluated to be in the range of 1000°C, subject to reevaluation on the basis of new data. Option B4 is rather doubtful whereas option B6 is not acceptable. Reduction of the peak electron temperature would allow more confident acceptance of B4 but not of B6.

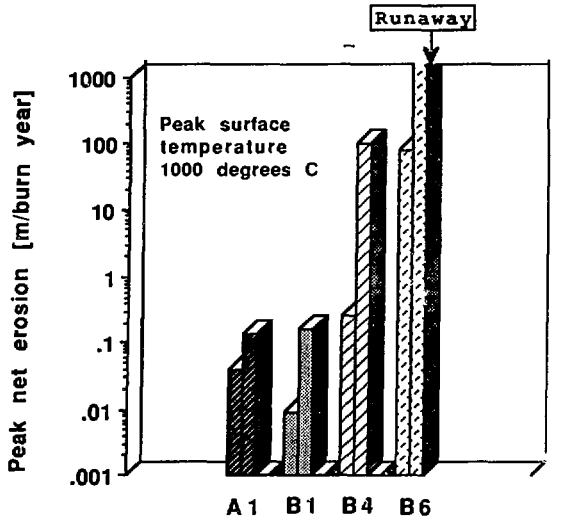

FIG. 3-16 Peak values of net erosion of the outer divertor plates of ITER scenarios A1, B1, B4 and B6. Upper and lower values indicate the spread in erosion arising from differences in the predicted divertor plasma conditions.

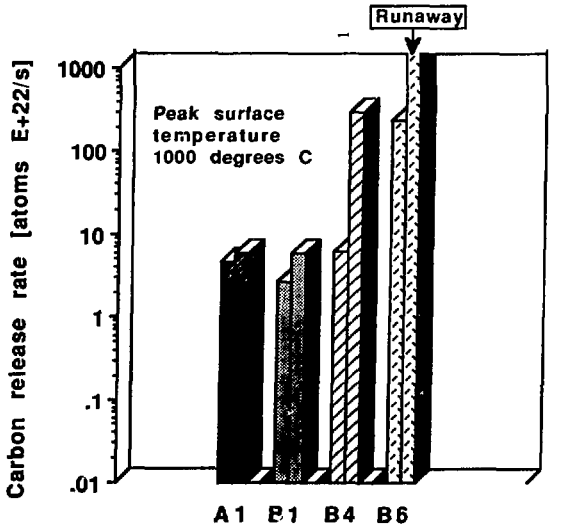

FIG. 3-17 The total release rates of carbon for ITER scenarios A1,B1, B4 and B6. The upper and lower values correspond to those used in Fig. 3-8-16

Beryllium has not yet been examined in detail for use in ITER. As a low-Z material, many aspects of its behaviour will be similar to carbon, but differences such as the following are important. Thermal sublimation occurs for beryllium at surface temperatures below the onset of radiation enhanced sublimation for carbon. Self-sputtering yields are higher but beryllium radiates less than carbon. The advantage of high pumping by evaporated or bulk beryllium observed in present-day machines may saturate for ITER pulse lengths. In principle, however, beryllium possesses the advantage of potential in-situ repair.

3.8.2 High-Z materials

Tungsten is a particularly attractive material because its threshold energy for physical sputtering by D^+/T^+ ions is relatively high (>150 eV), the yield is much lower than that of low-Z elements, and self sputtering exceeds unity only at an incident energy of about 1 keV. Also there is no RES and no chemical erosion by D/T. Oxygen can cause chemical erosion at high surface temperatures but the yield is small relative to that of carbon, and it might be reduced because of the presence of the intense flux of accompanying D^+/T^+. Use of tungsten is expected to lead to higher sheath temperatures because of the increased particle and energy reflection coefficients for D/T on W.

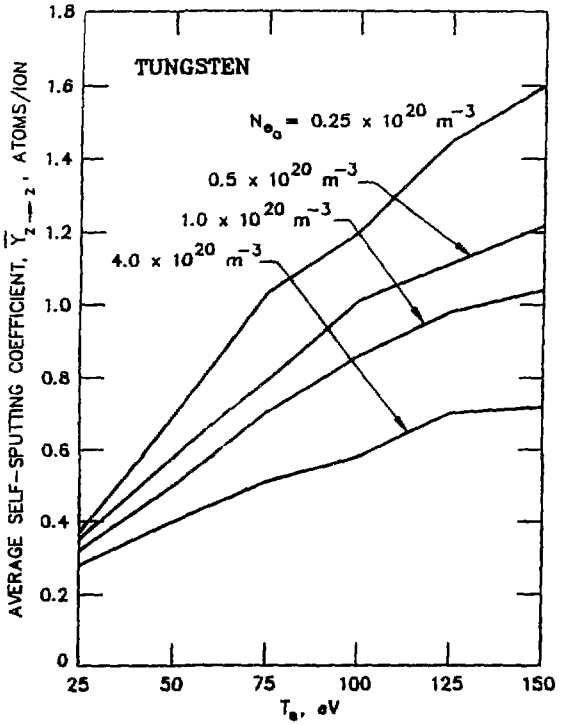

FIG. 3-18 The average self-sputtering yield of tungsten plotted as a function of T_e for plasma density in the range 0.25 to 4.0 x $10^{20}m^{-3}$.

In principle, it is desirable to operate with D^+/T^+ ion energies below the threshold for physical sputtering by D^+/T^+ (i.e. at a local plasma temperature of ~25 eV) but in practise the broad spread of the velocity distribution of the incident ions may impose more severe restrictions upon the temperature. Also, kinetic effects may enhance the D^+/T^+ ion energy so that operation close to the threshold may not be practical. It is likely that incident He ash and relatively highly charged impurity ions will have incident energies that are well above their sputtering thresholds. (This could be a problem if edge radiation were to be enhanced by injected impurities). However, the beneficial effect of the long range of the magnetic sheath relative to the short ionisation range of the slowly moving sputtering tungsten atoms appears to reduce substantially the risk of runaway erosion. The results of a very detailed analysis of the sheath and self-sputtering effects are shown in Fig. 3-18 where the average value of the self-sputtering yield of tungsten is plotted as a function of T_e for a range of values of local plasma density. The implication is that operation at temperatures as high as ~100 eV may not cause the self-sputtering yield to exceed unity, in the absence of impurities.

Both experimental and modeling data indicate that sputtered tungsten ions may be retained within the divertor of ITER. But it is not yet possible to quantify the allowable rate of plate erosion for ITER. It may well be that this is dominated more by plasma contamination than by erosion of the surface. Extensive experimental and theoretical exploration of the compatibility of tungsten and other high Z elements with tokamak operation is urgently required

3.9 HELIUM EXHAUST

Prior to being evacuated from the tokamak, He particles pass through three regions with different transport properties. First, they must leave the closed magnetic surface region of the torus where they originated in D-T reactions. Here they are transported across the magnetic surfaces as He ions. The second region is the scrape-off layer and the divertor volume, where two-dimensional flows both along and across the magnetic surface must be considered. Ions and neutral atoms are of equal importance in transport. Finally, there are pumping ducts and downpipes, bringing gas to the pumps, where all the He flow is carried by atoms. Because of the principal difference in the particle transport in these three regions, it is practical to describe them in separate models and to match the solutions via the proper boundary conditions set at the separatrix, at the divertor plate, and at the duct entrance. Efforts have been made during the ITER Definition Phase to assess the He transport in all these regions and the impact on the design. The approaches and results are summarized below.

3.9.1. Helium Transport in the Bulk Plasma

Helium transport inside the separatrix in ITER has been considered in Refs.[3.64,65]. Both studies are based upon a one-dimensional diffusion approach with an inward pinch of He ions taken into account, the diffusivity being specified as a function of the magnetic surface. In Ref.[3.64], the complete set of transport equations, describing the transport of energy, particles, and current in the plasma column, is solved numerically. It was shown that both sawteeth and soft-β limits may significantly reduce the He density in the bulk plasma in the case of small He

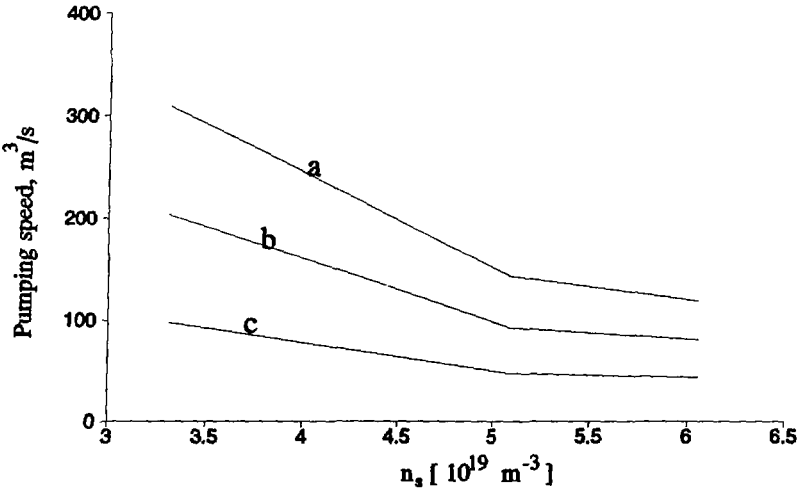

FIG. 3-19 Required pumping speed for He for sceenario A1 with edge He/DT density ratio calculated from core transport model to be 0.2. (a) reference plate geometry with end of plate horizontal (b) intermediate geometry, end of plate angled (c) divertor plate flat, i.e. no bend at end.

diffusivity or large pinch velocity. A simple analytical model used in Ref.[3.65] assumes negligible level of He recycling in the main plasma, but it takes into account finite He ion density at the separatrix, $n_{s,He}$. This model gives an appropriate linear relation between the bulk and edge He densities, which is used in the calculations of the required pumping speed. The models lead to optimistic values of the ratio $n_{s,He}/n_s$ = 0.2 for scenario A1 (see Table 3-9). To obtain a more conservative figure, the assumption that $n_{s,He}/n_s = 0.1$, the same as in the core, is made. This leads to the higher quoted He pumping speed for each of the scenarios in Table 3-9.

3.9.2. Helium Transport in the Edge Plasma

There are four 2-D codes: ZTRANS [3.66], UEDA [3.41], HELIUM [3.67], and B2 [3.40], which have been used for He transport modeling. The first three perform Monte-Carlo simulations of He atom transport and rely on a test-fluid approximation for He ions. ZTRANS and HELIUM are stand-alone codes which model the He transport on a specified background of the hydrogen components. The equations for all species are solved simultaneously in UEDA and B2. Monte-Carlo/ Fokker Planck techniques are used in ZTRANS.

The results show at least qualitative agreement about the He distribution in the edge plasma. A general feature of predicted He behaviour is a considerable outward shift of the He flow onto the target with respect to the flow of the background plasma. Such a shift, originating from both the existence of drag and thermal forces, impeding the flow of He along the hot region of the scrape-off layer and making it spread radially over the whole layer [3.57], and the directed transport of atoms due to the plate inclination with respect to the magnetic surfaces, greatly alleviates the necessary

TABLE 3-9. RESULTS OF PUMPING CALCULATIONS

Scenario	A1	B1	B6	B4
Fusion Power (MW)	1080	860	750	865
$\langle n_e \rangle$ (10^{20} m^{-3})	1.22	1.06	0.64	1.31
$n_{He}(0)/n_e(0)$	0.1	0.1	0.1	0.1
$n_e(a)$ (10^{20} m^{-3})	0.35	0.30	0.18	0.37
$n_{He}(a)$ (10^{18} m^{-3}) from core transport model[a]	7.9	7.2	3.4	9.7
$n_{He}(a)$ (10^{18} m^{-3}) from $n_{He}(a)/n_e(a) = 0.1$[b]	3.5	3.0	1.8	3.7
Required pumping speed C_p (m^3/sec)	310[a]–700[b]	340[a]–800[b]	1060[a]–1970[b]	180[a]–470[b]

[a] Edge He density determined by core transport model twice
[b] Edge He density set to 0.1 of assumed edge electron density

pumping requirements because the source of He atoms is displaced closer to the entrance of the pumping duct.

The main questions 2-D modeling should answer are: what is the pumping speed C_p necessary to maintain the specified value of He concentration in the bulk plasma $n_{He}(0)/n_{DT}(0)$? what is the He fraction in the evacuated gas? and how do these figures depend on the plasma parameters and divertor geometry? The results reveal high sensitivity to the upstream density of the background plasma n_s (see Fig. 3-19, where the dependence of C_p on n_s for scenario A1 is given), and to the shape and position with respect to magnetic surfaces of the divertor target.

3.9.3 Helium Transport in the Pumping Duct

Calculations of the required pumping speed for different scenarios, plate inclinations, and duct opening, assuming the He density in the duct to be constant and its backflow to the divertor to be uniform, isotropic and consisting of cool thermalized atoms, was made in Refs. [3.65,67]. The values of necessary pumping speed for different scenarios are listed in Table 3-9. The values in the Table are for the reference configuration (Rev A04), with a horizontal part to the plate (see Fig. 3-20) and do not take into account the constriction ("nose") at the entrance to the pump duct. The new reference configuration (Rev. A05) with an angled part to the plate is expected to resemble the intermediate case of Fig.3-20.

Note that the pumping speed of 700 m^3/sec provided at the torus [3.63] is marginally adequate for all these scenarios except B6. While the exhaust requirement for the steady-state, long-pulse scenario, B1, is somewhat larger than the provided speed in the reference design, improvements in plate shape and pump duct conductance, as discussed before [3.68,69], are expected to provide an adequate margin. Nevertheless, this must be verified.

All codes show that efficient He separation in the divertor region can be expected, so that the He concentration in the exhaust gas will likely exceed 2.5%.

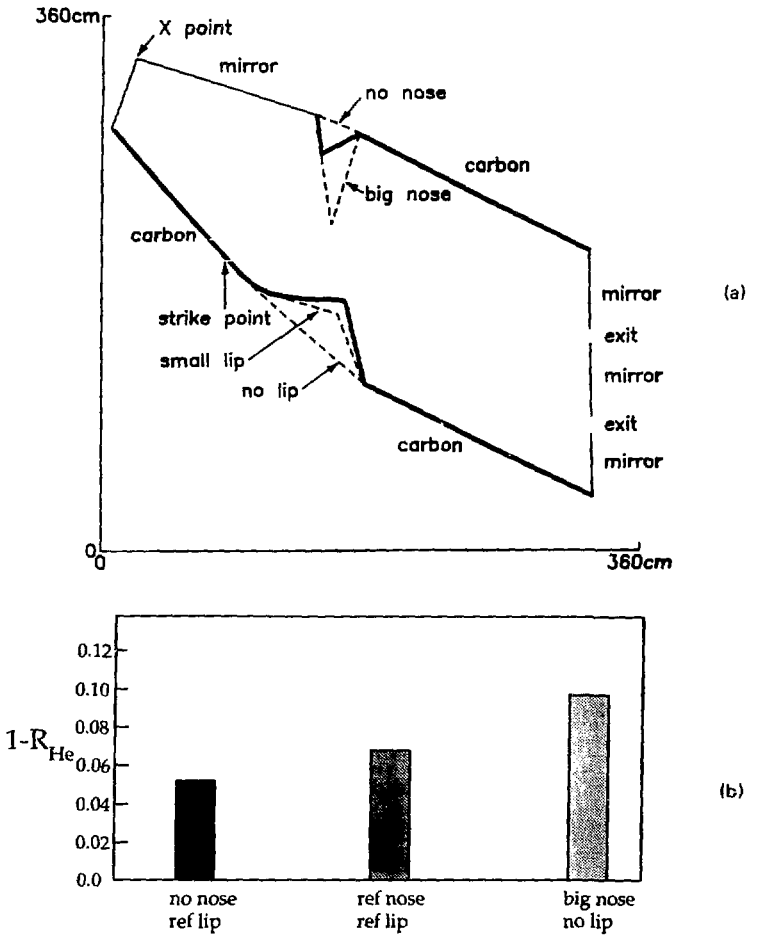

FIG. 3-20 (a) Pump duct geometries investigated with DEGAS (b) He pumping coefficient (complement of He recycling coefficient) for three geometries.

3.10 FIRST WALL OPERATING CONDITIONS

3.10.1 Heat Loads on the First Wall

Bremsstrahlung, cyclotron, synchrotron, and line radiation from the plasma are predicted to cause a nearly uniform power loading of <0.1 MW/m^2 on the first wall, assuming that less than 50% of the input power, alphas plus auxiliary heating, will be radiated from inside the separatix. Uniform charge-exchange losses would increase this by 0.001 MW/m^2 ; localized losses, as due to pellet injection and neutral beams would cause little additional power load, provided the penetration of these was more than ~0.1 m inside the separatrix. The wall near the divertor may see a twice higher

power load if radiation from the divertor region is ~30% of the input power there. Prompt loss of fast alphas are predicted to cause peak power loads in both the physics and technology phases of ~ 0.1 MW/m^2 on 1% of the wall, and ~0.5 MW/m^2 on specially shaped sublimiters (or wall segments) located at both edges of access ports. Ripple-trapped alphas would impact between TF coils on the outer wall of the vessel, about 45° above the plasma midplane. Stochastic diffusion of banana orbit alphas would cause a broader power loss profile causing a peak power load less than ~0.1 MW/m^2 (except on sublimiters as previously noted); the exact profile will depend on the shape of the wall. The divertor may intercept some of the lost alpha orbits.

3.10.2 Erosion

From energy-dependent particle charge exchange neutral particle fluxes to the wall, calculated with the DEGAS and B2 codes [3.70], < 10^{20} /m^{2}s at E ~ 100 eV, the gross erosion of a carbon outer wall in the entire technology phase is <0.03 cm from physical sputtering by D/T. This is based on the expectation that T_e at the wall sheath will be less than 30 eV, thus ion impacts will not cause more sputtering than neutral impacts. TF ripple at the outer midplane would locally increase the erosion by a factor of 3 to reach 0.1 cm/(integrated burn year), provided the wall is not contoured to match the ripple. The inner wall would have twice the average erosion rate due to higher average fluxes but no ripple enhanced erosion. Sputtering due to impurity ions at ~10% concentration levels would increase the erosion about a factor of 5. The gross erosion of carbon-based materials due to RES and chemical sputtering by D/T is approximately the same as that impurity ions, <5 cm/(integrated burn year) for wall temperatures < 1500°C. The gross erosion of tungsten tiles would be 100 times less rapid. About 1/2 of eroded material is expected [3.71] to be redeposited on the wall and the rest is likely to be deposited on the divertor.

3.10.3 Plasma Contamination

Using the Post/Lackner model [3.72] for diffusive transport in a SOL, the impurity content of the core plasma has been evaluated for both C and W wall tiles. It is assumed that the W ions moves along the field at $0.1c_s$, as do the C, D, and T ions. The radial transport coefficients are the same as used in §3.4. The estimated core concentrations of C and W are $n_C/n_e = 10^{-3}$ and $n_W/n_e = 3 \times 10^{-6}$, which do not pose a serious contamination problem.

3.10.4 Effects on the Divertor

The main effect on the divertor is expected to be the contamination of the divertor with wall material. About 1/2 of the eroded wall material is expected to be transported down field lines onto the divertor plate. The region of most intense deposition would be near the wall, but ample material would be deposited closer to the strike point. Hence, if a high-Z wall material was used, the shielding of divertor impurities must be sufficiently good that high-Z divertor tiles are also acceptable. The charge state of the impacting wall impurities will be higher than those which originated at the divertor plate because of the longer residence time in the plasma and the higher electron temperature near the midplane. This is particularly important near the separatrix.

3.11 STARTUP SCENARIO AND STARTUP LIMITER CONSIDERATIONS

The startup phase of an ITER plasma is the initial ~30 seconds in which the current is ramped up from 0 to about half current (12–15 MA). During this period the plasma is limited by either inboard or outboard startup limiters rather than the divertor plates because it is not possible to form a diverted configuration at very low plasma currents. Subsequently, the divertor configuration is established and considerations similar to those applied elsewhere in §3.4 apply.

For Ohmic startup at medium densities (volume-average density increases with time to 4×10^{19} m^{-3}, e.g. Fig. 3-21) the transport code ASTRA [3.73] was used to model the initial phase of the discharge when the plasma is in contact with the wall. With ASTRA, self-consistent calculations of plasma parameters in both bulk and edge plasma regions may be performed [3.74]. The evolution of the edge plasma parameters, i.e. temperature, density, and particle outflows from the bulk plasma as well as the peak power load at the inner wall (assuming toroidal symmetry) are shown in Fig. 3-22. For Ohmic startup, a power of 8–10 MW and ideal heat loads of 0.7–1.0 MW/m^2 are predicted for inboard startup. This is consistent with estimates [3.75] scaled from the physics ignition case using an analytic model [3.47] and also consistent with the resistive volt-second consumption. Ideal heat loads of 0.3–0.5 MW/m^2 are obtained for outboard startup. Increased radiation would improve the heat loads.

The ideal heat load must be modified by factors which take into account asymmetries and uncertainties. While toroidal field ripple may be neglected for inboard startup, for outboard startup toroidal ripple leads to a peaking factor of 2.6 at $q = 3$ (increasing with q up to $q \approx 5$ and then flattening off), i.e. an ideal heat load of 0.8 MW/m^2, comparable to the heat load obtained for inboard startup. If outboard startup is used, it is therefore recommended that the startup limiter be shaped to match the ripple corrugation of the magnetic surfaces. For both outboard and inboard startup, the limiter should be circular and concentric with the toroidal field to an accuracy of the order of one mm. Once this is done, the heat load for both outboard and inboard startup is dominated by mechanical considerations requiring that the angle of incidence of the magnetic field not be less than 1.5°. For Ohmic startup, this results in acceptable values of the heat loads: $\approx$ 1 MW/m^2 for outboard startup with shaping (about 2.5 MW/m^2 without shaping at $q \approx 3$) and $\approx$ 2 MW/m^2 for inboard startup. These values must still be multiplied by: a left-right asymmetry factor of 1.3 because experiments show an asymmetry in power loads between electron and ion sides in the ratio of 2:1; a factor for uncertainty in transport coefficients of 1.3 (similar to §3.4.3); and a toroidal peaking factor associated with MHD effects of 1.3. The engineering peaking factors, to associated with the angle of 1.5° is expected to be 1.3. Reduction of the area of the startup limiter by access ports and edge effects are not yet taken into account. No credit is taken for power reduction by radiation.

For startup with lower hybrid assist at medium densities, only outboard startup is considered because of coupling. Startup at 20 MW appears possible (4 MW/m^2 before application of asymmetry and uncertainty factors above). 40 MW yields a value of 10–13 MW/m^2 before application of these factors.

Lower-hybrid-assisted startup at lower densities is evoked in some alternate scenarios. While the present scaling can not be applied to these relatively collisionless plasmas, a tendency to higher heat loads at lower densities is expected. Furthermore,

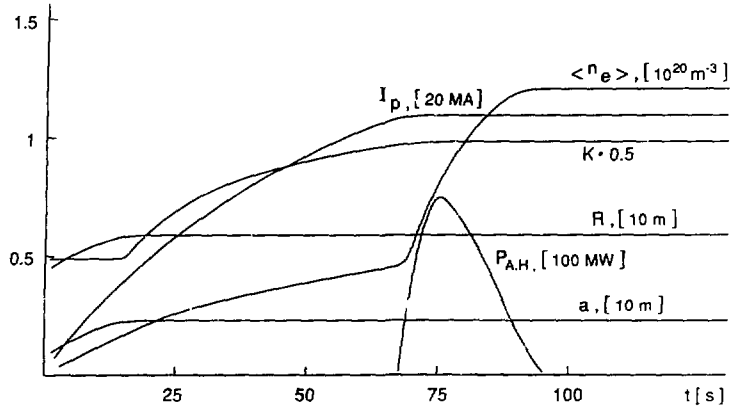

FIG. 3-21 Time evolution of plasma parameters (current, density, elongation, major radius, minor radius, and auxiliary heating power) during startup for ITER scenario examined by ASTRA code.

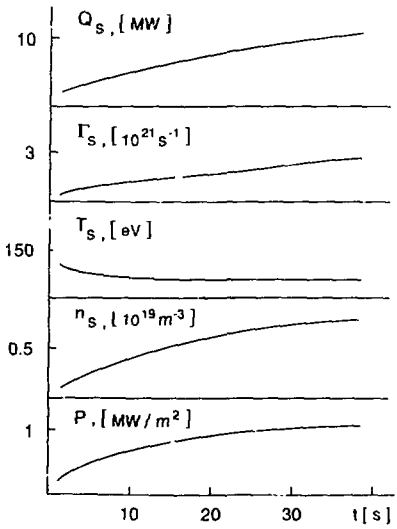

FIG. 3-22 Time evolution of edge plasma parameters (power flow to edge, particle flux to edge, temperature, density) and power per unit area deposited on startup limiter during plasma startup.

the effect of suprathermal electrons, ignored in the scaling above, would be exacerbated.

Erosion problems related to the higher temperature of a limiter plasma relative to a deep divertor plasma remain to be worked out, and 2-D modeling of a startup limiter equilibrium is desirable.

Calculations of the divertor plate heat loads at the final stage of the discharge start-up were based on scaling laws and have been normalized to 2-D modeling results for the nominal divertor operating regimes [3.74]. The results obtained have shown that for the discharge startup scenario considered, the peak heat loads are not in excess of those typical for the burn phase.

3.12 CONDITIONING

Conditioning procedures are *in vessel* techniques required to remove loosely bound surface impurities, such as oxygen, water, and hydrocarbons, which might readily contaminate the plasmas, and also to reduce the hydrogen (isotope) concentrations in the plasma-facing components, thus improving density control, particularly during plasma startup.

3.12.1 Baking

After the initial evacuation of the vacuum vessel, or after a major opening, an extended baking of the vessel and all its components to an elevated temperature is required to speed up the desorption of loosely bound and physisorbed molecules. The required temperature is material dependent. Generally a higher temperature is better, though certain materials, e.g., stainless steel, suffer loss of strength or other desirable properties by extended stays within certain temperature ranges (~500–700°C for steel). For carbon and carbon-based materials,. a temperature above 350°C for 24 hours is recommended. For most metals, only a temperature above 150°C is necessary.

3.12.2 Conditioning Techniques

Conditioning techniques generally rely on the exposure of plasma-facing components to plasmas. The higher energy of plasma particles relative to room temperature gases speeds up kinetic and chemical processes which clean surfaces and desorb atoms adsorbed within the bulk. Based on the desired effects, i.e., surface cleaning or bulk desorption, different techniques have been developed for tokamaks. However, not all are applicable in ITER, mainly because of its extended pulse length and continuously present toroidal field.

Conditioning methods which do not rely on plasma exposure, e.g., gettering, boronization, beryllium coating, and heating with rf waves, are not considered suitable for ITER, in part because of the tritium inventory issue, and in part because of their inherent transient effects. For the latter technique, radiatively cooled tiles would have to be used exclusively, in contradiction to the present plans, or cooling would have to be interrupted during this infrequent conditioning and probably the cooling channels would have to be drained.

Conditioning to remove oxygen-bearing molecules and hydrocarbons should be required only after large quanitites of O have entered the vessel, by an air or water leak, or if they have been exposed internally, as by a disruption. The two main methods that have been successful in the past are Taylor discharge conditioning (100 kA plasma current, 100 ms pulse duration, 10^{18} m^{-3} plasma density, 1 Hz repetition rate) and pulse discharge cleaning (2 MA plasma current, 2 s pulse duration, 10^{19} m^{-3} plasma density, 0.01 Hz repetition rate). Both make use of the steady-state toroidal field, but generally at reduced values. The pulsed nature of these techniques requires more extensive fatigue and eddy current analyses. Both techniques have been used in tokamaks with room-temperature, as well as 300°C , walls. Other plasma techniques, ECH, ICRH, and DDC (disruptive discharge cleaning) may be applicable. It is considered that conditioning to remove loosely bound impurities will be needed less frequently than once per week.

The desorption of hydrogen atoms trapped within the bulk requires either elevated temperatures, particularly for carbon, or bombardment by atoms/ions with sufficient energy to penetrate into the bulk. Glow discharges, generally in He, have been very useful for this in the absence of a magnetic field. However, glow discharges in a magnetized configuration have only been tested in one tokamak (Tore Supra). The results are not conclusive. Pulsed discharge cleaning with He has also been successfully used to desorb trapped hydrogen. A variation on this technique would be to change over the working gas from D/T to He at the end of plasma burn. The 30-50 s period of the plasma shutdown may purge the PFC of retained D/T. However, this technique has not yet been demonstrated and the detailed shutdown scenario remains to be elaborated.

If plasma conditioning techniques prove too difficult to implement, then elevated temperature can be used. The same guidelines as stated before apply. Carbon-based materials would have to be held above 350°C and metals above 150°C. Bulk doping methods may, however, alleviate the conditioning requirements.

3.13 PASSIVE SHUT-DOWN

It is important that the fusion plasma be shut-down by some passive process in the event of a failure of the divertor plate cooling system. Engineering analyses show that 2500° C is the maximum allowable surface temperature for carbon-based plates bonded to a water-cooled molybdenum alloy structure. The rate at which carbon is released from the plates increases non-linearly with increasing surface temperature and so one potential method for passive shutdown is to rely upon the associated increase of impurity contamination in the edge plasma to enhance energy loss or to trigger a disruption. The latter would cause a rapid shutdown of the fusion power. (In the ideal case the disruption should be a minor one, but this aspect is not considered here.) Impurity transport rates are not sufficiently rapid for the core to be contaminated in less than ~10 s, a period considered marginally too long in the case of a loss-of-coolant accident. The magnitude of the required impurity release to cause a disruption has not yet been assessed but it is reasonable to assume that the onset of runaway carbon erosion of the divertor plate would be adequate, though not necessary. It is used as a criterion in the following discussion.

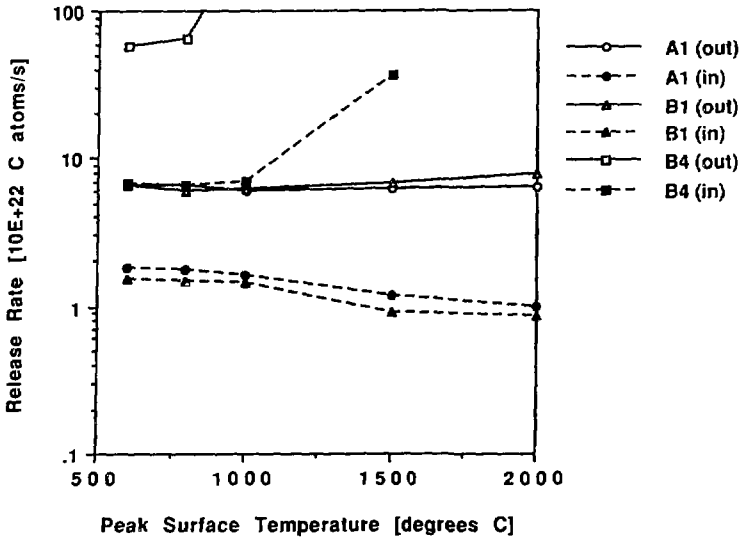

FIG. 3-23 Dependence upon the peak surface temperature of the release rate of carbon from the outer divertor plates of ITER options A1, B1 and B4. Upper and lower values reflect the spread in the predicted plasma conditions, see §3.8

The erosion processes of carbon are briefly described in §3.8. It can be deduced that runaway conditions occur when

$$Y_C(E_i) + Y_{RES.C}(E_i, T_s) > 1. \qquad (11)$$

Here $Y_C(E_i)$ is the self-sputtering yield due to recycling carbon ions which is non-linearly dependent upon the incident ion energy, $E_i \sim 2.5 \langle Z \rangle T_e$, assuming the recycling carbon ions remain cold. Here $\langle Z \rangle$ is the average charge state of the recycling ion. $Y_{RES.C}(E_i, T_s)$ is the yield for radiation enhanced sublimation caused by the recycling carbon ions and it is dependent upon both E_i and the surface temperature T_s. Analyses show that $\langle Z \rangle$ is about 2 for self sputtering and 1 for RES. It is evident that the critical surface temperature for runaway carbon release is governed by the relationship and

$$Y_{RES.C}(E_i, T_s) \approx [1 - Y_C(E_i)]. \qquad (12)$$

The critical temperature is therefore sensitive to E_i and hence to T_e which is itself dependent upon the plasma operating conditions. (T_e and T_i are expected to be similar in the sheath region.) Fig. 3-23 shows the dependence upon peak surface temperature of the release of carbon neutrals from each of the outer divertor plates of the A1, B1 and B4 options of ITER (see Table 3-5 and also §3.8). The upper and lower values show the spread arising from differences in the predicted divertor plasma conditions. The steady-state scenario B6 is not included because of its excessive erosion even at room temperature. Neither the physics ignited scenario (A1) nor the long-pulse hybrid

scenario (B1) exhibit runaway conditions in the surface temperature range up to 2000°C. In the case of B4, the lower T_e condition (25 eV) approaches runaway erosion at 2000°C, but the higher T_e case (75 eV) does so at about 1100°C.

In general it is concluded that runway carbon erosion is not a reliable mechanism for passive shutdown in all conditions. This unreliability is further aggravated by the sensitivity of runaway conditions upon $\langle Z \rangle$ and upon cooling and other effects which occur in the local plasma due to the release of substantial quantities of carbon as the runaway threshold is approached.

Release of carbon due to thermal sublimation can exceed that due to particle bombardment when the surface temperature approaches 2000°C.This effect has not been modelled explicitly for ITER conditions but it is clear that thermal sublimation can cause a gross release of carbon although it does not *per se* lead to runaway conditions. Thus at the present time it is not possible to guarantee that an increase in the surface temperature of the divertor plate will lead to a rapid shut down of the plasma, although gross erosion is expected at about 2000°C.

3.14 PHYSICS R&D REQUIREMENTS

The area of power and particle control requires a particularly directed, continuous, and vigorous R&D program to provide and augment experimental data, improve modeling, investigate materials, demonstrate experimentally operational aspects and new concepts, and thereby improve the design and the confidence in the predictions for ITER.

A particular effort is required in the area of scrape-off layer measurements to provide an experimental database for improving modeling of effects already taken into account (diffusion, pinch, impurities, etc.) and to permit inclusion of effects not presently included (kinetic effects, drifts, current flows, etc.). In addition, measurement of poloidal and toroidal dependences of the divertor power loads and sheath electron temperatures and variations of divertor geometry (single null, double null, divertor length, impact on exhaust, etc.) are crucial for the final design of ITER. Related tasks explore the effect of hot spots, and the impact of radio frequency and fueling method on the edge plasma. In view of the necessity of ELMy H-mode conditions, as well as other transients such as thermal instabilities or impurity-related effects, the dynamic characteristics of the edge plasma must be investigated.

Experimental and modeling data of impurity transport and radiation is important to predict impurity reflux toward the main plasma and to generate scenarios able to radiate more than 2/3 of the plasma power produced in the core plasma to reduce the heat load transferred to the divertor plates. Transport of He toward and in the plasma edge, and exhaust from the plasma, remains a crucial topic to extrapolate the degree of alpha-particle dilution of the central plasma. Final materials choices for the physics and technology phases will depend on new measurements of DT retention, pumping, erosion, startup behaviour, and extrapolated disruption survivability and will be strongly conditioned by the experimentally determined impurity reflux characteristics. The latter problem is particularly relevant for the choice of plate material for the technology phase.

Demonstration of active control and optimization of divertor conditions to improve the severe conditions associated with the ITER parameters is crucial. This

includes gas recirculation, powerful pumping, biasing and current injection, impurity seeding, preferential fueling at one divertor, ergodic edge concepts, RF impurity control, and innovative He pumping techniques. In addition, promising alternative divertor plate concepts should be brought to a level of development adequate for comparison with "classical" designs. Presently applied wall conditioning concepts (for O removal and for DT depletion to facilitate startup) are generally difficult or impossible to apply with the required frequency in ITER. Innovative concepts must be developed in this area.

REFERENCES (§3.0)

[3.1] M. NAGAMI et al., Plasma Physics and Controlled Nuclear Fusion Research 1980 (Proc. 8th Int. Conf. Brussels, 1980) Vol. 2, IAEA, Vienna (1981) 367.

[3.2] M. KEILHACKER et al., Plasma Physics and Controlled Nuclear Fusion Research 1980 (Proc. 9th Int. Conf. Baltimore, 1982) Vol. 3, IAEA, Vienna (1983) 183.

[3.3] L. DE KOCK et al., Plasma Physics and Controlled Nuclear Fusion Research (Proc. 12th Int. Conf. Nice, 1988) Vol. , IAEA, Vienna (1989)

[3.4] S.K. ERENTS et al., *Nuclear Fusion* **28** (1988) 1209.

[3.5] K. ALEXANDER et al., *Nuclear Fusion* **26** (1986) 1575.

[3.6] D. GOEBEL et al., *Plasma Physics and Controlled Fusion* **29** (1987) 473.

[3.7] I.S. LEHRMAN et al., *Plasma Phys. and Controlled Fusion* **32** (1990) 51.

[3.8] ASDEX Team, Annual Report of Max-Planck-Institute for Plasma Physics (1987) 8.

[3.9] L. DE KOCK et al., IAEA- TECDOC-536 (Proc. of a Technical Committee Meeting on impurity control in toroidal devices) IAEA, Vienna (1990) 37.

[3.10] N.L. VASIN et al., *J. Nucl. Mater.* **162-164** (1989) 300.

[3.11] G.K. MCCORMICK et al., *J. Nuclear Materials* **162-164** (1989) 264.

[3.12] N.TSOIS et al., Proc. 16th European Conference on Controlled Fusion and Plasma Physics, Venice (1989),Vol. III, 907..

[3.13] S.K. ERENTS et al., Proc, 17th European Conference on Controlled Fusion and Plasma Heating, Amsterdam (1990) 1385.

[3.14] ASDEX Team, Annual Report of Max-Planck-Institute for Plasma Physics (1988).

[3.15] D.N. HILL et al., *Nuclear Fusion* **28** (1988) 902.

[3.16] K. ITAMI et al., IAEA-TECDOC-536 (Proc. Technical Committee Meeting on Impurity Control in Toroidal Devices) IAEA, Vienna (1990) 67.

[3.17] D.N. HILL et al, "DIII-D data for SOL modelling," ITER Physics R&D Reports (Contribution by DIII-D Team), Task PH-01, Power and helium exhaust conditions, ITER-TN-PH-9-7/PH01 (1989).

[3.18] J. NEUHAUSER et al., "Edge and divertor studies on ASDEX," Proc. 13th Int. Conf. on Plasma Physics and Contr. Nuclear Fusion Research, Washington 1990, (IAEA, Vienna), paper A-5-2.

[3.19] T. SHOJI et al. "EML and Divertor Bias Studies on JFT2-M," ITER Physics R&D Reports (Contribution by JFT2-M Team), Task PH-01, Power and helium exhaust conditions,ITER-TN-PH-0-3-PH01 (1990).

[3.20] K. BEHRINGER et al., Proc. 8th Intl. Conf. on Plasma-Surface Interactions in Contr. Fusion Devices, Jülich, Germany, *J. Nucl. Mater.* (1989).

[3.21] T. HIRAYAMA, et al., "Database on Z_{eff} and radiation power in JT-60, and numerical simulation study of radiation performance based on self-consistent model," ITER-IL-Ph-13-0-J-1 (1990).

[3.22] ITER Physics R&D Reports (Contribution by TFTR Team), Task PH-05, Characterization of low-Z materials for plasma-facing components, ITER-TN-Ph-9-7/PH05 (1990).

[3.23] J.L.LUXON et al., "Recent results from DIII-D and their implications for next generation tokamaks," Proc, 17th European Conference on Controlled Fusion and Plasma Heating, Amsterdam (1990), to be published in Plasma Physics and Controlled Fusion (1990), in press.

[3.24] K. J. DIETZ et al., "Beryllium in JET," in ITER Physics R&D Reports (Contribution by JET Team), Task PH-05, Characterization of low-Z materials for plasma-facing components, ITER-TN-PH-0-3-PH05 (1990).

[3.25] J. WINTER et al., J. Nuclear Materials **162-164** (1989) 713.

[3.26] H. NAKAMURA et al, "Experiments with TiC coated Mo limiter and divertor plate," in ITER Physics R&D Reports (Contribution by JT-60 Team), Task PH-06, Characterization of high-Z materials for plasma-facing components, ITER-TN-PH-9-7/PH06 (1989).

[3.27] J. ROTH, G. JANESCHITZ, *Nuclear Fusion* **29** (1989) 915.

[3.28] M. IDA et al., *Phys. Rev. Lett.*, **58** (1987) 116.

[3.29] G. FUSSMANN, "Impurity Transport in Tokamaks (Overview), presented at the *ITER Workshop on Power anmd Particle Control*, Garching July 1990, ITER-IL-Ph-9-0-E-11

[3.30] M. SHIMADA et al., 9th Intl. Conf. on Plasma-Surface Interactions in Contr. Fusion Devices, Bournemouth, UK, *J. Nucl. Mater.* (1990), in press.

[3.31] C. E. BUSH et al., Princeton Plasma Physics Laboratory Report PPPL-2616 (1989).

[3.32] Y. SHIMOMURA et al., *Nuclear Fusion* **23** (1983) 869.

[3.33] P.H. REBUT et al., Proc. 13th Int. Conf. on Plasma Physics and Contr. Nuclear Fusion Research, Washington 1990, (IAEA, Vienna), paper A-1-2

[3.34] R. BUDNY et al., private communication, presented at the Transport Task Force Meeting, Hilton Head, USA, Feb. 19, 1990.

[3.35] E.J. SYNAKOWSKI et al., Princeton Plasma Physics Laboratory Report PPPL 2700 (1990).

[3.36] H. NAKAMURA et al., "Helium transport and exhaust experiments in JT-60, ITER-IL-PH-9-0-J-4. (1990)

[3.37] J. HOGAN et al., "Helium transport in TEXTOR," ITER-IL-PH-9-0-U-5. (1990).

[3.38] M. SHIMADA et al., *Phys. Rev. Lett.* **47** (1981) 796.

[3.39] H. NAKAMURA et al., Proc. IAEA Technical Committee Meeting on α-Particle Confinement and Heating, Kiev, (1989).

[3.40] B.J. BRAAMS, "Computational studies in tokamak equilibrium and transport," Thesis, State University at Utrecht, The Netherlands, June 1986;

and B.J.BRAAMS, "A multi-fluid code for simulation of the edge plasma in tokamaks," NET Report 68, EUR-FU-XII-80/87/68 (Comm. of the European Communities), Jan. 1987.

[3.41] K.ITOH et al., *Jap. J. Applied Phys.* 27(1988) 1750.

[3.42] YU. IGITKHANOV AND V. POZHAROV, in Summary of ITER Specialists' Working Session on Model Validation and Development of Edge Plasma Models, ITER-TH-Ph-9-4 (1989).

[3.43] YU. IGITKHANOV et al., Proc. 11th European Conference on Controlled Fusion and Plasma Physics, Aachen (1983) 397.

[3.44] R. SIMONINI et al., Proc. 17th European Conference on Controlled Fusion and Plasma Physics, Amsterdam (1990), Vol. III, p. 1369.

[3.45] T. ROGNLIEN, Communication presented at the *PPPL/ITER Workshop on Plasma Edge Modeling* Princeton, USA, (Jan 1989).

[3.46] S.A. COHEN et al., Proc. 9th Intl. Conf. on Plasma-Surface Interactions in Contr. Fusion Devices, Bournemouth, UK, *J. Nucl. Mater.* (1990), in press.

[3.47] M.F.A. HARRISON, E. HOTSTON, Proc. 9th Intl. Conf. on Plasma-Surface Interactions in Contr. Fusion Devices, Bournemouth, UK, *J. Nucl. Mater.* (1990), in press.

[3.48] H.D. PACHER et al., "Status of divertor considerations," ITER-IL-PH-13-0-31, 1990.

[3.49] H.D.PACHER, G.W. PACHER, "Evaluation of effective power load safety factors with sweep, and with sweep and ergodization," ITER-IL-PH-13-0-30, 1990.

[3.50] H.D.PACHER, G.W.PACHER, "Reduction of Divertor Plate Heat Loads by Sinusoidal X-point Sweeping," ITER-IL-Ph-13-0-24, 1990.

[3.51] M. AZUMI et al., "Reduction of heat load at the divertor plate by magnetic fields perturbation with active coils--preliminary results," ITER-IL-PH-13-0-J-5, Aug. 1990.

[3.52] M.F.A. HARRISON, E. HOTSTON, "Simulation of edge ergodization for ITER options A1 and B6," ITER-IL-PH-13-0-E10, August 1990.

[3.53] S. KRASHENNINIKOV, T.K.SOBOLEVA, "Influence of kinetic effects on the sheath potential and divertor plasma parameters in ITER, ITER-IL-PH-13-0-S-14, 1990.

[3.54] K.A. WERLEY, B. BRAAMS, S.A. COHEN, "2-D edge plasma parametric studies of the ITER physics phase device", ITER-IL-PH-13-9-U-1 (1989).

[3.55] D.N. RUZIC, K.A. WERLEY, S.A. COHEN, *J. Nucl. Mater.* (1990), in press.

[3.56] B.J.BRAAMS, Communication to US Workshop on Power and Particle Control for ITER, Princeton, USA, 1989.

[3.57] S.I.KRASHENINNIKOV, Issues of Atomic Science and Technology, Series Thermonuclear Fusion, 1988, No 2, p.8 (in Russian).

[3.58] J. BROOKS, Proc. 9th Intl. Conf. on Plasma-Surface Interactions in Contr. Fusion Devices, Bournemouth, UK, *J. Nucl. Mater.* (1990), in press.

[3.59] V.A.POZHAROV, et al., "Calculation of thermal loading onto divertor plates in the presence of impurities, ITER-IL-Ph-13-0-S-21, (1990).

[3.60] V. ABRAMOV, YU. IGITKHANOV, V. PISTUNOVITCH, "Feasibility of carbonic divertor plates," ITER-IL-PH-13-9-S-12 (1989).
[3.61] A. MAHDAVI et al., Communication to *ITER Workshop on Advanced Divertor Concepts*, Garching, Germany, October 1990.
[3.62] J. CUMMINGS et al., Proc. 9th Intl. Conf. on Plasma-Surface Interactions in Contr. Fusion Devices, Bournemouth, UK, *J. Nucl. Mater.* (1990), in press.
[3.63] N.A. UCKAN and ITER Physics Group, *ITER Physics Design Guidelines: 1989*, ITER Documentation Series, No. 10, IAEA, Vienna, 1990.
[3.64] M.REDI, S.COHEN. "Influence of edge conditions on ITER helium ash accumulation and sustained ignition," ITER-IL-PH-13-0-U-1.13 (1990).
[3.65] A.S.KUKUSHKIN, "On He transport inside the separatrix and its impact on pumping requirements in ITER," ITER-IL-PH-13-0-S-13 (1990).
[3.66] J.N.BROOKS, M.PETRAVIC, G.KUO-PETRAVIC, *Contributions to Plasma Physics* **28** (1988) 465.
[3.67] A.S.KUKUSHKIN, "Once more on He pumping and divertor geometry," ITER-IL-PH-13-0-S-10 (1990).
[3.68] D.N.RUZIC, K.A.WERLEY, S.A.COHEN, "Variation of neutral gas temperature and densities in the divertor region and pump duct of ITER as a function of geometry: physics and technology phases" ITER-IL-PH-13-0-U-9 (1990).
[3.69] A.YU.PIGAROV, "Parametric study of helium pumping for ITER," ITER-IL-PH-13-0-S-18 (1990).
[3.70] Y. SUN et al., "Calculations of particle fluxes to the ITER divertor plates and walls: A Progress Report," ITER-IL-Ph-13-9-U-4 (1989).
[3.71] V. VOJTSENYA, S. COHEN, Proc. 9th Intl. Conf. on Plasma-Surface Interactions in Contr. Fusion Devices, Bournemouth, UK, *J. Nucl. Mater. (1990), in press.*
[3.72] D.E.POST, K.LACKNER, "Plasma models for impurity control systems," in Physics of Plasma-Wall Interactions, D.E.Post and R.Behrisch, Ed., Plenum Press, NY (1986), p. 627.
[3.73] A.Yu.DNESTROVSKIJ et al., "Analysis of 0-dimensional dependences for the tokamak SOL parameters and their effect on transport processes in the main plasma," ITER-IL-Ph-13-0-S-11, (1990).
[3.74] A.Yu.DNESTROVSKIJ et al., "Edge plasma parameters and heat loads at the first wall and divertor plates for the discharge startup in ITER," ITER-IL-Ph-13-0-S-12 (1990).
[3.75] H.D.PACHER, G.W.PACHER, M.F.A.HARRISON, "Startup limiter considerations," ITER-IL-Ph-E-0-6 (1990).

4.0. DISRUPTIONS

4.1 CHARACTERISTICS OF TYPICAL DISRUPTIONS

4.1.1 Classification of Disruptions

Disruptions appear in all tokamaks under various conditions. They can be classified according to cause.

Density limit disruptions are thought to be caused by a thermal instability of the edge plasma in machines with metal or carbon plasma-facing components. Recent experiments on JET [4.1] with beryllium show that the density limit under those conditions is often given by a more benign series of highly radiating localized MARFE's rather than by disruptions. Impurity accumulation may also lead to disruption by effectively lowering the density limit.

Low-q disruptions usually limit operation to $q > 2$, although $q_\psi(95\%) = 1.9$ has been attained in single-null operation (DIII-D, [4.2]).

Beta-limit disruptions occur near the Troyon limit, $\beta\ (\%) = 2.8\ I/aB$ for high I/aB. Soft, i.e. disruption-free, beta limits are sometimes observed, e.g. on JET with Be operation (JET, [4.3]).

Disruptions also occur during transient phases. Ramp-up disruptions occur during startup and can often be avoided by following appropriate trajectories in the l_i-q plane (JET, [4.4]). Changes of configuration (transition from limiter to separatrix-bounded plasma), large sawtooth crashes particularly at low q, and strong ELM activity can lead to disruptions. The transients associated with plasma current rampdown or termination of additional heating are also a major source of disruptions in present devices (78% of all disruptions in JT-60, [4.5]).

4.1.2 Evolution of Disruptions

The evolution of disruptions can be divided into 4 phases, which are most clearly seen in density limit disruptions (for other disruptions, the pre-precursor and precursor phases sometimes do not appear explicitly or coalesce). Major characteristics of these phases are as follows:

i) Pre-precursor phase. This precedes a density limit disruption. A slow increase in radiation (up to a significant fraction of the input power during times up to 1 s) at the plasma edge, SOL, or divertor and/or an increase in recycling leads to a decrease in edge temperature and a shrinking of the current channel.

ii) Precursor phase and MHD activity. During this phase, MHD modes are frequently observed (usually 2/1 [4.2] although in some cases 1/1 (TFTR, [4.6]) or absent). Usually for density limit disruptions the modes grow, slow down, lock to an error field, continue to grow, and then lead to the next phase. In devices which exhibit locked modes, suppression of mode locking (error field compensation, adding neutral beam power) has been found to suppress (or delay) disruptions. Some devices (notably TFTR) do not appear to exhibit precursors or locked modes in many

disruptions. Low-q disruptions often exhibit n = 1 precursors (JET, [4.4]) or purely growing 2/1 modes (DIII-D, [4.2]) before thermal quench occurs near q = 2.

iii) Energy quench phase. A first phase of energy quench is often a redistribution (flattening with strong edge gradients (JET [4.2], Tore-Supra [4.7]), but also erosion on one side; JET) of the electron temperature profile lasting several ms. During the energy quench proper, the electron temperature drops rapidly, to a final temperature between 50 and 100 eV (Tore Supra [4.8]) and possibly lower in other experiments. The time scale for this quench, during which the plasma loses the major portion of its thermal energy, is usually from 100 to several hundred microseconds but may be as long as several ms. (In some cases, multistage partial thermal quenches are observed). Typically 50%, but in some cases (JT-60 [4.5]) up to 80%, of this energy is lost to the plasma-facing components, and the remainder is presumably radiated. The cause of the energy quench remains unclear, and proposed explanations based on turbulent processes or impurity influx remain contradictory. The loss of plasma pressure in this phase results in a rapid inward motion of the plasma to a new equilibrium position, determined by the vertical field and the eddy currents in the surrounding conducting structures.

iv) Current quench phase. After the energy quench, an increase of the total current, accompanied by a negative voltage spike, is observed and normally attributed to a flattening of the current profile. The duration of the current quench is variable, but the fastest quench times observed in various devices are 5–15 ms, depending on the device but independent of the plasma current in that device (except for JT-60 [4.5], where an increase of the fastest decay time with current is observed). Usually, a fastest decay time rather than a maximum decay rate is quoted. Typical quench times in each device are often much longer than the fastest quench times. Although the fastest quench times appear to be of the order of the vacuum vessel time constants of these devices, this may be fortuitous. Most (over 75%) of the magnetic energy is lost by radiation during this phase. Usually, current quench is accompanied by inward motion of the plasma (DIII-D [4.2,9]) and often by vertical displacement (also DIII-D). During rapid current quench, runaway electrons can be generated carrying a significant fraction of the plasma current (see Section 4.3), and having energies exceeding 50 MeV [4.4,10,11], although in some cases (DIII-D [4.9]), a large density rise during current quench appears to prevent runaway formation. Poloidal currents in plasma-facing components are inferred (DIII-D [4.2,9]) when vertical displacements occur (for a more detailed discussion , see §4.2 of this report).

4.1.3 Disruption Frequency

Disruption frequency statistics on JT-60 [4.5] show that 30% of discharges disrupt when the operation covers the entire operational region and that 20% of additionally heated (NB) disruptions occur during power on. 2.2% of disruptions of NB heated shots (0.8% of all NB heated shots) could not be attributed to any identifiable cause. Identifiable causes for disruptions during power on included mis-injection of pellets, exceeding the density limit after pellet injection, impurity gas injection, operation in abnormal conditions (at low toroidal field, low plasma current, or low q), locked mode during current ramp-up, NB port aging, unusual configurations, and Ti or Mo influx with limiter plasmas and metal walls. Most of the disruptions attributed to identifiable causes are in principle avoidable in routine operation. Disruption fre-

quency statistics on TFTR [4.6] show a disruption frequency of 2–4% for shots over a time period for which a significant fraction of the shots was far from the operating limits (supershots at low-n, high-q, high-temperature). JET [4.1] has reported a reduction of the occurrence of disruptions, particularly density limit disruptions, when Be is employed but no figures are presently available. Considering the disruption frequency database on these and other machines and the uncertainties inherent in the extrapolation to ITER parameters (much longer pulse length, elongation, coupling to vacuum vessel, relative importance of locked modes), the disruption frequency must be estimated ~5% of all shots in the physics phase of ITER. The best experimentally demonstrated value in the absence of active control and extrapolable to well-controlled routine ITER operation would be either the best TFTR value (2–4%) or a value of 2% extrapolated from JT-60 on the assumption that unavoidable disruptions consist of those due to unidentified causes (0.8% of shots) and an additional 1.2% of shots due to identified causes (i.e., up to 20% of flat-top disruptions due to identified causes or a smaller number combined with some accidental and power-off disruptions). For the technology phase, present data would therefore suggest a disruption frequency of 0.8% of shots if (1) all operation is far from the operational limits, (2) disruptions during discharge shutdown and additional heating power-off can be essentially avoided, and (3) if some measure of active control of disruptions is implemented.

4.1.4 Characterization of Disruptions for Representative ITER Scenario

The data summarized in Sect. 4.1 as well as in the other subsections of Sect.4 have led to the characterization of disruptions for ITER given in Table 4-1.

4.2 CHARACTERISTICS OF VERTICAL DISPLACEMENT EVENTS

The strongly elongated plasma configurations to be used in ITER ($\kappa \sim 2$) are vertically unstable unless active feedback on the vertical position is applied. A malfunction of this feedback system for any of a variety of reasons, such as noise in the position detection circuits, saturation of the control or power supply system, or abrupt changes in plasma parameters, can lead to a rapid displacement vertically at full plasma current. As the plasma contacts the plasma-facing components at the top or bottom of the vacuum vessel, the current is rapidly forced to zero, similar to the behaviour of the plasma after the thermal quench of a disruption (DIII-D [4.2,9], JET [4.12,13]). This phenomenon constitutes the vertical displacement event. A rapid vertical displacement normally also occurs during the current quench phase of a normal disruption (DIII-D) in elongated plasmas.

Although the causes for vertical displacement events and disruptions are different, the effects on the machine are similar, in that the total plasma energy (thermal and magnetic) is lost in a short time. The forces created by the vertical displacement event on machine components are frequently greater than those encountered in a conventional disruption because the displacement of the plasma current increases its magnetic interaction with the first wall and vacuum vessel components (JET, [4.14]).

The time scale for vertical displacement is governed by the electromagnetic interaction of the plasma current with nearby conducting structures and by the decay time constants of the eddy currents produced in these structures by the motion of the

TABLE 4-1. SUMMARY TABLE: TENTATIVE CHARACTERIZATION OF DISRUPTIONS FOR REPRESENTATIVE ITER SCENARIO

Thermal Quench:

• Typical duration: *(occasionally as long as 3 ms)* *(design values: 0.1; 0.5; 3 ms)*	0.1–1 ms
• Energy to divertor plate: typical *(design value: 500 MJ)*	250 MJ
– width of energy deposition on inclined divertor plate at ≈15°	0.25 m
– peak energy load on divertor plate inclined at ≈ 15° *(for 250 MJ; 4 plates; poloidal peaking factor 2; no toroidal peaking)*	12 MJ/m^2
• Energy to first wall:	250 MJ
– peaking factor	5
– peak energy load on first wall	2 MJ/m^2

Current Quench:

• Typical duration: *(occasionally as short as 5 ms)* *(design values: 5 ms; 20 ms; 200 ms)*	20-to–several 100 ms
• Energy to divertor:	up to 200 MJ
• Energy to first wall: *(mainly radiation)*	500 down to 300 MJ
– peak energy load on first wall *(excluding runaway electrons)*	up to 3 MJ/m^2
• Runaway electrons:	
– particle energy	up to 300 MeV
– total energy content	100 MJ
– peak energy load due to runaway electrons	30 MJ/m^2
• Poloidal currents in first wall elements:	up to 0.2 × I

Disruption Frequency:	number	%
• Ignition studies: *(10^4 discharges)*	1500	(15%)
of which: – at nominal parameters:	500	(5%)
– at reduced W_{th} (≈ 200 MJ):	1000	(10%)
• Long pulse/steady-state operation studies: *(5×10^3 discharges)*		
– at nominal parameters	250	(5%)
• Technology testing phase: *(up to 4×10^4 discharges)*		
– at nominal parameters	300	(≈ 1%)

[Note: Disruption frequency numbers assume only "non-avoidable" disruptions (Physics Phase) and some active control (Technology Phase). Improvement by factor of 10 to rare fault status requires near-perfect active disruption control systems (R&D program).]

plasma current. Modelling the plasma of ITER as a rigid body and taking into account the interaction with the conducting structures predicts a growth rate for vertical displacement of the order of 35 s^{-1} [4.15], equivalent to a time of the order of 100 ms.

This simple picture of the time development of the vertical displacement event is complicated by the response of the plasma to the motion. Two effects must be taken into account self-consistently. The first is the change in plasma shape and edge q value, and therefore in coupling to external elements, as the plasma moves vertically. To evaluate this effect, 2-D numerical simulations of the motion including MHD effects in the plasma and eddy currents in the passive structures (with EDDYC-2 [4.16] and TSC [4.17]) have been performed and give growth rates for vertical displacements of the order of 30 s^{-1}.

The other complicating effect is the existence of currents in the plasma periphery closing through the first-wall components which the plasma touches (Fig. 4-1). These currents are force-free in the plasma periphery, but they modify the force distribution on the plasma [4.17,18,23]. During the vertical displacement event, the destabilizing force on the plasma resulting from the poloidal field curvature is balanced by the forces on the plasma resulting from the induced currents in the passive conducting structures and in the vacuum vessel, including the poloidal currents. The total force acting on the vacuum vessel, equal and opposite to the destabilizing force, is therefore

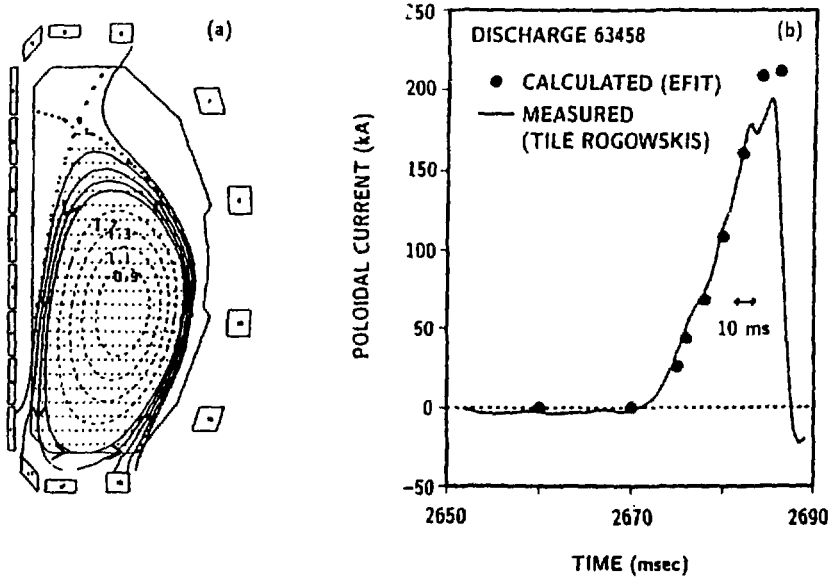

FIG. 4-1 Example of vertical displacement event from DIII-D [Fig. 4 fom paper IAEA-CN-53/A-1-4, "DIII-D Research Program Progress," by DIII-D Team, in Plasma Physics and Controlled Nuclear Fusion Research (Proc. 13th Int. Conf., Washington, D.C., 1-6 October 1990) IAEA, Vienna (to be published)]. In (a), the poloidal direction of current flow is indicated. In (b), the measured current through first-wall elements is compared with currents inferred from equilibrium fitting.

TABLE 4-2. SUMMARY TABLE: TENTATIVE CHARACTERIZATION OF VERTICAL DISPLACEMENT EVENTS FOR REPRESENTATIV ITER SCENARIO

- Duration of event:
  - given by vertical displacement and low-q disruption
- Thermal quench
  - occurs when q at the last closed flux surface reaches ~1.5
- Vertical motion
  - described by an exponential form before the thermal quench
  - given by results of simulations with eddy currents
  - expected growth rate $\gamma = 30\ s^{-1}$ $z(t) = z(0) \times \exp(\gamma t)$
- Current quench
  - occurs after thermal quench
  - total current I(t) is almost constant up to thermal quench $I(t) \approx I(0)$
    ($I(t) \approx I_a(t) + q_a(t) \times I_h(t)$, where I_h = *halo current – see below*, $I_a(t)$ = *current inside last closed flux surface*)
  - duration (after $q_a = 1.5$) 5–20 ms
- Energy deposition
  - during thermal quench
    100 % of thermal energy may be lost at point of contact 500 MJ
    width of layer ~0.25 m on divertor plate, or 0.05 m on first wall
  - during current quench
    - *50 % of magnetic energy lost at point of contact* 250 MJ
      width of layer ~0.25 m on divertor plate, or 0.05 m on first wall
    - *50 % of magnetic energy radiated* 250 MJ
- Runaway electrons may be produced during the current quench
  - energy up to 300 MeV
  - current up to 11 MA
  - energy deposition (see also Table 4.1) up to 30 MJ/m^2
- Poloidal currents in first wall elements (halo currents)
  - poloidal current value - scaling tbd up to $0.2 \times I$
    [poloidal current depends sensitively on electron temperature of the halo (unknown, assumed to be between 2 and 30 eV), driving terms for halo current are time rate of change of toroidal flux due to change in plasma cross-section and time rate of change of plasma current during current quench]
  - toroidal distribution ~ uniform
    [if plasma resistance determines current distribution, i.e., other impedances in poloidal circuit are small.]
    Recommendation: in-vessel components should have interconnections with low impedance in poloidal direction. Insulation of poloidal current paths is undesirable (arcing).
- Vertical displacement event frequency non-zero
  depends on reliability and dimensioning of position control system, but spontaneous peaking of the current profile, or spurious noise in control system can initiate a VDE. Also, disruptions in elongated plasmas terminate in VDE-like manner, therefore the effects of a full VDE must be designed for. Number of VDE's can probably be minimized by operating a reasonable distance from the vertical stability limits.

expected to be unchanged by the existence of poloidal currents. However, the force distribution on the vacuum vessel is modified, and the time constant for vertical motion is changed because of the resulting different resistive dissipation.

The poloidal currents are produced in the plasma-facing components as the plasma moves against them. These currents have been directly measured in DIII-D [4.2,9] and code simulation of measurements has been shown to be insufficient if their effect is not included [4.18]. These "halo currents" have also been deduced from measurements in JET [4.12]. Two driving terms for these currents have been identified. One is the decrease of toroidal flux enclosed by the plasma periphery connected to the plasma-facing conducting components as the plasma area is forced to decrease [4.19]. This creates a poloidal electromotive force. The other driving term is the toroidal electromotive force induced by the decrease of the plasma current [4.13,20]. Because the plasma periphery has only a very small beta, the currents are force-free and follow the magnetic lines of force in the plasma. In the plasma-facing components, however, they close on the shortest path, i.e., poloidally, and create local forces on these components. The size of the current produced is determined from the induced electromotive force and the plasma resistance in the plasma periphery ("halo;" for edge parameters reasonable for ITER, e.g., $T_e \sim 10$ eV, $n_e \sim 10^{20}$ m^{-3}, the effect of ion saturation current in determining the current distribution is expected to be unimportant). Because the distribution of current is determined by the largest resistance in the circuits, the plasma resistance for conducting first-wall components, the current distribution is expected to be toroidally uniform. The total halo current is predicted to attain up to 20% of the initial plasma current in ITER.

The strong wall contact of the plasma as it is pushed against the plasma-facing components will increase the plasma impurity content during the vertical displacement event, leading to enhanced radiation losses. As in the case of normal disruptions, part of the stored energy will therefore be radiated to the plasma-facing components. Although this effect will tend to equalize the power distribution on the walls, the area of contact with the plasma will still absorb a considerable fraction of the total energy.

A vertical displacement event can thus be described by the following sequence of events. Upon loss of vertical position control, the plasma moves vertically with a growth rate for vertical displacement determined by eddy currents in the passive structures (expected growth rate ~ 30 s^{-1}). The total measured current, consisting of the current in the confined plasma plus the contribution to toroidal current resulting from halo currents, is nearly constant during this phase, until the safety factor of the confined plasma current reaches 1.5 [q(a) ~ 1.5] due to decrease of the plasma cross-section. This corresponds to experimental observations on DIII-D [4.20]. A thermal quench is then expected, and a low-q disruption is initiated. The duration of the ensuing current quench is between 5 and 20 ms, like a normal disruption. The thermal energy of the plasma is expected to be lost essentially at the point of contact during the thermal quench, whereas 50% of the magnetic energy is expected to go into radiation, the rest being lost at the point of plasma contact during current quench. During the vertical displacement, after the plasma touches the first-wall surfaces, and during the thermal quench, halo currents are expected to occur, whose maximum size is approximately 20% of the initial plasma current. Their toroidal distribution is expected to be uniform if the largest resistance in the circuit is the resistance of the halo plasma (with a temperature expected to be between 5 and 30 eV).

The preceding discussion is summarized in the characterization of vertical displacement events ITER, Table 4-2. A major uncertainty remains the anticipated frequency of occurrence of the phenomenon, which is essentially determined by the dimensioning and reliability of the vertical position control system. Zero frequency is unlikely because VDE's can be initiated by spontaneous peaking of the current profile or noise in the position control system, even if the system is very reliable. It is expected, however, that the number of VDE's could be reduced by operating a reasonable distance from vertical stability limits. Future work should establish a more quantitative criterion. Vertical displacement events are therefore seen to be strongly dependent on the detailed design as regards both their characteristics and their frequency of occurrence.

4.3 SPECIFIC ASPECTS OF DISRUPTIONS

4.3.1 Energy Deposition During Thermal Quench

During the thermal quench phase, most of the thermal energy (typically 80%) of the plasma is lost very rapidly, in times between 0.1 and 3 ms [4.4,5,21]. Experimental observations to define the energy loss channel differ in different experiments, and vary from 100% radiated power (JET [4.4]) through 50% radiated, 50% to the limiter (TFTR [4.21]) to more than 100% of stored thermal energy deposited on the divertor (JT-60 [4.5] — this last observation has some magnetic energy transferred to the divertor during the thermal quench).

The reason for these differences in experimental observations are not clear. It should, however, be noted that the disruptions extensively studied in JET and which exhibited mainly radiative power loss during this phase were density-limit disruptions, whereas those in JT-60 with high divertor heat load took place at low density.

Observations of the temperature of the divertor plates during the thermal quench phase indicate that the width of power deposition becomes appreciable wider than normal (by a factor of three in JT-60 [4.5]) and its peak lies outside that obtained for stationary power flow conditions. Neither the toroidal distribution of heat conducted to the divertor nor that radiated to the first wall is well known, nor is direct information on the quench of ion thermal energy and the loss of fast ions available.

In the light of this fragmentary information, the heat load distribution during the thermal quench is necessarily uncertain in the characterization of disruptions for ITER. The power radiated is likely to be below 100%, because avoiding disruptions in ITER will require the normal operating regime of ITER to be a safe distance away from the density limit. One hundred percent of the power load onto the divertor plates in this phase is equally unlikely, because at reasonably high density, radiation losses will be larger. It is therefore expected that approximately equal power will go to first wall (partly by radiation and partly by particles) and to the divertor (mainly by particles), as given in the guideline.

4.3.2 Energy Deposition During Current Quench

During the current quench, the major channel for loss of the magnetic energy from the plasma is radiation, because the plasma is heavily contaminated with impurities (e.g. JET [4.4], JT-60 [4.5]). The other major loss channel is dissipation

in the conducting structures due to eddy currents. This channel is expected not to be important in ITER. Accordingly, the radiated power will normally dominate the power balance and the power deposition would therefore be relatively uniform. Nevertheless, if rapid vertical motion occurs (as is observed in e.g. DIII-D [4.2,9] and JET [4.4,12]), due to vertical instability and failure of vertical position control in response to the rapid changes in plasma parameters, a large fraction of the remaining energy stored in the plasma may be lost directly to the divertor plates.

The guideline for ITER for the distribution of the magnetic energy during the current quench gives 75% of the energy remaining in the plasma at the beginning of current quench going to the first wall, with an appreciable peaking factor to account for toroidal and poloidal asymmetries of the radiated power. The remaining 25% normally goes to the divertor. However, since rapid vertical motion can not be ruled out, the divertor plates must be capable of withstanding the deposition of the total remaining plasma energy on one divertor.

4.3.3 Runaway Electrons

In the thermal quench of a major disruption, central electron and ion temperatures in the plasma drop to values in the range of 5–200 eV. The upper value has been measured by LIDAR on JET during Be operation [4.1] and in Tore Supra during density limit disruptions [4.8]; the lower value is not directly measured, but inferred from general behavior, e.g. diamagnetism and limits of Thompson scattering sensitivity, on a number of tokamaks. Ion temperatures are less well documented. Values near 25 eV have been inferred on Tore Supra from density decay rates [4.8]. Charge exchange measurements on JET [4.22] also have shown temperatures below 100 eV at 10 ms after the thermal quench. The drop in electron temperature greatly increases the plasma resistivity while the plasma current remains fixed. This greatly increases the toroidal electric field as seen by electrons in the plasma.

Also a result of the thermal quench is a change in the plasma electron density. DIII-D routinely finds factor of ~2 increases in electron density during 1-5 ms after the thermal quench of major disruptions [4.20,24]. It is not known whether the density increase is caused by an impurity (most likely carbon) or a hydrogen influx. In contrast, Tore Supra reports a steady drop in density for a period of 20-200 ms after the thermal quench i.e., during the current quench phase [4.8]. Additionally, for minor disruptions on JET, decreases in electron density are well documented [4.25].

Electron temperature and density and Z_{eff} enter sensitively into the determination of the Dreicer field, the electric field above which electrons accelerate to relativistic energies. Furthermore, these quantities, along with the MHD stability and inductive energy of the plasma and the geometry of the tokamak, set the duration of the increased electric field. Because of these sensitivities, the variability of observations on the number and energy of the runaway electrons that exist in tokamaks after disruptions should not surprising. Auxiliary heating, lower hybrid in particular, makes the generation of runaway electrons more likely following a disruption.

In Tore Supra [4.11], most of the 130 plasma disruptions during 1990 with $I > 0.4$ MA generated runaway electrons. In contrast, during the lower toroidal field operation period of 1989, less than 5% of the disruptions were followed by runaways. DIII-D [4.20] has never observed runaway electrons, and operates at similar plasma parameters and toroidal fields as the first, lower toroidal field, phase of Tore

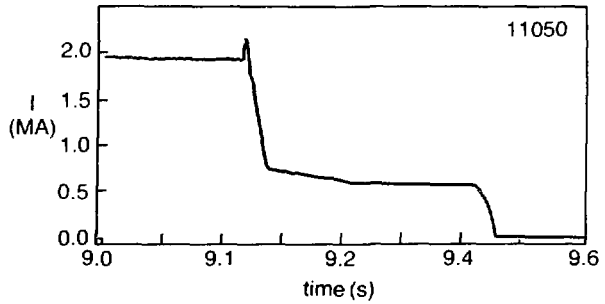

FIG. 4-2 Decay of plasma current after a major disruption in JET, showing a runaway electron current plateau (from. Ref. 4.4)

Supra. This may be attributed either to the density behavior seen in DIII-D, or to low toroidal field operation [4.11]. (DIII-D has similar diagnostics, e.g., hard x-ray and neutron detectors, to Tore Supra.)

The total runaway electron current following a disruption has been measured on JET to be up to 1/2 of the plasma current for I up to 6 MA [4.4]. The termination of the discharge then frequently exhibits a plateau, as shown in Fig. 4-2. Similar values for runaway current are found on JT-60 [4.5] and TFTR [4.6]. More generally, the runaway current is < 1/4 of the initial plasma current. The runaway current has been observed to persist for 10–1000 ms. The longer time is associated with better control of plasma position (JT-60 [4.26], JET [4.1],...) as well as the application of lower hybrid for current drive (Tore Supra [4.11], PLT [4.27],...).

Peak energies of the runaway electrons are measured by determination of activation products formed in the tokamak materials by photoneutron interactions. In PLT [4.27] and Tore Supra [4.11], these values were found to be ~20–45 MeV. JET has found evidence for runaway energies of ~100 MeV [4.28]. For the present generation of devices, the energy gain of runaway electrons is ~20 MeV/s, as calculated by the change in inductive energy. From the measured location of the activation products in the Tore Supra first wall, the runaway electron gyroradius was determined to be ~1 mm, corresponding to < 5% of the runaway energy [4.11].

Motivated by these types of observations, predictions have been made of the runaway electron energies and currents expected in ITER after major disruptions. The models developed included classical collisions, and synchrotron radiation resonances with the rippled toroidal field [4.29,30]. The upper limit for the runaway energy is ~300 MeV and the average energy is ~40 MeV. The total runaway current is predicted to be up to 1/2 of the plasma current. This last value is very sensitive to the assumed plasma density, temperature, and impurity content after the disruption. These models give good agreement with the data described earlier. The maximum total energy in the runaways, calculated from their total current (assumed to be 11 MA) and the inductance, is 100 MJ. This energy is assumed to be distributed uniformly on the divertor plates or on the first-wall tiles depending on the equilibrium after the thermal quench. The typical width of energy deposition is assumed to be ~10 cm. This gives a peak power load of 30 MJ/m^2. The implicit assumptions of no toroidal peaking (as might

occur due to small gyroradii and mechanical tile alignments) and the 10 cm width across the divertor plate must be carefully re-examined in on-going experiments.

The damage to PFC due to runaway impact has been modeled and comparisons made with simulation experiments. Details are described in Sect. 3.2.3. In brief, runaway electron impacts on carbon divertor plates are predicted to cause severe erosion of the surface as well as damage to water cooling tubes 2 cm below.

Methods to reduce the generation of runaway electrons and to avoid damage are under consideration. Techniques to address the first issue include reduction of the frequency of disruptions by active control of MHD and plasma operation away from density and beta limits. Further suggestions, still awaiting experimental test are: increases in plasma density or increased speed of plasma ramp-down, either upon detection of a thermal quench. Proposed methods to reduce runaway electron damage include: better control of plasma position; use of special sublimiters; and use of high Z materials, either as inserts in the divertor plate structure or as divertor plate tiles.

4.4 CONTROL AND AVOIDANCE OF DISRUPTIONS

4.4.1 Active Control Method

The methods of disruption control that are proposed for ITER are categorized into two ways: (1) by using external circuits and passive structures [4.31-34], and (2) by using external beam or RF sources [4.35, 36, 37].

In DITE [4.31], disruption control has been demonstrated by using a fast magnetic feedback system with 15 kHz and 5 kA for I = 60–120 kA. In Ohmic discharges, the amplitude of saturated m = 2 modes was reduced by a factor of 6 and the disruptive density limit was extended by up to 20%. The effectiveness was larger at low q. Even during the feedback control in Ohmic discharges, there appears a disturbing effect on m = 2 modes by sawteeth. The sawteeth that enhance m = 2 activity were stabilized by LH waves. However, the soft X-ray signals show the presence of a continuous m = 1 oscillation that couples with m = 2 modes. Application of feedback to this discharge reduces the m = 2 mode amplitude by a factor of 8. In addition, the amplitude of the coupled continuous m = 1 modes is also reduced and the confinement in the plasma center is improved as indicated by peaking of soft X-ray signals. The limit to the control appears to be due to a combination of plasma noise, abrupt change in m = 2 modes induced by a sawtooth, available feedback current and the system bandwidth.

In DIII-D [4.3], compensation of a static error field by a correction field has been found to prevent the onset of n = 1 locked modes, particularly those that occur at low density and low internal inductance. The discharge thereby becomes much more robust against disruptions. The effect persists even as q is decreased.

In COMPASS-C [4.33], resonant magnetic perturbations were applied at the density limit. The helicity is m/n = 1/1, 3/2 or 3/1. The perturbation levels are typically 10 Gauss, while the error field is reduced to less than 0.5 Gauss. The density limit is increased by 15% for q(a) = 3.5 when 2/1 perturbation is applied in the Ohmic discharge. Other perturbations do not affect the MHD activity; there is no extended period of oscillatory precursor to disruption.

For highly elongated plasmas, external kink modes are the most unstable modes near the beta limit. The effect of a passive stabilizing shell has been studied in PBX-M [4.34]. The longest growth times of n = 1 modes are longer by an order of magnitude than those in PBX without the passive structure near the outboard side of the plasma boundary, and they are comparable to L/R time of the passive shell. The current quench times during disruptions are also longer than in PBX. The characteristics of disruptions in PBX-M indicate that a close-fitting passive shell soften disruptions.

The m = 2 modes are often destabilized when the m = 1 modes are stabilized by applying LH-current drive in ASDEX [4.35, 36]. Current profile measurements show that the region with steep current density gradient extends to the location of the q = 2 surface. The disruption induced by m = 2 modes is preceded by a period (lasting several 10's of ms) of slow growth of the amplitude before locking. Unlocking of the modes and prevention of disruptions has been demonstrated by applying unidirectional neutral-beam injection in order to obtain plasma rotation.

Theory [4.37] indicates that disruption control by using electron cyclotron current drive should be possible. The m = 2 tearing modes may be suppressed by adding current (with a density of the order ~10% of the total current density) near the q = 2 surface with a width of the order of 10-20% of the plasma minor radius [§5.10].

In Ohmic discharges, reduction or suppression of m = 2 modes by feedback has been shown to avoid disruption and to increase the density limit. However, in a plasma with additional heating, a series of minor disruptions often occur followed by a major disruption. Studies of auxiliary-heated plasmas are therefore required. In a strongly shaped plasma, kink modes may be the trigger of high beta disruptions especially for lower l_i. The highly conductive structure of ITER may soften disruptions, i.e., increase the growth time of kink modes to values close to the skin time of the vacuum vessel. This effect may, however, be reduced because the separation between plasma and vacuum vessel is large in ITER (60-80 cm).The method of unlocking tearing modes by using neutral beams as demonstrated in ASDEX [4.35] may also be applicable to ITER.

4.4.2 Stable Operational Range

It is important to evaluate the operational region of the present tokamaks in order to define a strategy for minimizing the frequency of disruptions.

In JT-60, the disruption frequency was about 30% on average during 1985 to 1989 for about 9000 shots. Most of these disruptions are considered to be avoidable with sufficiently reliable plasma control and auxiliary heating systems (see also §4.1.3). Disruptions tend to become more frequent as operational boundaries are approached [4.38,39]. This is illustrated in Fig. 2.2-8.

The DIII-D tokamak shows the stable region to the density limit disruption in an l_i-q plane. As the discharges approach the density limit, the current profile peaks on a global scale, the internal inductance l_i increases and m = 2 tearing modes are destabilized prior to the disruption. All stable DIII-D discharges have lower l_i than the critical one at the same q. As q(95%) decreases, the DIII-D high beta experiments show a general trend toward lower l_i and narrower range of l_i for stable discharges (see Fig. 2.2-7). In particular, at q(95%) < 4, the operating range for l_i becomes narrower at high g [where g = β(%)/(I/aB) = Troyon factor] than at low g: g = 2.5

for $0.8 < l_i(1) < 1.1$ and g = 3.5 for $0.9 < l_i(1) < 1$ when q(95%) = 3.1, and g = 3.5 for $0.9 < l_i(1) < 1.3$ when q(95%) = 4.1. The value of g that has been sustained for at least 1 second is g = 2.7 at q(95%) = 2.3 and g = 3.4 at q(95%) = 3.8. For a database of 50 discharges with g >1.8 at q ~ 3.1, it was found that more than 90% survived during the high beta phase for g ~ 2.5. For g > 3.1, more than 25% disrupted and more than 30% of shots showed saturation or collapse of the beta value. For the lower q region (2.2 < q < 2.8) the reliability was worse [4.39].

Based on present experiments, it is recommended that the machine should not be operated near the operational boundary such as for l_i, q, beta and density to reduce the disruption frequency and to minimize the impact on the device.

4.5 REQUIREMENTS IN R&D

Many of the characteristics of disruptions are still incompletely understood. These include aspects of the thermal quench, the current quench, runaway production and energy distribution, and expected disruption frequency. Research is required in all of these areas.

The detailed mechanism of thermal quench must be investigated so that the duration of this phase can be confidently scaled to ITER and the contribution of the different energy loss channels to energy balance must be clarified. Information on the loss of ion energy and fast ions during the thermal quench phase must be obtained. The toroidal distribution of heat and particle loads must be determined for ITER-like conditions.

Radiation loss to the first wall during the thermal quench may be the limiting factor for the lifetime of the first wall if no protective tiles are used in the technology phase of ITER [4.39]. Therefore, the characteristics of disruptions not followed by a fast current quench are equally important.

It has been pointed out that many of the characteristics of the current quench phase are determined by the electromagnetic interaction of the plasma with the coils and the surrounding structures. The driving term, however, is the decrease of plasma current which is a consequence of the increased resistance of the plasma (due to the low temperature after thermal quench and the high impurity concentration). The relationship between wall materials and plasma resistance (impurity content) in this phase, as well as the penetration of the impurities into the plasma, must still be elucidated in order to extrapolate convincingly to ITER conditions.

Because of the impact of high-energy runaways on plasma-facing components, it is necessary to investigate the scaling of disruption-produced runaway currents and energies with plasma current, plasma current decay rate, coupling to external circuits, error fields, etc. in order to be able to predict the runaway content for disruptions in ITER conditions. At the same time, procedures must be developed which will reduce these currents and energies in order to minimize damage to first-wall components.

Vertical displacement events must be classified according to their causes, and control methods should be developed to limit their severity. The poloidal currents produced during vertical displacement events in plasma-facing and first wall components must be studied to enable their extrapolation to ITER conditions, since the insulation and anchoring of these elements must be designed in consequence.

The effect of disruptions on the first wall and divertor plates of ITER is major and severely limits the lifetime of these components, so that minimizing the number of disruptions is a major goal. As a step towards this goal, the statistics of disruptions must be further investigated, in an attempt to determine their causes, and the types of disruptions difficult to avoid must be identified. As a further step, a method for near 100% identification of a pre-disruptive state of the plasma should be developed in order, to be able to shut down without a disruption, to activate control mechanisms to avoid a disruption, or, at the least, to be able to reduce the impact of the disruption on the machine.

Methods of avoiding and/or controlling disruptions must be developed and tested in an ITER-relevant regime. Current profile control and feedback control of MHD modes have been proposed. The input or activation signals for each control method must be identified, and the reliability of the different methods must be investigated.

Finally, for safety reasons, it should be shown that it is possible to extract the energy of the plasma (kinetic and magnetic) in an orderly and reliable fashion on several different timescales. It is advantageous to accomplish this without disruption and to develop means of shutting down the plasma on a time scale of the order of 10 s without disruption. Equally, means should be developed to quench the ITER plasma in a very short time by reliably inducing a soft disruption. These concepts should be tested in an ITER-relevant regime.

The topics discussed here are included in the long-term Physics R&D program for ITER [4.40] and discussed in more detail in another section of this report.

REFERENCES (§4.0)

[4.1] P. THOMAS et al., PSI Meeting June 1990, to be published in *J. Nucl. Mater.* (1990).

[4.2] ITER Physics R&D Reports (contribution by DIII-D Team), Task PH07, Disruptions, ITER-TN-PH-9-7-PH07-U3, Sept. 1989.

[4.3] K. J. DIETZ et al., 17th EPS Conf. on Cont. Fusion and Plasma Heating, Amsterdam, 1990, to be published in *Plasma Physics and Controlled Fusion.*

[4.4] J. WESSON et al., *Nucl. Fusion* **29** (1989) 641.

[4.5] ITER Physics R&D Reports (contribution by JT-60 Team), Task PH07, Disruptions, ITER-TN-PH-0-3-PH07-J1, March 1990.

[4.6] ITER Physics R&D Reports (contribution by TFTR Team), Task PH07, Disruptions, ITER-TN-PH-9-7-PH07-U1, Sept. 1989.

[4.7] ITER Physics R&D Reports (contribution by TORE Supra Team), Task PH07, Disruptions, ITER-TN-PH-0-3-PH07-E2, March 1990.

[4.8] J. VALLET et al., "First Results on Disruptions in Tore Supra," presented at ITER Specialists' Meeting on Disruptions, Garching, Sept. 1989.

[4.9] A. KELLMAN et al., in Proc. 16th Symposium on Fusion Technology, London England, Sept. 1990 (to be published).

[4.10] P. JOYER, G. MARTIN, in Proc. of 17th EPS Conference on Controlled Fusion and Plasma Heating, Amsterdam, 1990, Vol. I, 303.

[4.11] G. MARTIN et al., "Disruption-induced runaway in TORE-Supra," presented at ITER Specialists' Meeting on Vertical Displacement Events and Disruption-Generated Runaway Electrons, Garching, July 1990.

[4.12] P. NOLL et al., *Fusion Technol.* **15** (1989) 259.

[4.13] P. NOLL et al., "VDE's and Halo Currents on JET," *op. cit.* [4.11], ITER-IL-PH-8-0-12.
[4.14] P. NOLL, private communication.
[4.15] J. LEUER et al., "ITER Rigid Body Vertical Stability," presented at ITER PF Specialists' Meeting, Feb. 1990, ITER-IL-PF-9-0-2.
[4.16] A. ASTAPKOVICH et al., "Simulation of VDE's with EDDYC-2," *op.cit.* [4.11], ITER-IL-PH-8-0-18.
[4.17] R. SAYER et al., "TSC Modeling of Vertical Displacement Episodes," *op. cit.* [4.11], ITER-IL-PH-8-0-17.
[4.18] T. JENSEN, D.G. SKINNER, "Support of model for vertical displacement episodes from DIII-D experimental results," GA Report GA-A19882.
[4.19] G.W. PACHER, H.D. PACHER, in Proc. of 17th EPS Conference on Controlled Fusion and Plasma Heating, Amsterdam, 1990, Vol. I, 423.
[4.20] A. KELLMAN et al., "Vertical displacement events, disruptions, and runaway electrons in DIII-D," *op. cit.* [4.11], ITER-IL-PH-8-0-13.
[4.21] M. ULRICKSON, in "U.S. Contributions to the INTOR Phase -2A, Part 3 Workshop, 1988," USA INTOR/88-1, Chapter 3, pp 33-35.
[4.23] E.J. STRAIT et al., "Observation of poloidal current flow to the vacuum vessel wall during a tokamak vertical instability," submitted to *Nucl. Fusion.*
[4.24] A. KELLMAN et al., "Operating limits and disruptions in DIII-D," *op. cit.* [4.8]
[4.25] S. COHEN et al., *Plasma Physics and Controlled Fusion* **29** (1987) 1205.
[4.26] T. KIMURA et al., "Disruption-Induced Hard X-Rays in JT-60," *op. cit.* [4.11], ITER-IL-PH-8-0-23.
[4.27] J. STRACHAN, private communication.
[4.28] O.N. JARVIS et al., *Nucl. Fusion* **28** (1988) 1981.
[4.29] A.J. RUSSO, "Disruption Runaway Modeling, Ripple Effects and Energy Limits," in *op. cit.* [4.11], ITER-IL-PH-8-0-26.
[4.30] L. LAURENT et al., *Europhys. Letters* **11** (1990) 219
[4.31] A.W. MORRIS et al., *Physical Review Letters* **64** (1990) 1254
[4.32] ITER Physics R&D Reports (contribution by DIII-D Team), Task PH08, Disruption Control, ITER-TN-PH-9-7-PH08-U2, Sept. 1989.
[4.33] ITER Physics R&D Reports (contribution by COMPASS Team), Task PH16, MHD Activity, ITER-TN-PH-0-3-PH16-E4, March 1990.
[4.34] ITER Physics R&D Reports (contribution by TFTR Team), Task PH16, MHD Activity, ITER-TN-PH-9-7-PH16-U1, Sept. 1989.
[4.35] ITER Physics R&D Reports (contribution by ASDEX Team), Task PH16, MHD Activity, ITER-TN-PH-9-7-PH16-E3, Sept. 1989.
[4.36] ITER Physics R&D Reports (contribution by ASDEX Team), Task PH16, MHD Activity, ITER-TN-PH-0-3-PH16-E3, March 1990.
[4.37] L.E. ZAKHAROV et al., "M=2 tearing mode stabilization with local current drive in ITER," *op. cit.* [4.8]
[4.38] ITER Physics R&D Reports (contribution by JT-60 Team), Task PH16, MHD Activity, ITER-TN-PH-0-3-PH16-J1, March 1990.
[4.39] ITER Physics R&D Reports (contribution by DIII-D Team), Task PH16, MHD Activity, ITER-TN-PH-0-3-PH16-U2, March 1990.
[4.40] G. VIEIDER et al., "ITER Plasma Facing Components," *op. cit.* [4.8].
[4.41] *Research and Development Needs for ITER Engineering Design,* IAEA/ITER/DS/20, ITER Documentation Series, IAEA, Vienna (1991).

5.0. CURRENT DRIVE AND HEATING

5.1 INTRODUCTION

The ITER current drive and heating (CD&H) systems are required for: ionization, preheating, and current initiation; noninductive current ramp-up assist; heating the plasma to the desired operating point; steady-state operation with full non-inductive current drive; current profile control (both in steady-state operation, and in combination with inductive current drive); and burn control by modulation of the auxiliary power. Steady-state current drive is the most demanding requirement, so this requirement has driven the choice of the ITER current drive and heating systems; these systems are described in detail in Ref. [5.1]. The reference and alternate systems scenarios are as follows:

Reference:	75 MW, 1.3 MeV neutral beam system
	50 MW, 5.0 GHz lower hybrid system
	20 MW, 120 GHz electron cyclotron system
Alternate:	130 MW, 15–80 MHz ion cyclotron system
	50 MW, 5 GHz lower hybrid system
	20 MW, 120 GHz electron cyclotron system

During plasma startup the electron cyclotron (EC) system must assure breakdown and current initiation at a low loop voltage (≤ 0.3 V/m). No more than 10 MW of EC power at 120 GHz is needed for reliable start-up with a large initial plasma major radius, and with a magnetic field error of less than 50 G. The ITER EC system is also considered for disruption control. Modeling indicates that a localized current layer driven with EC waves will maintain a plateau in the current density near the $q = 2$ surface to stabilize tearing modes (a precursors to disruptions). Disruption control is more demanding than start-up assist, requiring about 20 MW of injected power with real-time control of the injection angle (or frequency). An experimental demonstration of this disruption-control scenario is still required.

Volt-seconds saved with noninductive current ramp-up assist will be available for lengthening the current flat top or extending ITER operation to higher plasma current. Three constraints have been identified that limit the usefulness of non-inductive current ramp-up assist in ITER: (i) stresses in the central Ohmic transformer coils can limit the number of Volt-seconds available at the beginning of the current flat-top; (ii) the peak heat flux and/or electron temperature at the diverter plate or start-up limiter can exceed limits for safe divertor operation; and (iii) the power applied to the plasma for current ramp-up also heats the plasma and slows current penetration. The total lower hybrid (LH) system power was chosen to be adequate for current ramp-up assist in ITER.

A combination of neutral beams (NB) and LH waves was chosen for the reference operating scenario because this combination provides control of the current

profile and yields the highest current drive efficiency or figure of merit ($\gamma = nI_{CD}R/P_{CD} \approx 0.45\text{–}0.5 \times 10^{20}$ A/m^{2}W). Central current drive is provided by NB, while LH waves are used to drive current in the outer region. Current profile control is provided both by varying the relative neutral beam and lower hybrid power; and by varying the vertical aiming of the neutral beams. The NB energy is chosen to assure penetration to the magnetic axis for central current drive in the reference steady-state discharge. The frequency of the LHW is chosen to minimize difficulties in generation and transmission, to ensure good coupling between the launcher and the plasma, and to avoid damping on fast alpha particles. The neoclassical bootstrap current plays an important role in ITER steady-state scenarios; both by reducing the current that must be driven with neutral beams and lower hybrid waves, and by helping to broaden the current profile. Key physics issues include penetration of lower hybrid waves into reactor plasmas, and expanding the experimental database for neutral beam current drive (particularly to beam velocities greater than the Alfvén velocity), and experimental demonstration of steady state bootstrap current.

The alternate operating scenario differs in that central current drive is provided by ion cyclotron (IC) waves. Fast wave current drive scenarios at low (~17 MHz), medium (~55 MHz) and high (~120 MHz) frequencies were examined. A low frequency (~17 MHz) fast wave current drive scenario was chosen because this scenario gives the best current drive figure of merit ($\gamma \approx 0.3 \times 10^{20}$ A/m^{2}W), and avoids ion damping. About 130 MW of IC power is needed for steady-state operation. Key unresolved physics issues include an experimental demonstration of IC current drive, and current profile control.

5.2 IONIZATION, PREHEATING, AND CURRENT INITIATION

The unique feature of discharge start-up in ITER is a rather low loop voltage, $V_{loop} < 10$ V. This constraint follows, on the one hand, from a vacuum chamber design having a very low toroidal resistance (about 20 μΩ), and on the other hand, from the difficulty of achieving a rapid current change in the superconducting poloidal field coils. Such a low loop voltage severely constrains inductive start-up of the discharge, putting severe limitations on the magnitudes of stray poloidal fields within the chamber. Under these conditions it will be necessary to use special preionization techniques for the reliable and reproducible start-up of the discharge. One should say in advance that the "preionization" here does not mean only the creation of seed electrons to assist the emergence of an avalanche breakdown. Rather, we take the term "preionization" to mean the solution to the main discharge start-up problem: production of a completely-ionized plasma having a temperature of a few tens of eV and a density in the range 10^{18} m^{-3}.

At present, the most attractive and best developed technique to solve this problem is EC resonant heating (ECRH), although there are some experiments in which LH and Alfvén waves have successfully been used. For EC discharge start-up, there is a wide experimental base [5.2] and a rather well-developed theory of wave-plasma interactions [5.3]. Although there has been no detailed comparison between the theory and the experiment yet, the main results from both theory and experiment are in a qualitative agreement. This allows us to rely upon a favorable theoretical prediction for utilization of this technique in ITER.

The main advantages of the discharge start-up using the EC preionization are:

(1) Under ITER conditions one can provide a reliable and reproducible discharge start-up in a wide range of parameters (n_e, T_e, V_{loop}, P, B_{crr});
(2) The stray field limit is reduced by at least one order of magnitude;
(3) One can exclude the emergence of run-away electrons by control of the plasma temperature and density at the ionization stage;
(4) Loop voltage reduction to ~3 V and a corresponding reduction of currents in the vacuum chamber walls.

One should also add that the saving of a poloidal flux is often considered as an additional advantage of the EC start-up. However, under ITER conditions this saving is 1–2 V-s only, i.e., ~1% of the total flux.

5.2.1 Experimental Results

The greater part of the experiments can be generalized in the following way :

(1) EC preionization reduces the necessary loop voltage, V_{cr}, at very low levels of launched power (P_{EC} = 150 kW on DIII-D, P_{EC} = 40 kW on CLEO). In this case, an increase in P_{EC} has a weak effect on the further reduction in V_{cr}.
(2) Results have a weak dependence on the type of polarization, place of microwave energy launch, or pulse duration.
(3) The position of a resonance zone in the majority of experiments is not critical.
(4) The neutral gas pressure in the chamber, as well as the resulting plasma density, can be varied in a wide range.
(5) It is possible to arrange the discharge in such a way that run-away electrons and hard X-ray radiation are absent.
(6) A toroidal current is observed in the plasma when microwave power is launched into the chamber and the primary winding is short-circuited. The magnitude of this current depends on the applied vertical magnetic field.
(7) A current to the rail limiter located in the lower (or upper) part of the chamber is registered.
(8) Fast electrons with energies up to a few tens of keV are produced, when the microwave power is absorbed in a resonance zone.
(9) A steep rise in the electron temperature after the rotational transform emergence is observed, when an inductive electric field is applied to the microwave-produced plasma.
(10) Utilization of EC preionization allows one to reduce the inductive electric field strength to the values of the order of 2[d(LI)/dt]. For example, this allowed discharge start-up at E ~ 0.1 V/m on T-10, and E ~ 0.15 V/m on DIII-D.

5.2.2 EC Start-up Theory: Status and Predictions for ITER

The EC-wave energy absorption in a tokamak is provided by the existence of two plasma resonances: the electron cyclotron and upper hybrid. From the point of view of practical application to ITER these two absorption mechanisms do not differ much from each other, since the electrons accelerated by the wave have time to transfer their energies to a thermal plasma component in both cases. Therefore one can assume that the whole radiated microwave power or its greater part is absorbed in the plasma volume.

Transport of the absorbed energy is determined by the mechanisms of heat and particle confinement in a toroidal magnetic field without a rotational transform. This differs from confinement in the usual tokamak configuration that has a rotational transform. In a purely toroidal magnetic field, an inertial plasma drifts across the field lines under the effect of the ballooning force, and emerges along the major radius with a velocity of the order of the sound speed. Such a rate of plasma loss would be catastrophic. Such losses are not observed under real conditions. Instead, an equilibrium configuration is produced in which the ballooning force is compensated and the inertial drift is suppressed in spite of the absence of rotational transform.

Thus one should find an equilibrium in order to determine the plasma confinement time at the EC ionization stage. Then, one should consider the possible loss channels and single out the most dangerous of them. The equilibrium mechanism was studied in [5.4]. It can be qualitatively explained in the following way: the force of interaction between a vertical plasma current (closing through the vacuum vessel) and the toroidal magnetic field, or that between a toroidal current and a vertical magnetic field can be used for compensation of the ballooning force. The vertical current emerges as a result of the toroidal drift of electrons and ions in opposite directions. The origin of the toroidal current is similar to the origin of the Pfirsch-Schlüter current in the ordinary tokamak configuration. Both mechanisms are observed in experiments. However, the opportunities to sustain an equilibrium by both techniques are limited. The point is that the vertical current is not a divergence-free, and so violates quasi-neutrality. The toroidal current is related to the plasma diamagnetism with respect to the vertical magnetic field. Therefore, the pressure of the plasma confined due to the toroidal current cannot exceed the pressure of the confining vertical magnetic field.

A number of qualitative conclusions from this equilibrium theory have been confirmed by experiments that allows one to build up a model of energy and particle confinement at the EC plasma ionization stage in the tokamak discharge [5.5]. According to this model, the plasma temperature and density at the ionization stage are such that the plasma pressure is balanced by the vertical magnetic field pressure. Therefore, with a rise in the vertical magnetic field, B_v, the pressure rises until the losses related to a longitudinal plasma flow begin to dominate. Further increases in B_v then lead to increased longitudinal losses. Hence, there is an optimum in B_v whose value depends on the plasma density and on the absorbed power. The optimal vertical field for ITER is calculated to be in the range B_v = 50–150 Gauss, and show that an ECRH power of about 10 MW is needed to produce an ITER plasma with a density of 10^{19} m^{-3} and a temperature of 100 eV. Thus a microwave preionization system at a frequency with an EC-resonance within the torus, having a power 10 MW and a pulse duration $\leq$ 1 s is sufficient for preionization in the ITER vacuum chamber.

5.3 LOWER HYBRID PHYSICS

Lower hybrid heating, current drive, and current ramp-up assist have been demonstrated in present day tokamaks [5.6]. In addition, lower hybrid waves (LHW) have been used for preionization and current initiation during start-up. The highest

current drive figure-of-merit ever obtained, 0.34×10^{20} A/m^{2}W, was achieved in JT-60 [5.7] with LHW. This level is adequate for ITER applications. Other important recent results include H-mode discharges obtained with LHW in JT-60 [5.8]; flexible current profile control by tailoring the wave spectra, suppression of sawteeth with moderate LHW power levels, and strongly peaked electron temperatures profiles with high central temperatures obtained by stabilization of the $m = 1$ MHD mode with LHW in ASDEX [5.9]; very long LHW current drive discharges (TRIAM-1M: 1 hr, low density[5.10]; Tore-Supra 22 s, 2×10^{19} m^{-3} [5.11]). Current ramp-up has been investigated and found in good agreement with theory in a number of experiments (PLT, Alcator-C, PETULA, JT-60, WT-3).

Agreement between theory and experiment is good in most areas, including the current drive efficiency in the presence of a toroidal electric field. Questions that require further experimental effort include the origin of the spectral broadening during wave propagation and the enhanced current penetration observed in some experiments. The on-going experimental programme includes large-scale (JET, Tore-Supra, JT-60), and medium-scale experiments (FTU, PBX-M), which should provide complementary information in both LHW physics and RF technology required for ITER.

Extrapolating from present results, it appears that LHW cannot penetrate into the high β core of a burning D-T plasma in ITER. For standard ITER scenarios, LHW are predicted to penetrate to $r/a \approx 0.6$. Hence, during the high β phases of the discharge LHW will be used for current drive and current profile control in the outer regions of the plasma. This restricted penetration, together with the requirement of a monotonic q-profile, limits the total current which can be driven by LHW.

Lower hybrid waves are also the method chosen for ohmic current ramp-up assist in ITER, which will have a range of plasma parameters close to those of present experiments.

5.3.1 Physics Issues Relevant for High-β Operation.

The penetration of LH wave into hot, dense plasmas is restricted by (i) strong wave damping and (ii) toroidal propagation effects. These are discussed below.

5.3.1.1 Penetration limit due to wave damping.

Strong Landau damping causes total single pass absorption of the LH wave in moderate temperature and density plasmas. An estimate of the maximum reachable temperature $T_{e,max}$, in good agreement with more refined modeling, is obtained by using simple quasi-linear formulae [5.12,13]. This yields in the range of parameters for interest to ITER [5.14] that

$$N_{\|,max}^2 T_{e,max} \approx \text{60-to-90 keV}, \qquad (1)$$

where $N_{\|,max}$ is the highest wave parallel refractive index in the local LHW spectrum. In order to maximize this temperature, one has to choose the smallest possible parallel refractive index, which is given by the "accessibility limit," defined by

$$N_{\|,acc} = \omega_{pe}/\omega_{ce} + [1 + \omega_{pe}^2/\omega_{ce}^2 - \Sigma_i \omega_{pi}^2/\omega^2]^{1/2},$$

where ω_{pe}, ω_{ce}, ω_{pi}, and ω are the electron plasma and cyclotron frequencies, the ion

plasma frequencies for the different ions in the plasma, and the wave frequency, respectively. In the range of parameters considered for ITER, this index is practically a function of the ratio n_e/B^2 alone. Consequently, when $N_{||,max}$ is chosen close to the accessibility limit, $N_{||,max} = N_{||,acc} + \Delta N_{||}$, the above equation gives a β limit rather than a temperature limit, as illustrated in Fig. 5-1. $\Delta N_{||}$ is the width of the launched spectrum, as determined by the launcher characteristics.

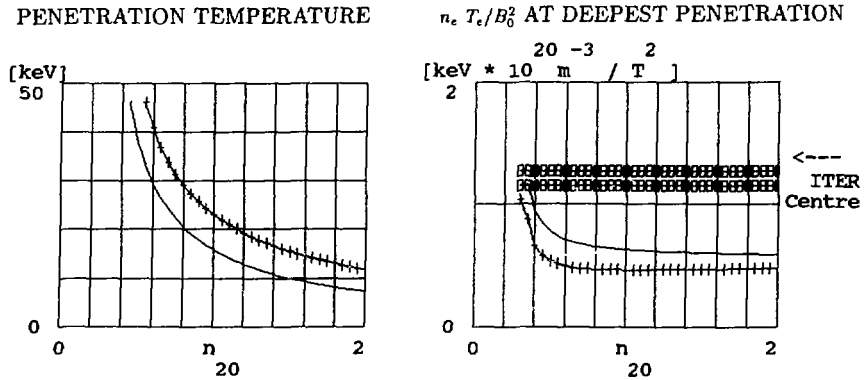

FIG. 5-1 Damping limit of penetration of the LH waves [5.14]. P = 50 MW, $\Delta N_{||}/\langle N_{||}\rangle = 0.1$; B = 5 T (solid) and B = 7 T (crossed) lines

This estimate shows further that the β limit decreases rapidly with increasing spectral width. The spectral width of the launched spectrum is inversely proportional to the number N_{wg} of waveguides stacked in the toroidal direction in a grill (about 100 in ITER), leading to $\Delta N_{||}/N_{||} \leq 0.1$. A narrower spectrum, apart from being technically demanding, would be illusory since a number of mechanisms can broaden the spectrum during wave propagation (see §5.3.1.3). Increasing the launched power level also improves the penetration.

For an injected power of 50 MW, and a spectral width of 0.1, Fig. 5-1 shows that (except for very low density, $n_e(0) \leq 0.4 \times 10^{20}$ m^{-3}, where high temperature operation is precluded because it violates power exhaust system requirements) the local β where the LH wave power is deposited is about half of the values expected at the plasma center for the ITER reference scenarios [the product $n_e(0)T_e(0)$ is close to 30×10^{20} m^{-3} keV for the scenarios A1, B1 and B6, c.f. §9.0]. This means that, for the standard ITER profiles, the LH wave during flat-top will be totally absorbed before reaching $r/a \approx 0.6$. Note that wave absorption will not limit penetration to the plasma core during the current ramp-up phase because β need not be high during current ramp-up.

5.3.1.2 Penetration limit due to propagation effects in toroidal geometry

Ray-tracing analyses made for ITER [5.15,16,17,18] show that propagation effects impose a limit to the wave penetration comparable to that due to absorption. The penetration improves with increasing aspect ratio, $N_{||}$, and ω/ω_{pe}, and depends on the poloidal position of the launchers. Off-midplane launch leads to either very

poor ray penetration (associated with dominantly $N_{||}$ downshift), or to rather good ray penetration (with upshift). The launcher position (top or bottom) for good penetration is given by rotating the direction of the toroidal field by 90° in the positive direction (for co-acting current drive). The actual penetration is determined by the point where the up- or down-shifted spectrum meets the limit of Eq. (1). This favors the rays launched from the position with dominant upshift because it avoids accessibility problems, insures single-pass absorption and a better control of the deposition zone. This corresponds to the bottom half-port for the particular choice of current and toroidal field directions in ITER.

A LHW launcher designed for coupling the total power through a single port would fill it completely in the poloidal direction, causing a large spread of trajectories. Coupling the power by using two half-ports is thus preferred. Further reasons are the requirements of the ramp-up phase and maintenance and safety considerations. Toroidal propagation effects do not impede central wave penetration in low density plasmas representative of the ramp-up phase or low β operation in ITER [5.15,16].

5.3.1.3 Spectral broadening issue

The spectral width influences the LHW penetration. To explain the magnitude of the absorbed power and of the driven currents observed in many experiments, it is necessary [5.19,20] to invoke an "upshift" of the wave power spectrum $P(N_{||})$, i.e. to assume the presence of some wave power at considerably lower phase velocity than expected from the launched spectrum (by typically a factor of 2 to 3).

A number of possible explanations for the occurrence of the upshift have been proposed, including edge bouncing of the rays [5.21], strong edge density fluctuations [5.22], nonlinear effects in caustics [5.23], effect of Parail-Pogutse instability [5.24], ponderomotive effects [5.25], diffraction effects [5.26], ray stochasticity [5.27], wave scattering on toroidal inhomogeneities like the magnetic ripple [5.28], parametric decay, and electron-electron scattering[5.29].

Some of the mechanisms invoked would not affect the propagation in the high β phases of ITER (e.g., "edge-bouncing," since full absorption occurs in a single pass). Others would be deleterious to LHW penetration (e.g., scattering off of toroidal field ripple [5.30] or density fluctuations, and diffraction broadening).

The experimental database does not allow us to identify a specific mechanism causing the observed spectral shift. It is necessary to understand the cause of the spectral shift or broadening in order to predict the penetration of the LHW in ITER. An experimental effort is recommended in this area [5.31].

5.3.1.4 Consequences of restricted penetration: restricted total power and current

Restricted penetration limits the total current which can be usefully driven by LHW since the q-profile will become non-monotonic if the local current density is too high. A monotonic q-profile is required for MHD stability [5.32, and §2.2].

When used in conjunction with neutral beams for central current drive, this limits the LHW current [5.17] to about 2.5–3 MA and the injected LHW power to 30–40 MW in the standard discharges with the safety factor at center $q(0) \approx 1$. A typical example is shown in Fig. 5-2.

However, if q(0) in the range 1.7–2 can be tolerated, MHD equilibria with a large fraction of bootstrap current (e.g. 70%) can be obtained [5.33] using a narrow

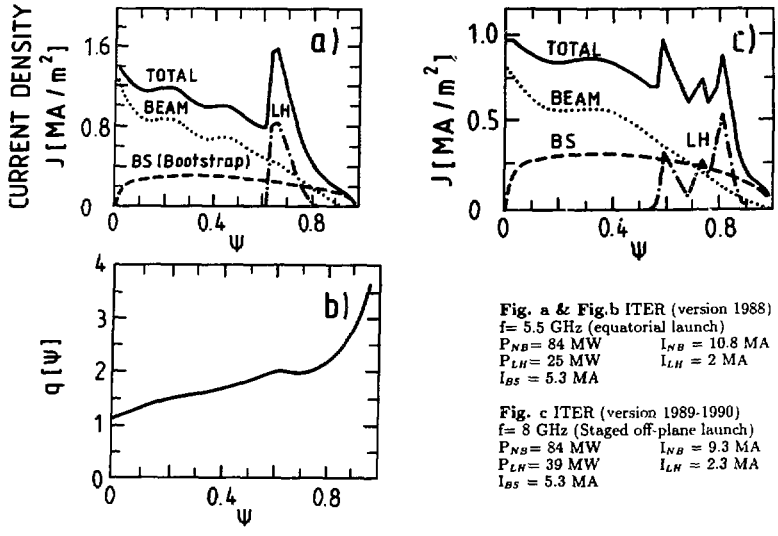

Fig. a & Fig.b ITER (version 1988)
f= 5.5 GHz (equatorial launch)
P_{NB}= 84 MW I_{NB} = 10.8 MA
P_{LH}= 25 MW I_{LH} = 2 MA
I_{BS} = 5.3 MA

Fig. c ITER (version 1989-1990)
f= 8 GHz (Staged off-plane launch)
P_{NB}= 84 MW I_{NB} = 9.3 MA
P_{LH}= 39 MW I_{LH} = 2.3 MA
I_{BS} = 5.3 MA

FIG. 5-2 Combined use of neutral beam injection and LH waves in ITER [5.17]: (a) and (c) LH waves, NB, bootstrap, and total current density profiles. (b) safety factor profile.

central seed current (driven by neutral beams or by fast waves injection). In these cases, the LHW power deposited in the outer zones controls the total current, acceptable equilibria are found for ratios of LHW to central (fast-wave) current drive powers in the range (60 MW)/(8 MW) to (85 MW)/(55 MW) as illustrated Fig. 5-6. Two critical points have to elucidated before adopting this type of operation: (1) is operation at $q(0) \geq 1$ acceptable?, and (2) can high bootstrap currents persist in stationary states?

5.3.1.5 Current diffusion

Spatially resolved measurements of the fast electron tails created by the LHW in present-day experiments (e.g. using X-ray bolometry), often show the presence of fast electron tails in interior regions that modelling predict to be inaccessible to LHW. The commonly accepted explanation for this is that the slowing-down time $\tau_s(s)$ of the fast electrons is comparable to their radial confinement time τ_f (which is expected to be ~ τ_E). The resulting delocalization of the RF current is predicted to occur [5.34] even when τ_s is somewhat less than τ_E (as is the case in JT-60). These estimates are, however, very uncertain due to the uncertainties of τ_f. No enhanced penetration of the current is expected during high β operation in ITER due to the strong inequality $\tau_s \ll \tau_E$. More experimental and modelling data are required to establish the validity of this or an alternative explanation (e.g., anomalously deep power deposition)[5.31].

5.3.2 Selection of Frequency, Interaction with α-Particles

The frequency of the LH system for ITER has been selected to be 5 GHz; a number of physical and technical criteria were considered in making this choice.

5.3.2.1 Lowest frequency for avoiding interaction with α-particles

A major physical constraint is the necessity to avoid absorption by energetic ions, in particular by α-particles, which would decrease the current drive efficiency, reduce the penetration, and might increase fast α losses. This imposes a lower bound on the frequency for ITER operating conditions.The physics underlying the onset of interaction of the LHW with thermal and fast ions is well understood [5.35]. The interaction of LHW with injected neutral beams has been investigated in a number of tokamaks. Recent experiments in JT-60 [5.36,37] confirm the dependency of the onset of fast-ion-damping on wave and plasma parameters.

LH waves can only interact with α-particles when the perpendicular phase velocity of the wave, $v_{\phi\perp} = c/N_\perp$ is smaller than the birth velocity $v_\alpha=(2E_\alpha/M_\alpha)^{0.5}$ of the α-particles (i.e., for $N_\perp > 23.1$). $N_\perp$ is given by the dispersion relation as a function of $N_\parallel$ and the plasma parameters; it increases roughly like $N_\parallel n_e^{1/2}/\omega$. For a given maximum operating density and maximum $N_\parallel$ a minimum frequency is required to avoid this interaction (in evaluating $N_\perp$, the electrostatic approximation to the dispersion relation is not sufficient, due to the proximity of the launched spectrum to the fast wave conversion layer). A frequency of 5 GHz is sufficient to avoid any interaction with α-particles for a wave spectrum extending up to $\Delta N_\parallel = 0.2$ above the (central) accessibility limit and for densities up to 1×10^{20} m^{-3} (which is more than the density at the deepest penetration radius even when $\Delta N_\parallel = 0.1$).

This result is confirmed by several calculations performed for ITER [5.38] in which the amount of LHW power absorbed by α-particles was evaluated when the strict condition $v_{\phi\perp} < v_\alpha$ was not obeyed in the plasma. Note that when the strict condition is obeyed, interaction with beam deuterons or tritons injected at 1.3 MeV is also avoided.

5.3.2.2 Coupling density

Coupling of a grill launcher to the plasma is well described by the theory [5.39]. To minimize the reflection coefficient, a plasma density at the surface of the launchers corresponding to $\omega_{pe} \approx N_\parallel\omega$ is required. The optimal density in the front of the grills for tolerable LH power reflection is of the order of 2×10^{18} m^{-3} at 5 GHz. The multijunction launcher [5.40]—used in most large present LHW systems and in the ITER design—is a self-matching system. Good matching is expected to extend from 5×10^{17} m^{-3} to 4.5×10^{18} m^{-3} at 5 GHz [5.41] (vs ~1.3×10^{18} m^{-3} to 8×10^{18} m^{-3} at 8 GHz [5.42]).

The expected wall density falls into the required range for 5 GHz, so that the LHW launcher can be positioned flush to the first wall in this case. However, large uncertainties exist in these evaluations, and provision for radial motion of the grill is included in the launcher design. The power loading on the side limiters of the launchers--including the α-particle loading--appears to be barely within the present technical capability if the launcher has to protrude into the scrape-off layer to obtain acceptable power reflection. Preferred solutions are to use the plasma position control system to move the plasma edge closer to the launcher, or to use a separate broad "alpha particle scraper" (also envisaged to protect the port sides) that should protrude with the antenna.

5.3.2.3 Selection of the frequency for the ITER LHW system: summary

A frequency of 5 GHz is sufficiently high to avoid interaction of the LHW with α-particles and beam ions in all ITER operation scenarios. The possible occurrence of parametric decay instabilities at the plasma edge, which might prevent the wave penetration has also been theoretically investigated [5.43] and found unlikely at both 5 GHz and 8 GHz. A slight improvement of the LHW penetration in the upper frequency range (8 GHz) has been predicted [5.17]. However, two main penalties would have to be paid if the higher frequency were selected: the plasma density required at the launcher mouth for good grill matching would increase, and RF transmission losses increase with frequency. In both frequency ranges the development of dedicated RF power tubes would be required. While not considered problematic at either frequency, klystrons (usable in the lower range up to about 6 GHz) benefit from large experience, while for higher frequency gyrotrons, phase control is a new requirement that would require development. The selected frequency of 5 GHz is convenient for all functions of the LHW system on ITER.

5.3.3 Current Drive Efficiency

The local current drive efficiency (in absence of an electric field) is well represented by the theoretical formula [5.44]

$$\gamma \equiv n_e R I_{driven}/P_{abs} = \gamma_0 F(x, Z_{eff})\, G(\varepsilon, x)\,,$$

where γ_0 is the "Fisch-Boozer" efficiency

$$\gamma_0 = [(2m_e\varepsilon_o{}^2c^2/(e^3\, ln\, \Lambda)](1/\langle N_{||}\rangle^2)[4/(5 + Z_{eff})]\,,$$
$$1/\langle N_{||}\rangle^2 = [1/N_{||min}{}^2 - 1/N_{||max}{}^2]/ln\,(N_{||max}{}^2/N_{||min}{}^2)\,,$$

which is an average over the wave spectrum extending from $N_{||min}$ to $N_{||max}$. $N_{||min}$ is taken as the refractive index at the accessibility limit, $N_{||acc}$ (using volume-averaged density and magnetic field on axis). This expression has been used in most evaluations of the experimental data up to now. $F(x, Z_{eff})$ is a temperature correction term [with $x = v_{phase}/v_{eth} = v_\phi/v_{eth} = c/(\langle N_{||}\rangle v_{eth})$, $v_{eth} = (T_e/m_e)^{0.5}$]

$$F(x, Z_{eff}) = 1 + (1/x)^2\,[(5 + Z_{eff})/4 + 3(5 + Z_{eff})/2(3 + Z_{eff})] + (1/x)^3[3(2\pi)^{0.5}(5 + Z_{eff})/8Z_{eff}]$$

and $G(\varepsilon, x)$ is a correction accounting for trapped electrons (ε being the local inverse aspect ratio r/R), which reads for slow LHW [5.45]

$$G(\varepsilon,x) = 1 - [\varepsilon^{0.77}(12.25 + x^2)^{0.5}]/(3.5\varepsilon^{0.77} + x)$$

(These expressions are valid only for narrow wave spectra). For ITER technology phase conditions ($N_{||acc} = 1.85$), with $N_{||} \approx 2$, $Z_{eff} \approx 2$; $\gamma_0 \approx 0.3 \times 10^{20}$ A/m^{2}W. For temperatures near the deepest penetration point, $N_{||}{}^2T_e \sim 60$–90 keV, F ($N_{||}{}^2T_e \sim 60$–90, $Z_{eff} \sim 2$) ~ 1.55–1.85 and G ($\varepsilon \sim 0.25$, $N_{||}{}^2T_e \sim 60$–90) ~ 0.7. Thus the calculated efficiencies are of order $\gamma = 0.32$–0.38×10^{20} A/m^{2}W These values are also consistent with the value obtained in JT-60 of 0.34×10^{20} A/m^{2}W.

5.3.4 Current Ramp-up Assist with LHW

There is an extensive experimental database for LHW for this application [5.6]. Recent results [5.36] give further support to the selection of LHW as the method of choice to assist the ohmic current ramp-up since ITER ramp-up assist would be performed in a range of plasma parameters close to those of present experiments (the main difference being the time scales involved--a longer ramp-up duration and skin time in ITER).

The physical constraints to be considered in a LHW assisted current ramp-up scenario include:

(i) achievement of a transformer flux saving significant as compared to the flux consumption during the reference inductive burn phase in order to provide an extension of the inductive burn duration (note that a saving of the order of 30 V-s would extend the burn duration by 190 s and 460 s in the reference technology phase scenarios B1 and B6, respectively);

(ii) avoidance of non-monotonic q profiles;

(iii) evolution of the discharge in a stable region of the q–l_i diagram to ensure the stability of the discharge,

(iv) achievement of a ramp-up duration compatible with the operation scenarios requirements.

Technical constraints must also be considered, the main ones are:

(i) Power exhaust considerations: to minimize the additional power requirements the current ramp-up shall be performed at sufficiently low density. However, the total power acceptable in the divertor decreases rapidly with density decrease. During the early phases of the ramp-up, the plasma must be close to the launchers and thus will lean on an outboard limiter. The power handling capacity of such a device will impose a severe restriction on the total power conducted to the limiter [5.46, and §3.0]. The low density power handling limits of both divertor and limiter operation have still to be assessed.

(ii) Stress in the poloidal field system also limits the maximum flux swing saving obtained by noninductive means. Present estimates [5.47] show that a flux saving of up to 50 V-s is tolerable from this point of view.

(iii) Finally, the technical requirements imposed by the LHW assisted current ramp-up system, especially the required wave spectrum flexibility and the geometry of the launchers, shall be made compatible with the design of the LHW system developed for burn phase current drive.

When the current is ramped up at a rate comparable to the ohmic ramp-up (about 0.35 MA/s), modelling studies [5.48,49,50,51] have shown consistently that 20–40 V-s can be saved by ramping the injected LHW power up to 20–35 MW when operating at a low density ($\langle n_e \rangle \approx 2 \times 10^{19}$ m^{-3}), or about 20 V-s using up to 45 MW of current drive power when operating at $\langle n_e \rangle \approx 4 \times 10^{19}$ m^{-3}. The physical constraints mentioned above can be satisfied, partly due to the fact that account is taken of the evolving plasma geometry.

"Slow" ramp-up scenarios have also been studied (ramp-up times of several hundred seconds, at zero surface voltage [5.51]), aiming at large flux savings to minimize the number of shots for a given fluence. According to this work, it appears possible to decrease the number of shots in the technology phase by up to a factor 6,

with savings of 100 to 130 V-s (which might be beyond the limit imposed by the poloidal field system), using up to 40 MW power. However, these long ramp-up times may not be consistent with the short dwell time and high availability desired in the ITER technology phase.

In conclusion, LHW assisted current ramp-up is attractive and the physical constraints can be respected. The main point of concern is the ability of the power exhaust system to withstand the additional power in the low density range.

5.4 NEUTRAL BEAM PHYSICS

5.4.1 Introduction

Neutral beams with an energy of 1.3 MeV have been chosen as the primary system for noninductive current drive in the core of plasma and heating plasma to ignition. Critical issues in evaluating the performance of NBs for ITER include current drive efficiency, flexibility of tailoring a driven current profile, beam penetration, beam stopping cross section, the possibility of an Alfvén wave instability which might decrease the current drive efficiency substantially, plasma rotation induced by beam injection, and beam shinethrough. Those issues have significant impact on physics requirements for the NB system, such as beam energy, beam power and beam power profile.

5.4.2 Status of Database

5.4.2.1 Neutral beam current drive

During the definition phase of the ITER conceptual design period in the summer of 1988, the database for NB current drive experiments was assessed [5.52]. Since then, there has been no substantial progress in beam driven experiments, although neutral beams have been used routinely as a reliable heating method in tokamak experiments. A brief summary of the status of the database for neutral beam current drive experiments from this definition phase report is repeated here.

Experiments on noninductive current drive by NB have been done in TFTR, DIII-D and JET. In all experiments, only the change of the loop voltage was measured. The driven current was inferred using sophisticated modelling codes that include the effects of both resistive current penetration and a bootstrap current.

In TFTR a significant change in loop voltage was observed, even with balanced injection. The quantitative analysis shows that the results can be understood with a model which includes both beam driven currents and neoclassical bootstrap currents. The plasma does not reach resistive equilibrium during the 0.7 s NB injection pulse.

In JET, 14 MW of NB has been injected into both H-mode and L-mode plasmas with currents up to 4 MA. The measured loop voltage can be best explained if both bootstrap currents and beam driven currents are taken into account.

Recent DIII-D [5.53] NB current drive experiment concentrated on discharges at high β_p, in which fully noninductive discharges have been studied with NB driven current and bootstrap current. Double-null divertor discharges ($\kappa \approx 1.9$, I = 500 kA, H-mode) have been established with $\beta_p = 5.1$ and $\varepsilon\beta_p = 1.8$, using up to 14 MW of NB injection. During the ELM-free phase, excellent H-mode confinement is obtained

($\tau_E \sim 2.3 \times \tau_{ITER89\text{-}P}$). When $\beta_p > 1$, fishbone-like bursts of MHD activity occur and plasma internal inductance starts to decrease. During the ELM-free phase the loop voltage is negative but there is insufficient time to reach a stationary state. After the onset of ELMs a stationary state is reached with a slightly positive voltage. For a typical 500 kA discharge, there is a 55% beam driven, a 35% bootstrap, and a 10% ohmic fraction.

Analyses of the experimental results on NB noninductive current drive show that experimental results are consistent with neoclassical theory, i.e., the experimental results fit best with calculations which include the beam driven current, bootstrap current and plasma rotation. It should be noted that the beam driven currents are estimated only by fitting to the measured loop voltage and the direct measurement of driven current profiles and/or experiments that drive the current for a time long compared to the resistive skin time are necessary to improve confidence in NB current drive performance. To confirm the present scaling of the NB current drive efficiency, it is recommended that current drive efficiency should be studied in a wide range of plasma temperatures. Furthermore, the beam injection pulse length is rather short and discharges are still developing, not stationary, therefore experiments with a longer pulse length are needed [5.31].

5.4.2.2. Alfvén wave instability and beam slowing down

The deceleration of neutral beam ions through Coulomb collisions is a fundamental process in plasma physics and is assumed classical. Conceivably, however, the excitation of beam driven instabilities such as Alfvén wave instabilities could lead to enhanced deceleration rates with resultant reduction of current drive efficiency and a different partition of the beam energy between electrons and ions.

In ITER with a beam energy $E_b = 1.3$ MeV Alfvén wave instabilities are predicted to occur simply because of the beam energy exceeding the Alfvén velocity. In the definition phase report [5.52], the T-11 experimental results are analyzed. Different conclusions are drawn from the two separate analyses: one suggests no possibility of instabilities, and the other suggests their influences on observed spectra of high energy neutrals. Since then new experimental results relating to this subject have been reported and a lot of theoretical effort has been made as well.

Experiments

In DIII-D[5.54,55], short pulses (2 ms) of deuterium neutral beams were injected into deuterium plasmas. After ionization, the beam ions produce 2.5 MeV neutrons in beam-plasma fusion reactions. Because the fusion cross section falls rapidly with decreasing energy, the neutron emission is simply related to the beam-ion slowing-down time τ_s. In the first experiment , the neutron decay time τ_n was found to agree with classical theory (to within 30%) for an order of magnitude variation in τ_n. The study was restricted to the regime $E_b > E_{crit}$, where E_{crit} is the critical energy at which ion drag equals electron drag.

The second experiment extended the previous study into the regime where beam ions slow down primarily upon thermal ions ($E_b < E_{crit}$). The regime, $E_b < E_{crit}$, was assessed by reducing the beam energy and by employing electron heating to raise the electron temperature, which raised E_{crit}. The classical prediction was calculated numerically using fits to the experimentally measured profiles with a code developed

for this purpose. The ratio of the experimentally measured decay time to calculated decay time, plotted versus E_b/E_{crit}, indicated no systematic variation as the beam ions switch from slowing primarily upon electrons to slowing primarily upon ions. Systematic dependencies upon E_b, T_e and n_e were also absent.

In conclusion, beam ions in the regime $v_e \gg v_b \gg v_i$ and $n_b/n_e < 0.1\%$ were seen to decelerate classically in the DIII-D tokamak experiments. The ~25% agreement between theory and experiment for the range $0.5 < E_b/E_{crit} < 2.4$ suggests that the distribution of beam power between ions and electrons was classical, and no indications of enhanced scattering associated with the excitation of beam driven instabilities such as Alfvén instabilities were observed. The experimental results are still limited and further experimental observations are necessary on this subject [5.31].

Theoretical work

A lot of theoretical effort has been made to investigate Alfvén wave instabilities in ITER and present experiments [5.56,57,58]. These include local mode analyses, which point to the possibility of instability at long wavelength, and a global mode analysis.

In the framework of the local mode analyses [5.56], the excitation of Alfvén waves by neutral beam injection was examined for ITER and T-11 experiments. Attention was focused on the low frequency ($\omega \ll \omega_{ci}$) shear and compressional modes, and the higher frequency ($\omega \leq \omega_{ci}$) anomalous Doppler mode. Although there can be waves which absorb substantial power from the beam ions resulting in wave growth, in most cases the power transferred from the waves to electrons (Landau damping) is larger, resulting in a stable system. The primary conclusion is that for ITER at a power level of 100 MW, the shear and compressional modes are stable, and the anomalous doppler mode has a band of only weak instability in the range $1.4 < E_b(\text{MeV}) < 2.5$. The beam parameters for ITER, 75 MW at 1.3 MeV, are such that the Doppler mode would be stable. The analysis however points out that the largest ratios of growth to damping occur for small $k_\perp$, where the local analysis begins to break down. The same model was applied to the T-11 tokamak, which indicates that it was stable to all three modes.

Global Alfvén Eigenmode (GAE) stability theory is applied, including an anisotropic distribution function produced by NB injection, as well as arbitrary background density and temperature profiles [5.57]. The electron damping term is always stabilizing. Only the toroidal (n) and poloidal (m) pairs (0, -2), (0, -1), and (1, -1), are considered because the growth rates for other mode numbers are much smaller. For ITER at the baseline parameters, the (1, -1) mode appears to be the most problematic and sensitive to the introduction of anomalous loss of beam particles. However, by relatively small adjustments in background density profile, safety factor profile, beam energy, or by including effects related to quasilinear diffusion, this mode can be made stable. The changes required are well within ranges which will maintain good ITER MHD stability and current drive performance.

5.4.2.3. Neutral beam stopping cross section

The profile of NB heating and current drive depends upon the accuracy of calculations of deposition profiles of beam heat and momentum in the plasma. These calculations in turn depend on the accuracy of relevant atomic cross sections which

determine the location of beam deposition. A correct determination of these cross sections is therefore essential for analyzing and optimizing the performance of NB heating and current drive systems for ITER. The definition phase report [5.52] concludes that the effective ionization cross section is enhanced by a factor 1.4-1.6 for $E_b \sim 1$ MeV, $Z_{eff} \sim 2$, $n_e \sim 10^{20}$ m^{-3}. Since then our understanding of and ability to model these processes have improved [5.59].

The atomic processes involved in stopping neutral beam atoms have been considered, including both the ground state and the excited states of beam atoms, thus allowing for the multistep ionization of beams in collisions with plasma constituents and impurities. The effective beam stopping cross section has been calculated for a wide variety of beams and plasma parameters. The stopping cross section data are also given in terms of a convenient analytic fit, which can be used either in computers or for simpler analytic estimates of neutral beam penetration. The beam attenuation can be characterized by the effective cross section, which can be conveniently defined as $\sigma_s = 1/(n_e\lambda)$, where λ is a mean free path. The primary atomic collision processes contributing to the cross section are charge exchange and ionization of the ground state beam by plasma ions. For plasma density $n_e \leq 10^{19}$ m^{-3} and beam energy $\leq$30–40 keV/u the above approach is adequate. With increasing n_e and beam velocity, the radiative decay time for excited atoms becomes comparable to the collisional time, and the beam and plasma particles are in a collisional radiative equilibrium. Multistep processes, such as excitation with subsequent ionization, start to play an important role in the beam attenuation and may considerably enhance the effective stopping cross section.

The effect of multistep processes on the stopping cross section can be represented in terms of the fractional beam stopping increment $\delta = [\sigma_s - \sigma_s^{(0)}]/\sigma_s^{(0)}$, where the superscript (0) indicates that the corresponding quantity is calculated by using only ground state beam atoms, excluding excitation and subsequent electron loss. The effective beam stopping cross section depends on the beam energy, the plasma density and the plasma effective ionic charge, and very weakly on the plasma electron temperature.

It is concluded that in the case of $n_e \approx 10^{20}$ m^{-3} and $E_b > 0.5$ MeV/u, δ amounts to almost 0.4. The new, lower value for δ may relax, to a certain extent, the requirement on the beam energy in ITER.

5.4.2.4. Plasma rotation

Plasma rotation, induced by NB injection, has been observed in many devices. Plasma rotation tends to reduce the relative speed of NB with respect to the plasma and therefore the current drive efficiency deteriorates. In the definition phase of the ITER conceptual design, the experimental data were assessed [5.52] and since then no new analysis has been made. The conclusions from these assessments are briefly summarized here.

Central rotation speeds have been studied by using data from ISX-B, PLT, PDX, DIII, JT-60, and TFTR for a wide range of plasma conditions. The conclusion is that, for estimating the central rotation speed in ITER, it is appropriate to assume the momentum confinement time τ_ϕ equal to the energy confinement time τ_E. The projected central rotation speed for ITER is then $v_\phi = 3.1 \times 10^5$ m/s, i.e. only 29% of the thermal velocity and only 3% of the beam velocity. Such a rotation speed will not

affect beam attenuation, the beam deposition profiles, or the current drive efficiency to any significant degree. However, it may have a small (~10%) effect on the MHD equilibrium. In conclusion the present experimental data show that the momentum confinement time does not exceed the energy confinement time. On this basis the effects of plasma rotation in ITER should be small. However, further attention should be paid to this subject [5.31].

5.4.3. Design Issues

5.4.3.1. Current drive efficiency

The Mikkelsen-Singer (MS) model for NB current drive [5.60] was recommended for estimating the ITER neutral beam current drive efficiency in the ITER Physics Design Guidelines. The MS model has been reviewed by comparing it with results from two dimensional calculations [5.61] and new calibration coefficients are proposed taking into account some dependence on profiles of densities and temperatures, and beam energy.

The current drive figure-of-merit, $\gamma_{NB}(10^{20}\ A/m^2W) = n_{e20}IR/P_{beam}$, is given as,

$$\gamma_{NB} = (5A_{bd}T_{10})(1 - f_s)(R_{tang}/R)[J(x, y)/0.2]F_b(Z_b, Z_{eff}, \bar{\varepsilon})$$

where $x = (E_b/B_{bd}E_{crit})^{0.5}$, $y = 4Z_{eff}/5A_b$, $\bar{\varepsilon} = a/2R$, f_s = shine-through fraction,

$J(x, y) = x^2/[4 + 3y + x^2(x + 1.39 + 0.6y^{0.7})]$,

$F_b(Z_b, Z_{eff}, \bar{\varepsilon}) = 1/Z_b - [1 - G(Z_{eff}, \bar{\varepsilon})]/Z_{eff}$

$G(Z_{eff}, \bar{\varepsilon}) = (1.55 + 0.85/Z_{eff})\sqrt{\bar{\varepsilon}} - (0.20 + 1.55/Z_{eff})\bar{\varepsilon}$,

and other notations follow Mikkelson and Singer. The calibration coefficients, A_{bd} and B_{bd}, have been determined by comparing γ_{NB} with the drive efficiency γ_{NB} obtained from the 2D calculations for ITER-like parameters. The density and temperature profiles are assumed as $n(\psi) = n_o(1 - \psi)^{\alpha_n}$ and $T(\psi) = T_o(1 - \psi)^{\alpha_T}$ with $T_e = T_i$. The normalized flux variable, ψ, varies from 0 to 1. The parameter ranges covered are $0.6 \le n_o(10^{20}\ m^{-3}) \le 1.6$, $20 \le T_o(keV) \le 35$, $0.2 \le \alpha_n \le 1.1$, $0.5 \le \alpha_T \le 1.5$. Other parameters varied were: $0.7 \le E_b(MeV) \le 1.5$, $1.5 \le Z_{eff} \le 2.2$, $5 \le He(\%) \le 10$, $5.2 \le R_{tang}(m) \le 6.2$. Some dependences have been observed in A_{bd} on profiles and beam energy. The proposed calibration coefficients are (E_b in MeV)

$$A_{bd} \approx 0.11(1 - 0.35\alpha_n + 0.14\alpha_n^2)(1 - 0.21\alpha_T)(1 - 0.2E_b + 0.09E_b^2),$$
$$B_{bd} = 1.0,$$

As the above current drive efficiency with newly proposed coefficients is applied for the ITER technology phase plasma, the so-called current drive figure of merit γ_{NB} is around $0.5 \times 10^{20}\ A/m^2W$.

5.4.3.2. Beam energy, beam aiming, and beam penetration

In choosing the beam energy and beam aiming for ITER, consideration of both physics and engineering issues is necessary. The following constraints should be taken into account for the selection for the beam energy and aiming: (1) the require-

ment of $Q > 5$ for a steady state operation, (2) the need for flexibility in tailoring current profiles to cover a wide range of operation space, (3) the shinethrough power should be within the allowable level of a first wall, and (4) the selection of the beam energy should be consistent with a realistic development plan for the NB system.

In the definition phase of the conceptual design the range of beam energy was selected as $0.7 \leq E_b(\text{MeV}) \leq 2.0$, based on preliminary studies on the above issues [5.52]. During the conceptual design phase, the beam energy has been chosen to be $E_b = 1.3$ MeV, considering improved investigations of physics and engineering critical issues [5.61,62].

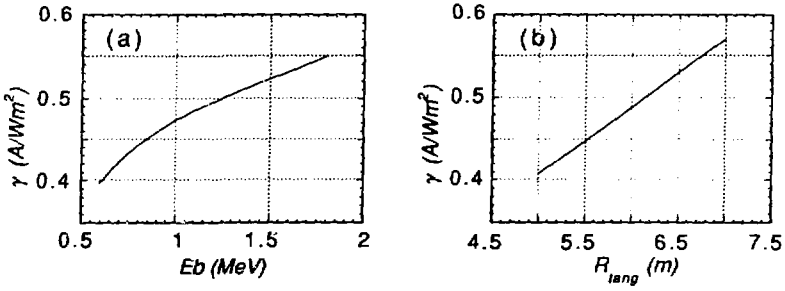

FIG. 5-3 Figure of merit for NB current drive efficiency, γ, is plotted for ITER technology phase plasmas and NB configuration, based on MS formula [5.61].

The figure of merit for NB current drive efficiency γ_{NB} is plotted in Fig.5-3, based on the MS formula with the new coefficient derived in the previous subsection. γ_{NB} increases with beam energy. For $E_b = 1.3$ MeV, γ_{NB} reaches almost 0.5, which might meet the above requirements, although it depends on parameters in evaluations. The figure of merit also increases with the tangency radius, R_{tang}, at which the beams aim, so a large value of R_{tang} is favorable from the viewpoint of current drive efficiency. However, when R_{tang} increases in the range of $R_{tang} < R_{mag}$ (R_{mag} is the plasma magnetic axis), the beam path to the plasma axis becomes long and the deposition of beams in the plasma central region becomes difficult, although it depends on beam energy and plasma parameters, especially plasma density, as discussed later. Further increase of R_{tang} results in a hollow driven current profile, and the space available for beams between toroidal coils is narrower. Based on those considerations the beam aiming point is selected as $R_{tang} \sim R_{mag}$.

Sufficient beam penetration into the plasma center is essential for developing various profiles of beam driven current. The beam penetration is dependent upon many parameters, such as a beam energy, beam aiming, plasma parameters, especially plasma density, and beam stopping cross section. For steady state operation in the ITER technology phase, where a plasma with a low density of $\langle n_e \rangle \sim 0.7 \times 10^{20}$ m^{-3} and high temperatures of $\langle T \rangle \sim 20$ keV is selected to increase the current drive efficiency, the above beam energy of 1.3 MeV is sufficient for providing enough flexibility for various operation modes. For steady-state operation with these plasma parameters, however, concern must be expressed about sound divertor operation, from both the viewpoint of physics and engineering (unless a

considerable part of power from a plasma can be radiated uniformly before reaching the divertor plate). Another possible operation mode, the hybrid operating mode, has been proposed for the ITER technology phase to cope with this divertor problem [5.63, and §3.0]. While it is not true steady-state operation, it does allow a few thousand seconds of operation per plasma pulse. The hybrid operating mode, where a plasma current will be supplied with a combination of an inductive and a noninductive drive in a relatively high density plasma, provides high probability of a low temperature divertor plasma, and sound divertor operation. However, at these higher densities beam penetration becomes important.

Spatial beam deposition profiles were investigated with various densities and beam energies while keeping a square root of parabolic density profile (the reference profile for ITER) to study accessible plasma density for the 1.3 MeV beams. The results show that a density of $n_{eo} = 1.5 \times 10^{20}$ m^{-3} ($\langle n_e \rangle \sim 1.0 \times 10^{20}$ m^{-3}) is marginal for good penetration of beams. For the hybrid operation mode an inductive current mainly runs in the central region of the plasma, therefore it is not necessary for the beam to penetrate fully into the plasma center, and a somewhat hollow profile of the beam-driven current should be used for the hybrid operation mode, filling the middle region of the plasma radius with current. The LH and bootstrap currents are mainly located at outer part of the plasma. The 1.3 MeV beam could be used for density $\langle n_e \rangle \geq 1.0 \times 10^{20}$ m^{-3} for a hybrid operating scenario. However considering the fine arrangement of the current profile this density region could be marginal for the 1.3 MeV beam.

To improve beam penetration the beam line can be rearranged to aim toward smaller R_{tang}, e.g., $R_{tang} < R_{mag}$, instead of the present arrangement of $R_{tang} \sim R_{mag}$. This shortens the length covered by a beam from plasma surface to plasma center. The disadvantage with this rearrangement is a reduced current drive efficiency, approximately proportional to R_{tang}. The reduction of the plasma minor radius is also effective in improving the beam penetration to the plasma center.

Instead of a deuterium beam, a hydrogen beam was also studied, because the higher velocity of hydrogen (relative to deuterium) at the same beam energy improves penetration to the plasma center [5.64]. The penetration of a hydrogen beam, its current drive efficiency, and fuel dilution due to hydrogen beam injection were compared with deuterium beam operation. Regarding the penetration, a hydrogen beam at 1.3 MeV can easily penetrate into the center of a plasma with $\langle n_e \rangle \approx 1.0 \times 10^{20}$ m^{-3}. The current drive efficiencies for hydrogen and deuterium beams coincide at the beam energy of $E_b = 0.85$ MeV. Below this beam energy the hydrogen beam has a higher current drive efficiency than the deuterium one. However at the energy of 1.3 MeV the deuterium beam is superior by ~10% to the hydrogen beam. The plasma dilution is dependent upon particle exhaust performance and particle transport characteristics of the plasma. Assuming the same characteristics for hydrogen and helium particles, the dilution by the hydrogen beam exceeds the helium dilution. The steady state mode would be operated near the beta limit boundary and therefore the hydrogen dilution would play a significant role.

5.4.3.3. Profile controllability of beam driven currents

The plasma expected in the technology phase of ITER, which may be restricted to a rather limited operation space near the plasma beta limit in order to satisfy various requirements and constraints, will need a specific range of plasma current profiles. In the present understanding, a rather flat profile of total current is favorable for steady-state operation from the MHD stability viewpoint [§2.2].

Various cases of NB power profiles (NB power footprint) and resultant plasma current profiles have been studied with changing plasma densities [5.61,62], because as mentioned in the previous subsection the NB power deposition is very sensitive to plasma density. The results show that a NB power deposition profile produces an approximately similar beam driven current profile for a low density case, like $\langle n_e \rangle \leq 0.7 \times 10^{20}$ m^{-3}. This means that, for steady-state operation at relatively low density, significant flexibility of tailoring the driven current profile could be provided and a specific total current profile could be realized if the beam power profile can be adjusted from a peaked to a hollow profile. With increasing plasma density it becomes difficult to produce a flat profile of the beam driven current due to weak beam penetration. For instance, in a case of $\langle n_e \rangle \sim 1.0 \times 10^{20}$ m^{-3} a flat profile of beam-driven current is realized by a peaked beam power profile, i.e., all the beams must aim at the plasma center. Therefore the physics requirement is that the beam power profile (footprint) should cover a wide range of profiles, very peaked to hollow.

5.4.3.4. Beam shinethrough

Neutral beam shinethrough power has been evaluated for two cases with different plasma densities for ITER [5.65]. For a relatively flat beam power profile (beam footprint) with a 30 MW beam going through each port, a lower density case, $n_{e0} = 10^{20}$ m^{-3} ($\langle n_e \rangle \sim 0.65 \times 10^{20}$ m^{-3}), has a peak shinethrough power of 0.02 MW/m^2, measured at a plane perpendicular to a beam line. At a higher density, $n_{e0} = 1.5 \times 10^{20}$ m^{-3} ($\langle n_e \rangle \sim 1.0 \times 10^{20}$ m^{-3}), the shinethrough power is remarkably reduced and central beam power is fully absorbed.

In conclusion, the beam shinethrough power is quite small, except for extreme low density plasma less than 0.5×10^{20} m^{-3}, which is not envisioned in ITER.

5.4.3.5. Consistency with lower hybrid waves

The reference scenario of ITER steady state current drive is the combination of beam-driven current, LH-driven current and neoclassical bootstrap current. It has been demonstrated that a desirable total current profile can be realized for ITER parameters [5.17,18]. In order to maintain a monotonic q profile, it is necessary to distribute the LH power deposition over a broader range of ψ surfaces. The desirable monotonic $q(\psi)$ has been demonstrated, although the current profile has sharp peaks around $\psi = 0.6$–0.8; the central and edge safety factors, 1.33 and 3.33, respectively, probably meet criteria for ideal MHD stability; and a large fraction of the current is generated by the neoclassical bootstrap effect (0.36), as shown in Fig. 5-2.

5.5 ION CYCLOTRON PHYSICS

5.5.1 Theory and Modeling of Fast Wave Current Drive

The modeling of fast wave heating and current drive is based on a well-developed theory of wave propagation and damping in inhomogeneous plasmas. Waves with frequencies in the ion cyclotron frequency range (10-100 MHz) can deposit their energy either on electrons (primarily through the mechanism of transit time magnetic pumping at lower frequencies, with Landau damping becoming progressively more important as the frequency is increased), or on ions (either through minority heating scenarios, or cyclotron damping at surfaces where the wave frequency is an integer multiple of the ion cyclotron frequency). While it is possible to drive current by damping fast waves on either electrons or on ions, it was found that the optimum fast wave current drive scenarios are those in which the wave damps on the electrons. We therefore concentrate on these scenarios [5.66]. Figure 5-4 shows a survey of the partition of wave power between electrons and various ion species as a function of the wave frequency [5.67]. There are three potential windows for fast wave current drive in ITER: one at low frequency (below the tritium ion cyclotron resonance frequency), a second between the second harmonic of tritium and the second harmonic of deuterium, and a third above the third deuterium cyclotron harmonic.

5.5.1.1 Low frequency fast wave current drive scenarios

The low frequency scenarios have the advantage that there are no ion cyclotron resonances within the plasma. Hence, the wave power is entirely deposited on the electrons. It is therefore possible to choose relatively high wave phase velocities (where the damping per pass is relatively low), and achieve a higher current drive figure-of-merit. Because the plasma opacity is low in this frequency window, the wave energy is mainly deposited in the center of the plasma, where the temperature and density are highest. When the ion cyclotron power is launched from the midplane of the tokamak this tends to result in a rather peaked driven current profile. It is possible to broaden the current profile somewhat by launching the waves from a location above (or below) the midplane. However, these off-midplane launch scenarios have a substantially lower current drive figure-of-merit, and only a marginally broader driven-current profile [5.68].

The low frequency current drive scenarios have been modeled both with full-wave codes and with ray-tracing codes. The optimum scenarios obtained from the the ray-tracing codes [5.69] can be summarized by the formula

$$\gamma_{FWCD} \approx 0.57[(\langle T_e \rangle/10\ \mathrm{keV})/(2 + Z_{eff})] \times 10^{20}\ \mathrm{A/m^2W},$$

where γ_{FWCD} is the current drive figure of merit, and $\langle T_e \rangle$ is the density weighted, volume-averaged temperature. This formula includes current drive efficiency degradation due to realistic antenna spectra.

When similar scenarios were modeled with existing full-wave codes, a current drive figure of merit 50% higher was obtained when careful attention was paid to coupling to cavity eigenmodes [5.70]. Increasing the current drive efficiency is important to achieving attractive fast wave current drive scenarios; hence, these

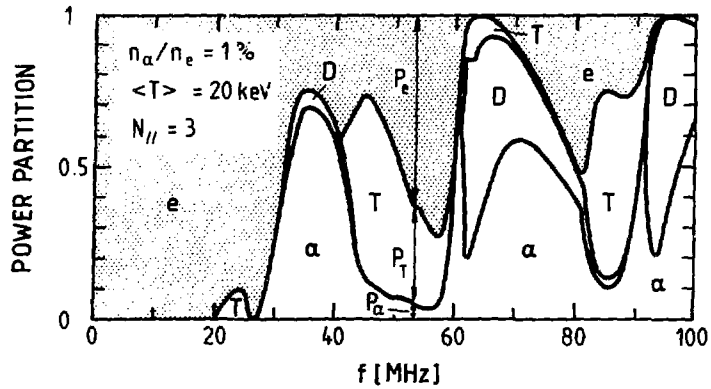

FIG. 5-4 The fraction of fast wave power absorbed by various ions species vs. frequency [5.67].

scenarios should be examined in more detail. However, it should be noted that there are important deficiencies in the present full wave codes. Toroidal effects are not fully retained, and relativistic effects (which can significantly limit the current drive efficiency) have also been ignored. The toroidal effects are particularly important because they lead to an up-shift in $N_{||}$ (i.e., a down shift in the local phase velocity of the wave) which is not included in the full wave codes. The ray-tracing analysis of similar scenarios (which includes the up-shift in $N_{||}$) indicates that the fast wave power is absorbed in regions where the local phase velocity is low. When similar toroidal effects are included in the full wave codes we can expect the $N_{||}$ up-shift to substantially reduce the current drive figure-of-merit. It should also be noted that maintaining coupling to cavity eigenmodes in an actual tokamak experiment may pose severe technical problems.

5.5.1.2 Intermediate frequency fast wave current drive scenarios

The second window (at ~55 MHz for the reference design) offers somewhat improved opacity [5.52]. At these higher frequencies ray-tracing codes provide sufficient accuracy for modeling wave propagation, absorption, and current drive efficiency. It is necessary to deposit the bulk of the wave energy in the electrons on the first pass through the plasma in order to achieve a high current drive efficiency, since any energy not deposited on the electrons on the first pass will be absorbed at the second harmonic of the deuterium cyclotron resonance. Largely because of incomplete absorption of the waves by electrons on the first pass, and subsequent absorption of the waves at the ion resonance, the current drive figure of merit in this frequency range was calculated to be lower than that of the low frequency scenarios by about 10–20%.

5.5.1.3 High frequency fast wave current drive scenarios

Finally, we consider the window above the third deuterium cyclotron harmonic. At these higher frequencies the plasma opacity has substantially improved, and more

control is available on the driven current profile [5.71]. However, damping on fusion-produced fast alpha particles becomes a substantial concern. For ITER conditions, alpha particles can absorb 50% of the incident rf power, rendering current drive efficiencies very low [5.72]. In the absence of α-particles, however, this technique is calculated to work well.

5.5.2 Experimental Database

A mature technology exists for generating waves in this frequency range, and there is a large experimental database on ion cyclotron heating. Perhaps the most impressive results are those from JET [5.73] in which both combined neutral beam and ICRF heated, and only ICRF heated H-modes have been obtained. An automated matching network is able to maintain coupling between the fast wave antenna and the plasma through the H-mode transition. Work on both JET [5.73] and JFT-2M [5.74] have demonstrated wave absorption on electrons by transit-time magnetic pumping (the absorption mechanism invoked for most fast wave current drive scenarios).

The experimental database for fast wave current drive (as opposed to fast wave heating) is very sparse. The improvement of the experimental database on fast wave current drive is the single most important R&D task relating to the alternate ion cyclotron system to be undertaken during the ITER EDA [5.31]. Such experiments are necessary to demonstrate the physics of fast wave current drive, and to provide operational experience with plasmas in which the full plasma current is supported with RF power.

5.5.3 Ion Cyclotron Heating

Ion cyclotron waves have significant applications to reactor plasmas beyond current drive. Ion cyclotron heating has been demonstrated as an effective means of achieving high power deposition in the center of a large, hot tokamak plasma, in H-mode as well as in L-mode [5.73,75]. Extensive theoretical work correlates well with experiment, providing confidence that the basic mechanisms of minority and second-harmonic heating using the fast wave are well understood [5.76]. At present, the highest achieved fusion power output (100 kW) has been obtained with ICRH minority heating in a D-He^3 mixture on JET [5.73]. Demonstrated scenarios for fast wave heating include minority heating, second harmonic heating, and heating at higher cyclotron harmonics, in addition to electron heating experiments that resemble our fast wave current drive scenarios. The unique ability of fast waves to deposit power directly on ions in the center of the plasma suggests that fast waves would be useful both for start-up (when a dense D-T plasma must be heated to thermonuclear temperatures) and for burn control [5.77].

5.5.3.1 Deuterium minority heating

Fundamental heating of a deuterium minority is an attractive option for heating D-T plasmas in ITER to ignition. With this method of heating it is possible to create a non-thermal tail on the deuterium distribution function with energy in the range of 100 keV. This tailoring of the deuterium distribution function enhances the reactivity of the plasma. In addition, there is some experimental evidence that the electron channel dominates energy losses in tokamaks [5.78]. Hence, it is advantageous to

heat ions directly and to insure that the characteristic energy of any non-thermal ion tails created by the heating process is less than the critical energy so that drag power goes to thermal ions (rather than directly to electrons).

Deuterium minority heating scenarios have been compared with electron heating scenarios in transport simulations using the JETTO code [5.77,79]. It is found that the D concentration $[n_D/(n_D + n_T)]$ is not critical and can be taken as high as 30-50%. This mode is seen to lead more quickly to ignition than electron heating. The main advantage of the direct ion heating scheme is that it is much less affected by confinement degradation, rather than from the enhanced reactivity. Higher thermal ion temperatures are obtained by direct ion heating than in electron heating scenarios because in electron heating schemes equipartion of energy from electrons to ions has to compete with transport losses. As a result, $Q \approx 15$ is reached with ion heating, while $Q \approx 10$ is obtained with electron heating. Note that the advantage of this scheme follows mainly from the assumptions made regarding ion thermal transport, i.e., that $\chi_i = \chi_{nc} + 1.5(T_e/T_i)^{1.5}\chi_e$, where χ_e is chosen to be consistent with a Kaye-Goldston like scaling in which the confinement is degraded only by the power flowing to the electrons.

With respect to burn control, electron heating can become inefficient because of its loose coupling to ions [5.77], compared the total reaction rates obtained with a different fractions of (Power coupled to ions)/(Total power). He shows that putting 80% of the power into fuel ions provides ± 25 % control over the reaction rate, while pure electron heating provides almost no control over the reaction rate in his model. There is also a slower response of the reaction rate to electron heating due to the energy equipartion time. Thus, direct ion heating (as obtained with ICH) should have significant advantages for feedback control of a burning plasma.

5.5.3.2 He^3 and other minority heating schemes

The use of fast wave minority He^3 heating ($f \approx 44$ MHz) during the physics phase of ITER operation will allow central power deposition with little generation of radioactivity. In addition to regular heating, physics studies can include the simulation of alpha-particle heating by using a low concentration of He^3 in a He^4 or H background plasma, and stabilization of the sawtooth regime by fast particles (as is seen in the monster sawtooth operation on JET). Minority heating of H in a D or He^4 background can be done at about 65 MHz. This frequency can also provide a credible method of heating a hydrogen plasma, via minority second harmonic He^4 heating. He^3 or H minority heating is also a second option for start-up and heating of D-T plasmas to ignition.

5.5.3.3 Heating and current drive at high frequency

For a frequency range of 70–110 MHz, heating and current drive scenarios are as follows: $2\omega_{cD}$ at 74 MHz can be used for burn control, local current profile control in combination with NBCD, heating of hydrogen plasma (He^4 minority second harmonic heating), heating of deuterium plasma (H minority heating), and D-He^3 burn; $2\omega_{cHe3}$ at 98 MHz can be used for D-He^3 burn; $3\omega_{cD}$ at 110 MHz can be used for burn control and local current profile control in combination with NBCD [5.72,80].

Power partition among species and power deposition profiles were calculated with a one-dimensional full-wave code and a two-dimensional bounce-averaged Fokker-Planck code. For physics ignition parameters ($\langle T \rangle$ = 10 keV, $\langle n_e \rangle = 1.4 \times 10^{20}$ m^{-3}), the ratio of the power absorbed by alphas and deuterons in the central region to the total RF power (from the 1D full-wave code) is ~70% with $2\omega_{cD}$ heating and ~55% with $3\omega_{cD}$ heating.

Power partitions among species in the central region taking quasi-linear velocity diffusion and trapped particle effects into account are almost the same for both heating regimes, i.e., ~20% to alphas and ~80% to deuterons, from the 2D Fokker-Planck code. Collisional power transfer to ions and electrons is as follows: (i) $2\omega_{cD}$ heating: ~86% to ions and ~14% to electrons; (ii) $3\omega_{cD}$ heating: ~72% to ions and ~28% to electrons. The collisional power transfer with $2\omega_{cT}$ heating is almost the same as the one with $2\omega_{cD}$ heating. Thus central ion heating is expected in both $2\omega_{cD}$ and $2\omega_{cT}$ regimes. The central power density is comparable to that of the alpha heating. Thereby efficient burn control can be expected.

Local current profile control is possible by accelerating deuterium beam ions with second or third harmonic ICRF waves in NBCD plasma. The cyclotron resonance layer is located slightly to the high field side in order to enhance absorption by passing particles and to increase the driven current by ICRF waves. Enhancement of the current density by ICRF waves is localized near the cyclotron resonance layer. The current drive figure-of-merit is rather low, about 0.13. This application may be useful to provide a method of local current profile control with ICRF waves, and to drive current near the center of the plasma at high density when the neutral beams cannot penetrate well.

The extrapolation of the heating results to ITER appears to be straightforward. Calculations by Batchelor [5.70,81] and Bhatnagar [5.82] indicate that the power deposition profile can be tailored by changing the frequency of the launched waves. We conclude that ICRH is an attractive and versatile method for heating and burn control.

5.6 BOOTSTRAP CURRENT

5.6.1 Status of Database

Significant amounts of bootstrap current have recently been observed in large tokamak experiments. The existence of a neoclassical, diffusion driven current was predicted by Galeev [5.83] and Bickerton et al. [5.84] in the early 1970's. However, experimentally this neoclassical bootstrap current proved very elusive [5.85]. While bootstrap currents were not observed in tokamaks, they were observed in the other toroidal confinement devices, such as the stellarator [5.86], Heliotron [5.87], and Multipole [5.88].

In the collisionless (banana) regime of neoclassical theory the bootstrap current may be roughly estimated as

$$I_{bs} \approx \varepsilon^{0.5} \beta_p I$$

where ε is the inverse aspect ratio. To obtain a significant bootstrap current, both high poloidal beta ($\beta_p \gg 1$) and low collisionality ($\nu_* \ll 1$) are needed.

TFTR: The existence of a bootstrap current in a tokamak was reported from TFTR in low current operation (the so called "super shot") [5.89], with a plasma current I = 0.8–1.1 MA. With neutral beam power P_b ~10-to-15 MW, T_{eo} = 8 keV, T_{io} = 15–30 keV. These plasmas are in the collisionless regime with $\nu_{*i} < 5 \times 10^{-3}$, $\nu_{*e} < 5 \times 10^{-2}$ at r = 0.3 m and β_p = 2. The time behavior of the one-turn loop voltage is compared with TRANSP code analyses of the predicted loop voltage under various assumptions. The best fit to the experimental data is obtained when both the bootstrap and beam driven currents are included. From this analysis a bootstrap current of up to 500 kA (about 50% of the total current) is inferred.

Significant bootstrap current with the possibility of improved confinement was recently reported [5.90]. Plasmas near the equilibrium limit with $\varepsilon\beta_p \sim 1.5$ and $\beta/(I/aB) \sim 4$ have been produced in high temperature plasmas ($T_{io} \sim 20$ keV, $T_{eo} \sim 8$ keV) with confinement times significantly enhanced ($\tau_E/\tau_L \sim 3.5$). The central q value is observed to be $q_o = 1.6 \pm 0.5$ in 400 kA plasmas. In those collisionless high β_p plasmas, transport analysis shows that the bootstrap current accounts to about 70% of plasma current for several hundred milliseconds during heating pulse.

JET: In low density limiter discharges with I = 1 MA and P_b = 5 MW [5.91], $I_{bs} \approx 250$ kA at $\beta_p \approx 0.8$ is obtained. The measured surface voltage is also compared with value estimated using several driven current models. Again, measured loop voltages are best fit by a model which includes bootstrap and beam-driven current together with electric-field diffusion. JET also observed a bootstrap current of 700 kA in H-mode discharges (I = 2 MA, P_b = 9 MW).

JT-60: Using 20 MW of perpendicular neutral beam injection, JT-60 obtains very high beta poloidal (β_p = 3.2) in very low current operation (I = 500 kA) [5.92]. Up to 80% of the total plasma current is driven by the bootstrap current. The beam driven current is negligible in the JT-60 case. The measured loop voltage, normalized to that predicted using the neoclassical resistivity (including OH, L, and high-T_i discharges), decreases with β_p as neoclassical bootstrap current theory suggests.

DIII-D: Very high values of β_p = 5.1 and $\varepsilon\beta_p$ = 1.8 were produced by 14 MW NB at low plasma current, I = 0.54 MA [5.53]. The discharge is approaching the equilibrium limit. The high β_p, with confinement equal to $2.4 \times \tau_{ITER89\text{-}P}$, was realized during the ELM-free phase. For a typical discharge, there was a 55 % beam driven, a 35 % bootstrap, and a 10 % ohmic current.

To explain the observed loop voltage in TFTR, JET, JT-60, and DIII-D, the contribution from neoclassical effects are essential. However, under the present plasma parameter, usually $\tau_{skin} > \tau_{heating}$. The effects of conductivity change near the edge and equilibrium changes due to the increase in β_p on the loop voltage are comparable to or larger than the bootstrap current. More delicate diagnostics, including current profile measurements, may be needed to clarify the accuracy of the present bootstrap current theory [5.31].

5.6.2 Bootstrap current in ITER

The bootstrap current in ITER plays an important role in the technology phase operating scenario since it reduces the required current drive and thereby reduces the

power load on the divertor plates. For typical plasma parameters of $\langle T \rangle = 20$ keV, $\langle n_e \rangle = 0.7 \times 10^{20}$ m^{-3}, and an average current drive efficiency of $\langle \gamma \rangle = 0.42$ (10^{20} A/m^{2}W), each MA of plasma current requires 10 MW of current drive power. Therefore a careful, accurate evaluation of the bootstrap current is necessary since it has such an impact on the design. Furthermore a simple formula for bootstrap current, rather than a complete time intensive 2-D calculation, is needed by the system code, which systematically studies a range of design concepts. Here we describe a simple formula obtained from an empirical fit to a series of 2-D calculations for the ITER technology phase.

It is well known that the bootstrap current is proportional to the product of poloidal beta and the fraction of trapped to circulating particles (proportional to the square root of the inverse aspect ratio in the large aspect ratio limit). In addition to this dependence, studies on current drive in ITER during the conceptual design phase showed that the bootstrap current is also significantly dependent upon the profile of the total plasma current. This behavior is primarily related to the fact that flux surfaces are pushed out as the current profile is flattened and the area inside a given flux surface increases. This behavior can easily be seen from the following expression for the total bootstrap current,

$$I_{bs} = \int d\psi \, q(\psi) \langle\langle \mathbf{B}\cdot\mathbf{J} \rangle\rangle_{bs} / \langle\langle B^2 \rangle\rangle$$

The area effect comes from the q dependence, i.e., flat current profiles raise q in the interior of the plasma. In the above expression $\langle\langle\ \rangle\rangle$ refers to a flux average and $\langle\langle \mathbf{B}\cdot\mathbf{J} \rangle\rangle_{bs}$ is the bootstrap source with the dependence described above.

A typical example is shown in Fig. 5-5 [5.93]. Here the bootstrap current is calculated by a 2D equilibrium code for a given plasma current profile. The bootstrap current in this figure is not included self-consistently in the total plasma current, consequently there may be some minor changes. Comparisons with a self consistent calculation produced similar results. It is evident that for fixed current profiles (α_J = constant), the bootstrap current is proportional to the poloidal beta, β_p, as expected. The total bootstrap current indeed changes drastically as the current density profile exponent, α_J, is varied at fixed β_p. Effects of density and temperature profiles have been also studied. Their impact on the total bootstrap current are much smaller than that of the current profile, although the bootstrap current profile changes significantly as the density and temperature profiles are changed. An empirical formula of the bootstrap current has been derived from a series of calculations [5.94], in which the bootstrap current is included self-consistently in the 2D equilibrium calculation. The current profile is changed from peaked to hollow by varying peak densities, temperatures and their profiles, and by varying the beam energy. The empirical formula is expressed as

$$I_{bs}/I = C_{bs}(\epsilon^{1/2}\beta_{pa})^{1.3},$$

where

$$C_{bs} = 1.32 - 0.235[q_\psi(95\%)/q_\psi(0)] + 0.0185[q_\psi(95\%)/q_\psi(0)]^2,$$
$$\beta_{pa} = \langle p \rangle / (B_{pa}^2/2\mu_o) \quad \text{with } B_{pa} = I/5\langle a \rangle \text{ and } \langle a \rangle = [V/(2\pi R)]^{0.5} \approx a\kappa^{0.5}.$$

In the empirical formula the effect of the current profile is expressed as the ratio,

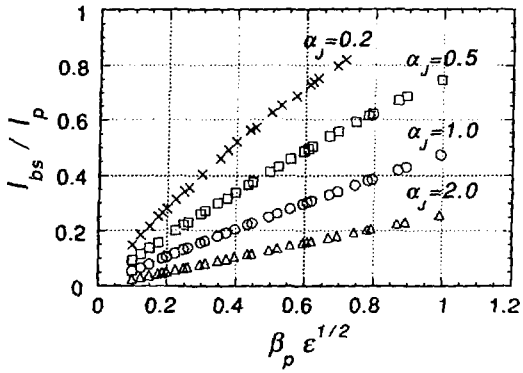

FIG. 5-5 The fractions of the bootstrap current, I_{bs}/I_{tot}, are plotted as a function of the product of poloidal beta, β_p, and square root of inverse aspect ratio, $\varepsilon^{1/2}$. The bootstrap current is calculated for a given total current profile and is not solved in a consistent way. The profiles of total currents, densities and temperatures are assumed as $[1 - (r/a)^2]^{\alpha_i}$, i = J, N, T, and $\alpha_n = 0.5$ and $\alpha_T = 1.0$. The total plasma current is fixed to I = 20 MA, and the poloidal beta is changed with varying peak densities and temperatures [5.93,94].

$q_\psi(95\%)/q_\psi(0)$, and the formula is valid in a range of $1.0 < q_\psi(95\%)/q_\psi(0) < 5.0$. This formula applied to the ITER technology phase predicts a 30% fraction for the bootstrap current. It should be noted that recent studies on the current profile effect suggest that the exponent of 1.3 is somewhat high and that a formula using the internal inductance might be preferable to that of the ratio of q_ψ's [5.94].

Further work is required on the bootstrap formalism to properly treat the energetic particles [5.31].

5.7 REFERENCE OPERATING SCENARIO

The ITER steady-state and hybrid operating scenarios are constrained by the need to maintain acceptable operating conditions at the divertor. Hence, great emphasis was placed on minimizing the power required for steady-state operation and/or current profile control, while maintaining the average plasma density in the range $(0.7–1) \times 10^{20}$ m^{-3}; i.e., one must maximize the current drive figure-of-merit, $\gamma \equiv \langle n_e \rangle IR/P_{inj}$. A combination of NB and LHW was chosen for the reference operating scenario because this combination provides for control of the current profile and yields the highest current drive figure of merit [$\gamma \approx (0.45–0.5) \times 10^{20}$ A/m^{2}W]. Central current drive is provided by NB, while LHW are used to drive current in the outer region. An electron cyclotron system is provided to assist in start-up and for controlling disruptions.

Bulk current profile control is provided both by varying the relative NB and LH power, and by varying the vertical aiming of the NB. The NB energy is chosen to assure penetration to the magnetic axis for central current drive in steady-state

operating scenarios. The frequency of the LHW is chosen to minimize difficulties in generation and transmission, to ensure good coupling between the launcher and the plasma, and to avoid damping on fast alpha particles.

The neoclassical bootstrap current plays an important role in ITER steady-state and hybrid operating scenarios, both by reducing the current that must be driven with NB and LHW, and by helping to broaden the current profile. Key physics issues include penetration of LHW into reactor plasmas, and expanding the experimental database for both NB current drive (particularly to beam velocities greater than the Alfvén velocity and critical velocity, above which the interaction of beam with the electrons begins to dominate) and the neoclassical bootstrap current.

Key physics issues for EC waves include expanding the experimental database on electron cyclotron current drive, and developing and experimentally demonstrating the details of disruption control scenarios.

5.7.1 Current Profile Control

Non-inductive current drive methods promise to allow greater control over the current profile in ITER than has been the case in most tokamak experiments to date. Possible benefits from current profile control include reduction in the inductive Volt-second requirements, improved energy confinement both due to a reduction in anomalous transport rates [5.95] and the elimination of sawtooth oscillations [5.96], and a reduction in the disruption frequency through stabilization of 2/1 tearing modes [5.97].

It is useful to divide current profile control into two categories: bulk current profile control (by which we mean control of the safety factor at the magnetic axis, q(0), and bulk parameters such as the internal inductance, l_i, while maintaining a monotonic q-profile) and detailed current profile control (e.g., control of the gradient in the current density at key locations like the q = 2 surface).

5.7.1.1 Bulk current profile control

The ITER physics specifications call for a relatively low internal inductance, in the range $0.55 < l_i < 0.75$. This relatively low value of l_i has been chosen because MHD studies [5.98, and §2.2] indicate that this range will provide optimum stability at relatively high values of β. It has the further advantage of somewhat reducing the inductive Volt-seconds required for current ramp-up, and the vertical field required from the poloidal field system.

A relatively peaked temperature profile (at least parabolic) is expected in ITER. If no measures are taken to control the current profile, this peaked temperature, together with the neoclassical degradation in the plasma conductivity away from the magnetic axis, will lead to a very peaked Ohmic current profile, and an internal inductance in excess of unity. At high plasma currents I ≥ 22 MA, (e.g., for the ITER ignition operational scenarios), the tendency toward strong peaking of the current profile will lead to sawtooth oscillations. With large sawtooth oscillations, peaking of the current profile can be avoided at the expense of a substantial degradation in energy confinement. Control of the current profile through noninductive current drive in ITER will allow either the elimination of sawtooth oscillations [e.g., by holding q(0) > 1] or the substantial reduction of the sawtooth mixing radius, while holding the internal inductance in the desired range.

Generally, the goal is to maintain a broad current profile. The neoclassical bootstrap current is very helpful in this regard since theoretical calculations indicate that it will help broaden the current profile. Hence, we are motivated to maximize the bootstrap current in order to minimize the auxiliary power requirement while maintaining a broad current profile. During the conceptual design work has centered on scenarios in which $q(0) \approx 1$. However, recent work (see §2.2) shows that broader current profiles with higher values of q(0) may be desirable. An operating scenario with q(0) in the range 1.5–2 would have a substantially higher bootstrap current. If such scenarios are found to be acceptable in other respects they would have positive impact on ITER technology phase operation.

The β-limit is of particular concern in the ITER steady-state and hybrid operating scenarios. In these scenarios the plasma current is reduced ($I \approx 15$ MA) and the fusion power is limited by MHD stability considerations [operation is at the β-limit, which is taken as $\beta\ (\%) \leq 3I/aB$ in these operating scenarios]. At these lower currents sawtooth oscillations are less effective in broadening the current profile, and noninductive current drive will be necessary to maintain the internal inductance in the desired range. Recent theoretical and experimental studies [5.99, 100] indicate that substantial increases in the β-limit (up to $\beta \leq 5I/aB$) are possible if the internal inductance can be adequately controlled. Such an extension of ITER's operating limits would have a substantial positive impact on ITER operating scenarios.

Finally, it should be noted that recent experimental results from TFTR [5.95] indicate that substantial improvement (or degradation) in the energy confinement is possible through control of the current profile. It is not yet clear what relationship exists between the current profiles that are optimum with respect to MHD stability and the current profiles that yield the best energy confinement.

Bulk current profile control requires that a substantial fraction of the total plasma current be driven noninductively (it is easily seen that a small perturbation in the plasma current profile can only result in a small perturbation in l_i, while efforts to increase q(0) by local current drive at the magnetic axis can only result in a non-monotonic q-profile which would be unstable to double-tearing modes). Hence, the efficiency with which injected power produces current, and some degree of control over where the current is generated are major considerations in choosing a system for bulk current profile control. In the ITER reference design this function will be carried out with a combination of lower hybrid waves and neutral beams. At the temperatures and densities envisioned for ITER operation the lower hybrid waves are limited to driving current in the outer portion of the plasma, while the neutral beams are used to drive current in the plasma interior.

It was decided to aim the neutral beams tangent to the magnetic axis of ITER in order to maximize the current drive efficiency and thereby alleviate conditions at the divertor. This leads to a reduction in the ability to control the current profile at densities $\langle n_e \rangle \geq 1 \times 10^{20}\ m^{-3}$ (see §5.4.3). Current profile control could be maintained at these higher densities if the neutral beams were aimed somewhat inboard of the magnetic axis. These options should be considered in future work on the ITER reference current drive and heating scenarios

5.7.1.2 Detailed current profile control

The safe and reliable operation of ITER will require the suppression of major disruptions. One means by which this might be accomplished is through modification of the current profile in the neighborhood of the q = 2 surface in order to stabilize m = 2 tearing modes (which are a precursor to disruptions). In evaluating scenarios for disruption control through noninductive current drive, attention must be paid to the minimum width of the driven current profile in addition to the efficiency of current drive. The power requirements are minimized by minimizing the ratio of the square of the width of the driven current profile to the current drive efficiency [5.101,102,103]. When this criterion is applied, electron cyclotron current drive, which has a relatively low current drive efficiency but a yields narrow driven current profile, is found to be quite attractive for this application. The ITER electron cyclotron system has been designed to allow real-time adjustment in the aiming of the microwave beam to allow tracking of the q = 2 surface. Modeling of ITER disruption control scenarios indicate that the 20 MW EC system should be capable of stabilizing m = 2 tearing modes at plasma currents less than about 22 MA (see §5.9). At higher currents the q = 2 surface moves closer to the plasma surface, where the aspect ratio is lower. Trapped particle effects lead to a substantial degradation in the electron cyclotron current drive efficiency at these lower aspect ratios, so that the present ITER electron cyclotron system is not expected to be effective for disruption control at currents above 22 MA. Other electron cyclotron disruption control scenarios, in which the microwave beam is aimed tangent to the q = 2 surface, promise superior performance at high plasma currents. These new scenarios are currently under study.

5.7.2 Start-up Assist

In addition to disruption control, the ITER electron cyclotron system is also designed to assist in plasma start-up. This is necessary because the thick ITER vacuum vessel limits the loop voltage available for plasma break-down and current initiation. This is a particular problem for start-up using the outer wall as a limiter since the toroidal electric field is reduced for fixed loop voltage at larger major radius. Start-up on the outer wall will be necessary when lower hybrid current ramp-up assist is employed to reduce the Volt-seconds required from the poloidal field systems for current ramp-up.

A theory of the equilibrium of very low current toroidal plasmas has been developed (see §5.2) and applied to the study of start-up in ITER. It is found that the required start-up power varies with the vertical magnetic field. For ITER the minimum start-up power occurs with a vertical field in the neighborhood of 50 G. Hence, it is necessary to keep magnetic field errors in ITER below 50 G during start-up to avoid substantial impact on the start-up power. At the optimum vertical field, and with magnetic field errors of the magnitude expected in ITER the required start-up power lies in the range 5–10 MW, well within the capability of the ITER electron cyclotron system.

5.7.3 Non-Inductive Current Ramp-up and/or Current Ramp-up Assist

In addition to its role in current profile control, the ITER LH system can be used for noninductive current ramp-up or current ramp-up assist (see §5.3.4). Lower

hybrid current ramp-up assist can provide the 20 (or more) Volt-seconds needed to provide an adequate current flat-top for ITER ignition scenarios at currents in excess of 22 MA, and may have a role in long-pulse operating scenarios for the ITER technology phase. Lower-hybrid assisted current ramp-up scenarios require that the plasma be positioned near the outer wall so that contact can be maintained between the plasma and the lower hybrid launcher (hence, the need to maintain the option of initiating the plasma break-down near the outer wall of the plasma chamber).

5.7.4 Plasma Heating and Burn Control

The auxiliary power requirements for maintaining steady-state operation in ITER are substantially higher than what is required for heating the plasma to ignition, or maintaining control of a sub-ignited operating point. Depending on the plasma density, the set of methods which could be used for central plasma heating changes. All four methods could be used for heating if the density is less than 5×10^{19} m^{-3}. Three methods could provide electron heating (NB, EC, LH) while IC waves can be used for both ion and electron heating (depending on the frequency selection). With increasing density the problem of penetration of LHW first appears. Then, if density becomes greater than 1×10^{20} m^{-3}, NB with an energy of 1.3 MeV ceases to penetrate into the central part of plasma column. While there is evidence that direct ion heating schemes are superior for heating to ignition and for burn control (see §5.5.3), extensive modeling of ITER operating scenarios indicates that the neutral beam system in the ITER reference scenario should be adequate for this task [5.104].

The reference ITER hybrid scenario (B1) lies on the low temperature unstable part of the ignition curve and therefore requires active method for suppression of burn instability. The variation of heating/current-drive power is at the present time the principal method for burn control. The rate of power variation, which is the most important parameter for this method, is presently under discussion [5.105]. Similarly to the plasma heating, the most effective method of burn control is ion cyclotron heating, which directly puts its power to energetic ions. All other methods deliver power to electrons which in turn pass it to ions with the characteristic delay time of the order of the ion-electron collision time. In a dense plasma (like the reference hybrid scenario B1) this delay time is much less than the characteristic time of the burn instability (of the order of energy confinement time) and could not influence the choice of heating method. Much more important could be the limitation on the heating method caused by the plasma density. It was shown [5.106] that, because of the deterioration of NB penetration at high density, neutral beams with energy 1.3 MeV could provide efficient burn control if the plasma density is less than 1.5×10^{20} m^{-3}. In such a way the ITER NBI system could control the burn in all reference scenarios. At the present time the possibility of NBI power variation with the maximum rate of change 10 MW/s is foreseen.

5.8 ALTERNATE OPERATING SCENARIO

The alternate operating scenario differs from the reference scenario in that central current drive is provided by ion cyclotron (IC) waves. A low frequency (~17 MHz) fast wave current drive scenario was chosen because this scenario gives the

best current drive efficiency [$\gamma \approx (0.25\text{-}0.3) \times 10^{20}$ A/m^{2}W], and avoids ion damping (see §5.5.1.1). The ITER fast wave system will be designed to deliver 130 MW of fast wave power to the plasma for frequencies in the range 15–80 MHz. Hence, the alternate scenario will have sufficient flexibility to investigate intermediate frequency current drive scenarios as well (see §5.5.1.2). Key unresolved physics issues include an experimental demonstration of IC current drive, and current profile control.

The fast wave system could also be used for plasma heating and burn control (see §5.5.3). Important heating scenarios include deuterium minority heating at $f \approx 33$ MHz, He^3 minority heating (particularly during low activation studies during the physics phase) at $f \approx 44$ MHz, and second harmonic deuterium (or first harmonic hydrogen) heating at $f \approx 74$ MHz.

5.8.1 Fast Wave Current Drive

The low frequency current drive scenarios have the advantage that there are no ion cyclotron resonances within the plasma. Hence, the fast wave power is entirely deposited on the electrons. It is therefore possible to choose relatively high wave phase velocities (where the damping per pass is relatively low), and achieve a relatively high current drive figure-of-merit. Because the plasma opacity is low in this frequency window, the wave energy is mainly deposited in the center of the plasma, where the temperature and density are highest. This results in a rather peaked driven current profile. It is possible to broaden the current profile somewhat by launching the waves from a location above (or below) the midplane, but only at a substantial decrease in the current drive figure-of-merit. Hence, our ability to control the driven current profile with fast waves alone remains limited. The situation is similar (although the over-all current drive figure-of-merit is somewhat lower) with intermediate frequency current drive scenarios. There are two ways to deal with this problem: either attempt to maximize the bootstrap current , or abandon steady-state operating scenarios and focus on long-pulse ignition and hybrid operating scenarios.

5.8.1.1 Scenarios with a high bootstrap current

The bootstrap current is maximized by operation at high β_p, and by raising q(0) into the range 1.5–2.0 [5.33]. In these scenarios fast waves are used to drive the "seed" current on axis. A broad current profile is maintained through a combination of lower hybrid wave current drive in the outer regions of the plasma, and the bootstrap current itself (which has a characteristic broad profile). Relatively large amounts of lower hybrid power are needed, so that lower hybrid wave penetration becomes an issue as discussed in §5.3.1 (particularly §5.3.1.4). However, it appears that self-consistent MHD equilibria with monotonic q-profiles can be obtained with a reasonable total current drive power (in the range 120–160 MW). If q(0) is allowed to rise above 2.0, then it is possible to obtain self-consistent MHD equilibria with only 7.5 MW of current drive power, as shown in Fig. 5-6. These scenarios show great promise, and reinforce the need for further experimental investigations of the bootstrap current, and improved modeling of bootstrap currents for ITER operating scenarios.

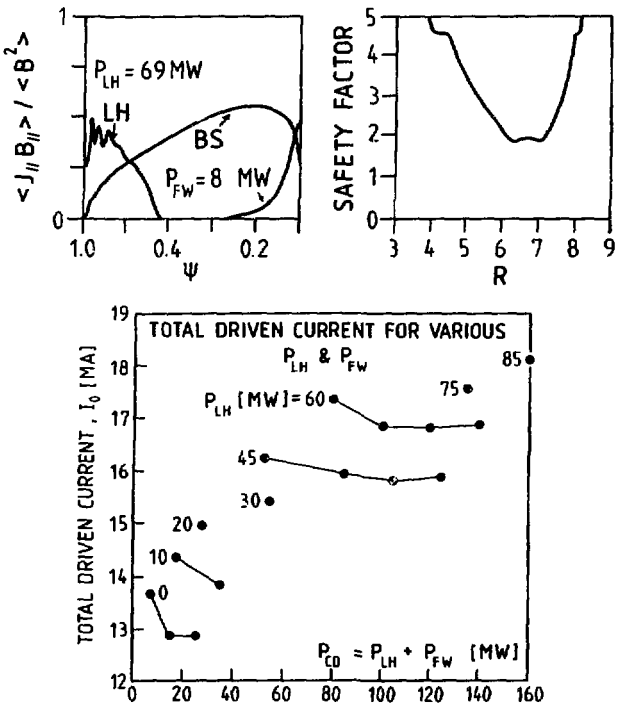

FIG. 5-6 MHD steady-state equilibrium with large bootstrap current [5.33]. Upper left: normalized current density of current driven by LH waves (69 MW), IC fast waves (8 MW), and bootstrap effect ($\langle n_e \rangle = 0.65 \times 10^{20}$ m^{-3}). Upper right: profile of the safety factor for the same case. Bottom: total plasma current for various LH and total injected LH + IC fast wave powers.

5.8.1.2 Long-pulse ignition and hybrid scenarios

Current profile control is required for long-pulse ignition and hybrid operating scenarios because, at times long compared to the resistive skin time when the plasma has reached resistive equilibrium, the Ohmic current profile will be very strongly peaked at the plasma center. One way of dealing with this problem would be to drive the current *backwards* in the plasma core, thus reducing the current density near the magnetic axis [5.107]. A relatively small total driven current (about 38 kA) appears to be sufficient to raise q(0) above one (thus suppressing sawtooth oscillations) and maintain an overall current profile consistent with MHD stability requirements. Fast wave and electron cyclotron current drive are well suited for this task precisely because the driven current profile tends to be strongly peaked near the magnetic axis. The overall current drive efficiency is of less concern in these scenarios because the total driven current is small compared to the plasma current.

5.8.2 Experimental Database

The experimental database for fast wave current drive (as opposed to fast wave heating) is sparse. The improvement of the experimental database on fast wave current drive is the single most important R&D task relating to the ion cyclotron system to be undertaken during the ITER EDA. Fast wave current drive experiments are planned on DIII-D and JET. Such experiments are essential to demonstrate the physics of fast wave current drive, and to provide operational experience with plasmas in which the full plasma current is supported with RF power [5.31].

5.9 CONTROL OF MAJOR DISRUPTIONS BY EC CURRENT DRIVE

The safe and reliable operation of ITER will require the prevention or suppression of major disruptions. The method proposed for the control of disruptions by electron cyclotron current drive relies on the stabilization of the m = 2, n = 1 tearing mode, which is generally regarded as a main cause for the occurrence of major disruptions. The stabilization of the m = 2, n = 1 tearing mode is achieved by control of the local current density profile around the q = 2 surface.

The effect of well-localized current perturbations around the mode rational surface has been analyzed in Refs. [5.97,108,102,103]. A particularly instructive expression for the tearing mode stability is obtained [5.103] using a cylindrical stability calculation. Assuming a Gaussian form for the current perturbation δj,

$$\delta j = I_{CD}/[(2\pi r_s)(\pi/\beta)^{1/2}] \exp[-\beta(x - x_0)^2], \qquad (1)$$

where $\beta^{-1/2}$ is a measure of its width and $x_0 = r_{CD} - r_s$ is the position of the center of the current perturbation with respect to the rational surface, the following expression for Δ' is obtained

$$\Delta' = \Delta_0' - I_{CD}[(r^2/q^2)(dq/dr)]^{-1}|_{r=r_s} \times 2\beta[(1 + \beta^{0.5}x_0 \, \mathrm{Re}\, Z(\beta^{0.5}x_0)], \qquad (2)$$

where Δ_0' is the stability parameter in the absence of the current perturbation, and $Z(z)$ is the plasma dispersion function. Including effects due to non-circular flux surfaces [5.109] will only lead to a change in Δ_0' and the appearance of an additional geometric factor, which is of order one, in the contribution from the current perturbation.

From consideration of Eq. (2), the integrated current in the perturbation I_{CD} that is required for stabilization is proportional to Δ_0', the shear at r_s, and to the square width β^{-1} of the current perturbation [5.101,102,103]. A co-driven current should be centered within the interval $r_s \pm (1/\beta)^{0.5}$, while a counter-driven current should be localized around $r_s \pm (2/\beta)^{0.5}$. A current driven in the co-direction is about 3 times as effective in stabilizing tearing modes as a counter-driven current [5.103]. Hence, only co-driven current perturbations were considered for ITER. A more quantitative estimate of the requirements for the stabilization of the m/n = 2/1 mode can be obtained by substitution of typical numbers for both Δ_0' and the shear at the q = 2 surface. This leads to a simple 'rule of thumb' with which the efficacy of a given current perturbation can be judged, namely,

$$I_{CD}/I \sim 5\beta. \qquad (3)$$

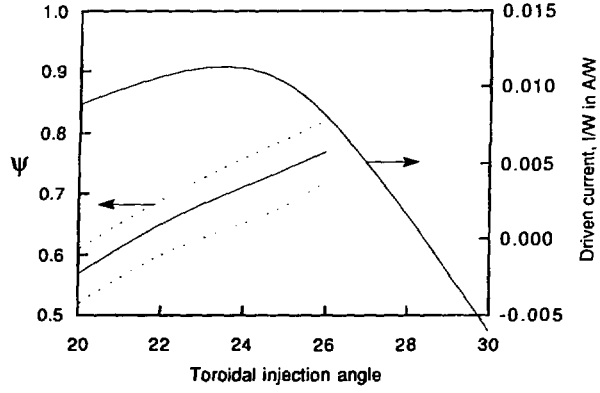

FIG. 5-7 Band of localization and total driven current as a function of toroidal injection angle ϕ for wave frequency f = 123 GHz [5.97].

Several computational codes [5.97,103,109] were used in order to analyze the power and deposition profile requirements for the ECW system to stabilize the m=2/n=1 tearing mode. Ray tracing with a weakly relativistic description of the dielectric tensor was usually used to calculate wave propagation and damping. Current drive efficiency was calculated taking into account both relativistic and toroidal effects. Two kinds of launching scenarios were analyzed: equatorial and tangential. The equatorial launch scenario has been adopted as the reference design.

Figure 5-7 shows the localization and current-drive efficiency for equatorial launch for the calculated optimum frequency of 123 GHz. For toroidal injection angles ϕ up to ~26°, the efficiency is high enough to satisfy the tearing-mode stabilization criterion in Eq. (3), but the current drive cannot be localized near $\psi = 0.8$ and stabilization cannot in fact be achieved if the q = 2 surface occurs at such a large value of ψ.

The following conclusions follow from the results of numerical simulations. Efficiency and localization of the current driven with the equatorial launch scenario is sufficient for tearing mode suppression if the plasma current I < 22 MA, so the q = 2 surface has a smaller trapped-electron population (i.e., larger aspect ratio). The tangential launch scenario has good current-drive efficiency and localization for all positions of the q = 2 surface (i.e., all values of I) if the microwave beam meets modest requirements of focussing and aiming.

REFERENCES (§5.0)

[5.1] *ITER Current Drive and Heating System*, IAEA/ITER/DS/32, IAEA, Vienna (1991).

[5.2] R. PRATER, B. LLOYD, "RF assisted breakdown in tokamaks," ITER Workshop, June 12-16 (1989); B. LLOYD et al., "Low voltage startup with ECH in DIII-D," ITER-IL-PH-6-0-U-5 (1990); V.V. ALIKAEV et al., *Proc. 17th EPS Meeting 1990*, Amsterdam, (1990).

[5.3] M.D. TOKMAN, "On ITER startup in a tokamak," ITER-IL-PH-6-9-S-13 (1989); A. ZVONLOV, A.V. TIMOFEEV, *Fizika Plazmy* **15**, 552 (1989).
[5.4] L.E. ZAKHAROV, G.V. PEREVERZEV, *Fizika Plazmy* **14**, 141 (1988).
[5.5] G.V. PEREVERZEV et al., "Plasma production in ITER by the method of microwave ionization," ITER-IL-PH-6-9-S-14 (1989).
[5.6] Review: N. FUJISAWA et al., INTOR Phase IIA, Part III, Vol. I, Ch. V, IAEA Vienna, 1988.
[5.7] M. NAGAMI et al., *Plasma Phys. Controlled Fusion*, **31**, 1597, (1989).
[5.8] S. TSUJI et al., "The Limiter H Mode with Lower Hybrid Current Drive," *Proc. 13th Int. Conf. on Plasma Physics and Controlled Nuclear Fusion Research*, Washington, D.C., Oct. 1-6, 1990, IAEA-CN-53/E-1-4.
[5.9] F.X. SÖLDNER et al., "Review of Lower Hybrid Experiments on ASDEX," *Proc. 13th Int. Conf. on Plasma Physics and Controlled Nuclear Fusion Research*, Washington, D.C., Oct. 1-6, 1990, IAEA-CN-53/E-1-1.
[5.10] S. ITOH, et al., "Experiments on Steady-State Tokamak Discharge by LHCD in TRIAM-1M," *Proc. 13th Int. Conf. on Plasma Physics and Controlled Nuclear Fusion Research*, Washington, D.C., Oct. 1-6, 1990, IAEA-CN-53/E-2-6.
[5.11] EQUIPE TORE SUPRA (presented by F. PARLANGE), "Progress to long pulse operation in TORE SUPRA," *Proc. 13th Int. Conf. on Plasma Physics and Controlled Nuclear Fusion Research*, Washington, D.C., Oct. 1-6, 1990, IAEA-CN-53/E-2-2.
[5.12] R.W. HARVEY et al., "Limitations on lower hybrid heating of dense, hot plasmas," *Proc. 3rd Topical Conf. on RF Heating of Plasmas*, Pasadena, p. A7 (1978).
[5.13] N.J. FISCH, A.H. BOOZER, *Phys. Rev. Lett.* **45**, 9 (1980).
[5.14] J.-G. WEGROWE, "Critical Issues for the Application of Lower Hybrid Waves to the Next Step Device,"*Proc. Workshop on Strong Microwaves in Plasmas*, Suzdal, USSR, Sept 1990.
[5.15] Y. BARANOV, A.R. ESTERKIN, "Lower hybrid current drive and optimisation of power spectrum," ITER-IL-PH-6-9-S-16 (1989).
[5.16] E. BARBATO, F. SANTINI, "Ray tracing and steady-state modeling," ITER-IL-PH-6-9-E-15 (1989).
[5.17] R.S. DEVOTO et al., "Modeling of lower hybrid current drive in self-consistent elongated tokamak equilibria," ITER-IL-PH-6-0-U-6 (1990).
[5.18] R. S. DEVOTO et al., "Current drive by neutral beams in ITER," ITER-IL-PH-6-9-U-8, Feb. 1989.
[5.19] IAEA Workshop on Non-Inductive Current Drive, Garching, 1987.
[5.20] J.-G. WEGROWE, G. ZAMBOTTI, *Proc. 16th. Eur. Conf. on CFPP*, Venezia, IV-1247 (1989).
[5.21] P. BONOLI, R.C. ENGLADE, *Phys. Fluids* **29**, 2937 (1986).
[5.22] P. BONOLI, E. OTT, *Phys. Fluids* **25**, 359 (1982).
[5.23] E. BARBATO, A. CARDINALI, F. SANTINI, in *Proc. of the 4th. Int. Symp. on Heating in Toroidal Plasmas*, Roma (1984).
[5.24] See e.g., J. VACKLAVIK et al., *Plasma Physics* **25**, 1283 (1983).
[5.25] R. CROCI, E. CANOBBIO, *Z. für Naturf.* **A-42**, 1067 (1987).
[5.26] G. V. PEREVERZEV, *JETP Lett.*, **44**, 549 (1986).
[5.27] D. MOREAU et al, *15th. Eur. Conf. on CFPP*, Dubrovnik, III-995 (1988); and *16th. Eur. Conf. on CFPP*, Venezia, III-1169 (1989).
[5.28] J.-G. WEGROWE, "Broadening of the Lower Hybrid Wave Spectrum due to Departure from Axisymmetry," *Proc. 14th Conf. Eur. CFPP*, Madrid, III-911 (1987).
[5.29] S. I. POPEL, V.N. TYSTOVITCH, "New theory of the spectral gap filling," presented at the *Int. Workshop on Strong Microwaves in Plasmas*, Suzdal, USSR, Sept. 1990.

[5.30] J.-G. WEGROWE, G. ZAMBOTTI, presented at the *8th. Topical Conf. on Application of RF Power to Plasmas*, Irvine, Calif., May 1-3, 1989.
[5.31] *Research and Development Needs for ITER Engineering Design*, IAEA/ITER/DS/20, IAEA, Vienna (1991).
[5.32] B.B. KADOMTSEV, *Sov. J. Plasma Phys.* **1**, 5 (1975); V.V. PARAIL, G.V. PEREVERZEV, *Sov. J. Plasma Phys.* **6** (1), (1980).
[5.33] D. EHST, "Fast wave current drive–ray tracing for ITER and simulations of the DIII-D experiment," ITER-IL-HD-7-7-10 (July, 1990); see also §5.6.
[5.34] J.M. RAX, D. MOREAU, *Nucl. Fusion* **29**, 10 (1989).
[5.35] J.-G. WÉGROWE, G. TONON, *IAEA Tech. Comm. Meeting on Non-inductive Current Drive in Tokamaks*, Culham, 1983; J.-G. WEGROWE, *Comments in Plasma Phys.*, **8**, 6 (1984).
[5.36] K. USHIGUSA, *17th CFPP - EPS Conf.* Amsterdam, 1990, to be publ. in *Plasma Physics & Controlled Fusion*, 1990.
[5.37] M. NEMOTO et al., "Acceleration of beam ions in simultaneous injection of NB, LH waves on JT-60," *Proc. 17th CFPP - EPS Conf. Contr. Fusion and Plasma Heating*, Vol. III, p. 1183 Amsterdam, (1990).
[5.38] YU. BARANOV, A.R. ESTERKIN, "LH current drive and optimization of power spectrum," ITER-IL-PH-6-9-S-16 (1989); E. BARBATO, F. SANTINI, "Quasi-linear effects on a absorption of LH waves," ITER-IL-PH-6-9-E-13 (1989); P. PAVLO, L. KRLIN, Z. TLUCHOR, "Influence of a particles on the LH current drive in a fully quasi-linear approach," ITER-IL-PH-6-9-S-23 (1989).
[5.39] M. BRAMBILLA, *Nucl. Fusion* **16**, 1 (1976).
[5.40] T.K. NGUYEN, D. MOREAU, *Proc. 12th Symopsium on Fusion Technology*, Vol. 2, p. 1381, Jülich, FRG (1982).
[5.41] G. TONON et al., ITER-IL-HD-3-9-E-1 (1989).
[5.42] J. YUGO et al., "Lower hybrid current drive system," ITER Heating and Current Drive Technology Meeting, July 18–22, 1988.
[5.43] A. CARDINALI et al., "Parametric decay instability for LH waves in large devices," NET Report (to be published).
[5.44] D.A. EHST, C.F.F KARNEY,"Neoclassical effects on RF current drive," Argonne Nat'l. Lab. Report ANL/FPP/TM-247, Apr. 1990.
[5.45] G. GIRUZZI, *Nucl. Fusion* **27**, 1934 (1987).
[5.46] H.D. PACHER, G.W. PACHER, M.F.A. HARRISON, ITER-IL-PH-13-0-E-6 (1990).
[5.47] R. YOSHINO, M. SUGIHARA, "Discharge scenarios in ITER and maximum V-s sparing due to PF system," ITER-IL-PH-6-0-J-4 (1990).
[5.48] P. BONOLI, "1-1/2 D transport code studies of lower hybrid assisted ramp-up in the ITER device," ITER-IL-PH-6-0-U-1 and U-3 (1990).
[5.49] G. PEREVERZEV, "Ohmic and LH Assisted Current ramp-up in ITER," ITER-IL-PH-6-0-S-5 and S-6 (1990).
[5.50] J.-G. WEGROWE, G. ZAMBOTTI, "Modelling of plasma current rampup by LH waves: comparison with experiments and application to NET," *Proc. 17th CFPP-EPS Conf.*, Amsterdam, 1990, Vol. III, p. 1235 (1990).
[5.51] G. PEREVERZEV, "Optimization and Operational Cycle with LH Ramp-up Assist in ITER," ITER-IL-PH-6-0-S-5, Feb. 1990.
[5.52] *ITER Concept Definition*, IAEA/ITER/DS/3, IAEA, Vienna (1989); J.R. GILLELAND et al., *Nuclear Fusion* **29**, 1191 (1989).
[5.53] J.L. LUXON et al., *Proceedings of 17th EPS Conference on Controlled Fusion and Plasma Heating*, Amsterdam, Netherlands, June, 1990.
[5.54] W.W. HEIDBRINK et al., *Nucl. Fusion* **28**, 1897 (1988).
[5.55] W.W. HEIDBRINK, "Measurements of classical deceleration of beam ions in the DIII-D tokamak," ITER-IL-PH-6-0-U-7 (1990).

[5.56] R.B. CAMPBELL, G.D. KERBEL, "A Study of Alfvén Waves Driven by Neutral Beam Injection in ITER," ITER-IL-PH-6-9-U-6 (1989).

[5.57] R.B. CAMPBELL, "A study of global Alfvén wave eigenmodes driven by energetic particles in the ITER and DIII-D," ITER-IL-PH-6-0-U-8 (1990).

[5.58] A.R. POLEVOY, S.E. SHARAPOV, "An analysis of the experiments on T-11 under super Alfvénic beam injection," ITER-IL-PH-6-9-S-6 (1989); P. POLEVOY, S.E. SHARAPOV, "Alfvén wave instabilitiy in ITER under injected high energy atoms with E > 1MeV," ITER-IL-PH-6-9-S-22 (1989); A.R. POLEVOY, S.E. SHARAPOV, "Alfvén wave instability in ITER with injected high energy atoms with E ≥ 1MeV," ITER-IL-PH-6-0-S-7 (1990); V.D. YEGORENKOV, K.N. STEPANOV, "Ion cyclotron instability supression in NBCD ITER plasma," ITER-IL-PH-6-0-S-8 (1990).

[5.59] C. BOLEY et al., "Convenient numerical fits for neutral beam cross section," ITER-IL-PH-6-9-U-1 (1989); R.K. JANEV, C. BOLEY, D. POST, *Nucl. Fusion* **29**, 2125 (1989); J.W. STERNS et al., "Penetration of an energetic D^0 beam into an ETR plasma," ITER-IL-PH-6-9-U-9 (1989).

[5.60] D.R. MIKKELSEN, C.E. SINGER, *Nucl. Technol./Fusion* **4**, 237 (1983).

[5.61] R.S. DEVOTO et al., "Current drive by neutral beams and lower hybrid in ITER," ITER-IL-PH-6-9-U-8 (1989); R.S. DEVOTO, "ITER current drive performance and power requirements under several neutral beam options," ITER-IL-PH-6-9-U-14 (1989); V.M. KULYGIN et al., "Steady state NB current drive in ITER," ITER-IL-PH-6-9-S-5 (1989); V.M. LEONOV, A.R. POLEVOY, "Calculation of the NBCD efficiency for the discharges with enhanced density," ITER-IL-PH-6-9-S-19 (1989); N. FUJISAWA, "Bootstrap current and NB current drive," ITER-IL-PH-6-9-J-1 (1989).

[5.62] V.M. LEONOV, A.R. POLEVOY, "NBCD in ITER–numerical simulations of the Possible Scenarios," ITER-IL-PH-6-9-S-25 (1989); V.M. LEONOV, A.R. POLEVOY, "Analysis of NBCD system possibilities to control the current profile," ITER-IL-PH-6-9-S-20 (1989); N. FUJISAWA, "Neutral beam power profile and resultant current profile," ITER-IL-PH-6-0-J-2 (1990); N. FUJISAWA, "Density limit for 1.3 MeV neutral beam," ITER-IL-PH-6-0-J-3, (1990); C.D. CHALLIS, "Simulations of neutral beam current drive and current profile in ITER," ITER-IL-PH-6-0-E-8 (1990)

[5.63] T. MIZOGUCHI, N. FUJISAWA, "Hybrid operation scenario using NBCD," ITER-IL-PH-6-9-J-4 (1989).

[5.64] N. FUJISAWA, "Possibility of hydrogen beam injection," ITER-IL-PH-6-0-J-4 (1990).

[5.65] N. FUJISAWA, "Neutral beam shinethrough power in ITER," ITER-IL-PH-6-0-J-1 (1990).

[5.66] D. W. SWAIN et al., "Fast wave current drive and ion cyclotron heating system for ITER - final report of the specialists' meeting," ITER-IL-7-0-20, Oct. 1990.

[5.67] A. FUKUYAMA et al., "A frequency survey for fast wave current drive in ITER," ITER-IL-PH-6-9-J-6 (1989).

[5.68] J. JACQUINOT et al., "FWCD new developments - EEC contribution," ITER-IL-HD-7-0-8 (July 1990); D. B. BATCHELOR et al., "Current drive calculation update for the fast ion cyclotron wave current drive system for ITER," ITER-IL-HD-7-0-7 (July 1990).

[5.69] Overall constant and temperature variation from FWCD benchmark runs reported at 30 July–1 Aug. 1990, ITER FWCD Design Meeting, particularly J. JACQUINOT, "FWCD: new developments"; H. KIMURA et al., "Update on calculations of the heating and current drive efficiency for high-frequency ion cyclotron system for ITER"; and D.A. EHST, "Fast wave current drive: ray tracing for ITER and simulations of the DIII-D

experiment." Z_{eff} dependence is a fit to data by J. JACQUINOT, "Summary of JET IC work," presented at the ITER Fast-Wave Current Drive Specialists' Meeting (5-9 March 1990, Garching), ITER-IL-HD-7-0-3. Note that this form also fits Z_{eff} dependence in intermediate frequency regime from V.L. VDOVIN, "Current drive in ICRF frequency range in tokamak-reactor ITER," ITER-IL-PH-6-9-S-11 (1989) and Y. KISHIMOTO et al., in Japanese Contributions to 15th Session of INTOR–IIA, Phase III, Vienna (Dec. 1986).

[5.70] D. B. BATCHELOR, E. F. JAEGER, M. D. CARTER, "Fast wave current drive for ITER using the ORION code," ITER-IL-HD-7-0-2 (Feb. 1990).

[5.71] D.A. EHST, "ITER equilibrium with bootstrap currents, lower hybrid current drive and fast wave current drive," ITER-IL-PH-6-9-U-2, (Feb. 1989); H. KIMURA et al., "ITER ICRF current drive and heating," ITER-IL-PH-6-9-J-2 (Feb. 1989).

[5.72] H. KIMURA, K. HAMAMATSU, A. FUKUYAMA, "High-Frequency Ion Cyclotron Heating and Current Drive System for ITER (Physics)," in ITER-IL-HD-7-0-3 (Feb. 1990).

[5.73] See, e.g., The JET Team (presented by D.F.H. Start), "ICRF Heating in Reactor Grade Plasmas," *Proc. 13th Int. Conf. on Plasma Physics and Controlled Nuclear Fusion Research* , Washington, D.C., 1-6 Oct. 1990, IAEA-CN-53/E-2-1-1.

[5.74] See, e.g., H. KAWASHIMA and the JFT-2M Group, "Fast Wave Current Drive Experiment on JFT-2M," presented at *The US/Japan Current Drive Workshop*, Lawrence Livermore National Laboratory, Feb. 1990.

[5.75] See J.C. HOSEA et al., "ICRF Heating in Several Regimes on TFTR," *Proc. 13th Int. Conf. on Plasma Physics and Controlled Nuclear Fusion Research* , Washington, D.C., 1-6 Oct. 1990, IAEA-CN-53/E-1-5; H. KIMURA et al., "Higher harmonic ICRF heating and beam acceleration in JT-60," IAEA-CN-53/E-1-3-1, ibid.

[5.76] See B. TUBBING et al., *Nuc. Fusion* **29**, 1953 (1989); P. COLESTOCK et al., *Proc. 8th Topical Conf. Radio-Frequency Power in Plasmas* (Irvine, CA, 1989), P. 189; A. M. MESSIAEN et al., ibid, p. 362.

[5.77] R. KOCH, "Fusion Reactivity Enhancement, Alpha and other fast Particle Effects in ICRF Heating of Reactor-Grade Tokamaks," *Proc. 13th Int. Conf. on Plasma Physics and Controlled Nuclear Fusion Research* , Washington, D.C., Oct. 1-6, 1990, IAEA-CN-53/G-2-9.

[5.78] See, e.g., P. REBUT, "Recent JET Results and Future Prospects," *Proc. 13th Int. Conf. on Plasma Physics and Controlled Nuclear Fusion Research*, Washington, D.C., Oct. 1-6, 1990, IAEA-CN-53/A-1-2.

[5.79] G. CENACCHI, A. TARONI, JET Report JET-IR88/03 (1988).

[5.80] H. KIMURA et al., "Update on calculations of heating and current drive efficiency for high-frequency ion cyclotron for ITER," ITER-IL-HD-7-0-9, Aug. 1990.

[5.81] D. SWAIN et al., "Fast wave heating and current drive system for ITER," ITER-IL-7-9-U-2, Aug. 89.

[5.82] J. JACQUINOT et al., "Current Drive for NET and ITER at 19 MHz," ITER-IL-HD-7-9-2, Aug. 89.

[5.83] A.A. GALEEV, *Sov. Phys. JETP* **32**, 752 (1971).

[5.84] R.J. BICKERTON, J.W. CONNOR, J.B. TAYLOR, *Nature Phys. Sci.* **229**, 110 (1971).

[5.85] J.T. HOGAN, *Nuclear Fusion* **21**, 365 (1981).

[5.86] M. MURAKAMI et al., *Proc. 13th Int. Conf. on Plasma Physics and Controlled Nuclear Fusion Research* , Washington, D.C., Oct. 1-6, 1990, IAEA-CN-53/C-1-3.

[5.87] S. BESSHOU et al, *Plasma Physics* **26**, 565 (1984).

[5.88] M.C. ZARNSTORFF, S.C. PRAGER, *Phys. Fluids* **32**, 298 (1986).
[5.89] M.C. ZARNSTORFF et al, *Phys. Rev. Letters* **60**, 1306 (1988).
[5.90] G.A. NAVRATIL et al, "Study of High Poloidal Beta Plasmas in TFTR and DIII-D," *Proc. 13th Int. Conf. on Plasma Physics and Controlled Nuclear Fusion Research* , Washington, D.C., Oct. 1-6, 1990, IAEA-CN-53/A-3-3.
[5.91] C.D. CHALLIS et al, *Nuclear Fusion* **29**, 563 (1989).
[5.92] M.KIKUCHI et al, *Nuclear Fusion* **30**, 343 (1990).
[5.93] N. FUJISAWA, "Comments on Bootstrap Currents in ITER and Improved Operation Scenario," ITER-IL-PH-6-0-J-10 (1990).
[5.94] N. FUJISAWA, "Bootstrap Current and Neutral Beam Current Drive," ITER-IL-PH-6-9-J-1 (1989).
[5.95] M.C. ZARNSTORFF and the TFTR group and collaborators, "Advances in Transport Understanding Using Perturbative Techniques in TFTR," *Proc. 13th Int. Conf. on Plasma Physics and Controlled Nuclear Fusion Research*, Washington, D.C., Oct. 1-6, 1990, IAEA-CN-53/A-2-2.
[5.96] F. X. SÖLDNER, "Profile control with LHW on ASDEX," ITER-IL-PH-6-0-E-7 (1990); K. USHIGUSA, "Current profile control by LHCD in JT-60," ITER-IL-PH-6-0-J-10 (1990); Y. TERUMICHI, "Sawtooth oscillation in ECH and LHCD plasmas in WT-3," ITER-IL-PH-6-0-S-11 (1990).
[5.97] G.R. SMITH, E. WESTERHOF, "Scenario for control of major disruptions by EC current drive," ITER-IL-HD-6-0-28 (July, 1990). See also §5.9.
[5.98] See, e.g., T. TSUNEMATSU et al., "Operational Limits and Disruptions in ITER," *Proc. 13th Int. Conf. on Plasma Physics and Controlled Nuclear Fusion Research* , Washington, D.C., Oct. 1-6, 1990, IAEA-CN-53/F-3-2.
[5.99] J. HOGAN, "Troyon coefficients g ~ 4 for ITER at high q (≥4)," ITER-IL-Ph-11-0-U-5 (1990).
[5.100] J.R. FERRON et al., *Phys. Fluids* B **2**, 1280 (1990); T.S. TAYLOR et al., "Profile optimization and high beta discharges in DIII-D," *Proc. 13th Int. Conf. on Plasma Physics and Controlled Nuclear Fusion Research*, Washington, D.C., 1-6 Oct. 1990, IAEA-CN-53/A-3-1. Note that the definitions of the internal inductance in these refs. differ from that given in this chapter.
[5.101] E. WESTERHOF, *Nucl. Fusion* **27** (1987) 1929. (Note that Figs. 3 and 4, but not their captions, have been interchanged in this reference.).
[5.102] L.E. ZAKHAROV, A.A. SUBBOTIN, "Tearing-mode stabilization by generation of an additional current layer in tokamaks," ITER-IL-PH-11-9-S-2 (1989).
[5.103] E. WESTERHOF, *Nucl. Fusion* **30** (1990) 1143.
[5.104] See S.K. HO, J. PERKINS, "Operating point control, fractional power operation, and sensitivity to confinement assumptions," presented at ITER Workshop on Burn Control, Garching (16-17 June 1990); V.E. LUKASH, "Stabilization of burn instabilities by feedback control of auxillary heating," ibid; S. HANEY, "ITER burn control studies with MACFAST," ibid; J. MANDREKAS, W. STACEY, "A full transport treatment of ITER burn control," ibid.
[5.105] S.W. HANEY, L.J. PERKINS, "Active control of thermonuclear burn conditions for the ITER," ITER-IL-SA-1-0-2 (1990).
[5.106] V.E. LUKASH, "Stabilization of burn instabilities by feedback control of auxiliary heating," presented at the ITER Workshop on Burn Control, Garching, 16-17 June 1990.
[5.107] S. TOKUDA, T. TSUNEMATSU, "Requirement for current density profile for sawtooth suppression," presented at the ITER Specialists' Meeting on Sawtooth Behavior at High Beta, Garching (6-8 August 1990); T. TSUNEMATSU, J. HOGAN, D. PEARLSTEIN, "Summary of specialists' meeting on sawtooth behavior at high beta," ITER-IL-PH-11-0-20 (1990).

[5.108] G. GIRUZZI, T.J. SCHEP, E. WESTERHOF, "Current Drive and Profile Control in NET Plasmas," FOM-Institute for Plasma Physics Report No. RR-PP-89/042, Nov. 1989.
[5.109] L.K. KUZNETSOVA, "Stabilization of m = 2 tearing modes by EC waves in ITER," ITER-IL-PH-6-0-S-1 (1990).

6.0. AXISYMMETRIC MAGNETICS

6.1 INTRODUCTION

The ITER concept is based on a non-circular plasma cross-section, with a vertical elongation of approximately 2. The axisymmetric magnetics design and plasma equilibrium aspects of such non-circular tokamaks are well understood, as evidenced by the successful construction and operation to specification of DIII-D, JET, PBX-M, JFT-2M, FT-1, and FT-2. The physics considerations involved -- electromagnetics, magnetic flux and current penetration within the plasma, and plasma pressure balance -- are fully understood, and sophisticated computer codes for axisymmetric magnetics design, optimization and data interpretation are available among all ITER parties. These design codes are generally well validated against experimental data, and hence the design tools needed for the axisymmetric magnetics design of ITER are available, and there are no truly critical physics issues or unknowns that require resolution prior to defining the ITER design concept. Application of this knowledge during the Conceptual Design Activity (CDA) has made it possible to develop complete and self-consistent axisymmetric magnetics design for the ITER device that meets all design requirements. This design gives high confidence that the plasma configuration, equilibrium control and inductive current drive capability needed to conduct all phases of the ITER operation and research programme will be successfully obtained.

6.1.1 Axisymmetric Magnetics Design Issues.

While the axisymmetric magnetics design of ITER poses no unknown physics, the device configuration and engineering aspects of the magnetics design have a significant impact on the overall ITER design concept. This is particularly true of the poloidal field (PF) system [6.1], where the central solenoid magnet coils [6.2] contribute significantly to setting the overall size (major radius) of ITER [6.3]. Accurate specification of the axisymmetric magnetics requirements for the PF system -- in particular the plasma flux-linkage (volt-seconds) to be supplied by the central solenoid -- is crucial to specifying the minimum size of ITER. Specification of the V-s requirements -- in particular the resistive V-s required for plasma current ramp-up -- is the first of four key axisymmetric magnetics design issues.

The device configuration and magnet technology requirements for ITER and the range of missions that ITER must be capable of also introduce three additional considerations into the axisymmetric magnetics design. The reactor-like device configuration -- with in-vessel blanket/shield modules [6.4] and superconducting poloidal field and toroidal field magnets [6.2] -- puts the PF coils relatively far from the plasma. Under these circumstances, design of the PF system to provide experimental flexibility -- the ability to provide plasma equilibrium over a range of plasma current density profiles and pressures -- to cover the full range of ITER operation conditions [6.5] becomes a second important design consideration.

Similarly, the need to rely on modular in-vessel conducting structures [6.6] for stabilizing the plasma against axisymmetric instabilities must be reconciled with the conflicting desire to design with the maximum allowable plasma elongation. Here it is necessary to balance considerations of reliable control of the vertical equilibrium of the plasma against nuclear performance and assembly/maintenance requirements for the in-vessel modules in which the stabilizing structures must be located. This trade-off, and the importance of elongation in minimizing overall device size, make accurate evaluation and optimization of the vertical stability properties of the ITER plasma a third important design consideration.

Finally, the need to use superconducting magnet technology, the requirement to have a relative thick torus vacuum vessel [6.6], and the large size of ITER all act to limit the toroidal electric field available for plasma breakdown and current initiation. Here the ITER design must necessarily operate at or below the E-field limits in the presently operating generation of tokamak experiments. Under these conditions, provision of a reliable plasma breakdown scheme and evaluation of the effectiveness of rf assist for plasma breakdown becomes the fourth important axisymmetric design consideration.

6.1.2 Topics and Organization

The balance of this chapter is organized in four sections. Section 6.2 introduces the key design considerations (the operational scenario parameters, the l_i-β_p "operations space" specification for experimental flexibility, and the volt-second balance requirements) that form the basis for the design of the PF coil system. The basis of the resistive V-s estimates used for ITER design is described here.

Section 6.3 introduces the ITER reference design double-null (DN) plasma configuration and presents a brief overview of the associated PF coil system design and performance analysis. The related topics of plasma configuration control, alternate plasma configurations (semi-DN and single-null) and the magnetic requirements for the plasma operation sequence are also presented here. Plasma breakdown, with and without rf assist, is given special consideration.

Section 6.4 summarizes the analysis of the axisymmetric mode stability of the plasma column and presents the "Twin Loop" modular stabilizing structure concept developed during the CDA. The subject of computational methods for evaluation of the dynamic evolution of the plasma column during transient events (disruptions and loss-of-vertical-control) is also presented here. Finally, Sect. 6.5 presents an overall summary of axisymmetric performance and identifies issues for further study.

6.1.3 Relation to Other Design Elements

The subject of axisymmetric magnetics is closely tied to the design of the PF system -- especially the PF coils and power supplies -- and the electromagnetic design of the in-vacuum-vessel blanket/shield modules, the primary torus vacuum vessel and the device cryostat. Engineering considerations associated with these systems determine much of the final plasma magnetics design for ITER. The design and performance summaries for these systems presented here are necessarily brief. Refer to the respective poloidal field system [6.1], magnet systems [6.2], and confinement systems [6.6] reports for more details of the considerations involved and the design

concepts developed. Important aspects of other physics task areas that are related to or affect axisymmetric magnetics will also be found in other parts of this report.

- Plasma Performance: MHD Stability [§2.2] -- discussion of plasma profile effects and plasma operation region;
- Power and Particle Control: Optimization of Divertor Geometry [§3.5] and SN/DN Comparison [§3.6] -- plasma magnetic configuration requirements and effects of up/down magnetic asymmetries;
- Disruptions: Characteristics of Vertical Displacement Events [§4.2] -- simulation of plasma evolution following thermal quench and/or loss of vertical position control;
- Heating and Current Drive: Ionization Preheating and Current Initiation [§5.2] -- breakdown considerations and the role of RF assist; and Noninductive Current Ramp/ Ramp-down Assist [§5.3.2] -- LH assist for V-s savings and/or high plasma current;
- Diagnostics: ITER Diagnostic System [§7.3] -- magnetic diagnostics; and 7.4, Diagnostic Access [§7.4] -- access requirements imposed on PF coils.

6.2 AXISYMMETRIC MAGNETICS REQUIREMENTS

6.2.1 Basic Requirements

The basic requirements for plasma axisymmetric magnetics are: (1) to provide the plasma configurations, static plasma equilibrium fields, slow equilibrium control and inductive flux-linkage (V-s) required to conduct the ITER Operations and Research Programme, (2) to provide a plasma operation cycle (sequence of events that comprise a single machine pulse) suitable to achieve the plasma configurations defined in (1), (3) to provide conducting structures and active control fields to reliably stabilize axisymmetric modes of the plasma throughout the operational cycle defined in (2), and (4) to provide sufficient operational flexibility with regard to a range of operational scenarios (plasma current, beta and pulse duration) and plasma profile variations within a given scenario to be able to (a) conduct the full range of missions foreseen within the ITER Operation and Research Programme, and (b) accommodate foreseeable degrees of physics and/or technological uncertainty. These requirements are quantified in more detail in the Sections that follow.

6.2.2 Equilibrium Analysis Method and Validation.

An accurate calculation of the plasma equilibrium underlies all of the axisymmetric magnetics design presented below. The plasma equilibrium and optimization studies carried out during the ITER CDA use free-boundary plasma equilibrium models. These models, which solve the Grad-Shafranov equilibrium equation, are implemented numerically in various design codes available among the ITER parties. Extensive studies with these codes have been conducted during the CDA. Comparison of equilibrium analysis results during the CDA has demonstrated that there is good agreement (to within ~1% in PF coil currents) among all of the equilibrium codes. The key requirements to obtain agreement are: (1) accurate representation of the PF coil geometry (including non-uniform current density in coils with structural grading) and (2) specification of the plasma current density profile, $j(\Psi^*,R)$ and the plasma pressure profile, $p(\Psi^*)$, in a manner that is independent of the

functional forms of $j(\Psi^*, R)$ and $p(\Psi^*)$ implemented in the equilibrium model. Here Ψ^* is the normalized poloidal flux within the plasma, and R is the major radius.

As is well known, to satisfy requirement (2), it is sufficient to specify the plasma profile parameters such that the dimensionless internal inductivity, l_i, and poloidal beta, β_p, have given values. Provided this is done, the plasma flux configuration and PF coil currents are essentially independent of the mathematical form implemented in a given code to parametrize $j(\Psi^*, R)$ and $p(\Psi^*)$. Here, the internal inductivity is defined in terms of the internal poloidal magnetic energy by

$$l_i(3) = 4U_p/\mu_o R_o I^2 \qquad (1)$$

where U_p is the poloidal magnetic energy internal to the plasma boundary. The value of $l_i(3)$ is a measure of the peakedness of the current profile, with lower (higher) values of $l_i(3)$ denoting a less (more) peaked profile. Poloidal beta is defined as

$$\beta_p(3) = 2\mu_o\langle p\rangle/\langle\langle B_p\rangle\rangle^2 \qquad (2)$$

where $\langle p\rangle$ is the volume-averaged plasma pressure, B_p is the poloidal magnetic field, and $\langle\langle B_p\rangle\rangle$ denotes the poloidal line average of B_p on the plasma boundary.

The notation (3) in $l_i(3)$ indicates that the definition adopted as an ITER design parameter is one of three possible definitions of inductivity in use within the fusion community. The alternate definitions, $l_i(1)$ and $l_i(2)$, result in different numerical values for a given current density profile j(r). The differences are significant (~30%) for the highly elongated plasmas characteristic of ITER design. If the definition of l_i being used is not explicitly given, or if only a "generic" l_i is used, some caution is needed in interpreting experimental data or comparing equilibrium analyses. A similar situation applies for β_p. There are three definitions in common use, with minor differences (~15%) in numerical value for a given pressure profile. Again, if the definition being used is not given, caution is needed. In this chapter, references to l_i or β_p always use the $l_i(3)$ and $\beta_p(3)$ definitions, even if the notation (3) is not explicitly included.

The values β_p required for the ITER scenarios adopted for axisymmetric magnetics design and the associated ranges of $l_i(3)$ and β_p that define the l_i-β_p "operational space" for each scenario are presented in the following two Sections.

6.2.3 A1 Operational Scenario and Plasma Profile Parameters.

The axisymmetric magnetics design of ITER is largely set by the requirements for a nominal 22 MA physics operational scenario. This scenario, denoted hereafter as the "A1 Physics" scenario, features sufficient inductive current drive capability to establish a 22 MA plasma and provide a burn pulse $\geq$ 200 s, and also explicitly provides experimental flexibility with regard to the ranges of l_i and β_p that can be accommodated during the fusion burn.

Profile parameters for the A1 scenario: The nominal internal inductivity and pressure profile parameters for axisymmetric magnetics design for the A1 scenario are $l_i(3) = 0.65$ and $\beta_p(3) = 0.6$. These values respectively correspond to the mean current profile for optimal MHD stability at high toroidal beta [§2.2], and the plasma pressure needed to give a fusion power of 1100 MW. These parameters are for the fusion burn phase [from start-of-burn (SOB) to end-of-burn (EOB)] with an ignited plasma and nominal plasma temperature, density and composition. Other profile parameters apply

for the pre-ignition start-of-current-flattop (SOFT) phase, for ignited operation with modified fusion power or plasma composition, and for alternate operation scenarios.

Range of plasma profile parameters for the A1 scenario: The nominal A1 profile parameters given above are estimated values based on the expected plasma conditions. These precise values of the profile parameters actually realized will likely be somewhat different from these design parameters, and in any case will vary over a range owing to variations in plasma conditions possible within the A1 scenario. For axisymmetric magnetics design purposes, the inductivity profile parameter range is $0.55 \le l_i(3) \le 0.75$. This range encompasses the range of current profiles that result in acceptable MHD stability at high toroidal beta [§2.2].

The range of plasma pressures selected corresponds to $0.4 \le \beta_p(3) \le 0.8$. This pressure range provides approximately a factor-of-two decrease or increase in the plasma reactivity for reference plasma composition (Z_{eff}, impurity and thermal helium fractions) [§1.3], or alternatively, the ability to maintain constant fusion power with corresponding variations in the plasma composition.

The plasma profile parameter ranges required for low-β operation (with ohmic heating only) is $0.55 \le l_i(3) \le 0.75$ and $0 \le \beta_p(3) \le 0.2$. These parameters apply for the start-of-current flattop (SOFT) state prior to the initiation of auxiliary heating.

The combination of the ranges of inductivity and poloidal beta define a rectangular l_i-β_p "operations space" for ignited plasmas in the A1 scenario, as shown in Fig. 6-1. This operations space region describes the expected region within which experimental operations can be conducted, and thus quantifies the axisymmetric magnetics requirements for "experimental flexibility."

Alternate operations scenarios: Alternate operations scenarios are required for high-current physics operation and long-pulse, steady-state technology phase operation. For axisymmetric magnetics design, it is necessary to specify both the scenario parameters and the expected range of the profile parameters within each scenario. Parameters of the five scenarios used for design are summarized in Table 6-1. The range of internal inductivity in all scenarios is $0.55 \le l_i(3) \le 0.75$. The range of

TABLE 6-1. OPERATIONAL SCENARIO PARAMETERS FOR AXISYMMETRIC MAGNETICS DESIGN (all with $0.55 \le l_i(3) \le 0.75$)

Scenario	Description	I(MA)	β_p(nom)	β_p Range	Feature or [Limitation]
A1	Physics	22	0.6	0.4-0.8	≥200-s burn @ $l_i(3)$=0.75
A2	Physics	25	0.6	0.4-0.8	~50-s burn @ $l_i(3)$ = 0.75
A3	Physics	28	0.5	0.4-0.6	[$0.6 \le l_i(3) \le 0.7$] [requires 20 V-s non-inductive CD assist during current rampup]
B1	Technology	15.4	1.4	1.0-2.0	~130 V-s for burn [$\beta_p \le 1.8$ for $l_i(3)$ = 0.55]
B2	Technology	21.4	1.0	0.6-1.4	wall load ~1.5 MW/m^2

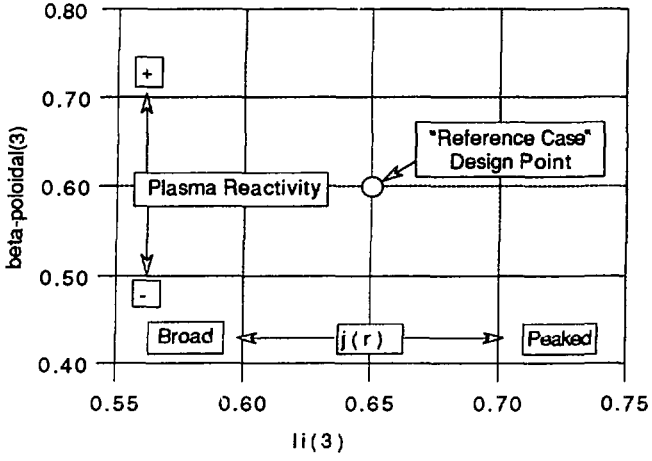

FIG. 6-1. Plasma profile operations space for the A1 physics scenario (ignition/burn)

plasma pressure is $0.7 \leq \beta_p/\beta_p(\text{nom}) \leq 1.4$, where $\beta_p(\text{nom})$ is the nominal design value of $\beta_p(3)$ for the respective scenario.

As summarized in Table 6-1, the design currents finally specified for the PF system (see §6.3) impose minor operational limitations on the A3 (28 MA) physics and B1 (15 MA) technology scenarios. The principal limitations are for the A3 scenario, where the inductivity range at 28 MA is restricted to $0.6 \leq l_i(3) \leq 0.7$ and 20 V-s of non-inductive current drive assist are required.

6.2.4 Plasma Volt-second Balance and Resistive Volt-second Requirements

Volt-second balance and analysis method: Calculation of the PF coil currents in the equilibrium analysis described in §6.3.2 below requires specification of the plasma flux linkage Ψ. For the calculated PF currents to be correct, this flux linkage must be consistent with (1) the inductive and resistive fluxes needed for each point in the plasma operation cycle and (2) the plasma profile parameters (l_i and β_p) that apply for the specific point in the operational space being evaluated.

For each of the operational scenarios used for the PF current analysis, equilibria are calculated for three fiducial points (SOFT, SOB and EOB) in the plasma operation cycle, with a range of profile parameters at each point. The flux linkage Ψ specified for each equilibrium calculation is consistent with the plasma V-s balance required at the corresponding fiducial point:

Fiducial point 1: Start-of-Current Flattop (SOFT)

$$0.55 \leq l_i(3) \leq 0.75, \quad 0 \leq \beta_p \leq 0.2$$

$$\Psi_{SOFT} = \Psi_{IM} - [L_p(l_i, \beta_p)I + 0.4\mu_o R_o I] \qquad (3)$$

Fiducial point 2: Start-of-Burn (SOB):

$$0.55 \leq l_i(3) \leq 0.75, \quad \beta_p(\text{min}) \leq \beta_p \leq \beta_p(\text{max}) \text{ per Table 6-1}$$

$$\Psi_{SOB} = \Psi_{IM} - [L_p(l_i, \beta_p)I + 0.4\mu_o R_o I + 10 \text{ V-s}] \qquad (4)$$

Here L_p is the plasma self-inductance, and L_pI is the inductive flux. The magnitude of L_p depends on l_i and β_p and must be evaluated within the equilibrium calculation for each combination of profile parameters.

The flux linkages at SOFT and SOB are the sum of the inductive flux linkage and volume-integrated resistive losses (see discussion below) needed to reach the respective points in the scenario. These fluxes are specified relative to the initial magnetization flux Ψ_{IM} (= 132.8 V-s) [6.1] provided by the PF system prior to plasma initiation. The SOB flux linkage represents the minimum flux required to reach start-of-burn.

Fiducial point 3: End-of-Burn (EOB)

$$0.55 \le l_i(3) \le 0.75, \quad \beta_p(\min) \le \beta_p \le \beta_p(\max) \quad \text{per Table 6-1}$$

$$\Psi_{EOB} = \Psi_{MIN} \text{ (with } I_{PF1} = I_{PF2} = -I_{MAX}) \qquad (5)$$

The flux at EOB is set by PF magnet performance rather than plasma requirements. For the EOB equilibrium calculation, the currents in coils PF1 and PF2 (see §6.3.1) are constrained to be equal, and the minimum (most negative) achievable flux linkage is determined by the peak current capability of PF1 and PF2 (see example calculation in Fig. 6-2), which is approximately –22.7 MA per coil [6.7]. This limit is set by superconductor quench protection.

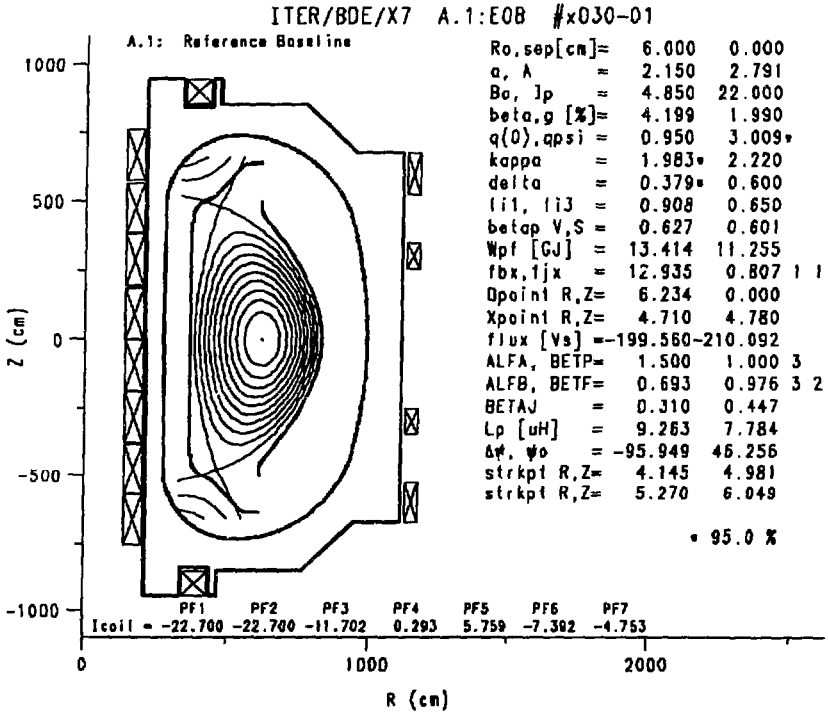

FIG. 6-2. Reference configuration plasma equilibrium and parameters for EOB

The EOB flux linkage calculated in this manner gives the minimum (most negative) PF V-s capability. The difference $\Psi_{IM} - \Psi_{EOB}$ gives the total PF system flux swing capability. The difference $\Psi_{SOB} - \Psi_{EOB}$ gives the V-s available for sustaining the fusion burn. These PF performance parameters depend on l_i, β_p and the scenario parameters. PF system performance is presented in §6.3.

Resistive V-s requirements: As shown in §6.3, about 1/3 of the total PF volt-second capability is allocated for resistive V-s consumption during plasma initiation, current ramp-up, heating, and fusion burn. An accurate estimate of the resistive V-s consumption in these phases is therefore essential for efficient design of the PF system and overall ITER device. The resistive V-s required are estimated as follows:

- Plasma initiation: The use of EC preionization is expected to reduce initiation loss to ≤ 1 V-s.
- Current-rampup: Cumulative resistive flux consumption to SOFT is estimated empirically using the Ejima scaling formula

$$\Delta\Psi_{res} = 0.4\ \mu_0 R_0 I \qquad (6)$$

This formula gives the minimum volume- and time-integrated (Poynting) resistive V-s to reach a stationary j(r) profile with q(edge) ≈ 3 and q(0) ≈ 1. The feasibility of achieving this near-minimum level of resistive consumption in large tokamaks has been verified in ITER Physics R&D experiments recently conducted in DIII-D [6.8], JET [6.9], JT-60 [6.10] and T-10 [6.11]. These experiments demonstrate (Fig. 6-3) that an Ejima coefficient of 0.4 is in fact a practical lower bound to resistive loss during current ramp-up. Resistive loss for 22 MA operation is 66 V-s.

- Heating: Resistive losses during the plasma heating period (~20 s) are estimated to be ≤ 10 V-s (time-average loop voltage ≤ 0.5 V).
- Burn: The plasma loop voltage during burn is estimated using [§1.3]

$$U_{loop} = 2.15 \times 10^{-3} (4.3 - 0.6\ R_0/a)\ Z_{eff}\ [I_{ind} R_0/\kappa_{95} a^2]/T_{10}^{1.5} \qquad (7)$$

Here $I_{ind} = I - I_{bs}$ is the net inductively-driven plasma current, I_{bs} is the bootstrap current and T_{10} is the density-weighted plasma temperature in units of 10 keV. The estimated burn loop voltage for nominal A1 scenario operation at 22 MA with I_{bs} = 3 MA, Z_{eff} = 1.66, and T_{10} = 1 is 0.117 V. A 200-s burn requires 23.4 V-s.

The basis for estimating the resistive V-s consumption during ITER current ramp-up received careful study during the first year of the CDA. The conclusions of this study [6.12] were:

(1) For the "engineering" V-s balance formalism adopted for ITER PF design, the appropriate measure of resistive V-s consumption is the Poynting (time- and volume-integrated) resistive V-s.

(2) Data complied by Ejima in 1986 [6.13] on the plasma surface V-s consumption in various tokamaks showed that the minimum surface V-s consumption is approximately 0.75 $\mu_0 R_0 I$. This is the sum of the internal inductive and resistive components. For typical ITER values of internal inductivity [$l_i(3) = 0.65$], the Ejima data implies $\Delta\Psi_{res} \approx 0.4\ \mu_0 R_0 I$, with an estimated uncertainty of approximately $0.1\ \mu_0 R_0 I$.

A guideline of $\Delta\Psi_{res} = 0.4\ \mu_0 R_0 I$ was recommended [6.14] for PF design. As shown in Fig. 6-3, subsequent analysis of resistive V-s consumption in DIII-D, JET,

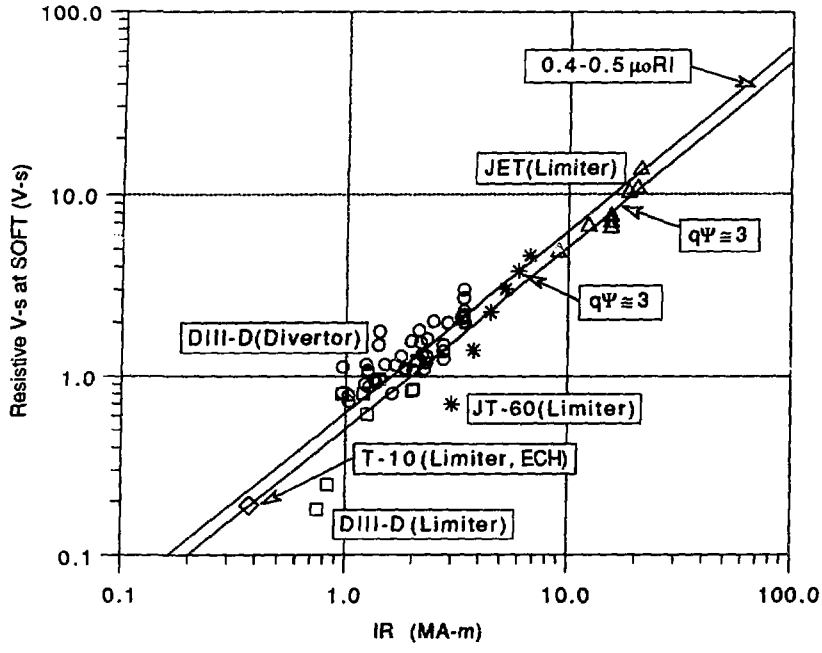

FIG. 6-3. Resistive V-s consumption (Poynting definition): DIII-D, JET, and JT-60.

and JT-60 and simulation studies has confirms this recommendation. Note that the recommended guideline is close to the absolute minimum consumption required to reach SOFT. Achieving this near-minimum consumption in ITER operations will require careful optimization of the current rise phase, and in particular, careful coordination of the plasma current rise and plasma cross-section expansion [6.1] and plasma density rise [6.15].

6.3 PLASMA EQUILIBRIUM

6.3.1 Reference Plasma Configuration and PF Coil Locations

The reference plasma configuration selected for the ITER conceptual design is an up/down symmetric DN divertor plasma with a nominal elongation (at 95% poloidal flux) of approximately 2. The plasma equilibrium fields and inductive flux linkage necessary to initiate and maintain this configuration are produced by a set of 14 superconducting PF coils that are located outboard of the toroidal field (TF) coil. The plasma flux surfaces, PF coil sizes and locations and nominal TF coil and divertor target geometries are shown in Fig. 6-2. Plasma configuration parameters are given in Table 6-2. PF coil parameters are given in Table 6-3. Further details of the PF coil design are given in [6.1,2].

Because of the complexity of the design considerations involved, the interaction of the PF magnet system with the balance of the tokamak, and the needed to assess

TABLE 6-2. PLASMA CONFIGURATION PARAMETERS
CONFIGURATION⇒DN DIVERTOR

R_o (m)	6.0	l_i (3)	0.65
a (m)	2.15	β_p(3)	0.60
I (MA)	22.0	κ_{95}	1.98*
R_x (m)	4.71	δ_{95}	0.38*
Z_x (m)	+/-4.78	q_{95}	3.00*
κ_x	2.22		
δ_x	0.60		

*Calculated from equilibrium analysis

TABLE 6-3. PF COIL SYSTEM PARAMETERS

Coil No.	R (m)	+/-Z (m)	ΔR (m)	ΔZ (m)	I_{max}(MA)	V_{max}(kV)	N(turns)
PF1U/L	1.725*	0.950	0.650*	1.840	22.8	12	520
PF2U/L	1.725*	2.850	0.650*	1.840	22.8	12	520
PF3U/L	1.725*	4.750	0.650*	1.840	22.8	20	520
PF4U/L	1.725*	6.650	0.650*	1.840	22.8	20	520
PF5U/L	3.900	9.000	0.900	0.899	18.5	20	480
PF6U/L	11.500	6.000	0.499	1.499	16.5	20	338
PF7U/L	11.500	3.000	0.499	0.900	9.7	20	208

* Radially graded winding pack, see [6.1],[6.2]

experimental flexibility, design of the plasma configuration and PF system has been an iterative process. The key design requirements and design features that emerge from this iterative process are as follows:

Magnet technology: Sustained fusion burn and the possibility of steady-state operation are essential considerations in the ITER design. Considerations of magnet performance (peak magnetic field, current density and stress levels) [6.2] and power demand during operation mandate the use of superconducting technology. The resulting PF magnet system, which is based on Nb_3Sn superconductor technology, operates at higher overall current densities and is more closely coupled to the plasma than an equivalent system with resistive magnets.

PF coil configuration: Considerations of initial assembly and maintenance of the TF and PF magnets [6.16] require that the PF coils be located outboard of the TF magnets. The need for vertical access gaps for assembly of in-magnet and in-vessel components, and radial access at the equatorial plane for heating and current drive systems [6.17] and for plasma diagnostic measurements [6.18] establish limitations on where the PF coils can be located. The requirement to produce a vertically

symmetric DN divertor plasma and considerations of structural symmetry and coil fabrication lead to a coil system design with up/down symmetry.

Plasma configuration: A DN divertor plasma configuration with divertor channel lengths (X-point to divertor target strike point) ≥ 0.6 m for the inboard divertor channel and ≥ 1.5 m for the outboard divertor channel is required to provide adequately low divertor plasma temperature, impurity control, and helium exhaust. Considerations of divertor geometry [§3.5] lead to a plasma configuration with moderately high triangularity: $\delta_x \approx 0.6$ at the X-point, and $\delta_{95} \approx 0.4$ at 95% poloidal flux. This triangularity is also consistent with the range $\delta_{95} = 0.3$–0.5 needed for optimal plasma stability at high-β [see §2.2]. Considerations for obtaining sufficient plasma current (≥ 22 MA) to insure ignition [§2.1] and minimal overall device size favor a plasma configuration with high vertical elongation. A limit on elongation of $\kappa_x \approx 2.25$ and $\kappa_{95} \approx 2.0$ is set by considerations of passive and active stabilization of the plasma vertical position [§6.4]. A lower limit on edge safety factor of $q_{95} \geq 3.0$ is set by considerations of MHD stability and avoidance of disruptions [§2.2 and §4.4].

Status Relative to Presently Operating Tokamaks: The plasma shape and safety factor of the reference configuration are consistent (or conservative) with respect to the results achieved in presently operating non-circular tokamaks. The relatively high safety factor at 22 MA allows for the possibility of higher current operation at lower q to provide improved confinement margin for ignition.

6.3.2 PF System Optimization and Performance Evaluation

PF optimization: The number, configuration, and location of the PF coils are optimized to meet operational requirements. The 7 independent coil groups, for DN operation, and the subdivision of the central solenoid (CS) into 4 groups is set by the need to control the equilibrium configuration over a range of plasma pressure and current profiles and to provide the range of plasma equilibria (circular ⇒ DN divertor ⇒ circular) needed for plasma start-up, burn and shutdown. The location and size of the gap between PF5 and PF6 is set by the access port needed for in-vessel assembly and maintenance. The gap between the PF7 coils is set by plasma heating and diagnostic access requirements.

PF coil current requirements: The scenario and profile parameters defined in Table 6-1 have been used as the basis of a comprehensive survey [6.19] of the PF coil current requirements. The current envelopes for each PF coil (max-to-min) required for the five scenarios and full range of profiles are shown in Fig. 6-4. The maximum ampere-turn capabilities provided by the PF system are summarized in Table 6-3.

Maximum currents for the individual coils are set by plasma flux linkage and equilibrium requirements at various points in the scenario. Maximum voltages are set by requirements to provide an open-circuit plasma loop voltage of 25 V/turn and plasma equilibrium control in the initial phase of the current ramp-up.

PF system performance: The design PF currents provide sufficient equilibrium and inductive current drive V-s capability to accommodate all major ITER operational requirements. PF coil system V-s capability and the V-s available for burn vary with the operational scenario and with $l_i(3)$ and β_p. The PF V-s capabilities for the five design scenarios at nominal β_p are summarized in Table 6-4. The nominal total V-s capability for the A1 physics scenario with "reference" profile parameters is 331 V-s, with approximately 52 V-s available for burn. The resistive V-s required for a 200-s

TABLE 6-4. PF SYSTEM V-s CAPABILITY AT NOMINAL BETA POLOIDAL

Scenario	I (MA)	Total Flux Swing(V-s)			Burn Flux Swing (V-s)		
	$l_i(3)$ =	0.55	0.65	0.75	0.55	0.65	0.75
A1	22.0	333.5	331.3	330.0	65.8	51.8	38.9
A2	25.0	340.9	338.5	336.9	38.0	22.2	7.4
A3	28.0*	343.6	341.2	339.2	27.7*	10.2*	-6.7*
B1	15.4	335.6	334.8	334.6	135.6	126.5	118.0
B2	22.0	348.9	346.5	344.9	74.4	60.1	46.8

* With 20 V-s non-inductive assist during current ramp-up

TABLE 6-5. SUMMARY OF PHYSICS PHASE V-s REQUIREMENTS

Parameter	Units	Value	Source/explanation
I	MA	22.0	Design plasma current
$l_i(3)$ (at SOB)	--	0.65	"reference" profile
$\beta_p(3)$(at SOB)	--	0.60	"reference" profile
L_p^{SOB}	μH	9.24	Plasma self-inductance
L_pI	V-s	203.1	Inductive V-s
Resistive loss:			
to SOFT	V-s	66.4	$= 0.4\mu_0 R_0 I$
SOFT to SOB	V-s	10.0	estimate
$\Delta\Psi$(to SOB)	V-s	279.4	SOB V-s requirement
I_{BS}	MA	3.0	per physics guidelines
$U_{loop}(I_{ind})$	V	0.117	" " "
t_{burn}	s	200	min. burn length req'nt
$\Delta\Psi$(burn)	V-s	23.4	to meet min. burn req'nt
$\Delta\Psi$(EOB)	V-s	302.8	EOB V-s requirement
$\Delta\Psi_{PF}$(EOB)	V-s	331.3	PF capability at EOB
Burn V-s margin	V-s	28.5	With full PF magnet performance

burn are estimated to be about 23 V-s. The remaining 29 V-s (~125% of the estimated burn V-s needed, or ~7% of the total flux swing) represent margin for increased resistive loss, extending the burn, or shortfalls in PF magnet performance. The allocation of the PF V-s capability among the various components of the plasma is summarized in Table 6-5. The PF design currents impose minor limitations on the B1 and A3 scenarios, as summarized in Table 6-1. The most significant limitation is limitation of the inductivity range for the A3 scenario to $0.6 \le l_i(3) \le 0.7$. The provision of additional non-inductive V-s during start-up allows A3 operation up to $l_i(3) = 0.75$.

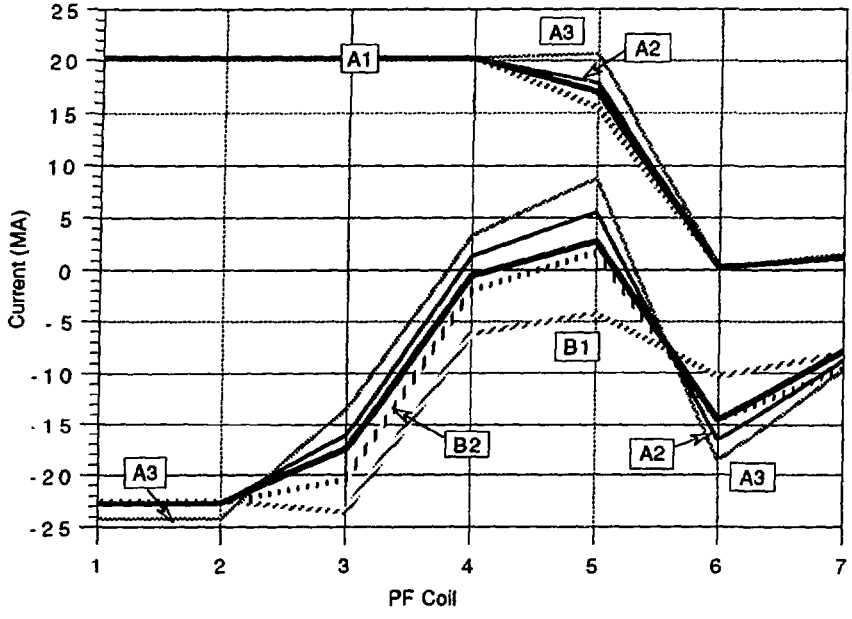

FIG. 6-4. PF coil current envelopes (maximum to minimum) for design scenarios. The envelopes include the effect of plasma profile variations within each scenario

6.3.3 Alternate Plasma Configurations.

The PF currents given in Table 6-3 are for operation with the reference DN plasma. The PF system can also produce semi-DN and single null (SN) plasma configurations. The amount of magnetic asymmetry required to obtain a SN plasma is small and the resulting magnetic configuration is, from the PF coil current and plasma configuration viewpoints, nearly identical to the reference DN case.

A symmetric DN configuration is the primary ITER operating mode, since this mode in principle allows equal sharing of power between the upper and lower divertor targets. However, it is also recognized that ion drift asymmetries will unbalance the heat loads to the upper and lower divertor targets. Operation in the "semi-DN" mode may help to rebalance the divertor heat loads. In this mode, the "inside" and "outside" (measured in poloidal flux) separatrices are no longer coincident, and more heat is expected to flow (in the absence of drift effects) to the divertor connected to the "inside" separatrix. (The definitions of "inside" and "outside" used here are not the usual ones referring to the small and large major radii divertor channels.)

Computational studies of the effect of magnetic asymmetries have demonstrated that for small displacements of the height of the magnetic axis (denoted by Z_0) from the device midplane, the "splitting" of the inside and outside separatrices is approximately $Z_0/(2.5\text{-}4)$ [6.1]. A 1.5-cm displacement of the magnetic axis "splits" the separatrices by about 0.5 cm at the outside midplane. This displacement is comparable to the power scrape-off length expected for H-mode plasmas, and hence should be

sufficient to obtain the desired semi-DN effect. The semi-DN regime will be obtained with $0 \leq Z_0 \leq 3$ cm. The same approximate relationship holds for larger axial displacements. A 5-cm displacement will probably be sufficient to thermally decouple the inside and outside separatrices. For this case, the power will flow only to the divertor connected to the inside separatrix and true SN operation should be obtained. The maximum obtainable axial displacement is limited to about 20 cm by the constraints imposed by the geometry of the reference design first-wall and divertor target contours. The PF system is magnetically capable of producing SN plasmas with a much greater degree of asymmetry and separatrix splitting, but operation with such "strong" SN configurations will require reconfiguration of the in-vessel components.

6.3.4 Plasma Operations Cycle

The reference and alternate plasma configurations described above apply for the portion of the plasma operation cycle from SOFT to EOB, in which the full plasma current is established at SOFT, the plasma is heated to ignition at SOB, and a sustained fusion burn proceeds. This burn can be maintained until the EOB current limit of the PF system is reached. The SOFT, SOB, and EOB fiducial points, together with the IM premagnetization configuration of the PF system, establish the operational envelope for the PF coil currents (see the [6.1] for more details) and are the design cases examined in detail in the l_i-β_p experimental flexibility studies described in §6.3.2.

The ITER plasma operations cycle (referred elsewhere as the plasma operations scenario, but called the plasma operations cycle here to avoid confusion with the operational scenario parameters presented in Table 6-1) includes plasma start-up and shutdown phases that respectively serve to prepare the SOFT plasma configuration and terminate first the fusion burn and then the plasma current following EOB. (Detailed considerations are discussed in [6.1]) The analysis presented there demonstrates that satisfactory start-up and shutdown sequences can be obtained within the PF current envelopes defined by Fig. 6-4 and Table 6-3. Highlights and key magnetic design considerations of the operational cycle are as follows.

PF system premagnetization and plasma breakdown: The reference design operational cycle begins with the PF system premagnetized to an initial magnetization flux linkage at the nominal plasma axis (R = 6.0 m) of 132.8 V-s. Plasma breakdown is initiated by the PF power supplies, which apply an open-circuit one-turn voltage of up to 25 V/turn. Open-circuit here denotes the voltage developed in absence of the torus vacuum vessel and the cryostat vessel.

Owing to the eddy currents induced by the one-turn voltage in the vessel and cryostat, the loop voltage within the torus is reduced and delayed relative to the PF voltage. Substantial in-torus poloidal error fields, up to several hundred G are also produced. To produce a satisfactory breakdown, the premagnetization currents and voltages applied to the PF coil system are adjusted to produce a multipole field null with low error fields ($\leq$ 5 G) in a 1-m diameter plasma breakdown region centered on R = 4.5 m. The desired breakdown condition with this field null and a toroidal electric field of approximately 0.4 V/m ($\approx$ 10 V/turn) develops within approximately 50 ms of application of the PF voltage (see §IV.9 in [6.1]).

Townsend breakdown: As shown by the analysis presented in Fig. 6-5, plasma breakdown via a Townsend avalanche is expected to occur for gas filling pressures that give an initial plasma density of 2×10^{18} m^{-3} if the mean-free path ($1/\alpha$, where α

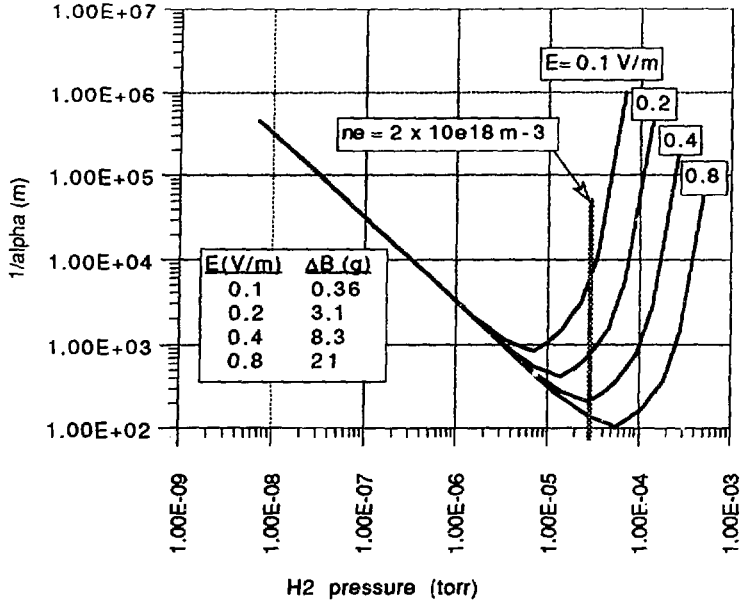

FIG. 6.5 Townsend avalanche characteristics for ITER

is the ionization probability per unit length) for escape of electrons from the breakdown region exceeds about 300 m. Allowing for a factor of ten conservatism on the mean-free-path, this implies that the average poloidal error fields over the breakdown region should be less than about 10 G. The field-null capability of the PF system is therefore sufficient to allow reliable plasma initiation by Townsend breakdown.

RF breakdown assist: While the above analysis suggests that breakdown in ITER can be achieved by a Townsend avalanche alone, finding the proper "tuning" of the experimental conditions may be time-consuming, and the resulting breakdown conditions may not be robust. For this reason, RF breakdown assist, with EC, is planned to supplement the Townsend breakdown. Studies conducted in various tokamaks have demonstrated the effectiveness of both EC [6.11,20,21] and LH [6.22–24] preionization in providing more reliable plasma initiation and a wider range of breakdown parameters at the low electric fields characteristic of ITER plasma start-up. In particular, experiments in T-10 [6.11] and DIII-D [6.20] have shown that application of ~0.05 MW/m^3 of EC power resonant in the center of the breakdown region reduces breakdown delay to less than 10 ms and provides reliable breakdown at E fields of 0.3 V/m, even with non-optimal error fields (up to 50 G) and filling pressures. Extrapolation of these results to ITER plasma initiation on the inside limiter implies an EC frequency of ~180 GHz and a power of ~1-2 MW.

Plasma current initiation and rampup to SOFT: An initial plasma current of 0.5 MA is expected within 0.5 s of breakdown. The rate of current rise achievable is set by the maximum loop-voltage available and the plasma energetics of gas ionization

and impurity burn-through. The availability of RF power for assistance in this phase is expected to help substantially in obtaining a favorable plasma energy balance.

The initial plasma configuration is a near-circular discharge on the inside first wall, which acts as a startup limiter. The plasma size is subsequently expanded and the divertor configuration formed at ~10 MA. The plasma current is then increased to 22 MA at SOFT. The total time to reach SOFT is estimated to be between 40 s and 100 s, limited on the lower bound by avoidance of a MHD-unstable skin current profile and on the upper bound by excessive resistive V-s consumption.

The PF coil current and power supply capabilities provide considerable flexibility in the rate of current rampup and, to a more limited degree, in the shape evolution sequence between initial breakdown to divertor formation. This flexibility is expected to be important in obtaining a current rampup scenario that simultaneously meets MHD stability requirements during rampup and also provides the near-minimum resistive V-s consumption assumed in the PF performance analysis.

Burn shutdown and current termination: The conclusion of the plasma operation cycle after EOB is reached reverses the start-up sequence. The fusion burn is first terminated and the plasma density is subsequently reduced. The divertor to limiter start-up transition is reversed once plasma density is reduced and power levels are low enough to return to limiter operation. Since the PF system reaches its V-s limit at EOB, the plasma current must be reduced simultaneously with the fusion power and density ramp-downs. Coordination of the various plasma operation factors involved to avoid a disruption is the principal operational objective.

Outside limiter start-up/shutdown: The reference plasma operation cycle is based on plasma initiation on the inside limiter. Plasma start-up sequences beginning and/or ending on the outside limiter are also magnetically possible. Here the primary concern is the breakdown phase: the larger major radius and slower E-field penetration through the torus vessel make Townsend breakdown and impurity burn-through on the outside limiter more difficult. RF assist in these start-up scenarios will probably be mandatory. The required EC frequency is ~120 GHz and the power required (extrapolated from T-10 and DIII-D experiments) is ~5-10 MW.

6.3.5 Equilibrium Control

The superconducting PF coils are capable of controlling the plasma current and shape on time scales > 1 s. This control time scale is set by the penetration time of the control fields through the vacuum vessel, and by limitations on peak PF power demand. The power demand limitation can be relaxed by adding PF power conversion modules and the provision of reserve line power capability for control transients.

Shape control parameters and control modes: The plasma shape during burn is defined in terms of five fiducial parameters: $R_{in} = R_o - a$, $R_{out} = R_o + a$, R_x, Z_x, and Z_o. The first four parameters define a symmetrical DN plasma. The fifth (Z_o), defines the degree of vertical asymmetry and applies for semi-DN and SN plasmas. During burn, R_{in}, R_{out}, R_x and Z_x must be controlled to a typical accuracy of +/- 1 cm. More precise control of Z_o (to +/- 3 mm) may be required to balance upper and lower divertor power loading when the plasma power scrape-off length is short (~0.5 cm).

Computational studies (see §4.3.2 and 4.3.3 in [6.1]) demonstrate that the fiducial parameters can be independently controlled by combinations of PF current perturbations that affect only one of the plasma shape parameters. The required con-

TABLE 6-6. PF COIL VOLTAGE (in kV) FOR PLASMA CONTROL

	Control Parameter (see note a for control rates)								Power Supply
Coil	R_{out}	R_{in}	R_x	Z_x	Z_o	I	β_p	l_i	Design (+/-)
PF1	0.0	-0.66	0.08	0.08	-0.30[b]	1.48	-0.53	0.60	2.0
PF2	-0.04	-0.34	-0.10	0.06	0.82[b]	1.40	-0.39	0.49	2.0
PF3	-0.19	0.53	-0.80	-0.02	-1.30[b]	1.02	0.08	0.13	2.0
PF4	-0.03	0.07	-0.10	-0.12	-0.40[b]	0.36	0.04	0.21	2.0
PF5	0.43	-1.37	1.60	-1.35	0.57[b]	0.46	-0.04	2.05	3.0
PF6	-3.13	3.70	-0.20	3.87	-3.20[b]	2.63	-1.43	-4.42	5.0
PF7	1.23	-0.93	-0.10	-0.57	0.79[b]	1.59	1.74	1.35	3.0

[a] Control rates:
R_{out}, R_{in}, Z_x, Z_o: 2 cm/s; R_x: +/- 3 cm at 0.2 Hz,
I: 400 kA/s; β_p: 0.05/s; l_i: 0.01/s

[b] U coil voltage; L coil voltage is less

trol voltages on the PF coils depend on the parameter being controlled and the rate of change of the control parameter. Control rates, PF voltages, and the capabilities provided by the PF power system are given in Table 6-6. Peak PF control power depends on the parameter being controlled and the control rate, typically ≤ 350 MW.

The R_x control capability allows sweeping of the X-point position at a low frequency (~0.3 Hz, set by ac losses in the SC magnets) for divertor peak power load reduction. The plasma current can be controlled via the "OH mode" that produces only a change in flux linkage. Plasma control during the start-up and shutdown portions of the operational sequence can be somewhat less precise. Control of R_{out} to +/- 1 cm is the most important requirement, since this parameter is critical to proper coupling of LH power to the plasma.

Feedback control: The plasma current and shape will be controlled by feedback from magnetic and other data (e.g., divertor heat load). A conceptual design for the control system is shown in Fig 6-6. Use of microprocessor-based numerical algorithms for both plasma shape reconstruction and PF control is envisioned. The control design incorporates a fast-response independent control loop for the vertical position, with a simplified control algorithm. This minimizes response delay in detecting and controlling vertical excursions and increases vertical control reliability. The error signal from the vertical control loop is also fed back into the main PF processor for slow control of the configuration symmetry via the SC coils

Control issues: A precision (+/- 0.5 cm error) real-time (~10 ms) algorithm for reconstruction of the flux surface geometry is essential for shape control. Several promising methods that can be implemented with microprocessors are being studied (see §IV.4 in [c.1]). Robustness of the algorithm and ability to accurately reconstruct a range of plasma shapes are highly desirable features. A final choice of algorithm is not yet possible. Accuracy of the magnetic data inputs is also critical: a precision of +/- 0.5% or better will be required. This includes absolute calibration and integration drift. Drift will become critical for pulse lengths >1000 s. Low-drift integrator

technology appears to be adequate up to this limit; improvements and/or true dc magnetic measurements will be necessary for longer pulses.

Overall reliability of the plasma control system must also be very high, since the consequence of loss of control will be a vertical displacement event and/or a disruption. Measures being studied to improve reliability include the use of redundant sensors and control processors and the adoption of multi-input control algorithms that maintain acceptable control even if a single input data is lost. Robustness of the control algorithm (the ability to maintain acceptable control even with degraded data or with off-normal plasma conditions) is also a key design requirement.

Status of plasma control in present experiments: Satisfactory control of ITER-like elongated plasmas has been demonstrated in the DIII-D and JET tokamaks. The absolute control accuracy (in cm) required for ITER is similar to that achieved in these tokamaks, and is frequently set by residual noise (electromagnetic pick-up, etc.) in the magnetic sensors. The relative control accuracy required for ITER is approximately a factor of two better than presently achieved. The electronic noise environment for ITER is presently unknown, and is an important issue for future study.

The reactor-like geometry and operating conditions expected in ITER also impose new complications. In general, the ITER magnetic sensors will be located further from the plasma surface than in present experiments. This imposes a need for more sophisticated flux surface reconstruction algorithms than are presently used.

6.4 AXISYMMETRIC STABILITY AND DYNAMIC EVOLUTION

The axisymmetric stability of the plasma column and the dynamic evolution of the plasma equilibrium in a loss-of-control situation have been important considerations in the axisymmetric magnetics design work during the ITER CDA. The principal consideration with regard to axisymmetric stability is development of stability models applicable to ITER plasmas and selection of a stabilization concept (passive and active) that provides reliable stabilization of the vertical position of the plasma.

The subject of dynamic equilibrium evolution is primarily one of development and validation of models suitable for predicting the evolution of the ITER plasma equilibrium in non-static situations such as plasma disruption or following loss of equilibrium control. These modeling predictions are crucial for estimating the dynamic behavior of the plasma following a disruption or loss of equilibrium control and for estimating the electromagnetic loads in in-vessel components.

6.4.1 Axisymmetric Stability

The axisymmetric-mode (n=0) stability of the plasma configuration is a key consideration in the overall design of the ITER device. The high-elongation plasma needed for maximum plasma performance is inherently unstable to vertical displacements, and must be stabilized by a combination of passive conducting structures and active control with in-vessel coils. These stabilization and control requirements are not unique to ITER. However, the nuclear and assembly/maintenance requirements of the ITER design impose limitations on the configuration of the stabilizing structures, and on where the stabilizing structures and control coils can be located. These limitations and the need to achieve reliable axisymmetric stability over

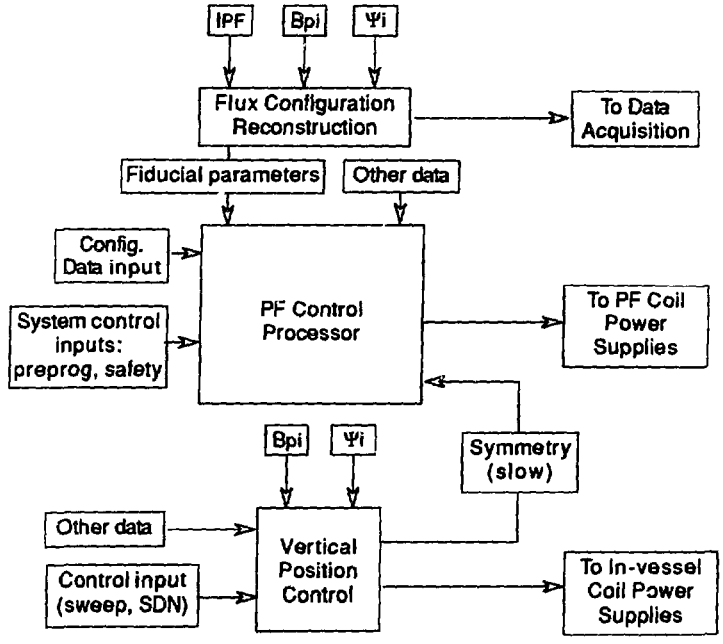

FIG. 6.6. Plasma control system concept

the full range of the plasma configurations required for ITER operation mandate a careful evaluation of the stability properties of the plasma.

Basic requirements: The basic requirement for axisymmetric stability is reliable stabilization and control of the plasma configuration. Major consideration is the stabilization of the vertical position of the plasma. For this mode, the plasma displacement is primarily an m = 1 rigid-body vertical shift. However, higher-order non-rigid modes are also important and must be considered in the stability assessment.

Models and stability margin and growth rate requirements: Most of the stability modeling during the ITER CDA has been with rigid-body displacement models [6.28], in which the stability of the plasma column is evaluated as if the plasma is an array of current-carrying wires, with fixed currents, that is displaced as a unit. While this type of model ignores the true MHD aspects of an m = 1 plasma displacement, it is found to accurately describe [6.25] (to within ~ 10% in DIII-D experiments) the stability properties of plasmas relevant to the ITER plasma configuration.

The rigid-body displacement models used during the ITER CDA allow calculations of two key parameters: the plasma stability margin

$$m_s = -F_{stab}/F_{destab} - 1, \tag{8}$$

and the instability growth rate γ_z defined by

$$Z = Z_o \exp(\gamma_z t). \tag{9}$$

Here F_{stab} is the restoring force on the plasma column produced by the currents induced in the PF coils and passive stabilizing conductors by a vertical displacement, F_{destab} is the destabilizing force on the plasma column produced by the static equilibrium field, and Z_0 is the initial displacement of the plasma from equilibrium at $Z = 0$. The value of m_s reflects the restoring force margin that the passive stabilizing structure provides. The stability margin requirement for ITER design is $m_s \geq 0.5$. This finite margin is required to (1) allow for inaccuracies in the stability assessment introduced by the rigid-body approximation (which overestimates stability relative to a true MHD displacement model), and (2) uncertainties in the properties of the passive stabilizing structure. The value of m_s is determined by the plasma and stabilizing structure geometry and the inductive coupling between the plasma and the stabilizing structure. The value of γ_z is determined by both m_s and the time-constant (L/R time) of the stabilizing structure. The growth rate is the parameter of ultimate importance to the engineering design and cost of the vertical position control system. A maximum permissible growth rate of $\gamma_z = 100\ s^{-1}$ is set as an ITER design requirement: this corresponds to a peak control power of approximately 1 GW for a 15 cm excursion.

Vertical stability assessment: Given the two requirements of $m_s \geq 0.5$ and $\gamma_z \leq 100\ s^{-1}$, the objectives of the vertical stability assessment and optimization conducted during the CDA were to (1) evaluate m_s and γ_z for the range of normal and off-normal plasma operating conditions to be encountered during ITER operations, and (2) to optimize the design of the passive stabilizing structure and active coil consistent with the other electromagnetic, nuclear performance, and assembly/maintenance requirements for the in-vessel and vacuum vessel systems in which the stabilizing structures and active control coils are respectively located. (For details see [6.1].) A brief summary is given below.

Vertical stability design and performance: The vertical position of the plasma column is stabilized by a set of modular "twin loop" structures incorporated in the outboard blanket/shield modules [6.26]. These structures, which are inductively coupled to the outboard wall of the torus vacuum vessel, act in conjunction with the additional stabilizing effect of the inboard wall of the vacuum vessel to reduce the vertical growth rate to $\gamma_z < 30\ s^{-1}$ and provide a stability margin of $m_s = 0.5$ or greater. These values define the worst-case performance for a deteriorated plasma shifted 0.15 m inboard of the normal equilibrium position, with $\beta_p \approx 0$ and $l_i = 0.9$. Stability margin and growth rate for the unshifted "reference case" 22-MA burn configuration plasma with $l_i = 0.65$ and $\beta_p = 0.6$ are significantly better: $m_s \approx 1.1$ and $\gamma_z \approx 15\ s^{-1}$.

Active control of the vertical position is provided by a pair of in-vessel resistive coils. A peak coil current of 300 kA allows vertical excursions of up to +/- 0.15 m to be controlled. Peak control power is approximately 1 GW.

Effect of non-rigid modes and plasma displacements: Preliminary evaluations of plasma stability and growth rate have been carried out with a trial function variational model (see §3.4 in [6.1]) and with the EDDYC-2 and TSC models [§6.4.2]. These models generally confirm the behavior seen in the rigid-body analysis. The plasma displacement for small perturbations is predominately an m = 1 mode, but with higher-order mode components near the boundary and X-point. Growth rates for the m = 1 component of the plasma displacement are higher, typically by ~20-50%.

All of the non-rigid calculations are subject to caveats owing either to the simplified models of the stabilizing structures and vacuum vessel that they

incorporate, or because of the non-rigorous treatment of MHD stability that they are based upon. Further study of these issues is needed during the ITER Engineering Design Activity. The present non-rigid stability results do, however, suggest that the rigid-body wire models used for the CDA studies give a reasonably accurate assessment of the stability properties of ITER plasmas. The non-rigid results also point out the prudence of maintaining $m_s = 0.5$ as a worst-case design requirement.

Status Relative to Present Experiments: Stabilization of the plasma vertical position with a twin-loop stabilizing element has not yet been demonstrated in an operating tokamak. However, the stability models used for ITER analysis have been validated against many tokamak experiments, including plasmas in DIII-D and PBX-M with elongations ≥ 2, and this validation, combined with the margins incorporated in the ITER design provides high confidence that the plasma vertical position can be reliably controlled throughout the ITER operation cycle.

6.4.2 Plasma Dynamics

The equilibrium control and stability analyses discussed above all assume either quasi-static (tens of seconds) evolution of the plasma configuration and/or small displacements. These conditions apply for the normal portions of the ITER plasma operation cycle. However, off-normal conditions such as a plasma disruption or a loss-of-equilibrium control event result in large perturbations to the plasma conditions and a much more rapid evolution of the plasma configuration. Here the evolution time scale is ≤ 1 s and the electromagnetic properties of the PF coil system, vacuum vessel and in-vessel components and also the evolution of the plasma current profile have a significant effect on the resulting dynamic evolution of the plasma configuration. A self-consistant analysis of these effects is necessary to assess the effects on this evolution on ITER components, particularly on the in-vessel blanket/shield modules and on the plasma-facing first wall and divertor plates. This analysis and application of some of the models is described §IV in [6.1].

Models for Dynamic Evolution Analysis: The EDDYC-2 [6.27], PROTEUS [6.28] and TSC [6.29] codes have been applied during the ITER CDA for analysis of dynamic evolution situations. All of these codes are 2-D axisymmetric plasma equilibrium models with the free-boundary plasma scrape-off assumptions. The models all incorporate 2-D axisymmetric representations of the tokamak structures. The 3-D components such as the ITER blanket/shield modules must be modeled as equivalent 2-D conductors. The EDDYC-2 and PROTEUS codes are dynamic equilibrium models with ad hoc plasma profile models. The time evolution of these profiles is specified as an input. The TSC model self-consistantly calculates the plasma evolution, including the current and pressure profiles, by solving the basic MHD equations of motion in conjunction with models for the plasma energy transport and magnetic diffusion. A plasma current "halo" model has recently been added to the TSC code [6.30].

These models have been calibrated against experimental data in situations relevant to analysis of ITER plasma dynamics, and thus have a certain degree of credibility when used in the predictive mode required for the ITER CDA. Sensitivity studies carried out in some of the ITER simulations have also demonstrated that the general characteristics of these models are not overly sensitive to the adjustable parameters that the particular models require. However, the details of some of the predictions that these models provide for ITER must remain subject to careful

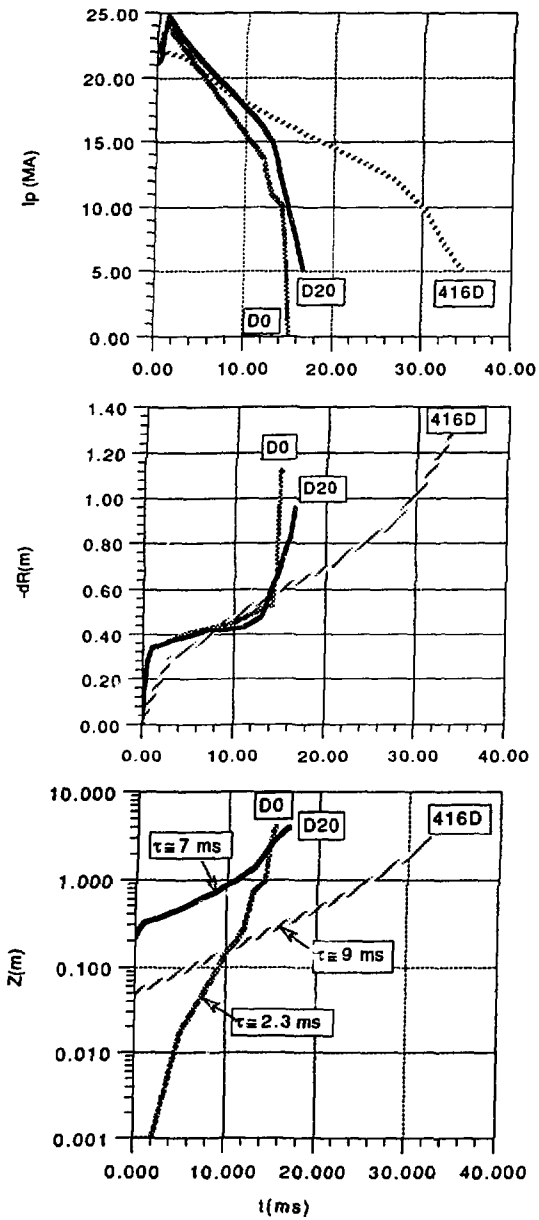

FIG. 6-7. Plasma current and configuration parameter evolution following disruption calculated with *EDDYC-2 (D0 and D20 traces)* and *TSC* (416D traces).

qualification, since the validation of all of the dynamic models is still a state-of-the-art R&D topic.

ITER Plasma Dynamics Simulations: Plasma dynamics during disruptions and loss-of-vertical-control events have been evaluated with simulation codes that calculate the equilibrium evolution self-consistantly with the electromagnetic properties of the vacuum vessel, twin-loop structures and other in-vessel components. These codes successfully predict the major characteristics of the plasma evolution in presently operating non-circular tokamaks, albeit with non-ITER-like stabilizing elements.

Results for the plasma configuration evolution during a vertical displacement event (after loss of vertical position control) from studies with the EDDYC-2 and TSC codes are shown in Fig. 6-7 [6.31]. The predicted plasma evolution in ITER following thermal quench is generally vertically unstable, with growth rates $\geq 100\ s^{-1}$ and a marked non-linear evolution as the axial displacement increases. A similar behavior applies if vertical control is lost owing to a control failure. Consequences of these relatively rapid displacements include significant localized electromagnetic loads developed in the in-vessel components and the likely formation of ex-plasma "halo" currents that will flow in in-vessel structures and rapid quench of the plasma current. The existence and importance of the halo currents in the overall equilibrium evolution is well documented in data obtained in DIII-D, JET and PBX-M [§4.2]. The consequences for ITER appear to be tractable if certain design features are provided, but further development of predictive models and more detailed evaluation is needed in future work. Additional details of the halo currents are discussed in §4.2 and [6.1].

6.5 SUMMARY AND FUTURE NEEDS

The axisymmetric magnetics design of the ITER PF system and in-vessel components meet all major design requirements. The poloidal field system uses superconducting coils, located outboard of the toroidal field coil, to provide the range of plasma equilibrium fields, slow equilibrium control and plasma flux linkage (V-s) needed to conduct the ITER operations and research programme. Double-null divertor plasma configurations and operational scenarios suitable for both 22-MA physics (high-Q/ignition) and 15-MA technology (high-fluence testing) phases are provided.

For 22-MA operation, the total PF flux swing is approximately 330 V-s. This provides sufficient inductive current drive capability for plasma start-up with 66 V-s of resistive loss and a 440-s (330-s minimum) sustained burn in 22-MA physics phase operation. The PF system is also designed to allow a range of plasma start-up and shutdown scenarios, and can maintain the reference 22-MA DN plasma during fusion burn over a range of current and pressure profiles. Increased plasma current (up to 25 MA with inductive current drive and up to 28 MA with non-inductive current drive assist) is also possible.

A modular twin-loop set of passive stabilizing conductors incorporated in the in-vessel blanket/shield modules and a pair of in-vessel resistive control coils provides reliable stabilization and control of the plasma vertical position. The plasma configuration during burn can be controlled or adjusted via the currents in the PF coils and divertor separatrix sweeping for divertor power load reduction and production of semi-DN and single-null plasmas for divertor optimization is possible.

Plasmas can be initiated via Townsend breakdown for inside limiter start-up, but the use of FR assist will enhance breakdown reliability and may be necessary to facilitate impurity burn-through and a prompt current rise in the first 0.5 s of the initiation. RF assist is probably mandatory for outside limiter initiation.

Existing plasma dynamic equilibrium models are generally adequate for the prediction of the evolution of the ITER plasma configuration in disruptions and loss-of-equilibrium control events. The predicted equilibrium evolution is relatively rapid and will result in significant conventional electromagnetic and/or thermal loads on in-vessel components, and the likely formation of ex-plasma halo currents that will flow in the first wall and divertor plates.

Future needs in the axisymmetric magnetics design area fall into three categories. The first category is the possible need for revision of the analysis conducted during the CDA to support modifications of the ITER design parameters -- either because of future changes to the ITER design guidelines, or for studies of alternate ITER designs with increased aspect ratio or other magnetic configuration changes. Repeating the CDA analysis for future design studies is straight-forward. The implementation of standard data formats for electronic exchange of equilibrium information among design codes and among the ITER parties, and for interfacing the resulting output data to engineering analysis codes will facilitate such future work.

The second major need is for more self-consistent coupling of axisymmetric magnetics analysis with other physics and/or engineering modeling. Self-consistent performance assessments that combine axisymmetric equilibrium calculations, energy transport modeling, and MHD stability coupled with calculations that combine dynamic modeling of the equilibrium evolution with plasma edge codes to predict heat and power loads on in-vessel components are needed to accurately quantify the effects of normal and off-normal operating conditions.

The third major need for future work is the improvement and further validation of the dynamic equilibrium models described in §6.4.2. Here improvements in the user interfaces and/or computational speed will facilitate more frequent use of such models for ITER simulations and design calculations. In addition, new physics effects such as the plasma halo currents need to be incorporated into these models and validated against experiments for conditions relevant to ITER design.

REFERENCES (§6.0)

[6.1] *ITER Poloidal Field System*, IAEA/ITER/DS/27, IAEA, Vienna (1991).

[6.2] *ITER Magnets*, IAEA/ITER/DS/26, IAEA, Vienna (1991).

[6.3] *ITER Parametric Analysis and Operational Performance*, IAEA/ITER/DS/22, IAEA, Vienna (1991).

[6.4] *ITER Blanket, Shield and Materials Database*, IAEA/ITER/DS/29, IAEA, Vienna (1991).

[6.5] *ITER Operation and Research Programme*, IAEA/ITER/DS/23, IAEA, Vienna (to be published).

[6.6] *ITER Containment Structures*, IAEA/ITER/DS/28, IAEA, Vienna (1991).

[6.7] J. MILLER, "Operating limits of the central solenoid," ITER-IL-MG-1-0-34 (1990).

[6.8] J. HOGAN, T. TAYLOR, J. LUXON, "Volt-second consumption during current ramp-up in DIII-D," ITER Physics R&D Report, Task PH11 (-U2),

Scaling of Volt-second Consumption During Current Rampup in Large Tokamaks, September 1989.
[6.9] P. LOMAS, "Current ramp-up in JET," Task PH11 (-E1), ibid.
[6.10] H. NINOMIYA, "Volt-second consumption in JT-60 in inductive and LHCD-assisted discharges," Task PH11 (-J1), ibid, March 1990.
[6.11] V.V. ALIKEAV et al, "Low-voltage plasma start-up with EC assist in T-10," ITER Physics R&D Report , Task PH11 (-S1), ibid, September 1989.
[6.12] J. HOGAN et al., ITER-TN-PH-8-6 (1988).
[6.13] S. EJIMA. et al., *Bull. Am. Phys. Soc.* **31** (1986) 1532.
[6.14] ITER Internal Document, ITER-IL-PH-10-9-1 (1989).
[6.15] T. KAISER, ITER Internal Document, ITER-IL-PF-9-0-12 (1990)
[6.16] *ITER Assembly and Maintainence*, IAEA/ITER/DS/34, IAEA, Vienna (1991).
[6.17] *ITER Heating and Current Drive System*, IAEA/ITER/DS/32, IAEA, Vienna (to be published)
[6.18] *ITER Diagnostics*, IAEA/ITER/DS/33, IAEA, Vienna (to be published)
[6.19] J. WESLEY, R. BULMER, L.D. PEARLSTEIN, ITER Internal Documents (ITER-IL-PF-1-0-31, 33, 36, 40, 42, 43, and 44).
[6.20] J. LUXON, B. LLOYD, G. JACKSON, "Low voltage start-up in DIII-D with and without EC assist," ITER Physics R&D Report , Task PH09 (-U2), RF Plasma Formation and Preheating, September 1989.
[6.21] S. TANAKA, "Electron cyclotron preionization and preheating experiments in the WT-3 tokamak," Task PH09 (-J3), ibid, March 1990.
[6.22] M. LARIONOV, "RF discharge in LH frequency range and its use as a preionization in a tokamak," Task PH09 (-S2), ibid.
[6.23] T. YAMAMOTO, "Summary of results from experiments on JFT-2M on plasma formation and current initiation by LH waves," Task PH09 (-J2), ibid.
[6.24] USHIGIUSA, K., "RF plasma formation with LH waves in JT-60," Task PH09 (-J1), ibid.
[6.25] E.A. LAZARUS et al., in Proc. Controlled Fusion and Plasma Heating, Amsterdam 1990, (European Physical Society 1990), p. 427.
[6.26] S. SADAKOV et al., "Twin-Loop for Vertical Control of Highly Elongated Plasmas," IAEA/ITER/DS/15, IAEA, Vienna (1990).
[6.27] L.D. PEARLSTEIN et al., ITER Internal Document, ITER-IL-PF-9-0-34.
[6.28] A. ASTAPKOVICH et al., "Numerical simulation of the plasma current disruption process in tokamak with shape and position evolution," ITER-IL-PF-4-0-13 (July 1990).
[6.29] R. ALBANESE et al., "Numerical studies of the NET via PROTEUS code," in Proc. 12th Conf. Numerical Simulation of Plasmas, San Francisco (1987).
[6.30] S.C. JARDIN et al., *J. Comp. Physics* **66**, 481 (1986).
[6.31] SAYER, R., "ITER Disruption Modeling with TSC," ITER-IL-PF-4-0-15 and PH-8-0-17 (1990).

7.0. DIAGNOSTICS

7.1 INTRODUCTION

During the ITER Conceptual Design Activity, three Workshops on Plasma Diagnostics, involving a total of about 60 physicists, were held [see Refs. 7.1 and 7.2]. Starting from reviews of operating experience with diagnostics on currently operating devices and early concepts of the requirements for plasma measurements, a set of diagnostics for ITER has been developed. Study of the issues has been shared between physicists in the different partner organizations with a wide experience being brought to this challenge.

This Chapter summarizes the results of these design and discussion activities, and also the design integration effort with the ITER Engineering team in trying to accommodate the diagnostics into the overall ITER concept. The proposed diagnostics have been grouped according to their need for operation, i.e., (i) for safety, control and performance in the high-radiation technology phase, and (ii) for plasma optimization and physics understanding during the preceding physics phase. In addition, a potential arrangement of the diagnostics around the tokamak has been developed, sharing the available port space amongst diagnostics and with other systems, such as the pellet fuelling system. The Chapter concludes with a short summary of the ITER-related diagnostic R&D requirements which are addressed extensively elsewhere [7.3]. The detailed description of ITER diagnostic systems including specifications to be placed on measurements of the plasma parameters is published separately [7.4].

7.2 SUMMARY

The ITER objectives of establishing the physics and technology data base for designing a demonstration fusion reactor, require that there should be reliable and detailed measurements of the plasma behavior for all phases of operation. This dictates an extensive and well coordinated set of diagnostics with appropriate spatial and temporal resolutions.

The diagnostics for ITER have been evaluated for their necessity and function during the different operational phases. During the physics phase these diagnostics will be needed to guide the experimental program through the exploration and optimization of various modes of operation. The goal will be to reach ignition in one or more of these modes, and subsequently to explore the ignited regime, both to establish the limits to the operational space and to advance the understanding of the physics of an ignited plasma. In addition to the information needed for the physics understanding of the plasma behavior, the plasma diagnostics on ITER must provide the signals necessary for being able both to control the plasma parameters during operation and to ensure device integrity under fault conditions. These special requirements for operation throughout the physics and technology phase, especially during

the latter with its extended pulses, long operation time and inhospitable environment, are very demanding. All these diagnostics must be radiation-insensitive, extremely reliable and remotely maintainable and must be used from first low power ohmic discharges through to the full burn condition with alpha-particle heating.

Thus, there will be a very extensive set of diagnostics during the physics phase to provide the full profile and multi-time information necessary to optimize the tokamak operation. A reduced set will remain for the technology phase to ensure control of plasma performance and safe operation. In fact there may be some interleaving of physics and technology experiments that will require the retention of adequate diagnostic capability for a longer period.

Several types of abnormal behavior of the discharge that may be dangerous for the machine integrity can be expected in ITER. Uncontrolled rise of the fusion power and plasma disruptions can produce unacceptably high thermal fluxes on the first wall and divertor plates. High mechanical stresses can arise in the first wall elements due to high poloidal currents flowing through these elements during the vertical displacement event. Development of safety diagnostics capable of detecting the onset of these events and controlling them are of primary importance for ITER. At this time, however, the detailed control requirements and response to off-normal events are not well specified. The Physics R&D program on operating tokamaks must improve the definition of the control requirements.

The diagnostics proposed for safety, control and plasma performance evaluation are listed in Table 7-1. This table, which also shows (in italics) many additional diagnostics needed in the physics phase, lists the plasma parameters to be measured, the technique and some comments on the applicability of this technique to the ITER conditions. Feasibility is based on knowledge of operation of diagnostics on current tokamaks, but it is clear that great attention will have to be paid to reliability of operation, internal calibration methods, and quality of signal processing in the implementation of these diagnostics. While it is presently assumed that the diagnostics being considered for safety are the same as those needed for physics measurements and control, duplication and redundancy may have to be provided to assure proper safety response.

Diagnostics that are suggested for control include (i) magnetic loops for plasma current, plasma position and plasma shape, (ii) interferometry for electron density; (iii) neutron spectroscopy for the ion temperature and for deuteron and triton density; (iv) neutron camera and (micro) fission chamber for fusion power; (iv) bolometers for radiative loss; (v) electron cyclotron emission (ECE) and magnetic loops for disruption precursors and (vi) infra-red detection and thermocouples for divertor plate temperatures and plasma vertical position. In addition methods for determining the profile of the current density and the helium concentration in the core and divertor regions must be provided. It is thought necessary to have full measurement of the profiles of electron temperature (by multi pulse LIDAR Thomson scattering and by ECE), electron density (by Thomson scattering and microwave reflectometry) and of the confined alpha-particles (possibly by collective scattering) during the technology phase.

Diagnostics that are suggested for the technology phase have to be accommodated in three large horizontal ports (i.e., ports #2, #10 and #14, the latter shared with the pellet injectors), in some top ports and pumping ducts at bottom. The

TABLE 7-1. DIAGNOSTICS FOR SAFETY, CONTROL AND PERFORMANCE

Plasma parameter	Candidate diagnostics	Comments
Plasma current	Magnetics	Needs methods of measuring steady-state fields
Plasma position and shape	Magnetics	See above
	Neutron camera	Needs validation
q(r) (current density)	Magnetics	$l_i(t)$; see above
	Motional Stark effect†	Needs diagnostic neutral beam
	Faraday rotation	Severe access limitations
	Reflectometry	Needs R&D to demonstrate feasibility
Electron density	Interferometry	Line-averaged; limited chord number
	Thomson scattering	Radial profile; limited time points
	Reflectometry	Radial profile; density fluctuations are issues
Ion/electron temperature	Neutron spectrometry	Core plasma ($r < 2a/3$) at DT phase
	Neutral particle analysis	Plasma periphery; needs diagnostic neutral beam
	CHERS	Needs diagnostic neutral beam and radiation resistant optics
	Thomson scattering	$T_e(r)$ profile; limited time points
	ECE	Suitable for T_e. Issues: harmonic overlap and supra-thermal emission
D/T density	*Neutral particle analysis*	Edge plasma; improves with neutral beam
	Neutron spectrometry	Core plasma; issue: S/N for DD neutrons
	Visible speciroscopy	Edge plasma; needs radiation resistant optics
Fusion power	Neutron yield monitor	Calibration methods need further development
Confined α-particles	Collective Thomson scattering	Needs validation on existing tokamaks and development of 1.5 THz radiation source
	CHERS	Needs diagnostic neutral beam
	Neutral particle analysis	Needs diagnostic neutral beam
Escaping α-particles	γ-spectroscopy	Needs R&D to demonstrate feasibility
	Thermocouples	Slow response time
	Faraday cups	Needs R&D to demonstrate feasibility
	Bolometers	Needs R&D to demonstrate feasibility
Divertor plasma	*Visible spectroscopy*	Needs radiation resistant optics
	Laser induced fluorescence	Needs R&D to demonstrate feasibility
	Langmuir probes	Severe erosion problems
	Reflectometry	Complicated plasma geometry

TABLE 7-1. DIAGNOSTICS FOR SAFETY, CONTROL AND PERFORMANCE (Cont'd.)

Plasma parameter	Candidate diagnostics	Comments
Divertor plasma	*Visible spectroscopy*	Needs radiation resistant optics
	Laser induced fluorescence	Needs R&D to demonstrate feasibility
	Langmuir probes	Severe erosion problems
	Reflectometry	Complicated plasma geometry
Erosion rate	*Visible spectroscopy*	See above
	Tile markers	Needs R&D to demonstrate feasibility
Heat loads	Thermocouples	Slow response time
	IR monitor	Needs radiation resistant optic
Helium concentration	*CHERS*	Needs dedicated neutral beam
	Residual gas analyzers	Relation to He density in the plasma is uncertain
Radiative loss	Bolometers	Limited access; low S/N ratio
Impurity content	*VUV spectroscopy*	For divertor view; access problematic
	X-ray spectroscopy	Key issue: radiation hardening of crystal
	Visible spectroscopy	Needs radiation resistant optics
Runaway electrons	ECE	Suitable in principle; needs validation
	X-ray monitor	Analysis of likely capability is required
Disruption precursors	Magnetics	Possible but not universal
	ECE	T_e fluctuations; uncertain
	Neutron camera	$n_i T_i$ fluctuations; uncertain
	Bolometers	Radiation increase; not universal
Edge localized modes (ELMs)	D(T)-light monitor	Needs radiation resistant optics
	Reflectometry	Suitable in principle; needs validation
	Langmuir probes	Severe erosion problems
	Magnetic probes	Need probes with good time response

† Diagnostics shown *in italics* are additional ones for the physics phase

more extensive set of diagnostics in the physics phase will be allocated on five large horizontal ports with additional access at the bottom. Sightlines through a pumping port are necessary for observations of the lower divertor and X-point region. Other diagnostics of the outer plasma regions and of the divertor need sightlines through the blanket gaps and detailed design is required to determine their feasibility.

Because of severe limitations for the vertical diagnostic access, tangential sightlines are proposed (e.g., for interferometer, n_t/n_d neutron spectrometer and Thomson scattering). A candidate design of the dedicated diagnostic port (i.e., port #10) that allows accommodation of the tangential-viewing diagnostics is shown in Fig. 7-1 along with the allocations and sightlines of the majority of ITER diagnostics.

During the conceptual design phase, the effort has been concentrated on the development of the diagnostic concepts. The studies of the combination of diagnostics sharing the same ports, with the necessary shielding implementation, and their requirements with respect to the rest of the facility, have been initiated. These studies

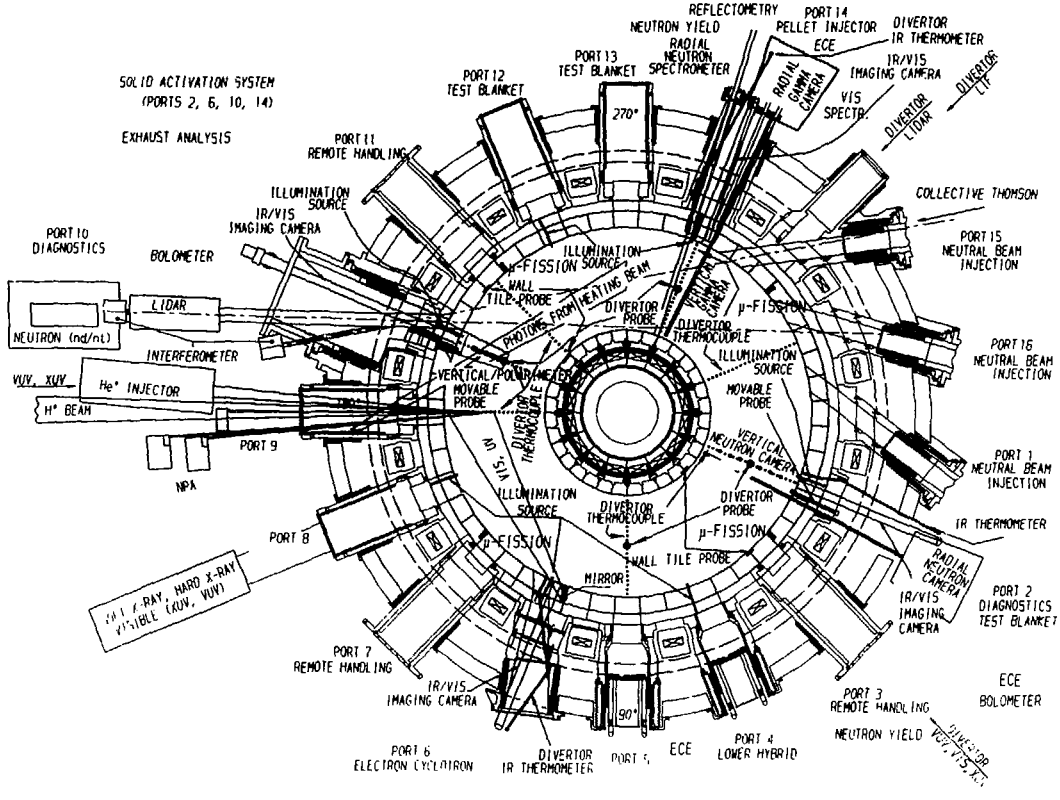

FIG. 7-1 ITER physics phase plasma diagnostics: equatorial plane projection.

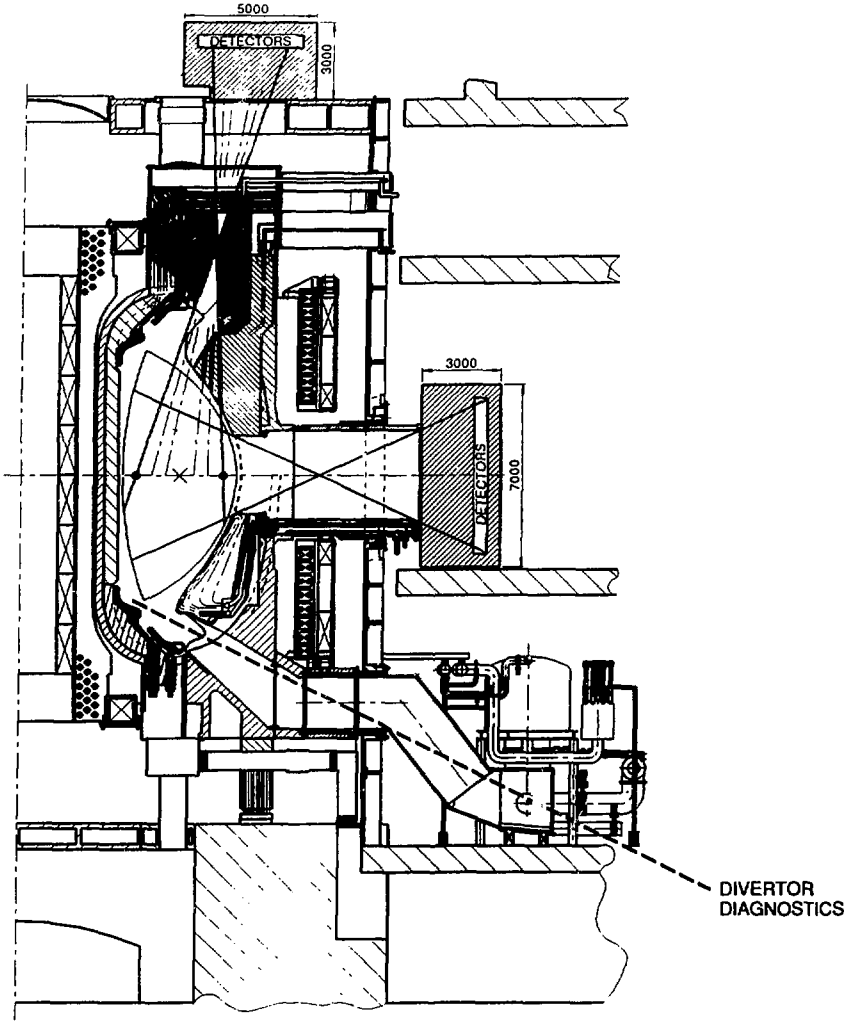

FIG. 7-2 Two-dimensional neutron camera and line-of-sight through pumping duct.

pointed to inconsistencies between the designs of some diagnostics and the reference tokamak design. Many diagnostics (e.g., bolometers and IR cameras for divertor view, interferometer/polarimeter, vertical neutron camera, micro-fission chambers, ECE and microwave reflectometry) require minor or significant changes to be made in the design of the blanket modules. One example is given in Fig. 7-2 that shows the lines of sight of the 2-dimensional neutron camera for measuring the space distribution of the neutron emissivity. This system consists of two collimator arrays that view the neutron emission of the plasma from the side (through a horizontal port) and

from above. The vertical camera needs neutron flux channels through the plug and top blanket module. The present concept involves 10 cm wide (toroidally) channels engineered into the plug, with a wider slot through the blanket segment. A possible compromise is the replacement of some upper and one lower outboard breeding blanket modules adjoining the diagnostic ports by shielding modules of a special design dictated by the diagnostic requirements.

The present approach, which relegated diagnostic systems to being minor modifications or additions to the machine, in comparison to other tokamak systems (heating, fueling, blankets, etc.) must be abandoned during the EDA.

7.3 DIAGNOSTIC ISSUES

There are serious issues involved in the diagnostic design and selection, and machine integration that must be reconsidered and resolved early in the next design phase. Some of these issues are summarized below.

1. The requirements for physical implementation of most of the diagnostics at the tokamak do not match the capabilities offered by the present reference design, developed before the diagnostic requirements could be defined. In particular, it is not possible to get the necessary sightlines for viewing the whole plasma cross-section or the divertor region without modifying the design. Changes in design of horizontal ports, of the sharing of the top and pumping-duct access, and of the blanket structures will be necessary at a number of locations. A special design for the dedicated diagnostic port and for blanket modules adjoining the diagnostic ports is a clear requirement.
2. Because of access limitations in the present conceptual design, a satisfactory solution for real-time measurement of the divertor plate temperature with a full view of the top and bottom divertor plates, which is essential from the point of view of the machine safety, was not found.
3. Some level of flexibility in the design of the ITER sub-systems will be necessary to allow optimization of the diagnostic capability while ensuring that the tokamak operation and shielding are not adversely affected.
4. The requirements arising from the very long pulses, the need to avoid disruptions, and the extensive use of localized non-inductive current drive have not yet been specified in details.
5. The impact of the radiation environment has not been taken properly into account in the selection of the measurement techniques. It is therefore critical that a "radiation effects" R&D program can start immediately.
6. The associated radiation-induced impact of the use of remote handling equipment for maintenance of diagnostics may significantly affect the capability to share ports and even affect the choice of diagnostic technique.
7. Many diagnostics have not been analyzed in detail (e.g., the use of reflectometry for off-axis measurement of the n_e, the use of one or more diagnostic neutral beams in the measurement of $T_i(r)$, $j(r)$, and low-energy confined alpha-particles, and laser-induced fluorescence for measurement in the divertor plasma region).

7.4 DIAGNOSTIC R&D PLAN

The principal tasks of this Diagnostic R&D Plan are listed in Table 7-2. The first and most urgent area of work is in the understanding of radiation effects on diagnostic equipment and demonstrating the feasibility of design concepts. A "Plan for ITER-related Plasma Diagnostic R&D during the Detailed Design Phase (1991-1995)" [7.3] has been prepared and has been reviewed by experts. In fact, the plan contains work which can be done in the later period (1996-2000) and, at some point the urgent scope, necessary to show feasibility of the diagnostic measurements, will be prioritized separately. This plan forms part of the documentation on the Technology R&D Needs [7.5].

7.4.1 Examples of Diagnostic R&D Needs

Examples from diagnostic R&D needs are as follows:

1. Fusion product measurement will have an increased importance in ITER relative to current devices, particularly as the device moves into the technology phase. Spectrometers for 14 MeV neutrons will be necessary for ion temperature measurement. Micro-fission chambers, developed for fission reactors will have to be upgraded for the fusion environment near the first wall, with special emphasis on the ability to cover the extreme dynamic range. Neutron detectors, appropriate to the several operating phases of ITER, must be prepared for the neutron camera. Detectors for measurement of 15 MeV D^3He gammas and 17 MeV DT gammas for use in the spatially resolving gamma camera must be developed for low sensitivity to low-energy background gammas.
2. Considerable improvement in reflectometry techniques will be required to apply the dual-polarization reflectometry for electron density and magnetic field profile measurements in ITER.
3. A ~ 1.5 THz laser source to operate with pulsed power of ~200 MW for 100 ns with repetition frequency ~20 kHz will be necessary for studying the confined alpha-particles and other accelerated ions in the plasma by the collective scattering technique.
4. The issue of calibrating, and checking on relative calibration, of the diagnostics for the highly activated tokamak and for the very long pulse lengths must be resolved to ensure that valid data can be assured. An in-situ calibration technique for 14 MeV neutrons has to be developed. This technique has to function during both phases of device operation with the following specifications:

(i) Calibration must be possible when the tokamak is fully activated;
(ii) It will work for both 2.5 and 14 MeV neutrons;
(ii) Calibration can be repeated once-a-week;
(iv) Accuracy, after extrapolation to full flux levels, must be better than 10%.
(v) There will be no safety hazard to users.

The specification of the hot-source calibration system for calibration of the ECE diagnostics is as follows:

(i) The source shall operate in vacuum with the vessel walls at 100°C;
(ii) The temperature uniformity over its surface of 20 cm diameter will be ±1%;
(iii) It can be deployed by the remote-maintenance equipment;
(iv) It can be cross-calibrated against a known standard periodically.

TABLE 7-2. COMPONENTS OF DIAGNOSTIC R&D PLAN

Radiation effects on components
Develop vacuum windows for diagnostics
Develop reflectors for diagnostics
Radiation sensitivity of ceramics
Radiation properties of fiber optics
Radiation hard dispersive and reflective methods
Data-base development for components in high radiation fields
Radiation capability of cabling
Radiation sensitivity of specific diagnostic hardware
New and significantly modified diagnostic methods
New fusion product techniques
Dual-polarization reflectometry for electron density and magnetic field profile studies
Source for collective scattering of fast ions
New calibration methods
In-situ calibration technique for 14 MeV neutrons
Hot source calibration of the ECE diagnostics
New diagnostic components
Many examples are given in the plan
Studies of new methods on operating fusion experiments
Provides funding to operating groups for installation of test diagnostic equipment on their devices
Development of diagnostic computer codes
Neutron transport codes
Analysis codes for the magnetic diagnostics
Interpretive diagnostic codes
Development of computer methods for real-time data-handling
Reliability studies of operating equipment

5. Prior to construction of many of the diagnostics, feasibility will have to be shown by developing, prototyping and testing of many of the components. These components will be defined during the design period of the diagnostic. At this time, some twenty components have been identified for development, but changes and additions can be expected as the program evolves. Some examples of the presently identified components are given below:

(i) Multi-pulse laser for the LIDAR Thomson scattering system;
(ii) Highly reliable rotating and vibrating, vacuum-compatible probe drives;
(iii) Magnetic sensor development;
(iv) Filter scope detectors of O and C in the XUV spectral range;
(v) Liquid activation detection system;
(vi) Measurement of atomic cross-sections for diagnostics dependent on charge-exchange reactions;
(vi) Method for removing carbon build-up on reflective optical equipment in vacuum;
(vii) High-throughput, high-contrast spectrometer for resolving UV helium spectral lines for alpha-particle diagnostics;
(viii) Helium diagnostic neutral beam (~100 keV) with large fraction of ground-state neutrals

6. The extensive set of new or greatly modified diagnostic techniques must be tested on operating fusion devices prior to final implementation on ITER. The R&D activity must prepare the necessary hardware and software interfaces so that the diagnostics can be tested in a timely fashion at such a device.

7. Two types of computer codes are required in demonstrating feasibility of diagnostics and in helping in their design. These are (i) specific hardware-related codes, such as neutron transport codes, relevant to the background noise and shielding of every diagnostic, and magnetic analysis codes establishing the location and quality of data of magnetic coils close to the first wall and (ii) interpretive codes to show the capabilities of the selected diagnostics for the relevant ITER physics parameters. The latter set, while crucial in the choice of diagnostic technique, will become a resource for the data analysis during operation.

8. Even in the physics phase, a large quantity of data will be accumulated during a 200 second pulse (even more in a week-long pulse in the technology phase). There is no question that the computer technology will be sufficiently advanced to cope with such data loads, even within the framework of providing analyzed data during the pulse. However, it is necessary to carry out a cybernetic and human-factors engineering study of the operation of ITER to optimize the computer hardware, software and data analysis prior to setting the computer hardware specifications.

REFERENCES (§7.0)

[7.1] V.S. MUKHOVATOV, S. YAMAMOTO, K.M. YOUNG, "Summary Report: ITER Specialists' Meeting on Plasma Diagnostics, July 1989" ITER Report, ITER-TN-PH-9-1.

[7.2] H. HOPMAN, V.S. MUKHOVATOV, S. YAMAMOTO, K.M. YOUNG, "Summary Report: ITER Specialists' Meeting on Plasma Diagnostics," ITER-TN-PH-0-1, February 1990.

[7.3] ITER Technical Report, "*Plan for ITER-Related Plasma Diagnostic R&D During the Detailed Design Phase, 1991-1995 (and Beyond). Part I: ITER Related R & D Needs*," ITER-TN-PH-0-3, November 1990.

[7.4] IAEA, *ITER Diagnostics*, IAEA/ITER/DS/33, IAEA, Vienna (1991).

[7.5] IAEA, *Research and Development Needs for ITER Engineering Design*, IAEA/ITER/DS/20, IAEA, Vienna, 1991.

8.0. FUELLING

8.1 FUELLING REQUIREMENTS

8.1.1 Required Particle Fluxes

The fuelling rate of deuterium (D) and tritium (T) must balance both the loss of particles burned in fusion reactions at a rate,

$$\Gamma_{fus} = 3.6 \times 10^{17} P_{fus}(MW)\ [particles/s] \quad (1)$$

and the loss of fuel particles exhausted together with the helium ash at a rate Γ^{ex}. In equilibrium, Γ_{fus} is equal to the pumped flux of helium Γ_α^{ex}. Thus the fuelling rate (Γ_{fuel}) of hydrogenic atoms (D or T) is determined by,

$$\Gamma_{fuel} = \Gamma^{ex} + \Gamma_{fus} \quad (2)$$

If the rate of fuelling and pumping is assumed to be the same for D and T, the fraction of helium ash in the exhausted gas defined by $f_\alpha = \Gamma_\alpha^{ex}/(\Gamma_T^{ex} + \Gamma_D^{ex})$ is related to the rate of fuelling by

$$\Gamma_{fuel} = \Gamma_{fus}[1 + 1/2f_\alpha] \quad (3)$$

When f_α is 0.015, the fuelling rate of deuterium and of tritium atoms becomes $34 \times \Gamma_{fus}$. Hence the efficiency of helium ash exhaust is the determining factor in the fuelling rate of hydrogenic ions. Note that the burn efficiency defined by $f_b = \Gamma_{fus}/\Gamma_{fuel}$ is almost equal to $2f_\alpha$. Thus an increase in the burn efficiency of the fuel requires an increase in the pumping efficiency of helium ash.

The preceding estimate can be applied to the different fuelling methods. It is expected that, for gas puffing in ITER, the fuelling efficiency of the bulk plasma will be comparatively low because the scrape-off layer is opaque to neutrals. Particle fuelling will be mainly in the form of ions, requiring a net inward ion flux from the scrape-off layer (SOL) plasma to the bulk plasma. Higher fuelling efficiency can be obtained by pellet injection with direct particle fuelling inside the separatrix, at the expense of decreasing the ratio of edge to central density.

8.1.2 Control of Density and Density Profile

- *Flat density profile*

Excessive radiation losses and dilution of the core DT plasma arising from accumulation of impurities and helium in the plasma core cannot be tolerated. A broad density profile of $n(0)/\langle n\rangle = 1.3–1.5$, where $n_e(0)$ is the central plasma (electron) density and $\langle n\rangle$ is the volume averaged density, is preferred during burn. This avoids the impurity accumulation predicted by neoclassical theory for a peaked density profile, and is consistent with high density at the separatrix that is required to reduce the heat load and temperature at the divertor plate. To produce a profile with the

required peaking factor, a combination of fuelling methods (see Sect. 8.3) will be required, depending on experimentally determined particle transport coefficients.

- *Peaked density profile*

Peaked density profiles allow improved energy confinement time in some conditions. They may therefore be attractive for approaching ignition, provided the constraints imposed by the β limit, divertor operating conditions and avoidance of impurity accumulation in the plasma core can be met.

8.1.3 Fuelling Requirements for Burn Control

The operating conditions are strongly influenced by the pressure profile, because the volume averaged α-heating power is proportional to the square of the volume averaged pressure, $\langle n(r)^2 T(r)^2 \rangle$ at $\langle T \rangle \sim 10$ keV. This suggests that a transient change in plasma density might be used for burn control (Section 2.4.3) by affecting the reactivity. Such a change in density does not change the volume average pressure at first, but after a characteristic time of the order of the energy confinement time, the pressure will adjust to the density profile. The particle fluxes needed to affect the reactivity are appreciably smaller than those needed for density profile control and rampup. The response of the core density to changes in fuelling by gas puffing or shallow pellet injection is expected to be slow (see Sect. 8.3.2), so that this method can only be used for burn control on longer time scales. Faster control could be provided, if required, by innovative fuelling methods such as compact toroids and/or ripple fuelling which are able to fuel inside ~0.6 of the plasma minor radius (see Sect. 8.3). Variation of DT mix to provide burn control should also be investigated.

8.1.4 Restrictions on Density Profile Choice

8.1.4.1 Edge density

To minimize erosion of the divertor target plate and impurity influx to the plasma and to maximize helium pumping, high recycling conditions (low temperature, high density plasma) are required at the divertor plate. High recycling conditions impose a lower bound on the density at the separatrix, about $(0.3–0.4) \times 10^{20}$ m^{-3} (see Sect. 3.0). In contrast, the disruptive density limit imposes an upper bound on the plasma edge density (see Sect.2.3). Therefore, ITER will probably be operated near the density limit, and control of the edge density will be important.

8.1.4.2 Beta limit

Operation at high average beta, or more appropriately high fusion power density, generally requires a broad pressure profile such as (Sect. 2.2)

$$p(r) \sim [1 - (r/a)^2]^{\alpha} \text{ with } \alpha = 0.7–1.5, \qquad (4)$$

since peaked profiles in the plasma core region attain the β limit at lower average β. To obtain a broad pressure profile, the temperature profile must be broad. The temperature profile is essentially determined by the local alpha heating power, which increases with the square of the density, again requiring the density profile to be rather flat.

8.1.4.3 Damage to the first wall

The neutral density at the plasma edge is predicted to be low, so that the average power flux convected by particles to the first wall is $\leq 10^{-3}$ MW/m^2. The associated wall erosion rate is small, giving a lifetime for carbon wall tiles >1 burn year. However locally intense fuelling (e.g. gas puffing or pellet injection) can increase local erosion rates. Detailed investigations must be carried out for each proposed fuelling scheme.

8.1.5 DT Mix Requirements and Tritium Inventory

Control of the DT mix is required both during the density rise phase during start-up and in the burn phase. Refuelling with an approximately equal mix of D-T will be needed to replace the expended fuel. To increase the tritium burnup fraction and to decrease tritium throughput, the nominal 50-50 DT fuel mix in the reacting plasma can be relaxed to 60-40 DT mix with little effect on fusion power and edge plasma density [8.1]. The DT mix can also affect the tritium inventory, which should be minimized for safety reasons. The major factor affecting the burn efficiency f_b, however, is the enrichment factor of helium in the pumped gas, which should be maximized to decrease the tritium throughput.

8.1.6 Wall Conditioning

Wall conditioning with H_2 or D_2 will be used to reduce tritium outgassing before maintenance. It will then be necessary to replace H or D with DT in the walls after maintenance. Fuelling requirements for conditioning are to be determined.

8.2 RELATION OF PARTICLE TRANSPORT TO FUELLING

Particle transport is one of the fundamental transport processes in plasmas. However the experimental database on particle transport remains limited, and therefore extrapolation to ITER is uncertain.

8.2.1 Particle Confinement Time

The normalized particle confinement time of JET, ALCATOR, JT-60 and TEXT shows that τ_p increases linearly with density until some critical density, and then decreases [8.2]. The critical density depends on the plasma minor radius. This density dependence can be explained by the penetration depth of the neutral particles. Penetration is relatively deep in plasmas having small minor radii and low density, and becomes shallow at large minor radii and at high density. In JT-60 [8.3], the particle confinement time in NB heated plasmas was found to scale empirically as

$$\tau_p \propto I^{\delta}/(\bar{n}_e P_{abs}^{0.5}); \quad \text{with } \delta = 0\text{–}1 \tag{5}$$

The deterioration of τ_p with density implicit in this scaling law is also consistent with the observation in TFTR that H_α emission in limiter plasmas touching the inner wall increases linearly with n_e^2 [8.4]. The same power dependence, $\tau_p \propto (1/P_{abs})^{0.5}$, is observed in JET with ICRF heated L-mode plasma [8.5].

Particle confinement in H-mode plasmas is improved. In ASDEX, τ_p rises from 0.01-to-0.15 s [8.6]. In JET τ_p rises to values 3 times higher than L-mode [8.7].

ITER is significantly different from present machines in that the scrape-off layer (density gradient scale length ~10 cm at the midplane) is relatively opaque to neutrals. The relation between density profile, fuelling method, and local transport coefficients is therefore significantly different in ITER than in present-day machines, so that care must be exercised in extrapolating experimental scaling laws for particle confinement to ITER.

8.2.2 Diffusivity and Inward Pinch

Local particle transport analyses are essential to investigate the controllability of the density profile and the burnup fraction. Local particle balance is given by

$$\partial n/\partial t = -(1/r)(\partial\, r\Gamma/\partial r) + S_{in} \tag{6}$$

$$\Gamma = -nv - D\,\partial n/\partial r \tag{7}$$

where S_{in} is the local particle source term, and v is the inward pinch velocity. In the case of electrons, S_{in} is given by the ionization of neutrals and impurities [8.8]. In the steady state, only the ratio of v/D can be estimated, so that dynamic modulation (pulsed or oscillating gas puffing, pellet injection, sawteeth) must be used to obtain D and v independently.

In TFTR [8.9], the density profile was modulated by a gas injection pulse of 50 ms, indicating D_e almost inversely proportional to the local density. D_e has the same profile as χ_e and the same value within a factor 2. The inward pinch velocity is nearly an order of magnitude higher than the neoclassical value. There was no clear difference in D_e between hydrogen or deuterium plasmas.

In JET [8.10], injection of small pellets indicated $D_e = (0.4\pm0.1)$ m^2/s, $v = 1.0(r/a)^4$ m/s, $\chi_e/D_e = 7.0\pm2.5$ at $r/a = 0.5$–0.6 consistent with the estimates obtained from analyzing transport in a sawtooth phase. Recent power balance estimates from anomalous transport triggered by electron temperature gradients suggest $\chi_i/D_i = 2$–3 [8.11]. The flat density profiles obtained when beryllium was used as the first wall material have been interpreted by the JET team to be consistent with absence of an anomalous inward particle pinch [8.11].

In ASDEX [8.12], sinusoidal modulation of the gas feed (5–20 Hz) was applied to investigate the radial profiles of D_e and v. A strong correlation between D_e and τ_E was observed in OH plasmas. In NB heated L-mode plasma, D_e in the outer region increased with P_{beam} and decreased with I. For these conditions, a strong inward convection is found. In H-mode with grassy ELMs, v at the periphery was larger by a factor 3–5 than the L-mode value even though D_e is similar for both modes.

Diffusion and convection alone are not sufficient to interpret the measurements. Other processes must be included, such as the off-diagonal term in particle transport coming from the temperature gradient, which can be investigated by modulating the RF power. Further processes that could affect the interpretation are ionization of inwardly convected impurities, deep penetration of neutrals [8.13], and direct ionization through molecular processes [8.14]. Inclusion of these processes is necessary to determine whether the inward electron pinch velocity is neoclassical or anomalous.

8.3 FUELLING METHODS

The ITER fuelling system depends on a combination of gas puffing and pellet injection, with some fuelling by the high-energy neutral beams. Alternative methods mentioned below could be examined if proven.

8.3.1 Gas Puffing

Gas puffing is the simplest fuelling technique and is used in all present-day tokamaks. Gas puffing into the divertor region is expected to be the main method of fuelling, because it is compatible with a high recycling divertor condition, and is probably compatible with H-mode operation. Gas puffing results in a flat density profile and a high edge density, leading to a high recycling regime in the divertor.

The potential problems of gas puffing are,

- Low fuelling efficiency of the bulk plasma, raising the tritium throughput
- Inadequate control of the density profile when gas puffing alone is used, leading to the possibility of too flat a profile, too high an edge density, and a resulting density limit disruption.

8.3.2 Pellet Injection and Pellet Ablation Physics

On JET and ASDEX [8.15,16], with pellet speeds of 0.5–1.5 km/s, it has been found that the pellet penetration depth is proportional to $v_p^{1/3}$. This experimentally obtained velocity dependence generally agrees with the prediction of the neutral gas shielding model. Extrapolating this formula to ITER suggests that direct particle fuelling by pellets is possible in the outer 1/3 of plasma minor radius with 8 mm diameter pellets having speeds of the order of 5 km/s [8.17]. Thus, investigations at higher speeds, 2.5–5 km/s, are required.

In burning plasmas, pellet injection at lower speeds, of the order of 1 km/s, may be useful to fuel just inside the separatrix at high fuelling efficiency. For this purpose, either a gas gun injector operated at low pressure or, alternatively, a centrifugal pellet injector could be used. Small pellets, 2–3 mm in diameter, should be used to avoid density limit disruptions caused by transient increase of the edge density.

Pellet ablation models previously developed (Neutral Gas Shielding model (NGS) [8.18,19] and Neutral Gas Plasma Shielding model (NGPS) [8.20]) have been improved recently. An example is the modification of the NGPS model using the calculated values of the confinement radius of the neutral cloud in [8.21]. A sensitivity study of the penetration depth using these ablation models yields ± 20% deviations in the predictions for ITER Physics Phase plasma [8.22]. Further improvements may be expected from use of a Magnetic Shielding Model. For example, a 1.5-D simulation suggests that the pellet traverses its own shielding cloud and a transient magnetic cavity may form inside the cloud [8.22]. However, many uncertainties that still exist in pellet ablation physics such as the deflection of the pellet path [8.23,24] or the change of velocity during the flight of the pellet [8.24] need further investigation. Furthermore, the effect of striations in the pellet cloud ahead of the pellet on the ablation rate and the size of the magnetic shielding effect need further study. To validate the ablation models, detailed measurements of the following are required: pellet cloud dimensions, expansion velocities ($\perp$ and $\parallel$ to B), time dependence and structure along

the field lines of density and temperature in the shielding cloud, location and size of the pellet inside the cloud, and magnetic field strength inside the cloud.

The potential problems of pellet injection are:

- Too low an edge density (Section 8.1.4); alleviation may require combined operation with gas puffing.
- Compatibility of edge density control by pellet injection in H-mode; experiments have been done on JFT-2M [8.25] and JET [8.11], but the effect of shallow pellet injection during the H-mode is not clear yet.
- Small size of the allowable density perturbation if operation is very close to the density limit.
- Charge exchange erosion induced by pellet injection; detailed ionization processes remain to be investigated experimentally and theoretically for typical ablation cloud parameters (10–20 eV and 10^{23}–10^{25} m^{-3}) [8.22].

8.3.3 Alternative Methods

8.3.3.1 NB injection

Neutral beam injection physics issues are sufficiently well established that the resultant particle deposition profile can be predicted with confidence. High energy beams which can penetrate the core plasma are not efficient simultaneously for both heating and fuelling. For example, the negative ion deuterium beam (1.3 MeV, 70 MW) to be provided for beam heating and current drive in ITER can supply only 3.8×10^{20} particles/s. While this is almost equal to the fuel particles consumed by fusion reactions (Section 8.1) for ~1 GW fusion power, the total number actually required is approximately 5×10^{21} particles/s, so that high energy beam fuelling alone is insufficient. Hence, it is necessary to augment this particle source with gas puffing.

Alternatively, a low-energy, low-power beam (10 keV, 6 MW) could supply ~4×10^{21} particles/s at relatively shallow penetration, i.e., could compete with shallow pellet fuelling. In combination with an inward pinch, this would have the potential of fuelling the plasma beyond the separatrix.

Both methods fuel the bulk plasma and thereby decrease the tritium throughput.

A potential problem of low energy NB injection is the erosion of the first wall caused by high energy halo neutrals (2–5 keV) produced at the plasma periphery.

8.3.3.2 Ripple fuelling

Neutral beam injection at low beam energy is better for fuelling since it demands less power for the same flux, but the neutrals then do not penetrate to the plasma core. Ripple injection [8.26] makes fuelling possible near the plasma center without cooling the plasma. This fuelling scheme is different from the higher energy scheme in [8.27]. In this scheme, the enhanced outward flow of the ripple-detrapped banana particles [8.28] is negligible owing to the short thermalization time of the low energy beam. For the ITER aspect ratio of 2.8, the field ripple inside the plasma is small. However, fuelling near half radius is possible with a beam energy of 50 keV [8.26].

The following problems exist in ripple fuelling:.

- The ripple loss of α-particles is ~6% when 6 ripple coils, equally spaced toroidally, are used. This could be reduced to ~3% by decreasing the number of ripple coils to 1 or 2.

- The net ion fuelling in this scheme charges up the plasma. This may be mitigated by α-particle loss and anomalous electron diffusivity.
- The first wall may be eroded by halo neutrals.

8.3.3.3 Compact toroids (CT)

In this innovative fuelling method, a compact torus (CT), produced by a plasma gun in conjunction with an accelerator and a system for compression, is injected into the tokamak. Following injection, the CT should come to rest and its magnetic field should reconnect with that of the core plasma. To supply from 4×10^{20} to 10^{22} particles for ITER, CT's with ~ 350 km/s and an injection rate from 4-to-100 Hz would be required. Experiments in the CALTECH ENCORE Tokamak (I = 2 kA, R = 0.38 m, a = 0.12 m) [8.29] on injection of dense spheromaks ($n_e \sim 5 \times 10^{21}$ m^{-3}, T_e = 5 eV, 30 km/s) have obtained a density increase by a factor of 6. However, more proof of principle experiments in conditions closer to those of ITER would be required. CT injection has a potential impurity problem due to substantial sputtering from the electrodes during the CT formation.

8.4 MODES OF OPERATION

In ITER, the baseline particle fuelling method is a combination of gas puffing and pellet injection. The modes of operation discussed in this section use only these two methods.

8.4.1 Fuelling During Burn

Due to the lack of sufficient experimental data, the density profile evolution can not yet be modelled with confidence. This implies that flexibility in the available fuelling methods will be required to produce the desired profiles.

8.4.1.1 Fuelling only by gas puffing

In gas puffing, hydrogenic ions burned in the fusion reaction will be fuelled mainly by the inward ion flux from the SOL plasma to the bulk plasma, since the scrape-off layer is relatively opaque to neutrals. The mechanism to produce the inward flux is a combination of inward pinch and diffusion. Consequently, flat density profiles will result, even becoming slightly hollow if the inward pinch is small. The characteristic time of this penetration may be the order of ~10 s, which is smaller than the fusion reaction time (of order of ~100 s).

8.4.1.2 Fuelling only by pellet injection

Pellet injection could be used to fuel the bulk plasma. The profiles obtained will be more peaked than in the preceding case. The frequency of pellet injection with a 50-50 DT mixture is expected to be 2–5 Hz with pellets of 6 mm dia. or 1–1.5 Hz with pellets of 7.4 mm dia., which corresponds to ~2×10^{22} particles/s with a burn efficiency of 3% at a fusion power of 1 GW.

8.4.1.3 Combination of pellet injection and gas puffing

A combination of pellet injection and gas puffing will provide a higher flexibility than either method alone for the control of the edge density. Tritium rich pellets combined with deuterium rich gas puffing may decrease the tritium throughput.

8.4.2 Compatibility of Pellet Fuelling with Lower Hybrid Current Drive (LHCD)

Lower hybrid waves will be used in ITER to provide current drive and current profile control. The superthermal electrons produced by LHCD would, however, reduce significantly the pellet penetration depth [8.30]. Thus, measures must be taken to ensure the compatibility of pellet fuelling with LHCD. Shallow penetration remains possible when pellets are injected in-phase, i.e. during LHCD operation, while deeper penetration is achieved with out-of-phase pellet injection, i.e., during brief interruption of the LHCD (notched operation).

Pellet injection with shallow penetration was found to be compatible with simultaneous LHCD in ASDEX [8.31] when small sized pellets, 4×10^{19}, were injected at a rate of 17–25 Hz. This suggests that shallow in-phase pellet injection may be possible for ITER.

To extrapolate to notched operation, it is noted that, in these experiments, recovery of deep pellet penetration after turn-off of LHCD required a relatively long time delay of ~200 ms [8.31]. This is possibly caused by the long slowing down time of superthermal electrons, as measured by a hard X-ray monitor. A very small population of superthermal electrons can still cause enhanced ablation of a pellet [8.30]. An acceptably short off time for notched operation for ITER (e.g., 0.1 s turn off each 1 s), is therefore of the order of the recovery time observed in present experiments, but this question requires further study. Optimization of off-time (lower limit: slowing down time of superthermal electrons) and frequency of interruption (lower limit from maximum pellet size) is required for ITER parameters.

8.4.3 Density Ramp-up to Ignition

The maximum particle flux required during rampup is mainly determined by the desired density ramp-up rate. Gas puffing produces higher peripheral densities, which may degrade the penetration of NB and may increase the possibility of a major disruption due to the density limit. Pellet injection yields deeper fuel deposition and lower edge density for the same average plasma density and may improve the conditions for ignition because of better NB penetration to the center. The NB penetration, the average plasma density evolution, and the evolution of the density profile determine the relative evolution of gas and pellet fuelling in time [8.32]. For example, for an initial deuterium plasma with a small diffusion coefficient, tritium supplied at the edge by gas puffing requires a finite time to mix sufficiently with the deuterium.

8.5 CONTROL OF DENSITY AND DT MIX

Feedback control of the density and its profile will be investigated for ITER. Double feedback control, as demonstrated on ASDEX [8.33], using a combination of pellet injection for core fuelling and gas puffing for edge fuelling is a possible scheme. Adding a cascade feedback loop between the central density and edge density could improve the control. Optimization of the pumping configuration for helium pumping changes the pumped DT flux and influences the profile. While changes in pumping may induce strong changes in recycling, this does not necessarily result in strong changes of the bulk plasma density profile, as shown by pumped limiter experiments in TORE SUPRA [8.34]. As input for density control, a combination of line integrated density from interferometry, density profile from the LIDAR system, and the density near the separatrix from reflectometry will provide adequate signals.

The absolute control of the DT mix may be difficult because the D/T ratio can be measured by a neutron spectrometer to an accuracy of only ~15% around the equilibrium state, and can be determined from the neutron yield by a fission chamber to only ~5% [8.35]. However, the relative control of the DT mix is expected to be possible with a combination of pellet injection (T and D) and gas puffing (mainly D).

8.6 PHYSICS R&D NEEDS

8.6.1 Particle Transport

The present database on particle transport of hydrogenic ions must be extended to include more data from improved confinement modes. Since ITER will be very different from present tokamaks, in that neutral particles will be unable to penetrate the scrape-off layer, direct extrapolation of particle confinement times to ITER is not valid, and the determination of the particle source profile in present experiments is crucial to obtain accurate expressions for the local transport coefficients (diffusivity and inward convective velocity). Impurity profiles must be measured to determine electron density and hydrogenic ion density profiles. This information should then be used to determine whether the particle inward pinch is neoclassical or anomalous. Local particle transport (convective velocity, diffusivity) of hydrogenic ions, helium and impurities are required both in the scrape-off layer (to predict SOL density and temperature profiles) and in the edge and core plasma (to predict the density profile as a function of fuelling method).

The compatibility of each fuelling method with He ash exhaust and H-mode plasma performance should be assessed. The level of first wall damage caused by charge-exchanged neutral particles should be also investigated for each fuelling method.

8.6.2 Pellet Ablation Physics

The velocity scaling of pellet penetration depth ($\propto v_p^{1/3}$) should be investigated at higher speeds, 2.5–5 km/s, to see whether improvement continues for the higher speeds.

More detailed measurements are required to improve the ablation model (e.g. measurement of size and location of the pellet inside the cloud with a shadowgram technique, measurement of time dependent ablation phenomena parallel and perpendicular to the magnetic field with a fast framing camera). Many effects in pellet ablation physics such as pellet deflection, striations, magnetic shielding effects, and enhanced ablation by superthermal electrons produced by LHCD must be investigated further. Furthermore, the problem of charge exchange neutrals produced in an ablation cloud should be studied.

8.6.3 Innovative Fuelling Methods

Direct fuelling in the core plasma can improve control of the density profile. Proof-of-principle studies of compact toroids and ripple fuelling with low energy NB injection should therefore be continued.

REFERENCES (§8.0)

[8.1] W. HOULBERG, M. GOUGE, "Pellet and gas puffing scenarios for ITER," ITER-IL-PH-9-0-U-9, presented at the ITER Specialists' Meeting on Fuelling and Density Control, 9–13 July 1990.

[8.2] A.J. WOOTTON et al., *Plasma Phys. Control. Fusion*, **30** (1988) 1479

[8.3] S. TSUJI and JT-60 Team, 14th EPS Madrid, Part I (1987) 57.

[8.4] D.H. HEIFETZ et al, *J.Vac. Sci. Technol.* **A6** (1988) 2564.

[8.5] M. BURES et al., *Plasma Phys. Control.. Fusion* **30** (1988) 1833.

[8.6] ASDEX Team, *Nucl. Fusion* **29** (1989) 1959.

[8.7] A. TANGA et al., *Nucl. Fusion* **27** (1987) 1877.

[8.8] G. FUSSMANN, "Impurity transport in tokamaks," ITER-IL-PH-9-0-E-11, presented at the ITER Specialists' Meeting on Fuelling and Density Control, 9–13 July (1990).

[8.9] P.C. EFTHIMION et al., Plasma Physics and Controlled Nuclear Fusion Research (Proc. 12th Int. Conf., Nice), IAEA, Vienna, Vol. 1, 307 (1989).

[8.10] A. GONDHALEKAR et al., *Plasma Phys. Control. Fusion* **31** (1989) 805.

[8.11] The JET Team (presented by P.H. Rebut), paper IAEA-CN-53/A-1-2, in Proc. 13th Int. Conf. on Plasma Physics and Controlled Nuclear Fusion Research, (Washington, D.C., 1–6 October 1990), IAEA, Vienna (to be published).

[8.12] K.W. GENTLE et al., "Determination of particle transport coefficients in ASDEX by gas modulation," to be published in *Nuclear Fusion.*

[8.13] A.GONDHALEKER, "Fuelling and density behaviors in JET," ITER-IL-PH-9-0-E-8, presented at the ITER Specialists' Meeting on Fuelling and Density Control, 9–13 July 1990.

[8.14] T. FUJIMOTO et al., *Nucl. Fusion* **29** (1989) 1519.

[8.15] W.A.HOULBERG et al., 31st Annual Meeting of the Division of Plasma Physics, Anaheim, (1989).

[8.16] R. LOCH et al., 17th EPS Conference on Controlled Fusion and Plasma Heating, Amsterdam, Vol. 1, 235 (1990).

[8.17] M.J.GOUGE, "Conceptual Design Description and Supporting R&D," ITER-IL-PH-9-0-U-10, presented at the ITER Specialists' Meeting on Fuelling and Density Control, 9–13 July 1990.

[8.18] P.B. PARKS et al., *Nucl. Fusion* **17** (1977) 539.

[8.19] S.L. MIROLA, C.A. FOSTER, *IEEE Trans Plasma Sci.* **PS-6** (1978) 578..

[8.20] W.A. HOULBERG et al., *Nucl. Fusion* **28** (1988) 595.

[8.21] L. LENGYEL, *Nucl. Fusion* **29** (1989) 37.
[8.22] L. LENGYEL, "Pellet ablation and shielding phenomena: state of the art," ITER-IL-PH-9-0-E-5, presented at the ITER Specialists' Meeting on Fuelling and Density Control, 9-13 July 1990.
[8.23] S.M EGOROV et al.,"Pellet ablation study in T-10 tokamak: experiments and theory development," ITER-IL-PH-9-0-S-1, ibid.
[8.24] G.A. WURDEN et al., "Pellet ablation studies in ASDEX," ibid.
[8.25] N.SUZUKI et al., 12th IAEA, Nice, Vol.1, 207 (1988).
[8.26] K. TANI et al., "Ripple-assisted fuelling in tokamak reactors," ITER-IL-PH-9-0-J-5, presented at the ITER Specialists' Meeting on Fuelling and Density Control, 9–13 July 1990.
[8.27] D.L. JASSBY, "Neutral Beam Injected Tokamak Fusion Reactor," PPPL-1280 (1976).
[8.28] R.J. GOLDSTON, D.L. JASSBY, "Phenomena Accompanying Gradient-B Drift Injection of Energetic Ions into Tokamak Plasma," MATT-1244 (1976).
[8.29] P.M. BELLAN, M.R. BROWN, "Compact torus injection for refuelling ITER," ITER-IL-PH-9-0-U-11, presented at the ITER Specialists' Meeting on Fuelling and Density Control, 9–13 July 1990.
[8.30] B. PEGOURIE, Y. PEYSSON, 17th EPS Conference on Controlled Fusion and Plasma Heating, Amsterdam, Vol. 3, 1217 (1990).
[8.31] F.X. SOLDNER et al., 17th EPS Conference on Controlled Fusion and Plasma Heating, Amsterdam, Vol. 3, 1217 (1990).
[8.32] L. LENGYEL, "Remarks on scenarios involving density ramp-up by pellet and NB-heating," ITER-IL-PH-9-0-E-11, presented at the ITER Specialists' Meeting on Fuelling and Density Control, 9–13 July 1990.
[8.33] R. LOCH et al.,17th EPS Conference on Controlled Fusion and Plasma Heating, Amsterdam. Vol. 1, 215 (1990).
[8.34] A.GROSMAN et al., "Plasma edge control in Tore Supra," 17th EPS Conference on Controlled Fusion and Plasma Heating, Amsterdam (1990).
[8.35] See V. MUKHOVATOV et al., *ITER Diagnostics*, ITER Documentation Series, IAEA/ITER/DS/33, IAEA, Vienna (1991).

9.0. TOKAMAK OPERATIONS

9.1 OPERATIONAL PLANS

ITER operations will be carried out in two phases: a physics phase devoted mainly to attaining the plasma physics objectives, and next, a technology phase devoted to fulfilling the engineering objectives and completing the testing programme. Before the initial operation in the physics phase, extensive commissioning tests of the tokamak components and the necessary support systems will have been carried out.

In the physics phase, ITER will initially aim to demonstrate controlled burn of more than 200 s duration in inductive operation. The burn pulse will then be extended towards longer burn duration, possibly up to steady-state, using non-inductive current drive, both to obtain the physics data base required for future reactors and to optimize the long-burn mode for the technology phase. Many of the preparatory experiments can be carried out at low neutron flux, so that the physics phase of ITER can be subdivided according to the activation of in-vessel components into: (i) a zero activation phase, i.e., operation in hydrogen, (ii) a low activation phase, in which deuterium is used; and (iii) a high activation phase, with deuterium-tritium operation and ignition. These phases are indicated on Table 9-1.

The technology phase is characterized by a specific fluence goal, required for attaining the testing objectives of the device. Operation in the technology phase will therefore be optimized to satisfy testing requirements concurrently with stress and fatigue limits of the machine. The determination of this optimal operation is one of the objectives of the physics phase .

9.1.1 Zero-Activation Phase

In the zero-activation phase, the operational space of the machine will be explored with ohmic heating, auxiliary heating, and non-inductive current drive. At the end of this phase, full-performance shots in hydrogen with optimized heating should demonstrate that ITER can attain the plasma parameters necessary for ignition.

Approximately six thousand discharges are expected to be required for the zero-activation phase (see Table 9-1), and a time span of three years is expected to suffice for this phase and the following low-activation phase.

9.1.2 Low-Activation Phase

Operation with deuterium (and some experiments with an admixture of He^3) in this phase allows confirmation of plasma confinement and radiation shielding with much reduced activation of the structures. The performance of the diagnostic systems in a moderate radiation environment will be verified and helium injection into the plasma will demonstrate helium exhaust and pumping from the divertor. About two thousand discharges are estimated for this stage.

TABLE 9-1. ITER PHYSICS PHASE OPERATIONAL PLAN

	ZERO ACTIVATION	LOW ACTIVATION	HIGH ACTIVATION
	OPERATIONAL CONDITIONS 6 000 Shots	PLASMA OPTIMIZATION 2 000 Shots	IGNITION AND DRIVEN OPERATION 7 000 Shots

I---Year 1---I----Year 2----I----Year 3-----I----Year 4----I----Year 5-----I----Year 6-----

H/He	H/He	H/He	H/He	H/He/D	D/T	D/T	D/T
Initial Ohmic Operation	Full Field & Heating System Tests	Physics Studies Wall Material Studies	Physics Studies Steady State Studies	He-Pumping Studies; Pre-Ignition Optimization	"Flash" Ignition Alpha Particle Studies	200 s Burn He-ash Removal	Final Parameters Definition Driven Operation
1500	500	2000	2000	2000	3000	2000	2000 shots
[]====[]==[]##[]====[]##[]=====[]=====[]###[]=====[]=====[]====[]###[]							
3.5 T	5 T	$\tau_E \geq 2$ s	$\Delta t \geq 1000$ s	$\tau_E \geq 3$ s	$\Delta t \geq 20$ s	$\Delta t \geq 200$ s	$\Delta t \geq 1000$ s
15 MA	22 MA	$\geq 10^{20} m^{-3}$	$<5.10^{19} m^{-3}$	$\geq 10^{20} m^{-3}$	$Q \geq 30$	$Q \geq 30$	$Q \geq 5$
10 MW	100 MW	100 MW	100 MW	100 MW	1 GW	1 GW	1 MW/m^2
[]====[]==[]##[]====[]##[]=====[]=====[]###[]=====[]=====[]====[]###[]							
	Hands-on Maintenance Test of Remote Maintenance	Internal Changes Remote Maintenance Tests		Internal Changes for DT Physics Studies by Remote Maintenance			Transition to Technology Phase

9.1.3 High-Activation Phase

The purpose of the high-activation phase, with deuterium/tritium plasmas, is twofold: to demonstrate controlled, ignited burn in a D/T plasma, and to define and optimize the long-pulse mode required for the subsequent technology testing program.

Controlled burn at high Q will be a new experimental situation. It is therefore reasonable to foresee an extended period of experimentation in order to develop and optimize the control until extended burn periods, of the order of 200 s, are achieved and helium ash accumulation becomes significant. The study of controlled burn conditions is therefore necessary to optimize the helium pumping and the divertor and first wall heat loads for the technology phase operation. During this stage, the physics of a burning plasma with an appreciable hot alpha-particle component will be investigated. This study will address energy and particle transport, MHD effects, changes in operational limits, and disruption control under these conditions.

The second major goal of the high-activation phase is the development of a long-pulse scenario suitable for the technology phase, using non-inductive current drive. An essential part of the program is the demonstration of plasma diagnostic capability over extended periods in full reactor conditions. The optimal mode of operation for the technology phase will be determined from the results of these experiments.

All of these investigations in deuterium/tritium plasma are expected to require seven thousand discharges over a span of three years. The integrated burn time in the physics phase is expected to be 1.5×10^6 seconds for a total first-wall fluence of 0.05 MWa/m^2.

9.2 OPERATIONAL MODES

The choice of the major device parameters and the criteia that have been applied are discussed in Ref. [9.1]. As stated there, the present ITER design emphasizes ignited performance. Optimization for long pulse operation with non-inductive current drive would result in somewhat different device characteristics. In this section, the reference (Table 9-1) and alternative operating points are presented.

The various operating points, which have been defined for the physics phase and the technology phase of ITER [9.1–9.3], are divided into three groups, i.e. preparation and low-activity physics operation, inductive operation (high activity), and long-pulse and steady-state operation (high activity), and are referred to as O, A, and B operating points respectively. The major characteristics of the inductive (type A) and long-pulse (type B) operating points are shown on Tables 9-2, 9-3, and 9-4. The type O operating points are commissioning scenarios, which will frequently have less than maximum fields and currents. Their extreme characteristics are equal to those of the type A (inductive operation) and type B (long-pulse) operating points.

In choosing the reference operating points, the minimum fusion power has been chosen to be approximately 1 GW. A trade-off must then be made between pulse length and divertor heat loads. This is clear especially for the case of non-inductive current drive, where the current drive efficiency decreases with increasing density, i.e. more input power is required to drive a given current. Efficient current drive therefore requires low-density, high-temperature operation. The peak power loads on the divertor increase as the density decreases and as the temperature increases. Two reference operating points are designated, the reference ignition (case A1) and the reference long-pulse mode (case B1). The other type A and B operating points do not satisfy all the constraints presently known, but they represent the likely operational envelope of ITER if some of the constraints can be relaxed and some of the goals can be changed (e.g. by increase of allowable divertor heat load, decrease of power to divertor, increase of current drive power, reduction of fraction of current driven non-inductively, increase of wall load). Some of these modifications are likely, since many of the models, such as divertor, bootstrap current, non-inductive current drive, ..., are still incomplete so that their extrapolation from present experiments is uncertain.

No steady-state operational mode presently identified satisfies the divertor constraints because of the low density necessary for efficient non-inductive current drive. Nevertheless, a typical operating point is chosen for steady-state operation (case B6), and will be referred to as the nominal steady-state case. The major

TABLE 9-2. REFERENCE OPERATING POINTS

Code description of operating point	A1 Reference Ignition*	B1 Reference Long-pulse	B6 Nominal Steady-state
Plasma current, I [MA]	22	15.4	19
Fusion power, P_{fus} [GW]	1.1	0.86	0.75
Average neutron wall load, L_w [MW/m^2]	1.0	0.8	0.7
Auxiliary power, P_{aux} [MW]	0*	110	115
$Q = P_{fus}/P_{aux}$	–	8	6.7
Pulse length, t_{burn} [s]	400	2500	ss
Bootstrap current fraction, I_{bs}/I	0.14	0.3	0.3
Noninductive current, I_{CD}/I	0	0.3	0.7
Loop voltage (V)	0.12	0.045	–
Z_{eff} (core plasma)	1.7	2.2	2.2
Safety factor, q_ψ (95%)	3	4.4	3.5
Troyon g-factor, g [=$\langle\beta(\%)\rangle/(I/aB)$]	2	2.7	3
Toroidal beta, $\langle\beta\rangle$ (%)	4.2	4	5.4
Poloidal beta, β_p	0.65	1.4	1.1
Average plasma density, $\langle n_e\rangle$ (10^{20} m^{-3})	1.2	1.1	0.64
Average temperature, $\langle T_e\rangle = \langle T_i\rangle$ (keV)	10	11	20
Confinement times: (s)			
τ_E (required)	3.8	2.6	2.7
τ_E (L-mode prediction from ITER89-P)	1.9	1.2	1.3
τ_E (ELMy H-mode prediction) = 0.75 τ_E(ELM-free H-mode)	4.4	2.8	3.1
P_{rad} (core) (MW)	67	90	49
P_{rad} (edge) (MW)	35	95	27
P_{div} (MW)	116	105	189
Peak divertor power load, P_{peak} [MW/m^2]**			
HHK model	14	17	54
2-D code	20	14	75
Swept and ergodized	7.7	5.6	17

---

* without burn control [cf. Table 9-3].

** Note: The divertor power loads are discussed in §3.4. All power loads include the physics safety factor (§3.4.3) and include no factor for engineering peaking. The first row (HKH model) gives the power loads as obtained from the systems code [9.1,2]. The second row (2-D code) gives the results of 2-D modelling (§3.4.1). The third row (swept and ergodized) gives the time-averaged peak power load with ±0.116 m sweeping and 0.06 m ergodization (see Table 3.2-2b and §3.4.4).

TABLE 9-3. INDUCTIVE OPERATING POINTS

code and description of operating point*	A1a	A1b	A2	A3	A4	A5
I [MA]	22	22	25	28	22	22
β_p	0.65	0.65	0.48	0.38	0.78	0.65
P_{aux} [MW]	0	25	0	0	0	110
P_{fus} [GW]	1.1	1.1	1.1	1.1	1.7	1.1
P_{peak} [MW/m^2]						
HKH model	14	11	18	20	40	47
2-D code	20					
swept&ergod.	7.7					
L_w [MW/m^2]	1	1	1	1	1.6	1
Z_{eff}	1.7	1.6	1.7	1.7	1.6	1.7
t_{burn} [s]	400	300	110	35	480	400

* Note:

A1a	reference ignition (without burn control)
A1b	reference ignition (with burn control)
A2	high current
A3	high current with 20 V-s savings by noninductive ramp-up assist
A4	beta at Troyon limit (g = 2.5) at nominal current
A5	driven operation at Q = 10

characteristics of the two reference operating points and of the nominal steady state case are shown on Table 9-2.

All heat loads quoted are in the absence of separatrix sweeping, and therefore only reflect changes in both total power to the divertor and scrape-off width. Sweeping of the X-point over several centimeters (3 cm are envisaged) will impose a lower limit on the effective power deposition width and thereby reduce some of the higher power load values. Separatrix sweeping is not expected to change the divertor plasma temperature, so that the large values expected in some of the cases (at low plasma density, particularly the steady-state cases) can cause severe erosion and impurity release problems (see §3.0) even if the power loading can be rendered acceptable by separatrix sweeping.

Common characteristics of the operating points are:

(a) Double-null divertor operation is assumed, a = 2.15 m, R = 6 m, with $\kappa(95\%) = 1.98$, $\delta(95\%) = 0.4$.

(b) The divertor heat load quoted is the peak physics heat load, including physics safety factors (model safety factor, physics toroidal peaking, physics time peaking, see Sect. 3.0), and excluding engineering peaking factors (resulting for instance from plate misalignment). The maximum heat load is quoted for the outside divertor plate, and refers to the maximum heat load in the absence of separatrix sweeping. This heat load is the result of an analytical scaling from existing 2-D model results and is to be confirmed by detailed 2-D modelling.

TABLE 9-4. LONG-PULSE AND STEADY-STATE OPERATING POINTS

code and description of operating point*	B1	B2	B3	B4	B5	B6	B7	B8
I [MA]	15.4	21.4	22	17.6	22	19	14.6	22
β_p	1.4	1	0.75	0.9	0.65	1.1	1.2	0.9
P_{aux} [MW]	110	115	115	115	0	115	115	130
P_{fus} [GW]	0.86	1.6	1.3	0.86	1.1	0.75	0.42	0.86
P_{peak} [MW/m^2]								
HKH model	17	17	78	31	14	54	17	72
2-D code	14			43		75		
swept&ergod.	5.6			13		17		
L_w [MW/m^2]	0.8	1.5	1.2	0.8	1	0.7	0.4	0.8
Z_{eff}	2.2	2.7	1.7	1.6	1.7	2.2	3.1	2
t_{burn} [s]	2500	1000	800	960	850	ss	ss	ss

* Note:

- B1 reference long-pulse (modest impurity seeding)
- B2 high wall load long-pulse (with impurity seeding)
- B3 long-pulse with lowest confinement enhancement (no impurity seeding)
- B4 long-pulse with minimum divertor load (no impurity seeding; 18% CD)
- B5 long-pulse inductive burn with 50 V-s savings by noninductive rampup assist
- B6 nominal steady-state (no impurity seeding)
- B7 steady-state constrained by divertor load (with impurity seeding)
- B8 steady-state at nominal current (no impurity seeding)

Reference total power input to all divertors is approximately 115 MW and values appreciably exceeding this are presently not considered to be allowable.

(c) Values for the wall load ≤0.8 MW/m^2 and burn times ≤800 s are considered to lie below the requirement for testing in the technology phase. Burn times considerably in excess of this minimum value are highly desirable from technology testing considerations.

(d) For evaluating the length of the burn phase, the resistive volt-seconds consumed to start of flat top are assumed to vary as the plasma current, with a constant of proportionality $C_{Ejima} = 0.4$. In other words, optimal programming of the start-up phase is assumed [§6.4]. The internal inductance $l_i(3)$ is equal to 0.65.

9.2.1 Major Characteristics of Operating Points: Inductive Operation

A brief characterization of the various operating points which are considered for inductive operation of ITER follows. The term "confinement enhancement factor" is used to denote the improvement in energy confinement time over ITER power law L-mode scaling that is required for each operating point [§2.1.3].

A1 Reference ignition. Full field and nominal current (22 MA), this case is calculated to satisfy divertor heat load and minimum wall load for technology testing requirements without the addition of impurities to the plasma to enhance radiated power ("impurity seeding") to reduce divertor heat load. At a plasma density of 1.22×10^{20} m^{-3}, the plasma temperature is 10 keV during the burn, this may constitute a thermally unstable operating point. Burn temperature control is therefore necessary. The Volt-seconds, at the expected $Z_{eff} = 1.66$ will suffice for ~400 s of burn.

A2 High current case (25 MA) at the same wall load as the reference ignition case. Ignition is obtained at a lower value of confinement enhancement above L-mode in this case (1.8 vs 2.0 for case A1) but the divertor heat load is somewhat beyond present constraints. The possible burn time is ~110 s.

A3 High current case with LH ramp-up assist to save volt-seconds during current ramp-up. This is the highest current case (28 MA) considered because of the q-limitations ($q_\psi \sim 2.4$) and has an expected divertor heat load beyond the presently allowed limit. For ignited burn, the required confinement enhancement is only 1.6–1.7 with 10% He concentration (and only ~1.3 for short burn with 0% He), but the burn duration is limited to ~35 s unless more than 20 V-s are saved by lower hybrid ramp-up assist.

A4 Beta-constrained case at nominal current (22 MA). The plasma beta is raised to correspond to a Troyon g-factor of ~2.5. The wall load then becomes 1.6 MW/m^2. The divertor heat load would then be far beyond the presently allowed limits.

A5 Driven operation at Q = 10. This case leads to the lowest required confinement enhancement factor (1.0–1.23 at start of burn) with 108 MW of auxiliary heating injected. As a result of the large auxiliary power requirements, the divertor heat loads would be well in excess of the present limits.

9.2.2 Major Characteristics of Operating Points: Long-Pulse Operation

The operating points chosen as candidate cases for technology phase operation are listed below. All of these operating points depend on non-inductive current drive, either during the flat-top or during ramp-up, in order to provide a burn duration long enough for technology testing. A brief characterization of the various operating points which are considered for long-pulse/steady-state operation of ITER follows:

B1 Reference long-pulse operation. The current is reduced to 15.4 MA. The fraction of current driven non-inductively is kept at 30%, sufficient to assure current profile control. The confinement enhancement factor is 2.2/1.8 (with respect to L-mode scaling according to ITER power/offset-linear scaling, see §1.0 and §2.1), and modest impurity seeding (0.7×10^{-3} Fe or similar medium-Z impurity, $Z_{eff} = 2.2$) is used to keep the divertor heat load down. The burn time deduced (from volt-second requirements) is ~2500 s. This scenario represents a compromise satisfying the constraints on divertor heat load, confinement, current drive fraction, wall load and burn time while requiring only modest impurity seeding. Some estimate for impurity radiation from the divertor is incorporated in the present model, but the uncertainty is large. If this radiation is greater, the additional impurity seeding could be reduced. Relaxation

of one or more constraints due to physics advances could lead to the various alternate scenarios B2 to B8.

B2 High wall load long-pulse (seeded). This scenario permits an increase of the wall load, with a decrease of the burn time to 1000 s, at constant current drive fraction but higher current (21.4 MA) than B1. The divertor heat load is maintained at acceptable values by stronger impurity seeding (1×10^{-3} Fe, Z_{eff} = 2.7). This procedure may not be compatible with other constraints, such as the density limit or confinement requirements.

B3 Long-pulse operation with lowest confinement enhancement factor (unseeded). In this case, the burn pulse is limited to 800 s and impurity seeding is not used. The plasma current is 22 MA, with a non-inductive current fraction of 30%. The required confinement enhancement factor is 1.6/1.2. However, the calculated divertor heat load would be far in excess of the constraint.

B4 Minimum divertor load with no impurity seeding. In this case, impurity seeding is not used, and a compromise between the non-inductive current fraction (18%, probably below the minimum required for profile control), pulse length (960 s), and the divertor heat load (25 MW/m^2, twice the present constraint) is struck.

B5 Long-pulse inductive burn with non-inductive ramp-up assist. The plasma parameters for this case are essentially the same as for the ignition reference case A1. In order to satisfy the divertor heat load constraint, current drive is applied only during startup. It is here assumed that 50 V-s can be saved by this means over purely inductive start-up. An inductive burn of 850 s would then be possible. However, no current profile control is applied during the burn.

B6 Nominal steady-state (with no impurity seeding). Presently, none of the steady-state scenarios satisfy the divertor heat load constraints. All three steady-state cases (B6, B7, and B8) have low densities, (0.6–0.65) $\times$ 10^{20} m^{-3} to allow steady-state non-inductive current drive (71–75% of total plasma current, the rest is provided by the bootstrap effect) at the nominal installed current drive power (115 MW). The nominal unseeded case would require a significant advance in divertor physics and technology because of the high heat loads predicted. The average wall load is 0.69 MW/m^2, somewhat below the minimum desired for technology testing. The burn time is expressed as seconds of burn for a given fluence, e.g., 4.6×10^7 s per MWa/m^2. The plasma current for this nominal steady-state case is 19 MA.

B7 Divertor-constrained steady state (seeded). The divertor heat load constraint is now satisfied, but at the cost of strong impurity seeding (1.3×10^{-3} Fe, Z_{eff} = 3.1) and the wall load (0.39 MW/m^2) is well below the minimum value required for technology testing. However, this case constitutes a mode of interest for physics experiments.

B8 Steady-state at nominal current (unseeded). Here, the wall load and the plasma current are fixed at their nominal values. Impurity seeding is not used. Consequently, the divertor heat load would rise to a value far beyond the presently accepted limit. Attainment of this minimum acceptable wall loading of 0.8 MW/m^2 also requires an increase of the installed current drive power to 127 MW from the nominal value of 113 MW.

9.2.3 Divertor Sweeping

The divertor heat loads calculated are the peak "physics" heat loads (i.e., without engineering peaking factors) resulting from scaling of 2-D model results. As the width of the power scrape-off decreases, however, it becomes possible to reduce the effective heat load on the divertor surface by sweeping the point of maximum heat load over a moderate distance on the divertor plate. Sweeping of this kind will be partially accomplished by unavoidable noise in the position control system. In a credible design, however, it must be possible to assure the desired sweep width actively. From considerations of eddy current losses in the coils and of power supply requirements, an active sweep of the X-point by ± 3 cm at a frequency of 0.2 Hz seems acceptable [9.4, 9.5]. This would assure a reduction of average power load from the maxima quoted by a factor of two to three.

9.3 OPERATIONAL SCENARIOS

The basic operational scenario in the physics phase of ITER is several hundred seconds of ignited burn with some external power (20–30 MW) for burn temperature control. Variations of this basic scenario include non-inductive ramp-up assist and non-inductive burn duration assist. As has been discussed, these latter modes must be developed in the physics phase to assure adequate burn pulse lengths in the technology phase. In addition, since the burn pulse duration is now comparable to or longer than the plasma current penetration time, current profile control becomes important. Even though no satisfactory steady-state operating point with the required characteristics for the technology phase has presently been identified, the possibility of steady-state operation will also be studied in the physics phase. The major difficulty for steady state operation resides in the predicted divertor conditions. However, present modelling of the scrape-off layer and of divertors is still incomplete, so that some improvement may be possible.

In the following, the time evolution of the discharge in the reference ignition, the reference long-pulse, and the nominal steady-state scenarios are described. The overall operation sequence can be divided into four phases: (i) start-up, in which the gas breaks down, the plasma current is ramped-up to the operating point value, and the plasma is heated to the working point; (ii) burn, the slowly varying period of plasma conditions in which fusion power is produced; (iii) shut-down, in which the plasma is allowed to cool and the density and current are decreased to zero; and (iv) dwell, the period during which the next shot is prepared.

9.3.1 Reference Ignition Scenario

The time evolution of the reference ignition scenario, with the coil current evolution as in reference [9.6] is shown on Fig. 9-1. In this reference scenario, plasma breakdown is programmed to occur towards the inner wall near the midplane, because the electric field is higher and the loop voltage in the presence of eddy currents builds up faster in this area [9.4]. More electric field is thus available more rapidly. Breakdown will normally be assisted by electron cyclotron heating power.

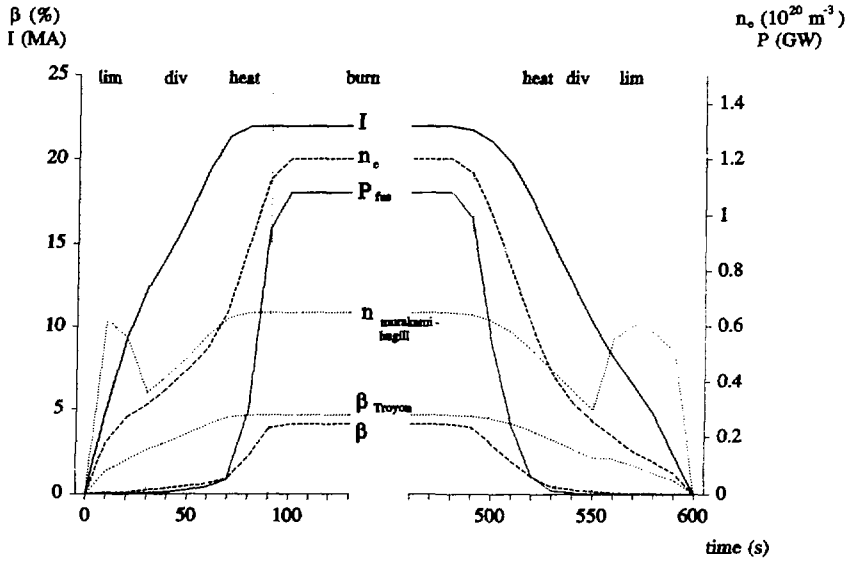

FIG. 9-1 Typical ignition scenario. The beta limit (β_{Troyon}) is calculated for g = 2.2. The density n_e is the volume average. At the top of the figure indicated are the phases for the discharge: limited, diverted, with additional heating, and burn.

With a loop voltage of approximately 10 V applied to the plasma, the plasma current attains 0.5 MA in about 0.5 s. Subsequently, the rate of current rise is decreased, to ~0.4–0.5 MA/s, to assure adequate current penetration. Establishment of the current profile is aided by expanding the cross-sectional area of the plasma during current ramp-up. The plasma minor radius is limited by inner wall contact during this stage, and is allowed to increase from the initial 0.8 m to the full minor radius of 2.15 m by a programmed increase of the plasma major radius as the plasma current rises to 10 MA. In the following phase, the plasma shape is changed from an essentially circular plasma, whose boundary is defined by start-up limiters at the position of wall contact, to the diverted cross-section with an elongation of 1.98 as the plasma current is raised to 15 MA. As can be seen on Fig. 9-1, this change from circular to strongly elongated cross-section results in a rapid variation of edge q. The final current increase to the nominal 22 MA level occurs with no change in plasma cross-section and at a reduced rate of current rise (0.15–0.25 MA/s) to assure current penetration.

From the preceding discussion, it is clear that a major constraint during the current rise phase is to control the plasma current profile. Avoiding unfavorable profiles (e.g. to minimize the likelihood of disruptions) effectively sets an upper limit to the rate at which the current can be raised. On the other hand, to minimize volt-second consumption, the current should be increased rapidly (see §6.0). From this point of view, it is advantageous to keep the plasma temperature low during this stage, and therefore to keep the average plasma density near the maximum practicable, i.e. close to the Murakami-Hugill limit for ohmic operation (indicated on Fig. 9-1, not

applicable with strong additional heating, see §2.3), hence at 3 to 6 × 10^{19} m^{-3} (note, however, the difficulty with non-inductive ramp-up assist, §9.3.4).

During the last stage of start-up, the plasma is heated to burn conditions. For the reference ignition scenario, the temperature is increased from typically 3 keV to 10 keV, and the plasma density is raised to 1.2 × 10^{20} m^{-3} in the space of about 20 s. The plasma stored energy thereby increases by approximately 400 MJ. The auxiliary heating systems must supply the necessary power to raise the stored energy as well as that required to cover the losses during this transition stage. Adjustment of the isotope concentration in the plasma fuelling system assures that the correct D/T concentration for the burn phase is attained at the end of this period. The parameters described here correspond to ignited operation. However, burn-control of the operating point [§2.4.4] may require somewhat different plasma conditions: n_e ~ 1.5 × 10^{20} m^{-3}, T_e ~ 8 keV, and auxiliary power of ~25 MW with feedback modulation (scenario A1a).

Because of current penetration and power supply considerations, the total time to ramp-up the plasma current to the 22 MA nominal current is expected to be about 70 s, of which the first ~30 s are in limiter configuration. With the ~20 s required to bring the full-current plasma to burn conditions, the start-up phase of the reference ignition scenario therefore requires about 90 s.

Since the reference ignition case uses only inductive current drive, the length of the burn phase is directly determined by the Volt-seconds remaining at the start of burn. The flux consumption as a function of time is seen on Figs. 9-2 and 9-3. For the given ramp-up scenario, with an impurity content giving a Z_{eff} of 1.66, and a 15% bootstrap current in addition to the inductively driven current, and an internal inductance $l_i(3)$ = 0.65 throughout the burn, a burn duration of nearly 400 s can be attained. In this scenario, the burn duration is therefore much shorter than the resistive time constant of the plasma (and somewhat shorter then the skin time), so that current profile control is not required. The desired current profile must instead be developed during current ramp-up, and then remains essentially unchanged until the end of burn, apart from the modifications due to bootstrap current. The low-temperature, high-density operating point (chosen because of divertor constraints) may require a form of burn temperature control to prevent the plasma temperature from run-away. Feedback control of auxiliary power, with a typical power of 20–30 MW (up to 75 MW for experimental purposes) is considered adequate to stabilize the burn (see §2.4.4).

At the end of the burn phase, all available volt-seconds of the transformer will have been expended in order to maximize the burn duration. The flux required for the plasma shut-down must therefore be supplied by the plasma inductive flux. The first phase of shut-down must be a decrease of the fusion power, by decreasing the density of the reacting particles and/or by cooling the plasma (e.g. by impurity injection or by changing the gas composition) with a modest decrease in the plasma current to recover Volt-seconds. During normal shut-down, the fusion power will be reduced and most of the thermal stored energy will be extracted over approximately 20 seconds (corresponding to ~5 energy containment times at burn conditions). As the fusion power decreases, the density limit also decreases. The plasma density must therefore be lowered to about half of that during burn. The speed of density decrease may well be much slower than the power decrease since it depends strongly on the recycling behaviour of the wall and plasma-facing components and on the available pumping speed. Some additional heating will therefore be required during this phase to avoid

exceeding the density limit. This may be seen on Fig. 9-1, where the Murakami-Hugill limit indicates the density limit for pure ohmic operation. When the plasma density is higher than this curve, some heating other than ohmic is required. As the plasma cools, the plasma current will be allowed to decay smoothly and the plasma shape will be gradually modified from the elongated divertor configuration of the burn phase to a circular configuration limited by the start-up limiters mounted on the vacuum chamber wall. The current decrease will resemble the time inverse of the start-up phase, and approximately the same length of time (70 s) is expected to be necessary. The overall time from end of burn to zero plasma current will therefore be approximately 100 s. (A variant has been proposed, in which, in order to improve density control during the start-up phase of the succeeding pulse, the discharge would be terminated in helium [9.7]. In this case, the burn phase would then be terminated by changing the working gas to helium, and the interaction of the helium plasma with the plasma-facing components during the shut-down phase would be used to reduce the adsorbed hydrogenic species.)

In the dwell phase, the next shot is prepared. This involves pumping the vacuum chamber to the required pressure, in the 10^{-5} millibar range, conditioning the plasma-facing components to provide the correct recycling characteristics for the next shot, and establishing the currents required for the plasma initiation phase in the poloidal field coils. From power supply and pumping considerations, approximately 100 s will be required for this phase.

In the scenario described, the total time during a tokamak cycle in which the plasma is not ignited is approximately 300 s. The duty cycle for the reference ignition case is therefore at best about sixty percent, as can be seen on Fig. 9-3.

Variations on the reference ignition scenario have been considered. Plasma start-up could take place on the outside wall with assistance from electron-cyclotron waves to aid in plasma formation and assistance from lower-hybrid current drive to reduce the Volt-seconds required for start-up. The variation of plasma current with the plasma cross-section can be programmed to attain a lower safety factor (e.g. below four) earlier in time and to remain low during the subsequent current profile development in order to avoid locked mode formation [9.8] (which could subsequently lead to disruptions). Elongation of the plasma and the transition to a diverted configuration could be started at lower plasma current to reduce power supply requirements. The rise of plasma stored energy (and poloidal beta) as the plasma is heated to ignition could be accompanied by a plasma current increase in order to alleviate the requirements on the poloidal field circuit in the preceding stage. A different current profile may develop, reducing the ignited burn duration if it is more peaked [by nearly 100 s if $l_i(3)$ is 0.75 instead of the reference value of 0.65] due to the increased flux necessary to establish such a current. During the shut-down phase, it might be preferable to limit the plasma by outer rather than inner wall contact to provide more margin against disruptions. However, the main characteristics of the reference ignition scenario are expected to remain those described in this section.

9.3.2 Reference Long-Pulse Scenario

The reference long-pulse scenario incorporates non-inductive current drive to prolong the duration of a sub-ignited burn phase (with $Q \sim 8$). Plasma start-up and current ramp-up is, however, accomplished inductively, so that the start-up phase of

this scenario is similar to that of the reference ignition case and the same constraints apply. Because of the lower current, 15.4 MA, chosen for this case, current ramp-up is stopped after about 45 s, and the plasma is heated to burn conditions over the next 20 s. Whereas the plasma density for this scenario is about 10% lower than for the reference ignition case, the plasma temperature is about 10% higher, so the total energy content of the plasma at start of burn and the power necessary in the heating phase are not greatly affected.

The Volt-seconds saved by working at lower plasma current alone would be sufficient to increase the flat-top duration to about 1000 seconds if the same loop voltage were required. The flux consumption of this scenario is compared with that of the reference ignition scenario on Figs. 9-2 and 9-3. With non-inductive current drive power at the 110 MW level providing 30% of the plasma current, and the bootstrap current providing another 30%, the burn duration can be extended to 2300 s, somewhat longer than the global resistive time constant of the plasma. Under these conditions, the current profile must be controlled to maintain the desired shape using the non-inductive current drive capability or local temperature profile control. In the reference long-pulse burn phase, auxiliary heating is therefore needed to control not only the burn parameters, as in the ignition case, but also the current profile.

In the shut-down phase, the time required for extracting the thermal energy from the plasma can be expected to be similar to that required for the ignition case. Because of the lower plasma current, however, the limiting density for purely ohmic operation is also lower (Murakami-Hugill limit is approximately 4.4×10^{19} m^{-3}), so that more time must be allocated to the density decrease. The plasma current decrease can proceed at the same rate as in the ignition case. The time for normal shut-down will therefore be in the range of 100 s.

The dwell time will not be shorter than for the ignition scenario, so that the total time during a tokamak cycle in which the plasma is not burning is also nearly 300 s. Because of the much longer burn duration, the duty cycle for the reference long-pulse case is appreciably higher than for the ignition case, close to 90 percent.

9.3.3 Nominal Steady-State

The nominal steady-state operation is defined in Sect. 9.2, where it is also clearly indicated that this mode of operation is not consistent with present divertor constraints. In this scenario, the plasma is also initiated and ramped-up inductively. The start-up scenario is therefore similar to the reference ignition case until the flat-top current of 18.9 MA is reached. The time required for this would be about 60 s. The energy input into the plasma to reach the burn conditions is again about the same, but for this case, the density is only increased by about 20% over the ohmic density limit. Instead, the plasma temperature is increased to about 20 keV, about twice that of the reference ignition case.

During the burn phase, the auxiliary heating systems at a 110 MW power level provide about 70% of the total plasma current by non-inductive current drive, the rest being supplied by the bootstrap current. For this mode of operation, current profile control as well as burn control must clearly be catered for in the design of the auxiliary heating systems.

Plasma shut-down is expected to be less delicate for this case because of the lower plasma density during burn. A violation of the density limit during shutdown is

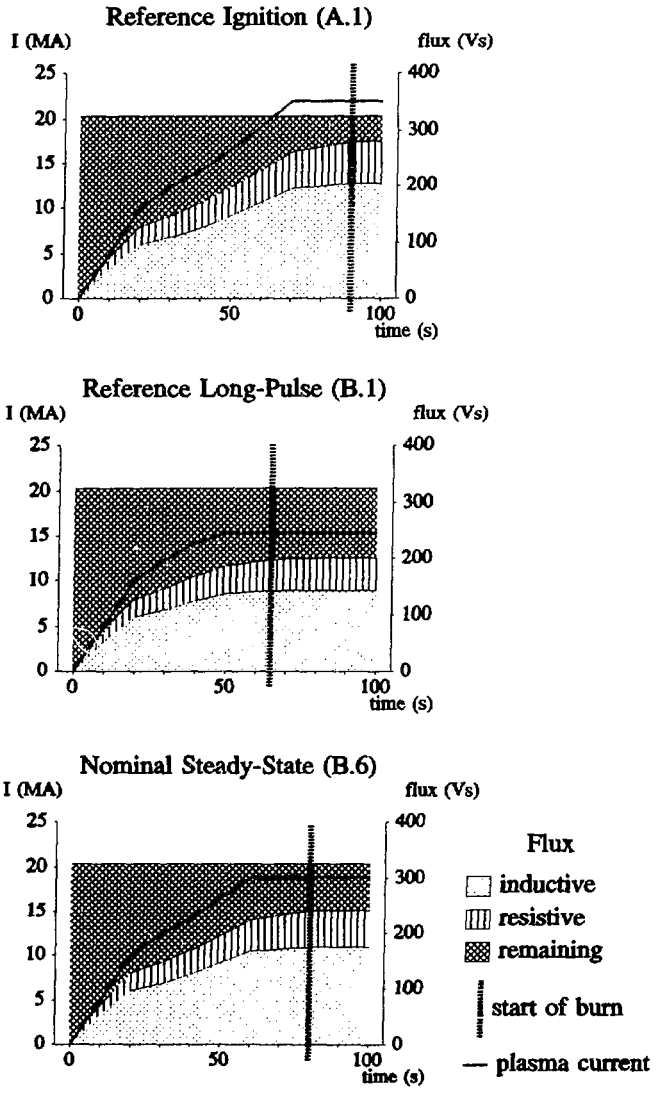

FIG. 9-2 Reference scenarios: first 100 seconds.

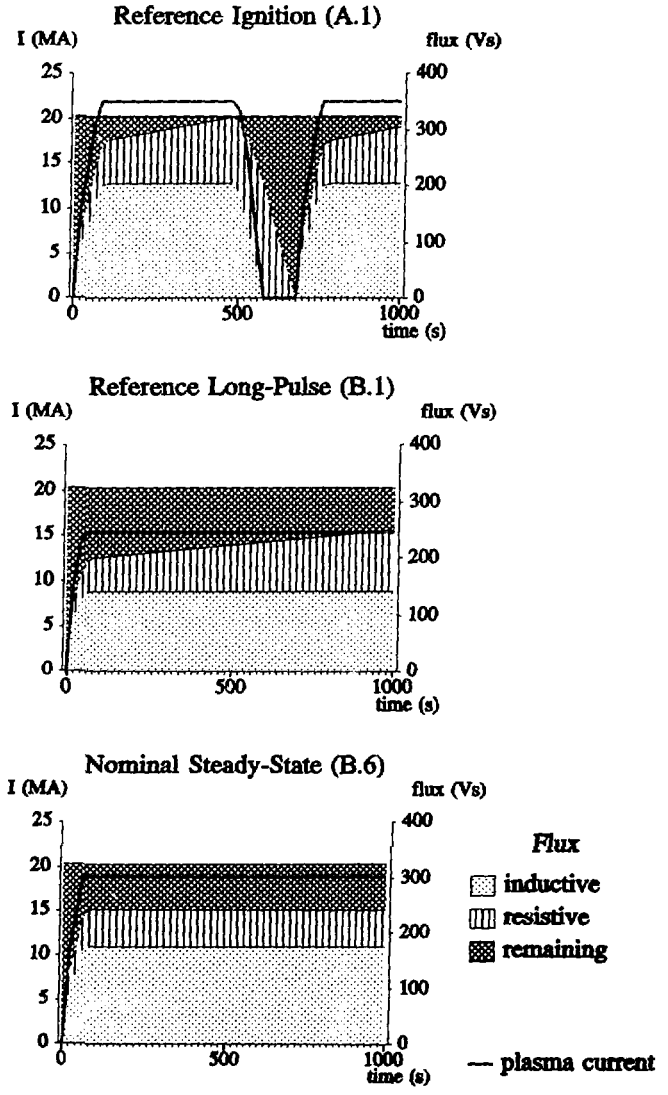

FIG. 9-3 Reference Scenarios: first 1000 seconds.

thus easier to avoid. A part of the current drive power can also be used to control the plasma behaviour during shutdown.

For this mode of operation, the duty cycle can clearly approach 100%. Nevertheless, it must be re-iterated that the nominal steady-state described here satisfies neither the presently known divertor constraints nor generates the neutron wall-loading level desired for technology testing.

9.3.4 Variants Based on Noninductive Ramp-up Assist

Two major variants of the basic scenarios exist, based on current ramp-up assisted by non-inductive means (see §5.0 and [9.2,3]). For both scenarios, careful programming of the plasma configuration and density during start-up is a prerequisite to maximize the efficiency of non-inductive current drive. The current ramp-up rate is taken to be the same as in the inductive ramp-up scenarios, and lower-hybrid current drive is used to reduce the Volt-seconds dissipated during the ramp-up. Present simulations indicate that about 1 V-s can be saved per MW of injected lower-hybrid power at an average plasma density of 2×10^{19} m^{-3}. Such a low plasma density is expected to present problems with the power-handling capacity of the start-up limiters and divertor. If the plasma density is raised to 4×10^{19} m^{-3} in order to improve the heat loads, the volt-second savings will be only half as big per MW of injected power. The heat load problem on limiter and divertor during these start-up scenarios is still under investigation.

In one of the variant start-up scenarios (case A3), the volt-second assist will be used to attain a plasma current of 28 MA in the reference ignition scenario. The higher plasma current provides ignition margin against an unfavorable confinement scaling. Most of the additional flux required for the higher current is provided by the poloidal field coils, but a net saving of ~20 V-s by lower-hybrid current drive is necessary to attain 28 MA and provide a burn duration of ~35 s. Ramp-up and ramp-down of current would each require about 85 s in this case, about 15 s more than in the reference ignition case. As this scenario is an extreme case for physics phase studies, duty-cycle considerations are not applicable.

In the other variant start-up scenario (case B5), lower-hybrid ramp-up assist would maximize the length of the inductive burn phase at the same plasma parameters (22 MA) as the reference ignition scenario (case A1) by reducing the V-s dissipated during ramp-up by 50 V-s. Apart from the different temporal density variation required to assure a current drive efficiency sufficient for saving 50 V-s, the evolution of the discharge is the same as the reference ignition scenario. Instead of a 400 s burn, 850 s are expected, and the total time during a tokamak cycle in which the plasma is not ignited is again roughly 300 s. The duty cycle therefore approaches 75%.

9.3.5 Outboard Start-up

In the scenarios presented in the preceding sections, break-down is always programmed to occur near the inner wall (small major radius side of the torus), except for LH assist rampup. As discussed, inboard start-up maximizes the electric field available for breakdown. For the variants with lower-hybrid assisted ramp-up in particular, and possibly to optimize volt-second consumption in inductively ramped-up scenarios, it may be advantageous to grow the plasma from an outboard start-up

limiter to the divertor configuration. The lower electric field available would necessitate breakdown assistance by electron cyclotron waves.

Outboard shut-down would be expected to be less sensitive to disruption than inboard shut-down, because a reduction of the plasma cross-section (and plasma current) due to inadequate position control would move the plasma away from the limiter. Exact position control at reduced plasma current thereby becomes less critical to avoid disruption. In addition, current profile control by lower-hybrid waves could be applied during this phase. The details of this outboard start-up/shut-down scenario remain to be defined.

REFERENCES (§9.0)

[9.1] *ITER Parametric Analysis and Operational Performance*, IAEA/ITER/DS/22, ITER Documentation Series, IAEA, Vienna (1991).

[9.2] L.J. PERKINS et al., "ITER operational performance: rationale for reference DT operational scenarios," ITER-IL-SA-1-0-9, March 1990.

[9.3] G.W. PACHER et al., "Reference operational scenarios," ITER-IL-PH-15-0-3, March 1990.

[9.4] *ITER Poloidal Field System,* IAEA/ITER/DS/27, ITER Documentation Series, IAEA, Vienna (1991).

[9.5] *ITER Magnets*, IAEA/ITER/DS/26, ITER Documentation Series, IAEA, Vienna (1991).

[9.6] N. MITCHELL et al., "Design basis for the plasma system," ITER-IL-PF-1-0-1, January 1990.

[9.7] J. EHRENBERG private communication.

[9.8] J. WESSON et al., *Nucl. Fusion* **29** (1989) 641.

10.0. PHYSICS R&D

10.1 INTRODUCTION

ITER-related Physics R&D Programmes [10.1] were set up in two steps: A first programme covering the latter part of the ITER conceptual design phase (1989 - 1990) was generated and agreed between summer 1988 and spring 1989, and partial results have been reported. A second programme is being developed, to provide the data base necessary for supporting the decision to start ITER construction and to be carried out in parallel with the ITER engineering design (1991 - 1995).

10.2 PROGRAMME 1989 – 1990

In 1988, physics areas in which the database was insufficient for the design of ITER or which, at that time, were not sufficiently covered by the ongoing programmes of the ITER Partners, were identified and a first R&D programme was set-up for the years 1989-1990 [10.2]. This was structured in 23 tasks. About one half of them were concerned with questions in three priority areas:

- power and particle exhaust physics (i.e., the combined fields of plasma edge physics and plasma-wall interaction as well as impurity behaviour);
- characterization and control of disruptions;
- long-pulse operation in regimes with low energy transport (in particular in the H-mode).

For some of the tasks (e.g., characterization of high-Z materials for plasma-facing components; electron cyclotron and ion cyclotron current drive), satisfactory coverage was not possible over the period in question, due primarily to the need to install new or to adjust existing equipment on various devices, but also, in some cases, to the necessity to perform the work in a staged approach.

A summary of the results obtained is given in Ref. [10.3]; of particular importance has been the information on:

(1) the analysis, in large tokamaks, of flux swing needs during optimized inductive current ramp-up, which has had a direct impact on ITER design, as well as the demonstration of substantial volt-second saving by lower hybrid wave current rampup assist;
(2) operation with Be coated walls, which has led to the serious consideration of Be as a design option as a plasma-facing material in ITER;
(3) the reasons for the appearance of the density limit;
(4) helium transport properties and measurements of the helium pumping efficiency of pumped limiters and divertors;
(5) feedback control of the 2/1 tearing mode using helical fields;
(6) long-pulse operation in H-mode with "grassy" edge localized modes (ELMs), avoiding appreciable impurity accumulation, as well as ways to control ELMs:

(7) the scaling of energy confinement, in particular first results for the H-mode (showing a similar dependence as typical L-mode scalings) and the scaling with aspect ratio for the L-mode; and
(8) plasma formation assist by electron cyclotron waves.

10.3 PROGRAMME 1991 - 1995

10.3.1 Approach

For the period 1991 - 1995 a framework programme was established that covers all R&D needs to support the engineering design of ITER [10.4,5]. Priority areas are those mentioned under Sect. 10.2 (including also the exploration of operational limits to devise operation scenarios for ITER which minimize the occurrence of disruptions), and in addition the physics of discharges containing a population of fast ions (representative for the conditions present during heating by fusion α-particles). In fact, the most crucial problems, to validate the ITER design concept and complete the physics data base required for starting ITER construction, in practical terms, are

- the demonstration in experiments prototypical for ITER, that operation with a cold divertor plasma ($T_e \leq 30$ eV) is possible, that the peak heat flux onto the divertor plate can be kept below about 10 MW/m^2, and that helium exhaust conditions corresponding to a fractional burnup larger than 3% can be ensured,
- a characterization of disruptions that allows specification of their consequences for the plasma-facing components, and demonstration that the number of disruptions can be reduced to a level yielding an acceptable lifetime of these components;
- the confirmation that steady operation in a regime with low energy transport (in particular in the H-mode) and satisfactory plasma purity is possible under ITER condition, as well as the capability to predict energy confinement for this mode in ITER with satisfactory accuracy;
- insurance that the presence of an appreciable population of fast ions does not jeopardize plasma performance in ITER.

Further areas covered are plasma heating and fuelling, long-pulse operation (including noninductive current drive) and optimization of discharge startup and shutdown, as well as plasma diagnostics.

The potential coverage of these R&D needs is satisfactory. There is redundancy in several areas, but concentration of efforts on some critical areas will be necessary to obtain all the information needed in time. These efforts will have to combine experiments, theoretical analysis and modelling; in particular systematic model development and validation, as a basis for extrapolation to ITER, is required.

10.3.2 Programme 1991 - 1992

An ITER-related R&D programme for the years 1991 and 1992 (but extending beyond as far as possible) is presently being developed from the framework programme 1991 - 1995. It is based on a detailed description of the R&D needs for ITER [10.5]. The programme covers five areas and is subdivided in 22 tasks, supplemented by subtasks where appropriate for a clear definition of the problems.

Ten of these tasks addressing the above crucial problems have been classified as high priority tasks. The other tasks are concerned with the optimization of ITER operation, including in a few areas (power and particle exhaust; fuelling; noninductive current drive) alternative and/or innovative schemes the development of which may extend beyond the end of ITER design.

The coverage of the tasks emerging from the contributions offered is generally good. However, studies of the edge plasma in ITER-relevant divertor configurations and operating conditions will be intensified only from 1992 on. Further improvement of the diagnostics for the edge plasma is needed. Work on the validation and development of models for the plasma edge as well as the characterization of candidate materials for plasma-facing surfaces (low and high Z) needs to be enhanced. The validation of theoretical predictions on the effects caused by a population of fast ions requires specific attention. The diagnostic means to characterize such a population must be improved. As far as operational issues are concerned, large-scale experiments on noninductive current drive by fast waves will only be done in 1993 and later, and work on fast (emergency) shutdown is not yet planned.

10.3.3 Diagnostics

A special process was adopted for developing an R&D programme for plasma diagnostics (see Sect. 7.0 and Refs. [10.6,7]). The activity will have to be closely related to ITER design, to a technology oriented R&D activity on nuclear properties of materials and components, as well as to the Physics R&D programme being undertaken at many tokamaks worldwide. It will draw on information arising from these programmes in evolving the requirements.

REFERENCES (§10.0)

[10.1] F. ENGELMANN et al., "Physics R&D Programme," Plasma Physics and Controlled Nuclear Fusion Research (Proc. 13th Int. Conf., Washington, D.C., 1990), IAEA, Vienna, paper IAEA-CN-53/F-3-18.

[10.2] ITER Technical Report, "*ITER-Related Physics R&D Programme 1989-1990*," ITER-TN-PH-9-2, Garching, 1989.

[10.3] *Physics and Technology R&D for ITER Conceptual Design*, IAEA/ITER/DS/19, ITER Documentation Series, IAEA, Vienna (1991).

[10.4] ITER Document, "Framework programme for ITER-related physics R&D during detailed design (1991-1995)," ITER-IL-PH-16-0-7(f), Garching, 1990.

[10.5] *Research and Development Needs for ITER Engineering Design*, IAEA/ITER/DS/20, ITER Documentation Series, IAEA, Vienna (1991).

[10.6] V. MUKHOVATOV et.al., "ITER operation and diagnostics," Plasma Physics and Controlled Nuclear Fusion Research (Proc. 13th Int. Conf., Washington, D.C., 1990), IAEA, Vienna, paper IAEA-CN-53/F-3-17.

[10.7] ITER Technical Report, "*Plan for ITER-Related Plasma Diagnostic R&D During the Detailed Design Phase, 1991-1995 (and Beyond). Part I: ITER Related R & D Needs*," ITER-TN-PH-0-3, Garching, November 1990.

11.0. ACKNOWLEDGEMENTS

This report on the physics basis of the ITER Conceptual Design has been compiled by the ITER Physics Group. We gratefully acknowledge the contributions of the many hundreds of physicists throughout the international fusion community upon which the report is based. The authors listed on the title page are the main authors of the report. In addition, we have listed below the major authors and major contributors to each section of the report so that it is clear to the reader who had the major responsibility for the work, and so that we could acknowledge the members of the home team who made substantial contributions in each area. Most of the conceptual design studies was carried out by the home team members, and we would like to thank and acknowledge them.

We would also like to give special thanks to the members of the international fusion community who shared with us the results of their experimental and theoretical research as participants in the ITER Physics R&D Program, and who participated in the many workshops that were held on each physics issue.

The authors and major contributors for each section are:

1.0 OVERVIEW: F. Engelmann, N. Fujisawa, V. Mukhovatov, G.W. Pacher, H.D. Pacher, V.V. Parail, D.E. Post, N.A. Uckan.

2.0 PLASMA PERFORMANCE

2.1 Confinement: V. Mukhovatov, J.D. Callen, J.G. Cordey, F. Engelmann, O. Kardaun, S.M. Kaye, A. Nocentini, H.D. Pacher, V.V. Parail, D.E. Post, K. Riedel, T. Takizuka, N.A. Uckan, P.N. Yushmanov; M. Azumi, G. Batemann, J.P. Christiansen, J. DeBoo, Yu. Esipchuk, H. Shirai, K. Itoh, S. Itoh, K. Lackner, T. Matsuda, Y. Miura, M. Mori, O. Naitoh, K. Odajima, K. Razumova, F. Ryter, D. Schissel, N. Suzuki, H. Tamai, A. Tanga, K. Thomsen, S. Tsuji, T. Taylor, T. Tsunematsu, F. Wagner, H. Yoshida, R. Yoshino.

2.2 MHD Stability: T. Tsunematsu, K. Borrass, J.T. Hogan, L.D. Pearlstein, L. Zakharov; A. Bondeson, L. Degtyarev, S. Ishida, J. Manickam, H. Matsumoto, S. Medredev, V.V. Parail, T. Ozeki, P. Savrukhin, S. Tokuda.

2.3 Density Limits: K. Borrass, S. Krasheninnikov, T. Tsunematsu, N.A. Uckan; D. Campbell, F. Engelmann, M.F.A. Harrison, J.T. Hogan, Y.L. Igitkhanov, Y. Kamuda, H. Niedermayer, J. Neuhauser, H.D. Pacher, V.V. Parail, T. Petrie, D.E. Post, A. Stäbler, D. Stotler, N. Suzuki, T. Tuda, G. Vlases, R. Yoshino, P.N. Yushmanov.

2.4 Alpha Particle Physics: S. Putvinskij, K. Borrass, F. Engelmann, L.J. Perkins, D.E. Post, D.J. Sigmar, T. Takizuka, K. Tani; M. Azumi, S. Bespoludenov, M. Chaniotakis, F. Cheng, S. Haney, L. Hively, S. Konvalov, V. Lukash, J. Mandrekas, H. Mynick, V.V. Parail,

A. Polevoy, J.A. Rome, D.A. Spong, A. Smirnov, T. Tsunematsu, T. Tuda, N.A. Uckan, R. White.

3.0 POWER AND PARTICLE CONTROL: S.A. Cohen, M.F.A. Harrison, Yu. Igitkhanov, S. Krasheninnikov, A. Kukushkin, G. W. Pacher, H.D. Pacher, V. Pistunovitch, D.E. Post, M. Sugihara, T. Takizuka, V. Abramov, K. Borrass, B. Braams, J. Brooks, J. Cummings, F. Engelmann, T. Hirayama, E. Hotston, K. Itami, Y. Koide, T. Mizoguchi, H. Nakamura, A. Pigarov, A. Pozharov, M. Redi, D. Ruzic, M. Shimada, T. Shoji, K. Tobita, N.A. Uckan, N. Ueda, K. Werley.

4.0 DISRUPTIONS: G.W. Pacher, A. Astapkovich, S.A. Cohen, F. Engelmann, H.D. Pacher, D. Post, R. Sayer, T. Tsunematsu, J. Wesley; H. Fleischmann, N. Hosogane, N. Ivanov, T. Jensen, A. Kellmann, T. Kimura, S. Krashenninikov, L. Laurent, M. Mori, A. Russo, J. Wesson. I. Yonekawa, L. Zakharov.

5.0 CURRENT DRIVE AND HEATING: N. Fujisawa , H.J. Hopman, W.M. Nevins, V.V. Parail, D.W. Swain, V.L. Vdovin, J.G. Wegrowe; D.B. Batchelor, S. Bernabei, C. Boley, P. Bonoli, R. Campbell, C. Challis, Yu.F.Baranov, E. Barbato, R. Devoto, D. Ehst, A. Fukuyama, G. Giruzzi, C. Gormezano, K. Hamamatsu, T. Imai, J. Jacquinot, R. Janev, M. Kikuchi, H. Kimura, Y. Kisimoto, R. Koch, L.K. Kuznetsova, A.V. Longinov, V.M. Leonov, T. Mizoguchi, Y. Ogawa, K. Okano, L.D. Pearlstein, G.V. Pereverzev, F. Santini, S.E. Sharapov, G. Smith, A.K.N. Stepanov, E. Suvorov, K. Tani, Y. Terumichi, A.V. Timofeev, G. Tonon, T. Tuda, K. Ushigusa, M. Yamagiwa, S. Yamamoto, T. Yamamoto, E. Westerhof.

6.0 AXI-SYMMETRIC MAGNETICS: J. Wesley, J.T. Hogan, G.W. Pacher, H.D. Pacher, L.D. Pearlstein, S. Putvinskij, M. Sugihara, R. Yoshino; V. Beljakov, R. Bulmer, Y. Gribov, W.A. Houlberg, T. Kaiser, J. Leuer, H. Ninomiya, T. Matsuda, Y. Nakamura, A. Kavin, V. Korshakov, A. Portone, D. Robinson, A. Roshal, Y. Shimomura, K. Shinya, N.A. Uckan, L. Zakharov.

7.0 DIAGNOSTICS: V. Mukhovatov, A. Costley, F. Engelmann, H.J. Hopman, S. Ishida, O.N. Jarvis, Yu. Kuznetsov, D. Manos, D.E. Post, H. Salzmann, P. Stott, P. Thomas, S. Yamamoto, K.M. Young; J.M. Adams, R. Barnsley, D.V. Bartlett, P. Batistoni, V. Belyakov, F. Casci, S.A. Cohen, A. Donné, T. Elevant, R. Giannella, C. Gowers, V. Gusev, M. von Hellermann, J.A. Hoekzema, T.P. Hughes, T. Iguchi, A. Izvozchikov, D. Johnson, R. Kaita, J. Källne, A. Kellman, A. Khudoleev, T. Kondoh, Y. Kusama, F. Levinton, J. Lohr, M. Maeno, M. Martone, T. Matoba, S. Medley, A. Nagashima, K. Nagashima, P. Nielsen, T. Nishitani, D. Orlinskij, O. Pavlichenko, N. Peacock, J.-P. Rager, G. Razdobarin, Y. Sano, M. Sasao, M. Sato, M. Satoh, J. Schlüter, D. Shcheglov, M. Sironi, V. Smirnov, R. Snider, M. Stamp, J. Strachan, D.B. Syme, K. Takeda, A. Weller, R. Yoshino.

8.0 FUELLING: R. Yoshino, F. Engelmann, H.D. Pacher; S.A. Cohen, M. Gouge, M. Harrison, W.A. Houlberg, K. Itoh, B. Kuteev, L. Lengyel, W. Nevins, V.V. Parail, K. Tani, K. Shimizu.

9.0 TOKAMAK OPERATIONS: G.W. Pacher, F. Engelmann, N. Fujisawa, V. Mukhovatov, H.D. Pacher, L.J. Perkins, D.E. Post, Y. Shimomura, M. Sugihara, T. Tsunematsu, J. Wesley, K. Young; S.A. Cohen, J. Galambos, J.T. Hogan, T. Mizoguchi, T. Nakazato, V.V. Parail, A. Polevoy, S. Putvinskij, R. Yoshino.

10.0 PHYSICS R&D:

Setting up and executing the ITER-related Physics R&D Programme was possible only due to the dedicated and efficient help of research workers both from experimental teams and theory groups of the fusion programmes of the four ITER Partners. A very large number of colleagues have given advice in the definition of the R&D needs, many more have made important contributions through their scientific work that generated the results of the first two years of the Programme. Particular mention must be made of all those who ensured the liaison between the contributing institutions(*) and the ITER Physics Group, which did the overall coordination.

(*) Contributing Institutions (the experimental devices operated are given in brackets):

EC:
AEA, Culham (DITE, COMPASS)
CCFM, Varennes, Canada (Tokamak de Varennes)
CEA, Cadarache (TORE SUPRA)
CIEMAT, Madrid (JT-1)
CRPP, Lausanne (TCA, TCV)
ENEA, Frascati (FT, FTU)
ERM-KMS, Brussels
FOM, Nieuwegein (RTP)
IPP, Garching (ASDEX, ASDEX Upgrade, WVII-AS)
JET, Abingdon (JET)
KFA, Jülich (TEXTOR)
NFR, Stockholm and Gothenburg
RNL, Risø

Japan:
ETL, Tsukuba (TPE-1RM-15, TPE-2M)
Hitachi Ltd., Hitachi (HT-2)
JAERI, Naka and Tokai-mura (JFT-60, JT-60U, JFT-2M)
Kyoto University, Kyoto (WT-3, Heliotron-E)
Kyushu University, Fukuoka (TRIAM-1M)
Nagoya University, Nagoya (Hybtok-II, CSTN-III, NAGDIS)
NIFS, Nagoya (JIPP-TIIU, CHS)
Okayama University, Okayama
The University of Tokyo, Tokyo (REPUTE-1, REPUTE 1Q)
University of Tsukuba, Tsukuba (Gamma-10)

U.S.S.R.:
FIAE, Troitsk (T-14)
Ioffe Institute, Leningrad (FT-1, FT-2, Tuman-3)
Kurchatov Institute, Moscow (T-10, T-15, TO-2, TVD)
SIA, Shatura (T-3M, T-3M-2)

U.S.A.: FRC, Austin (TEXT)
GA, San Diego (DIII-D)
LANL, Los Alamos (ZTH)
LLNL, Livermore (MTX)
MIT, Cambridge (VERSATOR, ALCATOR C/MOD)
ORNL, Oak Ridge (ATF)
PPPL, Princeton (TFTR, PBX/M)

In addition, many research groups at universities all over the world contributed to the Programme, either directly or through the above Institutions.

INTERNATIONAL
ATOMIC ENERGY AGENCY
VIENNA, 1991